

**For Official Use**

**NEA/CSNI/R(2010)7**

Organisation de Coopération et de Développement Économiques  
Organisation for Economic Co-operation and Development

**15-Dec-2010**

**English text only**

**NUCLEAR ENERGY AGENCY  
COMMITTEE ON THE SAFETY OF NUCLEAR INSTALLATIONS**

**Nuclear Fuel Behaviour during Reactivity Initiated Accidents**

**Workshop Proceedings**

**9-11 September 2009  
OECD Headquarters, Paris, France**

**JT03294450**

**Document complet disponible sur OLIS dans son format d'origine  
Complete document available on OLIS in its original format**



**NEA/CSNI/R(2010)7  
For Official Use**

**English text only**

## ORGANISATION FOR ECONOMIC CO-OPERATION AND DEVELOPMENT

The OECD is a unique forum where the governments of 33 democracies work together to address the economic, social and environmental challenges of globalisation. The OECD is also at the forefront of efforts to understand and to help governments respond to new developments and concerns, such as corporate governance, the information economy and the challenges of an ageing population. The Organisation provides a setting where governments can compare policy experiences, seek answers to common problems, identify good practice and work to co-ordinate domestic and international policies.

The OECD member countries are: Australia, Austria, Belgium, Canada, Chile, the Czech Republic, Denmark, Finland, France, Germany, Greece, Hungary, Iceland, Ireland, Israel, Italy, Japan, Korea, Luxembourg, Mexico, the Netherlands, New Zealand, Norway, Poland, Portugal, the Slovak Republic, Slovenia, Spain, Sweden, Switzerland, Turkey, the United Kingdom and the United States. The European Commission takes part in the work of the OECD.

OECD Publishing disseminates widely the results of the Organisation's statistics gathering and research on economic, social and environmental issues, as well as the conventions, guidelines and standards agreed by its members.

*This work is published on the responsibility of the Secretary-General of the OECD.  
The opinions expressed and arguments employed herein do not necessarily reflect the official  
views of the Organisation or of the governments of its member countries.*

## NUCLEAR ENERGY AGENCY

The OECD Nuclear Energy Agency (NEA) was established on 1<sup>st</sup> February 1958 under the name of the OEEC European Nuclear Energy Agency. It received its present designation on 20<sup>th</sup> April 1972, when Japan became its first non-European full member. NEA membership today consists of 28 OECD member countries: Australia, Austria, Belgium, Canada, the Czech Republic, Denmark, Finland, France, Germany, Greece, Hungary, Iceland, Ireland, Italy, Japan, Korea, Luxembourg, Mexico, the Netherlands, Norway, Portugal, the Slovak Republic, Spain, Sweden, Switzerland, Turkey, the United Kingdom and the United States. The European Commission also takes part in the work of the Agency.

The mission of the NEA is:

- to assist its member countries in maintaining and further developing, through international co-operation, the scientific, technological and legal bases required for a safe, environmentally friendly and economical use of nuclear energy for peaceful purposes, as well as
- to provide authoritative assessments and to forge common understandings on key issues, as input to government decisions on nuclear energy policy and to broader OECD policy analyses in areas such as energy and sustainable development.

Specific areas of competence of the NEA include safety and regulation of nuclear activities, radioactive waste management, radiological protection, nuclear science, economic and technical analyses of the nuclear fuel cycle, nuclear law and liability, and public information.

The NEA Data Bank provides nuclear data and computer program services for participating countries. In these and related tasks, the NEA works in close collaboration with the International Atomic Energy Agency in Vienna, with which it has a Co-operation Agreement, as well as with other international organisations in the nuclear field.

Corrigenda to OECD publications may be found online at: [www.oecd.org/publishing/corrigenda](http://www.oecd.org/publishing/corrigenda).

© OECD 2010

You can copy, download or print OECD content for your own use, and you can include excerpts from OECD publications, databases and multimedia products in your own documents, presentations, blogs, websites and teaching materials, provided that suitable acknowledgment of OECD as source and copyright owner is given. All requests for public or commercial use and translation rights should be submitted to [rights@oecd.org](mailto:rights@oecd.org). Requests for permission to photocopy portions of this material for public or commercial use shall be addressed directly to the Copyright Clearance Center (CCC) at [info@copyright.com](mailto:info@copyright.com) or the Centre français d'exploitation du droit de copie (CFC) [contact@cfcopies.com](mailto:contact@cfcopies.com).

## COMMITTEE ON THE SAFETY OF NUCLEAR INSTALLATIONS

Within the OECD framework, the NEA Committee on the Safety of Nuclear Installations (CSNI) is an international committee made of senior scientists and engineers, with broad responsibilities for safety technology and research programmes, as well as representatives from regulatory authorities. It was set up in 1973 to develop and co-ordinate the activities of the NEA concerning the technical aspects of the design, construction and operation of nuclear installations insofar as they affect the safety of such installations.

The committee's purpose is to foster international co-operation in nuclear safety amongst the NEA member countries. The CSNI's main tasks are to exchange technical information and to promote collaboration between research, development, engineering and regulatory organisations; to review operating experience and the state of knowledge on selected topics of nuclear safety technology and safety assessment; to initiate and conduct programmes to overcome discrepancies, develop improvements and research consensus on technical issues; and to promote the co-ordination of work that serves to maintain competence in nuclear safety matters, including the establishment of joint undertakings.

The clear priority of the committee is on the safety of nuclear installations and the design and construction of new reactors and installations. For advanced reactor designs the committee provides a forum for improving safety related knowledge and a vehicle for joint research.

In implementing its programme, the CSNI establishes co-operate mechanisms with the NEA's Committee on Nuclear Regulatory Activities (CNRA) which is responsible for the programme of the Agency concerning the regulation, licensing and inspection of nuclear installations with regard to safety. It also co-operates with the other NEA's Standing Committees as well as with key international organizations (e.g., the IAEA) on matters of common interest.



## FOREWORD

A reactivity initiated accident is a nuclear reactor accident that involves an unwanted increase in fission rate and reactor power. The power increase may damage the reactor core, and in severe cases, even lead to disruption of the reactor. A few such accidents occurred in the early days of research reactors. These early reactivity initiated accidents led to design improvements, which were implemented in later generations of research reactors and, more importantly, in commercial power generating reactors.

The NEA Working Group on Fuel Safety (WGFS) is tasked with advancing the current understanding of fuel safety issues by assessing the technical basis for current safety criteria and their applicability to high burnup and to new fuel designs and materials. The group aims at facilitating international convergence in this area, including as regards experimental approaches and interpretation and the use of experimental data relevant for safety.

To contribute to this task the Workshop on “Nuclear Fuel Behaviour during Reactivity Initiated Accidents” was held in Paris, France, on 9-11 September 2009. The workshop was organised jointly by the “Committee for the Safety of Nuclear Installations” of the OECD and the French “Institut de Radioprotection et de Sûreté Nucléaire” (IRSN).

The current proceedings provide summary of the results of the workshop with the text of the papers given and presentations made.

## ACKNOWLEDGMENTS

Gratitude is expressed to Marc Petit of IRSN for his help, skills and effort given to successful organisation and realization of the event.

Thanks are also expressed to the Workshop Organising Committee members, the Session Chairs and the workshop participants for their effort and cooperation.

### Organising Committee

Marc Petit (IRSN, France), Workshop Chair  
Toyoshi Fuketa (JAEA, Japan), Workshop Co-Chair and WGFS Chair  
Lothar Heins (Areva, Germany)  
Jose M. Rey (CSN, Spain)  
Wolfgang Wiesenack (IFE, Norway)  
Radomir Rehacek (OECD/NEA), Workshop Secretary



## EXECUTIVE SUMMARY

### 1. Introduction

This report documents the proceedings of the Workshop on “Nuclear Fuel Behaviour during Reactivity Initiated Accidents” held in Paris, France, on 9-11 September 2009. The workshop was organised jointly by the “Committee for the Safety of Nuclear Installations” of the OECD and the French “Institut de Radioprotection et de Sûreté Nucléaire”.

More than 90 specialists representing 19 countries and international organizations attended the workshop. A total of 25 papers were presented.

### 2. Background

A reactivity initiated accident is a nuclear reactor accident that involves an unwanted increase in fission rate and reactor power. The power increase may damage the reactor core, and in severe cases, even lead to disruption of the reactor. A few such accidents occurred in the early days of research reactors. These early reactivity initiated accidents led to design improvements, which were implemented in later generations of research reactors and, more importantly, in commercial power generating reactors.

Historically, the worst reactivity initiated accident took place on April 26, 1986 in reactor 4 of the Chernobyl nuclear power plant in Ukraine. The Chernobyl accident reminded the nuclear community of the destructive potential of RIAs, and it prompted much research into the subject.

In the early 1990s, experimental programmes were initiated in France, Japan and Russia to study the behaviour of highly irradiated nuclear fuel under reactivity initiated accidents. These test programmes were primarily intended to check the adequacy of regulatory acceptance criteria for RIA, which at the time were based largely on test results for un-irradiated or moderately irradiated fuel.

Our understanding of these damage mechanisms is based on RIA simulation tests, carried out on short-length fuel rods in pulse reactors. To date, more than a thousand pulse irradiation tests of this kind have been carried out on fresh (unirradiated) fuel rods, and about 140 tests have been done on pre-irradiated samples. Pulse irradiation tests generally show that cladding failure occurs at lower fuel enthalpies for preirradiated than for fresh fuel rods, and that the susceptibility to failure increases with increasing fuel burnup. The increased susceptibility to failure and the change from a high temperature to a low temperature failure mode are attributed to the combined effects of clad tube embrittlement and aggravated pellet-clad mechanical interaction (PCMI) in high-burnup fuel rods.

Modelling of reactivity initiated accidents involves the simultaneous solution of equations for neutron transport, heat transport within the fuel rods and across the clad-to-coolant interface, mechanical behaviour of fuel and cladding, and coolant thermal-hydraulics. These equations are strongly interconnected and dependent on both space and time. Since they cannot be solved in full detail in core-wide analyses on the computers available today, simplifications are needed.

Acceptance criteria for reactivity initiated accidents are defined by regulatory authorities to ensure integrity of the reactor coolant pressure boundary and maintenance of core coolability in the event of an accident. The limiting amount of damage is settled by the requirements to meet regulatory limits on radiation dose to the public, and to ensure integrity of the coolant pressure boundary and long-term coolability of the fuel.

The criteria are commonly defined in terms of limits on the radially averaged fuel pellet specific enthalpy, or the increment of this property during the reactivity initiated accident. Regulatory authorities usually (but not always) postulate two kinds of enthalpy limits:

- A definite limit for core damage, which must not be transgressed at any axial position in any fuel rod in the core.
- Fuel rod failure thresholds that define whether a fuel rod should be considered as failed or not in calculations of radioactive release.

In late 1993 and early 1994, two high-burnup PWR fuel rods failed at remarkably low fuel enthalpies under RIA simulation tests in the French CABRI facility and the Japanese Nuclear Safety Research Reactor (NSRR). Since then, burnup related effects on the enthalpy threshold for fuel rod failure have been extensively studied, and many RIA simulation tests on high-burnup fuel rods have been conducted in France, Japan and Russia. Separate effect test programmes were also performed. As of today, regulatory authorities in Japan and Switzerland have revised their acceptance criteria for RIA based on this research, while revisions are under way or planned in other countries.

### **3. Objectives and structure of the workshop**

The main objective of the workshop was to review the current status of the experimental and analytical studies of the fuel behavior during the RIA transients and the acceptance criteria for RIA in use and under consideration.

The workshop was organized in an opening session, five technical sessions:

- Recent experimental results and experimental techniques used.
- Modelling and Data Interpretation.
- Code Assessment.
- RIA Core Analysis.
- Revision and application of safety criteria.

Followed by a conclusion session.

### **4. Summary of the technical sessions**

Each technical session was terminated by a panel discussion moderated by the session Chairpersons. Based on this input, the Chairpersons elaborated a summary of the session. These summaries are reproduced below.

#### ***Session 1: Recent experimental results and experimental techniques used***

This session was chaired by Motoe Suzuki (JAEA, Japan) and Carlo Vitanza (HRP, Norway). Five papers were presented in this session.

The NSRR reactor continues to produce valuable RIA data and more RIA reactor testing will be needed in the future.

Compared with reactor tests, the very large deformations at failure obtained in the mechanical testing presented in this session raise the issue of applicability of such mechanical testing to actual cases.

The discussion pointed out that mechanical testing needs substantial interpretation in order to become applicable, and this requires use of validated codes. The quite different testing approaches presented in the session also indicate that a generally agreed and accepted testing method does not exist at present.

It was recommended that the NEA looks into the possibility to set up an expert group aimed to survey current laboratory test approaches and define methods that are most appropriate to complement in reactor testing. Considering the large deformation mentioned above, the expert group may also address how the results from mechanical testing should be “translated” into information practically applicable for reactor cases.

However, laboratory mechanical tests will not substitute reactor tests, which remain the pillar for RIA fuel studies.

### ***Session 2: Modeling and data interpretation***

This session was chaired by John Voglewede (NRC, USA) and Martin Zimmermann (PSI, Switzerland). Four papers were presented in this session.

Development and use of computer codes in the simulation and analysis of the reactivity-initiated accident have clearly been subject to considerable effort. The codes are useful in providing a better understanding of fuel behavior during the RIA. They are also useful in interpolating limited experimental data taken under test reactor conditions.

However, modeling the RIA has not yet advanced to the point of permitting extrapolation of experimental data beyond conditions actually tested. Nor has modeling advanced to the point of permitting confirmation of new alloys or new fuel designs under RIA conditions in the absence of experimental data.

It appears that still further work is needed. It can be grouped into the following areas:

- Transient DNB modeling.
- Fission gas behavior modeling, modeling of MOX effect (if confirmed).
- Consideration of more advanced thermal-hydraulic modeling to include azimuthally heterogeneous coolant conditions (likely to be implemented through proper coupling of already available thermal-hydraulic codes, sub-channel codes, or even CFD).

The response of a power reactor to a reactivity insertion is different from the response of the experimental reactors used in current tests. In future experimental programs, preference should be given to broader pulse widths, if feasible, in order to provide a better basis for the transfer to the power plant conditions.

These limitations give rise to the question of “When will the RIA codes be good enough?” The codes and models now in use appear to be adequate to be used in the process of establishing regulatory criteria. However, they do not appear adequate to resolve some technical issues, such as the role of transient gas release in determining cladding failure.

### ***Session 3: Code assessment***

This session was chaired by Zoltan Hozer (KFKI, Hungary) and Robert Montgomery (Anatech, USA). Three papers were presented in this session.

The presented papers underlined the importance of initial state conditions for RIA simulations. The correct initial state data for high burnup fuel rods can be obtained only by the detailed calculation of irradiation histories.

The boundary conditions for transient fuel calculations are determined mainly by thermal hydraulic phenomena. Since the heat removal from the cladding may significantly influence rod failure, close link with thermal hydraulic calculations is needed for RIA analyses (e.g. to better describe DNB conditions in such fast transients, when steady state correlations are no more valid).

The simulation of fission gas release and gaseous swelling of pellets during power ramps and RIA transients is still a challenge for the currently applied codes and needs further developments.

In the discussions it was agreed that extensive code validation must be performed before the application of transient fuel behavior codes for the safety analysis of NPPs.

Considering the significant differences in the capabilities of current transient fuel behavior codes, further discussions are proposed on key (important) behavior/phenomena to be included in the models.

### ***Session 4: RIA core analysis***

This session was chaired by Marek Stepniewski (Vattenfall Nuclear Fuel AB, Sweden). Two papers were presented in this session.

Having in mind the obligation of NPP utilities to provide generic enveloping case and reload safety evaluation including assessment of the design basis accident (DBA) for RIA: rod drop (BWR) or rod ejection (PWR) the low number of presentations submitted to the RIA core analysis session was unexpected. One possible explanation to that is that there is a gap between current level of codes and methods used for RIA analysis for safety evaluation when still “old” acceptance criteria are applied and codes and methods level used for development of failure thresholds based on the recent experimental evidences. Utilities are aware that new cladding performance based acceptance criteria for RIA will demand not only accurate coupled 3D kinetics nodal codes with advanced thermal-hydraulics (i.e. full heat transfer regime map) but also codes comparable with thermo-mechanical fuel rod design codes. Such codes are so far available for some institutions.

Another conclusion from this session is that application of statistical methods to gain margin to acceptance criteria is a way to go, however, one should be very careful applying statistical methods to RIA – the same level of knowledge and expertise is needed as it was done when statistical approach to LOCA was developed.

It was commonly agreed that there is still potential for improvement of codes and models applied to RIA simulation: DNB and post-DNB phase modeling, clad to coolant heat transfer modeling, coolant properties at RIA (rapid transition from CZP to local bulk boiling in BWR).

In previous sessions it was expressed strong need for a credible “translator” from laboratory data to reactor conditions. This would result in acceptance criteria based on fuel failure mechanisms which are relevant for conceivable accident scenarios (core and fuel conditions).

The recommendation is to go further and work for translation of these failure mechanisms to such formulation of new acceptance criteria that typical safety reload evaluation can be done without need for sophisticated fuel performance codes. Another possible way is development of suitable simplified thermo-mechanical models which can be implemented in current transient analysis tools.

#### ***Session 5: Revision and application of safety criteria***

This session was chaired by Jose Manuel Conde (CSN, Spain) and Nicolas Waeckel (EdF, France). Six papers were presented in this session.

The progress made in the development of new methods and approaches to determine the PCMI safety limits was acknowledged. The need to develop limits for the DNB and post-DNB phases was also highlighted.

One of the problems found when trying to verify the validity of the safety criteria is the lack of failed RIA experiments using non-spalled rods, as well as the low number of MOX experiments. The representativity of BWR experiments may also be improved.

The lack of accurate measurements of the mechanical properties of irradiated cladding materials is an additional problem to determine the PCMI safety limits. The need of fracture toughness values was specifically mentioned. This shortcoming is related to the need to determine adequate mechanical test methods representative of RIA situation.

A variety of variables are still being used to represent the PCMI safety limit. The figures of merit used are enthalpy rise, CSED and the J-integral, and the discussion about the adequacy of the CSED for this purpose is not closed. These variables are expressed in terms of corrosion layer thickness, cladding hydrogen contents or rod burnup, depending on the approach used. Other variables related to the fuel duty can be used, and the discussion is again not closed.

### **5. General conclusions and recommendations**

With reference to the previous OECD RIA workshop that was held in Aix-en-Provence in 2002, very significant progresses were made and documented during the present workshop. From the experimental point of view, new experiments with both BWR and PWR rods were conducted at high pressure high temperature (BWR conditions) in the new test capsule used by JAEA at the NSRR reactor in Japan. From the modeling point of view, transient

RIA fuel codes such as FRAPTRAN, FALCON, RANNS and SCANAIR were improved and validated against existing experiments. Furthermore, the close collaboration established between JAEA and IRSN will ensure that future experiments conducted in NSRR within the ALPS-2 program and in CABRI in the frame of the OECD Cabri Water Loop International Program (CIP) will be well coordinated and very complementary.

From a practical standpoint, it was shown as expected that the use of advanced alloys with higher corrosion resistance and, even more importantly, with lower in service hydriding greatly improve the fuel behavior under RIA conditions.

The analysis of the most recent experiments performed in CABRI and NSRR showed that the phenomenology of Pellet Clad Mechanical Interaction (PCMI) is adequately understood. Corresponding models were developed in RIA fuel codes. One difficulty in using these models is that the fuel clad failure threshold may depend on parameters that are difficult to derive (e.g. hydride rim thickness in the cladding). This may imply that a bounding approach still needs to be used for reactor applications given the broad scope of conditions fuel may experience during its residence time in the reactor.

Although they all show reasonably good agreement with existing experimental results, it was identified that different codes use different assumptions and this raises the question of the validity of extrapolations to reactor conditions. ***It was then recommended that the CSNI organize a benchmark between existing RIA fuel codes in order to evaluate further the pros and cons of the different approaches used.***

Further experimental efforts should then be devoted in priority to investigate both the behavior of fuel rods after boiling onset and the post-rupture phenomena under representative conditions. Additionally, the experimental database on MOX fuel behavior should be enriched as up to now, no consensus could be found among the experts on whether or not specific behavior of mixed oxide fuel (enhanced PCMI by gaseous swelling) is to be expected with respect to UO<sub>2</sub> fuel. The already planned experiments in NSRR and CABRI will address these issues. This will imply also additional work on clad to coolant heat transfer modeling under rapid transient conditions in order to be able to interpret the new experimental results. New models were developed recently, but the database for qualification remains very scarce.

In the recent years, a lot of efforts were devoted to develop separate effect mechanical tests on claddings in order to derive failure limits. Different solutions used in different laboratories were shown during the workshop. They all face the same difficulty: it is not yet possible to reproduce in laboratory scale experiments the loading conditions expected to exist during a RIA transient. Hence, the use of these experimental results for reactor applications remains an open issue. ***It was recommended that the CSNI set up a small writing group to produce a technical document explaining what are the outcomes of the different separate effect mechanical tests and how their results could be used.***

The question of RIA safety criteria was extensively discussed during the workshop. It appeared that most of the methodologies elaborated to propose renewed criteria rely on the heavy use of fuel codes in order to cover the broad spectrum of possible reactor conditions. Existing fuel codes appear robust enough to accommodate this approach: several tens of thousands of calculations were sometimes run to define the failure limits over the whole range of conditions. Consistently with the physical understanding of fuel rod behavior during RIA, the PCMI failure thresholds were investigated first, but plans exist to include post-boiling and post-failure phenomena in future versions of the criteria. Presently, it seems a bit premature to make a detailed comparison of the limits proposed in different countries because some of them are still under construction.

All of the above shows that in pile experiments, better knowledge of mechanical testing as well as RIA fuel codes improvement and qualification remain necessary in the upcoming years. It was recognized that the existing programs in NSRR and CABRI reactors address these needs adequately.



## Table of Content

<b>Foreward and Acknowledgements</b> .....	5
<b>Executive Summary</b> .....	7
<b>Opening Session</b> .....	17
Marc Petit – Workshop Chair (IRSN, France)	
Toyoshi Fuketa – Workshop Co-Chair and WGFS Chair (JAEA, Japan)	
<b>Opening and Welcome Address</b>	
Javier Reig, Head, Nuclear Safety Division, OECD Nuclear Energy Agency	
<b>Opening and Welcome Address</b>	
Jean-Claude Micaelli, Director of the Major Accident Prevention Division, IRSN .....	19
<b>NEA Activities in the Reactivity Initiated Accidents Area, Aims and Structure of the Workshop</b>	
Radomir Rehacek (NEA, France) .....	23
<b>The Nuclear Fuel Safety and the IAEA Safety Standards</b>	
Nicolas Tricot (IAEA, Austria) .....	29
<b>A Review of Experiments and Computer Analyses on RIAs</b>	
Lars Olof Jernkvist and Ali R. Massih (QT, Sweden); Jan In de Betou (SSM, Sweden) .....	43
<b>Current RIA-Related Regulatory Criteria in Japan and their Technical Basis</b>	
Toyoshi Fuketa and Tomoyuki Sugiyama (JAEA, Japan) .....	61
<b>Regulatory Analysis of Reactivity Transients</b>	
Carl Beyer and Ken Geelhood (PNNLs, USA) .....	81
<b>Session One – Recent Experimental Results and Experimental Technique Used</b> .....	97
Chair: Motoe Suzuki (JAEA, Japan)	
Co-Chair: Carlo Vitanza (HRP, Norway)	
<b>Microstructure and Mechanical Property Changes in Fuel Cladding during RIA-Type Temperature Transients</b>	
Fumihisa Nagase, Tomoyuki Sugiyama and Toyoshi Fuketa (JAEA, Japan).....	99
<b>Expansion-due-to-Compression Test Results on High Burn-up ZIRLO Cladding</b>	
Manuel Quecedo and M. Lloret (ENUSA, Spain); Jose Manuel Conde and Jose Manuel Rey (CSN, Spain). .....	113
<b>Ductility and Failure Behaviour of both Unirradiated and Irradiated ZIRCALOY-4 Cladding using Plane Strain Tensile Specimens</b>	
Sebastian Carassou, M. Le Saux, Xavier Averty, J.P. Pizzanelli and Christophe Poussard (CEA Saclay, France); Bernard Cazalis and Jean Desquines (IRSN, France); Christian Bernaudat (EDF, France).....	127
<b>Ductility Degradation of High Burn-up Cladding in PCMI-Simulating Condition</b>	
Sun-Ki Kim, Je-Geon Bang, Dae-Ho Kim, Ik-Sung Lim, Yong-Sik Yang, Kun-Woo Song, Do-Sik Kim and Hang-Seok Seo (KAERI, Korea) .....	149

<b>Applicability of NSRR Room/high Temperature Test Results to Fuel Safety Evaluation Under Power Reactor Conditions</b> Tomoyuki Sugiyama, Miki Umeda, Yutaka Udagawa, H. Sasajima, Motoe Suzuki and Toyoshi Fuketa (JAEA, Japan) .....	159
<b>Session Two - Modelling and Data Interpretation</b> .....	177
Chair: John Voglewede (US NRC, USA) Co-Chair: Martin Zimmermann (PSI, Switzerland)	
<b>Numerical Analysis and Simulation of Behaviour of High Burn-up PWR Fuel Pulse-Irradiated in Reactivity-Initiated Accident Conditions</b> Motoe Suzuki, Tomoyuki Sugiyama, Yutaka Udagawa, Fumihisa Nagase and Toyoshi Fuketa (JAEA, Japan) .....	179
<b>Influence of Initial Conditions on Rod Behaviour during Boiling Phase Following a Reactivity Initiated Accident</b> Vincent Georgenthum (IRSN, France); Tomoyuki Sugiyama (JAEA, Japan).....	197
<b>Application of the SCANAIR Code for VVER RIA Conditions – Boron Dilution Accident</b> Asko Arffman (VTT, Finland); Alain Moal (IRSN, France) .....	209
<b>Analysis of Mixed-Oxide Fuel Behavior during RIA Tests Using FALCON MOD01</b> Robert Montgomery and John Alvis (ANATECH Corp., USA); Ken Yueh and Odelli Ozer (EPRI, USA) ..	229
<b>Session Three - Code Assessment</b> .....	245
Chair: Zoltan Hozer (KFKI, Hungary) Co-Chair: Robert Montgomery (EPRI, USA)	
<b>Parametric Study of Fuel Rod Behaviour during the RIA using the Modified Falcon Code</b> Grigori Khvostov and Martin Zimmermann (PSI, Switzerland); Guido Ledergerber (KKL Switzerland) .....	247
<b>Major Sensitivities of Modelling a High Burn-up Fuel Rod with FRAPCON-3/FRAPTRAN Codes</b> Maria Teresa del Barrio, Isabel Vallejo and Luis Enrique Herranz (CIEMAT, Spain) .....	263
<b>Capabilities of Transuranus Code in Simulating Power Ramp Tests from the IFPE Database</b> Martina Adorni, Davide Rozzia, Alessandro Del Nevo and Francesco D’Auria (GRNSPG, Italy) .....	279
<b>Session Four - RIA Core Analysis</b> .....	297
Chair: Marek Stepniewski (Vattenfall, Sweden)	
<b>Analysis of PWR Control Rod Ejection Accident with the Coupled Code System Sketch-ins/trace by Incorporating Pin Power Reconstruction Model</b> Tetsuo Nakajima and Tomohiro Sakai (JNES, Japan).....	299
<b>A Survey of Available Margin in a PWR RIA with Statistical Methods and 3D Kinetics</b> Javier Riverola and Tomas Nunez (ENUSA, Spain) .....	321

<b>Session Five - Revision and Application of Safety Criteria .....</b>	<b>335</b>
Chair: Jose Manuel Conde (CSN, Spain)	
Co-Chair: Nicolas Waeckel (EdF, France)	
<b>Expectation to RIA Criteria to be Applicable for Fuel under High Duty</b>	
Hajime Fujii (MNF, Japan); Noyomu Murakami and Satoshi Imura (MHI, Japan) .....	337
<b>Swiss Regulatory RIA Criteria and the Verification Procedures by the Operators</b>	
Andreas Gorzel (ENSI, Switzerland) .....	349
<b>Example of Application of the IRSN Approach to Assess Safety Criteria for Reactivity Initiated Accidents</b>	
Christine Sartoris, Aude Taisne, Marc Petit, Francois Barré and Olivier Marchand (IRSN, France).....	361
<b>Burn-up Dependent RIA Criterion for VVER Fuel</b>	
Zoltan Hózer (KFKI, Hungary) .....	385
<b>An Analytical Criterion to Prevent PCMI Fuel Rod Cladding Failure during RIA Transients</b>	
Christian Bernaudat, S. Cambier, J. Guion and Serge Benjamin (EDF, France) .....	395
<b>Development of Acceptance Criteria for Safety Analysis of Control Rod Ejection and Control Rod Drop Accidents Using a Mechanistic Approach</b>	
Robert Montgomery and John Alvis (ANATECH Corp., USA); Ken Yueh and Odelli Ozer (EPRI, USA) ..	413
<b>List of Participants .....</b>	<b>421</b>



## **OPENING SESSION**

### **Welcome Address**

Javier Reig, Head, Nuclear Safety Division, OECD Nuclear Energy Agency (NEA)

Jean-Claude Micaelli, Director of the Major Accident Prevention Division (IRSN)

### **Introduction and Objectives of the Workshop**

Radomir Rehacek (NEA, France)

### **The Nuclear Fuel Safety and the IAEA Safety Standards**

Nicolas Tricot (IAEA, Austria)

### **A Review of Experiments and Computer Analyses on RIAs**

Lars Olof Jernkvist and Ali R. Massih (QT, Sweden); Jan In de Betou (SSM, Sweden)

### **Current RIA-Related Regulatory Criteria in Japan and their Technical Basis**

Toyoshi Fuketa and Tomoyuki Sugiyama (JAEA, Japan)

### **Regulatory Analysis of Reactivity Transients**

Carl Beyer and Ken Geelhood (PNNL, USA)





**OECD/NEA workshop**  
**Nuclear Fuel Behaviour during Reactivity-initiated Accidents**

Organised in cooperation with IRSN, Paris, France,  
 September 9-11, 2009

Contribution to the WS introduction  
 Jean-Claude MICAELLI, IRSN



Nuclear Fuel Behavior during Reactivity Initiated Accidents

**Fuel safety, industrial context**

- **More and more challenging demands on fuel and cladding material**
  - Increase the effective time that fuel remains in the reactor,
  - Increase the flexibility of operating mode (power variation) and adjust the energy produced to the demand.
- **Benefits:**
  - A reduction of the KWh cost,
  - A reduction of waste for ultimate disposal,
- **Counterparts:**
  - Higher mechanical thermal and chemical stresses,
  - The need of a constant search for improvement of fuel performance in particular in the challenging situations,
- **It results finally in:**
  - The need of increased attention to the adequacy of safety criteria and to the compliance to these safety criteria.

OECD/NEA Workshop, Paris, September 9-11, 2009 2/8 **IRSN**

Nuclear Fuel Behavior during Reactivity Initiated Accidents

**Fuel safety, a major concern for IRSN**

- **National public expert in nuclear and radiological risk**
- **Acting in particular:**
  - as support for the nuclear safety authorities,
  - as research operator in order develop the knowledge, tools and competence that are necessary for its expertise missions.
- **The fuel, a key parameter for three important factors of reactor safety :**
  - The control of the nuclear reaction,
  - The core cooling,
  - The FP retention (clad is the first barrier).
- **A large IRSN involvement in this field for more than 30 years for:**
  - FBR with in particular CABRI and SCARABBE in pile test programmes,
  - PWR:
    - LOCA with in particular PHEBUS-LOCA in pile test programmes,
    - RIA with in particular CABRI-REP-Na and CABRI-CIP in pile test programmes.

OECD/NEA Workshop, Paris, September 9-11, 2009 3/8 **IRSN**

Nuclear Fuel Behavior during Reactivity Initiated Accidents

### Fuel safety, RIA context

- **A clear need of revision of RIA safety criteria**
  - Already done in some countries, underway in particular in France, with the perspective of a new criteria around 2011-2012
    - It should be an "analytical" criteria:
      - Based on a deep understanding of involved phenomena,
      - Will involve the use of computational codes.
    - It should cover a wide spectrum of situations in terms of fuel materials (fuel pellets, clad), in terms of fuel irradiation (BU, corrosion, RIM, ...) and in terms of transient (energy deposit, pulse width, initial power, ...).
- **Beyond the safety criteria the quantification of the consequences of fuel dispersion should be investigated**

OECD/NEA Workshop, Paris, September 9-11, 2009 4/8 **IRSN**

Nuclear Fuel Behavior during Reactivity Initiated Accidents

### Fuel safety, RIA R&D needs

- **In depth understanding of phenomena that should result from a joint international effort, in order to:**
  - Develop, consolidate, assess adequate safety criteria and the tools that will be used to demonstrate and evaluate the compliance,
  - As far as possible, harmonize the safety criteria used or to be used in different countries,
  - A minima, clearly understand the differences,
  - Share the costs...
- **Internationalisation animated in particular by OECD, trough for example :**
  - The WGFS activities,
  - The OECD CABRI-CIP programme in which :
    - are discussed the CABRI tests that have been performed in a Na loop, the underway NSRR results,
    - will be discussed the CABRI tests in the water loop (first one foreseen end of 2010)
- **In depth understanding through:**
  - Adequate combination of in-pile integral tests and separate effect tests,
  - The development of simulation codes,
  - The support of advanced detailed simulation (multi-scale)
    - To back the elaboration of well grounded macroscopic models

OECD/NEA Workshop, Paris, September 9-11, 2009 5/8 **IRSN**

Nuclear Fuel Behavior during Reactivity Initiated Accidents

### The multi-scale approach, illustration

➢ **Advanced Simulation: Modelling and numerical simulation of onset and growth of cracks in irradiated fuel cladding during a RIA**

**Deriving an equivalent behaviour law**

- Local behaviour
- Zr<sub>2</sub>Ni<sub>3</sub> matrix with hydride platelets

Objectif : Adapter les codes macroscopiques (SCANAIR)

HOMOGE-NISATION

hydrides equivalent  
Zr/Ni  
déplacement anisotropie, ...

**Irradiated cladding failure criteria**

- Fracture mechanics not applicable
- Understand the mechanisms responsible for onset and growth of cracks
- Cladding failure predictive criteria
- 3D thermo-mechanical simulation
- Experiments:
  - Determine local behaviour of each phase
  - Determine micro et meso structural phenomena

OECD/NEA Workshop, Paris, September 9-11, 2009 6/8 **IRSN**

Nuclear Fuel Behavior during Reactivity Initiated Accidents

### The in pile experimentation

- Two key complementary tools: NSRR and CABRI
- Some news from CABRI
  - New core structure implemented in March 2009 ▶▶
  - Security tube implemented in May 2009 ▶▶
  - In pile part of the pressurized water loop implemented in June 2009 ▶▶
  - Pressure test of the whole water loop in July 2009
  - Building seismic reinforcement initiated in July 2009
  - Forthcoming events
    - Core load: first trimester 2010
    - Achievement of core criticality: second trimester 2010
    - First test (CIPQ): forth trimester 2010

OECD/NEA Workshop, Paris, September 9-11, 2009 7/8 **IRSN**



 Agence pour l'énergie nucléaire  
Nuclear Energy Agency
 OECD 

## NEA ACTIVITIES IN THE REACTIVITY INITIATED ACCIDENTS AREA, AIMS AND STRUCTURE OF THE WORKSHOP

Radomir REHACEK  
NEA, France

OECD/NEA RIA Workshop, Paris, France, September 9 – 11, 2009

 Agence pour l'énergie nucléaire  
Nuclear Energy Agency
 OECD 

## NEA ACTIVITIES IN THE REACTIVITY INITIATED ACCIDENTS AREA, AIMS AND STRUCTURE OF THE WORKSHOP

- Several NEA activities in direct link to RIA Workshop
- Set up of the RIA Workshop
- RIA Workshop outputs and organisation

OECD/NEA RIA Workshop, Paris, France, September 9 – 11, 2009

 Agence pour l'énergie nucléaire  
Nuclear Energy Agency
 OECD 

### Several NEA activities in direct link to RIA Workshop (1/5)

- Topical Meeting on RIA Fuel Safety Criteria
  - Aix-en-Provence, France, May 2002
  - Objectives
    - RIA fuel acceptance criteria, in particular to the fuel fragmentation enthalpy limit and the PCMI failure enthalpy limit in relation to high burnup fuel
  - Areas covered
    - "best estimate" core calculations for RIA energy deposition in high burnup fuels
    - technical background of current and new RIA fuel safety criteria
    - ongoing RIA experimental programmes

OECD/NEA RIA Workshop, Paris, France, September 9 – 11, 2009

OECD 

**Several NEA activities in direct link to RIA Workshop** (2/5)

□ **Topical Meeting on RIA Fuel Safety Criteria**

– Conclusions

- Not clear agreement about pin-by-pin calculations mainly because of high uncertainties in this approach
- General recommendation that future activities related to RIA should focus on appropriate methods for the evaluation of uncertainties on the best estimate RIA calculations in order to guarantee the global conservatism of safety demonstration

OECD/NEA RIA Workshop, Paris, France, September 9 – 11, 2009

4

OECD 

**Several NEA activities in direct link to RIA Workshop** (3/5)

□ **Topical Meeting on RIA Fuel Safety Criteria**

– Conclusions

- Some experts expressed their opinion that there has been a significant progress in the recent years in experimental research which improved our understanding of mechanical processes leading to failure of high burnup fuel during RIA, while some others argued that this may be true for existing cladding materials but for new alloys the data are missing.

OECD/NEA RIA Workshop, Paris, France, September 9 – 11, 2009

5

OECD 

**Several NEA activities in direct link to RIA Workshop** (4/5)

□ **State-of-the-art Report on Nuclear Fuel Behaviour under Reactivity Initiated Accident Conditions (SOAR-RIA)**

– Objectives

- Update of a State-of-the-art report on "PWR Fuel Behaviour in Design Basis Accident Conditions" published in 1986 which was devoted to the deformation, oxidation and embrittlement of PWR fuel cladding in a Loss-of-Coolant Accidents as since that a considerable world wide effort has been expended in the experimental modelling of PWR and BWR fuel behaviour in accident conditions, in particular high burnup fuel, which allows to update the state-of-the-art report and expand its scope including other types of DBA such as RIA, etc.

OECD/NEA RIA Workshop, Paris, France, September 9 – 11, 2009

6

 Agence pour l'énergie nucléaire  
Nuclear Energy Agency
 OECD 

## Several NEA activities in direct link to RIA Workshop (5/5)

- SOAR-RIA
  - Draft Report compiled by Lars Olof Jemkvist and Ali R. Massih with support of the Swedish Radiation Safety Authority (SSM)
  - Thoroughly reviewed by Working Group on Fuel Safety and approved by the Committee on Safety of Nuclear Installations (CSNI) in last June

OECD/NEA RIA Workshop, Paris, France, September 9 – 11, 2009

 Agence pour l'énergie nucléaire  
Nuclear Energy Agency
 OECD 

## Set up of the RIA Workshop (1/7)

- Objective
  - Workshop will focus on identifying the current status of the experimental and analytical studies of the fuel behaviour during the RIA transients and the acceptance criteria for RIA in use and under consideration.

OECD/NEA RIA Workshop, Paris, France, September 9 – 11, 2009

 Agence pour l'énergie nucléaire  
Nuclear Energy Agency
 OECD 

## Set up of the RIA Workshop (2/7)

- Organising Committee
  - **Marc Petit**, Institut de Radioprotection et de Sécurité Nucléaire, France, **Chair**
  - **Toyoshi Fuketa**, Japan Atomic Energy Agency, Japan, **Co-Chair**
  - **Lothar Heins**, AREVA NP GmbH, Germany
  - **Radomir Rehacek**, OECD Nuclear Energy Agency, France, **Secretariat**
  - **Jose Maria Rey**, Consejo de Seguridad Nuclear, Spain
  - **Wolfgang Wiesenack**, Halden Reactor Project, Norway

OECD/NEA RIA Workshop, Paris, France, September 9 – 11, 2009

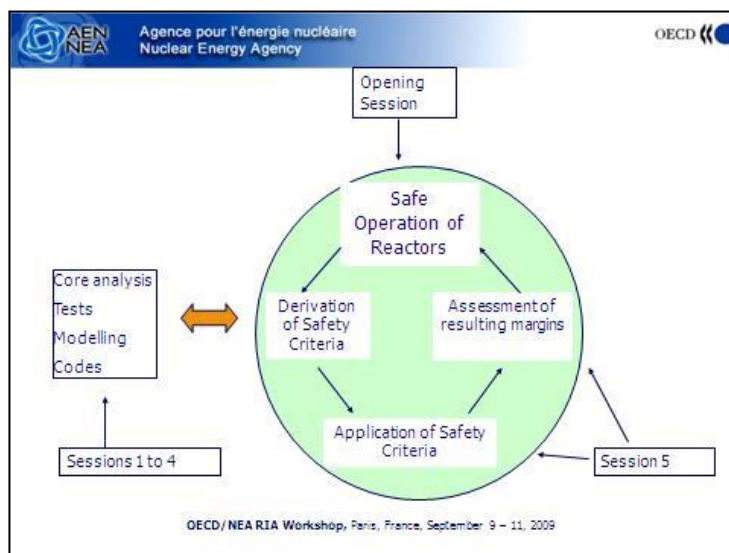
 Agence pour l'énergie nucléaire  
 Nuclear Energy Agency
 


## Set up of the RIA Workshop (3/7)

□ Workshop basis

- The starting point: safe operation of the reactors as a requirement
- Given this requirement, there is a logical chain of steps to follow to fulfil it:
  - A. Derivation of Safety Criteria
  - B. Application of the Safety Criteria: Demonstration of Compliance
  - C. Conclusion: Assessment of the resulting margins

OECD/NEA RIA Workshop, Paris, France, September 9 – 11, 2009 12



 Agence pour l'énergie nucléaire  
 Nuclear Energy Agency
 


## Set up of the RIA Workshop (5/7)

□ Workshop Sessions

- Opening Session
  - Chair: **Marc Petit** – Workshop Chair (IRSN, France)
  - Co-Chair: **Toyoshi Fuketa** – CSNI/WGFS Chair (JAEA, Japan)
- Session 1 – Recent experimental results and experimental technique used
  - Chair: **Motoe Suzuki** (JAEA, Japan)
  - Co-Chair: **Carlo Vitanza** (HRP, Norway)
- Session 2 - Modelling and data interpretation
  - Chair: **John Voglewede** (US NRC, USA)
  - Co-Chair: **Martin Zimmermann** (PSI, Switzerland)

OECD/NEA RIA Workshop, Paris, France, September 9 – 11, 2009 12

 Agence pour l'énergie nucléaire  
Nuclear Energy Agency
 OECD 

## Set up of the RIA Workshop (6/7)

- Workshop Sessions
  - Session 3 - Code assessment
    - Chair: **Zoltan Hozer** (KFKI, Hungary)
    - Co-Chair: **Robert Montgomery** (EPRI, USA)
  - Session 4 - RIA Core analysis
    - Chair: **Marek Stepniewski** (Vattenfall, Sweden)
  - Session 5 - Revision and application of safety criteria
    - Chair: **Jose Manuel Conde** (CSN, Spain)
    - Co-Chair: **Nicolas Waeckel** (EdF, France)
  - Summary Session
    - Chair: **Marc Petit** – Workshop Chair (IRSN, France)
    - Co-Chair: **Toyoshi Fuketa** – CSNI/WGFS Chair (JAEA, Japan)

OECD/NEA RIA Workshop, Paris, France, September 9 – 11, 2009

13

 Agence pour l'énergie nucléaire  
Nuclear Energy Agency
 OECD 

## Set up of the RIA Workshop (7/7)

- Workshop expectations
  - Assess progresses made in the physical understanding of fuel behaviour under RIA transients
  - Review how R&D results are used as a technical basis for setting up safety criteria
  - Identify potential need for new R&D actions in conjunction with safety criteria required evolutions/refinements
  - Formulate recommendations for future activities
  - Lay down RIA basis for an update of the NEA *Fuel Safety Criteria Technical Review* published in 1999 (under consideration within WGFS)

OECD/NEA RIA Workshop, Paris, France, September 9 – 11, 2009

14

 Agence pour l'énergie nucléaire  
Nuclear Energy Agency
 OECD 

## RIA Workshop outputs and organisation

- CD
  - Read file with instructions
  - Full papers, presentations included
  - Program, preliminary list of participants
- Handouts
- Proceedings
- Coffee and lunch breaks
- Assistant **Nicolina IANNOLO**

OECD/NEA RIA Workshop, Paris, France, September 9 – 11, 2009

15



  
**International Atomic Energy Agency**

---

**The Nuclear Fuel Safety and the IAEA Safety Standards**  
 Nicolas TRICOT – NSNI/SAS

*OECD/NEA Workshop  
 Nuclear Fuel Behaviour during Reactivity-Initiated Accidents  
 Paris, France, 9–11 September 2009*

**OUTLINE**

---

- Introduction
- The nuclear fuel safety and the IAEA Safety Standards (structure, hierarchy, application)
  - Safety fundamentals
  - Safety requirements
  - Safety guides
  - Safety series, Tec Docs
- Safety of Nuclear Power Plants : Design (NS-R1)
- Safety assessment for facilities and activities (GS-R Part 4)
  - Overall content
  - Selected examples vs. Generic Reactor Safety Reviews (GRSR)
  - Main findings
- Other IAEA fuel safety related activities and major events
- Concluding remarks

International Atomic Energy Agency 

**INTRODUCTION**  
Global context

---





OH, I'M NOT BROKEN DOWN. I JUST THOUGHT YOU'D BE CHEAPER THAN BUYING GAS...

- Fossil price rise
- Stable, competitive energy
- Energy supply security
- Environment

International Atomic Energy Agency 

### INTRODUCTION

#### World trend

---

➤ **Renewed interest for nuclear energy**

- projected number of new countries starting operation of NP
  - 8 by 2020
  - 23 by 2030 in high projection
  - growth estimate from 20% to 90% by 2030
- different country situation
  - countries having stopped construction but willing to resume soon,
  - countries having never stopped NPP construction,
  - nuclear power newcomers



■ Operating ■ Considering

International Atomic Energy Agency 

### INTRODUCTION

#### What does the IAEA do?

---

➤ **General Guidance**

- “MILESTONES in the Development of a National Infrastructure for Nuclear Power, NE series guide NG-G-3.1, September 2007
- “CONSIDERATION to launch a nuclear power programme” Brochure March 2007

➤ **Safety Standards**

- SF-1 “Fundamental Safety Principles”
- Requirements and guides

International Atomic Energy Agency 

### INTRODUCTION

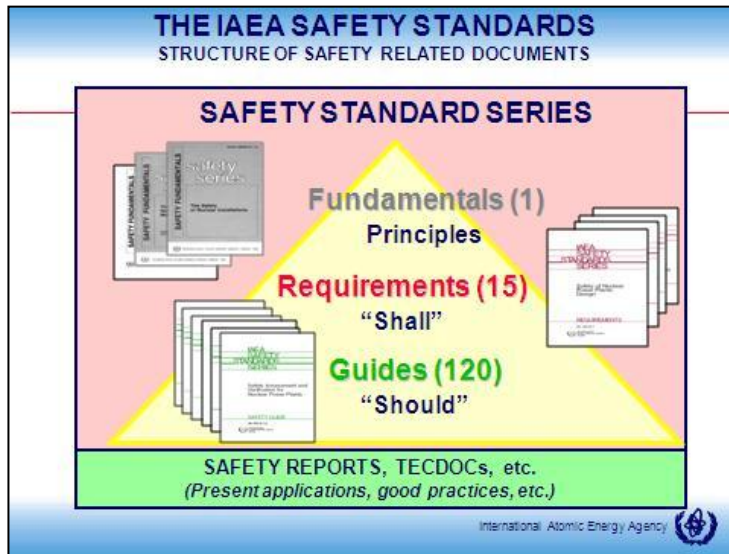
#### What does the IAEA do?

---

➤ **Services**

- Global guidance at early stages
- Facilitating competence building (staffing, identification of training needs, training)
- Assessment of the current status of the Governmental and regulatory framework and recommendations (Laws, regulations, rules and Regulatory Body's activities)
- Expert missions to review design aspects, feasibility study, site survey, site evaluation, construction, commissioning and operation
- Peers reviews to assess Safety Standards' uses (GRSR)

International Atomic Energy Agency 



### APPLICATION OF THE IAEA SAFETY STANDARDS

> Although the IAEA Safety Standards (SS) are recognized internationally, the degree of recognition varies significantly

> Big change is expected on further use and application of IAEA Safety Standards by Member States as:

- many MS started or will start a review process of their national Safety Requirements and a comparison between the new IAEA SS and their existing national SS
- the nuclear renaissance will lead to license new reactors designs worldwide (importance of the safety reviews against IAEA safety standards)

> IAEA trend to

- continue the development of safety standards
- use a technology neutral approach in developing or updating the safety standards

International Atomic Energy Agency

### OVERVIEW OF THE IAEA SAFETY STANDARDS

**THE SAFETY STANDARDS COVER SAFETY IN FIVE AREAS**

**NS** Safety of nuclear workers

**RS** Radiation protection and safety of nuclear

**WS** Waste management of radioactive waste

**TS** Safe transport of radioactive material

**GS** General safety (cross-cutting themes)

**Thematic areas**

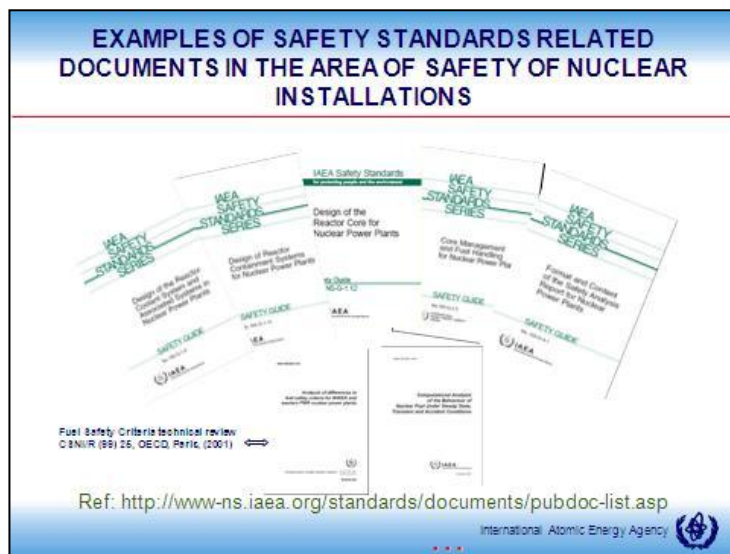
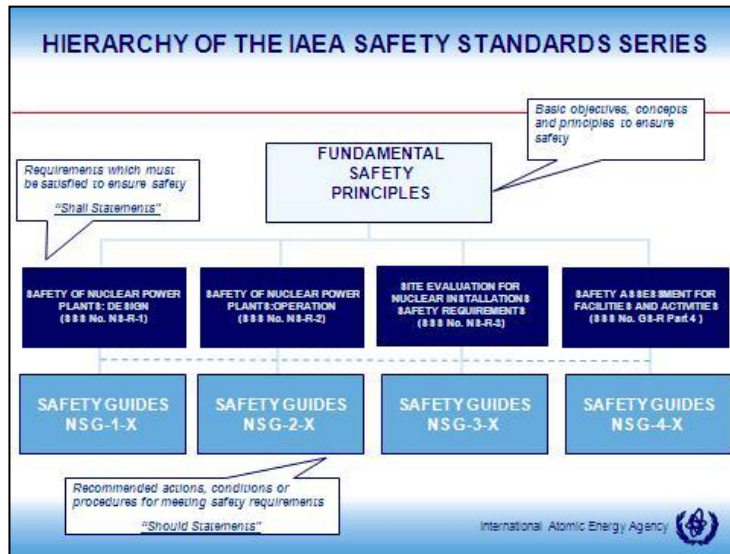
- Legal and governmental structures
- Emergency preparedness and response
- Regulatory systems
- Accidents and aftermath
- Incident investigation
- Radioactive waste management
- Decommissioning
- Establishment of conventions

**Facilities and activities**

- Production reactors
- Research reactors
- Medical and industrial radioisotopes
- Research reactors and accelerators
- Research and development
- Transport of nuclear material

IAEA Safety Standards are available on: [www.iaea.org](http://www.iaea.org)

International Atomic Energy Agency



### EXAMPLES OF SAFETY STANDARDS OR RELATED DOCUMENTS IN THE AREA OF NUCLEAR FUEL SAFETY

Related to NS-R-1

Related to NS-R-2

Related GSR Part 4

Ref: <http://www-ns.iaea.org/standards/documents/pubdoc-list.asp>

International Atomic Energy Agency

### IAEA DOCUMENTS RELATED TO SAFETY

Ref: <http://www-ns.iaea.org/standards/documents/pubdoc-list.asp>

International Atomic Energy Agency

### SAFETY OF NPPS: DESIGN (NS-R-1)

- Published in 2000, mainly devoted to LWRs
- Based on best practices worldwide at the time:
  - Deterministic safety assessment (DSA) plays a major role in demonstrating compliance with safety requirements, probabilistic safety assessment (PSA) supports DSA
  - Conservative DSA for anticipated operational occurrences and design basis accidents (DBA), best estimate (BE) approach for severe accidents
  - No established requirements for governing the selection of postulated initiating events
    - Categories of plant states typically cover:
      - Normal operation
      - Anticipated operational occurrences
      - Design basis accidents
      - Beyond design basis accidents (Severe accidents)
    - Acceptance criteria should be assigned to each category

International Atomic Energy Agency

## SAFETY REQUIREMENTS NS-R-1 SAFETY OF NPPs: DESIGN 1/5

**Chapter 6: Requirements for design of plant systems (fuel elements and assemblies)**

6.6: Fuel elements and assemblies designed to withstand satisfactorily the irradiation and environmental conditions in the reactor core (...) that occur in normal operation and AOCs

6.7: The deterioration considered shall include that arising from:

- ✓ Differential expansion and deformation,
- ✓ External pressure of the coolant,
- ✓ Additional internal pressure due to FP
- ✓ Irradiation of fuel and other materials in the fuel assembly
- ✓ Changes in pressures and temperatures (changes in power demand)
- ✓ Chemical effects, static and dynamic loading, including flow induced vibrations and mechanical vibrations,
- ✓ Changes in heat transfer performance (distortions or chemical effects)
- ✓ Allowance shall be made for uncertainties data, calculation and fabrication

IAEA  
SAFETY  
STANDARDS  
SERIES

Safety of Nuclear  
Power Plants:  
Design

---

REQUIREMENTS

No. NS-R-1

INTERNATIONAL ATOMIC ENERGY AGENCY

International Atomic Energy Agency

## SAFETY REQUIREMENTS NS-R-1 SAFETY OF NPPs: DESIGN 2/5

**Chapter 6: Requirements for design of plant systems (fuel elements and assemblies)**

6.8: Specified fuel limits, including permissible leakage of fission products shall not be exceeded in **normal operation**, and it shall be ensured that operational states that may be imposed in **anticipated operational occurrences** cause no significant further deterioration. Leakage of fission products shall be restricted by design limits and kept to a minimum

IAEA  
SAFETY  
STANDARDS  
SERIES

Safety of Nuclear  
Power Plants:  
Design

---

REQUIREMENTS

No. NS-R-1

INTERNATIONAL ATOMIC ENERGY AGENCY

International Atomic Energy Agency

## SAFETY REQUIREMENTS NS-R-1 SAFETY OF NPPs: DESIGN 3/5

**Chapter 6: Requirements for design of plant systems (fuel elements and assemblies)**

6.9: Fuel assemblies shall be designed to permit adequate inspection of their structure and components parts after irradiation. In the design basis accidents, the fuel elements shall remain in position and shall not suffer distortion to an extent that would render post-accident core cooling insufficiently effective, and the specified limits for fuel elements for DBAs shall not be exceeded

IAEA  
SAFETY  
STANDARDS  
SERIES

Safety of Nuclear  
Power Plants:  
Design

---

REQUIREMENTS

No. NS-R-1

INTERNATIONAL ATOMIC ENERGY AGENCY

International Atomic Energy Agency

## SAFETY REQUIREMENTS NS-R-1 SAFETY OF NPPs: DESIGN 4/5

**Chapter 6: Requirements for design of plant systems (fuel elements and assemblies)**

6.10: The aforementioned requirements for reactor and fuel element design shall also be maintained in the event of changes in fuel management strategy or in operational states over the operational lifetime of the plant

IAEA  
SAFETY  
STANDARDS  
SERIES

Safety of Nuclear  
Power Plants:  
Design

---

REQUIREMENTS

No. NS-R-1  
INTERNATIONAL ATOMIC ENERGY AGENCY

International Atomic Energy Agency

## SAFETY REQUIREMENTS NS-R-1 SAFETY OF NPPs: DESIGN 5/5

**Chapter 6: Requirements for design of plant systems (Fuel Handling and storage systems)**

For the record: Addressed in sections 6.96 through 6.98

IAEA  
SAFETY  
STANDARDS  
SERIES

Safety of Nuclear  
Power Plants:  
Design

---

REQUIREMENTS

No. NS-R-1  
INTERNATIONAL ATOMIC ENERGY AGENCY

International Atomic Energy Agency

## SAFETY GUIDE FOR THE DESIGN OF THE REACTOR CORE FOR NPPs - NS-G-1.12

**Guidance to achieve the requirements on nuclear fuel safety expressed in NS-R-1**

➤ **Chapter 2: General consideration in design**

- 2.7 The core design needs to be reviewed and, if necessary, modified accordingly when a significant configuration change occurs during the plant's operating lifetime, as a result of, for example:
  - ✓ The use of mixed uranium oxide and plutonium oxide (mixed oxide) fuel
  - ✓ An increase in burnup for a discharged fuel assembly
  - ✓ An increase in the duration of a fuel cycle
  - ✓ An increase in the rated power of the plant

IAEA Safety Standards  
*for protection people and the environment*

Design of the  
Reactor Core for  
Nuclear Power Plants

---

Safety Guide  
No. NS-G-1.12

IAEA  
*International Atomic Energy Agency*

International Atomic Energy Agency

## SAFETY GUIDE FOR THE DESIGN OF THE REACTOR CORE FOR NPPs - NS-G-1.12

**Guidance to achieve the requirements on nuclear fuel safety expressed in NS-R-1**

➤ Chapter 3: Specific safety considerations in design

- Fuel elements and assemblies (UO<sub>2</sub> and MOX fuel)
  - ✓ Thermal and burn-up effects
  - ✓ Effects of irradiation
  - ✓ Effects of variations in power levels
  - ✓ Mechanical effects in fuel elements
  - ✓ Effects of burnable poison in the fuel
  - ✓ Corrosion and hydriding of fuel elements
  - ✓ Thermal-hydraulic effects in fuel assemblies
  - ✓ Consideration of mechanical safety in the design

**IAEA Safety Standards**  
for protecting people and the environment

Design of the Reactor Core for Nuclear Power Plants

---

Safety Guide  
No. NS-G-1.12

IAEA  
International Atomic Energy Agency

International Atomic Energy Agency

## SAFETY REQUIREMENTS (GSR Part 4)

**SCOPE**

➤ Requirements to be fulfilled in the safety assessment of facilities and activities with special attention to:

- Defence in depth,
- Quantitative analyses and application of the graded approach
- Independent verification of the safety assessment

➤ Related Safety guides to be developed

**IAEA Safety Standards**  
for protecting people and the environment

Safety Assessment for Facilities and Activities

---

General Safety Requirements Part 4  
No. GSR Part 4

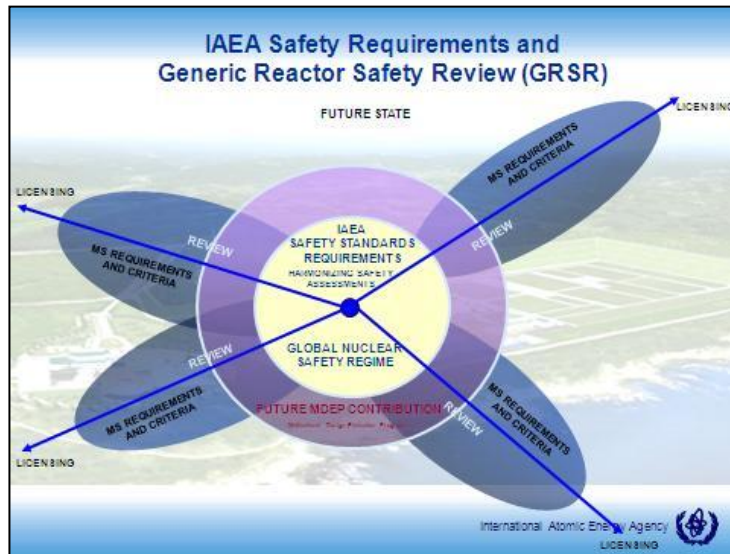
IAEA  
International Atomic Energy Agency

International Atomic Energy Agency

## SAFETY ASSESSMENT FOR FACILITIES AND ACTIVITIES (GSR Part 4)

- **Safety Assessment**
  - The safety assessment shall have the primary purpose of determining whether an adequate level of safety has been achieved for a facility or activity and whether the basic safety objectives and safety criteria established by the designers, the operator and the regulatory authority, reflecting the radiation protection requirements as laid down in the Basic Safety Standard have been complied with.
  - Therefore, (...) requirements are identified to be used in the safety assessment of nuclear facilities and activities with special attention to the defence in depth, quantitative analyses and the application of graded approach considering the range of facilities and activities addressed GSR-4)
  - Intended for application to all facilities (e.g. enrichment and manufacturing plants, NPPs) and activities (e.g. sources and their production, transportation)

International Atomic Energy Agency



### AP1000

Westinghouse AP1000

FOURTH-GENERATION (4G) incorporating passive safety systems and simplified operation:

- Electrical Power: 1,117 MWt
- Thermal Output: 3,400 MWt
- Plant Life: 60 Years
- Fuel Enrichment: 4-4.95%
- Plant Efficiency: 33.1% (32.7%)
- Operation Cycle: 18 months
- Plant Availability: 92%

Westinghouse

International Atomic Energy Agency

### EPR – European Pressurized Water Reactor

AREVA

AREVA EPR FEATURES

Evolutionary Generation II+ advanced pressurized water reactor

- Electrical Power: 1500-1600 MWt
- Thermal Power: 4200-4500 MWt
- Plant Life: 60 Years
- Fuel Enrichment: up to 5%
- Plant Efficiency: 36%
- Operation Cycle: up to 24 Months
- Plant Availability: 91%

International Atomic Energy Agency

### ESBWR — Economic Simplified BWR

**GE Hitachi ESBWR Features**  
 Natural circulation boiling water reactor with passive safety features.  
 Electrical Power: 1,500 MWe  
 Thermal Output: 4,500 MWt  
 Plant Life: 60 Years  
 Fuel Efficiency: 4.5%  
 Plant Efficiency: 36.5%  
 Operation Cycle: 18-24 months  
 Plant Availability: 87%

**Legend:**  
 ■ SATURATED WATER  
 ■ UNSATURATED WATER  
 ■ SATURATED STEAM

### ATMEA1

Reliable Generation III+ reactor worldwide

**ATMEA1/NEA ATMEA1 FEATURES**  
 Evolutionary Generation III+ reactor, simple and improved PWR, being advantage of both passive and active safety systems (2 loop configuration, 100% x 2 train safety system)

**Electrical Power:** 1,000-1,150 MWe  
**Thermal Output:** 2,850 - 3,150 MWt  
**Plant Life:** 60 Years  
**Plant Efficiency:** 37%  
**Operation Cycle:** 12 to 24 months

International Atomic Energy Agency **ATMEA1**

### APR1400

#### Advanced Power Reactor 1400

**Key to Power Station Category**

1. Reactor Building	2. Containment Building	3. Turbine Generator Building	4. Condenser Building	5. Cooling Water Building	6. Feedwater Building	7. Steam Building	8. Main Steam Building	9. Main Condenser Building	10. Main Feedwater Building	11. Main Steam Generator Building	12. Main Feedwater Generator Building	13. Main Condenser Generator Building	14. Main Feedwater Generator Building	15. Main Steam Generator Building	16. Main Feedwater Generator Building	17. Main Condenser Generator Building	18. Main Feedwater Generator Building	19. Main Steam Generator Building	20. Main Feedwater Generator Building	21. Main Condenser Generator Building	22. Main Feedwater Generator Building	23. Main Steam Generator Building	24. Main Feedwater Generator Building	25. Main Condenser Generator Building	26. Main Feedwater Generator Building	27. Main Steam Generator Building	28. Main Feedwater Generator Building	29. Main Condenser Generator Building	30. Main Feedwater Generator Building	31. Main Steam Generator Building	32. Main Feedwater Generator Building	33. Main Condenser Generator Building	34. Main Feedwater Generator Building	35. Main Steam Generator Building	36. Main Feedwater Generator Building	37. Main Condenser Generator Building	38. Main Feedwater Generator Building	39. Main Steam Generator Building	40. Main Feedwater Generator Building	41. Main Condenser Generator Building	42. Main Feedwater Generator Building	43. Main Steam Generator Building	44. Main Feedwater Generator Building	45. Main Condenser Generator Building	46. Main Feedwater Generator Building	47. Main Steam Generator Building	48. Main Feedwater Generator Building	49. Main Condenser Generator Building	50. Main Feedwater Generator Building	51. Main Steam Generator Building	52. Main Feedwater Generator Building	53. Main Condenser Generator Building	54. Main Feedwater Generator Building	55. Main Steam Generator Building	56. Main Feedwater Generator Building	57. Main Condenser Generator Building	58. Main Feedwater Generator Building	59. Main Steam Generator Building	60. Main Feedwater Generator Building	61. Main Condenser Generator Building	62. Main Feedwater Generator Building	63. Main Steam Generator Building	64. Main Feedwater Generator Building	65. Main Condenser Generator Building	66. Main Feedwater Generator Building	67. Main Steam Generator Building	68. Main Feedwater Generator Building	69. Main Condenser Generator Building	70. Main Feedwater Generator Building	71. Main Steam Generator Building	72. Main Feedwater Generator Building	73. Main Condenser Generator Building	74. Main Feedwater Generator Building	75. Main Steam Generator Building	76. Main Feedwater Generator Building	77. Main Condenser Generator Building	78. Main Feedwater Generator Building	79. Main Steam Generator Building	80. Main Feedwater Generator Building	81. Main Condenser Generator Building	82. Main Feedwater Generator Building	83. Main Steam Generator Building	84. Main Feedwater Generator Building	85. Main Condenser Generator Building	86. Main Feedwater Generator Building	87. Main Steam Generator Building	88. Main Feedwater Generator Building	89. Main Condenser Generator Building	90. Main Feedwater Generator Building	91. Main Steam Generator Building	92. Main Feedwater Generator Building	93. Main Condenser Generator Building	94. Main Feedwater Generator Building	95. Main Steam Generator Building	96. Main Feedwater Generator Building	97. Main Condenser Generator Building	98. Main Feedwater Generator Building	99. Main Steam Generator Building	100. Main Feedwater Generator Building
---------------------	-------------------------	-------------------------------	-----------------------	---------------------------	-----------------------	-------------------	------------------------	----------------------------	-----------------------------	-----------------------------------	---------------------------------------	---------------------------------------	---------------------------------------	-----------------------------------	---------------------------------------	---------------------------------------	---------------------------------------	-----------------------------------	---------------------------------------	---------------------------------------	---------------------------------------	-----------------------------------	---------------------------------------	---------------------------------------	---------------------------------------	-----------------------------------	---------------------------------------	---------------------------------------	---------------------------------------	-----------------------------------	---------------------------------------	---------------------------------------	---------------------------------------	-----------------------------------	---------------------------------------	---------------------------------------	---------------------------------------	-----------------------------------	---------------------------------------	---------------------------------------	---------------------------------------	-----------------------------------	---------------------------------------	---------------------------------------	---------------------------------------	-----------------------------------	---------------------------------------	---------------------------------------	---------------------------------------	-----------------------------------	---------------------------------------	---------------------------------------	---------------------------------------	-----------------------------------	---------------------------------------	---------------------------------------	---------------------------------------	-----------------------------------	---------------------------------------	---------------------------------------	---------------------------------------	-----------------------------------	---------------------------------------	---------------------------------------	---------------------------------------	-----------------------------------	---------------------------------------	---------------------------------------	---------------------------------------	-----------------------------------	---------------------------------------	---------------------------------------	---------------------------------------	-----------------------------------	---------------------------------------	---------------------------------------	---------------------------------------	-----------------------------------	---------------------------------------	---------------------------------------	---------------------------------------	-----------------------------------	---------------------------------------	---------------------------------------	---------------------------------------	-----------------------------------	---------------------------------------	---------------------------------------	---------------------------------------	-----------------------------------	---------------------------------------	---------------------------------------	---------------------------------------	-----------------------------------	---------------------------------------	---------------------------------------	---------------------------------------	-----------------------------------	--

ICHNP International Atomic Energy Agency

## Generic Reactor Safety Reviews vs. GSR Part 4 Selected Requirements

- Assessment of the possible radiation risks (Requirement 6)
- Scope of the safety analysis (Requirement 14)
- Deterministic and probabilistic approaches (Requirement 15)



International Atomic Energy Agency 

## SAFETY ASSESSMENT FOR FACILITIES AND ACTIVITIES (GS-R-4) SELECTED REQUIREMENTS vs. GENERIC REACTOR SAFETY REVIEWS

- Assessment of the possible radiation risks (Requirement 6)
  - The possible radiation risks associated with the facility or activity shall be identified and assessed

4.19. This includes the level and likelihood of radiation exposure of workers and the public and the possible release of radioactive material to the environment that are associated with anticipated operational occurrences or accidents that lead to a loss of control over a nuclear reactor core, nuclear chain reaction, radioactive source or any other source of radiation.

International Atomic Energy Agency 

## SAFETY ASSESSMENT FOR FACILITIES AND ACTIVITIES (GSR Part 4) SELECTED REQUIREMENTS vs. GENERIC REACTOR SAFETY REVIEWS

- Findings
  - Absence or limited scope of Level 2 PSA (or even Level 1 PSA)
  - Omission of certain initiating events (usually accidents at shutdown operational modes or accidents in radwaste treatment systems or spent fuel management systems)
  - Missing justification for categorization of initiating events
  - Missing data important for evaluation of radiological status prior the accident (cladding defects, excessive coolant radioactivity, and leaking steam generator tubes)
  - Assumptions used in safety analysis not presented in a clear and convincing way
  - Inconsistencies in transfer of data (without sufficient justification) from thermal-hydraulic analysis to containment analysis and to source term analysis
  - Unexpected rapid increase of doses in the environment with decreasing probability of occurrence in the range  $1E-6$  –  $1E-7/r$ .year (increase more than 2 orders of magnitude)
  - Over-conservatism used in analysis of design basis accidents (e.g. postulation of a core melt) leading to the conclusion that radiological consequences of design basis accidents are more severe than of severe accidents
  - Missing assessment of doses to control room staff in case of severe accidents

International Atomic Energy Agency 

## SAFETY ASSESSMENT FOR FACILITIES AND ACTIVITIES (GSR Part 4)

### SELECTED REQUIREMENTS vs. GENERIC REACTOR SAFETY REVIEWS

- **Scope of the safety analysis (Requirement 14)**
  - The performance of a facility or activity in all operational states and, as necessary, in the post-operational phase shall be assessed in the safety analysis.

*4.50 The safety analysis has to address both the consequences arising from all normal operational conditions (including start-up and shutdown where appropriate) and the frequencies and consequences associated with all anticipated operational occurrences and accident conditions shall be addressed in the safety analysis. This includes accidents that have been taken into account in the design (referred to as design basis accidents) and beyond design basis accidents (including severe accidents) for facilities and activities where the radiation risks are high. The analysis has to be performed to a scope and level of detail that corresponds to the magnitude of the radiation risks associated with the facility or activity, the frequency of the events included in the analysis, the complexity of the facility or activity, and the uncertainties inherent in the processes that are included in the analysis.*

International Atomic Energy Agency



## SAFETY ASSESSMENT FOR FACILITIES AND ACTIVITIES (GSR Part 4)

### SELECTED REQUIREMENTS vs. GENERIC REACTOR SAFETY REVIEWS

- **Findings**
  - No separate analysis of a category of BDBA without severe core damage
  - No concise description of which global or detailed acceptance criteria have been used, including criteria associated with high burn-up issues.
  - Missing full power Level 2 PSA
  - Limited scope LPSD PSA
  - Missing analysis of events related to accidents related to the spent fuel pool
  - Inconsistencies in targets for severe accidents

International Atomic Energy Agency



## SAFETY ASSESSMENT FOR FACILITIES AND ACTIVITIES (GSR Part 4)

### SELECTED REQUIREMENTS vs. GENERIC REACTOR SAFETY REVIEWS

- **Deterministic and probabilistic approaches (Requirement 15)**
  - Both deterministic and probabilistic approaches shall be included in the safety analysis.

*4.55. The objectives of a probabilistic safety analysis are shall be to determine all the significant contributing factors to the radiation risks arising from a facility or activity, and to evaluate the extent to which the overall design is well balanced and meets probabilistic safety criteria where these have been defined. In the area of reactor safety, probabilistic safety analysis uses a comprehensive, structured approach to identify failure scenarios. It constitutes a conceptual and mathematical tool for deriving numerical estimates of risk. The probabilistic approach uses realistic assumptions whenever possible and provides a framework for addressing many of the uncertainties explicitly. Probabilistic approaches may provide insights into system performance, reliability, interactions and weaknesses in the design, the application of defence in depth and risks that it may not be possible to derive from a deterministic analysis.*

International Atomic Energy Agency



## SAFETY ASSESSMENT FOR FACILITIES AND ACTIVITIES (GSR Part 4)

### SELECTED REQUIREMENTS vs. GENERIC REACTOR SAFETY REVIEWS

- Findings
  - Missing full power Level 2 PSA, limited scope of Low Power and Shutdown PSA
  - Use of old data sources, no evidence of analysing recent (national or international) operating experience (PIEs, failure rates)
  - Missing or insufficient uncertainty & sensitivity studies, no display of uncertainty bands
  - Insufficient documentation of phenomenological aspects
  - Unusually low Core Damage Frequency or Large Release Frequency results
  - Missing definition of core damage
  - Cliff-edge effects (releases)
  - Unusually large contributions from individual accident sequences
  - Inconsistencies between tables reporting results
  - Insufficient documentation of application of THERP methodology
  - Insufficient documentation of reliability data used
  - Missing information on truncation criteria used
  - Insufficient information about extrapolation of results from smaller to larger size reactors
  - Need for review of fire PSA

International Atomic Energy Agency 

## OTHER IAEA FUEL SAFETY RELATED ACTIVITIES AND MAJOR EVENTS (1/2)

➤ Technical Cooperation projects (2009-2011)  
 “Strengthening Safety and Reliability of Nuclear Fuel and Nuclear Materials In Nuclear Power Plants, Including Water-Cooled Water-Moderated Power Reactor Components and Piping” – (TC RER /3/008)

To provide Central and Eastern European countries with the necessary tools to:

- fulfill their own fuel and material licensing and safe management needs
- to ensure safe operation of Water-Cooled Water-Moderator Power Reactor (WWER) components and piping

- ✓ Improvement of regional fuel examination capabilities (Pilecti)
- ✓ Implementation of fuel examination and licensing in Romania (3 times 2 weeks)

➤ Safety aspects of future generation of reactors (HTGR, Fusion, etc...)

➤ Cooperation with OECD/NEA



International Atomic Energy Agency 

## OTHER IAEA FUEL SAFETY RELATED ACTIVITIES AND MAJOR EVENTS (2/2)

➤ IAEA Technical Meeting

SAFETY ISSUES RELATED TO THE USE OF HIGH-BURNUP FUEL AND TO THE  
LONG RESIDENCE TIME OF FUEL IN THE REACTOR  
IAEA HQ (1- 4 December, 2009)

- to discuss the safety issues related to high burnup fuel including the effects of a possible longer permanence of fuel in the reactor core and to review the existing IAEA related documents.
- will address both regulatory and licensing aspects, and the results will basically cover issues related to fuel acceptance criteria, accident study methodologies (verification and validation of computer codes, initial assumptions) and to the research and development programmes undergone to support the definition of the selected criteria

Scientific Secretary of the meeting is Mr Nicolas Triot of the Division of Nuclear Installation Safety.

Telephone # +43 1 2600 2592  
Email: n.triot@iaea.org

International Atomic Energy Agency 

## CONCLUDING REMARKS

- With the renaissance of Nuclear and the increased competition between designers, the solicitation of the nuclear fuel will be increased for:
  - Existing reactor designs,
  - New reactor designs (and possibly new fuel designs)
- In this regard, in order to meet the requirements of the Safety Standards (namely NS-R-1. GS-R- Part 4), the IAEA needs to review at the reactor design stage that the fuel safety criteria at high burn up, are underpinned by technical understanding
- The IAEA is supporting the efforts made by the international nuclear community in fuel safety activities and is developing dedicated safety standards (Tec Doc) and implementing a set of Meetings (CS, TM, etc) and Training Courses

International Atomic Energy Agency



## International Atomic Energy Agency



*...Thank you for your attention*

International Atomic Energy Agency



## A REVIEW OF EXPERIMENTS AND COMPUTER ANALYSES ON RIAs

**Lars Olof Jernkvist, Ali R. Massih**

Quantum Technologies AB, Uppsala Science Park, SE-75183 Uppsala, Sweden

**Jan In de Betou**

Swedish Radiation Safety Authority, SE-17116 Stockholm, Sweden

### 1. Introduction

Reactivity initiated accidents (RIAs) are nuclear reactor accidents that involve an unwanted increase in fission rate and reactor power. The power excursion may lead to failure of the nuclear fuel rods and release of radioactive material into the primary reactor coolant. In severe cases, the fuel rods may be shattered and large parts of the fuel pellet inventory dispersed into the coolant. The expulsion of hot fuel into water has potential to cause rapid steam generation and pressure pulses, which could damage nearby fuel assemblies, other core components, and possibly also the reactor pressure vessel.

Reactivity initiated accidents in power reactors may occur as a result of reactor control system failures, control element ejections or events caused by rapid changes in temperature or pressure of the coolant/moderator. Our knowledge of possible scenarios for RIAs in power reactors is based largely on best-estimate computer analyses and simulations on how the core and primary coolant system respond to postulated events. The fundamental output from the calculations is the space-time variation of power across the reactor core under the accident. To assess the consequences of the accident, these data are compared with results from pulse irradiation tests, carried out on instrumented fuel rodlets in dedicated research reactors. These tests are done to provide information on the fuel rod behaviour under RIA-like conditions, and in particular, on possible fuel failure mechanisms. Additional tests, performed under well-controlled out-of-reactor laboratory conditions, are sometimes used to supplement the pulse-irradiation tests.

Hence, our current understanding of reactivity initiated accidents and their consequences is based largely on three sources of information: i) best-estimate computer analyses of the reactor response to postulated accident scenarios, ii) pulse-irradiation tests on instrumented fuel rodlets, carried out in research reactors, iii) out-of-pile separate effect tests, targeted to explore key phenomena under RIA conditions. In recent years, we have reviewed, compiled and analysed these three categories of data. The results is a state-of-the-art report on fuel behaviour under RIA conditions, which is currently being published by the OECD Nuclear Energy Agency, Committee on the Safety of Nuclear Installations.<sup>1</sup> The report is concerned mainly with RIAs in light water reactors (LWRs), but Canadian Deuterium Uranium (CANDU) heavy water reactors and their fuel are to some extent also considered. The fuel pellet material of primary concern is UO<sub>2</sub>, but the report covers also (U,Pu)O<sub>2</sub> mixed oxide (MOX) fuel, gadolinium-bearing burnable absorber fuel, and inert matrix fuel. The report includes experimental data and calculated results, published in open literature up to March 2009. The purpose of the following presentation is to give a brief summary of the report.

---

<sup>1</sup> *Fuel Behaviour under Reactivity Initiated Accident (RIA) Conditions*, (In Press), Committee on the Safety of Nuclear Installations, Nuclear Energy Agency, OECD, Paris, France.

## 2. Best-estimate computer analyses of RIAs

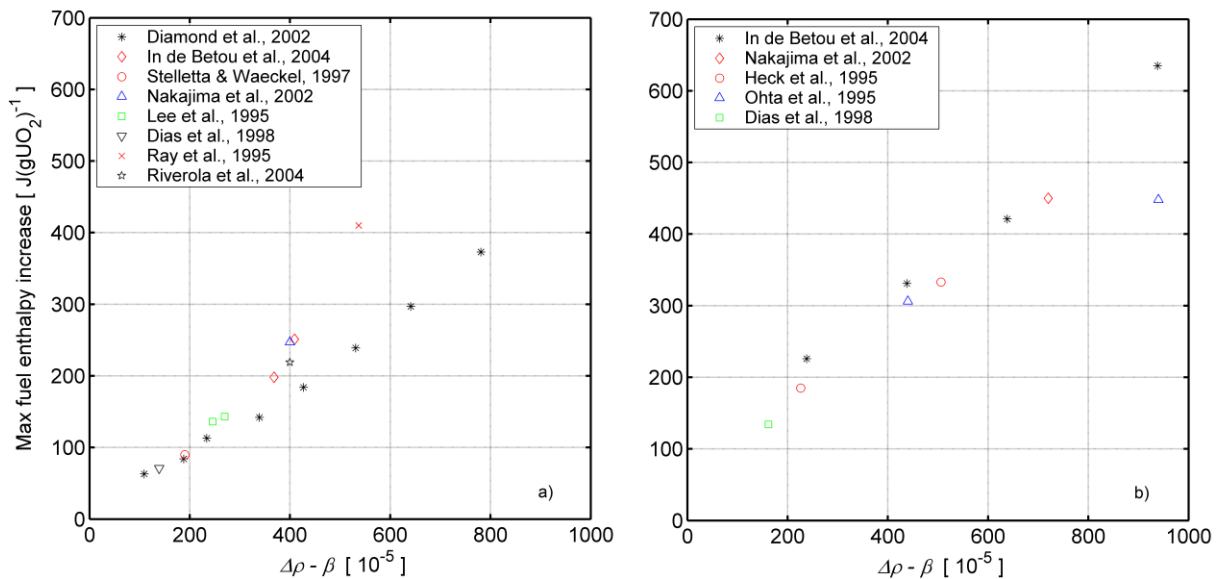
Modelling of reactivity initiated accidents involves the simultaneous solution of equations for neutron transport, heat transport within the fuel rods and across the clad-to-coolant interface, and coolant thermal-hydraulics. These equations are strongly interconnected and dependent on both space and time. Since it is difficult to solve the equations in full detail in core-wide analyses on the computers available today, various simplifications are usually employed in engineering analyses. The primary output from the core-wide analysis is the space-time variation of coolant properties and fuel assembly power. The power histories of individual fuel rods are then calculated from the fuel assembly power data by neutron flux reconstruction, and the pin power is integrated to obtain an estimate of fuel pellet radial average specific enthalpy, which is the parameter of primary concern in RIAs. Following the core-wide analyses, designated codes can be used to analyse the thermo-mechanical behaviour of particular fuel rods in detail, and to assess the risk for fuel rod failure.

Two RIA scenarios that have been closely analyzed over the years are the control rod ejection accident (REA) in pressurised water reactors (PWRs) and the control rod drop accident (RDA) in boiling water reactors (BWRs). The reactivity addition rates and the resulting power transients are much larger for these events than for other RIA scenarios, and they are therefore considered design basis accidents; i.e. postulated accident scenarios that are used to establish the design basis for the reactor and to define safety limits for its operation. The characteristics of a power pulse generated in an REA or RDA depend on the accident scenario - most importantly the reactivity worth of the ejected control rod, but also on the core and fuel design, reactor operating state, and the time at which the accident occurs under the fuel cycle. The most challenging conditions with respect to pulse amplitude are usually found at end of cycle (EOC).

Of particular interest to the fuel behaviour under an RIA are the width, shape and amplitude of the power pulse. Results from state-of-the art computer analyses of REAs and RDAs show that, while the width and shape do not vary significantly with position in the core, the pulse amplitude is a local property that falls off with increasing distance from the ejected control rod, and it also depends on fuel burn-up. In short, the local power generation within a specific fuel pellet is controlled by a reactive component and a driven component. The reactive component reflects the reactivity of the considered fuel pellet itself, which depends on its burn-up dependent content of fissile isotopes. The driven component stems from the external neutron flux, which depends on the burn-up dependent composition of fissile isotopes in nearby fuel assemblies and the distance from the ejected control rod. Consequently, the amplitude of the local power pulse depends on fuel burn-up, core loading pattern, the distance from the ejected control rod, and the reactivity worth of the ejected rod. Results of three-dimensional core kinetics analyses of postulated REAs and RDAs typically show that only 10-20% of the fuel within the core experiences a significant energy deposition under these accidents. The energy falls off rapidly with increasing distance from the failed control rod, and except for a 6×6 to 8×8 array of fuel assemblies around the rod, calculations suggest that the energy deposition is too low to cause fuel rod failure, even under very severe postulated accidents.

In figure 1, we summarise open-literature results on core-wide maximum values for the fuel enthalpy increase, obtained from independent three-dimensional core kinetics analyses of REA and RDA at EOC conditions. The core-wide maximum of fuel enthalpy increase under RIA, i.e. the largest increase of fuel pellet radial average enthalpy that is experienced by any fuel pellet in the core, is an important parameter for assessment of fuel integrity, and a key result in any analysis of RIA. The results are plotted with respect to prompt reactivity insertion,  $\Delta\rho-\beta$ , where  $\Delta\rho$  is the reactivity insertion caused by the ejected control rod, and  $\beta$  is the effective fraction of delayed neutrons. In the calculations, the REA was assumed to take place at hot zero power (HZIP) core conditions and the RDA at cold zero power (CZP). With regard to reactivity addition, these are the most severe initial conditions for control element ejections in PWRs and BWRs.

Figure 1. Calculated max fuel enthalpy increase under a) HZP REA and b) CZP RDA.<sup>1</sup>  
 In the calculations, both accidents are assumed to occur at end of cycle conditions.



The calculated results for the maximum fuel enthalpy increase in figure 1 follow a linear trend with respect to prompt reactivity insertion. For  $\Delta\rho-\beta$  beyond  $4\times 10^{-3}$ , there is an increasing spread in the calculated results. This is probably due to the fact that the results are sensitive to the unrealistic assumptions for model parameters and input data that are needed to achieve these very high reactivity additions in three-dimensional core kinetics calculations. For lower reactivity additions, the reported results from various investigators are, however, consistent.

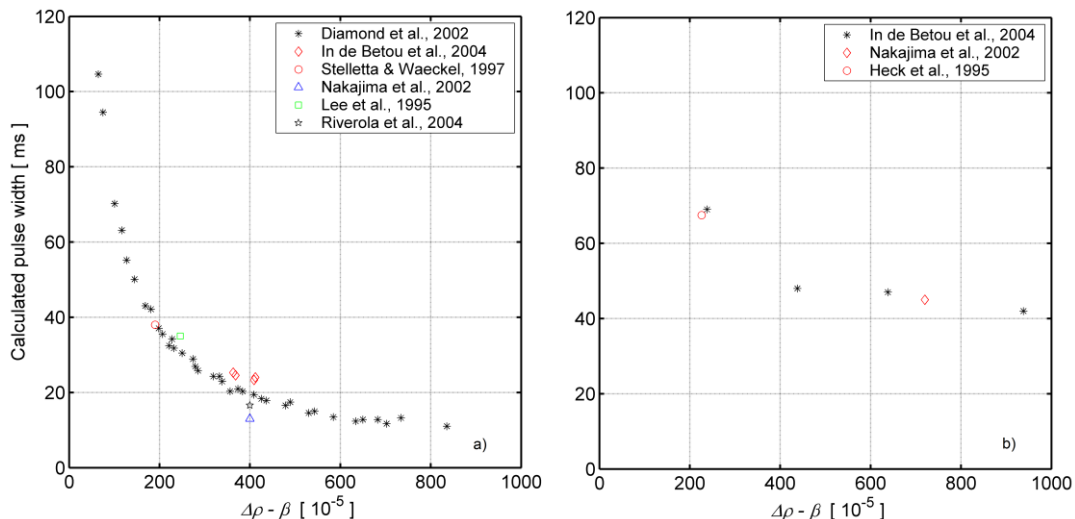
Figure 2 shows a compilation of calculated pulse widths (FWHM: Full Width at Half Maximum) for HZP REA and CZP RDA at EOC conditions, obtained from three-dimensional core kinetics analyses. The results are consistent, and we note that the calculated pulses for CZP RDA are wider than those for HZP REA at comparable reactivity additions. This is partly due to a slower rod ejection in the RDA, but also to the coarser core lattice for BWRs in comparison with PWRs, resulting in a longer effective neutron lifetime.

In conclusion, the consistency of calculated results in reported state-of-the-art analyses of postulated control rod ejection/drop accidents suggest that current computational methods used to analyse these accidents are mature and reliable. However, there are submodels in the codes that need refinement. For instance, prevalent submodels for vapour generation in the coolant are empirically based and rely on experimental data obtained under quasi-static test conditions. When these submodels are used in simulations of RIAs, they seem to overestimate the transient vapour generation and its associated reactivity feedback. Likewise, current submodels for clad-to-coolant heat transfer are generally designed for analyses of steady-state reactor operation and mild transients, and they are known to be inaccurate for modelling RIAs. More appropriate models for transient clad-to-coolant heat transfer, based on separate effect tests discussed in section 4.2, are underway, but have not yet been implemented in existing code systems for analyses of RIAs.

Finally, we note that fuel behaviour models used in computer codes for stand-alone analyses of fuel rod thermo-mechanical performance under RIAs are considerably more sophisticated than those used for fuel rod thermal analyses in large code systems for core-wide analyses of RIAs. Stand-alone codes for fuel rod transient analyses, such as FALCON, FRAPTRAN, SCANAIR and TRANSURANUS, are generally quite successful in reproducing the results of pulse-irradiation tests on single fuel rodlets, when it comes to temperatures and fuel rod deformations, provided that the cladding temperature remains low throughout

the tests. Also cladding failures are captured with a fair level of accuracy for the low temperature tests, if the degree of pre-test cladding corrosion is known and can be used as input to the analysis. However, due to the lack of appropriate clad-to-coolant heat transfer models for reactivity accidents, the codes usually fail to accurately reproduce measured temperatures and deformations in cases where a boiling crisis occurs. The new heat transfer models mentioned above could hopefully improve the situation.

Figure 2. Calculated power pulse width (FWHM) under a) HZP REA and b) CZP RDA.<sup>1</sup>  
In the calculations, both accidents are assumed to occur at end of cycle conditions.



### 3. Pulse-irradiation tests on instrumented fuel rodlets

To date, more than a thousand pulse-irradiation tests on un-irradiated LWR fuel rods and about 140 tests on pre-irradiated samples have been carried out in six different test facilities. Most of the data pertain to PWR type of rods, and the great majority of tests have been done on  $\text{UO}_2$  fuel. However, some data are also available for other kinds of fuel material, such as  $(\text{U,Pu})\text{O}_2$  mixed oxide fuel, gadolinium-bearing  $\text{UO}_2$  and inert matrix fuel. From these tests, it has been found that the fuel rod behaviour under a reactivity initiated accident is affected primarily by the:

- Characteristics of the power pulse, in particular the amplitude and pulse width.
- Core coolant conditions, i.e. the coolant pressure, temperature and flow rate.
- Burn-up-dependent state of the fuel rod. Among the most important properties are the degree of cladding waterside corrosion, the pre-accident width of the pellet-clad gap, the internal gas pressure in the fuel rod, and the distribution of gaseous fission products in the fuel pellets.
- Fuel rod design. Parameters of particular importance are the internal fill gas pressure, clad tube wall thickness, fuel pellet composition ( $\text{UO}_2/\text{PuO}_2/\text{Gd}_2\text{O}_3$ , enrichment) and the fuel pellet geometrical design (solid/annular).

These factors are important to the fuel rod behaviour during an RIA, and they also control what kind of damage is inflicted to the fuel rod under the accident. In the following subsections, we briefly summarise the main results from pulse-irradiation tests on un-irradiated and pre-irradiated fuel.

#### 3.1. Pulse-irradiation tests on un-irradiated fuel rodlets

Pulse-irradiation tests carried out on fresh (un-irradiated) fuel can be largely divided into two groups:

- Tests done to establish thresholds, in terms of peak fuel enthalpy, for cladding failure, fuel dispersal, melting, etc. Since these tests are generally aimed at establishing acceptance criteria for RIAs in power

reactors, the tests are done on fuel rods of prevalent commercial design and under conditions that, as closely as possible, resemble those expected for power reactor RIAs.

- Parametric studies, intended to shed light on the fuel behaviour and mechanisms of fuel failure under RIAs, and to generate data needed for verification and calibration of computer codes. The effects of selected parameters are studied by performing series of tests, in which a single parameter of interest is varied at a time. The impact of fuel rod design parameters as well as power pulse characteristics and reactor coolant conditions has been studied in this manner.

Tests within the first group generally show that the extent of damage inflicted to fresh fuel rods correlates well with the peak value of fuel pellet radial average enthalpy under the test. Regulatory acceptance criteria for RIAs are for this reason traditionally formulated in terms of limits for this parameter.

All failures observed in tests on fresh fuel are related to cladding overheating as a result of film-boiling and impaired clad-to-coolant heat transfer. Two limiting failure modes are observed: fracture of the overheated and oxygen-embrittled cladding upon quenching, or clad ballooning and burst at high temperature. The latter failure mode is restricting when there is a substantial gas overpressure in the fuel rod. Table 1 summarises enthalpy thresholds for the two failure modes, reported from pulse-irradiation tests on fresh  $\text{UO}_2$  fuel rodlets of various designs. Observed thresholds for dispersal of fuel into the coolant are also included in the table. An important conclusion is that cladding failure does not necessarily lead to fuel dispersal in tests on fresh fuel. This is particularly true for ballooning-type cladding failures.

**Table 1. Thresholds, in terms of fuel pellet radial average specific enthalpy, reported for limiting failure modes and fuel dispersal of fresh  $\text{UO}_2$  fuel rods.<sup>1</sup>  $\Delta P$  denotes the difference between fuel rod internal fill gas pressure in cold condition and coolant pressure (MPa).**

	SPERT US	PBF US	IGR KZ	HYDRA RU	NSRR JP
<b>Test conditions</b>					
Coolant temperature [K]	293	538	293	293	293 – 578
Coolant velocity [ $\text{ms}^{-1}$ ]	0	0.5	0	0	0 – 1.8
Coolant pressure [MPa]	0.1	6.45	0.1 – 16	0.1	0.1 – 16
Power pulse width [ms]	13 – 31	11 – 16	100 – 1000	4 – 8	4 – 7
Fuel rod type	BWR	PWR	VVER	VVER	BWR/PWR
<b>Test results</b>					
Failure enthalpy, quenching [ $\text{Jg}^{-1}$ ]	860 – 940	940 – 1050	1130	-	920
Failure enthalpy, ballooning [ $\text{Jg}^{-1}$ ]	-	-	670 ( $\Delta P=2.4$ )	670 ( $\Delta P=2.4$ )	900 – 590 ( $\Delta P=0.25-3.0$ )
Fuel dispersal threshold [ $\text{Jg}^{-1}$ ]	1005	1045	1130	-	1045

### 3.2. Pulse-irradiation tests on pre-irradiated fuel rodlets

Key data for pulse-irradiation tests on pre-irradiated fuel rodlets, as well as for the six pulse reactors in which the tests were done, are summarised in table 2. In short, these tests show that irradiated rods are more susceptible to cladding failure than fresh rods, i.e. they fail at lower fuel enthalpy. The tests also suggest that high-burn-up fuel rods fail either by cladding high-temperature ballooning and burst, or at low temperature, by pellet-clad mechanical interaction (PCMI) during the early heat-up stage of the accident. The high-temperature failure mode is observed for pre-irradiated VVER fuel rods, whereas pre-irradiated PWR and BWR rods fail almost exclusively by PCMI.

Table 2. Overview of pulse reactor tests on pre-irradiated LWR fuel rods.<sup>1</sup>

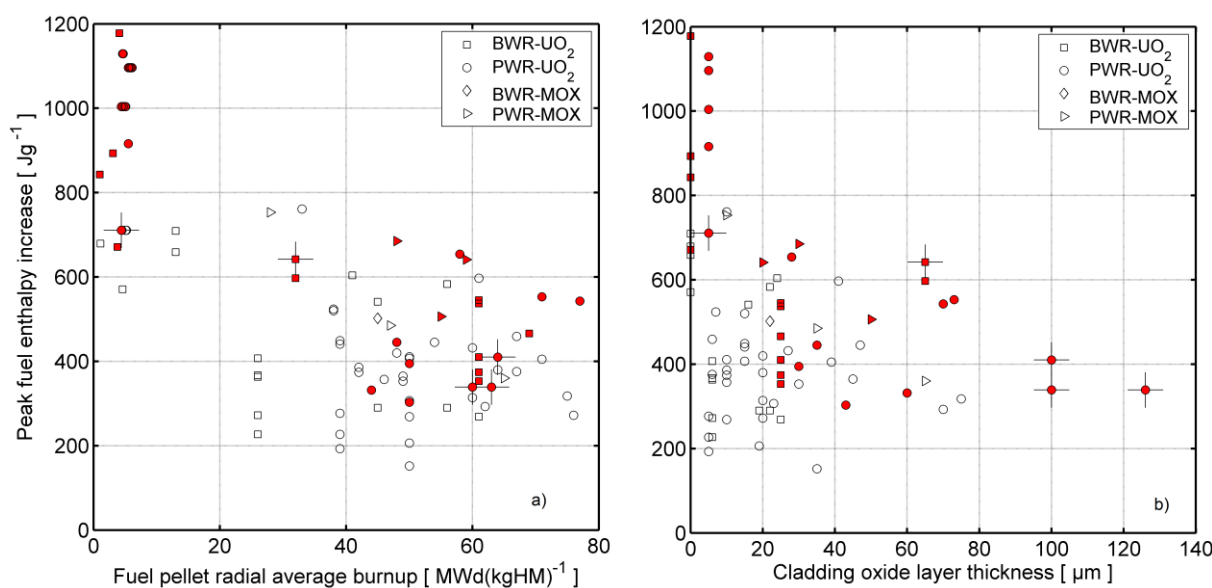
	SPERT US	PBF US	IGR KZ	BIGR RU	NSRR JP	CABRI FR
<b>Test conditions</b>						
Coolant medium	Stagnant water	Flowing water	Stagnant water	Stagnant water	Stagnant water	Flowing sodium
Coolant temperature [K]	293	538	293	293	293*	553
Coolant pressure [MPa]	0.1	6.45	0.1	0.1	0.1*	0.5
Power pulse width [ms]	13-31	11-16	600-950	2-3	4-7	9-75
<b>Fuel rods tested</b>						
Number of tests (PWR/BWR/VVER/MOX)	10 (0/10/0/0)	17 (17/0/0/0)	13 (0/0/13/0)	12 (0/0/12/0)	58 (32/17/0/9)	14 (10/0/0/4)
Burn-up [MWdkg <sup>-1</sup> HM <sup>-1</sup> ]	1-32	0-6.1	47-49	47-60	20-77	33-76
Clad oxide thickness [µm]	0-65	0-5	5	3-7	4-73	10-126
Rod active length [mm]	132	≈ 1000	150	140-150	122-135	440-1000
Peak fuel enthalpy [Jg <sup>-1</sup> ] (calg <sup>-1</sup> )	570-1180 (137-282)	770-1190 (185-285)	255-1051 (61-251)	481-787 (115-188)	155-657 (37-157)	343-832 (82-199)
Lowest failure enthalpy [Jg <sup>-1</sup> ] (calg <sup>-1</sup> )	356 (85)	586 (140)	737 (176)	687 (164)	222 (53)	117-151 (28-36)

\* Standard cooling conditions used in most of the NSRR tests on pre-irradiated fuel. A new test capsule, allowing high coolant temperature and pressure, has just recently been taken into operation.

The high-temperature failures observed for VVER fuel correlate well with peak fuel enthalpy: tests on VVER fuel with burn-up in the range 47-60 MWd(kgU)<sup>-1</sup> in the IGR and BIGR facilities suggest a failure threshold of about 650 Jg<sup>-1</sup>. The situation is much different for the PCMI-induced failures of PWR and BWR fuel. This is illustrated by figure 3a, which shows the results of all available pulse-reactor tests on pre-irradiated PWR and BWR rodlets with UO<sub>2</sub> and MOX fuel. The data are plotted in terms of peak fuel *enthalpy increase* during the test, rather than peak enthalpy, since the former parameter is more directly related to the PCMI-induced clad loading. From figure 3a, it is clear that failed rods and survivals are interspersed in the diagram, especially for fuel burn-ups beyond 40 MWd(kgU)<sup>-1</sup>. One reason for this scatter is that the degree of cladding corrosion has a strong effect on the susceptibility to PCMI-induced failure. However, the degree of cladding corrosion alone cannot explain the scatter, as evidenced by figure 3b, where the same data are plotted with respect to cladding peak oxide layer thickness. Also in this case, there is no clear demarcation line between failed rods and survivals. It is likely that part of the scatter in figure 3 is due to the fact that pre-irradiated test rods, which are re-fabricated from full-length fuel rods, are insufficiently pre-conditioned to reach an equilibrium pellet-clad contact state before testing. In most pulse reactors, it is not possible to operate the test rodlets at pre-conditioning power to reach the equilibrium state.

The assumedly insufficient pre-conditioning is not the only reason to question whether the performed pulse reactor tests reproduce the true fuel rod behaviour under RIAs: Firstly, most tests have to date been done with cooling by stagnant water at room temperature and atmospheric pressure. These cooling conditions are fairly close to those at cold zero power in BWRs, but much different from those connected with rod ejection accidents in PWRs. Secondly, about thirty of the pre-irradiated test rods, namely those in the SPERT and NSRR/JMTR tests, had atypical design and/or were pre-irradiated under atypical reactor conditions. Unfortunately, these rods make up most of the available test data for the burn-up range of 10 to 40 MWd(kgU)<sup>-1</sup>. It should also be remarked that all tests, except for those in the PBF and CABRI, were done on rodlets with very short (120-150 mm) active length. Finally, pulse widths in the NSRR (4-7 ms) and the BIGR (2-3 ms) were much smaller than those expected for control rod ejection/drop accidents; cf. figure 2. The pulse width affects the PCMI failure mode, most importantly because it controls the time lag between mechanical loading and heating of the cladding tube; a narrow power pulse leads to mechanical loading at a time when the cladding is insignificantly heated from its initial temperature and therefore potentially brittle.

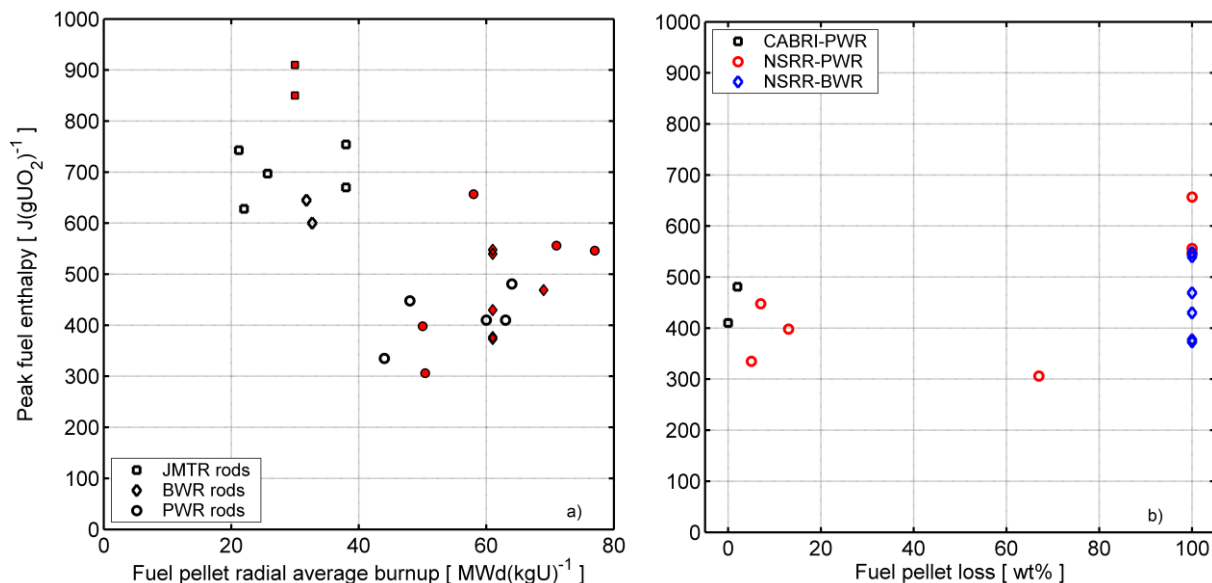
Figure 3. Peak fuel enthalpy increase versus a) fuel burn-up and b) clad oxide thickness for pre-irradiated PWR and BWR fuel rodlets.<sup>1</sup> Filled symbols represent failed rods, open symbols are survivals. Crosses indicate tests done on samples with hydride blisters in the cladding tube.



From table 1 in section 3.1, it is clear that RIA simulation tests on un-irradiated fuel rodlets generally result in fuel dispersal, when the peak fuel enthalpy exceeds roughly  $1000 \text{ Jg}^{-1}$ . Pulse reactor tests on pre-irradiated fuel rods show that fuel may be dispersed into the coolant at significantly lower fuel enthalpy, when the fuel burn-up exceeds approximately  $40 \text{ MWd(kgU)}^{-1}$ . The fuel dispersal occurs in connection with PCMI-type cladding failure; the ballooning and burst type of failure does not lead to significant fuel dispersal. Figure 4a shows the measured fuel dispersal from 25 pre-irradiated  $\text{UO}_2$  fuel rods that have failed through PCMI under pulse-irradiation tests in the SPERT, CABRI and the NSRR. Filled symbols represent rodlets, for which more than 10% of the  $\text{UO}_2$  fuel inventory was dispersed into the coolant under the tests, whereas open symbols are samples with no or marginal fuel loss. Obviously, for samples with fuel burn-up less than  $40 \text{ MWd(kgU)}^{-1}$ , there was no fuel dispersal for peak fuel enthalpies below  $800 \text{ Jg}^{-1}$ . However, the situation is much different at high burn-up. In the upper burn-up range of figure 4a, i.e. in the range of  $44$  to  $77 \text{ MWd(kgU)}^{-1}$ , we find that significant ( $>10\%$ ) fuel dispersal was reported for enthalpies far below  $800 \text{ Jg}^{-1}$  in eleven of the sixteen tests. These sixteen high-burn-up tests are plotted in figure 4b, which shows the percentage fuel loss versus peak fuel enthalpy under the test.

There are several reasons to why fuel dispersal is more extensive for high-burn-up than for low-burn-up fuel. Firstly, for a given fuel energy deposition, the cladding cracks are generally larger and wider for the high-burn-up fuel. This is most likely a result of hard PCMI and/or a more embrittled cladding in the high-burn-up fuel rods. The larger crack opening area eases the dispersal of fuel particles. Secondly, high-burn-up oxide fuel turns into fine fragments when subjected to an RIA, as a result of fission gas induced grain boundary decohesion. This fragmentation mechanism promotes fuel dispersal, since the fine fragments are easily expelled through cladding cracks under the power pulse.

Figure 4. Peak fuel enthalpy versus a) fuel burn-up and b) fuel pellet loss for pre-irradiated  $\text{UO}_2$  fuel rodlets that have failed by PCMI in pulse irradiation tests.<sup>1</sup> Filled symbols in figure 4a are samples with more than 10% observed fuel loss during the test, open symbols are samples with no or marginal fuel loss. Figure 4b shows only the tests with burn-up > 40  $\text{MWd}(\text{kgU})^{-1}$ .



#### 4. Out-of-reactor separate effect tests

In addition to pulse-irradiation tests, several out-of-reactor separate effect test programs have been conducted to explore the fuel behaviour under RIA conditions. These tests, which are briefly summarised below, are less costly than pulse-irradiation tests and allow key phenomena to be studied under well-controlled laboratory conditions.

##### 4.1. Tests on cladding mechanical properties

The cladding strength and ductility are of fundamental importance to fuel rod survivability under reactivity initiated accidents, and many separate effect test programs have been conducted to study these properties in detail. The objective has been to understand and quantify the observed degradation in fuel rod survivability at high burn-up, and most tests have therefore been focused on the embrittling effects related to cladding waterside corrosion, i.e. cladding oxidation and hydrogen uptake. These effects have been investigated by testing in-reactor corroded cladding, taken from high-burn-up fuel rods, as well as un-irradiated samples that have been artificially oxidized and hydrided under well-controlled laboratory conditions. Tests on the latter kind of samples provide a valuable supplement to the tests on irradiated cladding, which are costly and time consuming. Moreover, the hydride distribution in artificially corroded samples can be controlled in detail, which makes it possible to investigate the importance of e.g. hydride blisters to the cladding embrittlement.

Table 3 summarises seven test programs, which were aimed to study the mechanical properties of irradiated and/or corroded cladding tubes under RIA conditions. All tests were done at strain rates that were much higher than those normally used in mechanical testing, in order to reproduce the PCMI-induced loading conditions expected in high-burn-up fuel rod cladding during the early stage of an RIA. However, the rapid heat-up of the cladding during this stage of the accident was generally not simulated in the tests: except for a few tests with clad heating rates of either 100 or 200  $\text{Ks}^{-1}$  in the French PROMETRA program, all tests in table 3 were done at constant and uniform temperature. We note from

table 3 that a multitude of test methods were used, which makes it difficult to compare the results among different test programs. The main reason to this problem is that the stress biaxiality conditions, which are known to have a strong effect on cladding ductility, differ significantly between the test methods.

Table 3. **Summary of mechanical tests on cladding tubes, carried out at high strain rate.**<sup>1</sup>

Tests conducted by (country)	Test* method	Cladding material	Irradiated, un-irradiated	Strain rate [ s <sup>-1</sup> ]	Temperature [ K ]
IRSN/EDF/CEA (FR)	TAT, RTT, MAN, CBT	Zr-4, M5, ZIRLO	I+U	10 <sup>-3</sup> – 5	293 – 1373
Kurchatov Institute (RU)	TAT, RTT, CBT	E110	I+U	10 <sup>-3</sup> – 0.5	293 – 1400
GNF/Toshiba (JP)	OBT	Zr-2	I+U	10 <sup>-3</sup> – 8	293
JAEA (JP)	CBT	Zr-4	U	10 <sup>-4</sup> – 0.3	293 – 620
ANL/PSU (US)	RST	Zr-4	U	10 <sup>-3</sup> – 0.2	293 – 573
KAERI (KR)	RTT	Zr-4, HANA-4	U	10 <sup>-2</sup> – 1	293 – 623
Studsvik (SE)	EDC	Zr-4, ZIRLO	I	1 – 10	298 – 613

\* TAT: Tube axial tension test, RTT: Ring tensile test, MAN: Mandrel test, CBT: Closed-end burst test, OBT: Open-end burst test, RST: Ring stretch test, EDC: Expansion-due-to-compression test.

#### 4.2. Tests on clad-to-coolant transient heat transfer

Due to rapid heating and deformation of the cladding tube, clad-to-coolant heat transfer is different during RIAs than under steady-state operating conditions or slow overpower transients. As already mentioned in section 3, of particular concern with respect to fuel rod failure under RIAs is the occurrence of a clad-to-coolant boiling crisis, i.e. a transition to a regime with film-boiling and low heat transfer at the clad-to-coolant interface. This phenomenon has been studied in a series of out-of-pile experiments in the PATRICIA test loop of CEA, Grenoble, France. The test loop was operated at various coolant conditions, and comprised a test section in which a 0.6 m long electrically heated and instrumented Inconel tube was placed. Tests with heating rates up to 12000 Ks<sup>-1</sup> revealed significant kinetic effects in the clad-to-coolant heat transfer: The critical heat flux, i.e. the threshold heat flux at which a boiling crisis occurred, was 2-12 times higher in the transient tests than under steady-state conditions. The critical surface temperature, i.e. the surface temperature at which the transition to film-boiling took place, was also higher in the transient tests. In the film-boiling regime, the magnitude of the heat flux was 2-25 times higher than under steady-state conditions. The differences between transient and steady-state heat transfer were observed to increase with increasing heating rate.

The PATRICIA tests were carried out with an air-filled Inconel tube as a proxy for a true fuel rod. The Inconel tube was free from surface oxide, in contrast to most fuel rods. This remark is important, since pulse-irradiation tests in the NSRR on instrumented fuel rodlets with and without oxide show that, for comparable energy injections, corroded fuel rods reach lower cladding surface temperatures than fresh rods without a surface oxide layer. The effect is attributed to oxide-induced improvement of surface wettability, caused primarily by a change in chemical potential.

#### 4.3. Tests on fuel-coolant interaction

A major safety concern in reactivity initiated accidents is that the thermal energy of fuel particles, expelled into the coolant from failed fuel rods, is rapidly converted to mechanical energy in the form of destructive pressure pulses. The concern is that these pressure pulses may damage nearby fuel assemblies, other core internals and ultimately also the reactor pressure vessel.

By convention, the degree of fuel-coolant interaction is quantified with the energy conversion ratio, which is the ratio of the mechanical energy generated in the coolant to the thermal energy in the dispersed fuel. This ratio can be determined in pulse reactor tests, where the mechanical energy generated in the coolant is

estimated by measuring the motion of the water column in the test rig, as it is raised by rapid expansion of steam bubbles around dispersed fuel fragments. Such measurements have been made in the PBF and the NSRR, and notwithstanding the differences in coolant conditions between these facilities, the results are similar. Measured energy conversion ratios in PBF and NSRR typically fall in the range  $10^{-4} - 10^{-2}$ , and there is an inverse relationship between energy conversion ratio and mean size of the dispersed fuel fragments. Moreover, energy conversion ratios associated with dispersal of solid fuel particles are about an order of magnitude lower than for molten fuel, given a particular size of the dispersed fuel fragments.

## **5. Concluding remarks**

In this paper, we have discussed three categories of results and data on the behaviour of light water reactor nuclear fuel under reactivity initiated accidents. The presentation is a brief summary of a comprehensive report on this subject,<sup>1</sup> which is currently being published by the OECD Nuclear Energy Agency. The aforementioned report attempts to summarise the current state of knowledge on fuel behaviour under RIAs, and contains reviews and analyses of results from computer analyses on reactivity initiated accidents as well as from pulse-irradiation tests and out-of-pile separate effect tests. In addition, the report deals with the following issues:

- Scenarios and anticipated consequences of RIAs in major type of nuclear power reactors.
- Phenomena with particular importance to fuel behaviour under RIAs, e.g. fuel failure mechanisms.
- Influence of burn-up-dependent state of fuel and cladding on the response to RIAs.
- Methods and predictive computer codes for analyses of RIAs.

With more than 350 cited references to relevant works published up to March 2009, the report is a good entry to the subject.

## **Acknowledgement**

This work was funded by the Swedish Radiation Safety Authority.

## A review of experiments and computer analyses on RIAs

(summary of a report soon to be published by the OECD/NEA)

Lars Olof Jernkvist, Ali R. Massih  
Quantum Technologies AB, Uppsala Science Park, SE-75183 Uppsala, Sweden

Jan In de Betou  
Swedish Radiation Safety Authority, SE-17116 Stockholm, Sweden

OECD/NEA Workshop on Nuclear Fuel Behaviour during RIAs, Paris, Sept. 9-11, 2009



## Presentation outline

- Background and introduction
- Brief review of studies on LWR RIAs
  - Computer analyses of hypothetical RIAs
  - Pulse irradiation tests
  - Separate effect tests
- Summary and conclusions



## Background

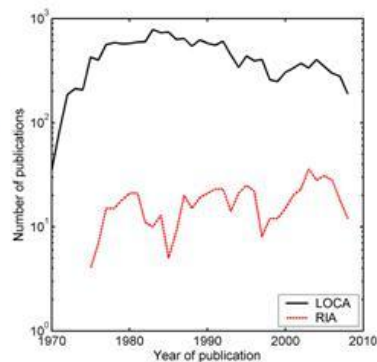
In 2003, the CSNI Special Expert Group on Fuel Safety Margins decided to work out state-of-the-art reports (SOARs) on nuclear fuel behaviour under accident conditions

LOCA:

- Update of 1986 NEA report
- Published June 2009

RIA:

- New report
- To be published late autumn 2009



Source: IAEA INIS database



## Introduction

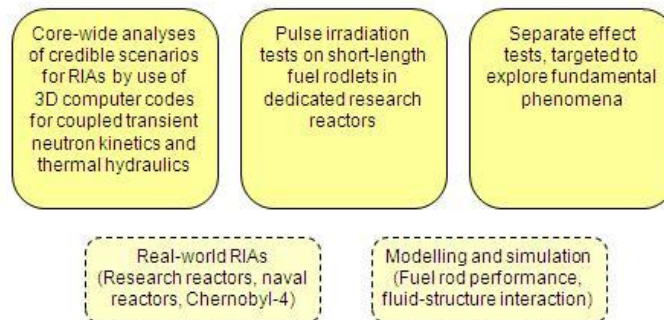
The new NEA report on nuclear fuel behaviour under RIA:

- Aims to summarize the current understanding of fuel behaviour under RIAs in light water reactors (BWR, PWR, VVER), based on results from experiments and state-of-the-art computer analyses
- Covers material published in open literature up to March 2009
- Deals with  $UO_2$ , (U,Pu) $O_2$  MOX, and burnable absorber fuels



## Introduction

What are the information sources on RIAs in light water reactors?



## Computer analyses of postulated RIAs

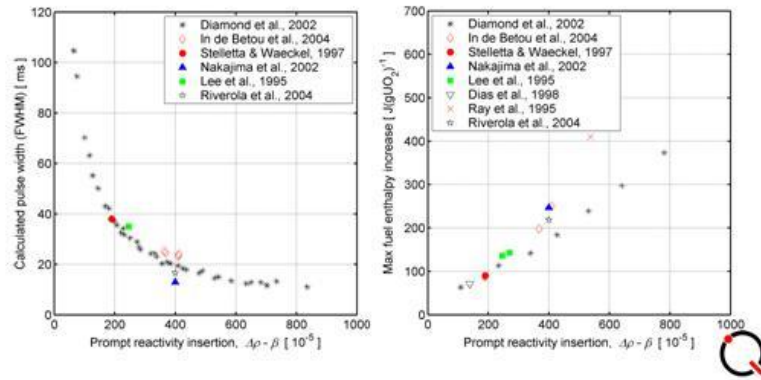
Reactor core analyses with state-of-the-art 3D methods

- Key results are the space-time variation of fuel power, fuel enthalpy and coolant properties → estimated number of failed fuel rods in the core
- Most reported studies are concerned with design basis RIAs
  - Control rod ejection accidents (REAs) in PWRs
  - Control rod drop accidents (RDAs) in BWRs



## Example: Calculated power pulse characteristics

REA at hot zero power, end-of-cycle conditions



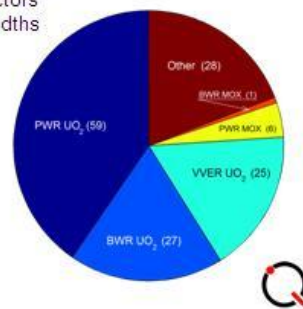
## Computer analyses of postulated RIAs

General observations:

- Reported results are fairly consistent
  - Power pulse characteristics
  - Power/energy distributions
  - Fraction of failed fuel rods
- Modelling issues concern
  - Fuel rod transient heat transfer
  - Clad-to-coolant transient heat transfer
  - Transient vapour generation in coolant
- Models for post-failure conditions are unavailable

## Pulse irradiation tests on fuel rodlets

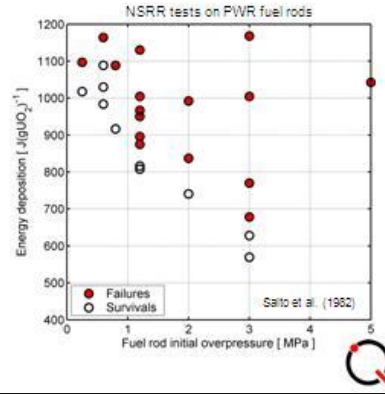
- Key results are fuel enthalpy thresholds for cladding failure, fuel dispersal and fuel melting
- Tests have been done in 9 power pulse reactors with diverse cooling conditions and pulse widths
- Current database comprises
  - > 1000 tests on un-irradiated fuel rods
  - ~ 150 tests on pre-irradiated fuel rods



### Tests on un-irradiated fuel rodlets

Key findings:

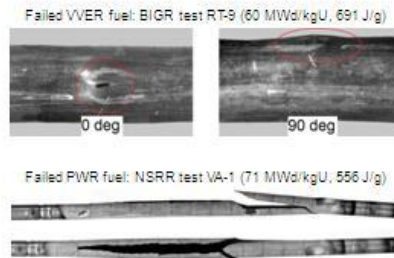
- Clear correlation between fuel rod damage and peak fuel enthalpy
- Two limiting failure modes, related to clad overheating:
  - Fracture of oxygen-embrittled cladding upon quenching
  - Clad ballooning and burst at high temperature



### Tests on pre-irradiated fuel rodlets

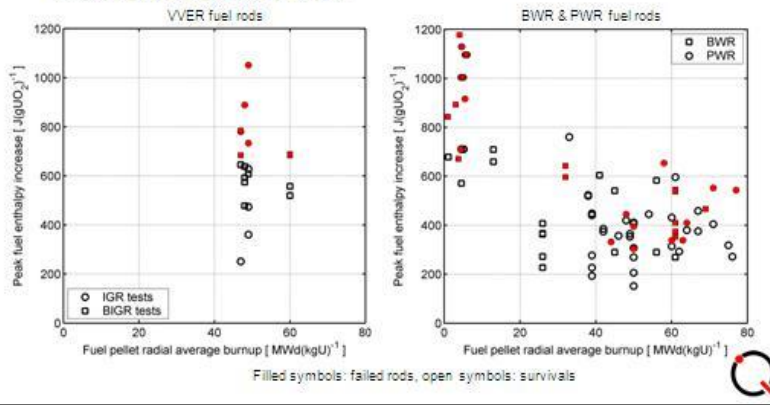
Key findings:

- Pre-irradiated fuel rods are more susceptible to failure than un-irradiated fuel rods
- Two limiting failure modes:
  - Clad ballooning and burst at high temperature (VVER)
  - PCMI-induced failure at low temperature (BWR & PWR)



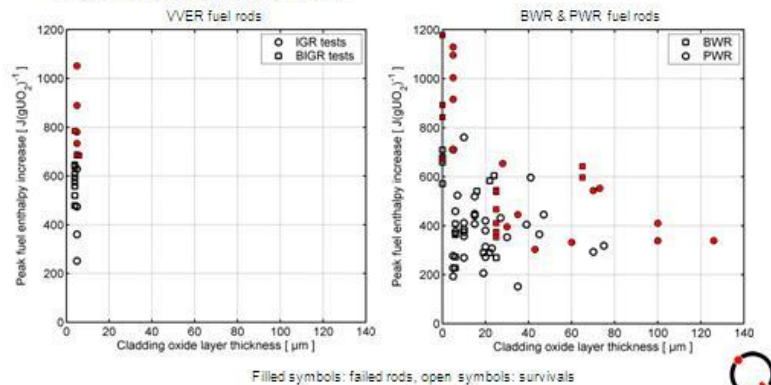
### Tests on pre-irradiated fuel rodlets

Results of tests on UO<sub>2</sub> fuel rods



## Tests on pre-irradiated fuel rodlets

Results of tests on  $\text{UO}_2$  fuel rods



## Pulse irradiation tests on fuel rodlets

General observations:

- Tests have been focused on cladding failure mechanisms; post-failure mechanisms have received less attention
- There is concern about the applicability of test results, due to differences between test reactor conditions and expected LWR RIA conditions
  - Power pulse width
  - Coolant conditions
  - Pre-conditioning of pre-irradiated fuel rods

## Separate effect tests

Tests targeted to explore RIA-relevant phenomena

- Cladding PCMI-induced failure
  - Embrittling effects of waterside corrosion and high strain rate
- Clad-to-coolant transient heat transfer
  - Effects of clad heating rate and surface conditions
- Fuel-coolant interaction (thermal to mechanical energy conversion)
  - Effects of fuel particle size and temperature

### Example: Cladding PCMI-induced failure

Out-of-pile mechanical property tests performed at high strain rate

Tests conducted by (country)	Testing* method	Cladding material	Irradiated, un-irradiated	Strain rate [ $s^{-1}$ ]	Temperature [K]
IRSN/EDF/CEA PROMETRA (FR)	TAT, RTT, MAN, CBT	Zr-4, M5, ZIRLO	I+U	$10^{-3} - 5$	293 - 1373
Kurchatov Institute (RU)	TAT, RTT, CBT	E110	I+U	$10^{-3} - 0.5$	293 - 1400
GNF/Toshiba (JP)	DBT	Zr-2	I+U	$10^{-3} - 8$	293
JAEA (JP)	RTT, CBT	Zr-4	U	$10^{-4} - 0.3$	293 - 620
ANL/PSU (US)	RST	Zr-4	U	$10^{-3} - 0.2$	293 - 573
KAERI (KR)	RTT, CBT	Zr-4, HANA-4	U	$10^{-2} - 1$	293 - 623
Studsvik (SE)	EDC	Zr-4, ZIRLO	I	1 - 10	298 - 613

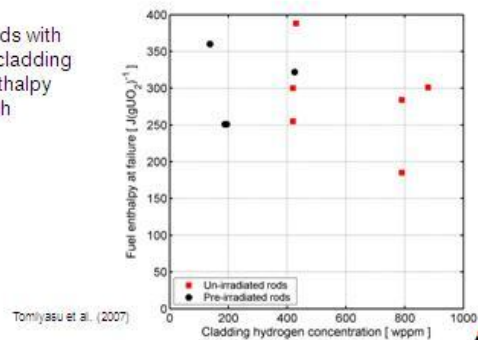
\* TAT: Tube axial tension test, RTT: Ring tensile test, MAN: Mandrel-type test, CBT: Closed-end burst test, DBT: Open-end burst test, RST: Ring stretch test, EDC: Expansion-due-to-compression test



### Example: Cladding PCMI-induced failure

NSRR tests on un-irradiated PWR rods with artificially hydrided cladding

- Un-irradiated fuel rods with artificially hydrided cladding fail at similar fuel enthalpy as pre-irradiated high burnup rods



Tomiyasu et al. (2007)



### Summary

What are the knowledge gaps concerning RIAs in light water reactors?

- No experiments on fuel assembly behaviour
  - Rod-to-rod interaction, following first cladding failure?
  - Long-term coolability of damaged fuel?
- Few pulse irradiation tests that initiate from hot coolant conditions and non-zero fuel rod power



## Summary

Topics considered in the new NEA report on LWR RIA:

- Scenarios for RIAs and their anticipated consequences
- Involved phenomena with relevance to fuel safety
- Data: Pulse reactor tests and relevant separate effect tests
- Calculations: Estimates of pulse characteristics and fuel damage
- Effects of fuel burnup and cladding corrosion
- Review of predictive computer codes for RIA



## Acknowledgements

Thanks are due to

- Many individuals and organizations, for contributing material to the report
- Members of the CSNI Working Group on Fuel Safety, for reviewing drafts to the report
- The Swedish Radiation Safety Authority, for funding the drafting of the report





## CURRENT RIA-RELATED REGULATORY CRITERIA IN JAPAN AND THEIR TECHNICAL BASIS

**Toyoshi Fuketa and Tomoyuki Sugiyama**  
Japan Atomic Energy Agency, Japan

### Abstract

This paper aims to provide a general outline of fuel behaviour during a reactivity-initiated accident (RIA) postulated in light water reactors (LWRs) and to show experimental data providing technical basis with the current RIA-related regulatory criteria in Japan. The safety evaluation guideline for the reactivity-initiated events in LWRs was established by the Nuclear Safety Commission (NSC) of Japan in 1984 based mainly on the results of the NSRR experiments. In the guideline, an absolute limit of fuel enthalpy during an RIA is defined in order to avoid mechanical forces generation. The guideline also defines an allowable limit of fuel enthalpy for fuel design as a function of difference between rod internal pressure and system pressure. All of the NSRR data used for the guideline were limited to those derived from the experiments with fresh, un-irradiated fuel rods. For this reason, the guideline noted that the failure threshold should be revised by further experimental efforts on irradiated fuel rods. A series of experiments with pre-irradiated fuel rods were accordingly initiated in 1989, and the NSC issued a regulatory report regarding behaviour of burn-up fuels during a postulated RIA in 1998. The PCMI-failure threshold in terms of fuel burn-up and enthalpy increase was defined in the report.

### 1. Introduction

In the first nuclear reactor CP-1, a person on the floor physically withdrew a control rod. If the reaction threatened to grow out of control he could re-insert his control rod, and an automatic control rod would also insert itself if the reaction reached a certain pre-set level. In case of emergency, another person, who stood on the balcony with an axe, would cut a rope and release another emergency control rod into the pile. The last line of defence consisted of a "liquid-control squad" that stood on a platform, ready to flood the pile with a cadmium-salt solution. The first nuclear reactor was equipped with multiple and diverse control system.<sup>1</sup> In the very beginning stage of developing power-producing reactors, a possible power excursion was one of primary concerns. A number of test reactors, such as the Boiling Water Reactor Experiment (BORAX) I to V and the Special Power Excursion Reactor Test (SPERT), were constructed in Idaho, United States in order to experimentally determine reactor kinetics and to demonstrate self-limiting characteristics. In July 1954, the BORAX-I, facility was destroyed during the final experiment with a rapid withdrawal of a control rod. Fuel plate fragments were scattered for a distance of 60 to 90 m. In January 3, 1961, the famous SL-1 accident occurred. A recent study analyzed that the core power level reached nearly 20 GW in just 4 ms, precipitating the reactor accident and steam explosion.<sup>2</sup> One could naturally expect that destructive forces may be triggered and generated by fuel failure and melting. It is not necessary to destroy a whole core in order to study the fuel failure and its consequences, the fuel crash test inside a rigid capsule or loop, such as the SPERT program in the Capsule Driver Core facility (SPERT/CDC), had been initiated and the Nuclear Safety Research Reactor (NSRR) program followed.

The current safety evaluation guideline for the reactivity-initiated events in LWRs was established by the Nuclear Safety Commission (NSC) of Japan in 1984 based mainly on the results of the NSRR experiments.

---

1 "The Manhattan Project; An Interactive History", [www.cfo.doe.gov/me70/manhattan](http://www.cfo.doe.gov/me70/manhattan), Office of History and Heritage Resources, U.S. Department of Energy.

2 "Supercritical", System Failure Case Studies, Vol.1, Issue 4, National Aeronautics and Space Administration, (2007).

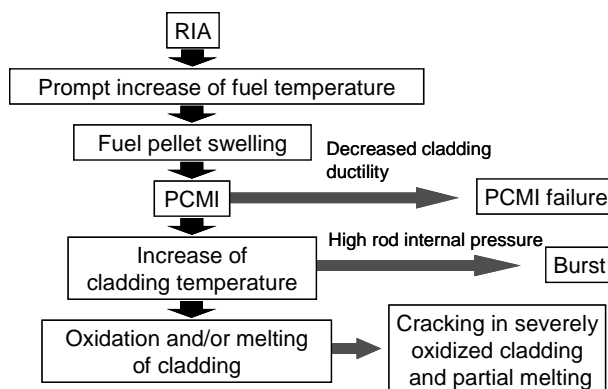
In the guideline, an absolute limit of fuel enthalpy during an RIA is defined in order to avoid mechanical forces generation. The guideline also defines an allowable limit of fuel enthalpy for fuel design as a function of difference between rod internal pressure and system pressure. All of the NSRR data used for the guideline were limited to those derived from the experiments with fresh, i.e. un-irradiated fuel rods. For this reason, the guideline had adopted a peak fuel enthalpy of 85 cal/g (0.36 kJ/g) as a provisional failure threshold of pre-irradiated fuel rod during an RIA; and this failure threshold is used to evaluate number of failed pre-irradiated fuel rods, and to assess source term regarding fission gas release in a postulated RIA. This failure threshold enthalpy of 85 cal/g was derived from only one experiment, i.e. the test 859<sup>3</sup> performed in the SPERT/CDC facility. Hence, the guideline noted that the failure threshold should be revised by further NSRR experiments with irradiated fuel rods. A series of experiments with pre-irradiated fuel rods were initiated in 1989, and the NSC issued a regulatory report regarding behaviour of burn-up fuels during a postulated RIA in 1998. The PCMI-failure threshold in terms of fuel burn-up and enthalpy increase was defined in the report.

## 2. Cladding failure

### 2.1. Failure modes

The processes of three different failure modes are shown in Fig. 1. After an onset of an RIA, rod ejection accident (REA) in PWRs or rod drop accident (RDA) in BWRs, fuel temperature increases promptly, and fuel pellets expand rapidly. The fuel pellets then contact with cladding inner wall and push it from inside. If the cladding has decreased ductility due to corrosion and subsequent hydrogen absorption during normal operations, it may fail due to the pellet/cladding mechanical interaction (PCMI). This “PCMI failure” occurs only in a very early stage of the transient, and the cladding temperature remains low at a time of the failure. Post-failed cladding has a long axial crack and its deformation is limited as illustrated in Fig. 2(a).

Figure 1. **Fuel failure modes in an RIA**



If the cladding is ductile enough to survive the stage of the PCMI loading and fuel enthalpy continues to increase, cladding temperature becomes higher after an occurrence of DNB. If the rod internal pressure is higher than the external, the cladding becomes ballooned due to the decreased yield stress of the cladding at the high temperature. The ballooned cladding may be ruptured and the fuel enthalpy at a time of the “rod burst” is determined as a function of rod internal/external pressure difference and cladding temperature. Failed cladding in this case has a short axial crack in a ballooned region as shown in Fig. 2(b).

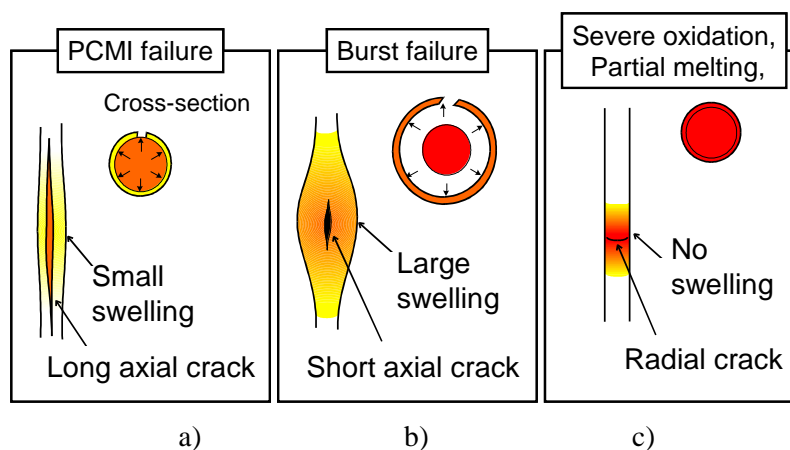
If the rod internal pressure is not higher and fuel enthalpy reaches much higher, the cladding may fracture due to severe oxidation and partial melting. The “brittle fracture” (or “melt failure”<sup>4</sup>) can occur in a late

3 Meyer, R., McCardell, R., Chung, H., Diamond, D. and Scott, H., “A Regulatory Assessment of Test Data for Reactivity-Initiated Accidents”, Nuclear Safety, Vol.37, No.4, pp.271-288, (1996).

4 Ishikawa, M. and Shiozawa, S., “A Study of Fuel Behavior under Reactivity Initiated Accident Conditions - Review”, J. Nuclear Materials, Vol.95, pp.1-30, (1980).

phase of the transient, and the fuel enthalpy at a time of the failure is relatively high. The failed rod has a radial crack as shown in Fig. 2(c).

Figure 2. Schematic diagram of failed rods



## 2.2. Thermal failure; brittle fracture and burst

The two failure modes “rod burst” and “brittle fracture” described in the latter of the previous section are categorised as thermal failure and can occur only after an occurrence of DNB. The Japanese regulatory criteria regarding the thermal failures are based on NSRR experiments performed with un-irradiated, fresh test fuel rods. The brittle fracture was observed in baseline experiments of the early phase of the NSRR program. The failure is principally caused by cladding embrittlement and the fracture generally occurs at the time of quench. The cracking is enhanced by cladding wall thinning. The duration of stable film boiling is several to ten seconds in the tests, and this is not sufficient to cause the cladding to become embrittled. Post-test rods showed that the cladding wall near cracked portion became thin with melting. In the baseline tests, where the cracking occurred, cladding melt was observed. Molten cladding moved to other locations inside the cladding, probably under gravity or by forces due to boiling. The variation of the wall thickness and the oxidation ratio along the axial direction in the cladding indicate that the oxygen pick-up becomes relatively higher in the thinner region. The cladding becomes more brittle in the thinner wall region and cannot withstand axial tensile stress upon quenching. Accordingly, Ishikawa and Shiozawa named this type of failure “cladding melt failure” instead of “cladding brittle fracture” in their review paper<sup>(4)</sup>.

As for the burst type of cladding failure, a series of NSRR experiments<sup>5</sup> had been conducted with un-irradiated, pre-pressurized fuel rods. The cladding ballooning is initiated at the point of the highest temperature, and once the ballooning starts it progresses rapidly. The rupture occurs at the point of ballooning initiation due to the extremely high strain rate. In the experiment, the burst split was located nearest the thermocouple which indicated the highest temperature at the time of the peak pressure but the lowest temperature at the time of the rod burst. Transient histories of the rod internal pressure during the experiments show a typical response in the case of a pre-pressurization of 2.0 MPa. As shown in Fig. 3, Saito et al.<sup>(5)</sup> characterised those into the following four phases:

Phase I: Rapid increase in accordance with the initiation of the power burst. Rod pressure increased from the rapid thermal expansion of the fuel pellet which coincided with the fuel heat-up caused by rapid energy insertion. During this period, the increase in the temperature of fill gas is thought to be negligibly small because of almost adiabatic heat-up of the fuel.

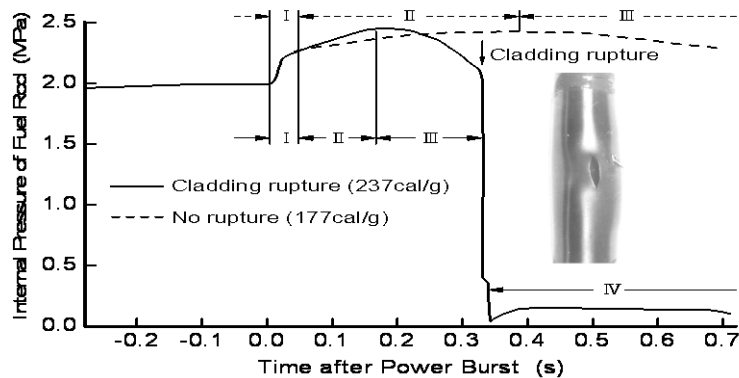
<sup>5</sup> Saito, S., Ishijima, K., Shiozawa, S. and Iwata, K., “Effects of Rod Pre-Pressurisation on Light Water Reactor Fuel Behavior during Reactivity Initiated Accident Conditions”, J. Nuclear Science and Technology, Vol.19, No.4, pp.289-306, (1982).

Phase II: Gradual increase up to maximum value for several hundred ms after the initiation of the power burst, depending on energy depositions, initial rod pressures, etc. Rod pressure increased due to the increase of gap gas temperature until the ballooning of the cladding became significant.

Phase III: Gradual decrease until rod rupture or until equilibrium was reached if the rod did not fail. The ballooning of the cladding became significant. Rod pressure decreased in accordance with the ballooning.

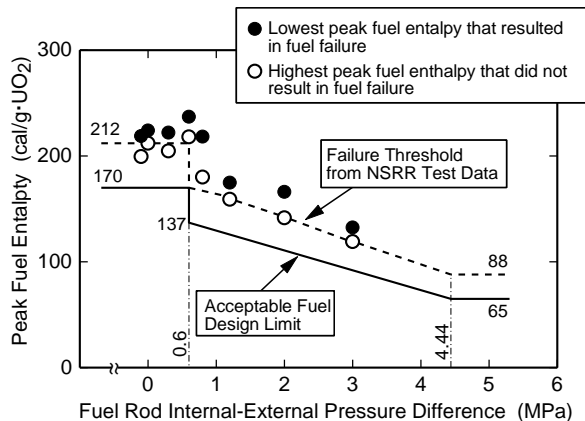
Phase IV: Sudden drop to coolant pressure if the rod ruptured. The rod pressure continued to decrease in accordance with the decrease in the temperatures of the fuel pellet and fill gas if the rod did not fail.

Figure 3. Transient histories of the rod internal pressureduring the experiments with pre-pressurised rods



A threshold of the thermal failures was defined in terms of the peak fuel enthalpy and rod internal/external pressure difference, as shown in Fig. 4.

Figure 4. Threshold of the thermal failures



The dashed-line in the figure is a failure threshold derived from the NSRR experiments with a single test pin. When the pressure difference was below 0.6 MPa, cladding fractured with partial melting at a peak fuel enthalpy of 212 cal/g (0.89 kJ/g) or higher. Above the difference of 0.6 MPa, the failure mode changes to the burst and the threshold decreases with pressure elevation. When a peak fuel enthalpy did not exceed 88 cal/g (0.37 kJ/g), DNB did not occur and therefore a rod did not experience the thermal failures. Since the thermal failures are strongly affected by rod cooling conditions, the single-pin experiments give a less conservative threshold. In another test series with rod bundle geometry, 15% reduction of the failure threshold appears due to the decreased coolability. With the 15% reduction and a 10 cal/g margin, the acceptable fuel design limit was determined as a solid-line of Fig. 4.

The rod ballooning was observed also in some experiments with irradiated test fuels, but no post-DNB failure occurred so far. Figure 5 shows residual hoop strain of post-test rods as a function of peak fuel enthalpy. In the test TK-1 the residual strain reached ~25%, and photographs in Fig. 6 showed pellet radial relocation.<sup>6</sup>

Figure 5. Residual hoop strain of post-test rods as a function of peak fuel enthalpy

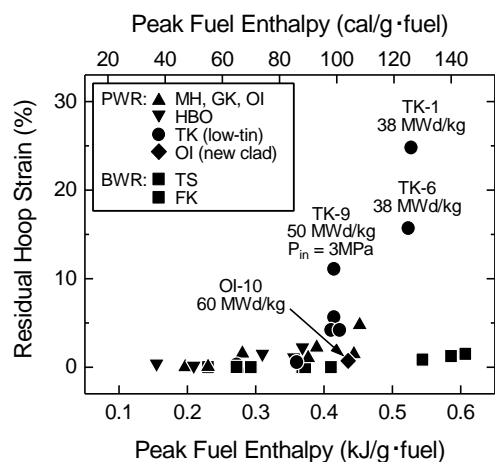
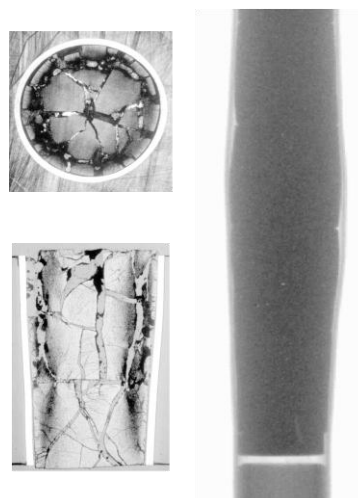


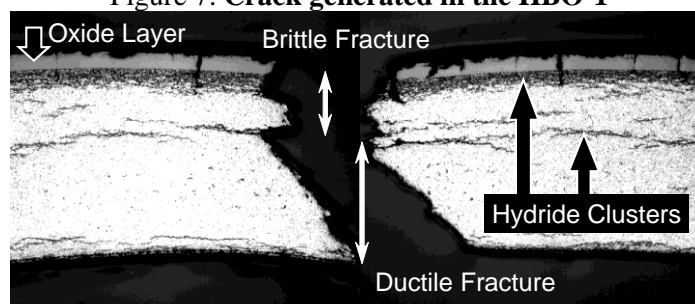
Figure 6. Post-test TK-1 rod



### 2.3. Mechanical failure; PCMI failure

As stated previously, a long axial crack appears in rods failed due to PCMI loading. Figure 7 shows a horizontal cross-section in the vicinity of a crack generated in the HBO-1 rod<sup>7</sup>. A brittle fracture appears in the cladding peripheral region where dense hydride clusters have precipitated, and propagates to inside with a ductile nature. The failure initiation is obviously influenced by the radially-localised hydride layer, i.e. hydride rim, so it is called “hydride-assisted PCMI failure”<sup>6,8,9</sup>. The HBO-1 rod was sampled from the 2<sup>nd</sup> highest span where the hydrogen concentration in the cladding was the highest in axial distribution, but the radially-averaged hydrogen concentration was ~400 ppm at most.

Figure 7. Crack generated in the HBO-1



- 6 Fuketa, T., Sasajima, H., and Sugiyama, T., “Behavior of High Burn-up PWR Fuels with Low-Tin Zircaloy-4 Cladding under RIA Conditions”, Nuclear Technology, Vol.133, pp.50-62, (2001).
- 7 Fuketa, T., Mori, Y., Sasajima, H., Ishijima, K. and Fujishiro, T., “Behavior of High Burn-up PWR Fuel under a Simulated RIA Condition in the NSRR”, CSNI Specialist Meeting on Transient Behaviour of High Burn-up Fuel, Sep. 12-14, 1995, Cadarache, France, OECD/GD(96)197, pp.59-85, (1996).
- 8 Fuketa, T., Nagase, F., Ishijima, K. and Fujishiro, T., “NSRR/RIA Experiments with High Burn-up PWR Fuels”, Nuclear Safety, Vol.37, No.4, pp.328-342, (1996).
- 9 Meyer, R., “An Assessment of Fuel Damage in Postulated Reactivity-Initiated Accidents”, Nuclear Technology, Vol.155, pp.293-311, (2006).

However, the local hydrogen concentration in the cladding peripheral region well exceeds 2500 ppm as shown in Fig. 8.<sup>(8)</sup> Incipient cracking occurs in this peripheral region due to the highly concentrated hydride clusters. Figure 9 illustrates the incipient cracks and an occurrence of stress concentration at a tip of the incipient cracks. The incipient cracks penetrate the oxide layer and a layer with high concentrations of hydride precipitates, “hydride rim”. A stress concentration at a tip of the incipient cracks drives the crack propagation to the inner part. Since the oxide layer has a negligibly low tensile stress, the thickness of the hydride rim controls the stress intensity factor. The hydride rim forms only in stress-relieved annealed (SRA) cladding, but the hydride-assisted PCMI failure occurs also in rods with recrystallisation annealed (RXA) cladding. In the RXA cladding the length of peripheral and radially-oriented hydrides may control the stress intensity factor. Figure 10 compares roles of the hydride rim in the SRA cladding and the radially-oriented hydrides in the RXA cladding on the incipient cracking. Fuel enthalpy at failure depends accordingly on the orientation of hydrides as well as on the amount of hydride precipitation.<sup>10,11,12</sup>

Figure 8. Radial profile of hydrogen concentration in HBO sibling rod

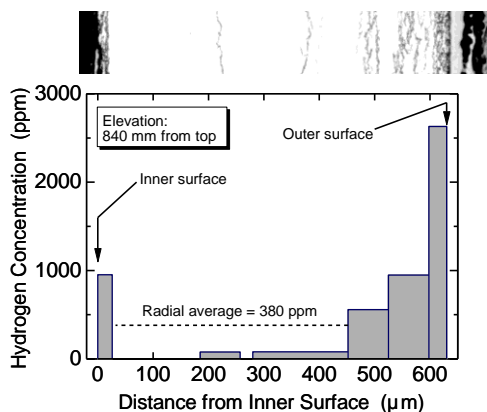


Figure 9. Stress concentration at a tip of incipient crack

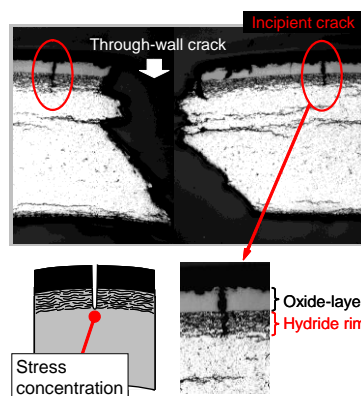
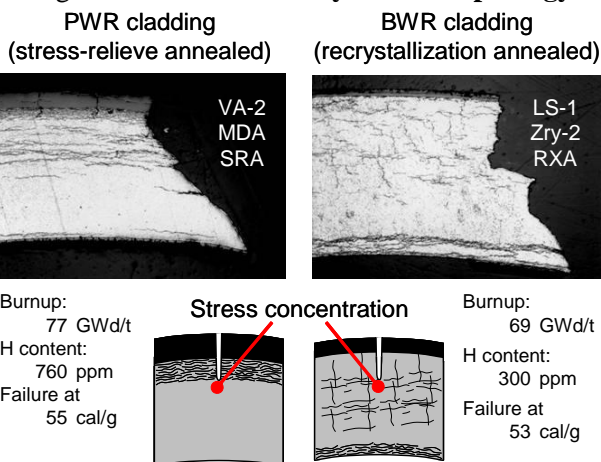


Figure 10. Influence of hydride morphology



10 Tomiyasu, K., Sugiyama, T. and Fuketa, T., “Influence of Cladding-Peripheral Hydride on Mechanical Fuel Failure under Reactivity-Initiated Accident Conditions”, J. Nuclear Science and Technology, Vol.44, No.5, pp.733-742, (2007).

11 Udagawa, Y., Suzuki, M., Sugiyama, T. and Fuketa, T., “Stress Intensity Factor at the Tip of Cladding Incipient Crack in RIA-Simulating Experiments for High Burn-up PWR Fuels”, J. Nuclear Science and Technology, Vol.46, No.10, (2009), to be published.

12 Sugiyama, T., Umeda, M. Fuketa, T., Sasajima, H., Udagawa, Y. and Nagase, F., “Failure of High Burn-up Fuels under Reactivity-Initiated Accident Conditions”, Annals of Nuclear Energy, Vol.36, pp.380-385, (2009).

Figure 11 shows the peak values of cladding residual hoop strain during the NSRR room temperature tests with PWR fuels. The nearly straight line in this figure indicates the strain level achievable only by the pellet thermal expansion. Tests, in which DNB did not occur, generally resulted in the PCMI-induced strains. When DNB occurs during the transient, the large cladding deformation is caused by the increase of the rod internal pressure in combination with the decreased yield stress of the cladding at an elevated temperature. In the phase of the PCMI, the deformation is driven only by solid thermal expansion of fuel pellets.

This hydride-assisted PCMI failure occurs only in the early stage of the transient when cladding surface temperature remains in the same level at the onset of the event. If the cladding survives this early phase, the behaviour proceeds to the late-phase, post-DNB process; then, cladding temperature increases rapidly and the ductility of the cladding increases. The data shown in Fig. 11 suggested that the cladding deformation was caused by the solid thermal expansion of pellets and fission-gas-induced pellet expansion was negligible in this early phase. The fission-gas-induced expansion is caused by thermal expansion of fission gas accumulated in fuel grain boundaries, and may have an important role on loading to the cladding only in the late phase.

Figure 11. Cladding residual hoop strain

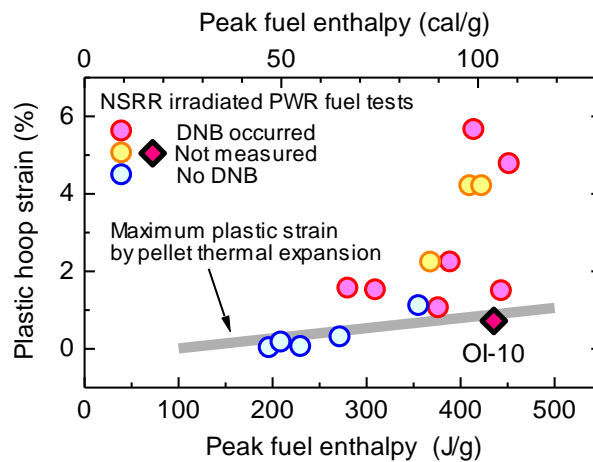
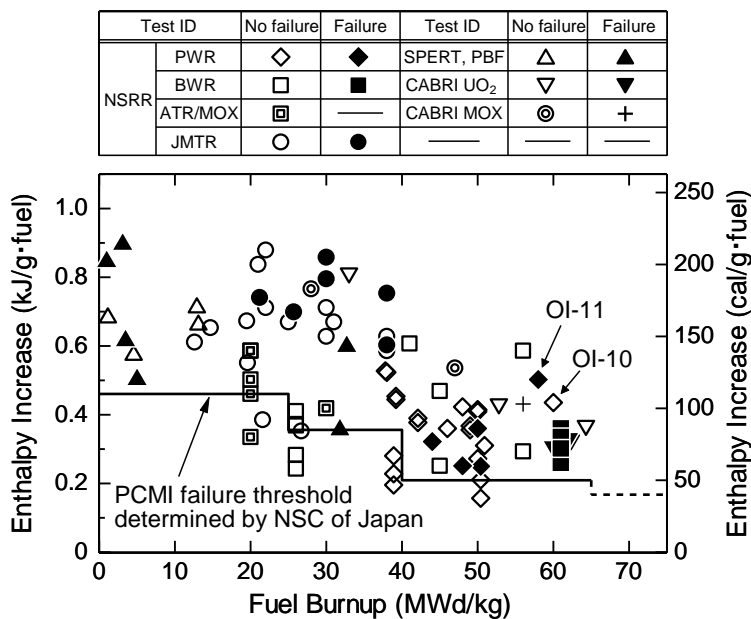


Figure 12 shows data of fuel enthalpy increases at failure as a function of burn-ups of tested fuel segments. A step function-like failure threshold defined in 1998 by Nuclear Safety Commission of Japan is shown in the figure.

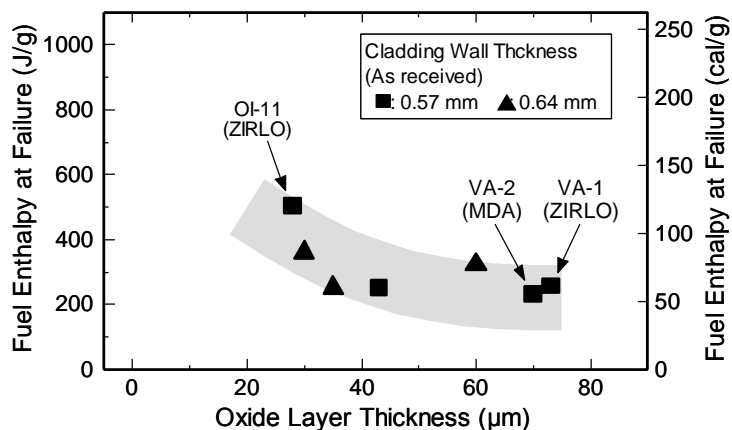
Figure 12. Burn-up dependent PCMI failure threshold



The enthalpy increase at a time of failure in the test OI-11 on a rod with ZIRLO cladding was much higher than those observed in previous tests with Zry-4 cladding in the same burn-up, about 60 MWd/kgU. The higher failure energy in the test OI-11 reflects the better performance of the new cladding materials in terms of corrosion, the thinner oxides and accordingly lower hydrogen content generated during irradiation in the PWR. It can be accordingly concluded that the rod with improved corrosion resistance have larger safety margin against the PCMI failure than conventional Zry-4 rods. Although a burn-up of the tested rod is much higher, 71 MWd/kgU, in the test VA-1, the enthalpy increase at failure was 64 cal/g (0.27 kJ/g) and remained in the same level comparing the data obtained in 50 to 60 MWd/kgU. The result suggests that high burn-up structure (rim structure) in pellet periphery does not have strong effect on reduction of the failure threshold because the PCMI load is produced primarily by solid thermal expansion.

Since the failure threshold formulated as a function of burn-up cannot reflect any improvements of fuel design, some proposals have made to describe the threshold with a different parameter. Figure 13 shows data of fuel enthalpies at failure from experiments on PWR fuels with SRA cladding as a function of cladding oxide layer thickness. The fuel enthalpy at failure correlates closely with the thickness of the hydride rim, and an amount of hydrogen introduced into the metal during a corrosion process is proportional to the oxide thickness. Accordingly, the fuel enthalpy at failure correlates well with the oxide layer thickness. It can be seen that the thinner oxide in the OI-11 results in the higher enthalpy at failure even with the high burn-up of 58 MWd/kgU. Although the ZIRLO sheathed rod tested in the VA-1 had a thick oxide layer of 73  $\mu\text{m}$ , the enthalpy at failure remained 64 cal/g which was at the same level with an oxide thickness of 40  $\mu\text{m}$ . The formulation of the threshold as a function of oxide thickness may offer an improvement in establishing a RIA failure threshold particularly for fuel designs with advanced cladding materials<sup>(13)</sup>. However, there is room for further improvement, since the formulation does not account for the other factors, e.g. hydrides distribution and orientation.

Figure 13. Fuel enthalpy at failure as a function of oxide layer thickness



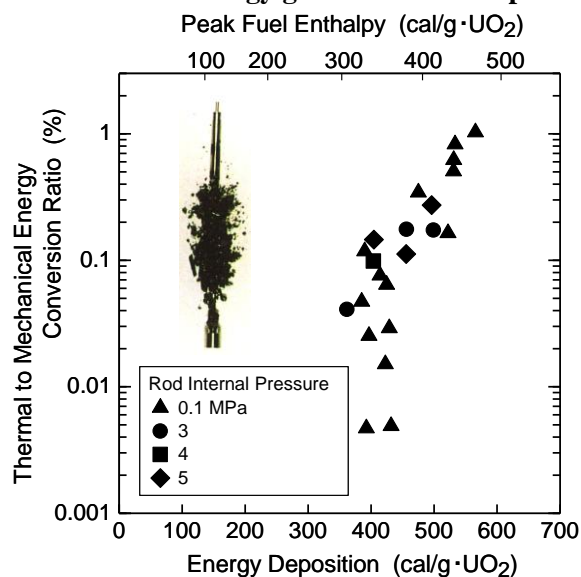
### 3. Fuel fragmentation and mechanical energy generation

Fuel fragmentation and mechanical energy generation occur when peak fuel enthalpy exceeds 285 cal/g (1.19 kJ/g) in the NSRR experiments with a fresh single-pin. Higher fuel enthalpy correlates with higher mechanical energy generated as shown in Fig. 14. Partial melting of pellets was always observed. In order to avoid incipient pellet melting, the Japanese regulatory guideline defines the absolute limit of maximum fuel enthalpy as 230 cal/g (0.96 kJ/g) in 1984. It is generally known that the pellet melting occurs at the lower temperature due to burn-up, additives, such as gadolinium, and Pu in MOX fuels. It was accordingly required that the reduction of the melting point was taken into the account for the absolute limit, when the NSC re-

13 Fuketa, T., Sugiyama, T. and Nagase, F., "Behavior of 60 to 78 MWd/kgU PWR Fuels under Reactivity-Initiated Accident Conditions", J. Nuclear Science and Technology, Vol.43, No.9, pp.1080-1088, (2006).

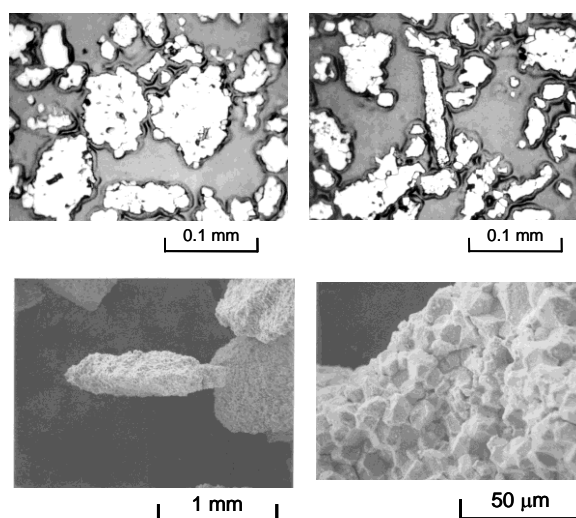
examined burn-up effects on RIA fuel behaviours and issued the regulatory report in 1998. As for the effect of burn-up on the melting point, the report noted that an assumption consisting of no reduction up to 30 MWd/kg and 3.2 degree/MWd/kg reduction above 30 MWd/kg was acceptable. It has been discussed that the assumption is overly conservative, but data regarding the melting point at higher burn-up are very limited for the moment.

Figure 14. **Mechanical energy generation due to pellet melting**



In NSRR experiments with high burn-up PWR and BWR fuels, which resulted in fuel failure, fuel pellets were dispersed from the rod, and were recovered as fragmented particles from capsule water after the experiment. Cross-sectional view and scanning electron microscopy images of the fragmented debris are shown in Fig. 15.

Figure 15. **Fuel particles collected after PCMI failure**



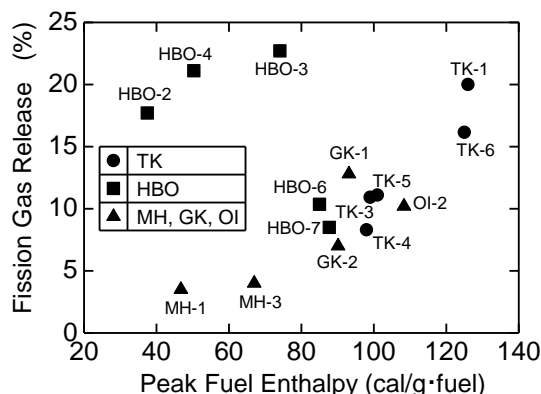
The appearance indicates that the collected fuel particles are not once molten, as can be expected from the low maximum fuel temperature (below ~2100 K in this case) during pulse irradiation. Although the fragmented particles remained in the solid phase, significant mechanical energy generations were observed in these experiments. The estimation of mechanical work due to rod internal gas release and expansion shows that the gas does not have enough potential to produce this level of mechanical energy. With an extreme assumption that

all of the rod internal gas reaches the maximum fuel temperature, gas internal energy is only limited, which is well below the mechanical energy generated. This suggests that rapid steam generation due to coherent thermal interaction of dispersed fuel fragments with coolant water is the primary source of the mechanical energy generated during the test. The postulated heat flux in this thermal interaction was compared with those in separate-effects experiments with powder fuels<sup>14</sup>, and the comparison corroborates that the heat flux in this process is realistic. In the current Japanese safety guideline, the mechanical energy generated in the PCMI failure is evaluated with a formula identical to that for mechanical energy produced by pellet melting.

#### 4. Fission gas release

After the pulse-irradiation experiments, rod-average fission gas release were measured for the test rods by rod puncture and gas analysis. The data are shown in Fig. 16 as a function of the peak fuel enthalpy. Except for HBO-2, -3, and -4, the higher fission gas release correlates with the higher peak fuel enthalpy. In HBO-2, -3, -4 and TK-1, the fission gas release reached ~20%, and this corresponds to all the fission gas accumulated in grain boundaries being released during these experiments. Rapid expansion of fission gas in grain boundaries causes grain boundary separation, and then results in fission gas release and fuel fragmentation. The experiments with the high fission gas release resulted in large rod deformation, except in HBO-2, -3, and -4. This fact indicates the significant role of fission gas in rod deformation. In HBO-2, -3, and -4, DNB did not occur, and cladding temperatures remained in low. (A transient signal from the thermocouple in HBO-3 showed ~670 K at maximum, but the duration of stable film boiling was very short and must have been limited to the local area.) Therefore, the significant role of fission gas in rod deformation appears only at high temperatures, where cladding ductility is enhanced.

Figure 16. Fission gas release (PWR/UO<sub>2</sub>) as a function of peak fuel enthalpy



The Japanese regulatory criteria do not formulate transient fission gas release during an RIA, because licensee's evaluations for fission gas release from pellets to rod internal gap during normal operations are conservative enough to encompass the transient release.

#### 5. Possible MOX effect

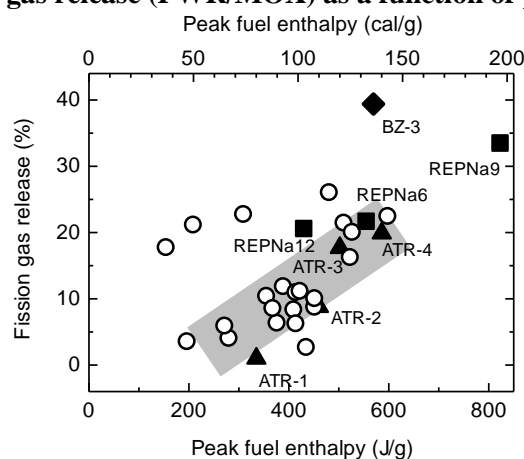
As stated previously, results from a series of the NSRR experiments on high burn-up LWR fuels show that the heavier corrosion of cladding during operations in nuclear power plants, in turn, the larger hydrogen absorption in cladding results in fuel failure at the lower enthalpy under RIA conditions. In particular, the thickness of hydride rim that appeared in high burn-up PWR fuel cladding, i.e. cladding peripheral layer containing dense hydride clusters, well correlates with fuel enthalpy at failure. Fuel enthalpies at failure in the two recent MOX

14 Sugiyama, T. and Fuketa, T., "Mechanical Energy Generation during High Burn-up Fuel Failure under Reactivity Initiated Accident Conditions", J. Nuclear Science and Technology, Vol.37, No.10, pp.877-886, (2000).

tests BZ-1 and -2<sup>15</sup> are consistent with a tendency derived from number of tests on UO<sub>2</sub> fuels, and indicate that any MOX effects do not appear regarding the PCMI failure. The threshold of fuel failure due to PCMI only depends on the cladding state with the PCMI loading dependent only on the pellet thermal expansion. Accordingly, the same failure limit is applicable to UO<sub>2</sub> and MOX fuels. Since the temperature escalation in an RIA is the most severe in pellet peripheral region, plutonium agglomerates uniformly distributed over MOX pellets may have weaker, negligible effect on the PCMI loading than high burn-up fuel structure.

On the other hand, data regarding the fission gas release indicate a possible MOX effect. The fission gas releases during PWR fuel experiments are plotted in Fig. 17 as a function of peak fuel enthalpy.

Figure 17. Fission gas release (PWR/MOX) as a function of peak fuel enthalpy



Data from NSRR experiments on ATR/MOX fuels<sup>16</sup> and REP-Na experiments<sup>17,18</sup> performed in sodium loop of French CABRI reactor are included in the figure. It can be seen that the fission gas releases of PWR fuels correlate with the maximum increase of fuel enthalpy. The ATR/MOX fuels have a homogeneous microstructure similar to that in SBR/MOX fuels, and the fission gas releases from the ATR fuels remain in the same level of those from UO<sub>2</sub> fuels. The MIMAS/MOX fuels tested in the REP-Na experiments and the most recent test BZ-3, on the other hand, show the larger fission gas releases. In particular, the fission gas release of 39.4% in the test BZ-3 is significantly large in comparison with those in tests on UO<sub>2</sub> fuels, even if one takes into consideration the initial fuel enthalpy of 70 J/g (17 cal/g) in the experiment started from a coolant condition of 281 deg C. The highest fission gas release among each UO<sub>2</sub> fuel ranged from 20 to 30% in the previous NSRR experiments, and it is generally accepted that the fission gas release achievable in an RIA-simulating test corresponds to the total amount of accumulated fission gas in grain boundaries. In the MIMAS procedure, a mother blend of uranium/ plutonium mixed oxide is added to natural or depleted UO<sub>2</sub>. Pelletizing and sintering of this powder mixture create an heterogeneous final product with mixed oxide (U,Pu)O<sub>2</sub> agglomerates embedded in the matrix of natural or depleted UO<sub>2</sub>. During operation cycles in a nuclear power plant, the fission occurs in the agglomerates which reach very high burn-ups compared to the burn-up averaged over the pellet. In the MIMAS/MOX fuels, a large amount of fission gas is accumulated in the Pu agglomerates, and in turn gives the large fission gas release during the RIA transient. It should be noted that further investigation is needed regarding gas inventories in the grain boundaries and in the Pu agglomerates in order to promote a better understanding of the fission gas release from MOX fuels.

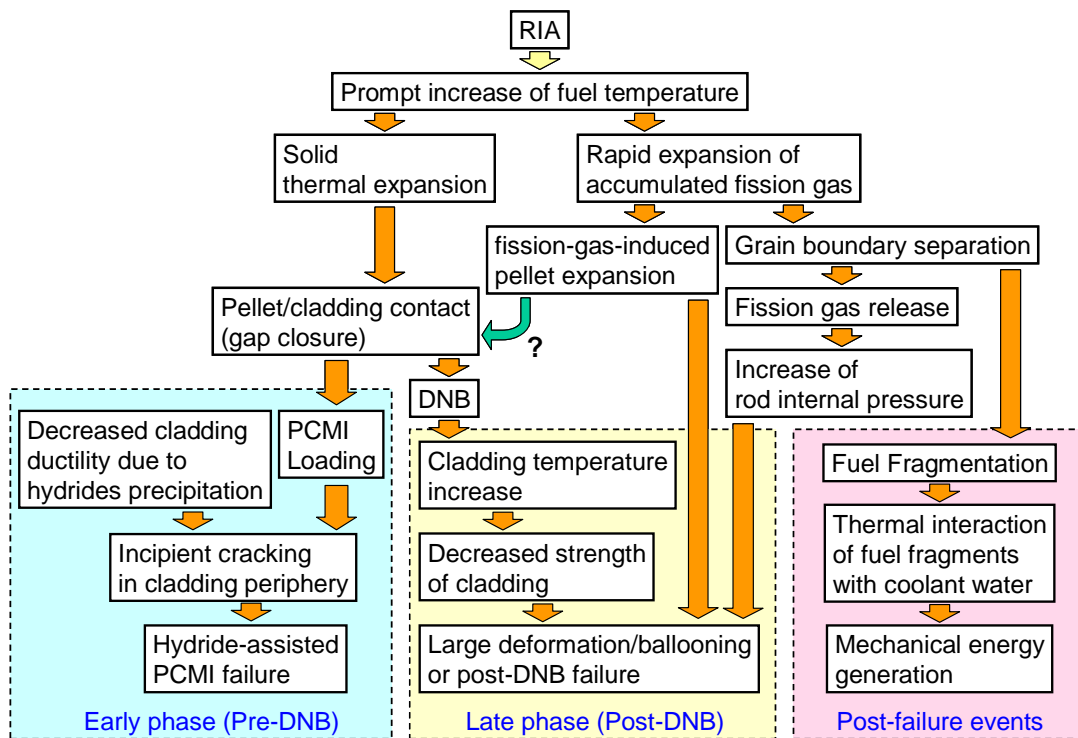
- 15 Fuketa, T., Sugiyama, T., Umeda, M., Sasajima, H. and Nagase, F., "Behavior of LWR/MOX Fuels under Reactivity-Initiated Accident Conditions", Paper 2083, TopFuel 2009, Sept. 6-10, 2009, Paris, France, (2009).
- 16 Sasajima, H., Fuketa, T., Nakamura, T., Nakamura, J. and Kikuchi, K., "Behavior of Irradiated ATR/MOX Fuel under Reactivity Initiated Accident Conditions", J. Nuclear Science and Technology, 37, 5, 455 (2000).
- 17 Schmitz, F. and Papin, J., "High Burn-up Effects on Fuel Behaviour under Accident Conditions: the Tests CABRI REP-Na", J. Nuclear Materials, Vol.270, pp.55-64, (1999).
- 18 Papin, J., "The Cabri Research Program for Study of Reactivity-Initiated Accidents", Scientific and Technical Report 2002, Institut de Radioprotection et de Sûreté Nucléaire, (2002).

**6. Summary**

Two failure modes can be observed with fresh rods. Both occur after cladding temperature escalation due to an occurrence of DNB. In case with a high rod internal pressure, ballooning and rupture is the mode, and a failure threshold in terms of fuel enthalpy depends on the pressure. In case with a low internal pressure, fuel fails due to severe oxidation of cladding in combination with a partial melting at a relatively high enthalpy level. Fuel fragmentation and mechanical forces generation is observed with a very high fuel enthalpy resulting in partial melting of pellets.

A pre-DNB failure, PCMI failure, is observed with high burn-up PWR and BWR fuel rods. Test rods with thicker oxide layer, higher hydrogen concentration, failed at a lower fuel enthalpy. The results indicate that the critical factor is whether cladding has enough ductility to survive until the time that cladding temperature reaches a certain level. Hydride rim, radially-localised hydride layer, in PWR/SRA cladding and radially-oriented hydride clusters in BWR/RXA cladding have important roles in failure of high burn-up fuels. In experiments resulting in the PCMI failure, fuel fragmentation and mechanical energy generation were observed as post-failure events. Collected fuel particles were not previously molten. The results indicate coherent thermal interaction between the particles and coolant water. Grain boundary separation was observed in extensive area of post-test fuel pellets. The separation can cause large fission gas release and post-failure fragmentation. PCMI load can be explained only by solid thermal expansion of pellets, but a role of fission gas in RIA fuel behaviour remains an important pending question as shown in Fig. 18.

Figure 18. Anticipated fuel behaviour during an RIA



## Current RIA-related Regulatory Criteria in Japan and Their Technical Basis

Toyoshi FUKETA and Tomoyuki SUGIYAMA  
Nuclear Safety Research Center  
Japan Atomic Energy Agency

OECD/NEA Workshop on  
Nuclear Fuel Behaviour during Reactivity Initiated Accidents  
OECD Headquarters, Paris, France  
September 9 - 11, 2009

**Introduction**

This presentation aims to provide a general outline of fuel behaviour during a reactivity-initiated accident postulated in light water reactors and to show experimental data providing technical basis with the current RIA-related regulatory criteria in Japan.

- Cladding failure
  - Thermal failure (Post-DNB)
  - Mechanical failure (Pre-DNB)
- Post-failure events (with and without pellet melting)
  - Fuel fragmentation
  - Mechanical energy generation
- Fission gas release

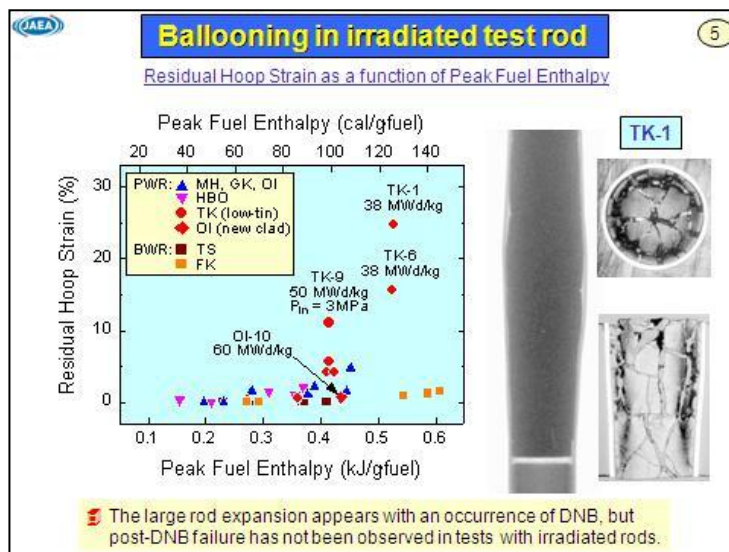
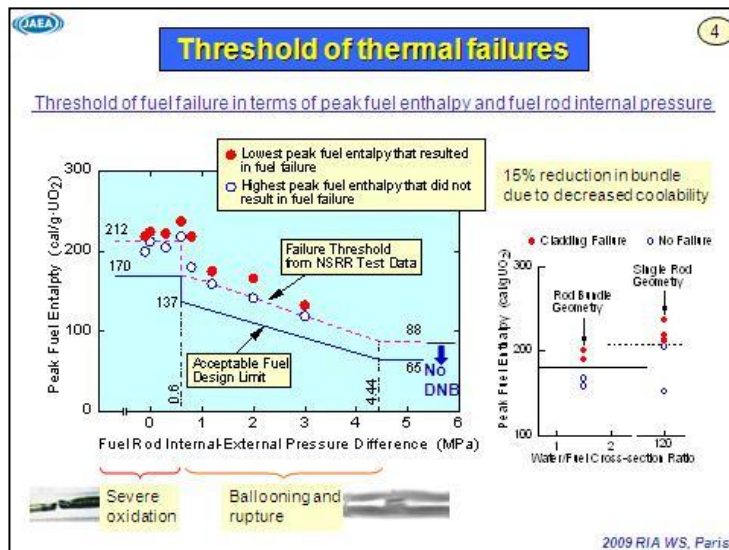
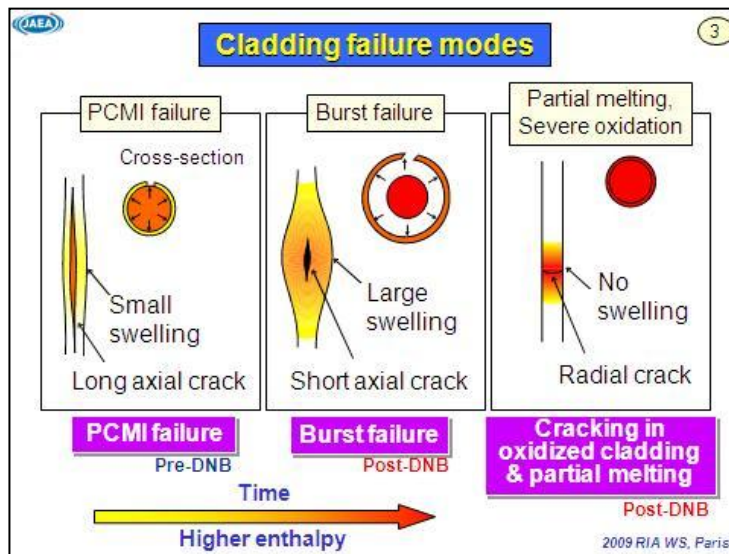
2009 RIA WS, Paris

**Cladding failure modes**

```

    graph TD
      RIA[RIA] --> Temp[Prompt increase of fuel temperature]
      Temp --> Swelling[Fuel pellet swelling]
      Swelling --> PCMI[PCMI]
      PCMI --> Ductility[Decreased cladding ductility]
      Ductility --> PCMI_Failure[PCMI failure]
      PCMI --> Temp2[Increase of cladding temperature]
      Temp2 --> FGR[Fission gas release]
      FGR --> Burst[Burst]
      Temp2 --> Oxidation[Oxidation and/or melting of cladding]
      Oxidation --> Cracking[Cracking in severely oxidized cladding and partial melting]
    
```

2009 RIA WS, Paris



**Hydride-assisted PCMI Failure** 6

PWR

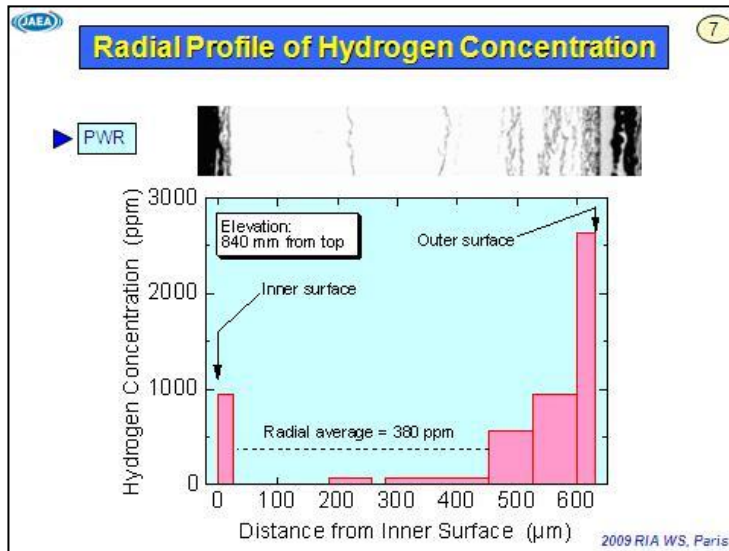
Oxide Layer

Hydride Clusters

Brittle Fracture

Ductile Fracture

A brittle fracture appears in the cladding peripheral region where dense hydride clusters have precipitated, and the crack propagates to inside.



**Stress concentration at a tip of incipient crack** 8

Through-wall crack

Incipient crack

Oxide-layer

Hydride rim

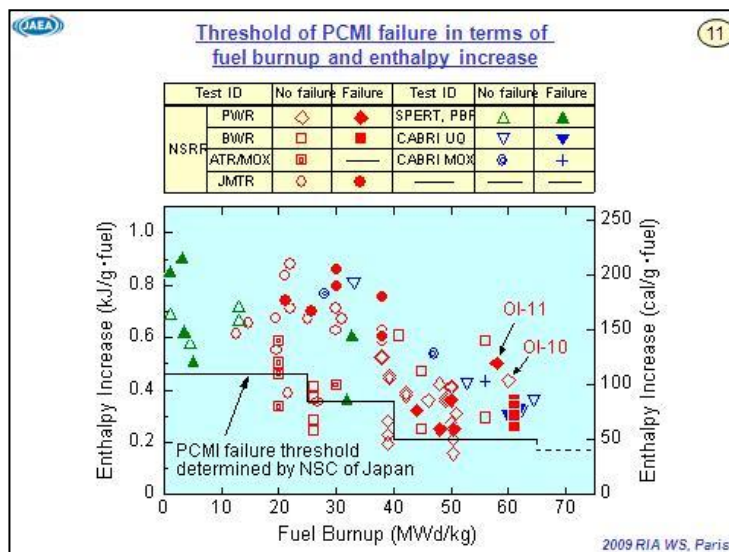
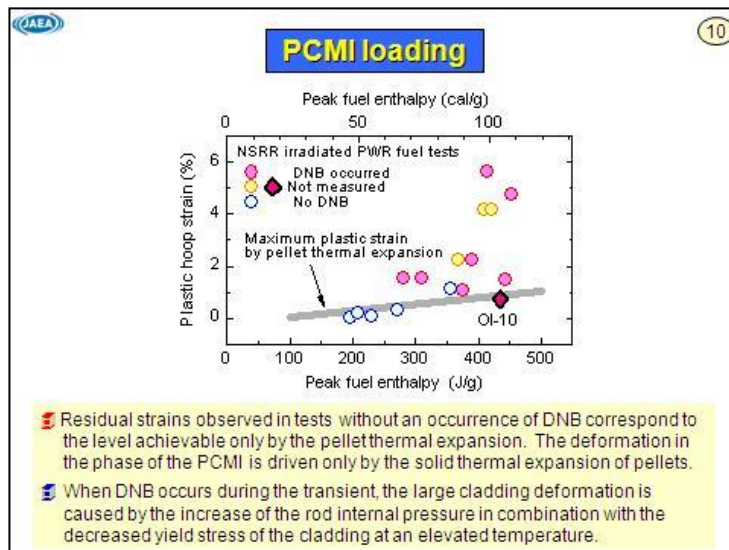
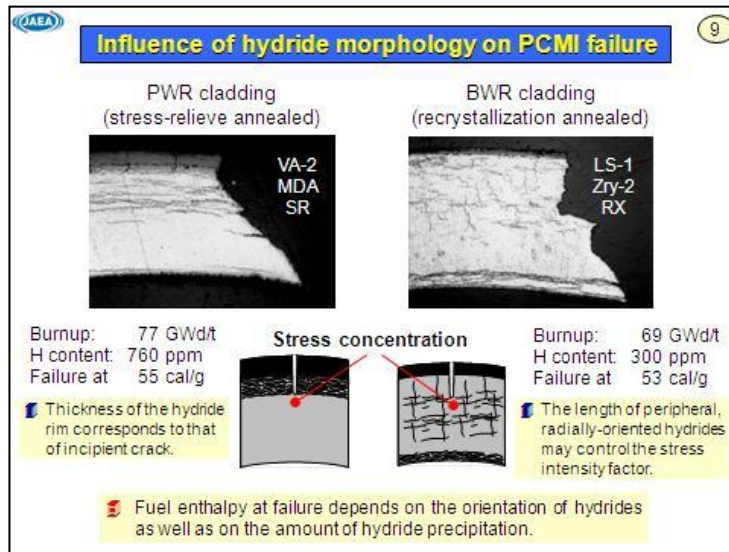
The incipient cracks penetrate the oxide layer and a layer with high concentrations of hydride precipitates, 'hydride rim'.

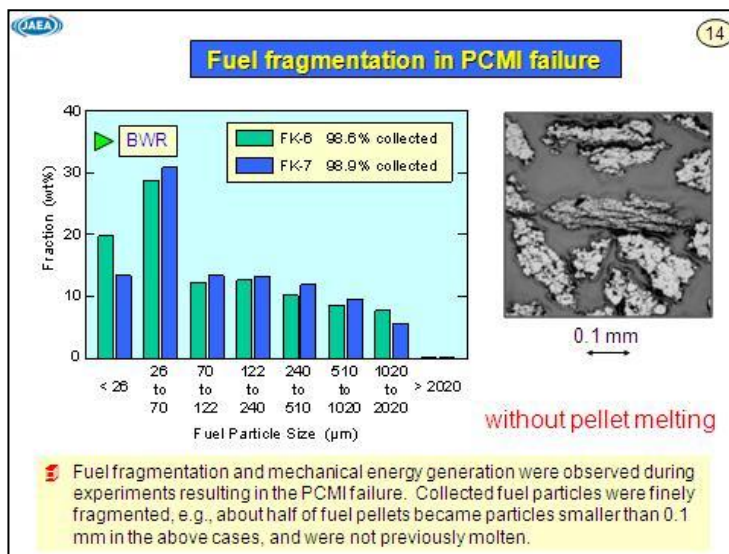
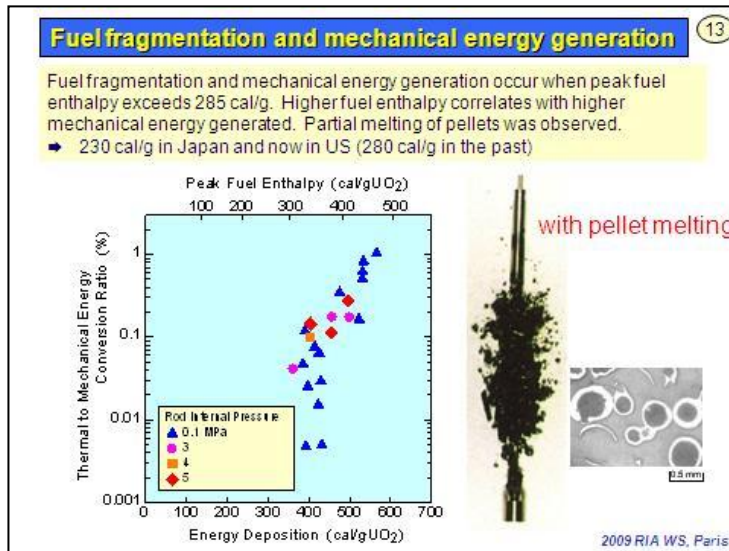
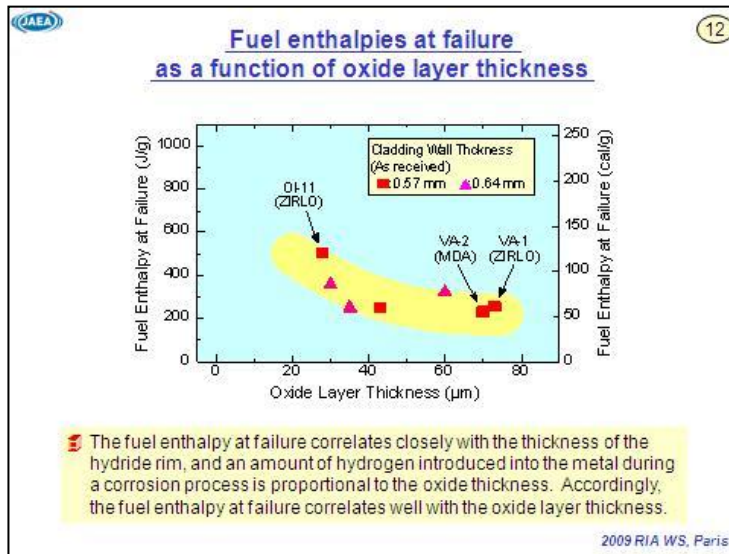
Stress concentration

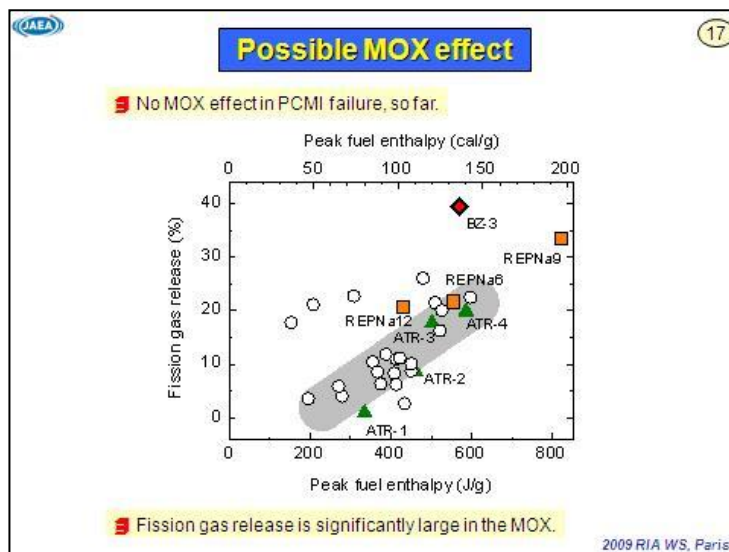
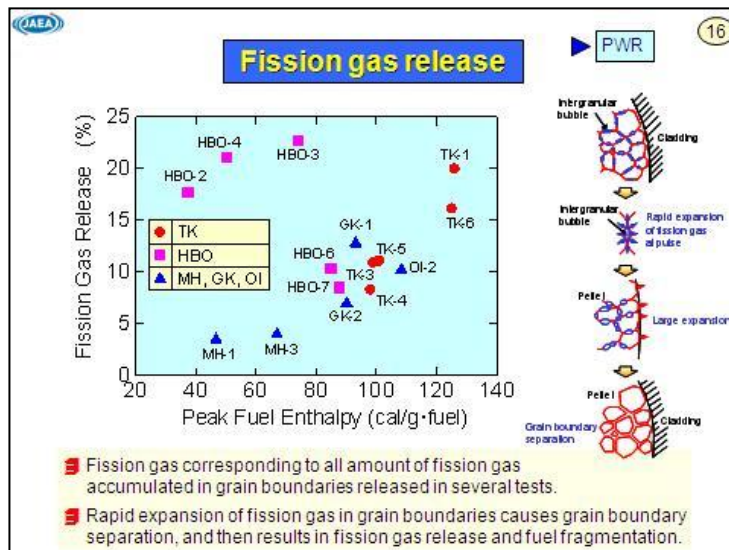
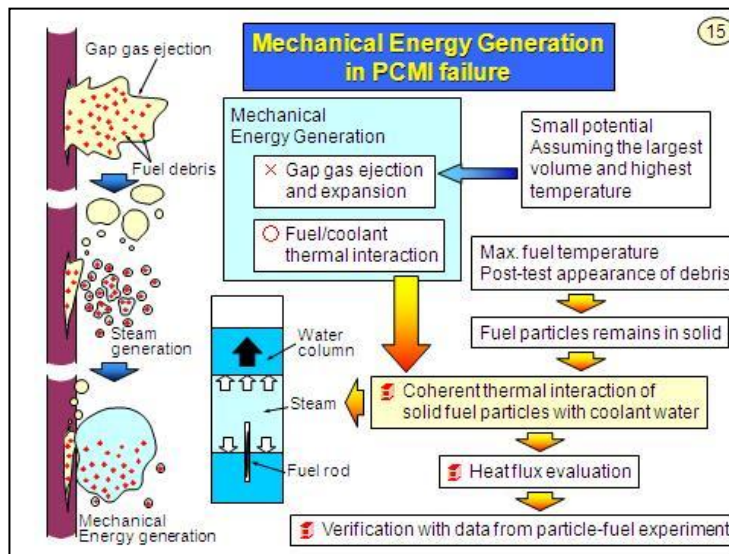
A stress concentration at a tip of the incipient cracks drives the crack propagation to the inner part.

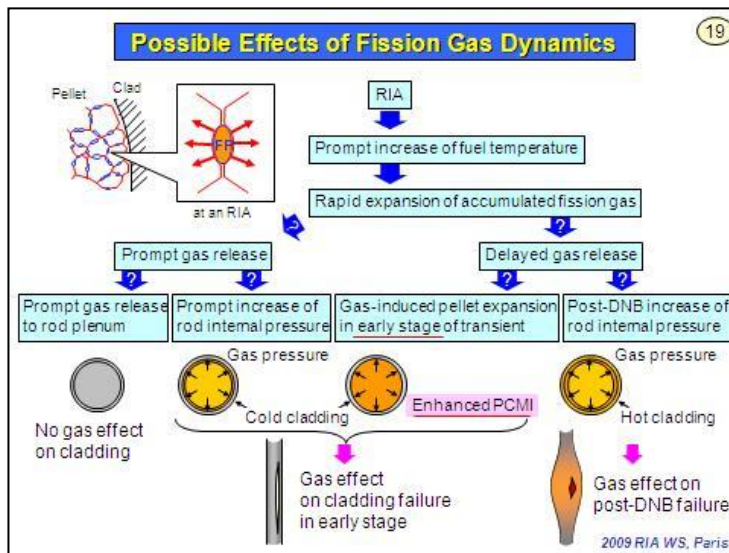
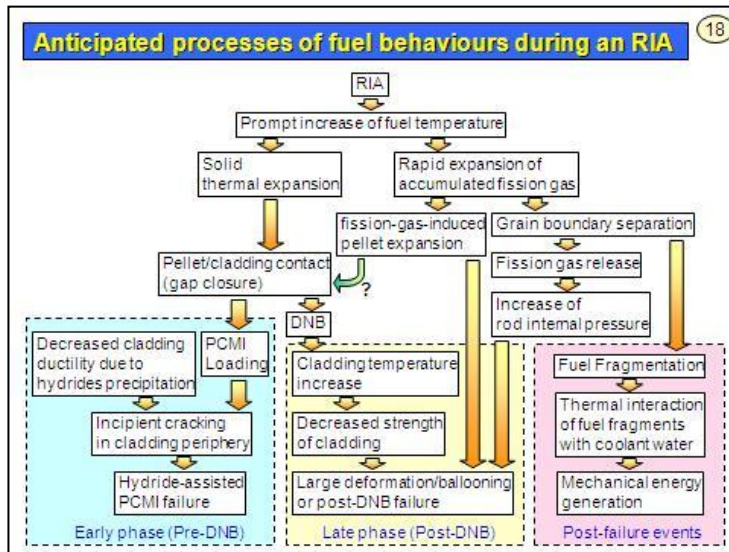
Since the oxide layer has a negligibly low tensile strength, the thickness of the hydride rim controls the stress intensity factor.

2009 RIA WS, Paris









**Summary** 20

- 1/2 -

- ❏ Two failure modes can be observed in tests with fresh rods. Both occur after cladding temperature escalation at an onset of DNB. In case with a high rod internal pressure, ballooning and rupture is the mode, and a failure threshold in terms of fuel enthalpy depends on the rod internal-external pressure difference. In case with a low internal pressure, fuel fails due to severe oxidation with partial melting of cladding at a high enthalpy level.
- ❏ A pre-DNB failure, PCMI failure, is observed with high burnup PWR and BWR fuel rods. Test specimens with thicker oxide layer, higher hydrogen concentration, failed at a lower fuel enthalpy. The results indicate that the critical factor is whether cladding has enough ductility to survive until the time that cladding temperature reaches a certain level.
- ❏ Hydride rim (radially-localized hydride layer) in SRA cladding and radially-oriented hydride clusters in RXA cladding have an important role in failure of high burnup fuels.

2009 RIA WS, Paris

 **Summary** 21

- 2/2 -

-  Fuel fragmentation and mechanical forces generation were observed at a very high fuel enthalpy resulting in partial melting of pellets.
-  Mechanical energy generated also in experiments resulting in the PCMI failure of high burnup fuels. Collected fuel pellets were finely fragmented, and were not previously molten. The results indicate an occurrence of coherent thermal interaction between the fine particles and coolant water.
-  Grain boundary separation was observed in extensive area of post-test high burnup fuel pellets. The separation can cause large fission gas release and post-failure fragmentation.
-  PCMI load can be explained only by solid thermal expansion of pellets, but a role of fission gas in RIA fuel behaviour remains an important pending question.

2009 RIA WS, Paris

## REGULATORY ANALYSIS OF REACTIVITY TRANSIENTS

**C. E. Beyer**

Pacific Northwest National Laboratory, USA

**K. J. Geelhood**

Pacific Northwest National Laboratory, USA

### 1. Introduction

This paper will describe modifications made to the FRAPCON-3 and FRAPTRAN fuel performance codes and models that impact reactivity initiated accident (RIA) analyses. The modified models include; 1) an upper bound empirical and best estimate release models for radioactive isotopes for fast transients, and 2) a revised cladding failure model that accounts for ductile and brittle failure. Because experimental data exists for discrete test conditions, the codes and models are used to interpolate and to some extent, to extrapolate these test conditions. An upper bound empirical model for release is used to establish new recommended release fractions for long-lived and short lived (radioactive) isotopes for RIA events. These bounding fission product inventory gap fractions will be included in the forthcoming Draft Guide (DG) 1199 to be published by the USNRC. The public is invited to comment on the proposed analysis methodology and gap fractions in DG-1199 during the upcoming public comment period. A best estimate release model is also used in FRAPTRAN 1.4 based on grain boundary gas concentrations from FRAPCON-3.4 to predict release for RIA events. Code and model predictions will be compared to failure and release data from RIA tests to demonstrate accuracy.

The release models for RIA analyses will be discussed, followed by the revised cladding failure model.

### 2. Fast transient (RIA) release models

The release of radioactive isotopes from a failed fuel rod during a RIA event is divided into long-lived (greater than 1 year half-life) and short lived isotopes (less than 1 year half-life). The total release of radioactive isotopes used for dose evaluations should include the steady-state gap inventory (present from normal operation prior to the RIA event) plus any fission gas released (FGR) during the RIA event. Therefore, the release is further divided into the gases released during steady-state operation and those gases released during the event itself due to the large temperature increase. The release of long-lived isotopes during steady-state and the RIA event will be discussed first followed by a discussion of release of the short-lived isotopes.

#### *2.1. RIA release of long-lived isotopes*

The release of long-lived isotopes during steady-state operation (i.e., krypton-85, cesium-134, and cesium-137) can be conservatively estimated with most fuel performance codes that predict the release of the stable noble gases. This assumes the release of the long-lived isotopes is equal to the release of the stable isotopes and using the recommended increase in diffusion coefficient for cesium-134 and cesium-137 of a factor of 2 compared to the noble gases release provided in the latest proposed ANS 5.4 standard. Bounding release values have been calculated for the noble gases and long-lived cesiums and provided in the latest recommended updates to gap release fractions for RIA events. These calculations have been done

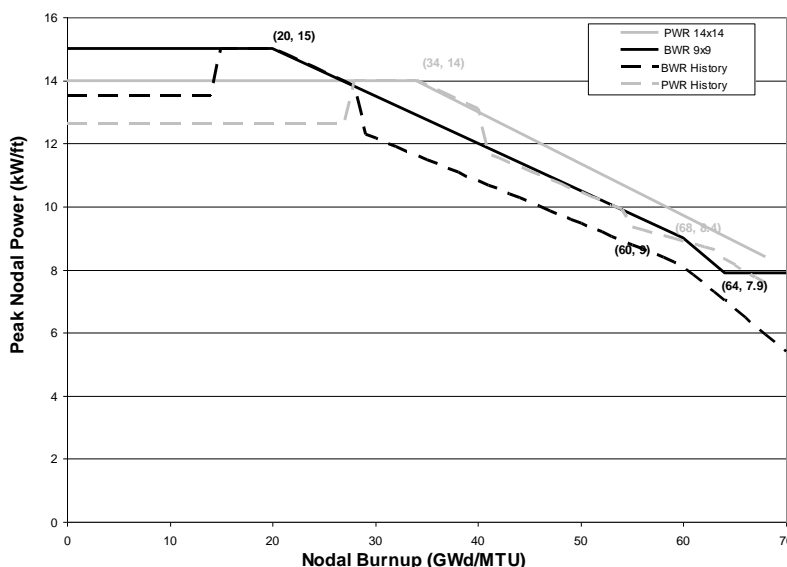
using the FRAPCON-3.3<sup>1</sup> fuel performance code for the most limiting of current PWR and BWR fuel designs (14x14 and 9x9, respectively) in terms of release and the guidance in the newly proposed ANS 5.4 standard<sup>2</sup>; the calculational results are presented in Table 1. A bounding spectrum of PWR power histories were used with partial power operation at an LHGR limit of 14 kW/ft up to 34 GWd/MTU (peak nodal burn-up). A bounding spectrum of BWR histories were used with partial power operation up to six months time at different points in the irradiation at an LHGR limit of 15 kW/ft up to 20 GWd/MTU (peak nodal burn-up). Example bounding histories used for PWR and BWR calculations are demonstrated in Figure 1. The highest release for the long-lived isotopes always occurred at or near the end-of-life (peak nodal burn-up of 68 GWd/MTU for PWRs and 70 GWd/MTU for BWRs) assumed for this calculation. Utilising the bounding power histories the stable release fractions were calculated to exceed the 0.10 fraction recommended in the current U.S. regulatory guides for a RIA event. This demonstrated the need to update the current regulatory guide for RIA events.

Table 1. PWR and BWR fuel rod peak gap release fractions, R/B, based on peak values from bounding power histories<sup>†</sup>

Isotope	Gap release fractions - 95/95 UTL			Current RG 1.183 table 3
	Calculated PWR 14x14 design	Calculated BWR 9x9 design	Maximum	
Kr-85	0.348	0.257	0.35	0.10
I-131	0.073	0.036	0.08	0.08
I-132	0.225	0.111	0.23	0.05
Other nobles	0.031	0.016	0.04	0.05
Other halogens	0.042	0.021	0.05	0.05
Alkali metals	0.457	0.336	0.46	0.12

<sup>†</sup>Gap fractions for non-LOCA events with exception of RIA events

Figure 1. Assumed PWR and BWR rod linear heat generation limits (solid lines) versus burn-up along with example assumed power history (dashed lines) used for FRAPCON-3.3 calculation of release



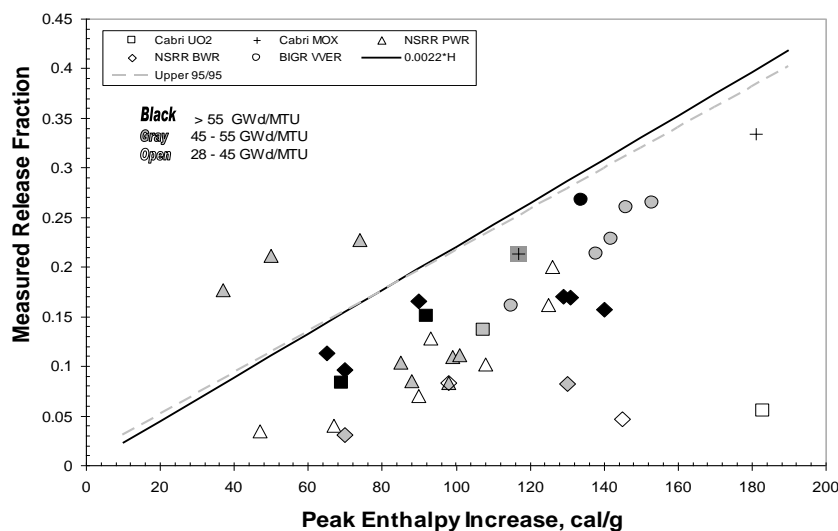
The release of long lived isotopes during a RIA event is based on stable noble gas release data from simulated RIA tests on PWR, BWR, and VVER test rods (shortened rod segments from actual commercially irradiated

<sup>1</sup> Lanning, D.D., C.E. Beyer, and K.J. Geelhood. 2005, *FRAPCON-3 Updates, including Mixed Oxide Properties*, NUREG/CR-6534 (PNNL-11513) Vol. 4, U.S. Nuclear Regulatory Commission, Washington D.C.

<sup>2</sup> Turnbull, J.A. and C.E. Beyer, *Background and Derivation of ANS-5.4 Standard Fission Product Release Model*, PNNL-18490, Pacific Northwest National Laboratory, Richland, WA.

rods) collected from tests in the CABRI<sup>3</sup>, NSRR<sup>4,5,6,7</sup>, and BIGR<sup>8</sup> test reactors. These release data for stable isotopes are plotted in Figure 2 as a function of enthalpy increase that demonstrates a strong dependence of release on peak enthalpy increase. The release of stable noble gases in this figure applies to the long-lived krypton-85 isotope and demonstrates that above an enthalpy increase of ~ 90 cal/gm some of the stable isotope release exceeds the recommended 0.10 fraction for RIA in the U.S. NRC regulatory guides (Regulatory Guides 1.183<sup>1</sup> and 1.77<sup>9</sup>). In addition, the release in Figure 2 is only the fraction of gas released during the RIA transient and does not include the release during normal operation (discussed above). It is noted that some of the BWR rod segments tested had local releases greater than 20% fission gas release (FGR) during their base irradiation and this did not appear to impact (reduce or increase) the release during the simulated test RIA event. The release fractions provided in Figure 2 are relative to the total gas produced in the fuel. Therefore, a new recommended release values will be provided in this paper to replace the value of 0.10 for krypton-85 and 0.12 for cesium-134 and cesium-137 specified in Regulatory Guides 1.77 and 1.183.

Figure 2. **Stable fission gas release data as a function of peak fuel enthalpy increase from simulated RIA tests in CABRI, NSRR, and BGR test reactors**



The pulse widths from these different test reactors varied considerably with the CABRI tests having the widest pulse width between 9 to 76 millisecond (ms), the NSRR tests between 4 to 7 ms, and the BGR

<sup>3</sup> Lemoine, F., J. Papin, J. Frizonnet, B. Cazalis, and H. Rigat, "The Role of Grain Boundary Fission Gases in High Burn-Up Fuel Under Reactivity Initiated Accident Conditions," Fission Gas Behavior in Water Reactor Fuels - Seminar Proceedings Cadarache France, 26-29 September 2000.

<sup>4</sup> Fuketa, T., H. Sasajima, Y. Tsuchiuchi, Y. Mori, T. Nakamura, and K. Ishijima, "NSRR/RIA Experiments with High Burn-up PWR Fuels," Proceedings of 1997 International Topical Meeting on Light Water Fuel Performance, Portland, Oregon, March 2-6, 1997.

<sup>5</sup> Fuketa, T., T. Sugiyama, H. Sasajima and F. Nagase, "NSRR RIA-simulating Experiments on High Burn-up LWR Fuels," Proceedings of the 2005 Water Reactor Fuel Performance Meeting, Kyoto, Japan, pp. 633-645, October 2-6, 2005.

<sup>6</sup> Nakamura, T., M. Yoshinaga, M. Takahashi, K. Okonogi, and K. Ishijima, "Boiling Water Reactor Fuel Behavior Under Reactivity-Initiated-Accident Conditions at Burn-up of 41 to 45 GWd/tonne U," *Nuclear Technology*, Vol. 129, pp 141-151, February 2000.

<sup>7</sup> Nakamura, T., K. Kusagaya, T. Fuketa and H. Uetsuka, "High-Burn-up BWR Fuel Behavior Under Simulated Reactivity-Initiated Accident Conditions," *Nuclear Technology*, Vol. 138, pp 246-259, June 2002.

<sup>8</sup> Yegorova, L. et al, *Experimental Study of Narrow Pulse Effects on the Behavior of High Burn-up Fuel Rods with Zr-1%Nb Cladding and UO<sub>2</sub> Fuel (VVER Type) under Reactivity-Initiated Accident Conditions: Program Approach and Analysis of Results*, NUREG/IA-0213, Vol. 1, May 2006.

<sup>9</sup> Regulatory Guide 1.77, Assumptions Used for Evaluating a Control Rod Ejection Accident for Pressurised Water Reactors, May 1974.

tests having the shortest pulse width of 2 to 3 ms. Examination of the data in Figure 2 in terms of pulse width reveals that pulse width does not appear to have a large influence on FGR between ~ 2 to 76 ms and that release primarily increases with increasing enthalpy. Also, power history and fuel burn-up may have an impact on release but the scatter in the data does not allow a definitive empirical relationship to be established. However, the FRAPCON-3.4 and FRAPTRAN 1.4<sup>10</sup> codes have been shown to provide a better prediction for a given power history and burn-up level than the empirical model (see discussion below). The release fractions are from test rods with very short fuel lengths such that the enthalpy increases and release values can be considered to be local rather than for a full-length LWR fuel rod.

An upper 95/95 tolerance level (empirical) curve is presented in Figure 2 that bounds the RIA release data with the exception of three data points from NSRR tests of PWR segmented rods. The upper tolerance curve does not intercept the origin (a small positive release of 0.01 at zero enthalpy increase); consequently, a slightly different relationship than the 95/95 tolerance curve is recommended that passes through the origin such that release fraction for long-lived isotopes can be bounded by the relationship:

$$F(\text{stable}) = 0.0022 * \Delta H$$

where  $\Delta H$  is the enthalpy increase in cal/gm

This relationship provides a zero release at zero enthalpy increase.

The three short fuel test rods that are not bounded by the 95/95 curve are HBO-2, HBO-3, and HBO-4. These three test rods were refabricated from the same full-length PWR rod and then RIA tested in NSRR. The Japan Atomic Energy Research Institute (JAERI) papers and reports on these tests note that the release data from these three HBO specimens were anomalous compared to the rest of the release data from the NSRR tests. It should be noted that they are also anomalous to the remainder of the 32 other RIA FGR data in Figure 2. These JAERI reports noted that the fuel fabrication process for HBO-2, -3, and -4 rods was different (labeled as Type-A fuel) than the rest of the HBO test series (labeled as Type-B fuel), but the Type-A fuel was used in some of the TK series test rods. For example, the TK-4 rod had Type-A fuel with similar burn-up of 50 GWd/MTU but peak enthalpy was over twice as high for TK-4 as for HBO-2 (98 cal/gm versus 37 cal/gm, respectively), thus suggesting that TK-4 should have significantly higher FGR. However, the FGR in HBO-2 was more than twice as high FGR as TK-4 (17.7 versus 8.3). This suggests that some unknown phenomenon caused higher FGR in HBO-2.

It has also been hypothesized that the higher FGR of the HBO-2, -3, and -4 rods may be due to their base irradiation (commercial reactor) powers being different from the other fuel rods in Figure 2 at equivalent burn-up levels. However, examination of reported histories for both TK-4 and HBO-2 test specimens demonstrated that they had similar base irradiation power histories. Therefore, base irradiation power histories do not appear to explain the high release in the HBO-2, -3, and -4 rods unless there are errors in the base irradiation powers. Consequently, there is no clear explanation for why the HBO Type A fuel experienced significantly higher FGR than any other RIA tests performed in CABRI, NSRR (including other NSRR tests with Type-A fuel), and BGR at low fuel enthalpies.

Further examination of Figure 2 also shows that two NSRR BWR specimens and one CABRI PWR specimen had significantly lower release than the majority of the other test rods. The largest deviation was from a PWR CABRI test rod (REP Na-2) with the lowest burn-up level (33 GWd/MTU) of the UO<sub>2</sub> test rods. The two NSRR BWR test rods (FK-1 and FK-3) were at relatively low burn-ups of 45 to 41 GWd/MTU, respectively. A qualitative theory of fission gas release can partially explain the lower release for these test rods based on increasing interconnected fission gas bubbles on grain boundaries with increasing burn-up. The fission gas release from the RIA test rods appears to be from the fracturing of the grain boundaries within the high burn-

<sup>10</sup> Geelhood, K.J., C.E. Beyer, and W.G. Luscher. 2009. "New Release of Fuel Performance Codes, FRAPCON-3.4 and FRAPTRAN 1.4, *Proceedings of Top Fuel 2009*, Paris, France, September 6-10, 2009.

up fuel rim and main body of the fuel and not due to diffusion during the RIA tests. These lower burn-up fuel rods have little or no fuel rim and have less grain boundary gas in the main body of the fuel. Therefore, the lower burn-up fuel will have less grain boundary gas than the higher burn-up fuel with the latter having more inventory for release during the RIA. It is further noted that the low burn-up (only 28 GWd/MTU) mixed oxide fuel (MOX) test rod from CABRI (REP Na-9) was within the release amounts of the higher burn-up UO<sub>2</sub> test rods. This can be explained by the bubble interconnection process, which appears to occur in MOX (in the PuO<sub>2</sub> rich particles) at much lower burn-ups than for UO<sub>2</sub><sup>3</sup>.

The newly released FRAPCON-3.4 code predicts the grain boundary gas as a function of burn-up more accurately than FRAPCON-3.3. The newly released FRAPTRAN 1.4 code utilises this boundary gas from FRAPCON-3.4 to predict the gas release during a RIA event. A comparison of release predictions from FRAPCON-3.4/FRAPTRAN 1.4 to four Cabri UO<sub>2</sub> rods (Na-2, Na-3, Na-4 and Na-5), four NSRR PWR rods (HBO-6, OI-2, MH-3 and GK-1), and two NSRR BWR rods (FK-1 and TS-5) demonstrates that this code combination provides a better prediction than a best estimate empirical (least squares) fit based only on fuel enthalpy increase. All of the best estimate code predictions are closer to the measured release values but the difference between the code predictions and a best estimate empirical model is only 1 to 3% release (absolute). For example, the NSRR OI-12 test rod measured 10.2% FGR while the code prediction was 10.35% and the empirical model predicted 13.3%. The exception to this is the Cabri Na-2 rod with a low burn-up (33 GWd/MTU) and high enthalpy (183 cal/gm) where the best estimate code model provided a significantly better prediction. For example, the best estimate empirical model provided an overprediction of 20% release (absolute) while FRAPCON-3.4/FRAPTRAN 1.4 predicted the release within less than 1% release (absolute) of the measured value. The remaining 23 Cabri, NSRR and BWR test rods, where base steady-state power histories are known, will be used in the future to further verify FRAPCON-3.4/FRAPTRAN 1.4 predictions of release during a RIA event. It is concluded that the bounding 95/95 empirical model is adequate for determining release values for licensing analyses but the FRAPCON-3.4/FRAPTRAN-1.4 code predictions may provide a better best estimate predictions for a specific fuel rod and RIA event.

There are no release data for the cesium, iodine, or short-lived noble gas isotopes from the RIA test rods. Therefore, their release fractions are estimated from the bounding relationship for stable noble gases and krypton-85 above. The release of the long-lived cesium isotopes (cesium-134 and cesium-137) can be estimated utilising the ANS 5.4 standard recommendation by assuming that cesium has a factor of 2 higher diffusion co-efficient than the noble gases. Because diffusional release is approximately proportional to the square of the diffusion coefficient, it is assumed that the cesium on the grain boundaries available for release during a RIA is proportional to the square root of the ratio of cesium-to-noble gas diffusion coefficients. The bounding release fraction for the long-lived cesium isotopes can be expressed as:

$$F(\text{cesium}) = 0.0022 * \Delta H * (2)^{0.5} = 0.0031 * \Delta H$$

where  $\Delta H$  is the enthalpy increase in cal/gm.

## ***2.2. RIA release of short-lived isotopes***

The iodine-131 short-lived isotope is the major contributor (>95%) that determines the level of dose in terms of release from the fuel. This is because iodine contributes a significant dose to the thyroid in terms of dose limits and iodine-131 is the longest lived of the iodine isotopes. There are no release data for the short-lived isotopes including iodine-131 for a RIA event, only release data for the stable noble gases exist; therefore, the short-lived isotope releases must be estimated from the stable noble gas release data and the newly proposed ANS 5.4 release model. For short-lived isotopes, the equilibrium release fraction is defined as R/B where R is the equilibrium release rate (e.g., atoms/sec) calculated assuming diffusional release at a given temperature (rod power) and B (atoms/sec) is the production rate at that rod power. The equilibrium diffusional release is achieved when the fuel temperature (rod power) remains relatively constant for 3 half-lives of the release isotope in question. For short lived isotopes, the shorter the half-life of the isotope the smaller the value of release, R/B, for a given fuel temperature. This is because the gas is held-up in the fuel until it diffuses to the

boundary where it remains until the boundary is saturated when it is then released from the fuel; this holdup allows for more decay of the isotope of the shorter lived isotopes before it can be released. Therefore, as a result of hold-up in the fuel, an isotope with a shorter half-life will decay more than an isotope with a longer half-life.

The release of the short-lived isotopes of the noble gases and iodine during a RIA is similar to that for steady-state power operation once the grain boundary is saturated. This is because once the grain boundaries are saturated during steady-state operation there is no holdup of the gas on the grain boundaries, and there is no holdup on grain boundaries during a RIA. The actual physical mechanism for release from the boundary is different between a RIA and that during steady-state operation. The RIA release is due to the large temperature increase within the fuel during this event that fractures the grain boundaries, thus releasing the gas on the boundaries immediately. The grain boundary saturation level for release decreases with fuel temperature for normal power operation such that an increase in fuel temperature over a few hours from a power ramp will also release grain boundary gas similar to a RIA event where the grain boundaries are fractured. Both mechanisms release all of the grain boundary gas (radioactive and stable). Therefore, there is a ratio between the radioactive R/B release and the stable release fractions that is primarily dependent on the fuel temperature increase (delta power increase) and burn-up for both a RIA event and a slow power increase during normal operation. This ratio can then be used to estimate the release for a given isotope, such as iodine-131, which is of primary importance for dose calculations for a RIA.

Several calculations have been performed with the FRAPCON-3.4 code and the proposed revised ANS 5.4 model to examine the ratio between stable noble gas release and the release of iodine-131 for the BWR 9×9 and PWR 14×14 fuel design at power increases of 14, 26, 31, and 41 percent and at rod average burn-ups between 12 to 38 GWd/MTU. The FRAPCON-3.4 release model estimates the stable gas release while the ANS-5.4 release model is used to estimate the iodine-131 release. The ANS 5.4 model is used for the latter because it predicts the decay of the isotope during the diffusion process from the fuel and has been verified against a large amount of short-lived isotope release data at burn-ups up to 80 GWd/MTU. Only the release of the iodine-131 isotope was examined because it has the highest R/B release of the short-lived volatiles that has the largest impact on dose calculations. The ratio of the best estimate predicted release fractions between the stable noble gases and iodine-131 at a given time step when power is increased provides an indication of the delay time between when a iodine-131 atom is produced to when it is released during normal power operation with little holdup on the grain boundary. Examination of the calculational results demonstrates that the ratio between the stable isotopes and iodine-131 release (e.g.,  $F_{\text{stable}}/R/B_{I-131}$ ), is typically between 6 to 15 when the power is increased between 14 to 41 percent and rod average burn-ups are between 12 to 38 GWd/MTU. An increase in power of 41 percent for steady-state power operation results in a delta increase in stable release fraction of 0.15, which is the upper range of delta release of a RIA for an LWR. The ratio of  $F_{\text{stable}}/R/B_{I-131}$  varies depending on power and burn-up. This suggests that the release fraction from decay for iodine-131 is reduced by a factor of 6 to 15 due to the time for diffusion to the grain boundary and release. Therefore, to be conservative, it is assumed that the diffusion from the fuel grain matrix to the grain boundary with no holdup on the grain boundary reduces the fractional release by a factor of 3 compared to the stable isotopes. As noted, the actual reduction in fractional release compared to the stable isotopes is most likely between a factor of 6 to 15, but without actual iodine-131 release data for test rods with simulated RIA power increases at various burn-up levels, it is difficult to determine the exact factor of reduction in release.

The bounding gap release fraction, R/B, for iodine-131 and the other short-lived isotopes is defined as:

$$F(\text{short life isotopes}) = (0.33) * 0.0022 * \Delta H = 0.00073 * \Delta H$$

where  $\Delta H$  is the enthalpy increase in cal/gm

The combined total RIA gap release fractions equals the steady-state gap fraction (Section 2) plus the transient releases provided in this section, as summarised in Table 2.

Table 2. Local gap release fractions for reactivity initiated accidents

Isotope	Combined RIA release fraction <sup>†</sup>
Kr-85	(( 0.35) + (0.0022 * )H )
I-131	(( 0.08) + (0.00073 * )H )
I-132	(( 0.23) + (0.00073 * )H )
Other Nobles	(( 0.04) + (0.00073 * )H )
Other Halogens	(( 0.05) + (0.00073 * )H )
Alkali Metals	(( 0.46) + (0.0031 * )H )

<sup>†</sup> Assumes no fuel melting,  $\Delta H$ = increased fuel enthalpy during RIA event

### 3. RIA failure models

The FRAPTRAN 1.4 code contains both ductile and brittle cladding failure models to predict failure during RIA. The ductile model is the same as that in FRAPTRAN 1.3. The ductile model predicts the cladding to fail when the predicted cladding plastic strain exceeds the predicted uniform elongation. This model is a function of temperature and hydrogen concentration.

$$UE = \min(UE_0, UE_{Hex})$$

Where:

UE = uniform plastic elongation, %

UE<sub>0</sub> = 2.2%

$$UE_{Hex} = A \cdot H_{ex}^{-p} \quad H_{ex} > 0$$

$$UE_{Hex} = UE_0 \quad H_{ex} = 0$$

$$A = 1211 \exp(-0.00927 \cdot T) \quad T < 700K$$

$$A = 1.840803 \quad T > 700K$$

$$p = 1.355231 - 0.001783 \cdot T \quad T < 700K$$

$$p = 0.107131 \quad T > 700K$$

$$H_{ex} = \max(0, H_{Tot} - H_{Sol})$$

$$H_{Sol} = 1.2 \times 10^5 \exp\left(\frac{-8550}{1.985887 \cdot T}\right)$$

H<sub>Tot</sub> = total hydrogen in cladding, ppm

T = temperature, K.

The predicted minus measured uniform elongation versus excess hydrogen concentration (concentration greater than solubility) is provided in Figure 3 to demonstrate the accuracy of the model. At hydrogen levels greater than approximately 600 ppm the uniform elongation is very low and the cladding typically fails in a brittle manner. This is illustrated in Figure 4 where uniform elongation (solid data points) is plotted as a function of the failure stress to the measured yield strength (measured yield stress is determined from data from similar irradiated cladding types at hydrogen levels less than 600 ppm). All of the uniform elongation data are below 0.45% except for one datum at 0.8%. Also, plotted is the total elongation data (open data points) that has some values that are relatively low but has four data points between 1 to 3.6% strain which is much higher than what would be expected for brittle cladding. This demonstrates that total elongation data has significant scatter and is not a good measure of the strain to failure.

Figure 3. Predicted minus measured uniform elongation from irradiated samples from the PNNL database as a function of excess hydrogen ( $293K \leq T \leq 755K$  and  $0 \leq \Phi \leq 14 \times 10^{25} \text{ n/m}^2$ )

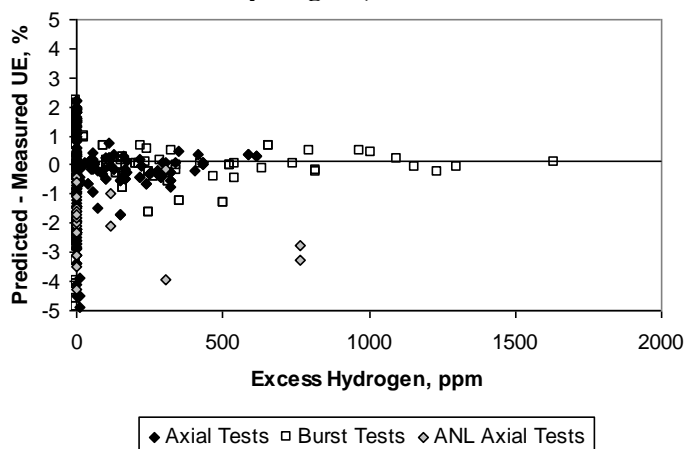
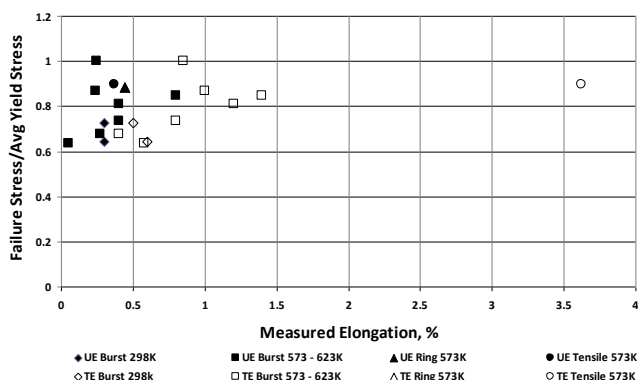


Figure 4. Mechanical tests at excess hydrogen levels greater than 600 ppm with failure at or below the yield strength (demonstrates little or no ductility) versus measured uniform and total elongation



A brittle failure model was added to FRAPTRAN 1.4 assuming that if the cladding excess hydrogen concentration is greater than 650 ppm, the cladding is predicted to fail when plastic strain exceeds 0.05%.

The failure predictions for 30 Cabri, NSRR and BGR RIA tests are listed in Table 3 utilising the ductile (uniform strain) and brittle failure models. It can be seen in Table 3 that failure or non-failure for these 30 tests is correctly predicted for 27 tests. For the remaining three tests, HBO1, RT10 and RT12, the deposited energy is within 5-10 cal/g of the enthalpy required to correctly predict failure or non failure. The first two tests are predicted to have not failed when failure was reported, while the reverse is true for RT12. This suggests that FRAPTRAN 1.4 provides a reasonably best estimate prediction of fuel rod failure due to a RIA.

Table 3. FRAPTRAN 1.4 failure predictions of CABRI, NSRR and BGR tests

Test	Observation	Prediction
<b>Cabri UO<sub>2</sub></b>		
NA1	Failed	Failed
NA2	Not failed	Not failed
NA3	Not failed	Not failed
NA4	Not failed	Not failed
NA5	Not failed	Not failed
NA8	Failed	Failed
NA10	Failed	Failed

Table 3. FRAPTRAN 1.4 failure predictions of CABRI, NSRR and BGR tests (Cont'd)

Test	Observation	Prediction
<b>Cabri MOX</b>		
NA6	Not failed	Not failed
NA7	Failed	Failed
NA9	Not failed	Not failed
<b>NSRR UO<sub>2</sub></b>		
FK1	Not failed	Not failed
GK1	Not failed	Not failed
HBO1	Failed	Not failed
HBO5	Failed	Failed
HBO6	Not failed	Not failed
MH3	Not failed	Not failed
OI2	Not failed	Not failed
TS5	Not failed	Not failed
<b>BIGR</b>		
RT1	Not failed	Not failed
RT2	Not failed	Not failed
RT3	Not failed	Not failed
RT4	Not failed	Not failed
RT5	Not failed	Not failed
RT6	Not failed	Not failed
RT7	Not failed	Not failed
RT8	Failed	Failed
RT9	Failed	Failed
RT10	Failed	Not failed
RT11	Failed	Failed
RT12	Not failed	Failed

#### 4. Conclusions

Bounding models at a 95/95 confidence level for release to the fuel rod gap were empirically derived from the Cabri, NSRR and BGR tests for predicting the release of long-lived isotopes (krypton-85, cesium-134 and cesium-137) and short lived isotopes (such as iodine-131) for dose determinations for RIA events. Dose calculations for RIA must include release during both steady-state as well as from the RIA event itself with examples provided in Table 2. The proposed fission product inventory gap fractions for RIA will be included in the forthcoming DG-1199. The public is invited to comment on proposed analysis methodology and gap fractions in DG-1199 during the upcoming public comment period.

The combination of using the FRAPCON-3.4 code to calculate grain boundary gas and the FRAPTRAN 1.4 code to predict the release from the grain boundaries during a RIA provides a better (best estimate) prediction of release for the long-lived and stable isotopes for this event than a best estimate empirical fit of the data only in terms of peak enthalpy increase. This is particularly true for the lower burn-up fuel rods where the grain boundary gas concentration is much lower and release is lower than for high burn-up fuel. The FRAPTRAN 1.4 code has demonstrated that it can accurately predict failure and non-failure for 27 out of 30 test rods from Cabri, NSRR and BGR tests. Those rods where FRAPTRAN 1.4 incorrectly predicted non-failure (HBO1 and RT10) and failure (RT12) were within 5-10 cal/g of the enthalpy required to correctly predict failure or non failure. This demonstrates that FRAPTRAN 1.4 can predict failure due to a RIA event in a best estimate manner with reasonable accuracy.

## Regulatory Analysis of Reactivity Transients

Carl Beyer, PNNL  
Ken Geelhood, PNNL

Presented at OECD/NEA Workshop on Nuclear Fuel Behavior during Reactivity Accidents  
Paris, France September 9 – 11, 2009



## Outline

- ▶ **Radioactive release to gap for RIA licensing analyses in forthcoming Draft Guide-1199**
  - ✓ Upper bound normal operational release to gap based on newly proposed ANS-5.4 standard
  - ✓ Upper bound transient release to gap based on empirical model
  - ✓ Best-estimate transient release to gap based on FRAPCON3.4/FRAPTRAN1.4 calculation
- ▶ **Cladding failure threshold for RIA**
  - ✓ Validation of FRAPCON3.4/FRAPTRAN1.4

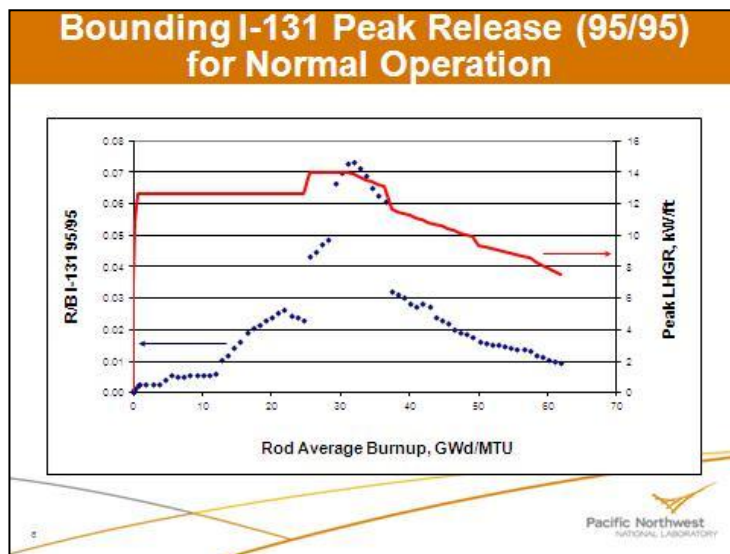
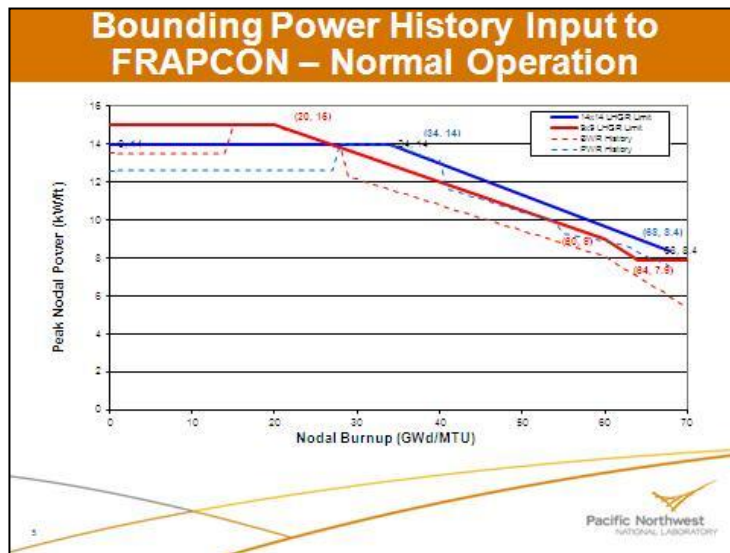
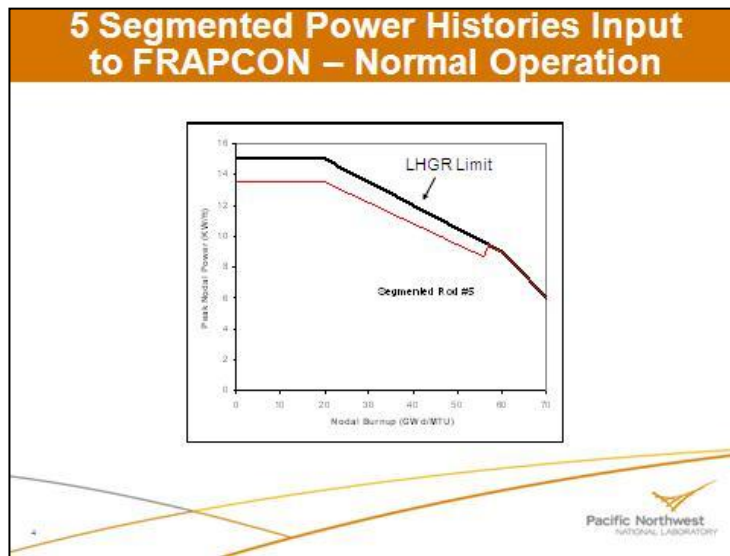


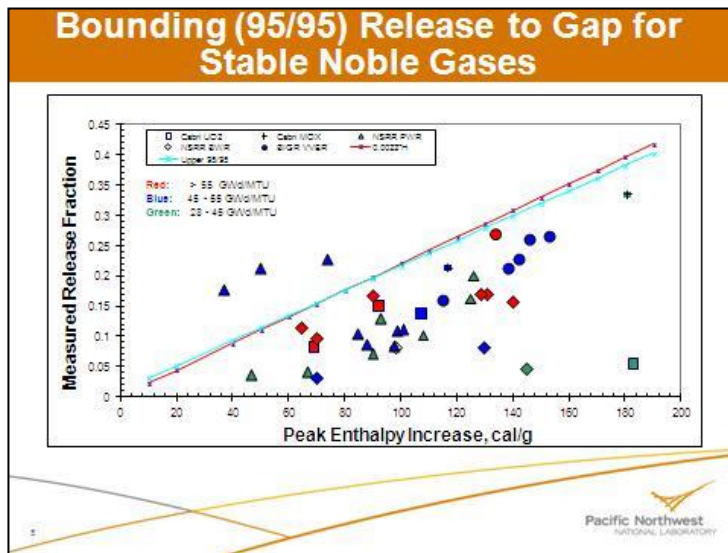
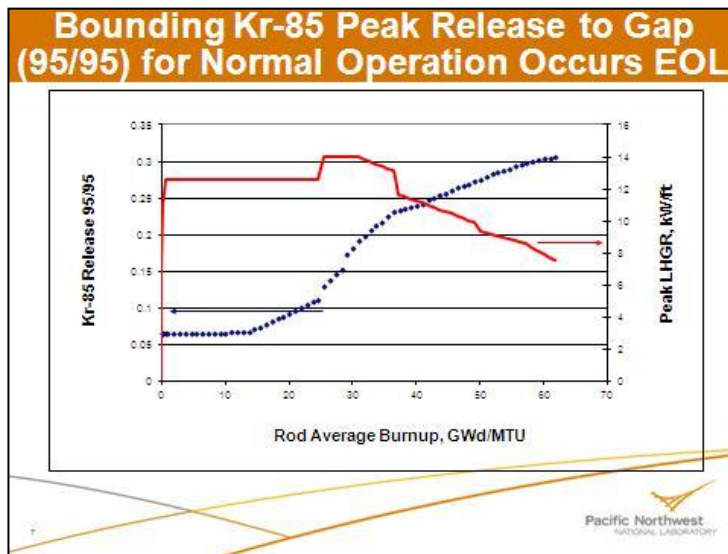
## Upper Bound Normal Operational Release to Gap

- ▶ 95/95 bounding relationship proposed in new ANS 5.4 Standard,\* temperatures predicted FRAPCON3.4
- ▶ Bounding power histories for 14x14 and 9x9 fuel designs
- ▶ Iodine-131 is the most limiting in terms of dose because it provides significant dose to the thyroid

\* Standard sent to ANSI for approval, background document for standard currently in publication as NUREG/CR and PNNL report (PNNL-18490)







- ### Transient Release to Gap of Short-Lived Isotopes
- ▶ RIA release data only from stable isotopes
  - ▶ Short-lived isotopes decay during diffusion to grain boundary, release is less than stables
  - ▶ Estimated ratio of stable isotopes to I-131 release based on ANS 5.4 diffusion coefficients
    - ✓ Varies between 6 to 15 for I-131 depending on burnup and power for range of LWR operation
  - ▶ Conservatively assumed I-131 release factor of 3 less than stables to estimate I-131 release to gap
- Pacific Northwest  
NATIONAL LABORATORY

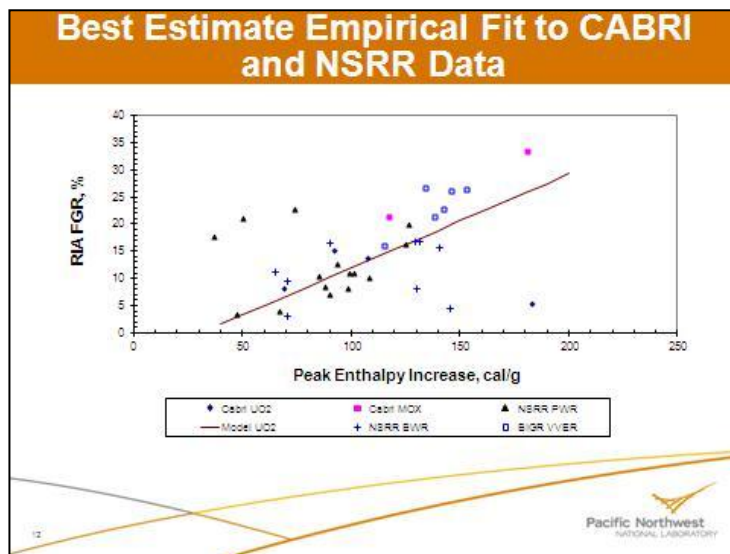
### RIA I-131 Release to Gap for Dose Consequences

95/95 upper bound from normal operation =  
 0.08 (for I-131 fraction)  
 +  
 95/95 upper bound from RIA transient =  
 $0.0022/3 \cdot \Delta H$  (for I-131 fraction)  
 $\Delta H$  = peak fuel enthalpy increase

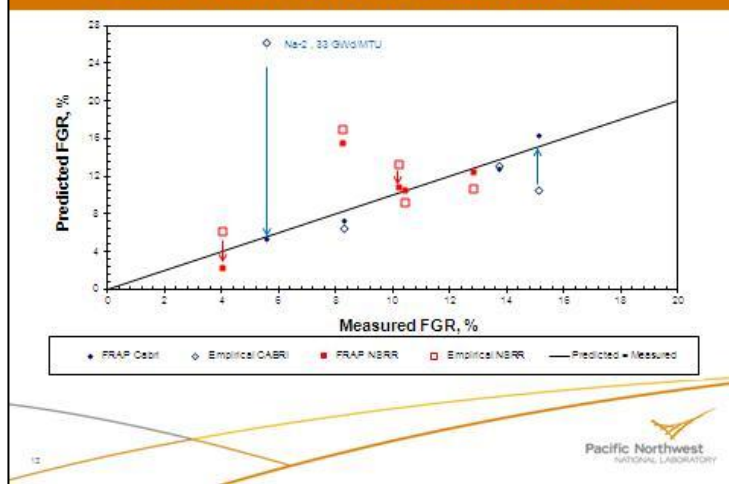


### FRAPCON3.4/FRAPTRAN1.4 Predictions of RIA Data

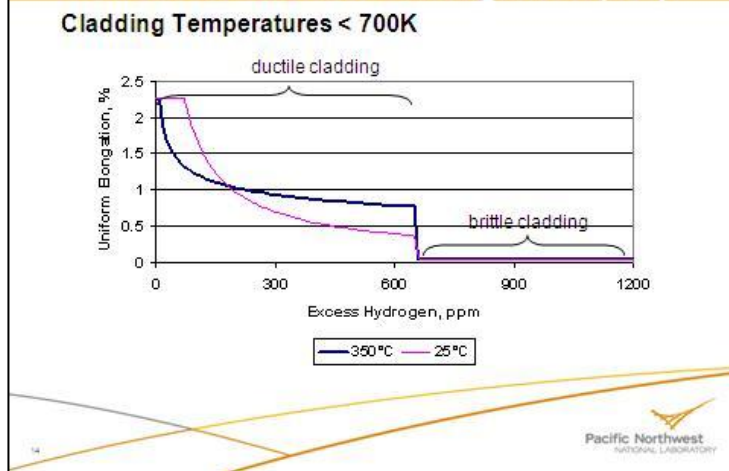
- ▶ Best-estimate release to gap predictions
- ▶ Best estimate failure predictions

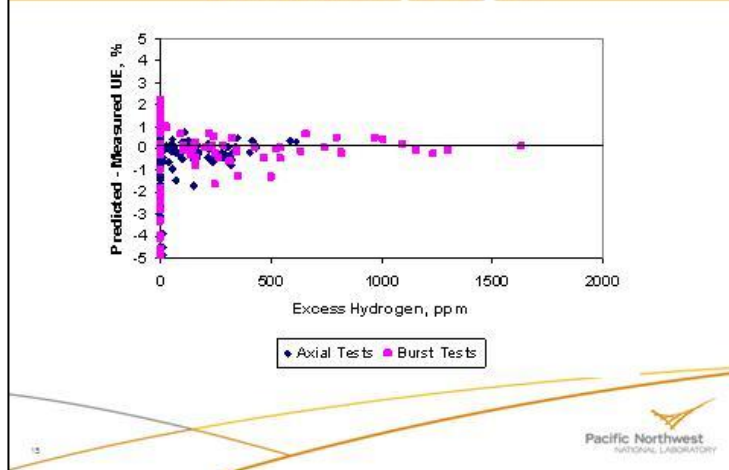
### FRAPCON3.4/FRAPTRAN1.4 Predicts RIA Release Better Than Previous BE Empirical Fit



### FRAPTRAN-1.4 Failure Model for RIA Based on Uniform Elongation (UE)



### Predicted - Measured UE vs. Insoluble Hydrogen



### FRAPTRAN1.4 Best Estimate Failure Prediction of 30 NSRR, CABRI and BGR Tests

- ▶ Successfully predicted failure/non-failure in 27 of 30 test rods
- ▶ NSRR HBO1 and BGR RT10 tests were predicted to not fail when failure was observed
- ▶ RT12 test was predicted to fail when failure was not observed
- ▶ Code predicted cal/gm failure threshold within less than 10 cal/gm measured of all three tests
- ▶ Predict recent CABRI and NSRR hot and cold capsule tests successfully



### Recent CABRI and NSRR Test Rod Comparisons

Rod	Test Conditions	Reported		FRAPTRAN 1.4	
		$\Delta H_{max}$	$\Delta H_{fail}$	$\Delta H_{max}$	$\Delta H_{fail}$
VA-1	NSRR 20°C stagnant water	133 cal/g	64±10 cal/g	132.5 cal/g	64.2 cal/g
VA-3	NSRR 285°C stagnant water	108 cal/g	82 cal/g	102.3 cal/g	75.4 cal/g
CIP0-1	CABRI 280°C flowing sodium	74 cal/g	no failure	71.6 cal/g	no failure

- ✓ All tests done on high burnup (72-75 GWd/MTU) rods with ZIRLO™ cladding
- ✓ FRAPTRAN 1.4 predicted failure or non failure correctly for each test
- ✓ FRAPTRAN 1.4 predicted maximum and failure enthalpies within less than 7 cal/g of reported values



## Summary

- ▶ New methodology proposed for determining release to gap for determining dose consequences for RIA in US reactors – Forthcoming Draft Guide 1199  
**Comments welcomed from public**
- ▶ FRAPCON3.4/FRAPTRAN1.4 provides best estimate failure predictions for RIA (assist in NRC in determining RIA failure thresholds)





## SESSION ONE

### **Recent Experimental Results and Experimental Technique Used**

#### **Microstructure & Mechanical Property Changes in Fuel Cladding during RIA-Type Temperature Transients**

Fumihisa Nagase, Tomoyuki Sugiyama and Toyoshi Fuketa (JAEA, Japan)

#### **Expansion-due-to-Compression Test Results on High Burnup Zirlo Cladding**

Manuel Quecedo and M. Lloret (ENUSA, Spain); Jose Manuel Conde and Jose Manuel Rey (CSN, Spain)

#### **Ductility and Failure Behaviour of both Unirradiated and Irradiated Zircaloy-4 Cladding Using Plane Strain Tensile Specimens**

Sebastian Carassou, M. Le Saux, Xavier Averty, J.P. Pizzanelli and Christophe Poussard (CEA Saclay, France); Bernard Cazalis and Jean Desquines (IRSN, France); Christian Bernaudat (EDF, France)

#### **Ductility Degradation of High Burnup Cladding in PCMI-Simulating Condition**

Sun-Ki Kim, Je-Geon Bang, Dae-Ho Kim, Ik-Sung Lim, Yong-Sik Yang, Kun-Woo Song, Do-Sik Kim and Hang-Seok Seo (KAERI, Korea)

#### **Applicability of NSRR Room/High Temperature Test Results to Fuel Safety Evaluation under Power Reactor Conditions**

Tomoyuki Sugiyama, Miki Umeda, Yutaka Udagawa, H. Sasajima, Motoe Suzuki and Toyoshi Fuketa (JAEA, Japan)



## MICROSTRUCTURE AND MECHANICAL PROPERTY CHANGES IN FUEL CLADDING DURING RIA-TYPE TEMPERATURE TRANSIENTS

**F. Nagase**, Nuclear Safety Research Center, Japan Atomic Energy Agency, Japan  
**T. Sugiyama**, Nuclear Safety Research Center, Japan Atomic Energy Agency, Japan  
**T. Fuketa**, Nuclear Safety Research Center, Japan Atomic Energy Agency, Japan

Fuel cladding temperature in a reactivity-initiated accident (RIA) widely varies depending on reactor type, accident scenario, and fuel burn-up. Since mechanical properties of the cladding is a key to the fuel performance and is greatly affected by the temperature, experimental data are necessary for a wide temperature range to estimate the fuel behavior under various RIA conditions. However, there are limits on the temperature and the number of tests in performing pulse irradiations at research reactors such as the NSRR of the Japan Atomic Energy Agency (JAEA) and the CABRI of the Institut de Radioprotection et de Sûreté Nucléaire (IRSN). Therefore, laboratory-scale experiments have been performed to complement the integral experiments. The present paper reports JAEA's experimental results on microstructure and mechanical property changes by temperature transients and discusses cladding behavior depending on the temperature under RIA conditions.

### 1. Introduction

In a postulated reactivity-initiated accident (RIA) of light water reactors (LWRs), a prompt power excursion of the reactor occurs by the insertion of a large amount of excess reactivity due to an inadvertent control rod withdrawal or ejection or to other causes. This reactor power excursion causes a rapid overheating of the fuel. The extent of overheating and the fuel cladding temperature in a RIA widely varies depending on reactor type, accident scenario, and fuel burn-up. Since mechanical property of the cladding is greatly affected by the temperature, experimental data are necessary for a wide temperature range to estimate the fuel behavior under various RIA conditions. High burn-up increases the amount of hydrogen absorbed in the cladding. Subsequent increase of hydrides precipitation reduces cladding ductility, and morphology and distribution of hydrides are also very important in reduction of the cladding ductility.<sup>1,2,3</sup> Morphology and distribution of hydrides can be altered by temperature transients expected in a RIA. Therefore, the information on behavior of hydrides as a function of temperature is also required for evaluating the fuel behavior under RIA conditions. However, there are limits on the temperature and the number of tests in performing pulse irradiations at research reactors such as the NSRR of the Japan Atomic Energy Agency (JAEA) and the CABRI of the Institut de Radioprotection et de Sûreté Nucléaire (IRSN). The NSRR and CABRI tests are performed under room temperature (RT; ~300 K) and high temperature (HT; ~550 K) conditions, respectively, though tests with higher initial temperatures (~550 K) are recently possible at the NSRR. Thus, laboratory-scale experiments have been extensively performed in the U.S.,

---

<sup>1</sup> F. Nagase, T. Fuketa, "Investigation of hydride rim effect on failure of Zircaloy-4 cladding with tube burst test," *J. Nucl. Sci. Technol.*, 42[1], 58, (2005).

<sup>2</sup> T. Fuketa, F. Nagase, K. Ishijima, T. Fujishiro, "NSRR/RIA Experiments with High Burn-up PWR Fuels Nuclear Safety, 37[4], 328, (1996).

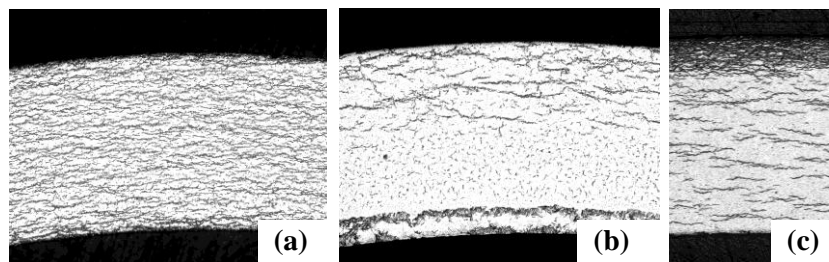
<sup>3</sup> T. Sugiyama, M. Umeda, T. Fuketa, et al., "Failure of high burn-up fuels under reactivity-initiated accident conditions," *Proc. International Conference on the Physics of Reactors (PHYSOR 2008)*, Interlaken, Switzerland, September 14-19, 2008.

France, Korea, Japan, etc.<sup>4,5,6,7</sup> to complement the integral pulse-irradiation experiments. The present paper reports experimental results obtained at the JAEA on changes of microstructure and mechanical properties of the fuel cladding during temperature transients, and discusses cladding behavior for a wide temperature range assumed under RIA conditions.

## 2. Experimental procedure

Unirradiated PWR cladding (Zircaloy-4) tubes and BWR cladding (Zircaloy-2 with zirconium liner) tubes were used in the present study. The cladding tubes were hydrided in mixture gas of hydrogen and argon at about 620 K for various times. The hydrogen concentration of the tested cladding ranged from about 10 (as-fabricated) to about 1000 ppm. Hydride morphology in radial cross sections of the hydrided cladding tubes is shown in Figure 1(a) and (b). Hydrides generally distribute homogeneously in the radial direction. Solid solubility of hydrogen is lower in zirconium compared with Zircaloy. Hydrides precipitate earlier in the zirconium liner than the Zircaloy during slow cooling. This causes difference in hydrogen concentration in solid solution, and hydrogen diffusion occurs from the Zircaloy to the zirconium liner. As a result, concentrations of hydrogen and hydride become higher in the zirconium liner of the BWR cladding as shown in Fig. 1(b).<sup>8</sup> Ring-like specimens cut from the hydrided cladding tubes were subjected to the ring tensile tests at temperatures ranging 300 to 573 K.<sup>9</sup> In addition, the hydrided cladding tubes were quickly heated up to 773 to 1273 K in an inert atmosphere, isothermally heated with holding times of 0 to 180 s and quickly cooled. Microstructure observation and ring tensile tests were performed after the heating. Cross-head speed in the ring tensile test was  $3.3 \times 10^{-3}$  mm/s and test temperature was about 300 and 573K.

Fig. 1 Hydride morphology in radial cross sections of the hydrided cladding tubes; (a) PWR cladding, (b) BWR cladding, (c) PWR cladding with hydride rim



Unirradiated PWR cladding (Zircaloy-4) tubes were hydrided in mixture gas of hydrogen and argon at about 600 K with a special charge method<sup>10</sup> to simulate the radial hydride distribution specific in the high

<sup>4</sup> R. Daum, S. Majumdar, et al., "On the embrittlement of Zircaloy-4 under RIA-relevant conditions," Zirconium in the nuclear industry, ASTM STP 1423, 702, (2002).

<sup>5</sup> J. Desquines, B. Cazalis et al., "Mechanical properties of Zircaloy-4 PWR fuel cladding with burn-up 54-64 MWd/kgU and implications for RIA behavior", Zirconium in the nuclear industry, ASTM STP 1467, 850, (2005).

<sup>6</sup> S. K. Kim, J. G. Bang, et al., "Hoop strength and ductility evaluation of irradiated fuel cladding," Nucl. Eng. Des., 239, 254, (2009).

<sup>7</sup> Grigoriev, V., Jakobsson, R. and Schrire, D., "Experimental Evaluation of Critical Strain Energy Density for Irradiated Cladding under Simulated RIA Conditions", *Proc. of ENS Topfuel 2001*, Stockholm, Sweden, May 2001.

<sup>8</sup> I. Takagi, S. Shimada, D. Kawasaki, K. Higashi, "A simple model for hydrogen re-distribution in zirconium line fuel cladding," J. Nucl. Sci. Technol., 39[1], 71, (2002).

<sup>9</sup> F. Nagase, T. Sugiyama, T. Fuketa, "Optimised ring tensile test method and hydrogen effect on mechanical properties of Zircaloy cladding in hoop direction," J. Nucl. Sci. Technol., 46[6], 545, (2009).

<sup>10</sup> T. Kido, M. Sugano, "Development of a method to charge hydrogen in zirconium alloys," Trans. Atomic Energy Soc. Japan, 1[4], 147, (2002).

burn-up fuel cladding. Radial cross section of the hydrided cladding tube is shown in Fig. 1(c). Hydrides are accumulated in layer at the cladding periphery and thickness of the hydrides layer is about 1/4 to 1/3 of the cladding thickness. The hydrides layer is called hydride rim, and the cladding tube with hydride rim is called simulated high burn-up fuel (SHB) cladding tube hereinafter. Average hydrogen concentration of the SHB cladding tube was estimated to range 890 to 1020 ppm, while local hydrogen concentration in the hydride rim is about 3000 ppm. Small specimens of 10 mm long and 5 mm wide were cut from the SHB and as-fabricated cladding tubes, and they were isothermally annealed in an inert atmosphere. The annealing temperature ranged 673 to 1173 K with holding times between 0 and 3600 s. Infrared furnace was used for rapid heat up, and temperature control and measurement were done with R type thermocouples which were spot-welded directly on the cladding tube specimens. Heat up rate was increased as much as possible to reduce the influence of the heat up phase and temperature overshoot of some degree was permitted in the shorter annealing. The overshoot was about 40 K at maximum. On the other hand, heat up rate was decreased to avoid the overshoot in the longer annealing. Finally, heat-up rates were changed from 60 to 100 K/s. After the annealing, microstructure observation was performed for the radial cross section of each cladding specimen.

### 3. Results and discussion

#### 3.1. Mechanical property change with temperature increase

Mechanical properties of Zircaloy have been investigated for a wide temperature range.<sup>11</sup> It was reported that strength decreases and ductility increases continuously with the temperature to about 1000K where  $\beta$  phase appears in  $\alpha$  phase. However, ductility (total elongation) increase of the hydride PWR cladding is not a simple function of temperature, but is complicatedly dependent on temperature and hydrogen concentration. Figures 2 and 3<sup>9</sup> show that ductility of the hydrided PWR cladding is relatively high and the temperature dependence is small below 573 K for the hydrogen concentration range below 500 ppm. On the other hand, ductility of the highly hydrided cladding (>700 ppm) is low at lower temperatures, significantly increases between 300 and 473 K, and the increase is smaller between 473 and 573 K.

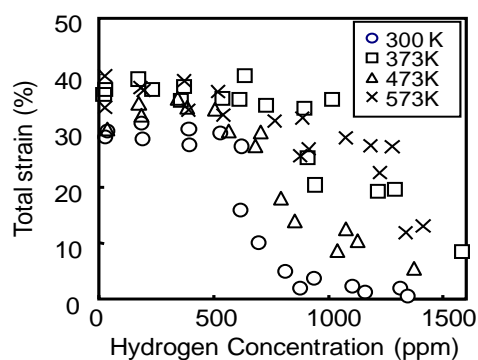


Figure 2. Total strain of hydrided specimens at temperatures from 300 to 573 K as a function of hydrogen concentration<sup>9</sup>

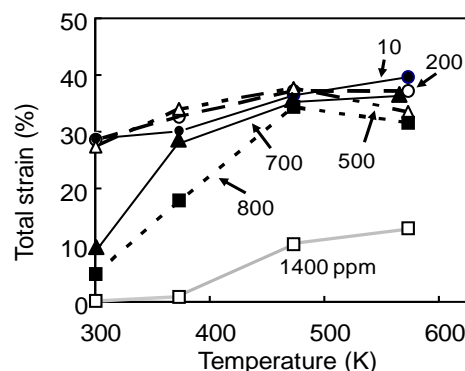
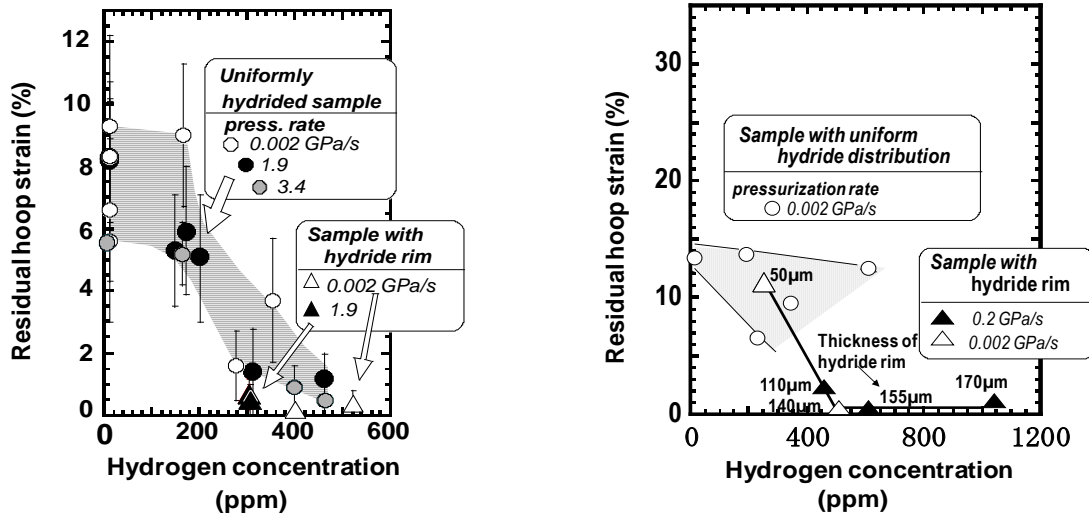


Figure 3 Total strain of hydrided specimens as a function of test temperature<sup>9</sup>

Figure 4 shows ductility (residual strain) measured in the burst tests of the hydride cladding with and without the hydride rim at room temperature and 620 K.<sup>1</sup> The figure shows that hydride rim decreases ductility of the cladding and the effect is still seen at 620 K when the hydride rim is thicker than 100  $\mu\text{m}$ .

<sup>11</sup> "High temperature materials program, part A – sixth annual report," GEMP-475A, p. 261, General Electric, (1967).

Figure 4. Residual hoop strain in samples failed in room temperature (left) and 620 K (right) burst test, as a function of hydrogen concentration <sup>1</sup>



3.2. Microstructure change with temperature increase

Figure 5 shows tensile strength and total strain at 573 K of the hydrided PWR cladding after the annealing at various temperatures for 180 s. The annealing at 873 to 973 K causes recrystallisation of the cladding regardless of the hydrogen concentration, which is indicated by increase of total strain and decrease in tensile strength. Effect of holding time on the recrystallisation is shown in Fig. 6 for the 400-ppm cladding tested at 573 K after the annealing at various temperatures. Figure 7 shows microstructure of the cladding after the heating at 973 K for 0 and 180 s. The progress of recrystallisation depends on the annealing time as well as the temperature, and the microstructure change is small even at 973 K with the holding time of 0 s. Therefore, ductility increase due to recrystallisation may not be expected below 1000 K in the RIA-type quick temperature transient.

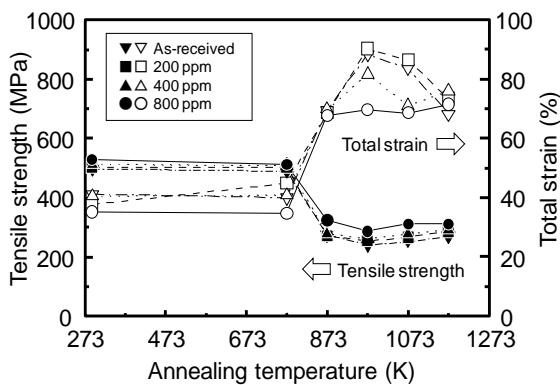


Figure 5. Tensile strength and total stress at 573 K of hydrided PWR cladding after annealing at various temperatures for 180 s

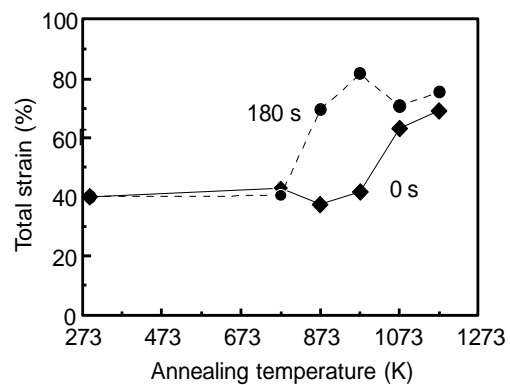


Figure 6. Total strain at 573 K of hydrided PWR cladding after annealing at various temperatures for 0 and 180 s

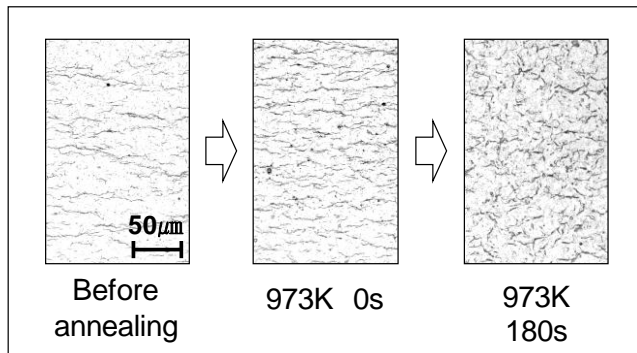


Figure 7. **Microstructure changes of hydrided Zircaloy-4 cladding after annealing at 973 K for 0 and 180 s**

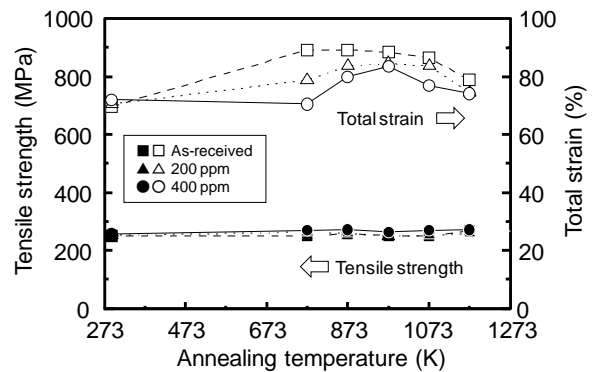


Figure 8. **Tensile strength and total stress at 573 K of hydrided BWR cladding after annealing at various temperatures for 180 s**

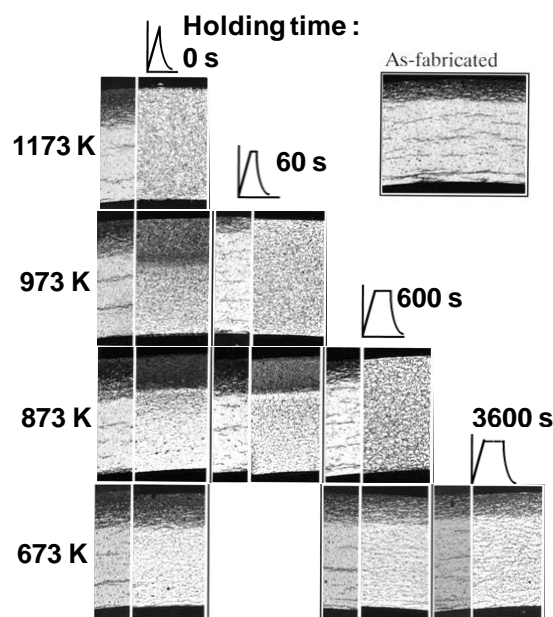
Phase transition to  $\alpha+\beta$  and  $\beta$  phases occurs during the transient to temperatures above 1100 K. Slight increase in strength and decrease in total strain possibly correspond to the phase transition. Since the phase transition shows no time dependence as shown in Fig. 6, it is considered that the transition occurs so quickly.

Similar microstructure and mechanical property changes are observed in the BWR cladding, though the changes due to progress of recrystallisation is much smaller (Fig. 8).

### 3.3. Behavior of hydride rim with temperature increase

Cross sections of cladding tube specimens with hydride rim (SHB specimens) before and after the temperature transients are compared in Fig. 9. The arrangement of the photographs corresponds to the test matrix vertically for the annealing temperatures from 673 to 1173 K and horizontally for the holding time from 0 to 3600 s.

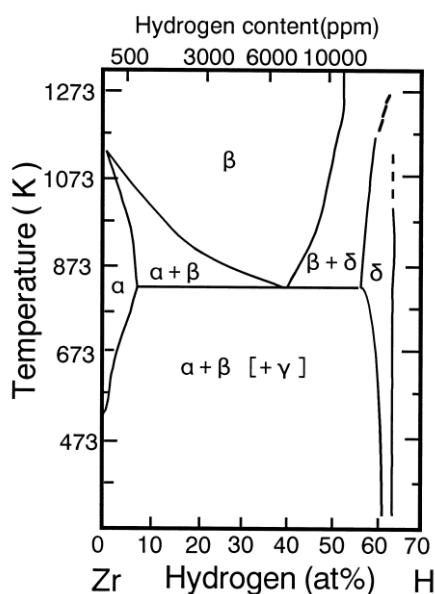
Figure 9. **Cross sections of cladding tube specimens with hydride rim before and after the temperature transients**



Thickness and morphology of hydride rim shows no change in the specimens annealed at 673K for the examined time range. Assuming that all of hydrogen is concentrated in the outer 1/4 of cladding thickness and hydrogen diffuses with diffusion coefficient in  $\alpha$ -Zircaloy which is determined by Kearns,<sup>12</sup> hydrogen concentration at the internal surface reaches 90% of the average concentration in the cladding after about 800 s. Namely, hydrogen concentration should be roughly constant through the cladding thickness at that time if all the hydrogen in the SHB cladding can diffuse according to the Fick's law. Solid solubility of hydrogen is about 200 ppm at 673 K.<sup>13</sup> Since local hydrogen concentration in hydride rim is estimated to be about 3000 ppm, most of hydrides were as precipitated there during the annealing at 673 K. The unchanged hydride morphology and radial localisation after the annealing at 673 K indicates that diffusion rate of hydrogen is negligibly small when it precipitated as hydrides. Since the hydrogen concentration in the inner part of the cladding thickness appears to increase after the annealing at 673 K, dissolved hydrogen in hydride rim is considered to diffuse to the inner part during the annealing.

Hydride rim is still distinguishable in the specimens that were annealed at 873 K for the holding times of 0 and 60 s and at 973 K for 0 s. However, hydride morphology obviously changed and the size of hydride became finer both in hydride rim and internal region. Hydride rim disappeared and radial hydride distribution became uniform in the cladding tubes annealed at 873 K for 600 s and at 973 K for 60 s. The binary phase diagram of zirconium-hydrogen system after Hall *et al.*<sup>14</sup> is shown in Fig. 10. The Zr-H alloy containing more than 1000 ppm of hydrogen transforms from  $\alpha+\delta$  to  $\alpha+\beta$  phase at about 850 K. Once the  $\alpha+\beta$  phase is formed, the solid solubility increases drastically as shown in the binary phase diagram. This transformation temperature may be different in Zircaloy containing some alloying elements and in the rapid heat up condition. However, it is reasonable to consider that the change of the hydride morphology in the hydride rim observed above 873 K was caused by the phase transformation and dissolution of hydrides during the annealing. Disappearance of the hydride rim after the annealing at 873 K for 600 s and 973 K for 60 s should be attributed to the dissolution of hydrides and followed diffusion of hydrogen in solid solution.

Figure 10. Binary phase diagram of Zr-H system<sup>14</sup>



<sup>12</sup> J.J. Kearns, "Diffusion coefficient of hydrogen in alpha zirconium, Zircaloy-2 and Zircaloy-4," J. Nucl. Mater. 43, 330, (1972).

<sup>13</sup> J. J. Kearns, "Terminal solubility and partitioning of hydrogen in the alpha phase of zirconium, Zircaloy-2 and Zircaloy-4," J. Nucl. Mater. 22, 292, (1967).

<sup>14</sup> E. Zuzek et al., Bulletin of Alloy Phase Diagrams, 11[4], 385, (1990).

At 1173 K, re-distribution and morphology change of hydrides occur rapidly. Hydride rim disappeared without holding time in the specimen heated to 1173 K. The microstructure of the cladding tube is basket-wave like and is apparently different from that annealed at temperatures below 973 K. Although hydride morphology is not clear in the figures, hydrides are considered to become very fine and precipitate on the boundary of needle-like  $\alpha$ -grain. Therefore, rapid disappearance of hydride rim and hydride morphology change can be correlated with the phase transformation to  $\beta$  phase. Assuming again that all of hydrogen is concentrated in the outer 1/4 of cladding thickness and hydrogen diffuses obeying the Fick's second law, hydrogen concentration change in the cladding thickness was estimated for the temperatures of 873, 973, and 1173 K. Diffusion coefficient in  $\alpha$ -Zircaloy was used for 873 and 973 K, though Zircaloy has the  $\alpha+\beta$  phase structure at those temperatures. Diffusion coefficient of  $\beta$ -zirconium<sup>15</sup> was used for the estimation of 1173 K because that of Zircaloy was not found. As a result, it was estimated that the hydrogen concentration at the internal surface of the cladding reaches 90% of the averaged concentration in the cladding, namely hydrogen concentration becomes nearly uniform, after about 150, 80, and 10 s at 873, 973, and 1173 K, respectively. The experimental results in Fig. 9 show that hydride rim disappeared and the hydride distribution in the cladding thickness became roughly uniform between 60 and 600 s at 873 K, between 0 and 60 s at 973 K, and by the transient heating to 1173 K (~0 s). The estimated period to obtain the uniform hydrogen distribution roughly agrees with that observed in the experiments. Consequently, redistribution of hydrogen by the temperature transient is explained by diffusion of hydrogen in solid solution, which is enhanced by the phase transition above 850 K.

### 3.4. Cladding property changes during temperature transient

Cladding mechanical properties which are directly connected to the fuel behavior and the failure limit under RIA conditions are dependent on neutron fluence, hydrogen absorption (hydrogen concentration, hydride morphology and hydride distribution) and temperature. Hydrogen content in the cladding increases with the burn-up increase. Solid solubility of hydrogen in zirconium and Zircaloy is low and excessive hydrogen precipitates as hydrides which have lower ductility at lower temperatures. Absorbed hydrogen tends to accumulate at the cooler cladding periphery, which forms hydride rim. The accumulation of hydrides is more significant in the PWR cladding in which the radial temperature gradient is steeper. Hydrides generally precipitate in parallel to the circumferential direction of the cladding due to the texture control on fabrication. However, fraction of the radial component of hydride orientation is rather high in the recrystallised BWR cladding which has grain boundaries, preferential site of hydride precipitation. These hydrides morphologies specific respectively in the PWR and BWR cladding as well as solid solubility are altered by the temperature increase under accidental conditions and consequently the cladding mechanical properties would be changed. Changes of the mechanical properties and the microstructure with temperature increase are summarised below based on the experimental results shown in 3.1 through 3.3, connecting with cladding behavior for a wide temperature range assumed in RIA conditions.

The highly irradiated and corroded fuel cladding exhibit lower ductility and fails at a lower energy deposition due to pellet-clad mechanical interaction (PCMI) from room temperature to about 400 K. Higher hydrogen concentrations, hydride rim and/or radially-oriented hydrides are the main causes of the failure at lower energy deposition, which has been experimentally confirmed.<sup>3,4,12</sup> Cladding ductility generally increases and strength decreases with the temperature.<sup>6,11,16</sup> However, the ductility increase complicatedly depends on hydrogen concentration as well as temperature. As shown in Fig. 2 and 3, the ductility obviously becomes high at about 473 K when the hydrogen concentration is below 800 ppm, while the ductility increase is insignificant between 473 and 573 K. The remarkable increase of the ductility occurs at higher temperatures when the hydrogen concentration is above 1000 ppm. Therefore, the failure limit of the high burn-up fuel may increase when the cladding temperature reaches over 500 K.

<sup>15</sup> M. Someno, Nippon Kinzoku Gakkai-shi, 24, 249 (1960), [in Japanese].

<sup>16</sup> A. Garde, "Effects of irradiation and hydriding on the mechanical properties of Zircaloy-4 at high fluencies," Zirconium in the nuclear industry, ASTM-STP 1023, 548, (1989).

However, it was reported that the cladding with thick hydride rim ( $> 100 \mu\text{m}$ ) showed lower ductility even at about 620 K.<sup>1</sup> It is considered that most hydrides still precipitate in the hydride rim and the ductility is low at those temperatures. Therefore, the high burn-up cladding with thick hydride rim may fail due to PCMI under RIA conditions even at about 620 K.

Solid solubility is about 450 ppm at 770 K and hydrides are dissolved in most part of the cladding. Ductility of Zircaloy is so high and hydrides exhibit plastic deformation above about 650 K.<sup>17</sup> Therefore, the cladding would not fail only by the thermal expansion of the pellet and may exhibit large hoop strain if the rod internal pressure increases at these temperatures.

Recrystallisation of the Zircaloy matrix in the PWR cladding and subsequent ductility increase, which generally occur above 870 K, may not be expected even at about 900 K under the fast temperature transient. However, strength is low at these temperatures and the phase transition to the  $\beta$  phase occurs in the single  $\alpha$  phase at about 1120 K. Therefore, possibility of the PCMI failure is zero at these higher temperatures, and the fuel may fail with cladding rupture due to significant increase of the internal pressure and embrittlement due to high temperature oxidation. Since hydrogen concentration is very high in the hydride rim and the  $\beta$  phase appears in the  $\alpha$  phase at as low as about 850 K, the hydrides are quickly in the solid solution in the hydride rim, though the cladding temperature would not reach so high in the high burn-up fuel due to decrease of the fissile material.

#### 4. Conclusion

The JAEA has been performed laboratory-scale experiments to complement the integral experiments at the NSRR and estimate the fuel behavior under various RIA conditions. The present issue summarised the experimental results on microstructure and mechanical property changes during temperature transients and discusses cladding behavior for a wide temperature range assumed in RIA conditions.

The highly irradiated and corroded fuel cladding fails at a lower energy deposition and exhibit lower ductility from room temperature to about 400 K. Cladding ductility generally increases and strength decreases with the temperature. The cladding ductility obviously becomes high at about 473 K when the hydrogen concentration is below 800 ppm, while remarkable increase of the ductility occurs at higher temperatures when the hydrogen concentration is above 1000 ppm. Therefore, the high burn-up cladding with thick hydride rim would fail with PCMI under RIA conditions even at about 620 K, though the failure limit of the high burn-up fuel may increase when the cladding temperature reaches over 500 K.

Solid solubility is about 450 ppm at 770 K and hydrides are dissolved in most part of the cladding. Ductility of Zircaloy is so high and hydrides exhibit plastic deformation above about 650 K. Therefore, the cladding would not fail due to the thermal expansion of the pellet and may exhibit large hoop strain if the rod internal pressure increases at these temperatures.

Recrystallisation of the Zircaloy matrix in the PWR cladding and subsequent ductility increase, which generally occur above 870 K, may not be expected under the quick temperature transient even at about 900 K. However, strength is low at these temperatures and the phase transformation to the  $\beta$  phase occurs in the single  $\alpha$  phase at about 1120 K. Therefore, possibility of the cladding failure due to PCMI is zero at these higher temperatures, and the fuel may fail with cladding rupture due to significant increase of the internal pressure and embrittlement due to high temperature oxidation. Since hydrogen concentration is very high in the hydride rim and the  $\beta$  phase appears in the  $\alpha$  phase at as low as about 850 K, the hydrides are quickly in the solid solution in the hydride rim, though the cladding temperature would not reach so high in the high burn-up fuel.

---

<sup>17</sup> K.G. Barraclough and C.J. Beevers, "Some observations on the deformation characteristics of bulk polycrystalline zirconium hydride," *J. Mater. Sci.*, 4, 518, (1969).



## Microstructure and Mechanical Property Changes in Fuel Cladding during RIA-Type Temperature Transients

**F. Nagase, T. Sugiyama, T. Fuketa**  
*Japan Atomic Energy Agency*

OECD/NEA Workshop  
Nuclear Fuel Behaviour during Reactivity Initiated Accidents  
Paris, France, September 9 – 11, 2009



### Background

- Reactor power excursion causes a rapid overheating of the fuel in an RIA.
- Microstructure including morphology and distribution of hydrides and mechanical property in high burn-up fuel can be altered by the temperature transient.
- Information on microstructure and mechanical property changes is required for evaluating the fuel behavior under RIA conditions.
- There are limits on the temperature and the number of tests in performing pulse irradiations at research reactors.
- Laboratory-scale experiments have been extensively performed to complement the pulse-irradiation experiments.

1



### Objective of this paper

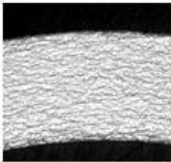
- To summarize experimental results obtained at JAEA on changes of microstructure and mechanical properties of the fuel cladding during temperature transients
- To discuss cladding behavior for a wide temperature range assumed under RIA conditions.

2

### Samples

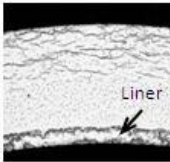


- Unirradiated PWR (Zircaloy-4) and BWR (Zircaloy-2 with Zr liner) cladding
- Pre-hydrating up to about 1000 ppm with H<sub>2</sub> or H<sub>2</sub>-He gas
- With uniform radial distribution and with localized hydride layer at periphery (Hydride rim)



PWR cladding

Uniform



BWR cladding

Liner

Uniform



PWR cladding

Localized

3

### Experiments



- Ring tensile test and burst test of uniformly hydrided samples and hydride-rim samples at 300 through 620 K
- Transient heating (773–1273 K) and ring tensile test (300 and 573 K) of uniformly hydrided samples
- Transient heating (673–1173 K) and microstructure observation of hydride-rim samples



Ring tensile test

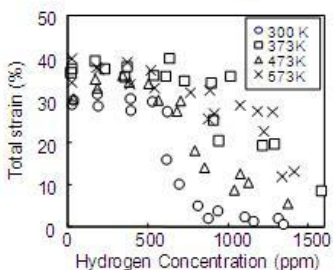


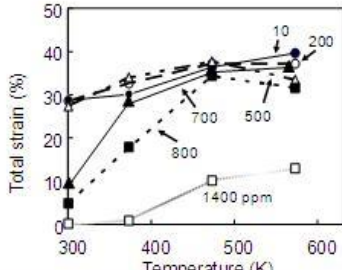
Tube burst test

4

### Mechanical property change with temperature increase

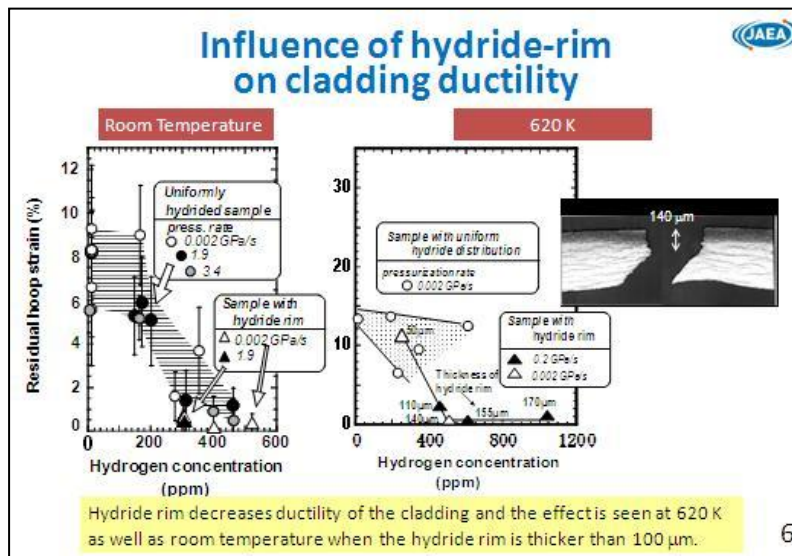




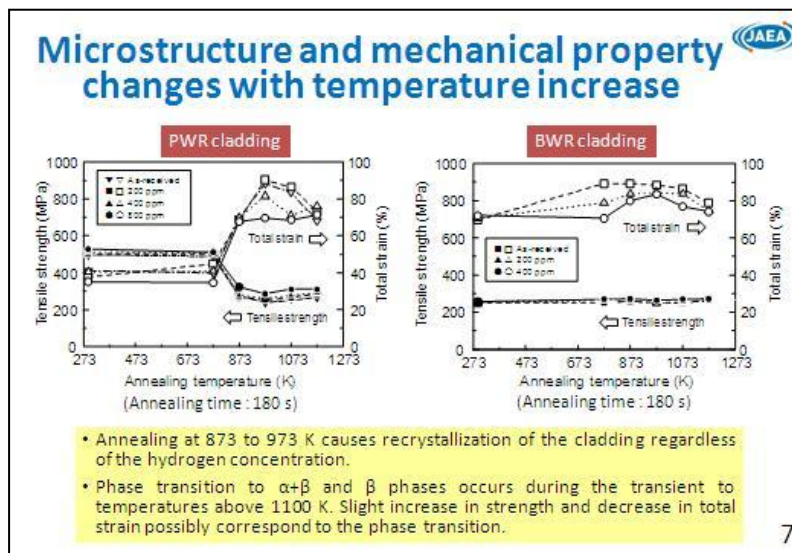


- Ductility is relatively high and the temperature dependence is small below 573 K for the hydrogen concentration range below 500 ppm.
- Ductility of the highly hydrided cladding (>700 ppm) is low at lower temperatures, significantly increases between 300 and 473 K, and the increase is smaller between 473 and 573 K.

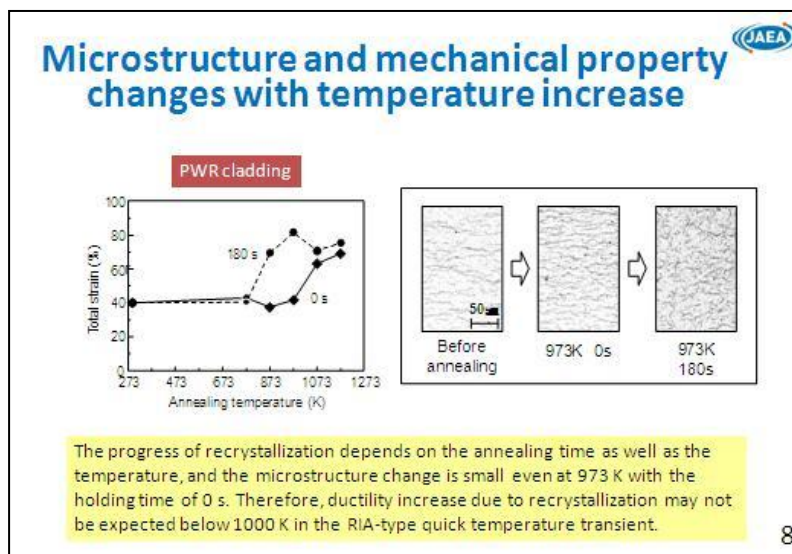
5



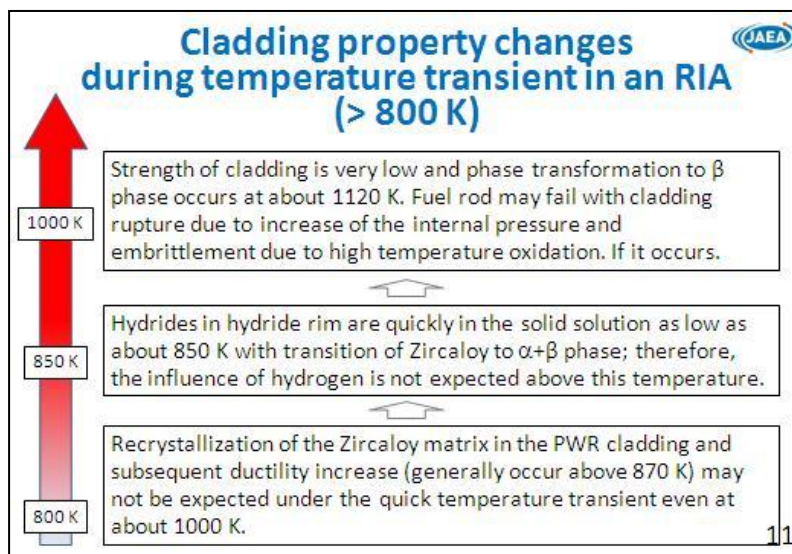
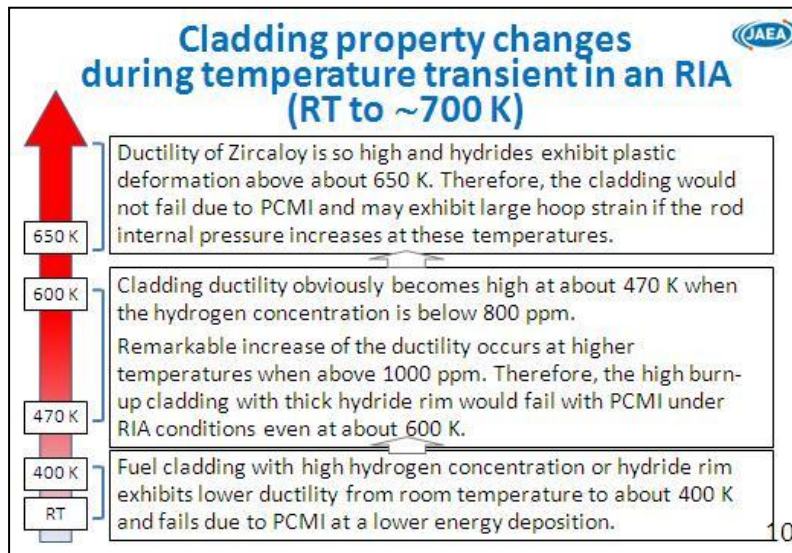
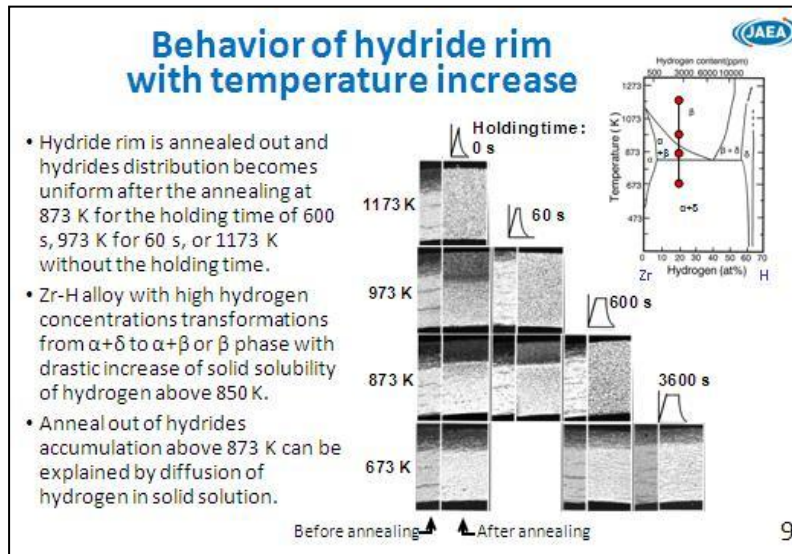
6



7



8



## Summary (1/2)



- JAEA has been performing laboratory-scale experiments on changes of microstructure and mechanical properties of the fuel cladding during temperature transients in RIAs
- Cladding behavior under RIA conditions was discussed in the present paper based on the obtained results.
  - Fuel cladding with high hydrogen concentration or hydride rim exhibits lower ductility from room temperature to about 400 K and fails due to PCMI at a lower energy deposition.
  - Cladding ductility obviously becomes high at about 470 K when the hydrogen concentration is below 800 ppm. However, remarkable increase of the ductility occurs at higher temperatures above 1000 ppm. Therefore, high burn-up cladding with thick hydride rim would fail with PCMI even at about 600 K.

12

## Summary (1/2)



- Ductility of Zircaloy is so high and hydrides exhibit plastic deformation above about 650 K. Therefore, the cladding would not fail due to PCMI and may exhibit large hoop strain if the rod internal pressure increases at these temperatures.
- Hydrides in hydride rim are quickly in the solid solution as low as about 850 K since  $\beta$  phase and the influence of hydrogen is not expected.

13



## EXPANSION-DUE-TO-COMPRESSION TEST RESULTS ON HIGH BURN-UP ZIRLO CLADDING

**M. Quecedo**

ENUSA Industrias Avanzadas SA, Spain

**J.M. Conde**

Consejo de Seguridad Nuclear, Spain

**M. Lloret**

ENUSA Industrias Avanzadas SA, Spain

**J.M. Rey Gayo**

Consejo de Seguridad Nuclear, Spain

### 1. Introduction

In the early 90's, the integral simulation tests of Reactivity Initiated Accidents (RIAs) on Light Water Reactor fuel performed in Cabri (France) and later on in the NSRR (Japan), pointed out as the cladding breach by the fast loading induced by the pellet expansion, known as Pellet Clad Mechanical Interaction (PCMI), as a new limiting failure mechanism for higher burn-up fuel. Indeed, the continuous trend to increase the fuel discharge burn-up and the more severe fuel thermal duty may result in a cladding embrittlement by irradiation damage and by the hydrogen absorption, and sometimes precipitated, from the cladding waterside corrosion process during power operation. The RIA safety limits in the PCMI phase in terms of maximum enthalpy increase are derived from the corresponding cladding failure criterion, fundamentally a cladding deformation<sup>1</sup> criterion and the Critical Strain Energy Density<sup>2</sup>, CSED. Therefore, there has been an increasing effort to characterise the cladding mechanical behaviour, such as the PROMETRA<sup>3</sup> program, and its embrittlement mechanism, under the fast loading conditions characteristic of RIA.

Among the available mechanical tests to achieve this goal, Studsvik developed the Expansion-Due-to-Compression<sup>4</sup> test, EDC. In this test, a polymer pellet is axially compressed inside a sample of the cladding tube, see Figure 1. The pellet produces a load in the cladding, basically in the circumferential direction. This experimental set-up, allows reaching a strain rate of the same order to that experienced by the cladding during a RIA, typically  $1 \text{ s}^{-1}$ . During the test, a data acquisition system records continuously the applied load and the cladding diameter such that the cladding deformation at rupture can be determined later. In addition, if pre-test calibrations are performed to determine the energy absorbed by the pellet and the machine, the work done to break the sample can be determined and the Critical Strain Energy Density, CSED, calculated. Therefore, the test also allows knowing the cladding deformation at fracture and the measured CSED.

---

<sup>1</sup> L. Jernkvist *et al.* "A Strain-based Failure Criterion for Reactivity Initiated Accidents in Light Water Reactors" SKI Report 2004:32.

<sup>2</sup> Y. Rassihd *et al.* "A Cladding Failure Model for Fuel Rods Subjected to Operational and Based Transients". *Proc. of a Technical Committee Meeting*, Windermere June 2000, IAEA-TECDOC-1233.

<sup>3</sup> B. Cazalis *et al.* "The PROMETRA Programme: Fuel Cladding Behaviour under under High Strain Rate", *Nuclear Technology*, Vol. 157, N° 3, March 2007, pp 215-229.

<sup>4</sup> V. Grigoriev *et al.* "Experimental evaluation of Critical Strain Energy Density for Irradiated Cladding under Simulated RIA", *Proc. of the ENS TopFUEL 2001*, Stockholm, Sweden, 2001.

Considering the interest of this mechanical characterisation, the CSN (Spanish Nuclear Commission) and ENUSA launched a program to perform EDC tests on irradiated cladding representative of nowadays PWRs in Spain. The ZIRLO cladding tested was obtained from a fuel rod irradiated in a demonstration program in CN Vandellós II up to ~ 70 MWd/kgU rod average burn-up and relevant oxide thickness/hydrogen content. This rod is a sibling rod for that providing the CIP0-1 rodlet tested in the Cabri International Programme<sup>5</sup> and also extensively characterised in PROMETRA<sup>3</sup>. Besides, another rod from the same fuel assembly has been subjected to simulated RIA tests, named as VA-2 and VA-3, in the JAEA ALPS programme<sup>5</sup>. Further conventional mechanical tests were also performed on this material in a bilateral framework.

This paper describes the EDC test campaign along with the post-test characterisation. The results are presented and discussed, including a comparison with the available conventional mechanical and full scale RIA simulation tests.

## 2. Experimental programme

### *EDC tests*

The scope of the experimental programme comprised EDC test on eight ZIRLO samples obtained from a fuel rod irradiated during five eighteen months cycles in CN Vandellós reaching 68 MWd/kgU rod average burn-up. The characteristics of ZIRLO have been described elsewhere<sup>6</sup>.

The position of the eight samples, with a length of ~20 mm, was selected from the upper rod elevation. Based on the detailed oxide profile, the samples were cut and prepared so that the peak strain in the clad during the EDC test were obtained in a mid pellet, MP, location for four of them while for the remaining four samples, the peak cladding strain aimed for a pellet to pellet, PP, interface. Indeed, the hydrogen content in the cladding and the oxide thickness are larger at PP positions, resulting in a more brittle cladding. Thus, the PP position may become the potential failure site as it has been observed in lower strain rate experiments<sup>7</sup>.

The test parameters were set to result in a cladding strain rate of ~1 s<sup>-1</sup> and, also, to produce the rupture of the sample. In this case, the measured SED at the moment of the break can be considered as the CSED. This CSED is calculated from the work done by the testing machine once the energy spent in processes different from breaking the cladding, such as polymer pellet extrusion and machine compliance is deducted. The resulting net work done to break the cladding is divided by the specimen volume to calculate an energy density and, following the methodology presented by Grigoriev<sup>4</sup> and Dufourneaud<sup>8</sup>, distributed in the axial direction proportionally to the post-test measured axial distribution of deformed cladding diameters. For this purpose the axial measured profilometry of each specimen is represented by

$$\Delta D(z) = \Delta D_{\max} \exp[-(a z)^2]$$

where  $\Delta D_{\max}$  is the maximum measured diameter

Considering that the limiting RIA in a PWR starts at Hot Zero Power, 280°C, and that the maximum temperature allowed by the pellet polymer is 340°C, this temperature range has been used for the tests. Using the lower range for temperature maximises the potential for brittle fracture of the cladding.

<sup>5</sup> M. Petit *et al.* "A Comparative Analysis of Cabri CIP0-1 and NSRR VA-2 Reactivity Initiated Accident Tests", *Proceedings of EUROSAFE Forum 2007*.

<sup>6</sup> G. Sabol, "ZIRLO-An Alloy Development Success", *Journal of ASTM International*, Vol. 2 N. 2, February 2005.

<sup>7</sup> M. Quecedo *et al.*, "Results of Thermal Creep tests on Highly Irradiated ZIRLO", *Nuclear Engineering and Technology*, Vol. 41, N° 2, March 2009.

<sup>8</sup> O. Dufourneaud *et al.* "Elastic-plastic Deformation of a Nuclear Fuel Cladding Specimen under Internal Pressure of a Polymer Pellet", *Proc. of the 5<sup>th</sup> World Congress on Computational Mechanics*, Vienna, 2002.

Table 1 summarises the main characteristics of the tested samples. It should be remarked that the oxide thickness ranges from 80 to 120 microns. The burn-up of the samples was ~75 MWd/kgU.

Figure 2 depicts a typical sample appearance after the test. All the samples became broken by a single axial crack, in a C-shape appearance.

Figure 3 plots the measured CSED and the permanent hoop strain as a function of the oxide thickness.

### ***Post-test characterisation***

Fracture characteristics have been examined in a fractography of the axial crack on specimens A and D. Figure 4 presents an example of the Secondary Electron Images obtained in specimen D, tested at 280°C.

The oxide layer and remaining wall thicknesses have been determined in a metallography on a radial-cross section at the peak axial strain, and on a far away one to be used as reference, on specimens D and H. Figure 5 presents Back Scatter Electron Images, BEI, at different contrast in order to show the oxide thickness and the hydrides.

Using these images, the azimuthal distribution of the hydrogen content in the cladding was measured by an image analysis technique<sup>9</sup>. Figure 6 plots the azimuthal distribution for the oxide and dense hydride rim thickness measured on the specimens D and H. There are no radial hydrides observed in the metallographies as it is expected from the cladding final manufacturing heat treatment: stress-relieved annealed, SRA.

### **3. Discussion of the results**

Figure 3 indicates that the measured CSED, as well as the hoop strain at failure, decreases with the cladding oxide thickness, as expected. This observation is also supported by an examination of the available cross-section metallographies, which indicates that the rupture of the specimen have occurred at the azimuthal position with the maximum oxide thickness. Furthermore, according to Figure 6, an even better correlation may be obtained if the dense hydride rim thickness is included. However, this dense hydride rim thickness cannot be known such as easily as the cladding oxide thickness, even more at irradiation conditions, and it is of low practical application. Finally, the larger oxide layer plus hydride rim thickness for Specimen H, see Figure 6, than for Specimen D may explain the lower CSED and hoop strain at failure for Specimen H than for D.

The available metallographies suggest also that failure takes place by two concurrent mechanisms:

1. At the beginning, the brittle oxide becomes broken resulting in radial cracks, perpendicular to the main stress/strain field, or existing radial cracks from the in-reactor irradiation propagate through the brittle dense hydride rim. This first step involves brittle, or quasi-brittle, materials and the energy used in this process is judged to be low.
2. As further energy is injected into the cladding, one of the previously formed cracks, initially the deepest one, propagates throughout the remaining more ductile base material by shear bands. The fractographies also support a ductile (nucleation, growth and coalescence of voids) failure. Most of the energy would be dissipated in this stage.

The measured CSED and hoop strain values are coherent with this brittle at-the-outer/ductile at-the-bulk cladding fracture behaviour. They also indicate that there is a significant amount of retained cladding ductility even considering the relevant oxide thickness and hydrogen content of the tested samples.

<sup>9</sup> D. Schrire and J.H. Pearce, "Scanning Electron Microscope Techniques for Studying Zircaloy Corrosion and Hydriding", *Zirconium in the Nuclear Industry: Tenth International Symposium*, ASTM STP 1245, Philadelphia, 1994, pp. 98-115.

Indeed, the CIP0-1 test performed in the OECD/NEA Cabri International Programme tested a rodlet from a mother rod sibling to the one used in this EDC Programme. The oxide thickness and hydride rim depth of the tested rodlet were equivalent to those in this EDC Programme. The permanent cladding deformation in the hoop direction was low, of the order of 0.5%, the calculated CSED was  $6 \text{ MJ/m}^3$  and the rod did not fail. The post-test characterisation revealed cracks that propagated through the hydride rim and were arrested at the more ductile underlying metal. Therefore, further energy would need to be injected during the Cabri test to propagate these cracks into the ductile remaining metal, *i.e.* a larger CSED, and also a larger permanent strain. Therefore, the CIP0-1 test results are coherent with those obtained in this EDC Programme.

As a result, the hydrogen content in the cladding is a key factor but so it is the radial distribution in the cladding thickness. A dense hydride rim would concentrate most of the absorbed hydrogen leaving the bulk of the cladding with a lower hydrogen concentration thus, behaving in a ductile manner. However, a homogeneous hydrogen distribution may decrease the overall cladding ductility, depending on the cladding area fraction covered by hydrides.

Figure 7 plots the measured CSED as a function of the hoop strain at failure. In the range covered by these tests there is an excellent linear relationship between both parameters. Therefore, either one may be used as a failure limit. This correlation may be different for macroscopic brittle failures with low or no plastic deformation and low CSED values, as the contribution from the plastic work would be low. A relationship between the CSED and the elongation at fracture can be expected from theoretical considerations as done in reference 1.

The analysis of the results from sibling tests performed in the same conditions, but aiming to strain a mid fuel pellet position and a pellet to pellet interface, does not show any additional effect of the PP position in the CSED or hoop strain at failure.

A trend with the temperature cannot be observed in the range of the tested temperatures, Figure 7.

The measured CSED can be compared to that calculated by integrating the stress-strain curve from conventional mechanical tests such as ring tensile (in the cladding circumferential direction), axial tensile tests and burst tests. Indeed, ZIRLO from the same or from a sibling fuel rod has been tested in a bilateral or join programmes, such as Cabri (PROMETRA) or ALPS. The details of this calculation can be found in reference 2. Therefore, a comparison between the measured and calculated CSED using the mechanical data available from this material has been carried out.

As regards the ring tensile tests, they have not been included in this comparison as their results may be contaminated by specimen bending at the gauge section and /or friction between the specimen and the mandrels. Besides, while in the axial tensile tests the total elongation can be calculated from the reduction in area thus including potential necking effects and resulting in a good estimation of the actual total elongation, in the case of the ring tensile tests the reduction in area is not available and it may not include necking effects.

As regards the axial and burst tests, only those performed at temperatures closed to that used in the EDC test, *i.e.* from 280 to 385°C, have been retained for the CSED calculation.

The CSED calculated from the conventional tests sometimes is corrected to incorporate the effects of the strain rate and biaxiality<sup>10</sup>. The strain correction aims to bring the results of conventional tests done at lower strain rate to an strain rates representative of RIA; the biaxility correction is applied to bring the strain field used in the conventional mechanical tests to a plane strain conditions, assumed to be more

---

<sup>10</sup> C. Bernaudat, P. Pupier, "A New Analytical Approach to Study the Rod Ejection Accident in PWRs", *Proceedings of the Water Reactor Fuel Performance Meeting*, Kyoto, 2005.

representative of that existing under PCMI during an RIA. During the recent years the most widely used correction has been based on the work of Yunchng and Koss.<sup>11</sup>

Figure 9 depicts the eight EDC measured avalues of CSED, and the calculated CSED from conventional tests. It is observed that the calculated values are typically below the measured ones for the same oxide thickness.

Figure 10 plots the uniaxial strain to failure measured in the axial, burst and EDC tests. A better agreement is observed in this case; one of the burst tests and the axial tests clearly that lie clearly below the general trend can be tracked back to more brittle failures at a pellet to pellet interface. As the burst test and the axial tensile tests are straining a larger volume of material there is more chance to pick a weaker cladding site.

Finally, figure 11 depicts the CSED as a function of the unaxial strain to failure. The linearity observed in the EDC tests (see Figure 7) is preserved when incorporating the CSED and hoop strain from the burst tests are incorporated but three axial tensile tests may be outside the general trend. Application of a biaxiality correction factor based on Yunchang and Motta will reduce the calculated CSED, leaving them even farther outside the general trend. Therefore, further development on the correction factor may be needed to bring those points into the general trend.

#### 4. Conclusions

A joint CSN and ENUSA EDC Programme has been performed in Studsvik on highly irradiated ZIRLO, with cladding sample burn-up of about 75 MWd/kgU, with relevant oxide thickness and hydrogen contents.

These tests and the post-test characterisation performed, indicate that oxide thickness and hydride rim thickness (hydride distribution) the cladding mechanical response under the fast PCMI loading during an RIA. The failure mechanism in the tested specimens was brittle at the cladding outer area (oxide+dense hydride rim) and ductile in the bulk cladding, with a much lower hydrogen concentration.

In the range of the parameters tested, the results show an excellent linear correlation between the measured CSED and the measured hoop strain at failure. Thus, any of both may be used as a failure indicator. On the other hand, no effect of temperature on CSED result can be observed.

The measured CSED and strain to failure and the twofold failure mechanism supports that significant ductility remained in the cladding after the commercial irradiation of the mother rod to support the PCMI loading of an RIA. Indeed, a rodlet, CIP0-1, from a sibling ZIRLO rod has survived an RIA simulation test in Cabri.

Finally, further work on potential correction factors for application to calculate the CSED from conventional mechanical tests is deemed necessary.

Table 1. **Sample and test characteristics**

Sample Id	Oxide thickness ( $\mu\text{m}$ )	Peak strain position	Test temperature ( $^{\circ}\text{C}$ )
A	125	PP	280
B	103	PP	280
C	89	MP	280
D	106	MP	280
E	104	PP	320
F	122	PP	340
G	91	MP	320
H	109	MP	340

<sup>11</sup> F. Yunchang and D.A. Koss, "The Influence of Multiaxial Satates of Stress, " on the Hydrogen Embrittlement of Zirconium Alloy Sheet", Metallurgical Transactions A, Vol. 16A, April 1985, pp 675-681.

Figure 1. EDC test sketch

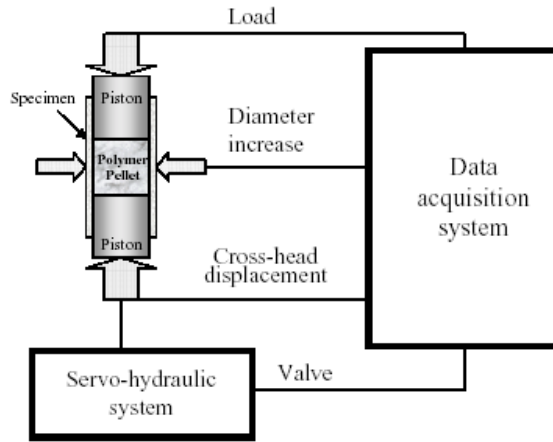


Figure 2. Post-test sample overall appearance



Figure 3. Measured CSED and hoop strain vs. oxide thickness

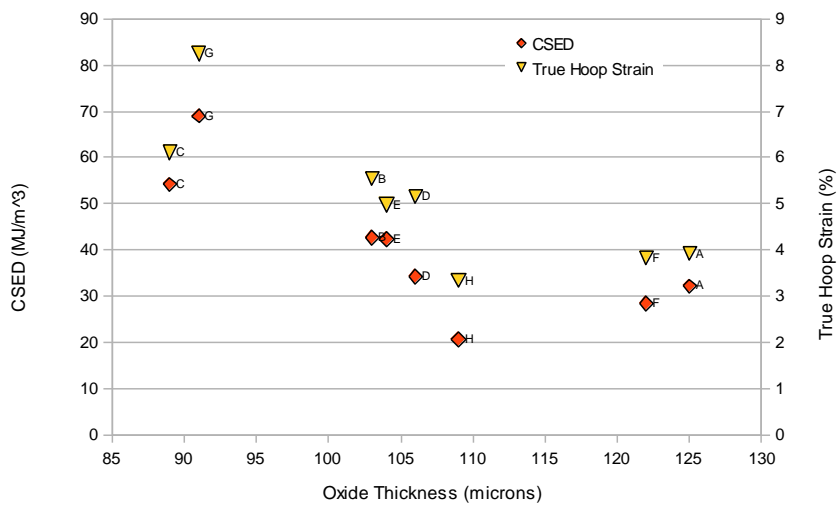
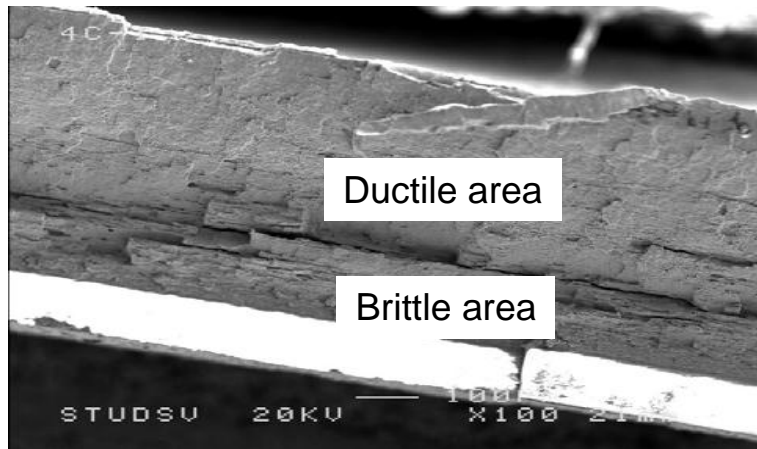


Figure 4. Example of fractography. specimen D

a) Secondary electron image (60x)



b) Secondary electron images (700x)

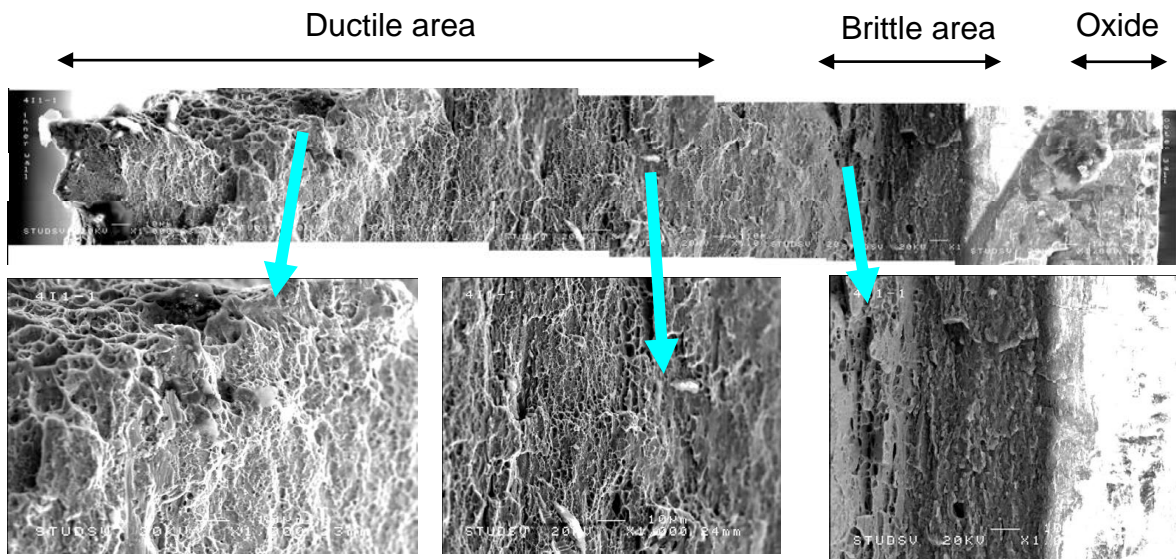
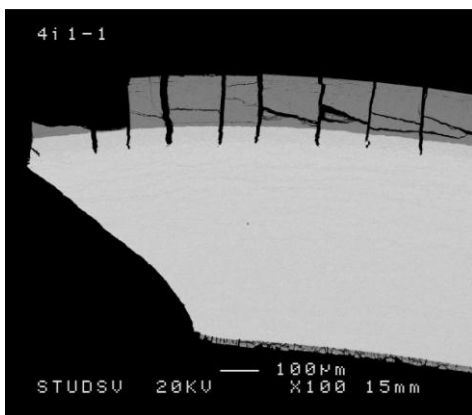


Figure 5. Cross-section metallography specimen D. rupture location

a) BEI showing oxide



b) SEI showing hydrides

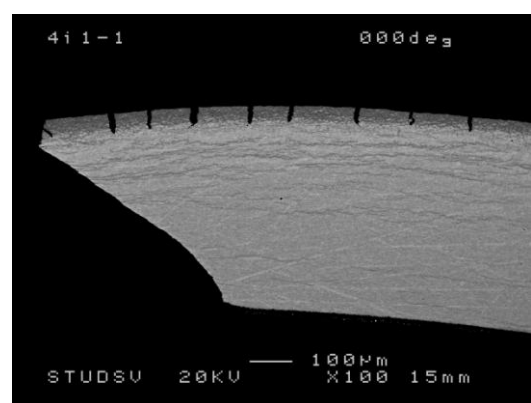


Figure 6. Azimuthal distribution of the oxide and hydride rim thickness  
 a) Specimen D  
 b) Specimen H

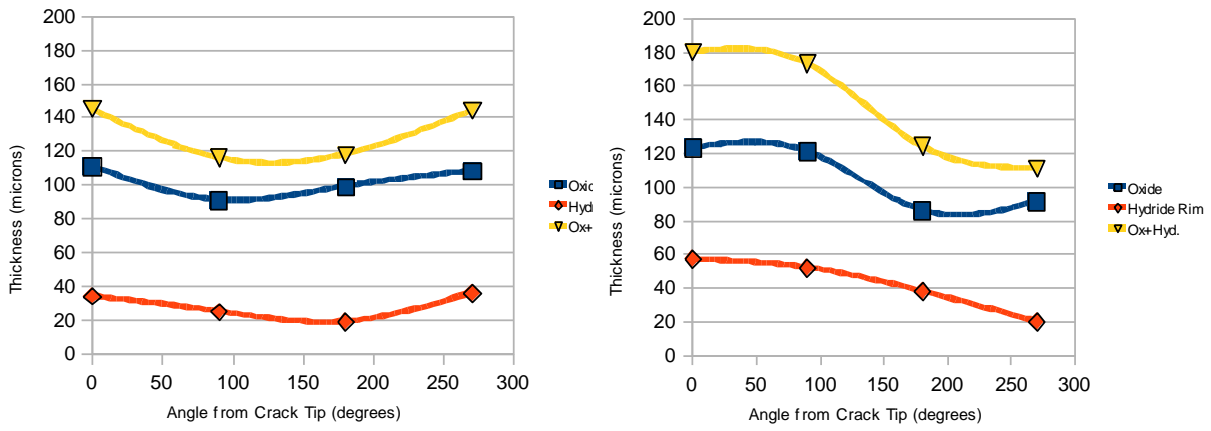


Figure 7. Measured CSED vs. hoop strain at failure

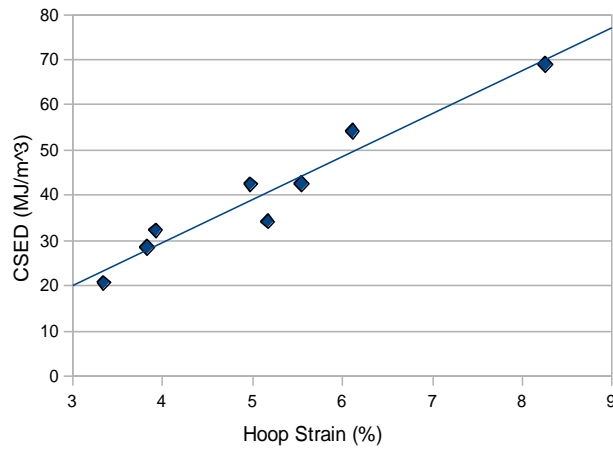


Figure 8. CSED vs. test temperature

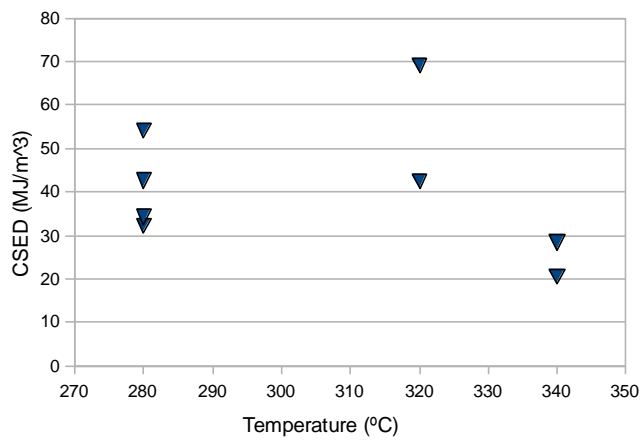


Figure 9. CSED measured and calculated from standard tests

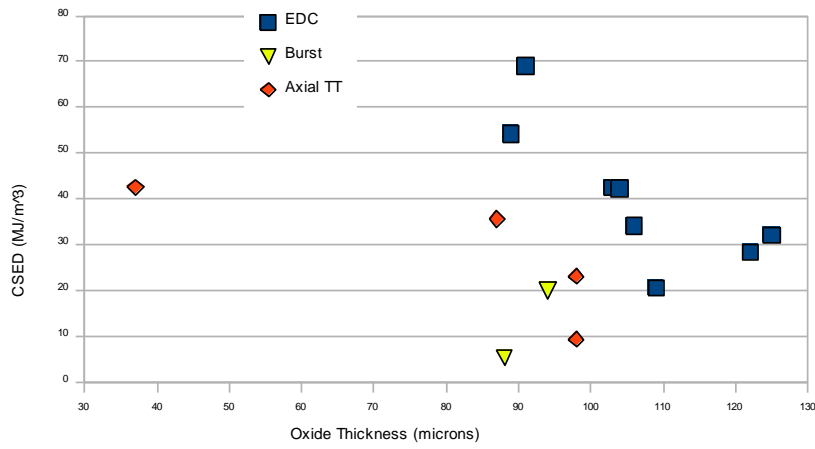


Figure 10. Comparison of EDC and conventional test strain to failure

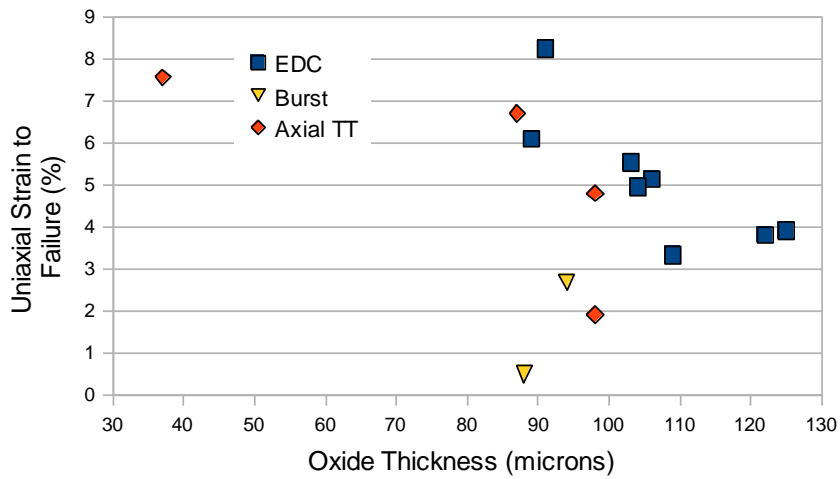
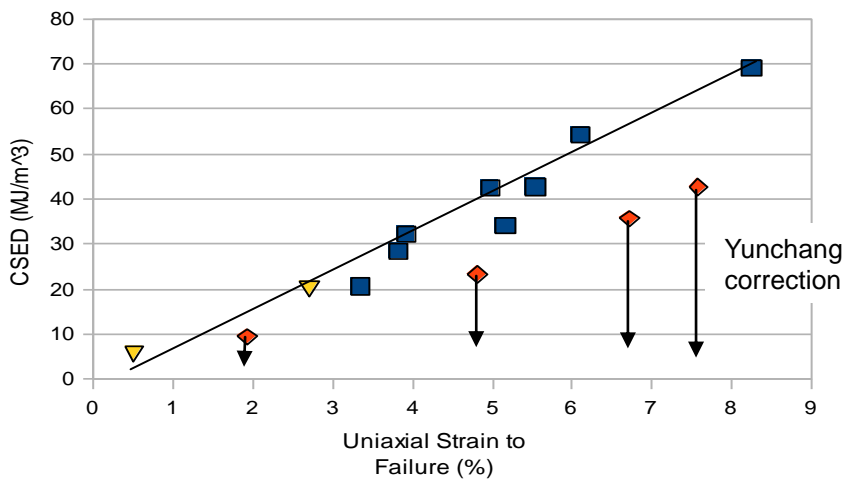


Figure 11. CSED vs.uniaxial strain to failure





## EDC test results on High Burnup ZIRLO

M. Quecedo, JM Conde,  
M Lloret, JM Rey

OECD-NEA RIA Workshop

**ENUSA** **CSN** CONSEJO DE SEGURIDAD NUCLEAR

### CONTENTS

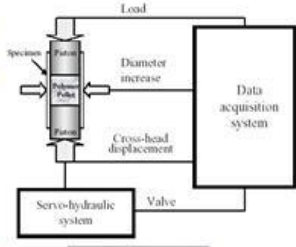
- Test and Specimen Description.
- Results and Pos-test Characterization.
- Analysis.
- Conclusions.

**ENUSA** **CSN** CONSEJO DE SEGURIDAD NUCLEAR

OECD-NEA RIA Workshop

### EDC TEST DESCRIPTION

- Cladding strained by internal expansion of a polymer pellet.
- Test Outcome:
  - CSED
  - Permanent hoop strain
- Loading state:
  - Mainly in Hoop direction.
  - Axially  $\sigma = F(\text{friction})$
- Fast loading:  $\dot{\epsilon} \approx \text{RIA}$ .
- Performed in Studsvik.





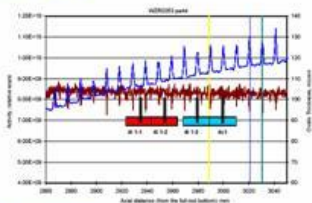
~20 mm

**ENUSA** **CSN** CONSEJO DE SEGURIDAD NUCLEAR

OECD-NEA RIA Workshop

### SCOPE DEFINITION

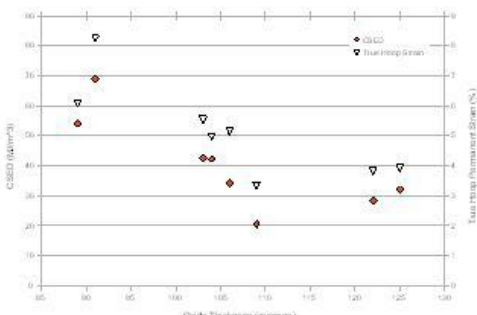
- Eight samples from ZIRLO rods from Vandellós:
  - Local burnup: 75 MWd/kgU
  - Oxide thickness: 90->120 μm
- Test conditions:
  - 280->340 °C
  - Strain rate: 1 s<sup>-1</sup>
- Post-test exams:
  - Profilometry.
  - Metallography & Fractography
  - Local hydrogen content.






DECO NEA RIA Workshop 4

### TEST RESULTS

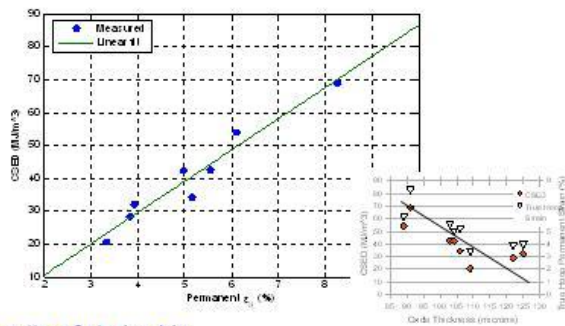


Some dependence on Oxide Thickness




DECO NEA RIA Workshop 5

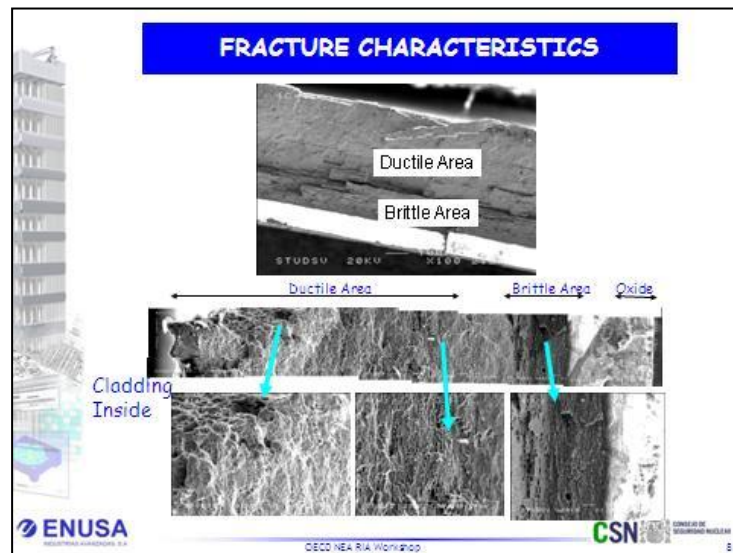
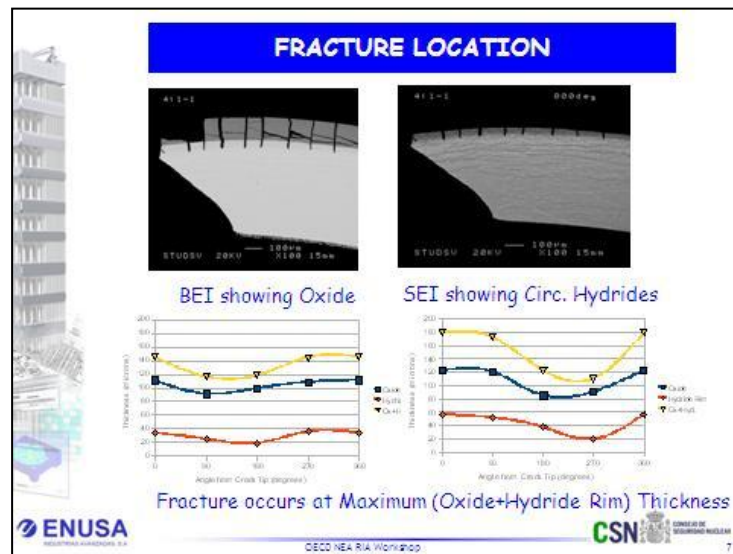
### Measured CSED vs Permanent Hoop Strain



Excellent Relationship:  
 Either parameter may be used as failure limit.  
 Ductility variability seems real.




DECO NEA RIA Workshop 6



### CSED CALCULATION

- Isotropic Hardening, Ramberg-Osgood.

$$\sigma_{eff} = K \left( \frac{\epsilon}{\epsilon_0} \right)^n (\epsilon_{eff})$$

- Strength Coefficient K adjusted to match measured yield strength.

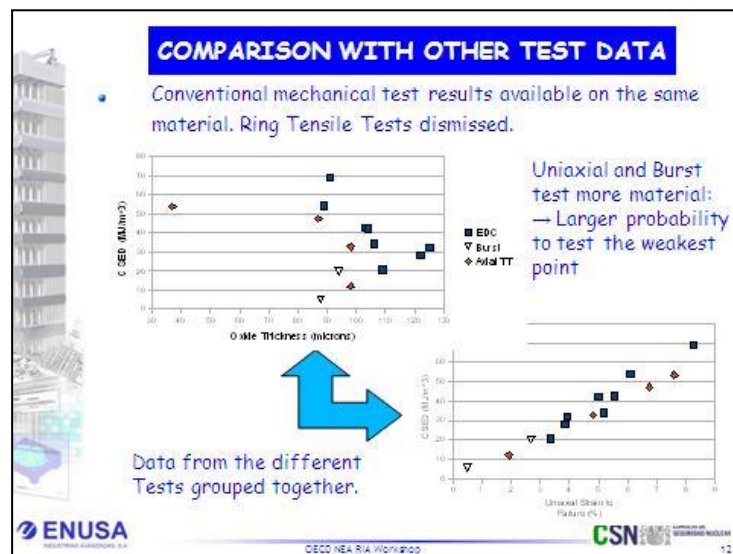
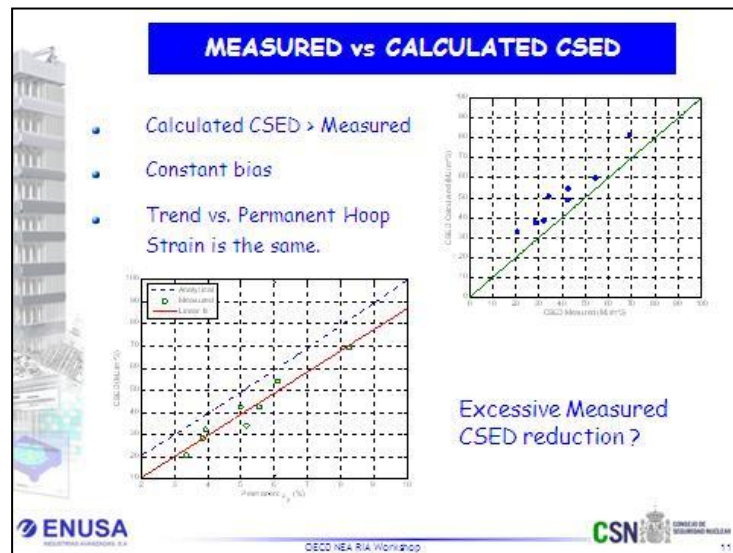
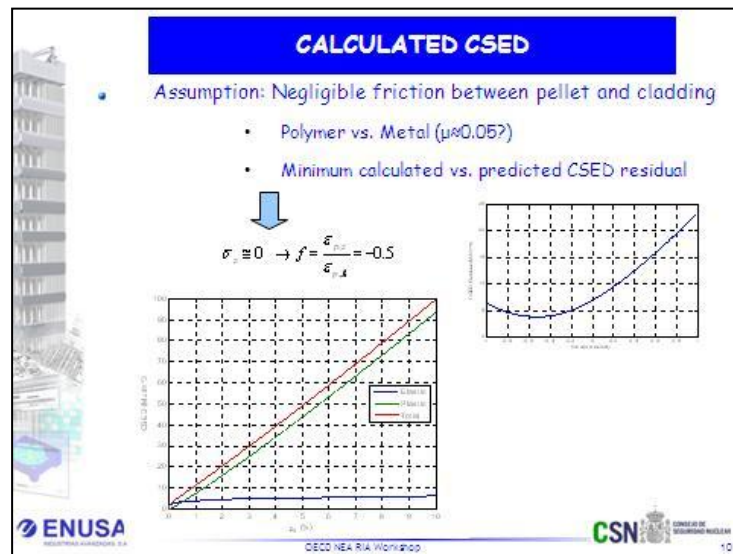
$$CSED = CSED_{elastic} + CSED_{plastic} = \frac{1}{2E} R_y (\sigma_{eff})^2 + K \left( \frac{\epsilon}{\epsilon_0} \right)^{1+n} \frac{1}{1+n} (\epsilon_{eff})^{1+n}$$

$$f = \frac{\epsilon_{pl}}{\epsilon_{pl,0}} \quad R = \frac{2}{3}(1+\nu) + 3(1-2\nu) \frac{1+f}{\sqrt{3}(1+f'+f)}$$

$$\epsilon_{eff} = \frac{2}{\sqrt{3}} \sqrt{1+f'+f} \epsilon_{pl,0} \quad \sigma_{eff} = K \left( \frac{\epsilon}{\epsilon_0} \right)^n (\epsilon_{eff})$$

ENUSA
 CSN

DECO NEA RIA Workshop 9





## CONCLUSIONS

- CSED and Permanent Hoop Strain measured in Eight ZIRLO specimens (75 MWd/kgU, 90-120  $\mu\text{m}$  oxide).
- CSED, Hoop Strain and fracture characteristics coherently indicate a significant retained cladding ductility.
- Measured CSED and Hoop Strain in good agreement with:
  - Theory.
  - Results from conventional (reliable) mechanical tests.
- Either CSED and Hoop Strain seem an appropriate failure limit.
- Local (Oxide + Dense hydride rim) thickness controls the failure location.
- Extension to RX material (hydride network) under way.

DECO-NEA RIA Workshop

## **DUCTILITY AND FAILURE BEHAVIOUR OF BOTH UNIRRADIATED AND IRRADIATED ZIRCALOY-4 CLADDING USING PLANE STRAIN TENSILE SPECIMENS**

**S. Carassou, M. Le Saux, J.P. Pizzanelli, O. Rabouille, X. Averty, C. Poussard**  
CEA Saclay, DEN-DMN, France

**B. Cazalis, J. Desquines**  
Institut de Radioprotection et de Sûreté Nucleaire (IRSN), DPAM-SEMCA, France

**C. Bernaudat**  
EDF, SEPTEN, France

### **1. Introduction**

As part of studies conducted in France on Reactivity Initiated Accident (RIA), IRSN and EDF have launched a large experimental project (PROMETRA) carried out by CEA in order to provide both material properties and material failure data [1]. During the first phase of a RIA event, the in-service loading deforms the cladding in the circumferential direction under multiaxial tension, in a situation close to an axial plane strain situation. In order to accurately evaluate the risk of rod failure during this stage, it is important to develop models able to predict the material behaviour under those representative loading conditions. Obviously, the fracture behaviour has also to be determined. To this end, uniaxial tensile data have been obtained between 20°C and 1100°C under high strain rates (0.01 to 5s<sup>-1</sup>) and high heating rates (up to 200°C.s<sup>-1</sup>) from specimens machined along the axis of the cladding or in the circumferential direction (ring specimens).

Material constitutive law formalisms are well adapted to reproduce the material behaviour in various mechanical loading conditions, especially when anisotropy is taken into account. Thus, as far as damage does not play a major role on the mechanical behaviour, the characterisation of the material mechanical behaviour can be achieved with standard uniaxial tests (axial and circumferential) performed under representative heating and strain rates. For instance, the PROMETRA database has recently been used to derive anisotropic viscoplastic constitutive relationships that take into account the influence of burn up, corrosion level, strain rate and temperature [2]. These relationships are applicable in a wide loading condition range including the RIA representative loading conditions.

On the other hand, as far as fracture is concerned, it is necessary to characterise the fracture behaviour in fully representative conditions, regarding both loading conditions (see figure [1]) and fracture mechanisms (see figure [2]).

Thus, the fracture data obtained up to now in the frame of the PROMETRA program using classical burst specimen or ring tensile specimens cannot be directly used to derive a material failure criterion convenient for RIA studies.

The aim of this study is to use a specific specimen geometry developed in order to assess fracture strain of irradiated Zircaloy-4 in conditions that are nearly representative of the loading (i.e. about zero axial strain) and fully representative of the fracture mode (i.e. outer diametral crack nucleation, then through-wall propagation of the crack) of the PCMI phase of an RIA.

Figure 1. Loading characteristics for RIA integral test (CABRI) and several mechanical testing (under the assumptions of isotropic material and proportional loading) [1]

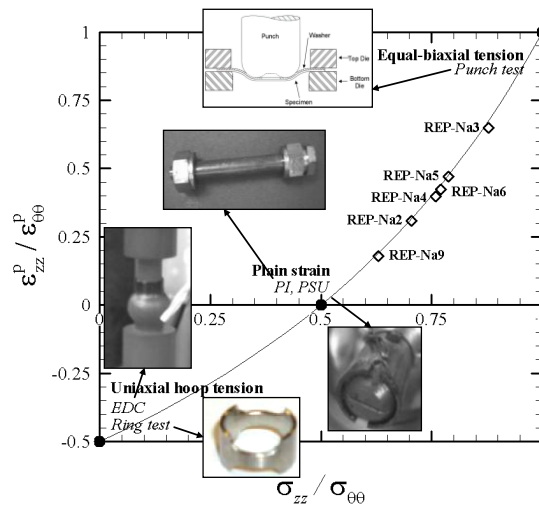


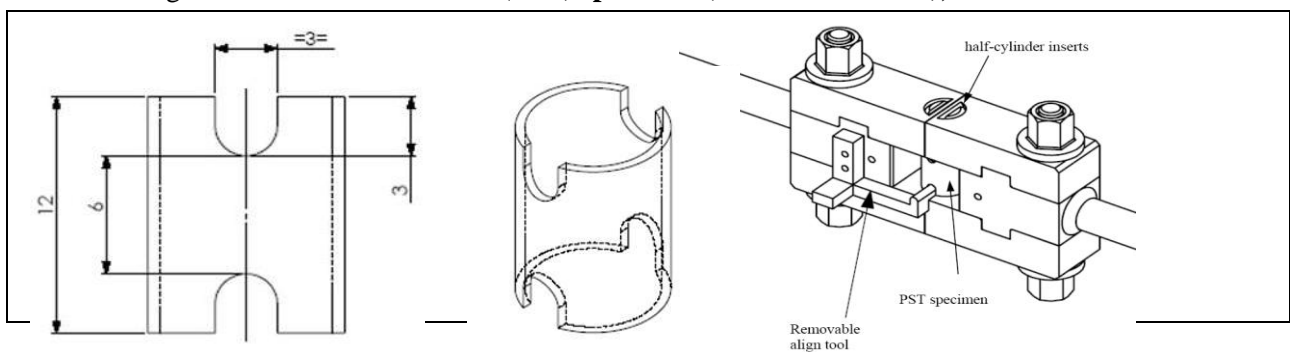
Figure 2. Fracture obtained after CABRI test REP-Na 8 [3]



## 2. Material and specimens

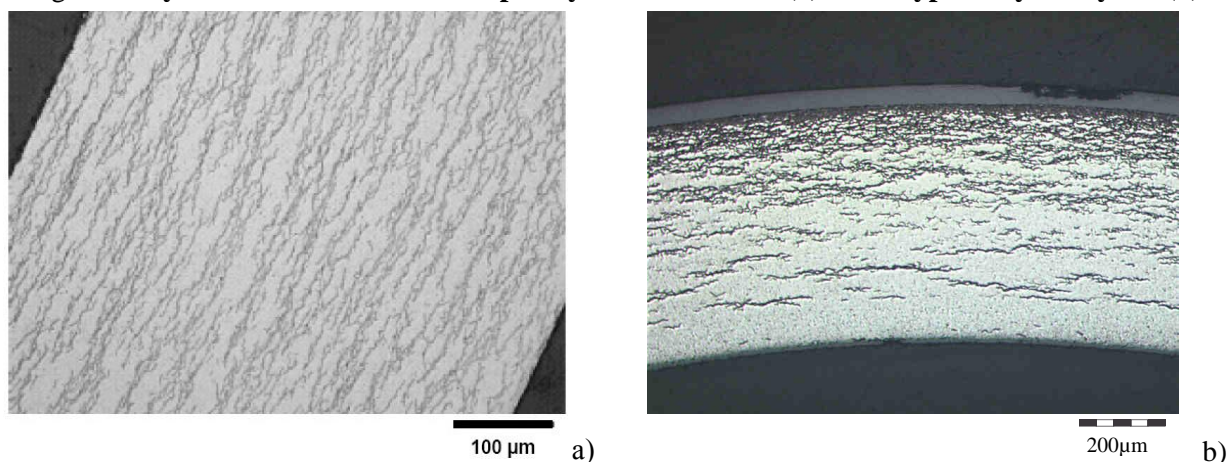
The Plane Strain Tensile (PST) specimen, initially developed at Pennsylvania State University [4], presents two notches, machined on each sides of the specimen (figure 3). The PST samples were machined from Zy-4 standard alloy, irradiated during 5 annual cycles in the French PWR CRUAS-2. The burn-up reached by the assembly is about 54 GWd/tU. The oxide layer (removed before machining of the specimen), was about 50 $\mu$ m, and the Hydride concentration can be estimated between 350 and 400 ppm.

Figure 3. Plane strain tensile (PST) specimen (dimension in mm), and cross-head



Before testing irradiated material, some tests were previously performed using the same methodology on non irradiated material in as received state, and homogeneously pre-hydrated ( $[H] = 700$  ppm, see figure 4).

Figure 4. Hydride distribution for the pre-hydrated material (a) and a typical Zy-4 5 cycles (b)



### 3. Methodology

The tensile tests were performed on a servo-hydraulic tensile testing machine located at the LECI hot cells, in CEA/Saclay. All the tests were performed with a displacement rate of  $0.003 \text{ mm}\cdot\text{s}^{-1}$  (corresponding to a strain rate of  $10^{-3} \text{ s}^{-1}$  for a specimen with a calibrated gauge length of 3 mm). The samples were placed around two half-cylinder inserts attached to the cross-heads and pulled apart inside the specimen (figure 3). Contrary to the testing procedure proposed by PSU [4,5], the notches were oriented perpendicularly to the pulling direction in order to minimise friction effects. No lubrication was used between the mandrels and the specimen. The specimens were previously painted with a speckling device, and the tests were filmed in order to perform local strain measurement by digital image correlation (DIC) method. Note that a microhardness indentation technique was used in [4,5], to measure local failure strains on the outer surface of PST specimens. Nevertheless, this technique is not well adapted for irradiated materials and/or for tests performed at high temperature.

Because the specimen does not have a well defined gauge length, a classical stress-strain curve would not be appropriate. Thus, the plastic displacement versus load curves were determined. The plastic displacement is obtained by removing the elastic part of the cross-head displacement measured during the experiments.

A 2-D Digital Image Correlation (DIC) technique was used to characterise the deformation of the PST specimens. DIC is an optical method that provides local displacement and strain fields on an object's surface by comparing digital images of the specimen taken before and after deformation. The surface of the specimen was illuminated with white-light and filmed with a digital video camera (resolution of  $1600 \times 1200$  pixels, image rate of 25 frames per second). The random patterns that offer the local contrast required for the identification of homologous points were obtained by speckling paint with an airbrush on the surface of the specimen. The spots of the specklegram have a diameter of about  $40 \mu\text{m}$ .

The CorrelManuV software developed at LMS/Ecole Polytechnique was used for the DIC. The gauge length of the measured local strain field is between  $150$  and  $200 \mu\text{m}$  (the typical domain used is 30 pixels square, each pixel corresponding to  $5 \mu\text{m}$  to  $8 \mu\text{m}$ , depending on the test). The expected accuracy of the strain measurement is approximately  $\pm 0.01$  (1%). The maximum strain that can be reliably measured is about 50%. For larger strains, the paint tends to flake off the specimen, leading to incorrect values. After the test, it is possible to compute the strain fields at a specific loading point, (including the image taken just prior to the fracture), provided that the strain do not exceed critical value.

Finite elements computations were carried out in support to the mechanical testing, using the finite element code Cast3M developed at CEA ([www-cast3m.cea.fr/cast3m/index.jsp](http://www-cast3m.cea.fr/cast3m/index.jsp)). Brick elements with quadratic interpolation (20 nodes, 27 Gauss points) were used for the calculations, based on a large displacement and

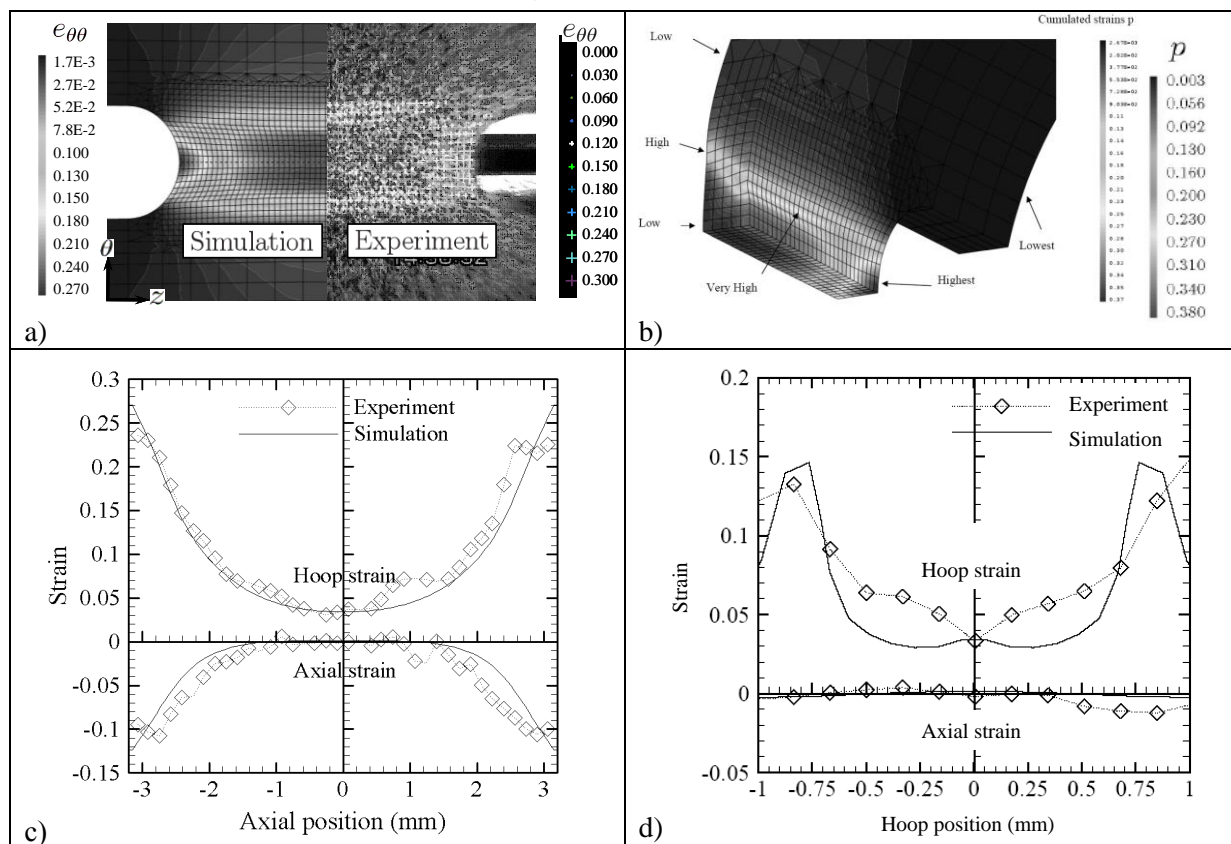
large strain formulation. According to the symmetries, only 1/8 of the system was considered. Standard boundary conditions were applied and a contact area involving sliding with friction was defined between the inner surface of the ring specimen and the outer surface of the die inserts. Friction was modelled by the classical Coulomb's friction law (friction coefficient,  $\mu=0.4$ ). The cross-head displacement is applied on the tangential direction of the sample gauge section. The set of constitutive equations proposed in [2] for fresh material was used to describe the mechanical behaviour of the cladding.

#### 4. Finite Element Analysis of the PST test

The mechanical PST tests performed on non irradiated material at room temperature were simulated, with the double goal to improve the knowledge of the structural behaviour of the specimen and to validate the DIC methodology.

At the early stage of elasticity, due to bending, the external surface of the specimen is loaded in hoop compression. Due to the presence of the notches that act as stress concentrators, tension stress bands then appear and link the two notches, surrounding a central compressive zone. Between the onset of global plasticity and the maximum load, the compressive zone disappears, and the bands grow up to promote a strong strain localisation pattern, symmetrical with respect to the axial direction of the specimen figure a). This strain localisation on external surface reflects shearing bands along the specimen width, promoted by the plane strain state [figures b) and d)]. After very large strain, the localisation bands became less sharp, and a nearly homogeneous stress and strain test appears in the middle of the specimen, where plane strain condition is fulfilled.

Figure 5. Calculated (FEA) and measured (DIC) hoop strain (results obtained on fresh Zy-4, tested at 25°C, at maximum load)



Figures a), c) and d), show the comparison between the hoop and axial strains calculated with finite elements and assessed by DIC. The good matching stands for cross-checking of both independent analyses,

and gives strong confidence on DIC measured strains. We can see from picture c) that, in these testing conditions, the plane strain state (zero axial stress) prevails in a large area between the notches, but is not fulfilled close to the notches.

## 5. Results and analysis of PST test

We can see from the global load-plastic displacement curves obtained on irradiated material shown in figure 6, that there is a strong temperature effect on the load (decreasing with temperature), and on the plastic displacement at fracture. The ultimate elongation increases between 280°C and 480°C, indicating an increase of the apparent ductility with temperature.

Figure 6. Load versus displacement on PST specimens machined from Zy-4 irradiated 5 cycles

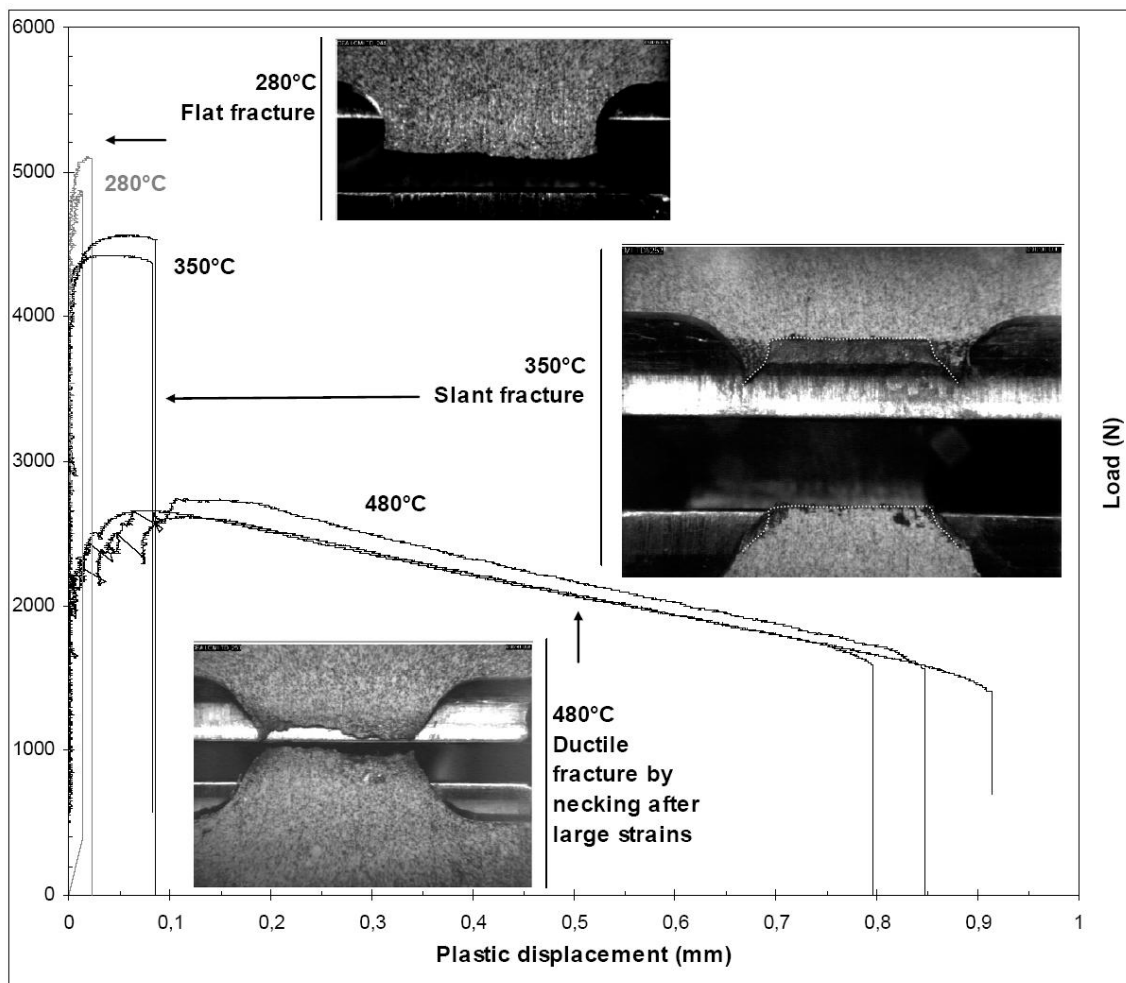


Table 1 summarises the fracture data obtained in this study on the hydrided and irradiated material, as well as data previously obtained [7]. When there is no clear evidence on the onset of fracture, the so-called “fracture strain” is the hoop strain value measured on the external surface at the middle of the specimen just prior to fracture. When cracks leading to fracture are detected, the fracture strain is the hoop strain at the location of the crack before it appears.

When comparing these values, care has to be taken of the different strain rates values, because of their well known effect on behaviour and ductility of zirconium alloys [8]. At room temperature, the ductility obtained

in this study on hydrided Zy-4 (10%), is two times greater than the value obtained in an equivalent material in a previous work (5%, obtained in [7]). This could be explained by the strain rate value that was  $10^2$  times greater in the previous work, leading to a lower ductility, enhanced by greater adiabatic heating. The very high value obtained on irradiated material at 480°C (more than 50% with necking, to be compared to 10% with slant for fresh hydrided and non hydrided material), could also be explained by the same reasoning, taking into account the decreasing effect of hydrides at this temperature. At 350°C, the values obtained in this study are very similar to these obtained previously, which is consistent with low values of strain rate sensitivity close to 350°C, caused by dynamic strain ageing of zirconium alloys [8].

Taking into account strain rate effects, we can assess that the effect of an homogeneous hydride distribution is visible at all the tested temperature (thus it becomes negligible at 480°C). Indeed, a strong effect of irradiation (or of the hydride non homogeneous distribution across thickness, as suggested by the results reported in [4] for non irradiated Zy-4 fuel cladding with a hydride rim) is clearly evidenced at 280°C and 25°C, by comparing fresh hydrided and irradiated material. This effect tends to disappear at 350°C.

Table 1. Fracture strains and fracture mode on PST specimens

T (°C)	Strain rates <sup>1</sup>	Zy-4 ; 0 ppm			Zy-4 ; 700-800 ppm			Zy-4 5 cycles (~400ppm)		
		Strain at fracture	Fracture mode	Source	Strain at fracture	Fracture mode	Source	Strain at fracture	Fracture mode	Source
25	$10^{-1}$	15%	slant	[7]	5%	flat	[7]	< 3%	flat	*
	$10^{-3}$				10%	flat	(1)			
280	$10^{-1}$	15%	slant	*	7%	?	*	3%	flat	(1)
	$10^{-3}$				8-10%	?	*			
350	$10^{-1}$	15%	slant	[7]	8%	slant	[7]	10%	slant	(1)
	$10^{-3}$				7 - 9%	slant	(1)			
480	$10^{-1}$	13%	slant	[7]	10%	slant	[7]	> 50%	necking	(1)
	$10^{-3}$									

(1) This study

\* no test at this temperature, but result are assumed from surrounding temperatures.

## 6. Failure mode and fracture process

At 480°C, the failure mode is ductile fracture by necking after large strains. A crack appears in the middle of the specimen after the maximum load. It appears to be a through-wall crack that propagated in a stable manner from the centre of the specimen (where a plane strain state prevails) toward the notches. The middle crack seems to appear on both sides of the specimen (the so-called “front side”, which is filmed, and the so-called “back side”), as suggested by the visible edges of an opened crack located at the back side of the specimen just after the fracture of the front side (see figure 7 –b).

At 280°C, fracture occurs prior to the development of necking. The fracture surface is macroscopically roughly perpendicular to the principal loading direction. The two specimens tested at 280°C exhibited either one or two cracks. Each crack started from a notch, near the plane of symmetry of the specimen, and propagated toward the centre of the specimen. The crack initiation occurred at the very onset of global plasticity, or just prior to the maximum load. The onset of the crack is located slightly away from the symmetry plane of the specimen, which is consistent with finite element calculations and measurement, which exhibit strain bands even at the early stage of plasticity (figure 7). In both cases, the crack exhibited a large stable axial propagation with no measurable reduction of the load (figure 7 –e shows a crack that propagated up to occupy nearly 80% of the width between the notches, without load reduction). If these cracks extended through the thickness of the specimen, we would expect a decrease in the load ranging from 40% (for a single crack) to 80% (if there were two cracks of the same length on both sides of the specimen). Therefore, at 280°C, the cracks must have propagated only along the outer surface of the specimen.

Figure 7. Pictures of Zy-4 irradiated 5 cycles PST specimens just prior to and just after fracture (see figure 8 for SEM examination of location “1” on figure 7-c)

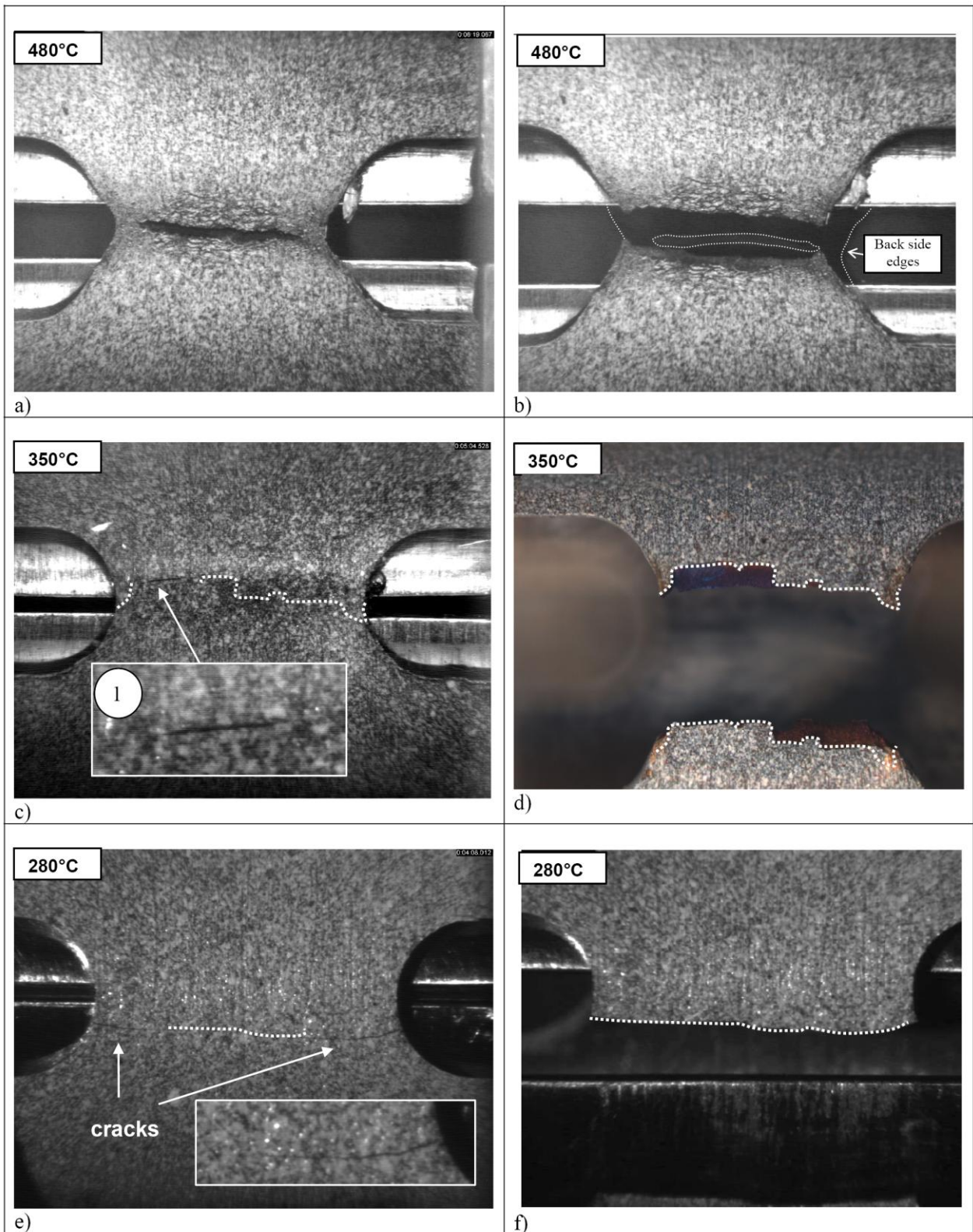
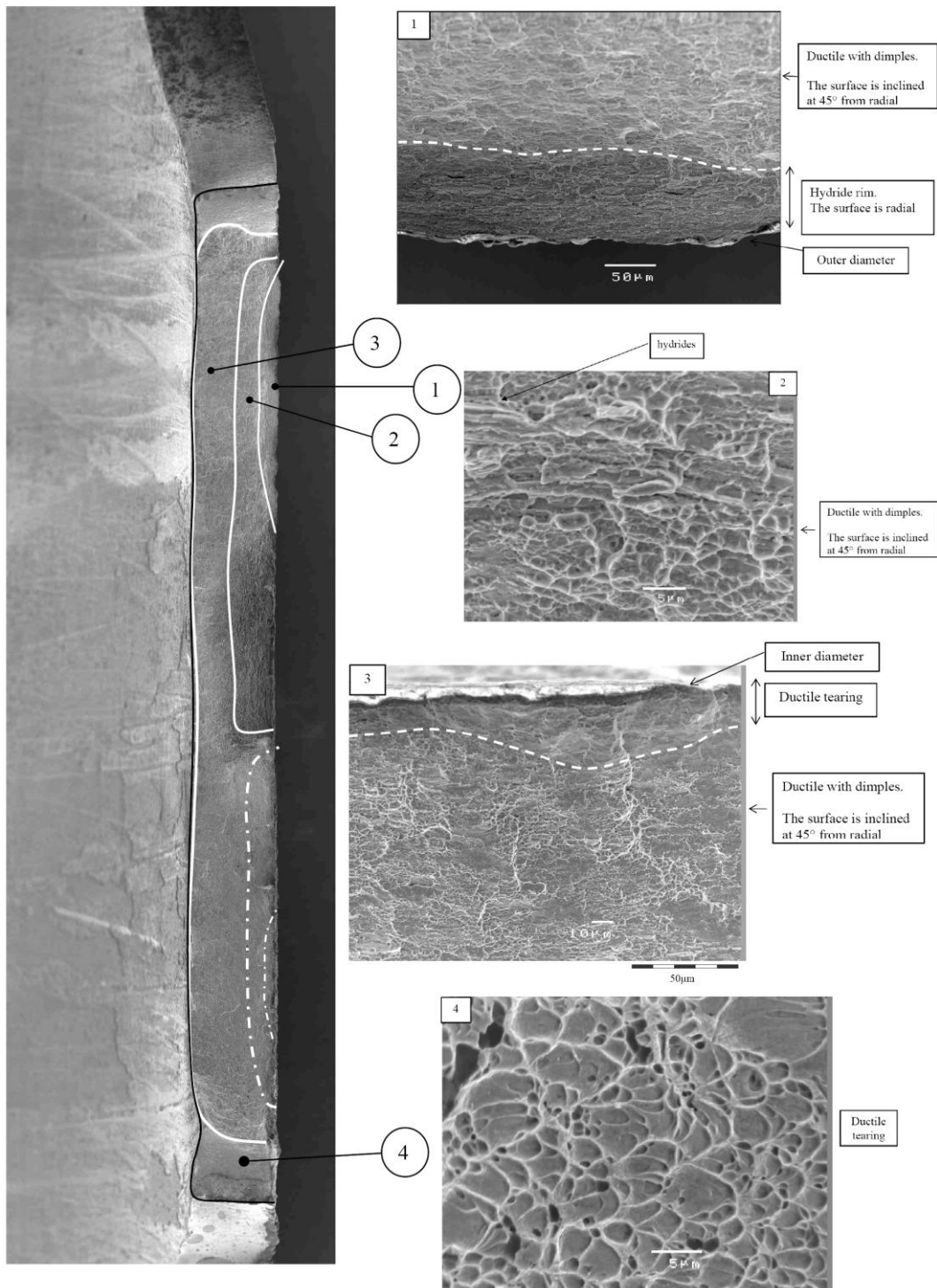


Figure 8. SEM examinations of Zy-4 irradiated 5 cycles PST tested at 350°C (location “1” in this picture is the same than area “1” in figure 7-c)



At 350°C, the specimens exhibit a so-called “through-thickness slant fracture” (figure 7), characterised by a plane inclined at 45° from the cladding thickness in the central area of the specimen, and inclined at about 45° from axial and hoop directions near the notches. Only one of the two specimens tested at 350°C failed on the front-side, and exhibited a “double through-thickness slant fracture” (see figure 7 –d). For this specimen, a crack was detected at the outer diameter slightly prior to the maximum load. This crack was located between the notches and the middle of the specimen. Between the onset of the crack and the final rupture, no drastic decrease of the load was observed. Just prior to fracture, the crack appeared to be roughly 1 mm in length (the initial distance between the notches being 6 mm). Following the same reasoning used in the previous section, if this 1mm crack extended through the whole thickness of the specimen, the section decrease would have caused a 10% to 20% reduction in the load (depending on the presence of a crack on the other side). Because no such decrease in load was observed before final fracture, we can reasonably infer that the crack observed was not a through-wall crack, but was instead limited to the external surface of the specimen.

SEM examinations were recently performed on the specimen exhibiting a double through-wall slant fracture, and preliminary results are presented in the following (see figure 7). The global view shows a double fracture, with two planes oriented at 45° from the radial direction but oriented at 90° from each other, intersecting in the middle of the specimen. When looking at the area located at the outer diameter of the sample, at the estimated axial position where a crack was observed during the test (see figure 7–c and location 1), a quasi-brittle fracture, characteristic of a high H<sub>2</sub> content, is observed at this location. A hydride rim, with a maximal thickness of 100 µm at this location was detected all along the outer diameter.

Moving toward the inner surface, following the assumed extension of the initial crack initiated within the brittle hydride rim (see Fig. 7, location 2), the fracture is ductile with dimples, in a plane oriented at 45° from the radial direction. Close to the inner diameter of the specimen, (see Fig. 7, location 3), the thin area of strong ductile tearing located at the top of the picture shows that the crack propagation along the radial direction occurs from the outer surface to the inner surface, with final fracture at the inner diameter. This failure process is consistent with the results of full-scale RIA experiments performed on high burn-up fuel rods, with hydride rims or blisters located near the clad outer surface, in the NSRR [6] and CABRI reactors [3].

The strong ductile tearing and the intense necking observed near the notches (see figure 7, location 4) shows that the crack propagation along the axial direction occurs from the area between the notches toward the notches.

## 7. Conclusions

In this work, eight PST tests machined from a Zircaloy-4 cladding irradiated up to 5 annual cycles have been performed at 280°C, 350°C and 480°C. The specimen displacements during the tests were filmed and digitally recorded to allow the use of a Digital Image Correlation (DIC) analysis technique to experimentally determine the local strains on the outer surface of the specimens. The plane strain conditions have been verified and prevail over a wide area between the notches of the specimen, as expected from full 3D FE numerical analysis performed in support of the tests.

For the first time, the location of the onset of fracture for this geometry on irradiated material has been experimentally observed: at 280°C, crack initiates in the vicinity of the notches, in an area where plane strain conditions are not fulfilled, and for a local circumferential strain value of about 5%. At 350°C and 480°C, cracks initiate at a location where plane strain conditions prevail, for circumferential strain values respectively close to 10% and greater than 50%. These results have been compared to results obtained previously by similar test on fresh and hydrided material, as well as tests performed as support to the study. At 350°C, the homogeneous 700ppm hydrided Zy-4 and the Zy-4 irradiated during 5 annual cycles exhibit similar fracture behaviour, for both fracture hoop strain values (10%) and fracture mode (through-wall slant fracture).

For the irradiated material, it has clearly been established that at 350°C, a brittle fracture occurs at the outer surface in the hydride rim. The crack propagates subsequently toward the inner surface and the notches, where final fracture occurs, providing a fracture process fully representative of a fracture during the PCMI phase of an RIA. This methodology can therefore be used to validate and develop further existing RIA material failure criteria.

## References

- [1] Cazalis, B., et al., *The PROMETRA program: Fuel cladding mechanical behaviour under high strain rate*. Nuclear Technology, 2007. 157: p. 215-229.
- [2] Le Saux, M., et al., *A model to describe the anisotropic viscoplastic mechanical behaviour of fresh and irradiated Zircaloy-4 fuel claddings under RIA loading conditions*. Journal of Nuclear Materials, 2008. 378: p. 60-69.
- [3] Papin, J. et al. *Summary and interpretation of the CABRI REP-Na program*. Nuclear Technology, 2007. 157: p. 230-250.
- [4] Daum, R.S., et al. *The influence of a hydrided layer on the fracture of Zircaloy-4 cladding tubes*. in *International Conference on Hydrogen Effects on Material Behaviour and Corrosion Deformation Interactions*. 2002. Moran, Wyoming.
- [5] Link, T.M., T.A. Koss, and A.T. Motta, *Failure of Zircaloy cladding under transverse plane-strain deformation*. Nuclear Engineering and Design, 1998. 186: p. 379–394.
- [6] Fuketa, T. et al. *Fuel failure and fission gas release in high burn-up PWR fuels under RIA conditions*. Journal of Nuclear Materials, 1997. 248: p. 249-256.
- [7] Le Saux, M., et al. *Failure of Hydrided Zircaloy-4 Fuel Cladding Tubes under RIA Loading Conditions*. in *17<sup>th</sup> European Conference on Fracture*. 2008. Brno, Czech Republic.
- [8] Prioul, C., ed. *Le vieillissement dynamique dans les alliages de zirconium. Conséquences sur les propriétés mécaniques*. « Le Zirconium », journées d'études : « Propriétés – Microstructure ». 1995: INSTN, Saclay. 25-34.


 DEN/Saclay/Département des Matériaux pour le Nucléaire

## Ductility and Failure Behaviour of both Unirradiated and Irradiated Zircaloy-4 Cladding using Plane Strain Tensile Specimens

S. Carassou<sup>(1)</sup>, M. Le Saux<sup>(1)</sup>, J.P. Pizzanelli<sup>(1)</sup>, O. Rabouille<sup>(1)</sup>,  
 X. Averty<sup>(1)</sup>, C. Poussard<sup>(1)</sup>,  
 B. Cazalis<sup>(2)</sup>, J. Desquines<sup>(2)</sup>  
 and C. Bernaudat<sup>(3)</sup>

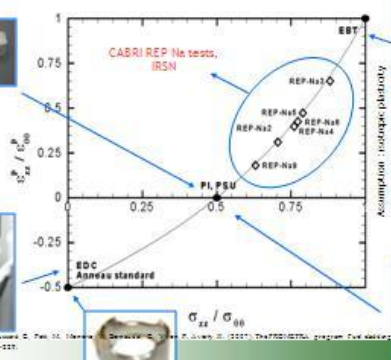
1 : CEA Saclay, Nuclear Energy Division  
 2 : IRSN/DBAM  
 3 : EDF/SEPTEN

WS RIA Paris, 10th September 2009
S. Carassou CEA/SEM/LCM
1




 DEN/Saclay/Département des Matériaux pour le Nucléaire

Many mechanical testing are available on cladding ...  
 ...But none of them fully represent actual RIA loading conditions


© Desquines, J. Poussard, C. Pélissier, M. Le Saux, B. Cazalis, C. Bernaudat, J. Averty, O. Rabouille, S. Carassou, 2009. The PROMETRA program Fuel cladding mechanical behaviour under irradiation. Nuclear Technology 167 217-229.

WS RIA Paris, 10th September 2009
S. Carassou CEA/SEM/LCM
3

DEN/Saclay/Département des Matériaux pour le Nucléaire

**cea**

### Test on Plane Strain Tensile specimen

- Usual short rings with machined gage sections induce uniaxial loading close to plane stress
- The PST specimen induces *plane strain* loading conditions at the middle of gage section.
- The plane strain (PST) failure conditions are supposed to be close to RIA failure conditions

*The objective is to provide fracture data on PST test in order to assess the influence of actual RIA loading conditions on failure strain*

---

WS RIA Paris, 10th September 2009 S. Carassou CEA/SEMI/LCM# 4

DEN/Saclay/Département des Matériaux pour le Nucléaire

**cea**

### Material description

- Zy-4 standard alloy, irradiated 5 cycles in the French PWR CRUAS-2
  - The burnup reached by the assembly is about 54 GWd/tU
  - Oxide layer thickness for our specimens can be estimated between 40µm and 50µm
- Non irradiated Zy-4 standard alloy
  - As received
  - Homogeneous pre-hydrated [H]~700ppm

---

WS RIA Paris, 10th September 2009 S. Carassou CEA/SEMI/LCM# 5

DEN/Saclay/Département des Matériaux pour le Nucléaire

**cea**

### Experimental Procedure

---

WS RIA Paris, 10th September 2009 S. Carassou CEA/SEMI/LCM# 6

DEN/Saclay/Département des Matériaux pour le Nucléaire

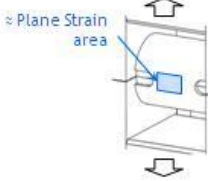
**cea**

### Mechanical Testing

- The tensile tests on irradiated materials were performed on a servo-hydraulic tensile testing machine (in M04 cell in LEC), with furnace heating
- The notches were placed at 90° from the loading direction, and no lubricant was used.
- The tests were filmed in order to perform local strain measurement by digital image correlation (DIC), using CorrelManuV software (developed at LMS/Ecole Polytechnique)



Dynamic tensile tests Machine  
(M04 cell in LEC)



Plane Strain area

WS RIA Paris, 10th September 2009
S. Carassou CEA/SEM/LCM
7

DEN/Saclay/Département des Matériaux pour le Nucléaire

**cea**

### Test Matrix

T° (°C)	Strain rate (s <sup>-1</sup> )	Zy-4 0ppm	Zy-4 700-800ppm	Zy-4 5 cycles
25	10 <sup>-1</sup>	x 2 <sup>(2)</sup>	x 2 <sup>(2)</sup>	
25	10 <sup>-3</sup>		x 2 <sup>(1)</sup>	
280	10 <sup>-1</sup>			
280	10 <sup>-3</sup>			x 2 <sup>(1)</sup>
350	10 <sup>-1</sup>	x 2 <sup>(2)</sup>	x 1 <sup>(2)</sup>	
350	10 <sup>-3</sup>		x 2 <sup>(1)</sup>	x 2 <sup>(1)</sup>
480	10 <sup>-1</sup>	x 1 <sup>(2)</sup>	x 1 <sup>(2)</sup>	
480	10 <sup>-3</sup>			x 3 <sup>(1)</sup>

(1) Test performed during this study 10<sup>-3</sup> s<sup>-1</sup>: 4 on fresh hydrided material (results discussed in this study)  
 (2) Test previously performed 10<sup>-1</sup> s<sup>-1</sup>

CEA-DRF/MT, Service 2, Travaux de base, 25105 Saclay, France. Université de Caen Normandie, Normandie Université, 14032 Caen Cedex 03, France. Institut de Mécanique des Matériaux, Université de Caen Normandie, 14032 Caen Cedex 03, France.

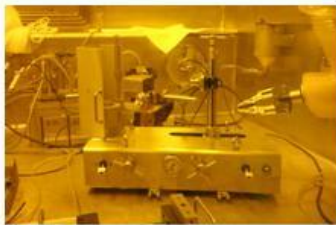
WS RIA Paris, 10th September 2009
S. Carassou CEA/SEM/LCM
8

DEN/Saclay/Département des Matériaux pour le Nucléaire

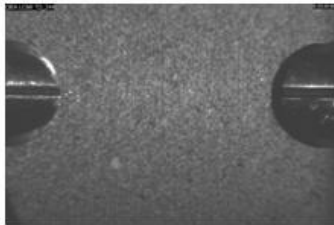
**cea**

### Strain assessment by Digital Image Correlation

- The specimens were painted with a speckling device, and the tests were filmed in order to perform local strain measurement by digital image correlation (DIC) method



Paint spraying device in LEC hot cell



random patterns obtained on a PST type specimen

WS RIA Paris, 10th September 2009
S. Carassou CEA/SEM/LCM
9

DEN/Saclay/Département des Matériaux pour le Nucléaire

cea

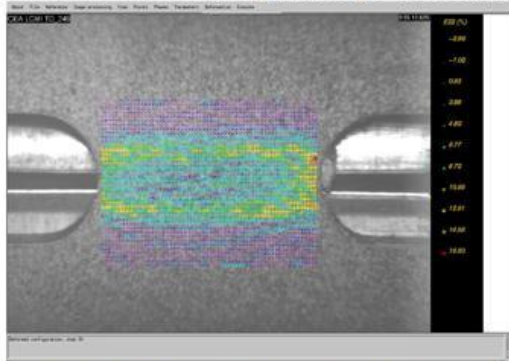
## Results and analysis of PST tests

WS RIA Paris, 10th September 2009 S. Carassou CEA/SEMI/LCMII 10

DEN/Saclay/Département des Matériaux pour le Nucléaire

cea

### Strain assessment by Digital Image Correlation



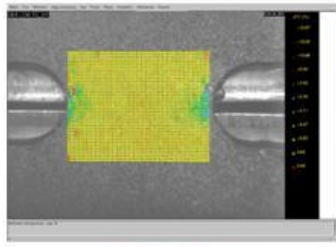
Test specifications : 480°C,  $10^{-3} \text{ s}^{-1}$  Test duration : 6 minutes (excluding furnace heating)  
 $\epsilon_{xx}$  evolution during the test obtained by DIC analysis

WS RIA Paris, 10th September 2009 S. Carassou CEA/SEMI/LCMII 11

DEN/Saclay/Département des Matériaux pour le Nucléaire

cea

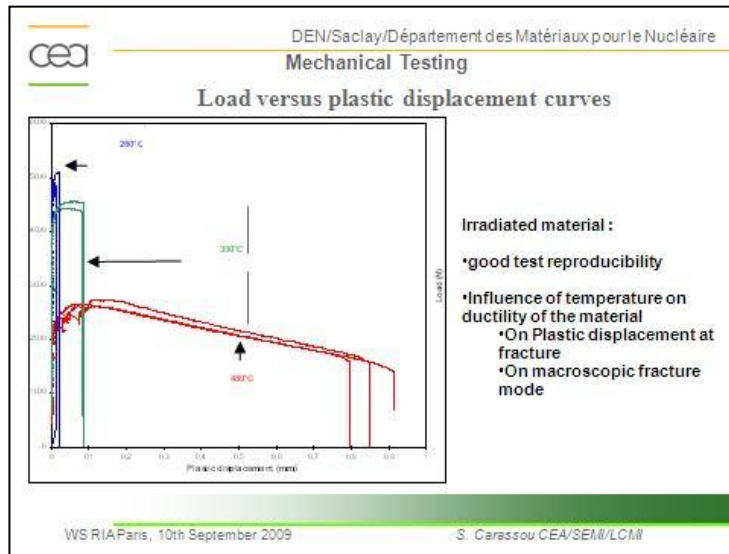
### Plane strain state of PST specimen



$\epsilon_{xx}$  obtained by DIC analysis

- 1) Cross checking of both simulations and experiment => confidence in DIC
- 2) As awaited, a large area between the notches is in a plane strain state

WS RIA Paris, 10th September 2009 S. Carassou CEA/SEMI/LCMII 12



DEN/Saclay/Département des Matériaux pour le Nucléaire

### Test Results : local fracture strain measurement

T° (°C)	Strain rate (s-1)	Zy-4 0ppm	Zy-4 700-800ppm	Zy-4 5 cycles
25	10 <sup>-1</sup>	15 % <sup>(2)</sup>	5% <sup>(2)</sup>	
25	10 <sup>-3</sup>		10% <sup>(1)</sup>	
280	10 <sup>-1</sup>			
280	10 <sup>-3</sup>			3% <sup>(1)</sup>
350	10 <sup>-1</sup>	15 % <sup>(2)</sup>	8% <sup>(2)</sup>	
350	10 <sup>-3</sup>		7.9% <sup>(1)</sup>	10% <sup>(1)</sup>
480	10 <sup>-1</sup>	13 % <sup>(2)</sup>	10% <sup>(2)</sup>	
480	10 <sup>-3</sup>			>50% <sup>(1)</sup>

(1) Test performed during this study  
(2) Test previously performed (results discussed in this study)

WS RIA Paris, 10th September 2009 S. Carassou CEA/SEM/LCM# 14

DEN/Saclay/Département des Matériaux pour le Nucléaire

### Test Results : local fracture strain measurement

T° (°C)	Strain rate (s-1)	Zy-4 0ppm	Zy-4 700-800ppm	Zy-4 5 cycles
25	10 <sup>-1</sup>	15 % <sup>(2)</sup>	5% <sup>(2)</sup>	
25	10 <sup>-3</sup>			
280	10 <sup>-1</sup>	15% <sup>(3)</sup>	7% <sup>(3)</sup>	
280	10 <sup>-3</sup>			
350	10 <sup>-1</sup>	15 % <sup>(2)</sup>	8% <sup>(2)</sup>	
350	10 <sup>-3</sup>			
480	10 <sup>-1</sup>	13 % <sup>(2)</sup>	10% <sup>(2)</sup>	
480	10 <sup>-3</sup>			

(1) Test performed during this study  
(2) Test previously performed (results discussed in this study)  
(3) Interpolated values for 10<sup>-1</sup> s<sup>-1</sup>

WS RIA Paris, 10th September 2009 S. Carassou CEA/SEM/LCM# 15

DEN/Saclay/Département des Matériaux pour le Nucléaire

**Test Results : local fracture strain measurement**

T° (°C)	Strain rate (s-1)	Zy-4 0ppm	Zy-4 700-800ppm	Zy-4 5 cycles
25	10 <sup>-1</sup>			
25	10 <sup>-3</sup>		10% <sup>(1)</sup>	< 3% <sup>(3)</sup>
280	10 <sup>-1</sup>			
280	10 <sup>-3</sup>		10-8% <sup>(3)</sup>	3% <sup>(1)</sup>
350	10 <sup>-1</sup>			
350	10 <sup>-3</sup>		7-9% <sup>(1)</sup>	10% <sup>(1)</sup>
480	10 <sup>-1</sup>			
480	10 <sup>-3</sup>			>50% <sup>(1)</sup>

(1) Test performed during this study  
 (2) Test previously performed (results discussed in this study)  
 (3) Interpolated values for 10<sup>-4</sup> s<sup>-1</sup>

WS RIA Paris, 10th September 2009 S. Carassou CEA/SEM/LCM# 16

DEN/Saclay/Département des Matériaux pour le Nucléaire

**Test Results : local fracture strain measurement**

T° (°C)	Strain rate (s-1)	Zy-4 0ppm	Zy-4 700-800ppm	Zy-4 5 cycles
25	10 <sup>-1</sup>	15% ←	5%	
25	10 <sup>-3</sup>		10%	< 3%
280	10 <sup>-1</sup>	15% ←	7%	
280	10 <sup>-3</sup>		10-8%	3%
350	10 <sup>-1</sup>	15% ←	8%	
350	10 <sup>-3</sup>		7-9%	10%
480	10 <sup>-1</sup>	13% ←	10%	
480	10 <sup>-3</sup>			>50%

**Hydride content effect (Homogeneous distribution) on fracture strain (PST specimens)**

Decreasing with increasing temperature

WS RIA Paris, 10th September 2009 S. Carassou CEA/SEM/LCM# 17

DEN/Saclay/Département des Matériaux pour le Nucléaire

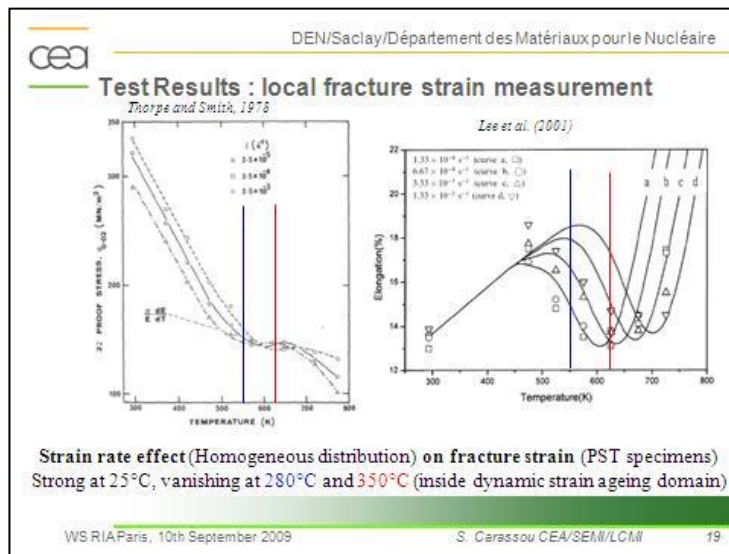
**Test Results : local fracture strain measurement**

T° (°C)	Strain rate (s-1)	Zy-4 0ppm	Zy-4 700-800ppm	Zy-4 5 cycles
25	10 <sup>-1</sup>	15%	5% ↑	
25	10 <sup>-3</sup>		10%	< 3%
280	10 <sup>-1</sup>	15%	7%	
280	10 <sup>-3</sup>		10-8%	3%
350	10 <sup>-1</sup>	15%	8%	
350	10 <sup>-3</sup>		7-9%	10%
480	10 <sup>-1</sup>	13%	10%	
480	10 <sup>-3</sup>			>50%

**Strain rate effect (Homogeneous distribution) on fracture strain (PST specimens)**

Strong at 25°C, vanishing at 280°C and 350°C (inside dynamic strain ageing domain)

WS RIA Paris, 10th September 2009 S. Carassou CEA/SEM/LCM# 18

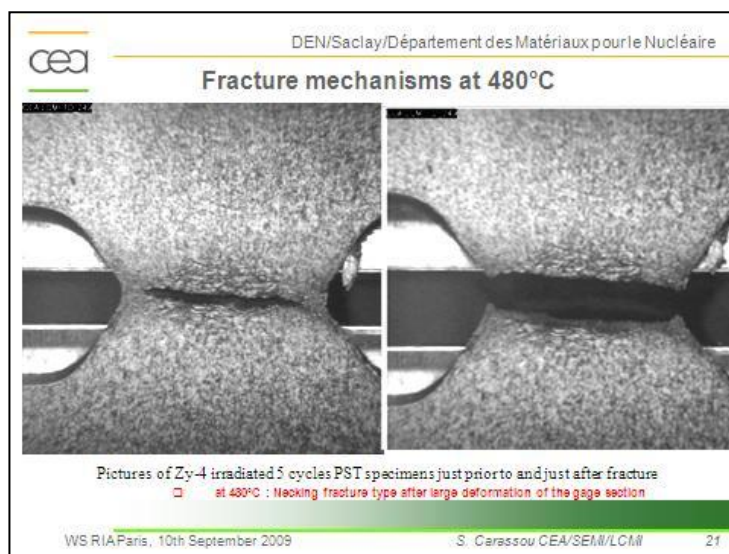


DEN/Saclay/Département des Matériaux pour le Nucléaire

**cea**

## Fracture Mechanisms Analysis

WS RIA Paris, 10th September 2009 S. Carassou CEA/SEMI/LCM# 20



DEN/Saclay/Département des Matériaux pour le Nucléaire

**cea**

### Fracture mechanisms at 480°C

Pictures of Zr-4 irradiated 5 cycles PST specimens just prior to and just after fracture

- at 480°C : Necking fracture type after large deformation of the gage section

---

WS RIA Paris, 10th September 2009 S. Carassou CEA/SEM/LCM 22

DEN/Saclay/Département des Matériaux pour le Nucléaire

**cea**

### Fracture mechanism analysis at 480°C

Ductile fracture by necking after large strains

1. Crack onset in the middle of the specimen at very large strain (ID ? OD ? Both ?)
  - > Local strain values at the onset of the crack : >50 %
2. The through-thickness crack propagates in a stable manner from the center of the specimen toward the notches.
3. Final fracture on the notches

---

WS RIA Paris, 10th September 2009 S. Carassou CEA/SEM/LCM 23

DEN/Saclay/Département des Matériaux pour le Nucléaire

**cea**

### Fracture mechanisms at 280°C

Pictures of Zr-4 irradiated 5 cycles PST specimens just prior to and just after fracture

- at 280°C : flat fracture type after very small strain

---

WS RIA Paris, 10th September 2009 S. Carassou CEA/SEM/LCM 24

cea DEN/Saclay/Département des Matériaux pour le Nucléaire

### Fracture mechanism analysis at 280°C

Mechanical Test result: Test number TD 244

Specimen picture at loading step 4: Test number TD 244

Micro Micro for Test number TD 244 at loading step n=4

For TD 244, the crack initiation occurred at the onset of global plasticity, prior to the maximum load

WS RIA Paris, 10th September 2009
S. Carassou CEA/SEM/LCM
25

cea DEN/Saclay/Département des Matériaux pour le Nucléaire

### Fracture mechanism analysis at 280°C

Mechanical Test result: Test number TD 244

Specimen picture at loading step 1 (fracture): Test number TD 244

Micro Micro for Test number TD 244 at loading step n=1 (fracture)

- large axial propagation (nearly 80% of the width between the notches)
- no measurable reduction of the load during the propagation.
- Therefore, these cracks must have propagated only along the **outer surface** of the specimen in those conditions

WS RIA Paris, 10th September 2009
S. Carassou CEA/SEM/LCM
26

cea DEN/Saclay/Département des Matériaux pour le Nucléaire

### Fracture mechanism analysis at 280°C

Three steps mechanism for the fracture of this PST specimen at 280°C :

1. Surface crack onset at or near the notch(es). This crack probably initiates on the hydride rim of the irradiated material.
  - > Local strain values at the onset of the crack : ~3 %
2. Stable axial extension of the surface (rim depth) crack(s). The surface crack occupies nearly the entire width between the notches.
3. Quick through-thickness propagation of the crack and final fracture.

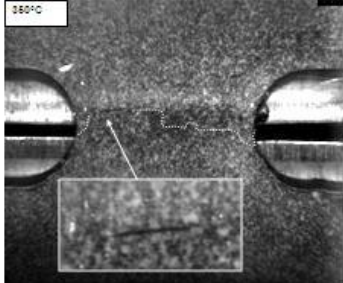
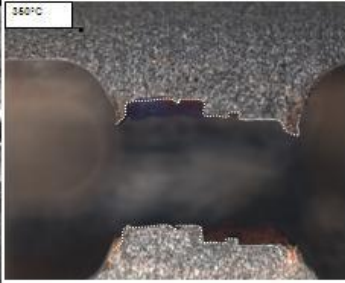
SEM analysis are planned in order to check the validity of this proposed mechanism.

WS RIA Paris, 10th September 2009
S. Carassou CEA/SEM/LCM
27

DEN/Saclay/Département des Matériaux pour le Nucléaire

**cea**

### Fracture type observed at 350°C

Pictures of Zy-4 irradiated 5 cycles PST specimens just prior to and just after fracture

- ☐ at 350°C : (double) Through-thickness slant fracture type after small strain

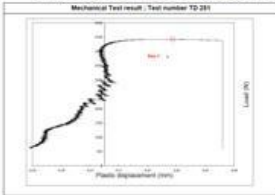
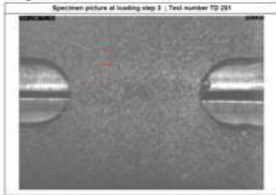
---

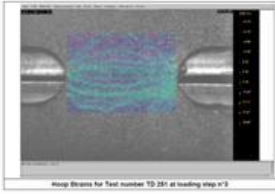
WS RIA Paris, 10th September 2009 S. Carassou CEA/SEM/LCM 28

DEN/Saclay/Département des Matériaux pour le Nucléaire

**cea**

### Fracture mechanism analysis at 350°C



- For TD 251, the crack initiation occurred at the outer diameter slightly prior to the maximum load
- Initiation in a plane strain area

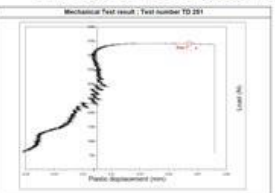
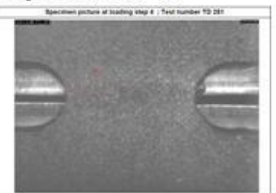
---

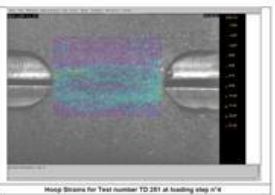
WS RIA Paris, 10th September 2009 S. Carassou CEA/SEM/LCM 29

DEN/Saclay/Département des Matériaux pour le Nucléaire

**cea**

### Fracture mechanism analysis at 350°C



- For TD 251, the crack initiation occurred at the outer diameter slightly prior to the maximum load
- Initiation in a plane strain area

---

WS RIA Paris, 10th September 2009 S. Carassou CEA/SEM/LCM 30

DEN/Saclay/Département des Matériaux pour le Nucléaire

**cea**

### Fracture mechanism analysis at 350°C

**Mechanical Test result - Test number TD 281**

**Specimen picture at loading step 6 (fracture) - Test number TD 281**

**hoop Strains for Test number TD 281 at loading step n°6 (fracture)**

\*Between the onset of the crack and the final rupture, no drastic decrease of the load (from step 5 to step 6) was observed.

\*Just prior to fracture, the crack appeared to be roughly 1mm long

\*If this 1mm crack extended through the whole thickness, the section decrease would have caused a 10% to 20% reduction in the load (depending on the presence of a crack on the other side)

\*Based upon a mechanical analysis: the crack observed between steps 5 and 6 was not a through-thickness crack

WS RIA Paris, 10th September 2009
S. Carassou CEA/SEM/LCM
31

DEN/Saclay/Département des Matériaux pour le Nucléaire

**cea**

### SEM inspections of the fracture surface at 350°C

- 1: A maximum 100µm depth rim is detected, that may have generated the crack. The rim is not only observed at this location, but at the whole outer diameter, (with smaller depth)
- 2: Mainly ductile with dimples
- 3: The thin area of strong ductile tearing located at the top of the zone "3" suggests that the fracture inner diameter is a place where final fracture occurs (the crack propagates from external diameter to internal diameter)
- 4: The strong ductile tearing suggests that the final fracture occurs on the notches  
*Possible crack propagation path*

WS RIA Paris, 10th September 2009
S. Carassou CEA/SEM/LCM
32

DEN/Saclay/Département des Matériaux pour le Nucléaire

**cea**

### Fracture mechanism analysis at 350°C

**Representativeness of fractures mechanisms :**

1. **Surface crack onset** between the notches and the middle part of the specimen **in a plane strain state**. This crack initiates **on the hydride rim** of the irradiated material
  - > Local strain values at the onset of the crack : ~10 %
  - > Local rim depth of 100µm
2. **Radial and axial extension** of the crack :
  - > from outer diameter to inner diameter at 45° from radial direction
  - > from the middle of the specimen to the notches
3. Final fracture on the notches

**Representative of expected fractures during RIA**

CABRI REP-N° 3 (Pépin et al., 2007)

HEC-1 in NSSR (Fuketa et al., 1996)

WS RIA Paris, 10th September 2009
S. Carassou CEA/SEM/LCM
33

DEN/Saclay/Département des Matériaux pour le Nucléaire

 **Synthesis and Conclusions (1/2)**

- ❑ Plane Strain Tensile specimens machined from Zircaloy-4 cladding irradiated up to 5 cycles have been tested at 280°C, 350°C and 480°C.
- ❑ The tests were filmed and digitally recorded to determine the local strains values using Digital Image Correlation method.
- ❑ The plane strain conditions have been verified and prevail over a wide area between the notches of the specimen.
- ❑ For the first time, the location of the onset of fracture for this geometry has been experimentally observed.

WS RIA Paris, 10th September 2009 S. Carassou CEA/SEMI/LCMI 34

DEN/Saclay/Département des Matériaux pour le Nucléaire

 **Synthesis and Conclusions (2/2)**

- ❑ At 280°C, a crack initiates in the vicinity of the notches, in an area where plane strain conditions are not fully fulfilled, and for a circumferential strain value of about 5%. The cracks initiate in the outer diameter.
- ❑ At 350°C and 480°C, cracks initiate at a location where plane strain conditions prevail, for circumferential strain values of approximately 10% and 50%, respectively.
- ❑ At 350°C, the cracks initiate in the outer diameter, and the propagate toward the inner diameter and the notches

**At this temperature, the fracture obtained is fully representative of expected fractures during RIA**

**These data can be used to validate and develop further existing RIA material failure criteria.**

WS RIA Paris, 10th September 2009 S. Carassou CEA/SEMI/LCMI 35

## DUCTILITY DEGRADATION OF HIGH BURN-UP CLADDING IN PCMI-SIMULATING CONDITION

**Sun-Ki Kim, Je-Geon Bang, Dae-Ho Kim, Ik-Sung Lim, Yong-Sik Yang,  
Kun-Woo Song, Do-Sik Kim, Hang-Seok Seo**

*1045 Daedeok Street, Yuseong, Daejeon, Korea, 305-600  
Korea Atomic Energy Research Institute*

### Abstract

The increase in fuel temperature resulting from an RIA induces a rapid fuel expansion, causing a severe pellet-cladding mechanical interaction (PCMI). This PCMI forces the cladding to experience a multiaxial tension such that the maximum principal strain is in the hoop (i.e., transverse) direction of the cladding tube. The survivability of a fuel cladding irradiated to a high burn-up under postulated RIA conditions is thus a response to a combination of the mechanics of a loading and the material degradation during a reactor operation. While such data is available for the axial deformation behavior of cladding tubes, relatively little has been reported in the open literature on the uniaxial tension behavior in the hoop direction of Zircaloy-4 cladding. Accordingly, it is essential to investigate the uniaxial tension behavior in the hoop direction of high burn-up Zircaloy-4 cladding. In this study, to evaluate the ductility and toughness degradation of Zircaloy-4 fuel cladding tubes under RIA, the hoop directional mechanical load which can simulate the PCMI load in RIA was applied to ring-type cladding specimen. That is, the ring tensile tests were performed in order to the ductility and toughness degradation of high burn-up fuel cladding under a hoop loading condition in a hot cell.

### 1. Introduction

With a trend of high burn-up operation, the safety issues on the nuclear fuel cladding are more important. One such postulated design-basis accident scenario is the reactivity-initiated accident (RIA) in a pressurised water reactor (PWR) caused by the ejection of a control rod from the core, which would cause a rapid increase of the reactivity and the thermal energy in the fuel [1]. The increase in fuel temperature resulting from an RIA induces a rapid fuel expansion, causing a severe pellet-cladding mechanical interaction (PCMI). This PCMI forces the cladding to experience a multiaxial tension such that the maximum principal strain is in the hoop (i.e., transverse) direction of the cladding tube. The survivability of a fuel cladding irradiated to a high burn-up under postulated RIA conditions is thus a response to a combination of the mechanics of a loading and the material degradation during a reactor operation.

While such data is available for the axial deformation behavior of cladding tubes, relatively little has been reported in the open literature on the uniaxial tension behavior in the hoop direction of Zircaloy-4 cladding. This technique was developed in 1990s by Arsene *et al.*[2, 3] and has been applied to Zircaloy-4. And also some experimental researches on hoop-directional mechanical properties for pre-hydrated Zircaloy-4 cladding were reported using ring tensile tests [4, 5]. But, they were not applied to irradiated materials. Accordingly, it is essential to investigate the uniaxial tension behavior in the hoop direction of high burn-up Zircaloy-4 cladding. In this study, ring tensile tests are applied to obtain the data regarding the uniaxial hoop direction deformation behavior.

## 2. Experimental procedure

The ring tensile specimen used in this study is a Westinghouse 17x17 type (Vantage-5H) Zircaloy-4 cladding irradiated for 3 cycles in the Ulchin Unit 2 pressurised water reactor, whose average burn-up was estimated to be approximately 65GWd/tU. The irradiated fuel rod was transferred to Post-Irradiation Examination Facility (PIEF) at KAERI, cut into approximately 13 cm length segments with a diamond low speed saw, and then the UO<sub>2</sub> pellet inside the fuel rod segment was removed by a mechanical grinding with a drill-attached defueling machine in a hot cell in Irradiated Material Examination Facility (IMEF). The dimensions and shape of the ring tensile specimen were designed in order to ensure that any deformation is limited to the gage section of the specimen, so that the uniform uniaxial hoop strain in the gage section could be at its maximal.

The ring tensile tests were performed in a hot cell with the Instron Servohydraulic System, Model 8562. The tests were performed at 25, 135, 200, 300, 350, 400, 600, and 800°C, and the initial strain rate was maintained at 0.01/s. The hydride morphologies were observed, which are shown in Fig. 1. These were representative images of the hydride rim taken before the mechanical tests. As seen in the figure, a hydride rim was formed around the metal substrate/oxide interface. This hydride rim is believed to cause a decrease of the ductility of the cladding tube [5].

Figure 1. Optical microscopy of the Zircaloy-4 from Ulchin unit 2



## 3. Results and discussion

To obtain the mechanical ductility such as UE (Uniform Elongation) and TE (Total Elongation) were evaluated for the ductility. The hoop stress-strain curves at 400°C among hoop stress-strain correlation results various temperatures are shown in Figure 2. The hoop stress-strain behavior of the irradiated cladding specimen was compared with unirradiated cladding specimens to investigate the degradation effect of mechanical properties by irradiation in nuclear reactor. Two runs were performed for unirradiated cladding specimens in order to confirm the reproducibility of the test results. As shown in the figure, the results for the unirradiated cladding specimens shows that mechanical strengths such as yield strength and ultimate tensile strength are in accord with each other even if there is some differences in total elongation. In case of unirradiated cladding specimens, ultimate tensile strength was ~570MPa, and ultimate tensile strength of the irradiated one was ~670 MPa. While, hoop strain of the irradiated one showed much lower value (~35%) than that of the unirradiated one (~80%), compared with the hoop strain of the unirradiated one. From this result, it was observed that the ductility of the irradiated cladding is sharply decreased as the fuel burn-up.

The evaluation results of the UE and TE are shown in Figure 3. The results show that both the UE and TE increase with an increasing temperature. Especially, they abruptly increase at 600°C, but become lower above this temperature. This peculiar behavior was also observed in the PROMETRA test program [6] which is a mechanical property relevant test program in conjunction with the CABRI program simulating RIA. It is believed that this behavior is caused by the elongation minimum phenomenon by the dynamic strain aging of the Zircaloy-4 cladding material above 600°C.

From a point of view of mechanical ductility, there were significant differences in both uniform elongation and total elongation between the irradiated Zircaloy-4 cladding (high burn-up Zircaloy-4 cladding) and the unirradiated Zircaloy-4 cladding. Especially, the decrease in total elongation of the irradiated cladding was

more remarkable, compared with the decrease in uniform elongation of the irradiated one. As the fuel burn-up increases, the nuclear cladding becomes brittle due to irradiation embrittlement, waterside oxidation and hydrogen pick-up [7-9]. Among these factors, the embrittlement by the hydrogen pick-up is dominant, and hydrogen effect on cladding embrittlement becomes a critical factor in high burn-up regime [10-13]. Figure 4 shows fracture surfaces of the un-irradiated and high burn-up fuel cladding at 400°C. The left one is a fracture surface of un-irradiated Zircaloy-4 cladding. A lot of dimples were observed, which means the ductile fracture. The middle one is a fracture surface of high burn-up Zircaloy-4 cladding with an oxide thickness of 20 μm and hydrogen pick-up of 150 ppm. The right one represents a fracture surface of high burn-up Zircaloy-4 cladding with an oxide thickness of 90 μm and hydrogen pick-up of 560 ppm. Dimples were not observed on the fracture surface of high burn-up Zircaloy-4 cladding with an oxide thickness of 90 μm and hydrogen pick-up of 560 ppm.

Figure 2. Hoop stress-strain curves of irradiated and unirradiated cladding at 400°C

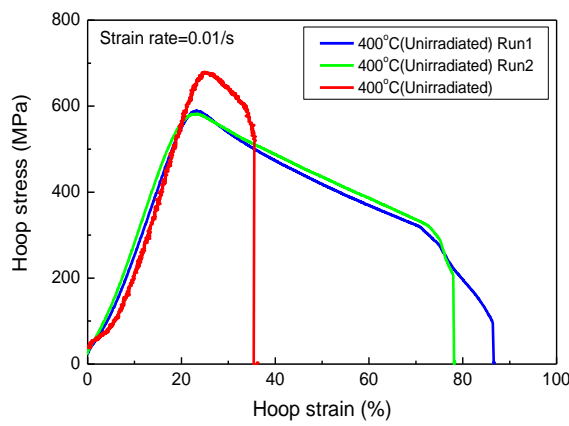


Figure 3. Ductility of the un-irradiated and high burn-up fuel cladding

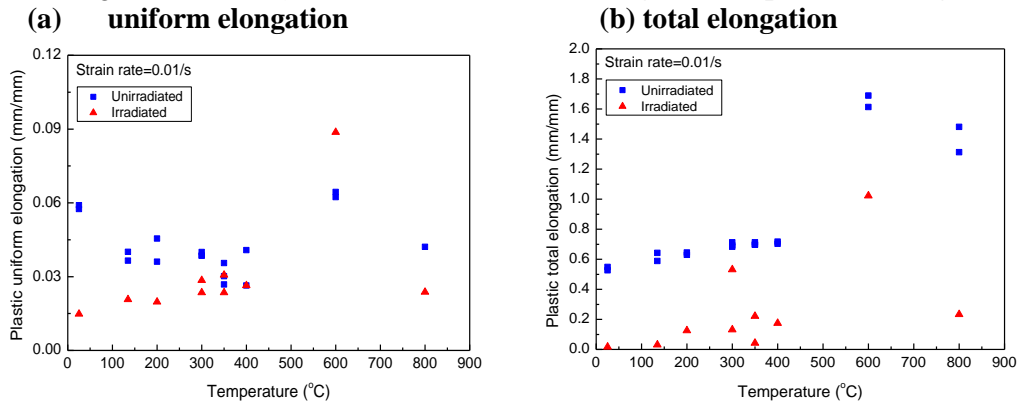
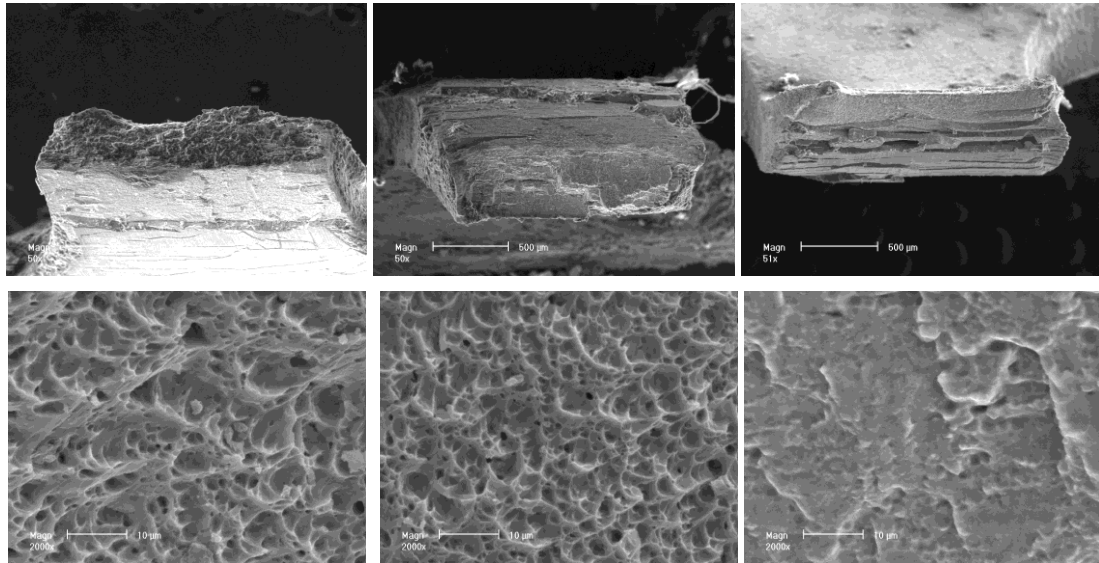


Figure 4. **Fracture surface of the un-irradiated and high burn-up fuel cladding**  
 a. un-irradiated                      b. high burn-up[20  $\mu\text{m}$ , ~150 ppm]                      c. high burn-up[90  $\mu\text{m}$ , ~560 ppm]



#### 4. Conclusions

On the basis of the PCMI-simulating ring tensile test for the high burn-up Zircaloy-4 cladding, the following conclusions were drawn.

First, there are significant ductility differences in both uniform elongation and total elongation between the irradiated Zircaloy-4 cladding (high burn-up Zircaloy-4 cladding) and the unirradiated Zircaloy-4 cladding, and especially, the decrease in total elongation of the irradiated cladding is more remarkable.

Second, the ductility is abruptly degraded above 600°C, which corresponds to a design basis accident condition such as a RIA.

## References

- [1] R. O. Meyer *et. al.*, “A Regulatory Assessment of Test Data for Reactivity Initiated Accidents”, *Nuclear Safety*, 37(4), 271-288 (1996).
- [2] S. Arsene and J. Bai, “A New Approach to Measuring Transverse Properties of Structural Tubing by a Ring Test”, *Journal of Testing and Evaluation*, 24(5), 386-391 (1996).
- [3] S. Arsene and J. Bai, “A New Approach to Measuring Transverse Properties of Structural Tubing by a Ring Test—Experimental Investigation”, *Journal of Testing and Evaluation*, 26(1), 26-30 (1998).
- [4] R. S. Daum, *et. al.*, “Mechanical Property Testing of Irradiated Zircaloy Cladding Under Reactor Transient Conditions”, *Zirconium in the Nuclear Industry: Small Specimen Test Technique: Fourth Volume, ASTM STP 1418*, PA, 195-210 (2002).
- [5] R. S. Daum, *et. al.*, “On the Embrittlement of Zircaloy-4 Under RIA-Relevant Conditions”, *Zirconium in the Nuclear Industry: Thirteenth International Symposium in the Nuclear Industry, ASTM STP 1423*, 702-719 (2002).
- [6] X. Averty, *et. al.*, “Tensile tests on ring specimens machined in M5 cladding irradiated 6 cycles” IRSN 2003/50 (2003).
- [7] Y. Fan and D. A. Koss, “The Influence of Multiaxial States of Stress on Hydrogen Embrittlement of Zirconium Alloy Sheet”, *Metallurgical Transactions A*, 16(A), 675-681 (1985).
- [8] L. A. Simpson, “Criteria for Fracture Initiation at Hydrides in Zirconium-2.5% Niobium Alloy”, *Metallurgical Transactions A*, 12(A), 2113-2124 (1981).
- [9] J. Bai *et. al.*, “Hydride Embrittlement in Zircaloy-4 Plate”, *Metallurgical and Materials Transactions A*, 25(A), 1185-1197 (1994).
- [10] A. M. Garde, *et. al.*, “Effects of Hydride Precipitate Localisation and Neutron Fluence on the Ductility of Irradiated Zircaloy-4”, *Zirconium in the Nuclear Industry: Eleventh International Symposium in the Nuclear Industry, ASTM STP 1295*, 407-430 (1996).
- [11] M. Grange *et. al.*, “Anisotropic Behavior and Rupture of Hydrided Zircaloy-4 Sheets”, *Metallurgical and Materials Transactions A*, 31(A), 679-690 (2000).
- [12] T. Fuketa, *et. al.*, “New results from NSRR Experiments with High Burn-up Fuels”, *Proceedings of the Twenty-Third Water Reactor Safety Information Meeting*, NUREG/CP-0149, 45-63 (1995).
- [13] F. Nagase and H. Uetsuka, “Hydride Morphology and Hydrogen Embrittlement of Zircaloy Fuel Cladding used in NSRR/HBO Experiment”, *Proceedings of the ANS International Topical Meeting on LWR Fuel Performance*, American Nuclear Society, Portland, OR, 677-687 (1997).

## Ductility Degradation of High Burn-up Cladding in PCMI-Simulating Condition

2009. 9. 10

Sun-Ki Kim\*, Je-Geon Bang, Dae-Ho Kim, Ik-Sung Lim, Yong-Sik Yang,  
Kun-Woo Song, Do-Sik Kim, Hang-Seok Seo

\*E-mail) kimsk@kaeri.re.kr

*Korea Atomic Energy Research Institute*

2009 OECD/NEA RIA Workshop

September 9-11, 2009, Paris, France

## Introduction

- The increase in fuel temperature resulting from an RIA induces a rapid fuel expansion, causing a severe pellet-cladding mechanical interaction (PCMI).
- This PCMI forces the cladding to experience a multi-axial tension such that the maximum principal strain is in the hoop (i.e., transverse) direction of the cladding tube.
- Ring tensile test was adopted as a PCMI-simulating method

2

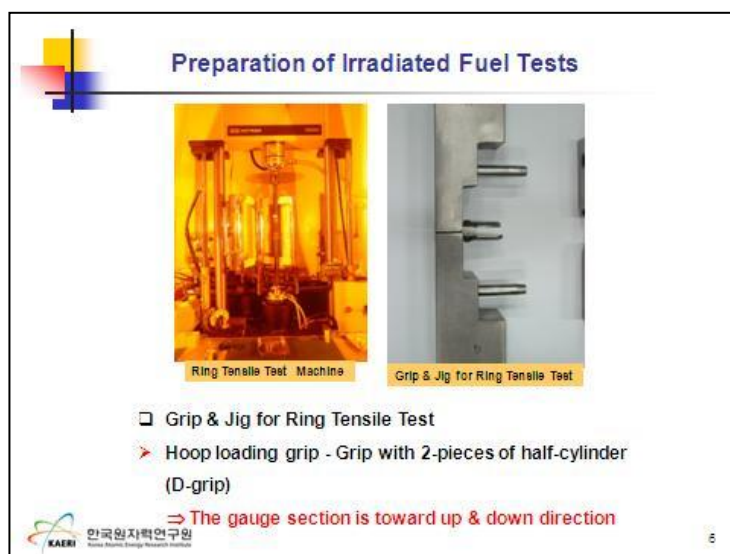
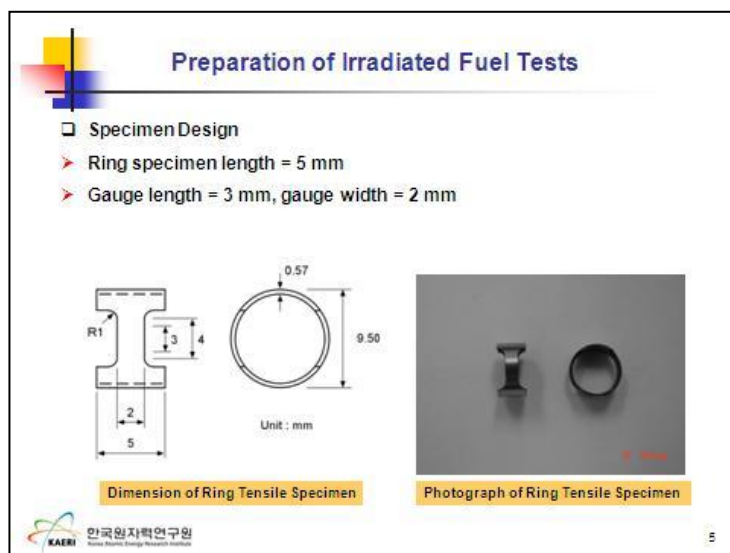
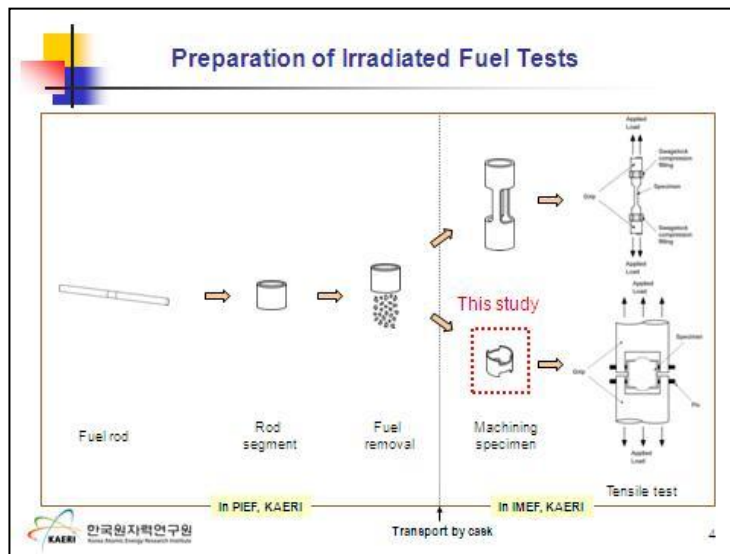
## Experimental Part

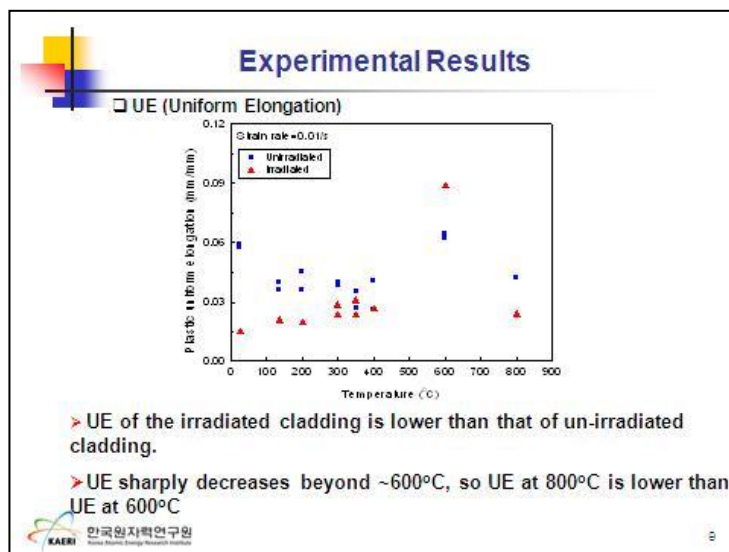
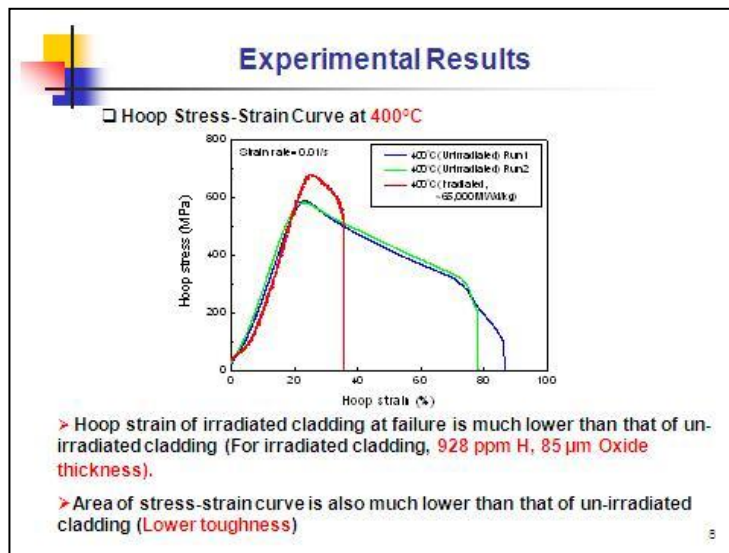
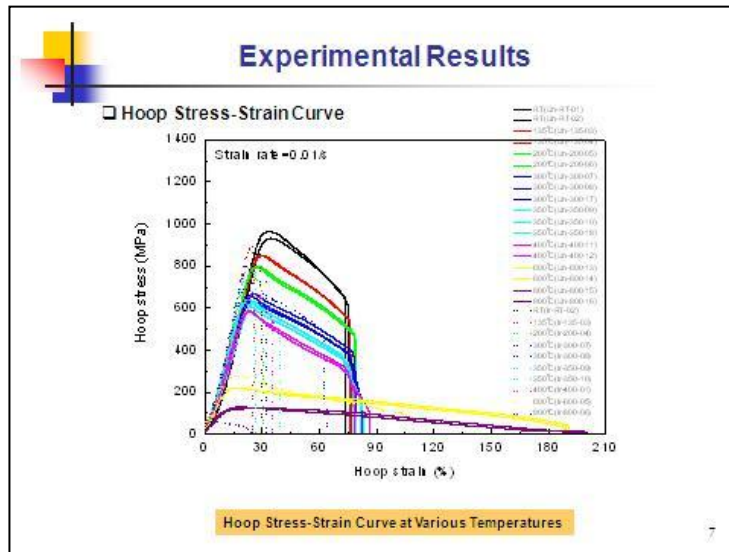
- High burn-up fuel cladding
  - Zircaloy-4 fuel cladding from Ulchin Unit 2 K23 in KOREA
  - Burn-up of tested rod = ~ 65 MWd/kg
  - Oxide thickness = 20 ~ 120 μm
  - H content = 150 ~ 1,160 ppm

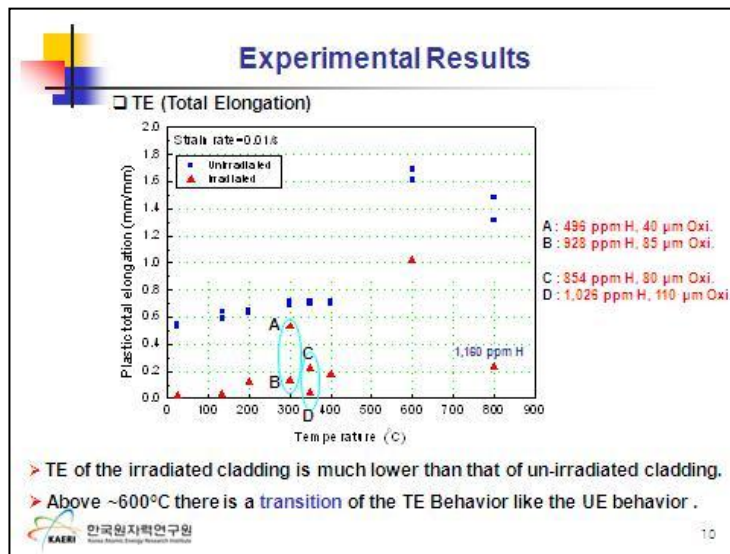
Unit: mm

Schematic diagram of Zircaloy-4 fuel rod discharged in Ulchin Unit 2

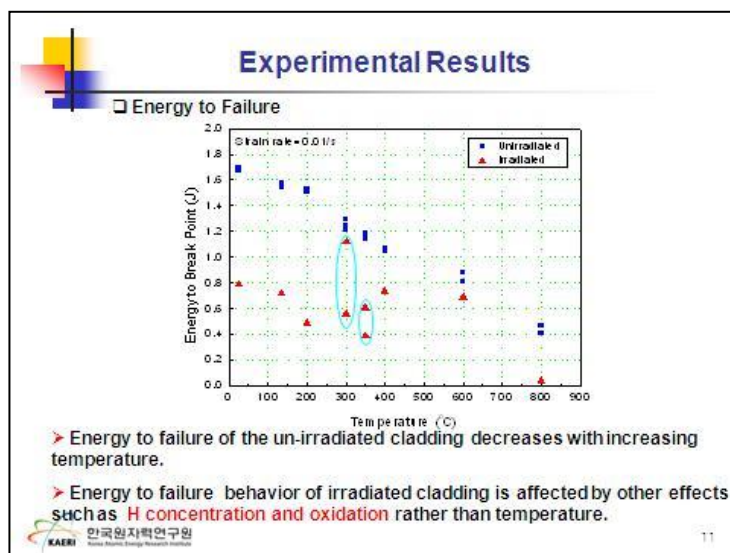
3



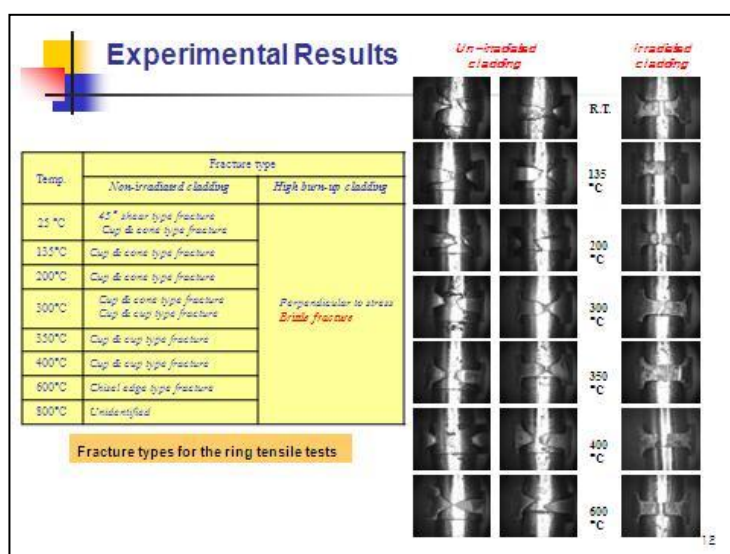




- TE of the irradiated cladding is much lower than that of un-irradiated cladding.
- Above ~600°C there is a transition of the TE Behavior like the UE behavior.



- Energy to failure of the un-irradiated cladding decreases with increasing temperature.
- Energy to failure behavior of irradiated cladding is affected by other effects such as H concentration and oxidation rather than temperature.



### Experimental Results

(a) (b) (c)

*Fracture surface of the un-irradiated and high burn-up fuel cladding  
 (a) un-irradiated (b) high burn-up[20 μm, ~150 ppm] (c) high burn-up[90 μm, ~560 ppm]*

한국원자력연구원  
Korea Atomic Energy Research Institute
13

### Conclusions

On the basis of the PCMI-simulating ring tensile test for the high burn-up Zircaloy-4 cladding, the following conclusions were drawn.

- First, there are significant ductility differences in both UE and TE between the irradiated Zircaloy-4 cladding (high burn-up Zircaloy-4 cladding) and the decrease in TE of the irradiated cladding is more remarkable than decrease in UE.
- Second, the ductility is abruptly degraded above 600°C, which corresponds to a design basis accident condition such as a RIA.
- Ductility and energy to failure (toughness) of irradiated cladding is affected by other effects such as **H concentration and oxidation** rather than temperature.

한국원자력연구원  
Korea Atomic Energy Research Institute
14

## APPLICABILITY OF NSRR ROOM/HIGH TEMPERATURE TEST RESULTS TO FUEL SAFETY EVALUATION UNDER POWER REACTOR CONDITIONS

**Tomoyuki Sugiyama**

Japan Atomic Energy Agency, Nuclear Safety Research Center  
Tokai-mura, Naka-gun, Ibaraki-ken, 319-1195, Japan

**Miki Umeda, Yutaka Udagawa, Hideo Sasajima, Motoe Suzuki and Toyoshi Fuketa**

Japan Atomic Energy Agency, Nuclear Safety Research Center

Pulse-irradiation tests of high burn-up light water reactor fuels have been performed at the Nuclear Safety Research Reactor (NSRR) in order to understand transient fuel behaviors and to evaluate the fuel failure limit under the reactivity-initiated accident (RIA) conditions. In order to investigate the initial temperature influence on fuel behaviors, especially on the failure limit due to the pellet-cladding mechanical interaction (PCMI), the high temperature test capsule was developed, which achieves the initial coolant temperature up to ~290°C. This paper describes the results from the room/high temperature NSRR tests performed on high burn-up fuels and discusses the initial temperature influence on the fuel behavior and the applicability of the NSRR data to the power reactor conditions.

### 1. Introduction

The Japan Atomic Energy Agency (JAEA) has performed pulse-irradiation tests of high burn-up light water reactor fuels at the Nuclear Safety Research Reactor (NSRR) in order to investigate transient fuel behaviors and fuel failure limit under the reactivity-initiated accident (RIA) conditions.<sup>1</sup> The coolant conditions in the NSRR tests was typically the room temperature (RT) of ~20 °C and atmospheric pressure of ~0.1 MPa, which are suitable to simulate RIAs assumed at the BWR startup. There have been, however, questions and arguments about applicability of the RT test results, especially the fuel enthalpy at failure due to the pellet-cladding mechanical interaction (PCMI), to the safety evaluation for RIAs at the PWR hot standby and BWR/PWR operation. On the basis of the RT test results, the PCMI failure is understood to occur when the hydride-embrittled cladding cannot sustain the hoop strain produced by the pellet thermal expansion at a power transient. In this process, initial cladding temperature can influence two factors related with the fuel failure limit; the amount of hydride precipitates and their distribution or morphology in the cladding,<sup>2</sup> and the mechanical properties of cladding metal matrix which determines the ductile fracture limit at the mid-wall and inner region where less hydrides are precipitated. In order to quantify the initial temperature effect on the failure limit through the above two factors, the high temperature (HT) NSRR test capsule was recently developed, which extended the initial coolant temperature range up to ~290 °C.<sup>3</sup>

This paper describes the results from five pairs of RT and HT tests performed on high burn-up fuels, including PWR-UO<sub>2</sub> rods with ZIRLO™, MDA and M5™ cladding, a BWR-UO<sub>2</sub> rod with Zircaloy-2

---

<sup>1</sup> T. Fuketa, H. Sasajima and T. Sugiyama, "Behavior of high-burn-up PWR fuels with low-tin Zircaloy-4 cladding under reactivity-initiated-accident conditions," Nucl. Technol., **133**, 1, 50 (2001).

<sup>2</sup> T. Sugiyama, M. Umeda, T. Fuketa, et al., "Failure of high burn-up fuels under reactivity-initiated accident conditions," Ann. Nucl. Energy, **36**, 3, 380 (2009).

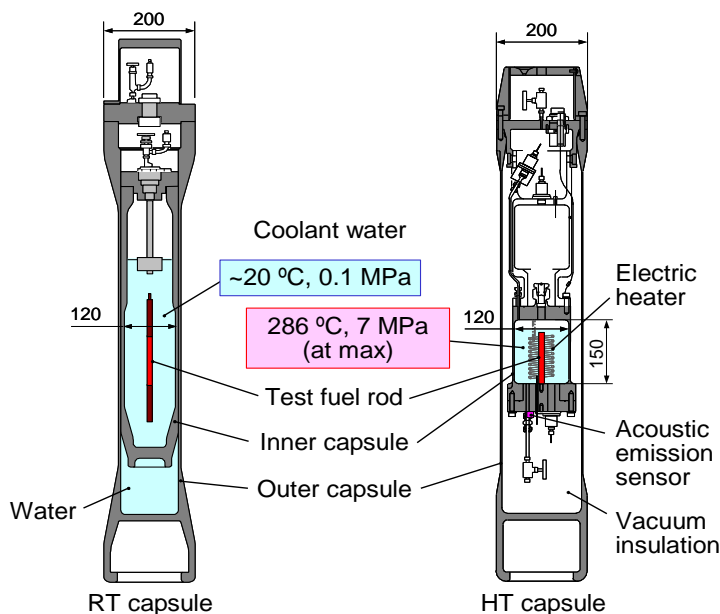
<sup>3</sup> T. Sugiyama, Y. Udagawa, M. Umeda, et al., "PWR fuel behavior in RIA-simulating experiment at high temperature," Proc. 2008 Water Reactor Fuel Performance Meeting, October 19-23, 2008, Seoul, Korea, #8108 (2008).

cladding and a PWR-MOX rod with Zircaloy-4 cladding. On the basis of these results, the initial temperature influence on the fuel behavior and the applicability of the NSRR data to the power reactor conditions are discussed.

## 2. Test facilities

The NSRR is a modified TRIGA<sup>®</sup> annular core pulse reactor which can simulate a power burst. At the maximum reactivity insertion, the peak power reaches ~21 GW and the corresponding pulse width is about 4 ms. The NSRR core has a large center cavity of 220 mm in diameter, which enables flexible design of the irradiation capsule containing a test fuel rod and various sensors. Figure 1 shows the schematics of the NSRR capsules for RT and HT tests. The both types of capsule are double containers made of stainless steel, which have enough air- and pressure-tightness. Only the HT capsule is equipped with an electric heater to raise the coolant temperature up to ~286 °C. The capsule internal pressure becomes the saturation pressure at the coolant temperature, and cannot be controlled independently. The space around the HT inner capsules is vacuum for thermal insulation, while the RT inner capsule is surrounded with water. The acceptable length of the test fuel rod is roughly 300 mm for RT capsule, but approximately 130 mm for HT capsule because of the short height of the inner capsule.

Figure 1. Schematics of NSRR room temperature (RT) and high temperature (HT) test capsules



## 3. Test fuels

Table 1 gives the description of test fuels used for the five pairs of RT and HT tests; the tests VA-1 and -3, VA-2 and -4, RH-1 and -2, LS-1 and -2, and BZ-2 and -3. The fuel rods irradiated in European countries were cut into segments of ~500 mm in length and transported to Japan. In the Reactor Fuel Examination Facility (RFEF) in JAEA-Tokai, these fuel segments were subjected to detailed fuel examinations and refabrication into the test fuel rods for the NSRR RIA-simulating tests. The test fuel rods for the paired RT and HT tests were sampled from close elevations of an identical mother fuel segment. The pellet stack length of the test fuel rod is typically ~110 mm for RT tests and ~50 mm for HT tests. All rods were filled with helium gas of ~0.1 MPa at ~20 °C.

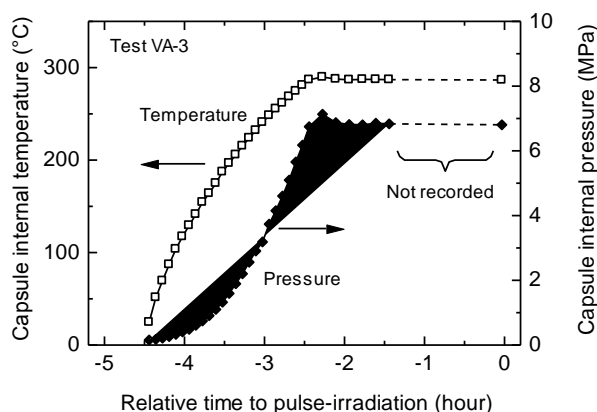
Table 1. Fuel descriptions, test conditions and main observations in NSRR high/room temperature tests

ID for test and test fuel rod	VA-1	VA-3	VA-2	VA-4	RH-1	RH-2
Descriptions of mother fuel rod						
Reactor, country	Vandellos, Spain				Ringhals, Sweden	
Fuel type	17x17 PWR-UO <sub>2</sub>					
Clad outer/inner diameter, mm	9.5/8.36					
Clad material	ZIRLO™		MDA		M5™	
Pellet burn-up, GWd/t	71		77		67	
Descriptions of test fuel rod						
Clad oxide thickness, µm	73	82	70	80	6	6
Clad hydrogen content, ppm	660	670	760	760	70	70
Pellet stack length, mm	112	61	111	61	117	50
Rod internal gas	helium of 0.1 MPa at ~20 °C					
Test conditions						
Power pulse width, ms			4.4		4.5	
Initial coolant conditions	18 °C 0.1 MPa	285 °C 6.8 MPa	28 °C 0.1 MPa	249 °C 4.0 MPa	16 °C 0.1 MPa	278 °C 6.4 MPa
Initial fuel enthalpy (20°C-based), $H_0$ , J/g (cal/g)	–	71 (17)	–	61 (14)	–	69 (16)
Max. increase of fuel enthalpy, $\Delta H_{max}$ , J/g (cal/g)	556 (133)	454 (108)	546 (130)	457 (109)	462 (110)	378 (90)
Main results						
Enthalpy increase at failure, $\Delta H_{fail}$ , J/g (cal/g)	268 (64)	344 (82)	231 (55)	no failure	no failure	no failure
Key observations	- PCMI failure - all pellets fragmented - mechanical energy detected	- PCMI failure - some pellets fragmented	- PCMI failure - all pellets fragmented - mechanical energy detected	- PCMI and gas-induced clad strain of 2.2%	- PCMI-induced clad strain of 0.96% - FGR 21.4%	- PCMI-induced clad strain of 1.06% - FGR 26.0% - DNB detected
ID for test and test fuel rod						
	LS-1	LS-2	BZ-2	BZ-3		
Descriptions of mother fuel rod						
Reactor, country	Leibstadt, Switzerland			Beznau, Switzerland		
Fuel type	10x10 BWR-UO <sub>2</sub>			14x14 PWR-MOX (MIMAS)		
Clad outer/inner diameter, mm	9.62/8.36			10.72/9.48		
Clad material	Zircaloy-2 (LK3) with Zr liner			Zircaloy-4		
Pellet burn-up, GWd/t	69			59		
Descriptions of test fuel rod						
Clad oxide thickness, µm	25	25	20	20		
Clad hydrogen content, ppm	300	290	160	160		
Pellet stack length, mm	107	52	110	51		
Rod internal gas	helium of 0.1 MPa at ~20 °C					
Test conditions						
Power pulse width, ms			4.4			
Initial coolant conditions	17°C 0.1 MPa	283 °C 6.6 MPa	18°C 0.1 MPa	281°C 6.6 MPa		
Initial fuel enthalpy (20°C-based), $H_0$ , J/g (cal/g)	–	70 (17)	–	70 (17)		
Max. increase of fuel enthalpy, $\Delta H_{max}$ , J/g (cal/g)	469 (112)	371 (89)	644 (154)	528 (126)		
Main results						
Enthalpy increase at failure, $\Delta H_{fail}$ , J/g (cal/g)	222 (53)	no failure	545 (130)	no failure		
Key observations	- PCMI failure - all pellets fragmented - mechanical energy detected	- PCMI-induced clad strain of 0.93%	- PCMI failure - all pellets fragmented - mechanical energy detected	- PCMI and gas-induced clad strain of 4.4% - FGR 39.4% - DNB detected		

#### 4. Initial coolant conditions in high temperature test

The coolant temperature is heated up to the target temperature in the HT tests, which is typically 280°C. The pre-heating takes about two hours and the target temperature is normally kept for ~one hour before the pulse-irradiation. Figure 2 shows the histories of inner capsule temperature and pressure during the pre-heating and temperature holding stages in the test VA-3. It should be noted that the temperature holding duration in the test VA-3 was longer than in other HT tests, because there was a sensor trouble and some attempts were made for recovery. No discernible influence, however, is anticipated from the difference of temperature holding duration.

Figure 2. Histories of capsule temperature and pressure during the pre-heating and temperature holding stages in test VA-3



#### 5. Results and discussions

Among the ten tests in Table 1, results from some tests are focused and compared from specific view points.

##### 5.1. Comparison between tests VA-1 and VA-3

This comparison aims at clarification of the initial coolant temperature influence on the PCMI failure limit. The tests VA-1 and VA-3 were performed on the sibling test fuel rods sampled from an identical ZIRLO-clad UO<sub>2</sub> rod irradiated up to 71 GWd/t in pellet burn-up. The initial coolant temperatures were 18 and 285 °C, respectively, in the tests VA-1 and VA-3. The two tests resulted in the PCMI failure at fuel enthalpy increases of 268 and 344 J/g, respectively. The fuel enthalpy at failure was higher in the test VA-3, in spite of thicker oxide layer at the cladding outer surface.

Figure 3 shows histories of linear heat rate (LHR) and radial average enthalpy of test fuel rods in the tests VA-1 and VA-3. The LHR history is based on the measurement of NSRR power, but the fuel enthalpy history is the calculation result using the RANNS code.<sup>4</sup> The initial fuel enthalpy ( $H_0$ ) is 71 J/g higher in VA-3, but the peak enthalpy ( $H_0 + \Delta H_{\max}$ ) is similar; 556 and 525 J/g. Cladding surface thermocouple was not attached in these tests because of difficulty to remove the thick oxide layer at the cladding outer surface. Hence, the history of cladding outer surface temperature in Fig 4 is also the estimation with the RANNS code. This figure shows that the fuel failure occurred before the elevation of cladding temperature in the both tests.

<sup>4</sup> M. Suzuki and T. Fuketa, "Analysis of pellet-clad mechanical interaction process of high-burn-up PWR fuel rods by RANNS code in reactivity-initiated accident conditions," Nucl. Technol., 155, 3, 282 (2006).

Figure 3. Histories of linear heat rate and enthalpy of test fuel rods in tests VA-1 and VA-3

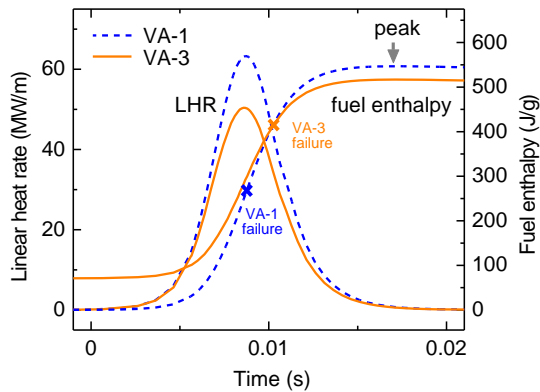


Figure 4. Histories of clad outer surface temperature in tests VA-1 and VA-3

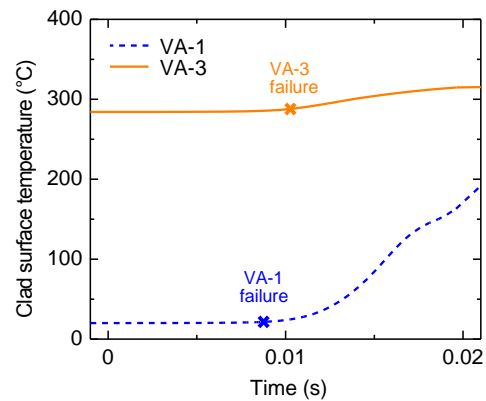
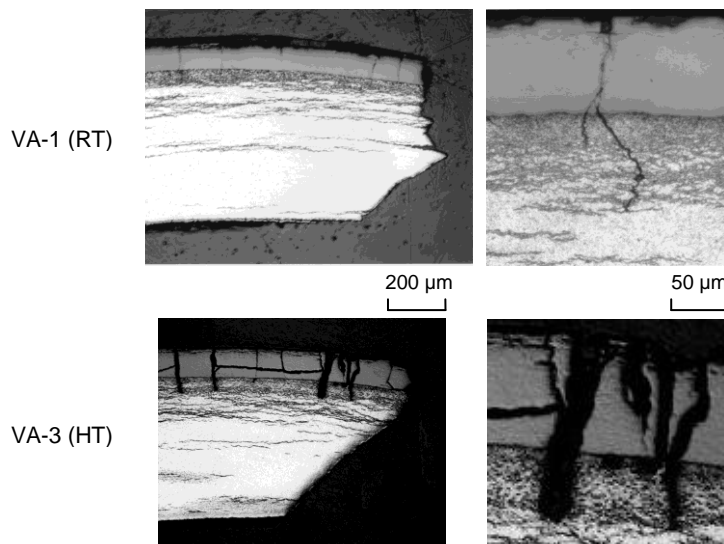


Figure 5 shows the metallographs of failed cladding in the tests VA-1 and VA-3. Both metallographs have common features; many radial cracks in the outer brittle zone comprising of the oxide layer and hydride rim, and tilted fracture surface suggesting a ductile fracture in the cladding inner region. On the other hand, the shape of the radial crack tips is clearly different. The radial cracks generated in the test VA-3 are widened and their tips are round, while they are sharp in the test VA-1. According to the previous studies<sup>5</sup>, the PCMI-induced cladding fracture in an RIA is initiated by the stress intensification at the incipient radial crack tip. The present observation suggests that many incipient cracks were generated in the cladding peripheral brittle zone both in the RT and HT tests, but the increased fracture toughness at high initial temperature delayed the further crack propagation and consequently raised the failure limits in terms of total (elastic + plastic) hoop strain and fuel enthalpy. As for the incipient crack depth which can be a primary factor for the failure limit when the crack tip is sharp, the initial temperature could affect the effective thickness of brittle zone because the hydrogen solubility limit in the cladding is dependent on temperature<sup>6</sup>. These temperature influences on the cladding mechanical properties through some mechanisms can be the reason of higher failure enthalpy in the test VA-3.

Figure 5. Metallographs of failed cladding in tests VA-1 and VA-3



<sup>5</sup> K. Tomiyasu, T. Sugiyama and T. Fuketa, "Influence of cladding-peripheral hydride on mechanical fuel failure under reactivity-initiated accident conditions," J. Nucl. Sci. Technol., 44, 5, 733 (2007).

<sup>6</sup> M. Petit, V. Georgenthum, T. Sugiyama, et al., "A comparative analysis of CABRI CIP0-1 and NSRR VA-2 reactivity initiated accident tests," Eurosafe 2007, November 5-6, Berlin, Germany (2007).

Regarding the mechanical load during the pulse-irradiation, Fig. 6 shows the evolution of cladding elastic/plastic hoop strain as functions of the fuel enthalpy ( $H_0 + \Delta H$ ) and of the fuel enthalpy increase ( $\Delta H$ ), which were calculated with the RANNS code. The both test fuel rods should have been at an identical mechanical state at the room temperature, or when  $H_0 + \Delta H = 0$ . The pre-heating to 285 °C in the test VA-3 caused the separation of the two traces in Fig. 6 (1), because the rapid pellet thermal expansion without cladding temperature rise fully contributed to the cladding elastic + plastic hoop strains in the test VA-1, while the cladding thermal expansion at 285°C mitigated the cladding hoop strain in the test the VA-3. Since the thermal expansion coefficient of pellet is larger than that of cladding, the initial hoop strain at the pulse-irradiation, or when  $\Delta H = 0$ , was larger in the test VA-3 than in VA-1, as show in Fig. 6 (2). Hence, the HT test always provides a slightly higher strain to the cladding than the RT test at a same level of fuel enthalpy increase. The gain of fuel failure limit at HT should, therefore, be slightly smaller than the gain evaluated from the differences of cladding mechanical properties between RT and HT. Fig. 6 shows that any of  $H_0 + \Delta H$  and  $\Delta H$  is not a perfect index to formulate the cladding mechanical load under the RT and HT conditions, but  $\Delta H$  seems more practical for safety evaluation.

Figure 6. Evolution of cladding hoop strain with fuel enthalpy ( $H_0 + \Delta H$ ) and with fuel enthalpy increase ( $\Delta H$ ) in tests VA-1 and VA-3

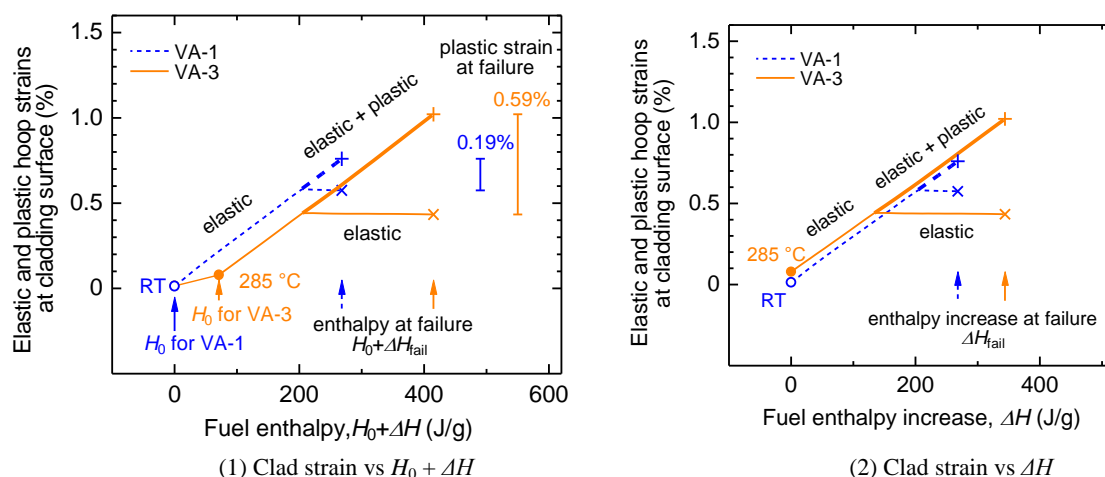


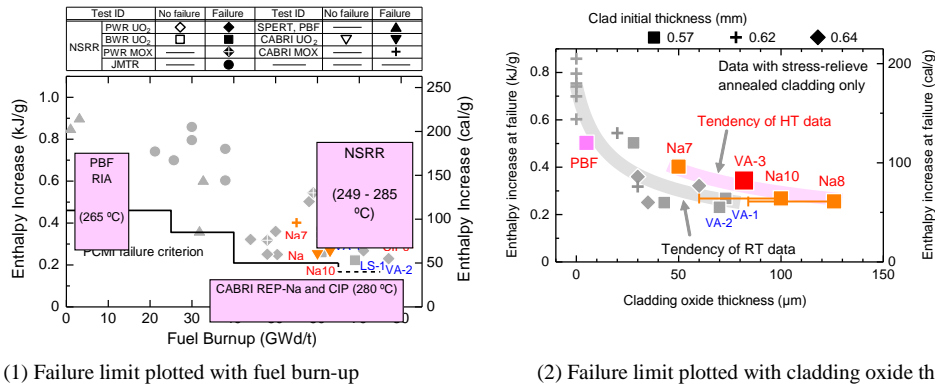
Figure 7 shows the fuel enthalpy increase at failure ( $\Delta H_{\text{fail}}$ ) as functions of fuel burn-up and cladding oxide thickness for all the available data including the VA-1 and VA-3. The initial temperature influence on the failure limit is not clearly observed in Fig. 7 (1). If NSRR data are focused, the VA-3 and other non-failure tests suggest some gain of the fuel limit. However, the CABRI REP Na-8 and 10 data<sup>7</sup> indicate no gain at the HT condition.

On the other hand, when the fuel failure limits are plotted with the cladding oxide thickness, as shown in Fig. 7 (2), two separate tendencies are observed for the RT and HT test data, if the PBF RIA 1-2 test can be treated as an exception because of the inner surface hydridation before the pulse-irradiation.<sup>8</sup> Hence, the gain of PCMI failure limit at HT is suggested, at least, for the stress-relieve (SR) annealed cladding, but the gain is not significant. As for the recrystallisation (RX) annealed cladding, in which hydrogen morphology is different from that in SR cladding, the evaluation of initial temperature influence is difficult at the present, because available data are limited.

<sup>7</sup> J. Papin, B. Cazalis, J. M. Frizonnet, et al., "Summary and interpretation of the CABRI REP-Na program," Nucl. Technol., 157, 3, 230 (2007).

<sup>8</sup> B. A. Cook, S. K. Fukuda, Z. R. Martinson, et al., "Reactivity initiated accident test series, Test RIA 1-2 fuel behavior report," NUREG/CR-1842, EGG-2073 (1981).

Figure 7. PCMI failure limit obtained in NSRR, SPERT-CDC, PBF and CABRI tests



### 5.2. Comparison between tests VA-3 and VA-4

This comparison aims at giving an explanation to the different results from the two similar tests VA-3 and VA-4. The mother fuels were irradiated in an identical fuel assembly through all the operation cycles. The only difference in the rod specification is the cladding material; ZIRLO for VA-3 and MDA for VA-4. As the pellet burn-up of the VA-4 test fuel rod was slightly higher than that of VA-3 (77 and 71 GWd/t, respectively), it was concerned that the residual fissile amount in the VA-4 rod was not enough to achieve a fuel enthalpy increase sufficient for the PCMI failure. Thus, the initial coolant temperature for the test VA-4 was lowered, in order to increase the coolant (that is, moderator) density and to enhance the thermal neutron flux coming to the test fuel rod. However, the initial temperature should have been high enough to achieve the primary objective, that is, the confirmation of the initial temperature influence on the fuel failure. Finally, the coolant conditions at the pulse-irradiation were 249 °C and 4 MPa, and the enthalpy increase reached 457 J/g which was similar to that in the test VA-3.

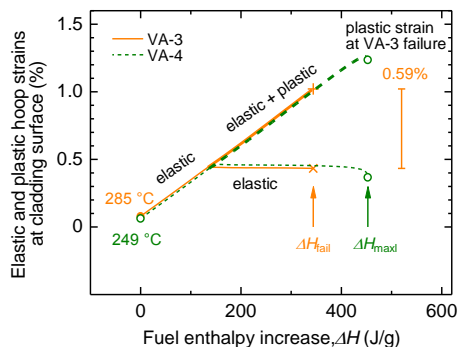
The VA-4 test fuel rod did not fail against the peak fuel enthalpy, and the cladding residual hoop strain reached 2.2%.<sup>9</sup> As this strain exceeded the level achievable only by the pellet thermal expansion at the peak fuel enthalpy in the test VA-4, the driving force of the strain would be the high rod internal gas pressure due to fission gas release from pellets. The cladding temperature was not measured in the test VA-4, but the large cladding strain suggested that the cladding temperature became high enough for the cladding deformation after the departure from nucleate boiling (DNB).

The present discussion focuses on the comparison of fuel behavior during the PCMI phase, that is, before the peak fuel enthalpy. Figure 8 shows the evolution of cladding elastic/plastic hoop strain with the fuel enthalpy increase up to the failure or to the maximum enthalpy in the tests VA-3 and VA-4. Although the strain histories of the two tests were almost common, the VA-4 test fuel rod survived the plastic hoop strain larger than 0.59% at which the VA-3 test fuel rod failed. As for the cladding mechanical properties, there is no factor which could lead to the higher ductility of the VA-4 cladding; the lower initial temperature in the VA-4 test and the slightly higher hydrogen content of the VA-4 cladding could be reasons for the higher brittleness rather than the ductility.

Any reasonable explanation cannot be given to the different results between the tests VA-3 and VA-4. However, the comparison between the two tests suggests that the test VA-4 was very close to the failure. The cladding metallograph of the VA-4 cladding is not available at present, but the widened cracks at the cladding periphery, which were observed in the VA-3 cladding, are anticipated also in the VA-4 cladding. The total number of the widened cracks can be larger, because the summation of all the crack widths should correspond to the large residual hoop strain, while the maximum width of a crack is probably similar in the two tests. The metallography of the VA-4 cladding is to be performed in this year.

<sup>9</sup> T. Sugiyama, M. Umeda, H. Sasajima, et al., "Effect of initial coolant temperature on mechanical fuel failure under reactivity-initiated accident conditions," Proc. Top Fuel 2009, September 6-10, 2009, Paris, France, #2086 (2009).

Figure 8. Evolution of cladding hoop strain with fuel enthalpy increase in tests VA-3 and VA-4



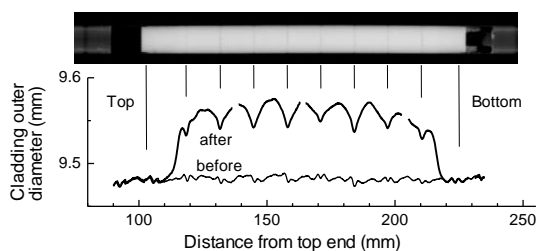
### 5.3 Comparison between tests RH-1 and RH-2

High temperature influence on the non-failure fuel behaviors, such as cladding deformation and fission gas release (FGR), is discussed on the basis of the comparison between the tests RH-1 and RH-2. The mother fuel rod is M5-cladded  $\text{UO}_2$  rod of 67 GWd/t. Because of the low sampling position and of the high corrosion-resistance of M5, the cladding oxide thickness was only 6  $\mu\text{m}$  and the hydrogen content was 70 ppm.

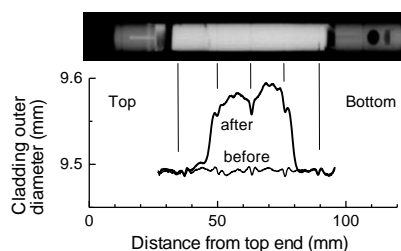
#### Cladding deformation

The two tests resulted in non-failure. Figure 9 shows the axial profiles of the cladding outer diameter before and after the pulse-irradiation. The shape of the both profiles reflects the barrel shape deformation of pellets. The cladding residual hoop strain reached 0.96% and 1.06% in the tests RH-1 and RH-2, respectively. Figure 10 shows the cladding residual hoop strain during the pulse-irradiation in the NSRR PWR fuel tests, including the tests RH-1 and RH-2. The nearly straight line is the strain level which is produced only by pellet thermal expansion, that is, the “PCMI-induced” strain level. If the cladding temperature rise was not so large, the hoop strain stayed on this level. On the other hand, when the cladding temperature reached high after the DNB and the fission gas release increased the rod internal pressure enough for the cladding ballooning, the “gas-induced” strain would occur additionally to the PCMI-induced strain. As for the RH tests, the strain of RH-1 is just on the PCMI-induced strain line, while the deformation mode in the RH-2 depends on which parameter is used for plotting; the maximum enthalpy increase ( $\Delta H_{\text{max}}$ ) or the peak fuel enthalpy ( $H_0 + \Delta H_{\text{max}}$ ).

Figure 9. Axial profiles of cladding outer diameter before and after tests RH-1 and RH-2



(1) Test RH-1: peak hoop strain = 0.96%



(2) Test RH-2: peak hoop strain = 1.06%

In order to determine the more appropriate index to plot the residual hoop strains under RT and HT conditions together, evolution of the elastic/plastic hoop strain with the fuel enthalpy is shown in Fig. 11. The residual strain is determined by the excess fuel enthalpy increase after the onset of the plastic deformation. The onset enthalpy is less sensitive to the temperature condition as shown in Fig. 11, because the decrease of elastic strain due to cladding thermal expansion and the reduction of yield strain with temperature rise almost cancel each other, as long as the cladding mechanical properties of the MATPRO

database<sup>10</sup> are used for the calculation. Therefore, the residual hoop strain should be correlated with the peak fuel enthalpy rather than the maximum enthalpy increase. Consequently, it is concluded that the residual strain in the test RH-2 was induced by the PCMI, and there is no particular influence of high initial temperature as long as the gas-induced strain does not start.

Fig. 10. Cladding residual hoop strain during pulse-irradiation as a function of fuel enthalpy

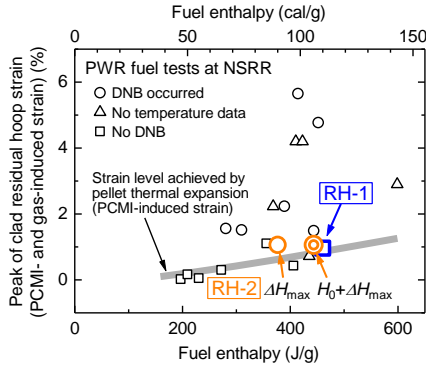
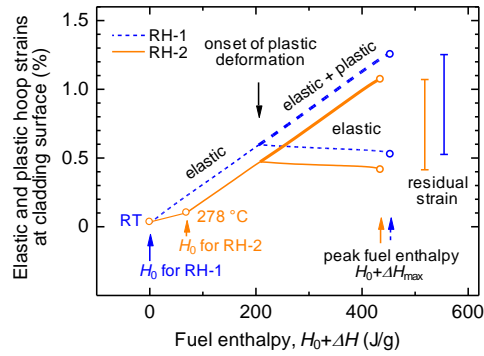


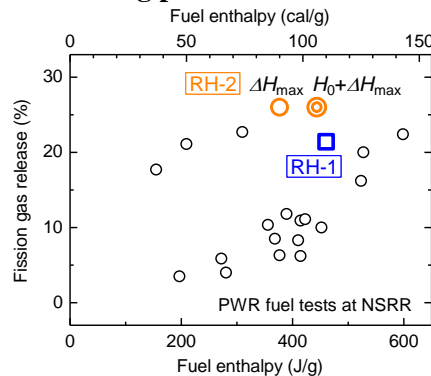
Fig. 11. Evolution of cladding hoop strain with fuel enthalpy in tests RH-1 and RH-2



*Fission gas release*

The fission gas release (FGR) during the pulse-irradiation was estimated as 21.4% and 26.0% for the tests RH-1 and RH-2, respectively. Figure 12 shows the FGRs during the NSRR pulse-irradiation tests with the PWR fuels, including the tests RH-1 and RH-2. Most results of the previous tests suggest that FGR increases with the fuel enthalpy. The RH-1 result is slightly high, but in agreement with the tendency. On the other hand, the FGR of RH-2 is higher than the tendency in either plot with  $\Delta H_{max}$  or  $H_0 + \Delta H_{max}$ . These results does not show which index is more appropriate. It is anticipated, however, that the gas release is driven by pellet temperature and possibly also by pellet internal tensile stress which is also temperature-driven. Since the pellet temperature is more correlated with the peak fuel enthalpy rather than with the maximum enthalpy increase, the more appropriate index to plot FGRs under RT and HT conditions together is the peak fuel enthalpy ( $H_0 + \Delta H_{max}$ ). The initial temperature difference should have less influence, because the peak pellet temperature is correlated with the peak fuel enthalpy. The reason of higher FGR in the test RH-2 than in the other tests could be due to the end pellet fragmentation which could occur in the NSRR tests [3]. This fragmentation occurs both in the RT and HT tests, but its influence can be more significant in the HT tests because the end pellets account for 33-50% of the total pellets.

Figure 12. Fission gas release during pulse-irradiation as a function of fuel enthalpy



<sup>10</sup> D. T. Hagrman, C. M. Allison, G. A. Berna, et al., SCDAP/RELAP5/MOD3.1 Code Manual Volume IV: MATPRO - A Library of Materials Properties for Light-Water-Reactor Accident Analysis, NUREG/CR-6150, EGG-2720 (1993).

### 5.4. Comparison between tests RH-2 and BZ-3

The comparison between the tests RH-2 and BZ-3 aims at discussion about cladding deformation modes.

The BZ-3 test was performed with the MIMAS MOX rod at a burn-up of 59 GWd/t. The same fuel was subjected to the RT test BZ-2 prior to the BZ-3. The test BZ-2 resulted in a PCMI failure when the increase of fuel enthalpy reached 545 J/g. On the other hand, fuel failure did not occur in the HT test BZ-3, but this could be due to the insufficient enthalpy increase, which was 528 J/g at the maximum, arising from the lower moderator density in the HT capsule. The test BZ-3 provided quite interesting data of non-failure fuel behaviors, such as a large cladding hoop strain of 4.4% at the maximum and a high FGR of 39.4% during the power transient. The axial profiles of the cladding outer diameter before and after the pulse-irradiation are shown in Fig. 13. Since the hoop strain of 4.4% is beyond the PCMI-induced strain level, the gas-induced strain should have occurred additionally. On the other hand, the cladding hoop strain in the test RH-2 was induced only by PCMI as discussed in the previous section.

Fig. 13. Axial profiles of cladding outer diameter before and after tests BZ-3

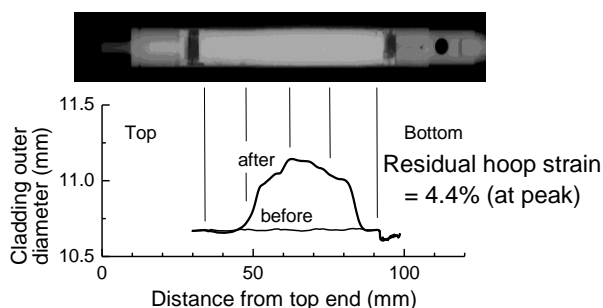


Fig. 15. Gas-induced clad residual hoop strain as a function of rod internal/external pressure difference during film boiling in tests RH-2 and BZ-3

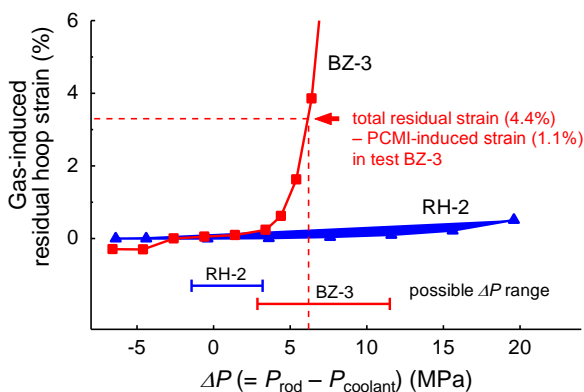


Fig. 14. Cladding surface temperature histories in tests RH-2 and BZ-3

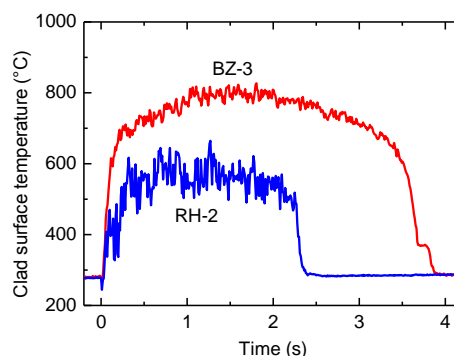
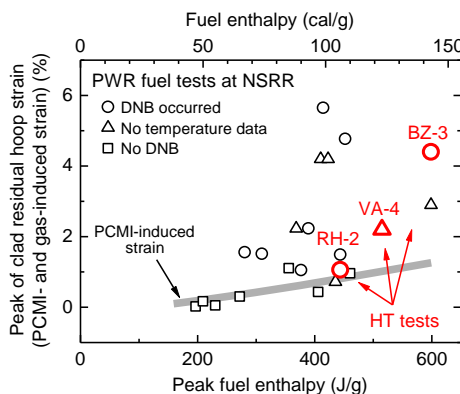


Fig. 16. Cladding residual hoop strain during pulse-irradiation as a function of peak fuel enthalpy ( $H_0 + \Delta H_{max}$ )



The occurrence and magnitude of the gas-induced strain are determined by the rod internal pressure, cladding temperature and the duration of high cladding temperature. Figure 14 shows the cladding surface temperature histories measured in the tests RH-2 and BZ-3. The peak cladding temperature was higher and its duration was longer in the test BZ-3 than in the RH-2. Anticipated gas-induced residual strains under the two cladding temperature histories are shown in Fig. 15, as a function of the rod internal/external pressure difference ( $\Delta P$ ) during the film boiling. These were evaluated with the RANNS analysis with the measured cladding temperature history as a boundary condition and with constant rod internal pressure as a driving force of the cladding ballooning. According to the calculation results, the gas-induced strain in the

test RH-2 becomes detectable when  $\Delta P$  is 10 MPa or higher, which is far beyond the possible  $\Delta P$  range estimated from the measured amount of rod gas and the possible range of gas temperature. On the other hand, the gas-induced strain in the test BZ-3 can be large within the possible  $\Delta P$  range. From the measured and evaluated strains,  $\Delta P$  in the BZ-3 film boiling is estimated as ~6.2 MPa (12.8 MPa in the rod internal pressure). This estimation, however, could have a considerable error, because the RANNS calculation assumed an axially uniform cladding deformation.

Figure 16 shows cladding residual hoop strain as a function of the peak fuel enthalpy. This figure is similar to Fig. 10, but the HT data are added. It was expected that HT tests would result in larger gas-induced strains than RT tests, because the cladding temperature can be higher and the film boiling duration can be longer under the HT conditions. However, Fig. 16 shows that the gas-induced strain is suppressed in the HT tests. This suggests that the rod internal pressures, which depend on the FGR and gas temperature, were similar in the RT and HT tests when compared at a same peak fuel enthalpy, and that the rod internal/external pressure difference was lower in the HT tests simply due to the higher coolant pressure.

Because the gas-induced strain is a complex phenomenon, it cannot be formulated with a single index, such as the peak fuel enthalpy and maximum enthalpy increase. Hence, conversion of the NSRR data to those under power reactor conditions requires some appropriate computer code which was verified with experimental data. Especially, the prediction of cladding temperature history requires accurate boiling transition models which consider coolant temperature, pressure, flow, effect of cladding surface oxide, cladding temperature increasing rate and so on.

## 6. Conclusions

In order to apply the NSRR room/high temperature test results to the safety evaluation under power reactor RIA conditions, possible influences of the initial coolant temperature on the failure/non-failure fuel behaviors were investigated, and the appropriate index to formulate the room/high temperature data consistently was discussed.

The comparison between the room temperature (RT) test VA-1 and high temperature (HT) test VA-3 suggested that the high initial coolant temperature raised the PCMI failure limit. The appropriate index for the failure limit is the maximum increase of fuel enthalpy, but it should be noted that differences arising from the initial conditions, such as cladding mechanical states, are not fully represented by the index. Regarding the different results in the two similar HT tests VA-3 and VA-4, no reasonable explanation was given at the present, but the comparison between the two tests suggested that the VA-4 was very close to the PCMI failure.

Non-failure behaviours during the RIA power transient were discussed on the basis of the RH-1, RH-2 and BZ-3 test results. The fission gas release (FGR) and the PCMI-induced cladding strain are correlated with the peak fuel enthalpy rather than with the maximum enthalpy increase. These results from RT and HT tests can be plotted together consistently by using the peak fuel enthalpy. On the other hand, the gas-induced cladding strain is a complex phenomenon and simple formulation with a single index is difficult. Conversion of the gas-induced strain data in the NSRR tests to the power reactor conditions requires well-verified computer codes for the transient fuel behavior analysis.

## Acknowledgments

All the tests presented in this paper were performed as parts of the fuel safety research program sponsored by the Nuclear and Industrial Safety Agency, the Ministry of Economy, Trade and Industry of Japan.

The fuel rods subjected to the VA and BZ tests and the fuel information on fabrication and base-irradiation were provided under the cooperation with Mitsubishi Heavy Industry, Ltd. The RH fuel rods and the fuel information on fabrication and base-irradiation were provided under the cooperation with AREVA NP. The LS fuel rod and the fuel information on fabrication and base-irradiation were provided under the cooperation with Kernkraftwerk Leibstadt AG and Paul Scherrer Institute.

P012

### Applicability of NSRR room/high temperature test results to fuel safety evaluation under power reactor conditions



T. Sugiyama, M. Umeda, Y. Udagawa,  
H. Sasajima, M. Suzuki and T. Fuketa

Nuclear Safety Research Center  
Japan Atomic Energy Agency

*OECD/NEA Workshop on Nuclear Fuel Behaviour during  
Reactivity Initiated Accidents, Paris, France, Sept 9-11, 2009*



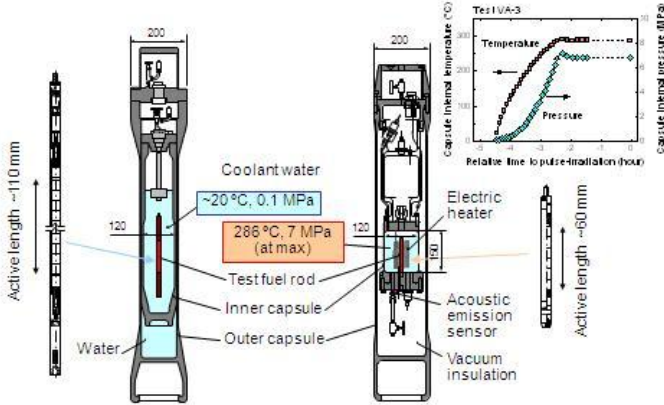
### Introduction

- The NSRR has provided data of transient fuel behavior during the reactivity-initiated accident (RIA) in LWR, but the test condition for high burnup fuels was limited to the room temperature (RT).
- The newly developed high temperature (HT) test capsule enabled assessment of possible initial temperature influences on the failure/non-failure fuel behaviors.
- This paper describes results from five pairs of RT and HT tests, and discusses the initial temperature influence and applicability of the NSRR data to the safety evaluation under power reactor conditions.



1

### NSRR test capsules



RT test capsule
HT test capsule



2

### RIA tests in ALPS\* program

Fuel	Type		Reactor (Country)	Burnup GWd/t	Cladding	NSRR test ID	
	Reactor	Spec				Room temp	High temp
UO <sub>2</sub>	PWR	17x17	Vandellos (Spain)	71	ZIRLO	VA-1 ★	VA-3 ★
				77	MDA	VA-2 ★	VA-4
			McGuire(USA) R2(Sweden)	71	NDA	MR-1	-
			Ringhals (Sweden)	67	M5	RH-1	RH-2
	BWR	10x10	Leibstadt (Switzerland)	69	Zry-2	LS-1 ★	LS-2
MOX	PWR	14x14	Beznau (Switzerland)	59	Zry-4	BZ-2 ★	BZ-3
				48	Zry-4	BZ-1	-
	BWR	8x8	Dodewaard (Netherlands)	45	Zry-2	DW-1	-

\* Advanced LWR fuel Performance and Safety research program sponsored by the Nuclear and Industrial Safety Agency (NISA) of the Ministry of Economy, Trade and Industry (METI) of Japan.      ★ PCMI failure

3

### Discussions based on test comparisons

**VA-1 vs. VA-3 :** temperature influence on failure limit

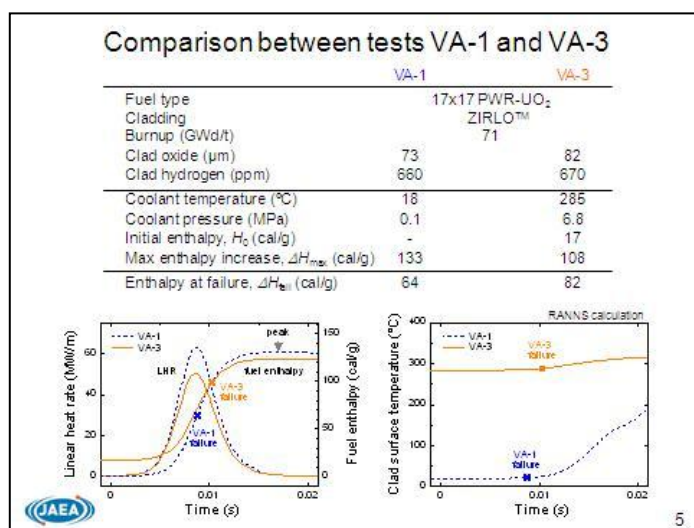
**RH-1 vs. RH-2 :** temperature influences on

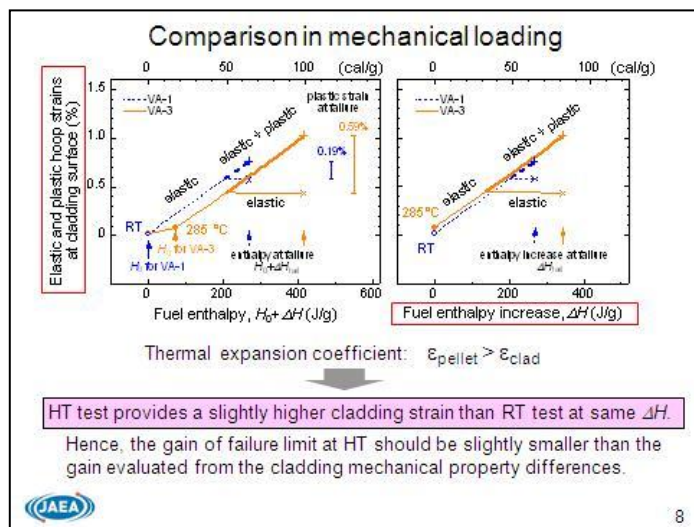
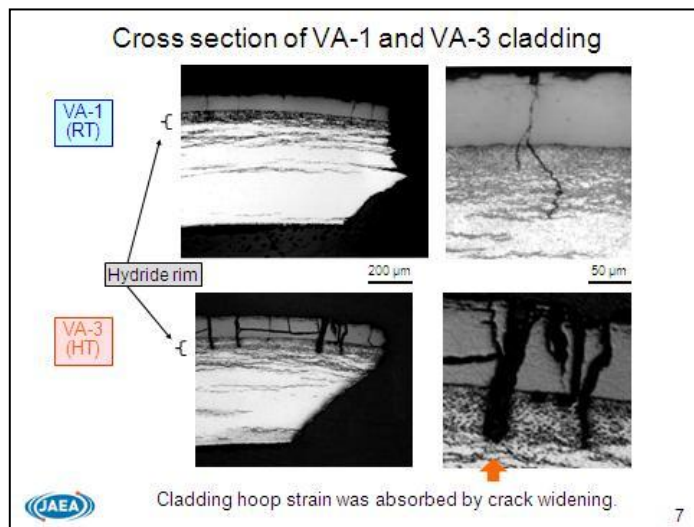
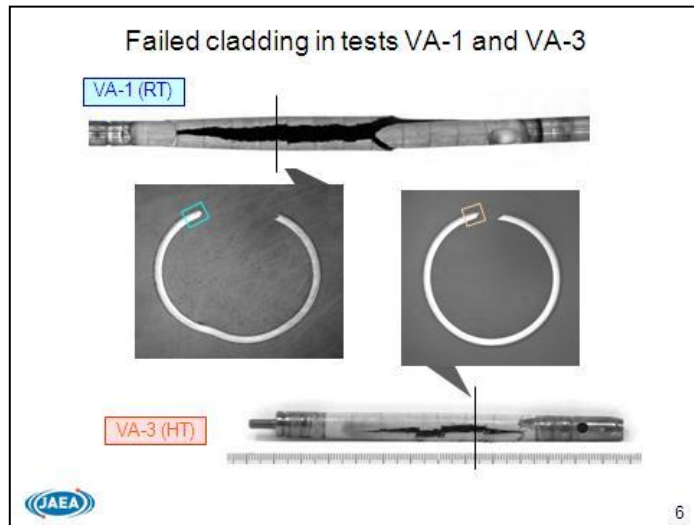
- cladding deformation
- fission gas release

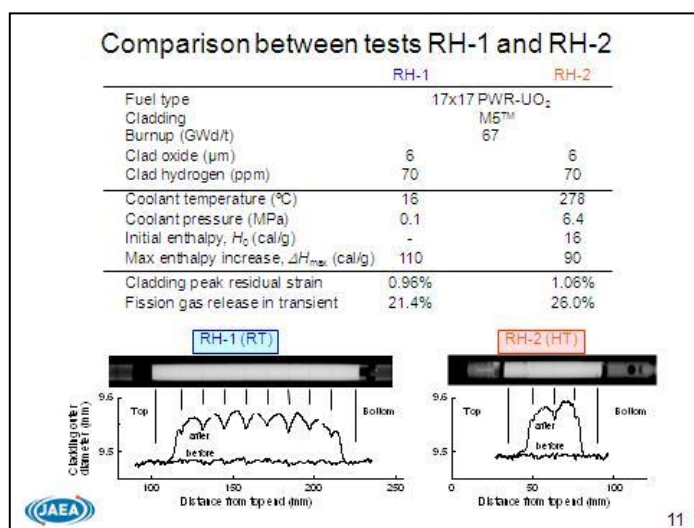
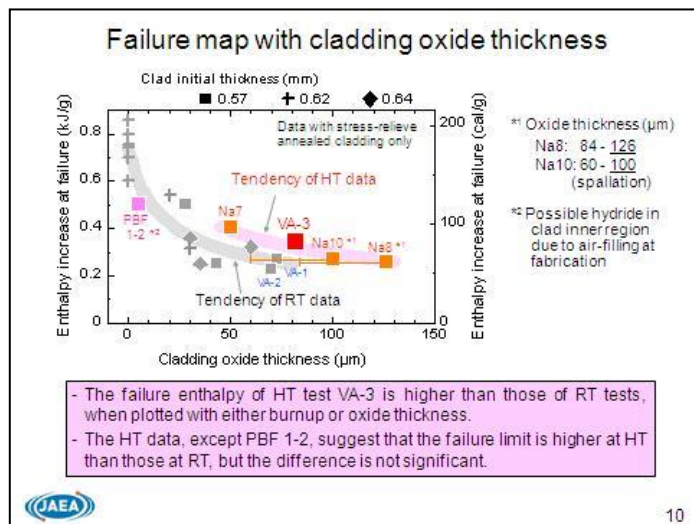
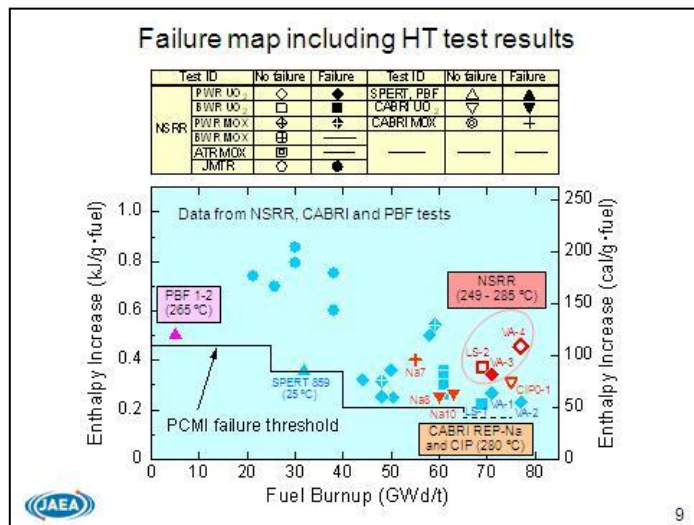
**RH-2 vs. BZ-3 :** driving forces of cladding deformation

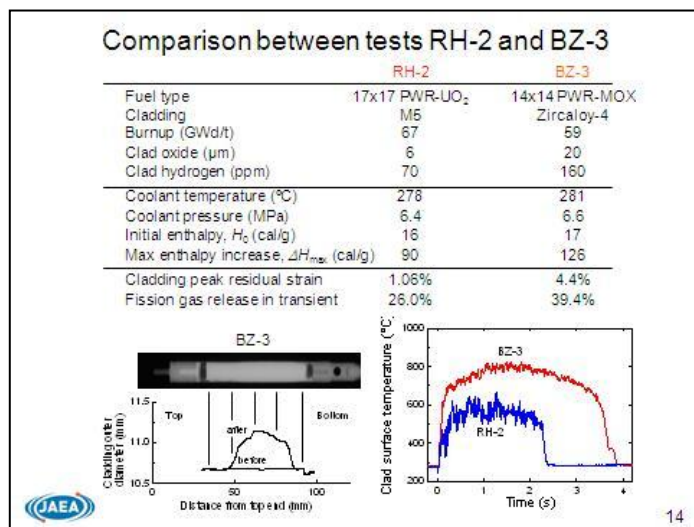
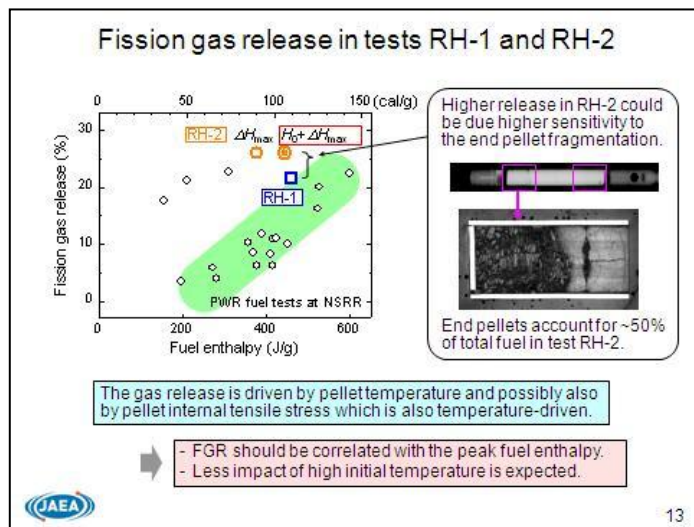
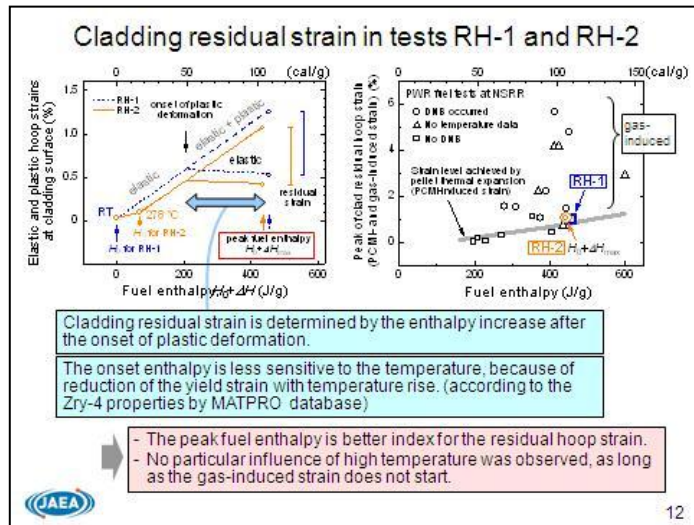
- pellet thermal expansion
- rod internal gas pressure

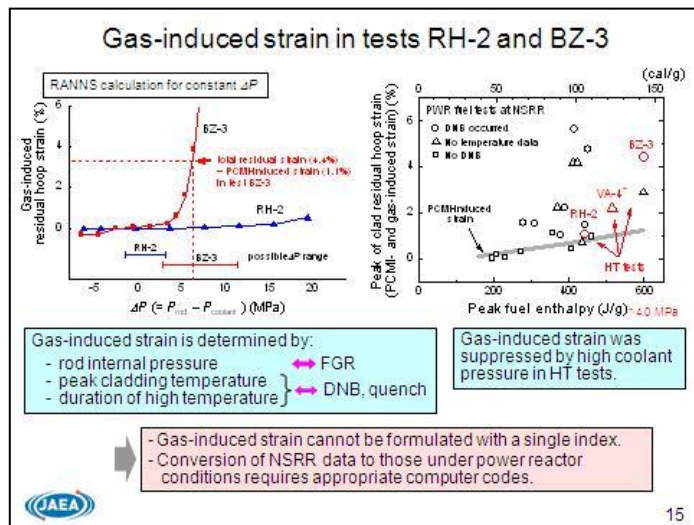
4











### Conclusions

- Comparison between tests VA-1 and VA-3 suggested that the high initial coolant temperature raised the PCMI failure limit. The appropriate index for the failure limit is the maximum increase of fuel enthalpy, but the cladding mechanical state are not fully represented by the index.
- Non-failure behaviors during the RIA power transient were discussed on the basis of the RH-1, RH12 and BZ13 test results. As for FGR and PCMI-induced cladding strain, results from RT and HT tests can be plotted together consistently with the peak fuel enthalpy. On the other hand, the gas-induced cladding strain is a complex phenomenon and simple formulation with a single index is difficult. Conversion of NSRR data of gas-induced strain to that under power reactor conditions requires adequate computer codes.

**JAEA** 16



## SESSION TWO

### Modelling and Data Interpretation

#### **Numerical Analysis and Simulation of Behaviour of High Burn-up PWR Fuel Pulse-Irradiated in Reactivity-Initiated Accident Conditions**

Motoe Suzuki, Tomoyuki Sugiyama, Yutaka Udagawa, Fumihisa Nagase and Toyoshi Fuketa (JAEA, Japan)

#### **Influence of Initial Conditions on Rod Behaviour during Boiling Phase following a Reactivity Initiated Accident**

Vincent Georgenthum (IRSN, France); Tomoyuki Sugiyama (JAEA, Japan)

#### **Application of the SCANAIR Code for VVER RIA Conditions – Boron Dilution Accident**

Asko Arffman (VTT, Finland); Bernard Cazalis (IRSN, France)

#### **Analysis of Mixed-Oxide Fuel Behavior during RIA Tests using FALCON MOD01**

Robert Montgomery and John Alvis (ANATECH Corp.); Ken Yueh and Odelli Ozer (EPRI, USA)



## NUMERICAL ANALYSIS AND SIMULATION OF BEHAVIOR OF HIGH BURN-UP PWR FUEL PULSE-IRRADIATED IN REACTIVITY-INITIATED ACCIDENT CONDITIONS

**Motoe Suzuki**

Nuclear Safety Research Center, Japan Atomic Energy Agency, Japan

**Tomoyuki Sugiyama, Yutaka Udagawa, Fumihisa Nagase and Toyoshi Fuketa**

Nuclear Safety Research Center, Japan Atomic Energy Agency, Japan

### Abstract

The four cases of the NSRR experiments, consisting of two room temperature tests and two high temperature tests, using high burn-up PWR fuel rods are analyzed by using the RANNS code to discuss the fuel behavior in hypothetical pulse-irradiation conditions.

A preparatory step is to calculate the fuel rod changes induced during the base-irradiation in commercial PWR by using the fuel performance code FEMAXI-6. Thus the fuel rod conditions, i.e. cladding diameter and oxide thickness prior to the NSRR experiment, are reproduced in accordance with the PIE results of the reference rods. The RANNS code adopts these changes as initial conditions, and calculates the temperature and thermal stress of pellet, and temperature and stress-strain of cladding during the fast transients in one-dimensional cylindrical geometry. These results were compared with the metallographic observations of failed part of the cladding, i.e. incipient crack depth and shear sliding deformation etc., to discuss the predominant factors causing cladding failure.

Based on these evaluations, two types of simulations are performed. One is with variable pulse heights (enthalpy), and the other is in commercial PWR conditions which assumes half-widths of power pulse as either 15ms or 30ms while the integrated energy of the pulse power is unchanged. The results are compared with each other and failure capability of cladding is discussed.

### 1. Introduction

As the reactivity-initiated accident (RIA) simulating experiments in the NSRR, the VA series of pulse irradiation tests were conducted using high burn-up PWR rods. In these tests, VA-1 and VA-2 were room temperature tests<sup>1)</sup>, and VA-3 and VA-4 were high temperature tests<sup>2), 3)</sup>. The results were that the VA-1, VA-2 and VA-3 caused cladding failure by pellet-clad mechanical interaction (PCMI), while VA-4 did not.

In these experiments, thermal and mechanical behavior of fuel is progressing in a very short period of time under complicate interactions among a number of factors<sup>4)</sup>.

Therefore, for the evaluation of the experimental results, numerical analysis is indispensable to investigate the mechanism or factors dominating in the fast transients of fuels.

As an extension of the analysis of failure mechanism, it is also significant to perform a predictive and exploratory simulation of fuel behavior in hypothetical conditions such as varied pulse power. In the present study, fuel behavior and failure conditions of the VA-series tests were analyzed by the RANNS code<sup>5), 6)</sup>, and the results are compared with respect to cladding temperature and stress-strain mainly during PCMI stage, and possible dominating factors in fuel failure are discussed.

## 2. Fuel rods and NSRR experiments

The major items of fuel specifications, test conditions and results of the VA-1 to VA-4 tests are listed in Table 1. The rods were obtained from a 17×17 type-assembly base-irradiated in Vandellós PPT in Spain<sup>1),2)</sup>.

Table 1. **Rod specifications, EOL conditions, test conditions and results**

	VA-1	VA-2	VA-3	VA-4
Cladding material	ZIRLO	MDA	ZIRLO	MDA
Pellet (BOL)	8.19 × 9.83 mm, 95% TD			
Cladding diameter (BOL)	9.50 mm O.D. - 8.36 mm I.D.			
Burn-up	71 GWd/t	77 GWd/t	71 GWd/t	77 GWd/t
Average thickness of oxide	73 μm	82 μm	73 μm	80 μm
Fluence	1.30 - 1.42 × 10 <sup>22</sup> n/cm <sup>2</sup>			
Initial rod pressure (He)	0.1MPa			
Coolant water condition	20°C, 0.1 MPa		285°C, 6.8MPa	250°C, 4MPa
Failure enthalpy increase	268J/g (64cal/g)	231J/g(55cal/g)	344J/g(82cal/g)	No failure

### 2.1. Method of analysis

#### 2.1.1. FEMAXI and RANNS

By using the fuel performance code FEMAXI-6<sup>7),8)</sup>, changes of the VA-series fuels induced during the base-irradiation are calculated, and the oxide thickness and rod diameter at EOL which were observed in the PIE of the reference rod were reproduced by adjusting the swelling rate of pellet and oxidation rate of cladding. Also, the power density profile in the radial direction of fuel pellet was calculated by using a burning analysis code<sup>9)</sup>. These EOL conditions were given to the RANNS analysis as initial conditions, and fuel temperature rise, thermal expansion, PCMI, and cladding stress/strain etc. were calculated with the pulse linear power and coolant conditions. In the FEMAXI-6 and RANNS codes, thermal analysis (heat conduction and internal pressure change) is performed with one-dimensional cylindrical geometry in each axial segment of pellet stack and cladding to obtain the temperature distribution, and on the basis of these thermal results a mechanical analysis for PCMI and elasto-plastic deformation of pellet and cladding is performed by using the finite element method (FEM).

Fig.1 shows the cylindrical geometry of one axial segment which is shared with both the codes, where pellet stack consists of 36 iso-volume ring elements, and cladding 8 iso-thickness ring elements and one outer oxide element. The power density profile of pellet is shown together in the figure. The analysis was performed with one axial segment only, because of the axial uniformity of the linear power. Fig.2 shows the pulse powers measured in the experiments and used in the RANNS analysis.

Figure 1. **One-dimensional geometry of FEMAXI-6 and RANNS, and power density profile**

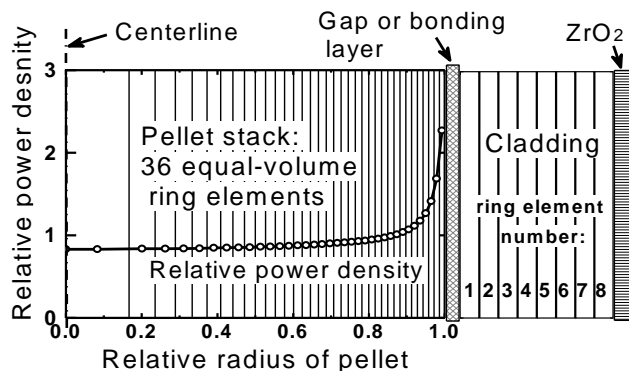
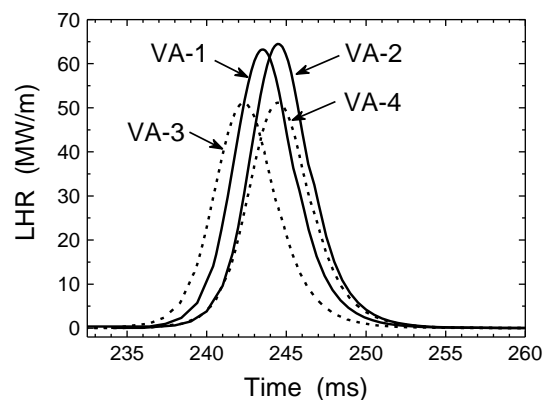


Figure 2. **Pulse linear powers of the VA-1, VA-2, VA-3 and VA-4 tests in the NSRR**



### 2.1.2. Metallography of cladding

Metallography observation of ruptured part of post-test cladding were conducted and process of cladding failure was considered in comparison with the analytical results.

### 2.1.3. Simulation with various pulses

Based on the conditions of high temperature tests VA-3 and VA-4, two types of simulation calculations were performed. One is with variable pulse heights (enthalpy), and the other adopts a commercial PWR condition which assumes half-widths of power pulse as either 15ms or 30ms while the integrated energy of the pulse power is unchanged.

## 3. Results and discussion

The following calculated results are those which are obtained in the condition assuming no cladding failure even if the actual test cladding did fail.

### 3.1. Cladding temperature

Fig.3 to Fig.5 show the calculated cladding temperatures of the VA-1, VA-3 and VA-4 tests, respectively. These temperatures are at the inner ring element 1, outer ring element 8, two ring elements 2 and 4 in between the 1 and 8, and outer oxide surface, which are indicated in Fig.1.

Figure 3. Calculated temperatures of the cladding ring elements #1, #2, #4, and #8, and of the oxide surface in the VA-1 test

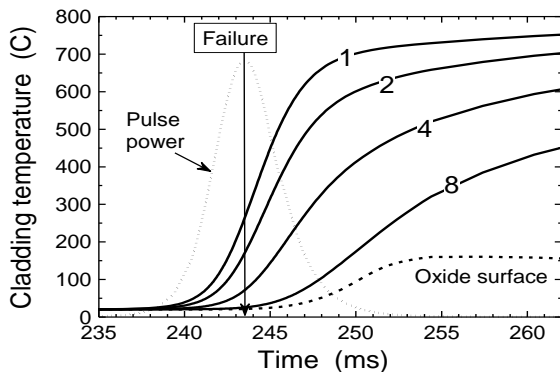


Figure 4. Calculated temperatures of the cladding ring elements 1, 2, 4 and 8, and of the oxide surface in the VA-3 test

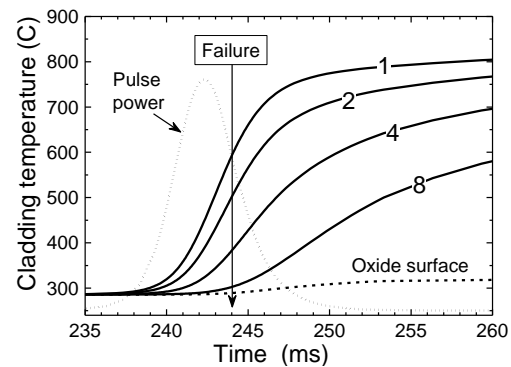
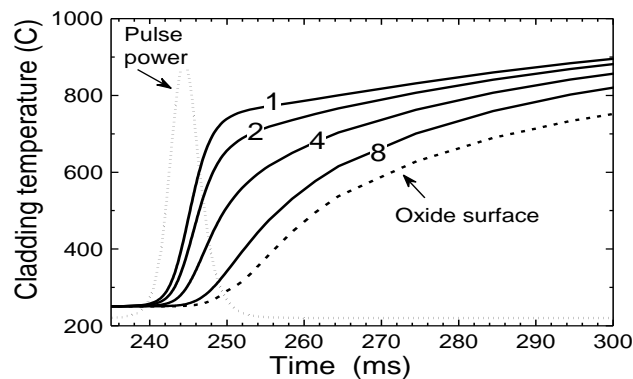


Figure 5. Calculated temperatures of the cladding ring elements 1, 2, 4 and 8, and of the oxide surface in the VA-4 test



On pulse power insertion, temperature of the inner element 1 rapidly rises due to the heat conduction through the solid bonding layer, while it is delayed in the outer element 8. The oxide surface temperature rise is much delayed because of the low thermal conductivity of the thick oxide. The failure instants

determined by measured data are indicated by vertical arrows. At failure instant, it is shown that the temperature at cladding outer region has scarcely elevated from the initial temperature. In the VA-4 test, PCMI failure did not occur, and departure from nucleate boiling (DNB) occurred and the cladding temperature is considered to have risen markedly. The calculation assumes an approximate condition for cladding surface heat transfer coefficient to reproduce the DNB.

### 3.2. Stress and strain of cladding

Since the pellet-clad gap has been closed and the bonding layer has been produced in the pre-test condition, the pellet thermal expansion induced by pulse power directly out-stretches the cladding, resulting in a strong PCMI and thus intense tensile stress in the cladding.

#### 3.2.1. Cladding stress

Figs.6 and 7 show the hoop stress (solid curves) and axial stress (broken curves) of the VA-1 and VA-3 claddings, respectively, together with the failure instant. They are the calculated values at the ring elements 1, 2, 4 and 8 indicated in Fig.1, similarly to those in Fig.3. Figure of the stresses in the VA-2 test are omitted because it is closely identical to that of the VA-1 test, Fig.6.

Figure 6. Calculated hoop and axial stresses of the cladding ring elements 1, 2, 4 and 8 in the VA-1 test

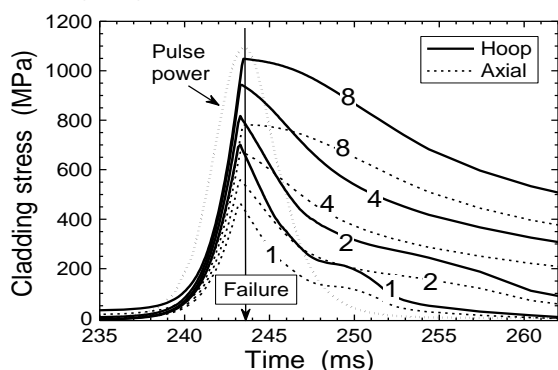
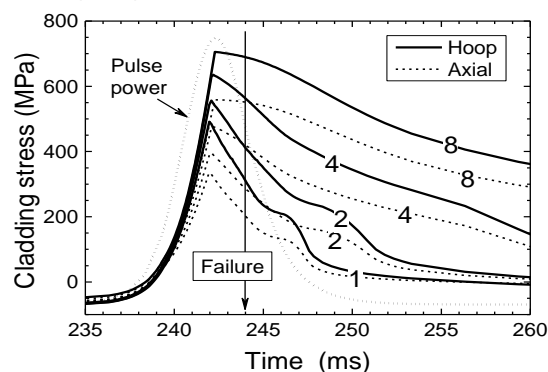


Figure 7. Calculated hoop and axial stresses of the cladding ring elements 1, 2, 4 and 8 in the VA-3 test



Immediately after the pulse power insertion, the tensile stress is increased rapidly due to PCMI, while the stress is falling after the temperature-dependent yielding. The yielding produces sharp inflection of the stress curves around 243ms (Fig.6) or 244ms (Fig.7).

In PCMI, the cladding is subjected to a bi-axial stress state, or combination of hoop stress and axial stress due to pellet stack expansion. It is also shown that the stress in the outer element is relatively higher than those in the inner element. This is mainly attributed to the enhanced thermal expansion of the inner region, for the expansion substantially cancels the tensile stress. This suggests that the crack is generated in the outer region which has high stress and low ductility due to lower temperature, which is consistent with the metallographic observation of cladding (Figs.14, 15 and 16).

#### 3.2.2. Cladding strain

Figs.8, 9 and 10 shows the total hoop strain, plastic hoop strain, creep hoop strain of the inner element #1 and outer element #8 in the VA-1, VA-2 and VA-3 claddings, respectively. The initial values of the creep strain are those at the end of base-irradiation. By the failure instant, no creep strains in the outer element are generated. In the present model, magnitude of the cladding plastic strain is dominated by the solid thermal expansion of pellet during the PCMI stage, which has been validated<sup>4)</sup>. If no failure would occur during the PCMI stage, the plastic strain would not proceed after the cease of PCMI. This plastic strain is an averaged value over the total circumference of cladding, since the calculation is performed in the cylindrical geometry. However, the actual cladding fractured at one site of the circumference, so that it can be considered that the plastic strain is localised in the neighboring area of fracture.

Figure 8. Calculated strains of the cladding inner element 1 and outer element 8 in the VA-1 test

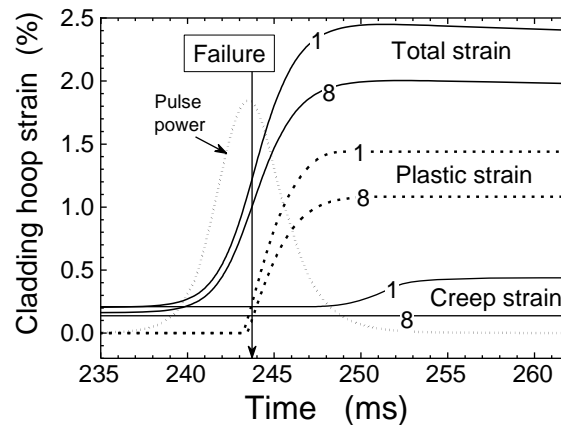


Figure 9. Calculated strains of the cladding inner element 1 and outer element 8 in the VA-2 test

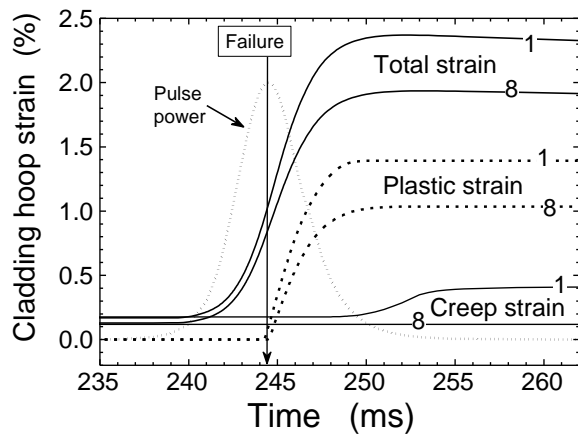
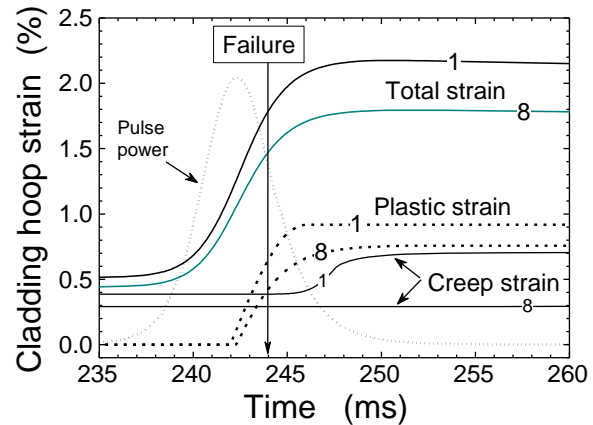


Figure 10. Calculated strains of the cladding inner element 1 and outer element 8 in the VA-3 test



### 3.2.3. Deformation of non-failed cladding in the VA-4 test

As shown in Fig.5 in the VA-4 test, cladding temperature is predicted to rise markedly and it is presumed that a burst release of fission gas occurred after the cease of PCMI. While the amount and rate of this release is not clear experimentally, calculated results are shown in Figs.11 and 12 assuming 12% fission gas release (FGR) at the early stage of transient. The cladding stresses in the inner and outer elements are in Fig.11, and hoop strains in Fig.12. These two figures suggests that the creep strain is enhanced during the high temperature period from 0.24 to 2.5s, i.e. hatched zones while the plastic strain remains unchanged after PCMI. Finally, the pre-test and post-test profiles of the cladding diameter are shown in Fig.13 together with the calculated values (horizontal broken lines) for comparison. In Fig.13, the calculated lines are for the two cases, i.e. Case-1 of no FGR yielding 0.73% plastic strain only, and Case-2 of 12% FGR yielding plastic strain of 0.73% and creep strain of 1.2%. In the case-1, amount of the plastic strain is determined by the pellet thermal expansion, which is clearly under estimate for the measured profile. On the other hand, in the case-2, creep strain induced by the enhanced internal pressure makes the bulk of deformation by about 60%, giving a better agreement to the measured profile.

However, the measured deformation at both the end of the pellet stack has a considerable difference from those in the middle region, suggesting the effect of axial temperature gradient. It is to be noted here that the prediction of cladding creep is sensitively dependent on a number of factors such as evolution processes of temperature and internal pressure, transient creep model, etc.

Figure 11. Calculated hoop stress of the inner ring element 1 and outer ring element 8 in the VA-4 test

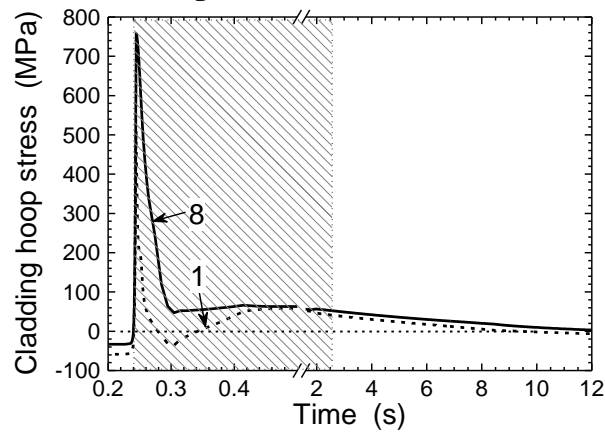


Figure 12. Calculated strains of the cladding inner element 1 and outer element 8 in the VA-4 test

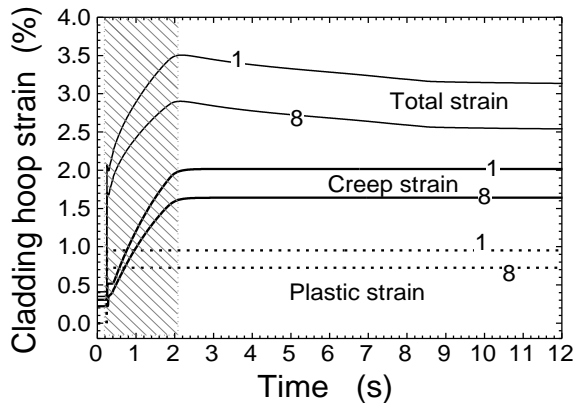
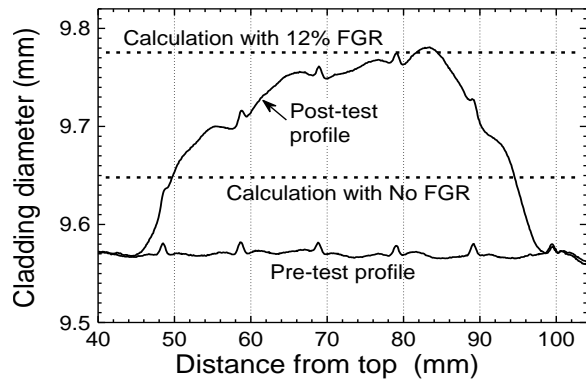


Figure 13. Comparison of cladding diameter profiles among the pre-test state, post-test state and 1-D calculations



### 3.3. Metallography of fractured cladding

A comparison is performed between the metallography of fractured claddings and calculations to assess the failure process predictability given by the present numerical analysis. Figs.14-16 show the fractured part of claddings of the VA-1, VA-2, and VA-3 tests.

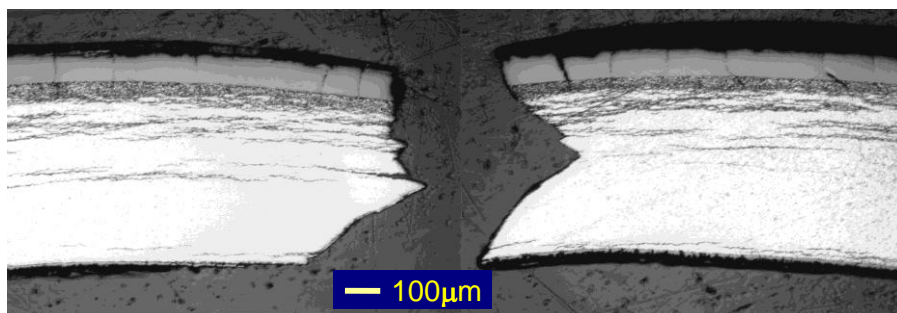


Figure 14. Cross section morphology of fractured part of the VA-1 cladding

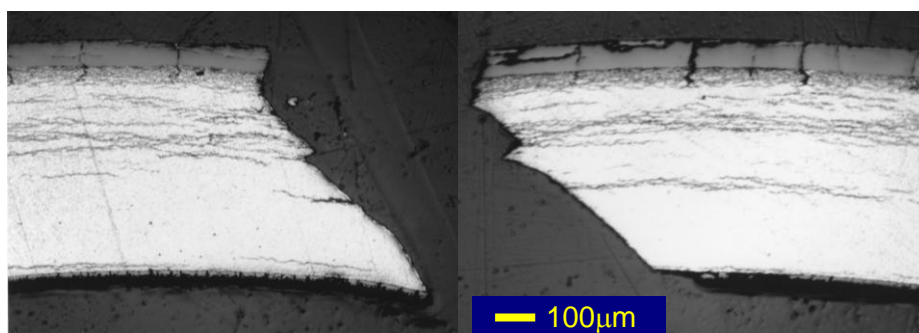


Figure 15. Cross section morphology of fractured part of the VA-2 cladding

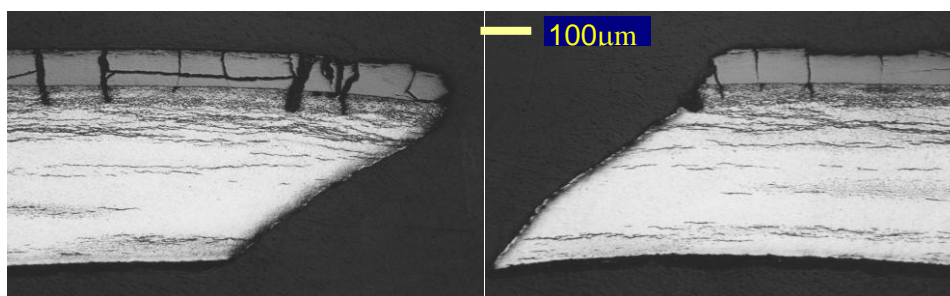


Figure 16. Cross section morphology of fractured part of the VA-3

### 3.3.1. VA-1 (Fig.14)

In Fig.14, thickness of the dense hydride layer appears to be in the range of 50-70  $\mu\text{m}$ . It is indicated that incipient crack of about 60 $\mu\text{m}$  depth was generated at the rupture site, and that the incipient crack grew to the 40% depth of cladding wall before a macroscopic shear sliding occurred through the rest of the wall.

### 3.3.2. VA-2(Fig.15)

In Fig.15 thickness of the dense hydride layer appears to be in the range of 40-45  $\mu\text{m}$ . It is indicated that incipient crack of about 40 $\mu\text{m}$  depth was generated at the rupture site, and that a shear sliding occurred from the tip of the incipient crack to the 30% depth of cladding wall before a macroscopic shear sliding occurred through the rest of the wall.

### 3.3.3. VA-3(Fig.16)

In Fig.16 thickness of the dense hydride layer appears to be in the range of 50-70  $\mu\text{m}$  similarly to the Fig.14. It is indicated that incipient crack of about 60  $\mu\text{m}$  depth was generated at the rupture site, and that from the incipient crack tip a macroscopic shear sliding occurred through the rest of the wall.

## 3.4. Condition and process of cladding rupture

### 3.4.1. Temperature and stress at crack tip

As shown in Figs.3, 4 and 5, the cladding outer temperature rise is slight at failure instant. The ring element thickness shown in Fig.1 is about 70  $\mu\text{m}$ , so that the incipient crack is assumed to be generated within the thickness of the outer element 8. In the followings, the temperature and stress of the crack tip is evaluated from interpolation of the calculated values of each ring element.

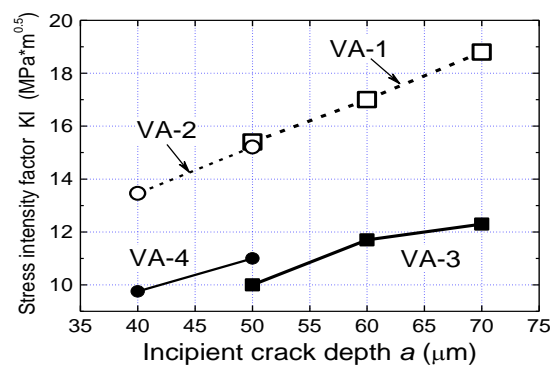
In the cladding of the VA-1 and VA-2 tests, temperature at the incipient crack tip is about 30-50°C, and calculated hoop (average) plastic strain at failure instant is 0.15-0.2% for VA-1 and 0.05-0.1% for VA-2. The 40% depth temperature at which shear sliding occurred is around 350C in the VA-1 test. At the failure

instant of the VA-3 test, the temperature is about 280°C at the outer element #8, about 310°C at the hydride layer bottom (about 12% depth of wall thickness), hoop plastic strain is about 0.4% (outer element) – 0.6% (inner element). This suggests that the VA-3 cladding was strained plastically to some extent owing to the ductility recovery at higher temperature over 300°C. As a result, the failure occurred somewhat behind the peak of pulse power and consequently the failure enthalpy increased significantly in comparison with those in the VA-1 and VA-2 tests.

### 3.4.2. Comparison of KI

The metallography images in Figs.14-16 indicate the followings: once an incipient crack is generated in the hydride rim layer, plastic strain is generated locally around the crack tip by the temperature rise and stress enhancement. Then the crack grows or if not, shear sliding occurs leading directly to the rupture. Therefore, it is necessary in principle to consider the condition to give rise to the local plastic strain around the crack tip. However, as a simplified and tentative criterion, the stress intensity factor KI at the crack tip is compared, assuming that KI has a reasonable correlation with the onset of local plastic strain around the tip. The incipient crack depths  $a$  in the VA-1, VA-2 and VA-3 tests obtained by referring to the Figs.14, 15 and 16, and calculated KI are shown in Fig.17. The figure indicates that the KI is a monotonously increasing function of  $a$ . Here, KI of VA-4( $a = 40\mu\text{m}$ ) is lower than that of VA-3 ( $a = 60\mu\text{m}$ , typically), which implies to coincide with the non-failure result of the VA-4 test.

1. Figure 17. KI as a function of incipient crack depth in the VA-1, VA-2, VA-3 and VA-4 tests

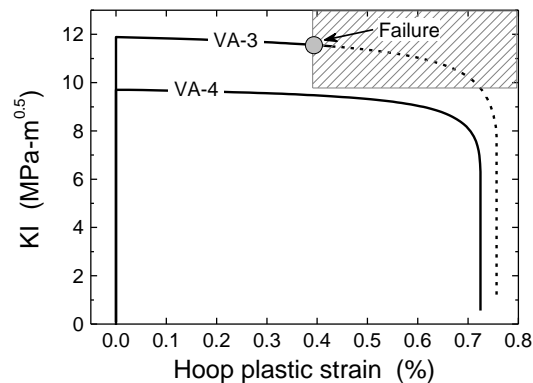


### 3.4.3. Comparison between VA-4 and VA-3

In the numerical analysis of the VA-4 test with non-failure result, macroscopic stress is to some extent higher than in the VA-3 test, as shown in Fig.11. Namely, at the hoop stress peak (244.3ms), temperature is 250°C and stress is ~750 MPa in the outer ring element 8, and the interpolated values are 270°C and ~800MPa at the crack depth (12% of the wall thickness), while the VA-4 cladding did not generate the macroscopic shear sliding even in the tensile stress which is by ~11% higher than that of the VA-3 cladding.

Here, assuming that a condition of onset of shear sliding consists of the two factors, i.e. local stress level at the crack tip represented by KI, and cladding ductility represented by the amount of hoop plastic strain  $\varepsilon_{\theta}^{pl.}$  in the outer element 8, KI of the incipient crack as a function of plastic strain increase induced by PCMI is compared between the calculations of VA-3 and VA-4 tests. Fig.18 shows this comparison of  $\varepsilon_{\theta}^{pl.}$ -KI curves, in which incipient crack depth is assumed to be typically 60 $\mu\text{m}$  in VA-3 and 40 $\mu\text{m}$  in VA-4. Supposing that in the VA-3 test the shear sliding occurred in the condition that the plastic strain is 0.4% at the tip and KI=11.7(MPa/m<sup>0.5</sup>), the hatched area in the figure could be a “failure zone”. It can be interpreted that the VA-4 cladding did not fail because the curve did not enter this area.

Figure 18. Evolution of hoop plastic strain of cladding vs. KI at the crack tip in the VA-3 and VA-4 tests



### 3.5. Failure/non-failure prediction with simulated pulse conditions

Based on the above discussion, the cladding mechanical conditions are considered by the following simulations.

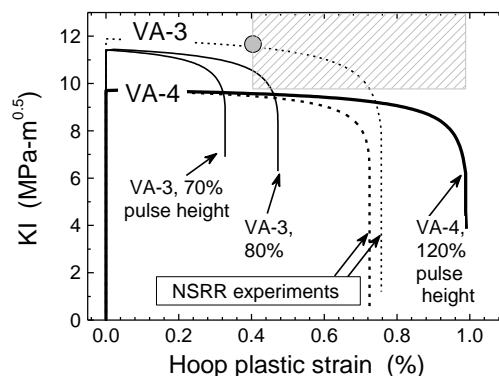
#### 3.5.1. NSRR test condition

In the first simulations, initial coolant temperature and pulse half-height width are unchanged from the NSRR test conditions. Results of the VA-3 and VA-4 tests with varied pulse height (fuel enthalpy increase) are shown in Fig.19.

#### 1) VA-3 simulation (crack depth=60 $\mu$ m)

To evaluate the pulse height allowing the VA-3 cladding to survive the PCMI, simulations with reduced pulse height, i.e. 70% or 80% magnitude of the original pulse height, are performed. In Fig.19, the  $\varepsilon_{\theta}^{pl.} - K_I$  curve corresponding to the original experimental condition is shown in a broken line, while the two simulation curves are shown in a thick line. Here, the 80%-height curve overpasses the “failure area”, suggesting the possibility of cladding failure, while the 70%-height curve does not.

Figure 19. Evolution of hoop plastic strain of cladding vs. KI at the crack tip in hypothetically varied pulse height in the VA-3 and VA-4 tests



This implies that a failure/non-failure boundary would exist in between the 70% and 80% height conditions. The fuel enthalpy increases of the two cases are: 80% case =  $454 \times 0.8 = 363$  (J/g), 70% case =  $454 \times 0.7 = 318$  (J/g). Though the measured failure enthalpy value of  $344$  (J/g)<sup>2</sup> (see Table 1) in the VA-3 test lies in between these two values, it can be considered that the pulse height, i.e. severity of transient, caused a strong PCMI resulting in failure.

## 2) VA-4 simulation (crack depth=40 $\mu$ m)

To evaluate the pulse height making the VA-4 cladding to fail by PCMI, simulations with increased pulse height by 20% from the original pulse height is performed. Even in this case, KI will not increase because the stress is not markedly enhanced due to cladding yielding and temperature rise, and the  $\varepsilon_{\theta}^{pl}$ -KI curve does not significantly exceed the experiment curve which is shown in a broken line. On the other hand, the plastic strain is enhanced due to larger thermal expansion of pellet, though the KI is rapidly decreasing with the plastic strain progress. Consequently, it can be estimated that the shear sliding would not occur and no PCMI failure would be predicted.

### 3.5.2. Simulation of RIA in a commercial PWR condition

A simulation was performed with the initial coolant condition being those of the commercial PWR, i.e. 285°C and 15.4MPa. Here, pulse half-width is changed into either 15ms or 30ms with the integrated fuel enthalpy increment of the VA-3 test being unchanged. Crack depth is assumed as 60 $\mu$ m. The resulted  $\varepsilon_{\theta}^{pl}$ -KI curves with the 15ms and 30ms widths are shown in Fig.20. In both the curves, the final values of plastic strain induced by PCMI are identical, while the lower KI values are resulted by attenuated stress in a mild transient. This allows the curves to be located mostly under the experiment curve, suggesting no possibility of cladding failure.

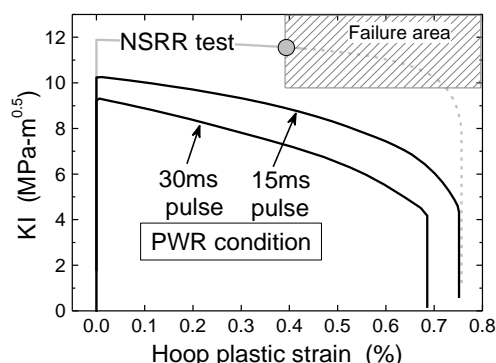


Fig.20 Evolution of hoop plastic strain of cladding vs. KI at the crack tip with hypothetically longer pulse width for the VA-3 test fuel in

### 3.6. Key factor dominating fracture of cladding

The discussions above would exhibit that in RIA of high burn-up PWR fuel, failure mode is a shear sliding induced by PCMI, and that for failure prediction it is essentially required to work out a criterion consisting of not only the KI at crack tip but also some parameter expressing the bound of shear sliding onset. Tomiyasu et al.<sup>10)</sup> and Udagawa et al.<sup>11)</sup> have pointed out that the local plastic deformation at the tip is a key factor to branch the cladding behavior into failure or non-failure.

As shown in Fig.16, at high temperature the cladding recovers ductility to some extent. This leads to the generation of shallow and larger number of incipient cracks, and local concentration of plastic strain is attenuated, while the fraction of wall thickness through which the shear sliding occurs becomes larger. Also irrespective of the initial fuel temperature in the test, magnitude of pellet thermal expansion is nearly identical if the pulse power shape (height, half-width and integral enthalpy) is unchanged, and consequently cladding deformation (strain) is identical, so that it can be considered that the failure criterion is significantly dependent on the onset condition of shear sliding as mechanical properties of cladding material.

## 4. Conclusions

Numerical analysis was performed on the pulse-irradiation tests with high burn-up PWR fuel in the NSRR by using the RANNS code, and the results were compared with metallography observations of ruptured claddings. The cladding rupture occurred by a shear sliding which starts from the tip of incipient crack generated in the hydride dense layer. The analyses reveals that the onset of shear sliding leading to cladding rupture can be closely associated with the stress intensity factor KI at the crack tip and local plastic strain evolution around the tip as well, and that these two factors depends also on the temperature of cladding.

Simulation calculations on the basis of experimental conditions reveals that the cladding stress is dependent on the height and half-width of pulse power, and for the same integral enthalpy of pulse a larger, half-width mitigates the severity of transient (PCMI) and decreases KI to allow plastic strain by temperature rise, thus failure possibility would be markedly decreased.

### Acknowledgement

The tests VA-1, VA-2, VA-3 and VA-4 have been conducted as a part of program sponsored and organised by Nuclear and Industry Safety Agency, Ministry of Economy, Trade and Industry. The fuel rods subjected to the VA test series and the fuel information on fabrication and base-irradiation were provided under the cooperation with Mitsubishi Heavy Industry, Ltd. In the whole process of the present analysis, the authors are much indebted to Mr.Hiroaki SAITOU of ITOCHU Techno-Solutions Corp., Tokyo, for his assistance in model development, coding and test-run of the RANNS code.

### Notes

- 1) Sugiyama, T., Umeda, M., Fuketa, Sasajima, H., Udagawa, Y., T., Nagase, F., “Failure of high burn-up fuels under reactivity-initiated accident conditions”, *Annals of Nuclear Energy*, 36, 380 (2009).
- 2) Sugiyama, T., “PCMI failure of high burn-up fuel under high temperature RIA conditions”, *Fuel Safety Research Meeting 2009*, Tokai, Japan, May20-21 (2009).
- 3) Sugiyama, T., Umeda, M., Sasajima, H., Suzuki, M. and Fuketa, T., “Effect of Initial Coolant Temperature on Mechanical Fuel Failure under Reactivity-Initiated Accident Conditions”, *Proc. TopFuel 2009*, Paris (2009).
- 4) Suzuki, M. and Fuketa, T., “Analysis of Pellet-Clad Mechanical Interaction Process of High-burn-up PWR Fuel Rods by RANNS Code in Reactivity-Initiated Accident Conditions,” *Nuclear Technology*, 155, 282 (2006).
- 5) Suzuki M., Saitou H. and Fuketa T., “Analysis on split failure of cladding of high burn-up BWR rods in reactivity- initiated accident conditions by RANNS code”, *Nuclear Engineering and Design* 236, p.128-139 (2006).
- 6) Suzuki, M., Sugiyama, T., and Fuketa, T., “Thermal Stress Analysis of High Burn-up LWR Fuel Pellet Pulse-Irradiated in Reactivity-Initiated Accident Conditions,” *Journal of Nuclear Science and Technology*, vol.45, p.1155-1164 (2008).
- 7) Suzuki, M. and Saitou, H., “Light Water Reactor Fuel Analysis Code FEMAXI-6 (Ver.1) -Detailed Structure and User’s Manual-”, JAEA-Data/Code 2005-003 (2005).
- 8) Suzuki M., Kusagaya K., Saitou H. and Fuketa T., “Analysis on Lift-Off Experiment in Halden Reactor by FEMAXI-6 Code”, *Journal of Nuclear Materials* 335, p.417-424 (2004).
- 9) Okumura K., Mori T., Nakagawa M. and Kaneko K., “Validation of a continuous- energy Monte Carlo burn-up code MVP-BURN and its application to analysis of post irradiation experiment”, *Journal of Nuclear Science and Technology*, Vol. 37, No. 2, p.128-138 (2000).
- 10) Tomiyasu, K., Sugiyama, T., Fuketa, T., “Influence of Cladding-Peripheral Hydride on Mechanical Fuel Failure under Reactivity-Initiated Accident Conditions”, *Journal of Nuclear Science and Technology*, 44, No.5 p.733-742 (2007).
- 11) Udagawa, Y., Suzuki, M., Sugiyama, T. and Fuketa, T., “Stress intensity factor at the tip of cladding incipient crack in RIA-simulating experiments for high burn-up PWR fuels”, submitted to *Journal of Nuclear Science and Technology*, (2009).

1

OECD/NEA Workshop on Nuclear Fuel Behaviour during Reactivity Initiated Accidents, Paris, France, September 9 – 11, 2009

**Numerical Analysis and Simulation of Behavior of High Burnup PWR Fuel Pulse-Irradiated in Reactivity-Initiated Accident Conditions**

Motoe SUZUKI, Tomoyuki SUGIYAMA, Yutaka UDAGAWA,  
Fumihisa NAGASE and Toyoshi FUKETA

Fuel Safety Research Group  
Nuclear Safety Research Center, Japan Atomic Energy Agency,  
Email: [suzuki.motoe@jaea.go.jp](mailto:suzuki.motoe@jaea.go.jp)

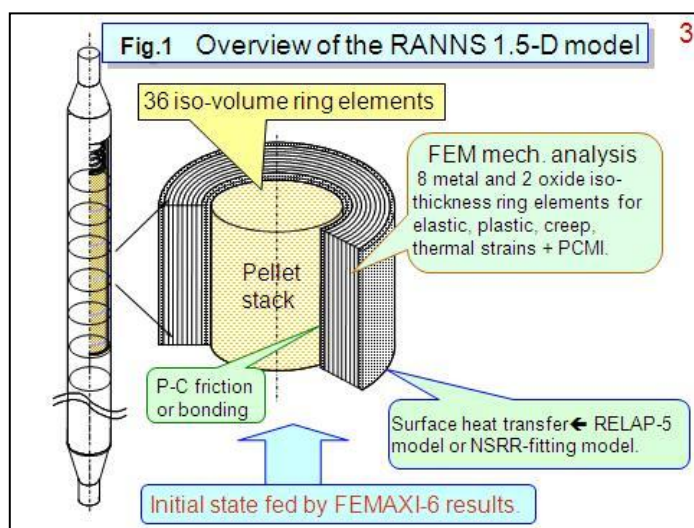
2

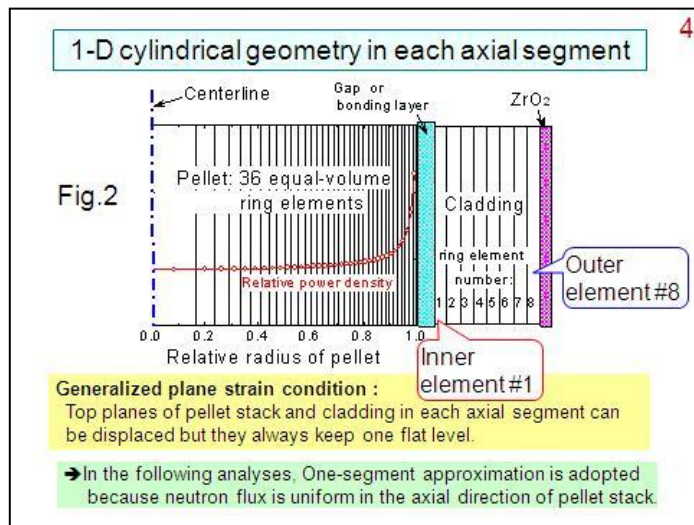
**Objectives**

- **Comparison** of fuel behavior in the NSRR experiment between high temperature condition and room temperature condition.
- **Simulation** to predict failure conditions on the basis of the comparison.

**Method of analysis**

- **Initial condition of fuel rod**  
Changes during base-irradiation is calculated by FEMAXI-6. Results such as cladding diameter, oxide thickness, etc. are fed to RANNS.
- **Transient calculation**  
Pulse linear power and coolant condition are given, temperatures and deformations of pellet and cladding, and PCMI are calculated.
- **Assumptions**  
Pellet is a continuum solid. Calculation continues even if the cladding failed in an actual experiment, not explicitly predicting rod failure.

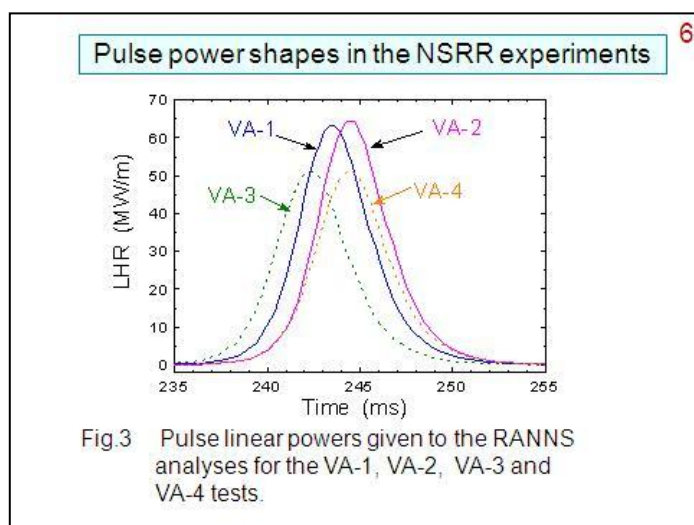




**5**

**Table 1 Rod specifications, EOL conditions, test conditions and results**

	VA-1	VA-2	VA-3	VA-4
Cladding material	ZIRLO	MDA	ZIRLO	MDA
Pellet (BOL)	8.19 x 9.83 mm, 95%TD			
Cladding diameter (BOL)	9.50 mm O.D. - 8.36 mm I.D.			
Burnup (GWdt)	71	77	71	77
Average thickness of oxide	73 μm	82 μm	73 μm	80 μm
Fast neutron fluence	1.30 - 1.42 x 10 <sup>22</sup> n/cm <sup>2</sup>			
Initial rod pressure	0.1MPa (He)			
Coolant water condition	20°C, 0.1 MPa	285°C, 6.8MPa	250°C, 4MPa	
Failure enthalpy increase	268J/g (64cal/g)	231J/g (55cal/g)	344J/g (82cal/g)	No failure



7

**VA-1 Room temperature tests**  
Results and analysis  
(71 GWd/t UO<sub>2</sub> and MDA cladding)

**VA-3 High temperature test**  
Results and analysis  
(71 GWd/t UO<sub>2</sub> and ZIRLO cladding)

RANNS analysis for temperature, stress/strain  
in one-segment approximation.

8

Calculated cladding temperatures of VA-1 and VA-3

VA-1

VA-3

Fig.4 Calculated temperatures of the cladding ring elements 1, 2, 4, and 8, and of the oxide surface in the VA-1 test.

Fig.5 Calculated temperatures of the cladding ring elements 1, 2, 4 and 8, and of the oxide surface in the VA-3 test.

At the observed failure instant, temperatures in the outer element are not significantly elevated.

9

Calculated cladding stresses of VA-1 and VA-3

VA-1

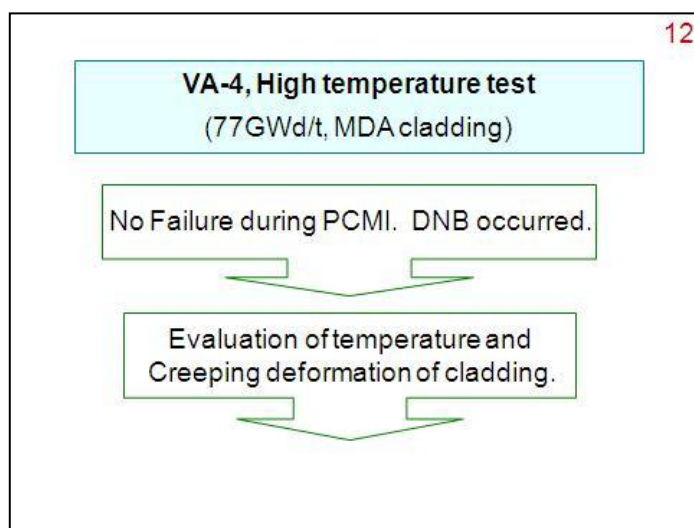
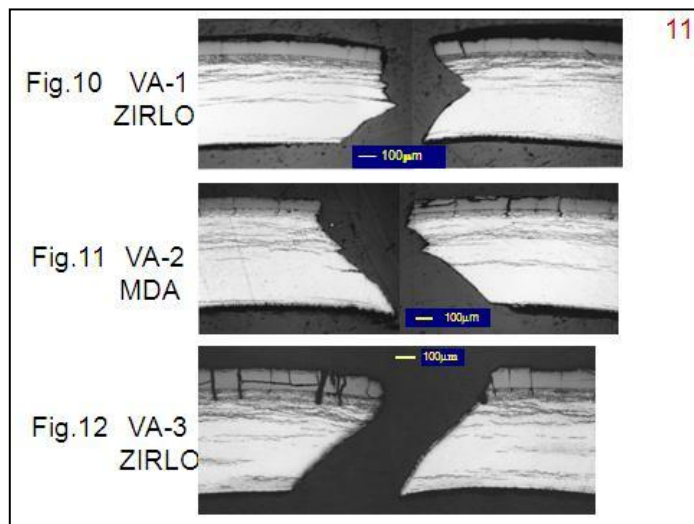
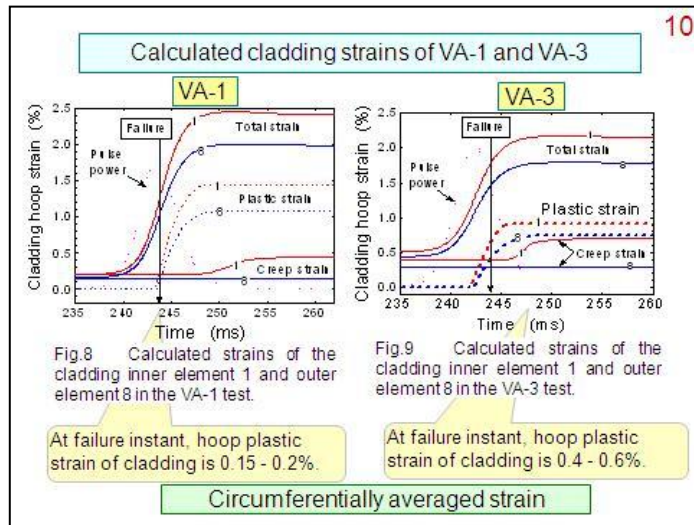
VA-3

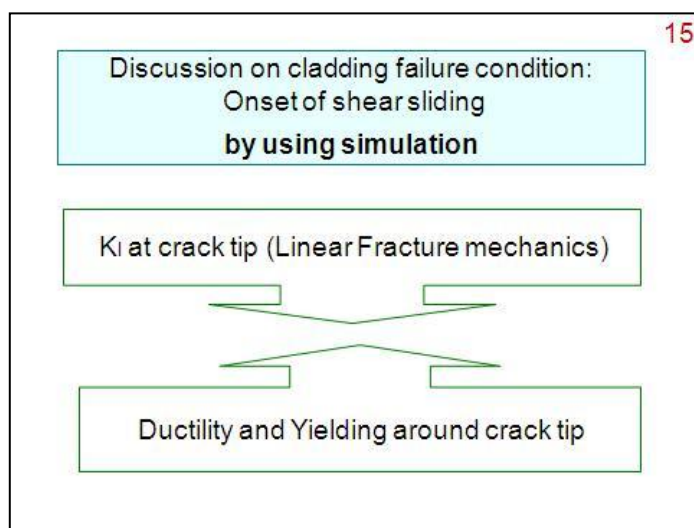
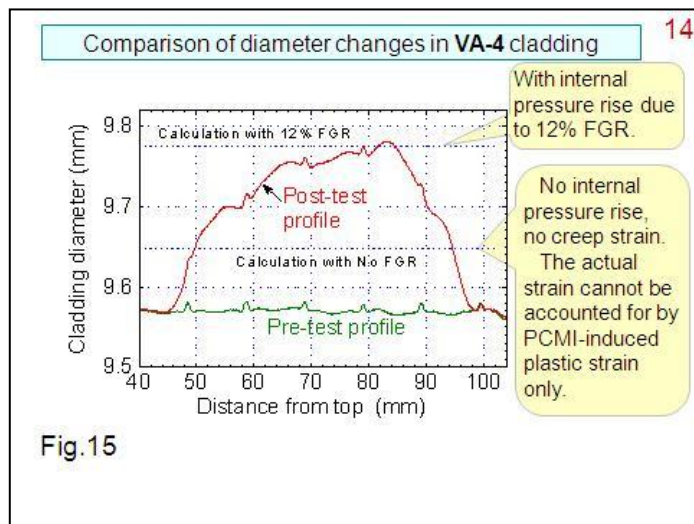
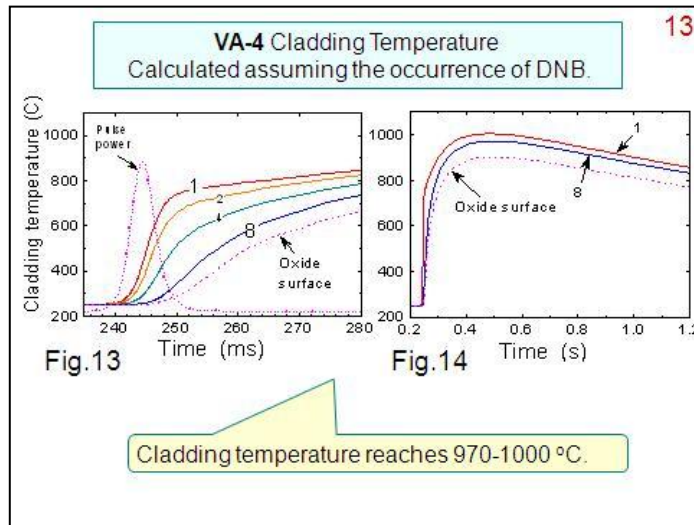
Fig.6 Calculated hoop and axial stresses of the cladding ring elements 1, 2, 4 and 8 in the VA-1 test.

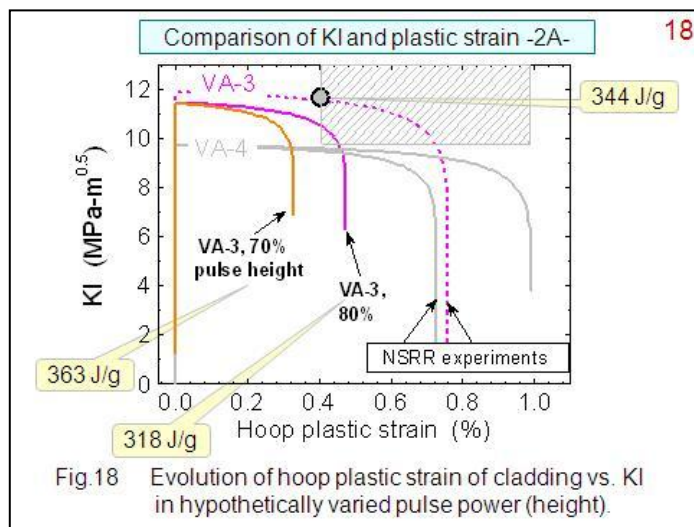
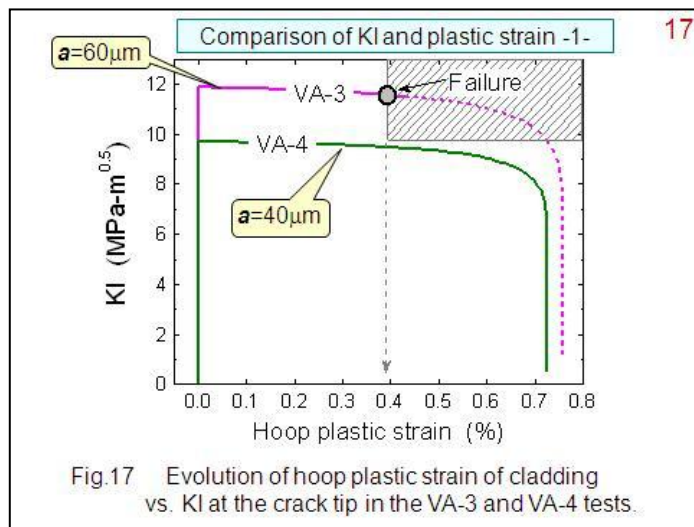
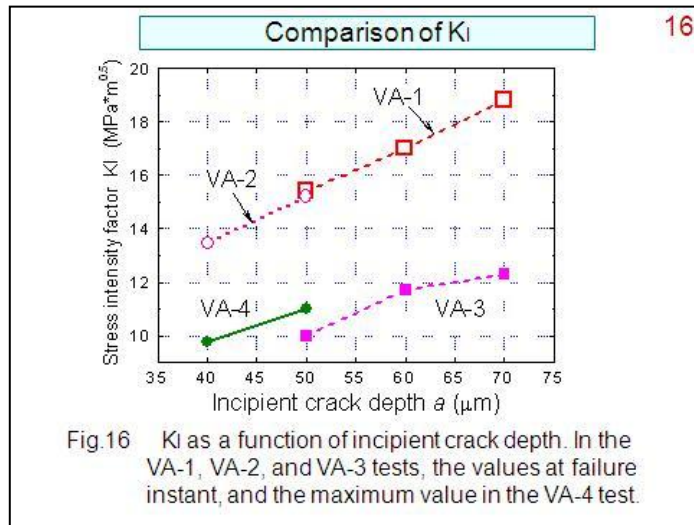
Fig.7 Calculated hoop and axial stresses of the cladding ring elements 1, 2, 4 and 8 in the VA-3 test.

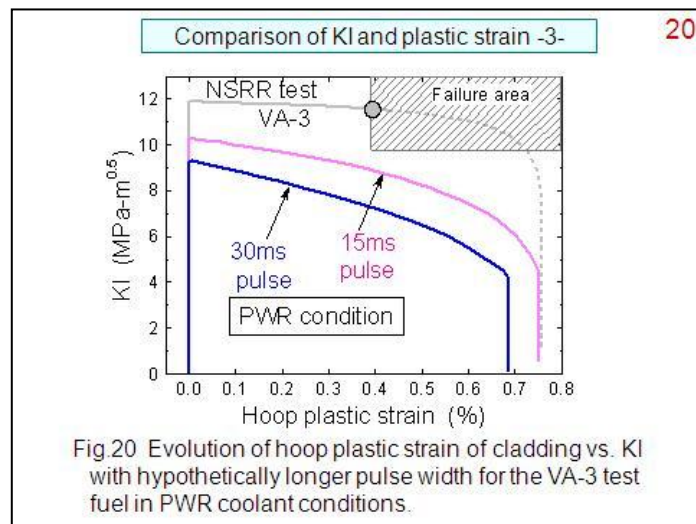
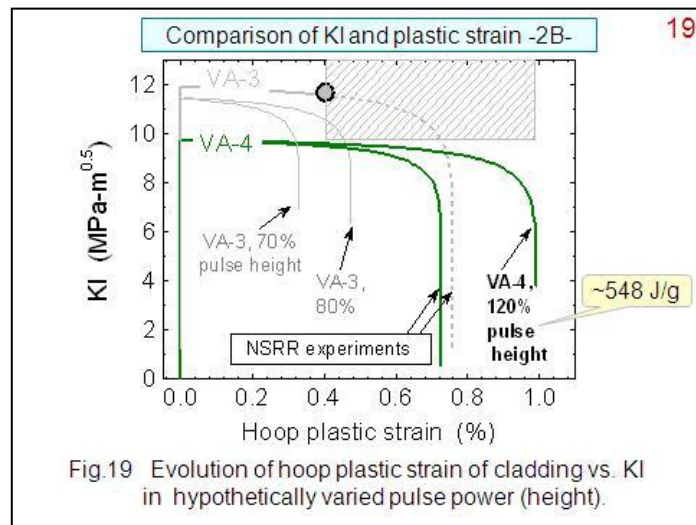
Failure occurred at the stress peak.

Failure occurred behind the stress peak.









**Conclusions** 21

The numerical analyses and simulations reveal:

- 1) Onset of shear sliding can be closely associated with KI at the crack tip and local plastic strain evolution as well.
- 2) These two factors depend also on the temperature of cladding.
- 3) A wider pulse mitigates the severity of transient, decreases KI, and allows plastic strain by temperature rise, thus failure possibility would markedly decrease.
- 4) Combination of numerical analysis and metallographic observation has a key role.

## INFLUENCE OF INITIAL CONDITIONS ON ROD BEHAVIOUR DURING BOILING CRISIS PHASE FOLLOWING A REACTIVITY INITIATED ACCIDENT

**Vincent Georgenthum**

*Institut de Radioprotection et de Sûreté Nucléaire, Direction de la Prévention des Accidents Majeurs  
BP3 13115 Saint-Paul-Lez-Durance Cedex, France*

**Tomoyuki Sugiyama**

*Japan Atomic Energy Agency, Nuclear Safety Research Center  
Tokai Mura, Naka-Gun Ibaraki-ken, 319-1195, Japan*

In the frame of their research programs on high burn-up fuel safety, the French Institut de Radioprotection et de Sûreté Nucléaire (IRSN) and the Japan Atomic Energy Agency (JAEA) performed a large set of tests devoted to the study of PWR fuel rod behavior during Reactivity Initiated Accident (RIA) respectively in the CABRI reactor and in the NSRR reactor. The reactor test conditions are different in terms of coolant nature, temperature and pressure. In the CABRI reactor, tests were performed until now with sodium coolant at 280°C and 3 bar. In the NSRR reactor most of the tests were performed with stagnant water at 20°C and atmospheric pressure but recently a new high temperature high pressure capsule has been developed which allows to performed tests at up to 280°C and 70 bar.

The paper presents discusses the influence of test conditions on rod behaviour during boiling phase, based on tests results and SCANAIR code calculations. The study shows that when the boiling crisis is reached, the initial inner and outer rod pressure have an essential impact on the clad straining and possible ballooning.

The analysis of the different test conditions makes it possible to discriminate the influence of initial conditions on the different phases of the transient and is useful for modelling and code development.

### 1. Introduction

In the frame of their research programs on high burn-up fuel safety, the French Institut de Radioprotection et de Sûreté Nucléaire (IRSN) and the Japan Atomic Energy Agency (JAEA) are performing studies on Pressurised Water Reactor (PWR) fuel rod behaviour during Reactivity Initiated Accident (RIA) induced by control rod ejection.

Such a RIA is characterised by a very rapid increase of reactivity and power in some rods of the reactor. After the initiating event (rod control ejection in PWR) the accidental sequence can be schematically represented in three phases (see Fig. 1):

- First, after the control rod ejection the energy deposition leads to a rapid rise of the fuel temperature which induces thermal swelling of the fuel pellets. During this phase the clad temperature is still close to initial temperature. The Pellet Clad Mechanical Interaction (PCMI) leads to a clad deformation and potentially to failure depending on fuel enthalpy increase and the level of clad embrittlement due to oxidation and hydriding.
- After the PCMI phase, the increase of cladding temperature leads to the Departure from Nucleate Boiling (DNB) and boiling crisis occurrence. In such a case, the clad to coolant heat transfer becomes very low and the clad temperature can reach a high temperature (>700°C). Depending on the internal gas pressure, the ductile clad can undergo an important deformation and a possible failure (see Fig. 2).
- Finally when the major part of the energy deposited in the fuel is transferred to the coolant the rewetting of the clad take place.

Fig. 1. Schematic representation of the sequence of a RIA

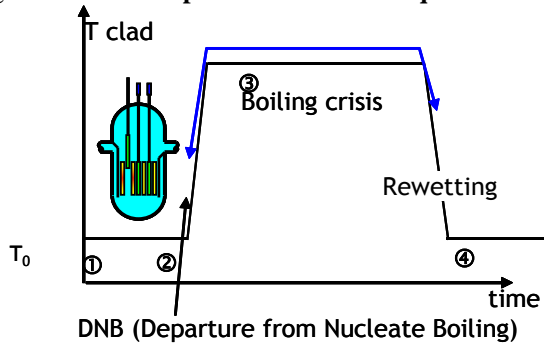
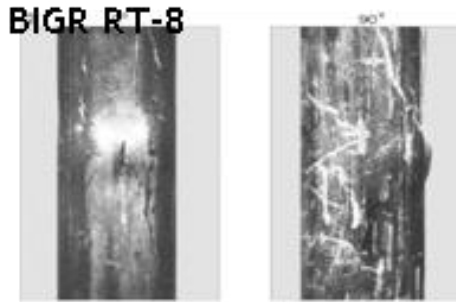


Fig. 2. Clad failure after a BIGR test [1]



In this paper we focus on the second phase, the so called post DNB phase. Among all the RIA experiments that have been performed in experimental reactors (NSRR, BIGR, IGR, SPERT, PBF, CABRI) none of them have been done with fully representative PWR conditions (coolant water at 280°C and 15,5 MPa pressure).

The goal of this paper is to study the influence of test conditions on the post DNB behaviour of PWR rods.

In Section 2, a description of non failed NSRR and CABRI results in terms of residual strain and fission gas release is presented. The development made in SCANAIR code for the post DNB modelling is described in section 3. In section 4, the SCANAIR code is used to analyse the difference between test conditions.

**2. Fission gas release and clad hoop strain in CABRI and NSRR PWR tests**

The CABRI and NSRR test conditions are gathered below:

- CABRI: tests have been performed in the former sodium loop with sodium at 280°C, flowing at 4 m/s under a 0.3 MPa pressure.
- NSRR room temperature capsule: most of the tests have been performed with stagnant water at 20°C and 1bar pressure.
- NSRR High Temperature High Pressure (HTHP) capsule: since 2006 some tests are performed with stagnant water at 250-280°C and 40-70 bar (saturation pressure at the achieved temperature).

Fig. 3 and Fig. 4 show the maximal clad residual hoop strain and fission gas release of CABRI and NSRR PWR tested rods as a function of fuel enthalpy increase.

Fig. 3. Maximal clad residual strain vs. burn-up using CABRI and NSRR tests results

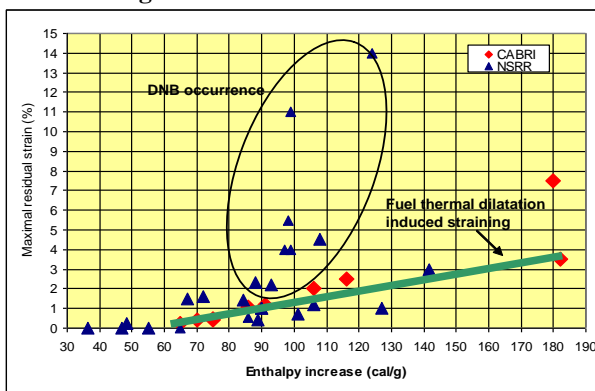
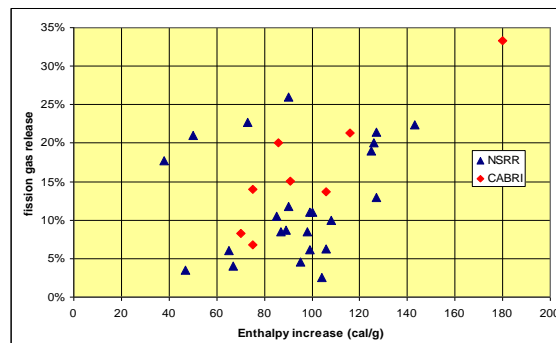


Fig. 4. Fission gas release vs. burn-up up using CABRI and NSRR tests results



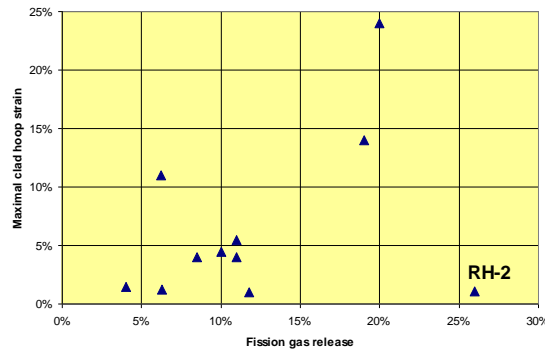
One can see from Fig. 3, that the clad hoop strain is increasing with fuel enthalpy, which is expected. In the CABRI tests the clad hoop strain is resulting from the fuel thermal swelling excepted for high enthalpy increase (>110 cal/g) where gas swelling in the fuel is supposed to enhanced the thermal swelling. In the

NSRR tests, when DNB occurred (from about 80-100 cal/g), the clad hoop strain is in some cases significantly increased.

It can be seen in Fig. 4 that the fission gas release is roughly a function of the enthalpy increase. The scattering of the result is certainly due to the fact that the figure gathered very different types of fuel ( $\text{UO}_2$  with different grain size and MOX) with different burn-up.

In tests that experienced boiling crisis, the maximal clad hoop strain is almost linear with the fission gas release excepted in the case of RH-2 test [3], where the fission gas release was high but the clad hoop strain remained low. The RH-2 strain resulted mainly from the fuel swelling (Figure 5).

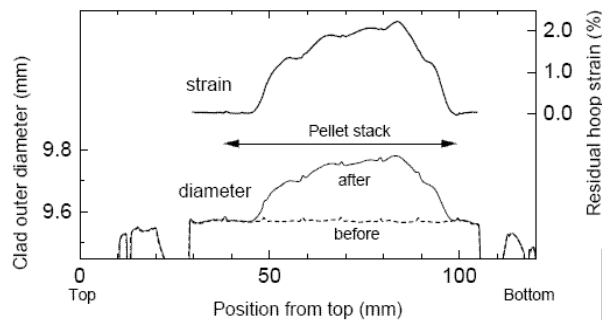
Figure 5. Maximal clad hoop strain vs. fission gas release for NSRR tests that experience a boiling crisis



The RH-2 test is the first test that has been performed in NSRR HTHP capsule. The test has been realised with an AREVA rod, M5 cladding with low corrosion ( $\sim 10\mu\text{m ZrO}_2$ ) and  $\text{UO}_2$  fuel irradiated at 67 GWd/t in Ringhals reactor in Sweden. The rodlet length was about 5 cm long containing 4 pellets. The high fission gas release (26%) with rather low enthalpy increase (90 cal/g) can be the consequence of the important fragmentation of the two end pellets that were not constraint by the fissile column and may be not representative of a 4 m rod behaviour in a PWR.

The VA-4 test has also been performed in the NSRR HTHP capsule [4]. The test has been realised with a MHI  $\text{UO}_2$  fuel at 77 GWd/t and MDA cladding with high corrosion level ( $\sim 80\mu\text{m ZrO}_2$ ) irradiated in the Vandellos reactor in Spain. In this case the initial coolant pressure and temperature were respectively 40 bar and 249°C. According to the diameter measurements the maximal residual hoop strain was 2.2% for an enthalpy increase of 109 cal/g. This level of strain exceeds the level resulting from the fuel thermal swelling and the added strain may result from the high internal pressure following the boiling crisis occurrence. Unfortunately the clad temperature was not measured and the fission gas release evaluation is not yet available.

Figure 6. VA-4 clad outer diameter measurement and residual hoop strain (from [4])

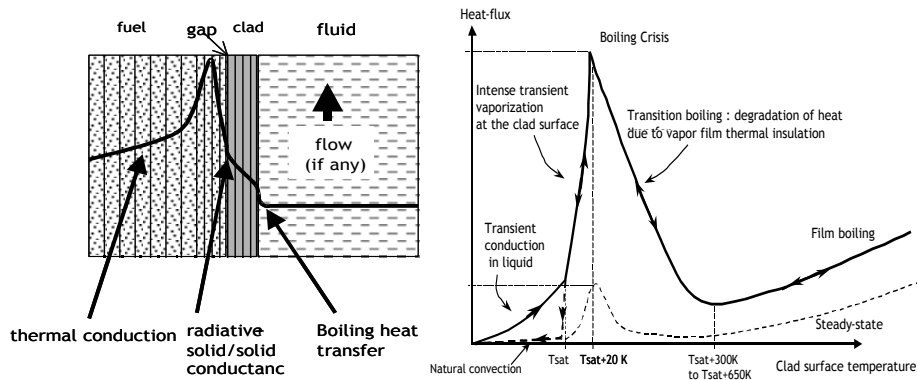


### 3. Modelling of boiling transition and post DNB clad deformation in SCANAIR code

In order to compute the post DNB behaviour, two developments have been performed in the SCANAIR code [5]:

1. Introduction of a clad visco-plastic law for high clad temperature: the partition of the mechanical deformation is written as the sum of an elastic, a plastic and a viscoplastic contribution. The plastic contribution is modelled with a perfect plastic law given by Prandtl Reuss' laws. The viscoplastic contribution is aimed at modelling the high temperature creeping (over 600°C) and is based on a Norton power law in which parameters are identified with burst tests [6].
2. Development of a transient clad-to-water heat transfer model on the basis of the physical interpretation of the NSRR and PATRICIA experiments [7], [8] for the NSRR and PWR thermal-hydraulic conditions: the clad-to-coolant heat transfer is described by a classical heat transfer coefficient approach which is estimated by correlations. The water boiling phenomena (that increase the heat transfer in nucleate boiling and degrade it in transition boiling) and film boiling are modelled. Heat transfer correlations are often semi or completely empirical and are validated in steady state conditions. During fast transient conditions, the radial temperature profile in the coolant can be much steeper than in steady state conditions and the shape of the boiling curve is different (see Figure 7). The maximal temperature reached during fast transient is mainly linked to the boiling crisis occurrence and film boiling coefficient. Thus a specific critical heat flux correlation has been developed for transient conditions, leading to higher critical heat flux compared to steady conditions. A specific film boiling coefficient derived from the Bromley correlation has also been implemented.

Figure 7. Clad-to-water heat transfer modelling in SCANAIR

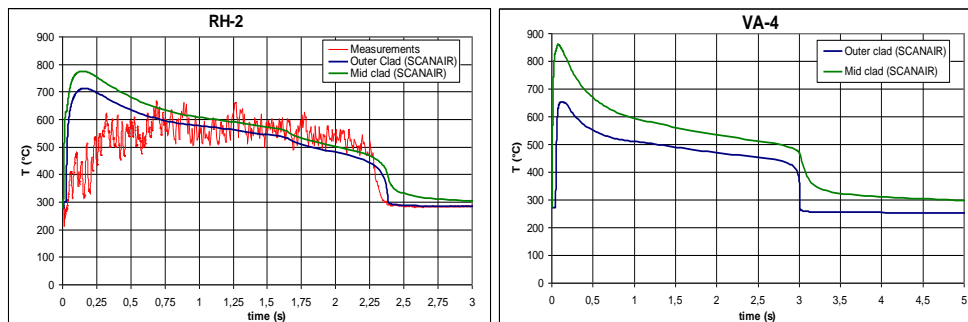


### 4. SCANAIR calculations

#### *RH-2 and VA-4 test calculations*

The new SCANAIR developments are used to recalculate the RH-2 and VA-4 tests. The calculated mid and outer clad temperature evolutions are represented in Figure 8 for RH-2 and VA-4 tests.

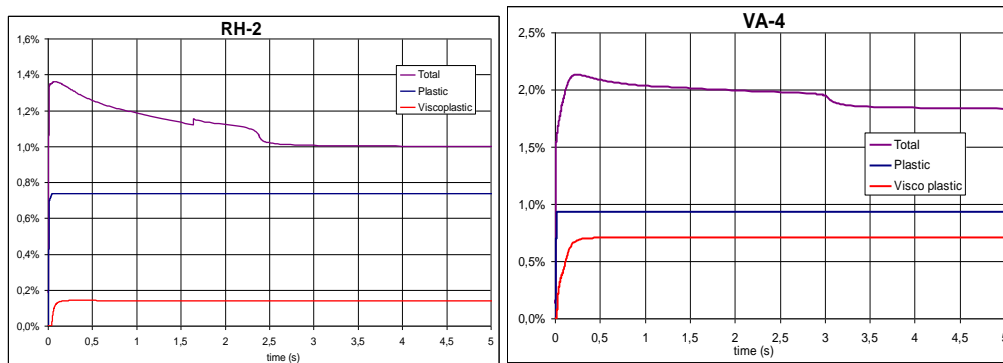
Figure 8. Outer clad temperature in RH-2 and VA-4 tests, SCANAIR calculations and measurements



In the RH-2 test, the outer clad temperature was measured. At the beginning of the post DNB phase, the calculation overestimates the thermocouple measurements but the boiling phase and rewetting is well simulated.

The clad hoop strain evolutions are represented in Figure 9.

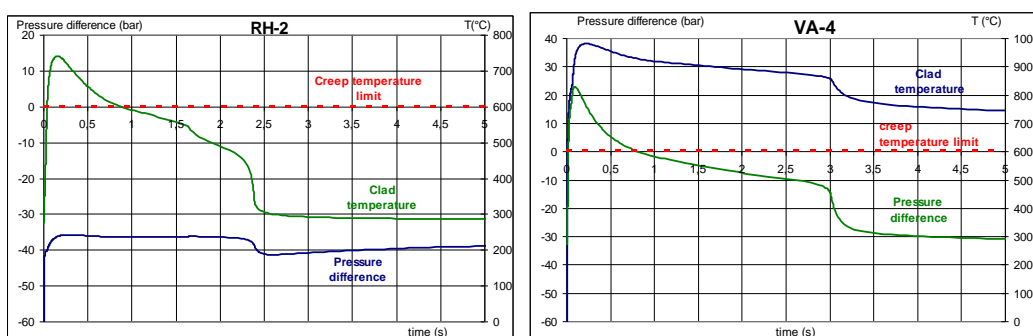
Figure 9. Clad hoop strain calculations in RH-2 (left) and VA-4 (right)



The residual hoop strain measurement and calculations are in very good agreement in the RH-2 case: about 1% in both cases. Almost all the hoop strain is obtained during the energy deposit and results from PCMI with fuel thermal swelling.

In the VA-4 test, the calculated residual hoop strain is slightly lower than the experimental one (1.8% vs. 2.2%). This discrepancy might be due to the use of Zircaloy mechanical laws while the VA-4 cladding is a MDA alloy. In this case a significant part of the hoop strain is obtained after the energy deposit due to the gap opening and positive pressure difference between inner and coolant pressure while the cladding temperature is higher to 600°C (temperature creeping limit). The high pressure reached in this case results from the high fission gas released at a high temperature (due to high enthalpy level). In RH-2 case, the inner pressure never over-passed the coolant pressure and really limited creep occurred (see Figure 10).

Figure 10. SCANAIR calculation of clad temperature and pressure difference evolutions in RH-2 test (left) and VA-4 test (right)



### PWR conditions calculations

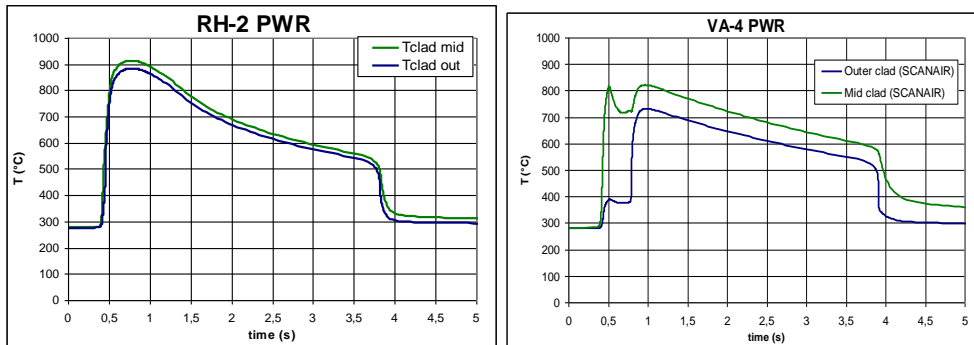
In order to evaluate the test conditions on the clad hoop strain, calculations have been done with RH-2 and VA-4 rods but with PWR conditions:

- Flowing water at 280°C and 155 bar.
- Inner pressure of 45 bar at room temperature.
- PWR pulse: 30 ms half width (the injected energy has been adjusted to reach the same maximal fuel enthalpy).

In this case the initial inner pressure at 280°C is ~ 90 bar and the initial pressure difference is ~60 bar that is to say similar to the HTHP case.

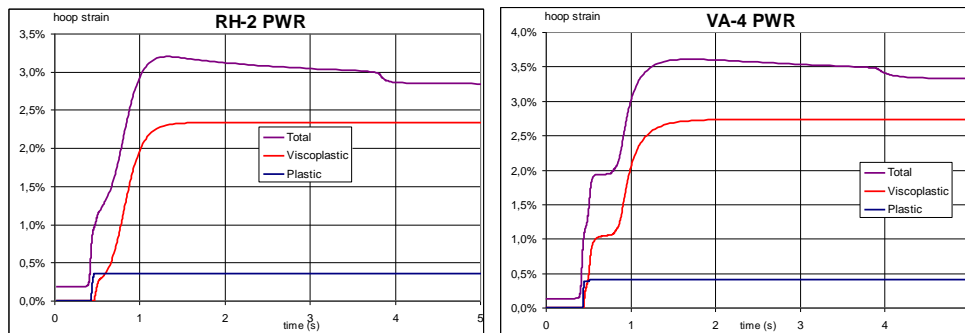
The clad temperature and the duration of boiling crisis are slightly higher in the PWR case than in the HTHP case (see Figure 11 compared to Figure 8). This phenomenon is mainly due to the fact than under PWR conditions the clad temperature increase is slower and then the transient effect on the boiling curve is less significant (see Figure 7 and [8]); the heat transfer in film boiling phase is for instance lower in this case.

Figure 11. Clad temperature evolution in PWR condition



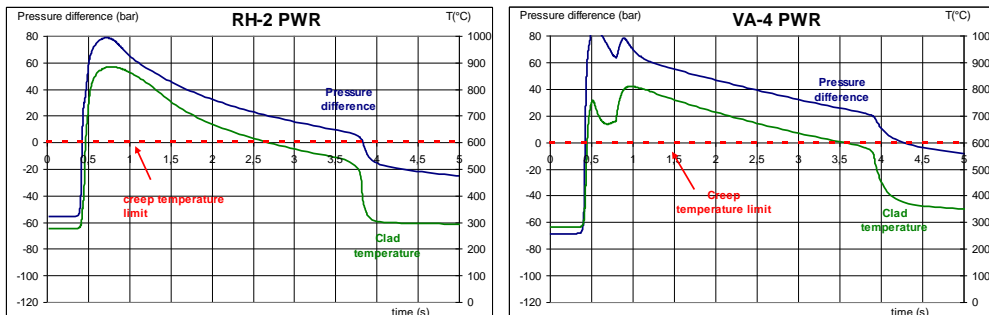
The important viscoplastic contribution leads to a significantly higher clad hoop strain in PWR conditions than in HTHP ones (Figure 12 compared to Figure 9).

Figure 12. Clad hoop strain evolution in PWR conditions



The high viscoplastic hoop strain is clearly linked to the high clad temperature and inner pressure reached during the transient (see Figure 13). Indeed, the pressure difference between inner and outside of the rod is significant while clad temperature overpassed 600°C, the temperature at which the clad creeping starts.

Figure 13. Clad temperature and pressure difference



## Conclusion

The analysis of the NSRR and CABRI REP-Na tests showed that:

- The clad residual hoop strain is linearly increasing with fuel enthalpy increase until about 110 cal/g, excluding the NSRR rod that experienced boiling crisis.
- The fission gas release is increasing with fuel enthalpy.
- In NSRR rods that experienced boiling crisis, the clad hoop strain is a function of enthalpy increase, except in the case of RH-2 test performed in the HTHP capsule.

The new thermal-hydraulic and mechanical developments made in SCANAIR made it possible to simulate the NSRR HTHP capsule and PWR conditions.

According to the calculations the clad hoop strain reached in PWR conditions is significantly higher than in HTHP conditions due to an important contribution of visco-plastic strain. Whereas in the two conditions the initial pressure difference between inner rod and coolant is equivalent, during the transient, the inner pressure becomes significantly higher than the outer one with a clad at a temperature overpassing 600°C leading to a significant clad creeping.

This study showed that test results can not be directly transposed to the PWR conditions without using code calculations.

The calculations have been done with short reconditioned rod assuming direct equilibrium of pressure between free volumes. IRSN is now developing a methodology to better evaluate the post DNB behaviour of the cladding especially with the introduction of gas axial flow modelling, which is essential for the calculations of a 4 m PWR rod.

In the new CABRI water loop (coolant water, 280°C, 155 bar) tests will be performed with more representative PWR conditions and will be useful for code modelling.

## References

- [1] L. Yegorova and al., “Experimental Study of Narrow Pulse Effects on the Behavior of High Burn-up Fuel Rods with Zr-1%Nb Cladding and UO<sub>2</sub> Fuel (VVER Type) under Reactivity-Initiated Accident Conditions: Program Approach and Analysis of Results”, *NUREG/IA-0213* Vol. 1 & 2, (2005).
- [2] F. Lemoine “Estimation of the Grain Boundary Gas Inventory in MIMAS/AUC MOX Fuel and Consistency with REP-Na Test Results” *Journal of Nuclear Science and Technology*, Vol. 43, No. 9, p. 1105–1113 (2006).
- [3] T. Sugiyama, Y. Udagawa, M. Umeda, T. Fuketa, “PWR fuel behaviour in RIA-simulating experiment at high temperature” *Proc of Water Reactor Fuel Performance Meeting*, (19-23 October 2008) Seoul, Korea.
- [4] T. Sugiyama, “PCMI failure of high burn-up fuel under high temperature RIA conditions” *Fuel Safety Research Meeting*, (20-21 May 2009) Tokai Japan.
- [5] E. Federici and al., “The SCANAIR Code Version 3.2: Main features and Status of Qualification”, *Proc of IAEA TCM on Fuel Behavior Under Transient and LOCA Conditions*, Halden, Norway, (10-14 September 2001).
- [6] T. Forgeron, J.C. Brachet, F. Barcelo and al “Experiment and modeling of advanced fuel rod cladding behavior under LOCA conditions: alpha-beta phase transformation kinetics and EDGAR methodology” *ASTM-STP 1354* – pp. 256-278 – (2000).
- [7] V. Bessiron, T. Sugiyama, T. Fuketa, “Clad to coolant heat transfer in NSRR experiments”, *J. Nuclear Science Technology* Vol. 44, No. 5, p. 723–732 (2007).
- [8] V. Bessiron “Modelling of Clad-to-Coolant Heat Transfer for RIA Applications”, *J. Nuclear Science Technology* Vol. 44, No. 2, p. 211–221 (2007).





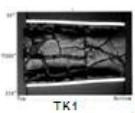
## INFLUENCE OF INITIAL CONDITIONS ON ROD BEHAVIOUR DURING BOILING PHASE FOLLOWING A REACTIVITY INITIATED ACCIDENT

V. Georgenthum - T. Sugiyama

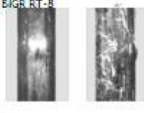
- Introduction
- NSRR and CABRI tests results
- SCANAIR code modeling
- Code results

### Introduction

#### The different phases during the RIA transient

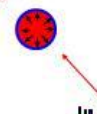


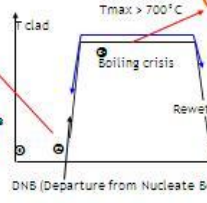
TK1



B1GR RT-8

PCM (Pellet Clad Mechanical Interaction)  
Risk of clad brittle failure





Time

DNB (Departure from Nucleate Boiling)

Boiling crisis

Rewetting

$T_{max} > 700^{\circ}C$

High fission gas release:  
risk of clad ballooning and failure



=> Emphasis on post DNB phase in this presentation

OECD-NEA workshop 9-11 September 2009

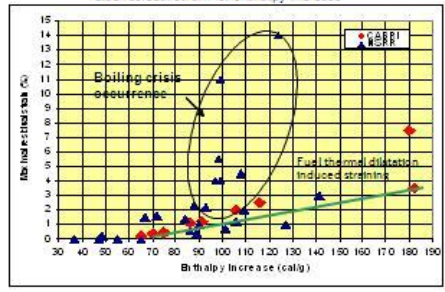
3/15



### Tests results in CABRI and NSRR

CABRI tests conditions: sodium loop at 280°C, flowing at 4 m/s under 0.3 MPa,  
 NSRR tests conditions: - Room temperature tests (stagnant water at 20°C, 0.1 MPa)  
 - High temperature high pressure tests (stagnant water at ~280°C, 7 MPa)

#### Clad residual strain vs. enthalpy increase

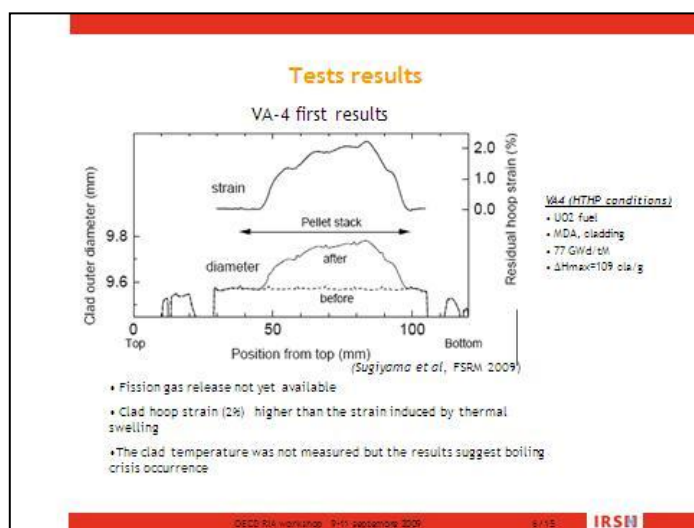
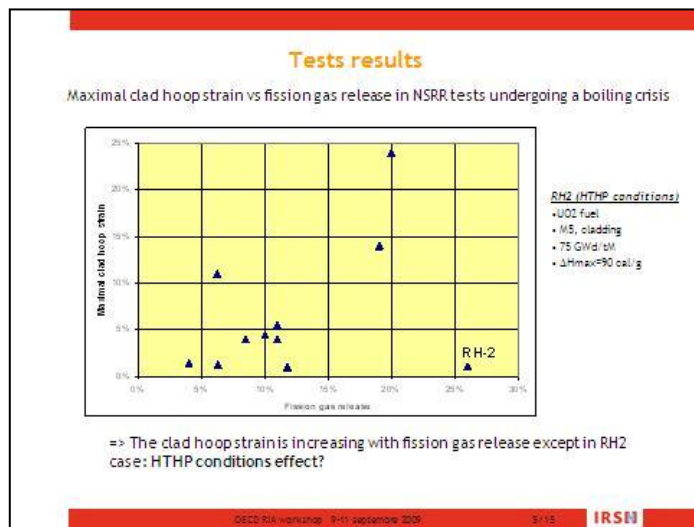
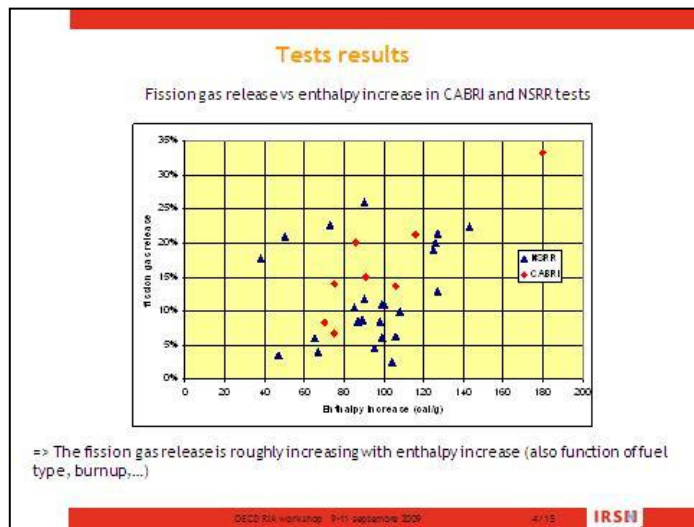


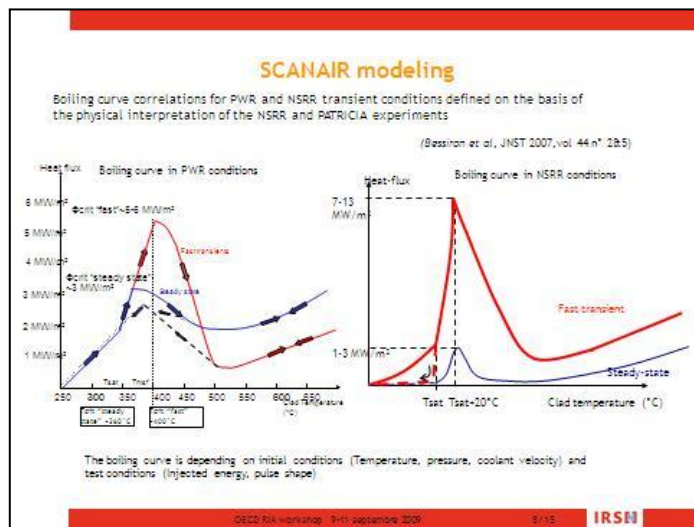
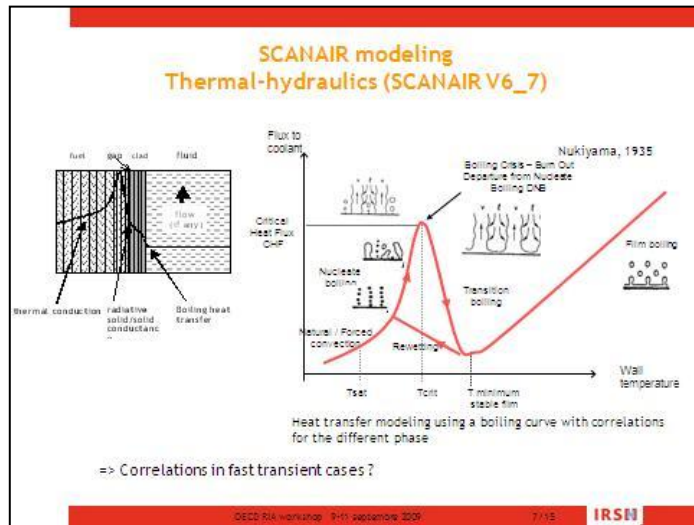
=> Significant clad residual hoop strain increase when boiling crisis occurs

OECD-NEA workshop 9-11 September 2009

3/15



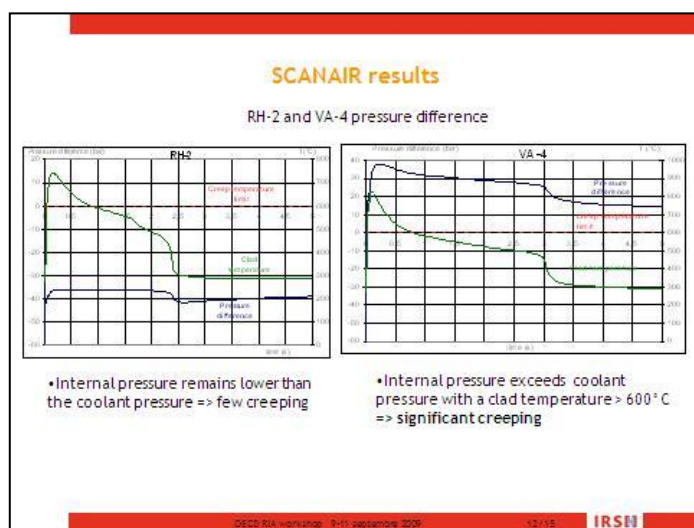
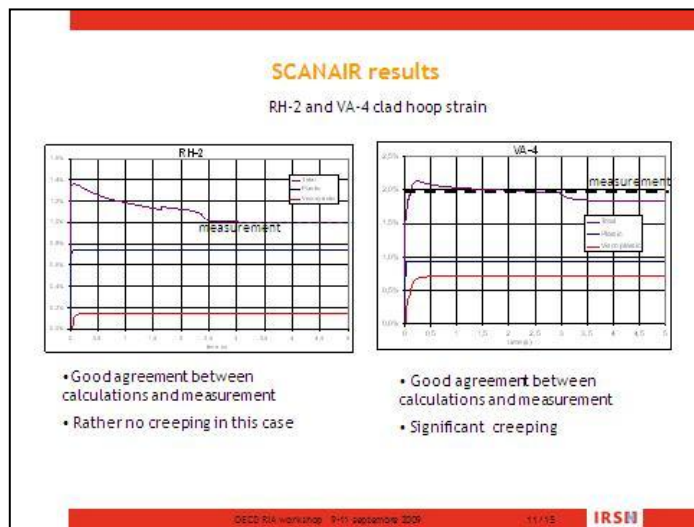
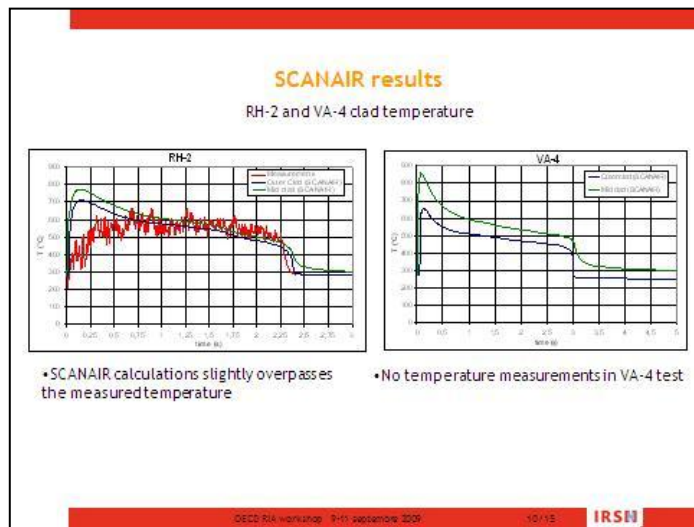


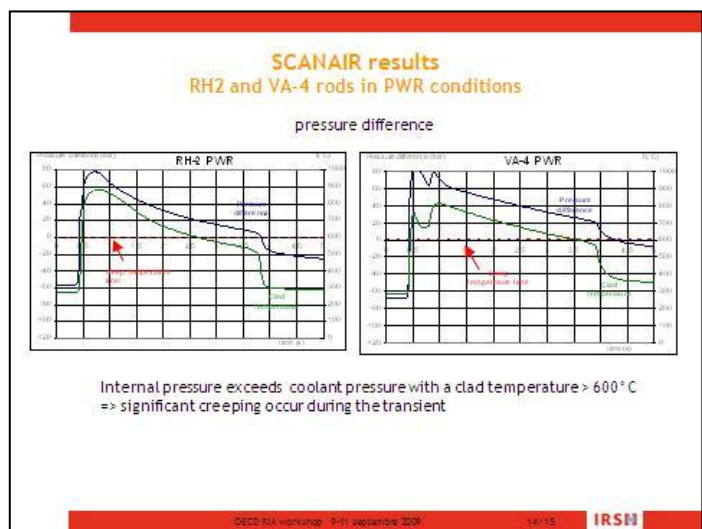
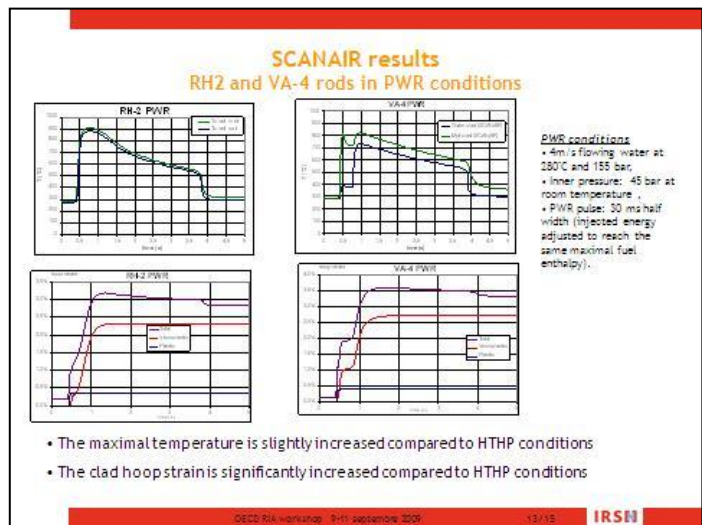


### SCANAIR modeling Mechanical modeling

- Partition of the mechanical deformation
  - $\epsilon_{mec} = \epsilon_{el} + \epsilon_{pl} + \epsilon_{vp}$
- Plastic contribution : perfect plastic law given by Prandtl Reuss' laws
- Visco-plastic contribution: based on a Norton power law in which parameters are identified with burst tests, *activated only over 600 °C*

DECD RA workshop 9-11 septembre 2009 9/15 **IRSN**





### Conclusion

- The new thermal-hydraulic and mechanical developments made in SCANAIR make it possible to simulate the NSRR/HTHP capsule and PWR conditions.
- In these two conditions the initial pressure difference between inner rod and coolant is equivalent, but during the transient, in PWR case, the inner pressure can become significantly higher than the outer one and lead to a significant clad creeping.  
=> Test results can not be directly transposed to the PWR conditions without using code calculations.
- IRSN is now developing a gas axial flow modelling, essential for the POST DNB calculations of a 4 m PWR rod.
- In the new CABRI water loop (coolant water, 280°C, 155 bar) tests will be performed with representative PWR conditions and will be useful for code modelling and gas axial flow model validation.

DECD RIA workshop 9-11 septembre 2009 15/15 **IRSN**

## APPLICATION OF THE SCANAIR CODE FOR VVER RIA CONDITIONS – BORON DILUTION ACCIDENT

**A. Arffman**

VTT Technical Research Centre of Finland

**B. Cazalis**

Institut de Radioprotection et Sûreté Nucléaire (IRSN), DPAM, SEMCA, LEC,  
13115 Saint Paul lez Durance, France

### Abstract

This paper consists of two parts. In part A, RIA pulse tests conducted at the Russian BGR reactor are being analysed at IRSN with SCANAIR V6 fuel performance code as a part of the code validation for VVER fuel. Recently a new version of the SCANAIR code was made available to VTT Technical Research Centre of Finland, and part B of the paper covers the introduction of the code version at VTT by a calculation of a hypothetical boron dilution accident in a VVER-440 power reactor.

### Part A. Analysis of the Russian BGR tests with SCANAIR V6

#### A.1. Introduction

The BGR/RIA test programme aimed to study the VVER high burn-up fuel behaviour in a wide range of fuel enthalpy generated by the narrow power pulse (2.5-3.1 ms) of the Russian BGR reactor [1]. In order to analyse these tests, the SCANAIR code [2], developed by the French Institut de Radioprotection et de Sûreté Nucléaire (IRSN), was improved through a BGR/NSRR heat transfer model, validated by Japanese NSRR experiments, and a Norton viscoplastic clad mechanical behaviour. The aim of this part of the paper is to present the SCANAIR improvements and to compare SCANAIR calculations with the BGR tests results.

#### A.2. BGR tests description

Twelve test rodlets (RT1-12), of fissile length of about 150 mm, were refabricated from the Russian VVER-440 and VVER-1000 fuel rods, irradiated respectively up to burn-ups of about 48 GWd/tU (NovoVoronezh Nuclear Power Plant) and 60 GWd/tU (Kola NPP).

VVER fuel rod geometry is annular with a hole radius of about 1.25 mm, an inner clad radius of about 3.8 mm and an outer clad radius of about 4.53 mm (see Figure A.1). Gap widths of irradiated fuel rods range between 0 and 30  $\mu\text{m}$ . Fuel rods were clad with Zr-1% Nb with an outer oxide layer of 3–5  $\mu\text{m}$  and were pressurized, before test, with pure Helium at an ambient pressure of 0.1 MPa (RT9, RT12) and 2 MPa (other tests).

In order to study the VVER high burn-up fuel behaviour during a RIA transient, the rodlets were subjected to pulse irradiation experiments in the Russian fast-pulse graphite-reactor (BGR). The internal volume of the capsule device was filled with water at room temperature and atmospheric pressure. The BGR test is characterised by the narrow pulse width of 2.5-3.1 ms (slightly lower than NSRR ones – see Figure A.2) and stagnant water under normal conditions.

Figure A.1. VVER fuel rod geometry

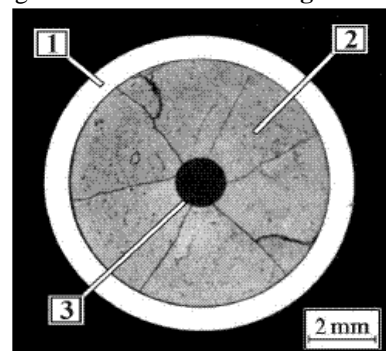
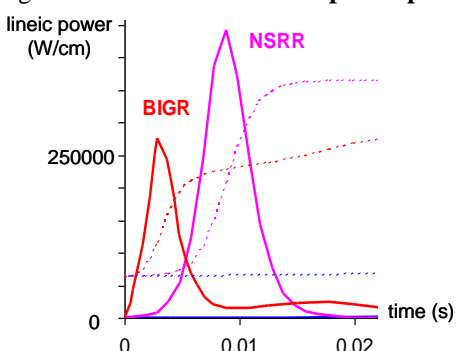


Figure A.2. BIGR and NSRR power pulse



### A.3. Presentation of SCANAIR V6

In order to analyse the BGR tests, the SCANAIR V6 version was implemented through two major developments:

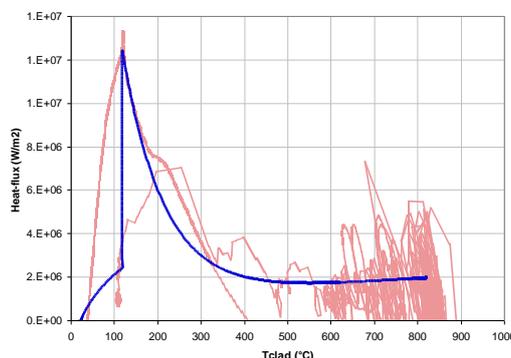
- A NSRR/BGR heat transfer model, with a transient boiling model developed on the basis of the physical interpretation of the NSRR boiling curves,
- An elasto-plastic clad behaviour incorporating a creep modelling.

#### A.3.1. NSRR/BGR heat transfer model

Specific NSRR experiments called Surface Effect Tests have been carried out in order to investigate the clad-to-coolant heat transfer in NSRR experiments [3]. These experiments highlighted the fact that pre-oxidized rods would exhibit a higher coolability than bare rods due to higher wettability. In particular, the dry out duration would be shorter for pre-oxidized rods. The tests also suggested an increase of the Critical Heat Flux (CHF) and Critical Temperature in the tests with high enthalpy deposit. The Figure A.3 shows an example of experimental boiling curve. The different heat transfer regimes can be identified on the graph:

- Boiling Crisis: presence of a peak of heat flux (CHF  $\sim 7$  to  $13 \text{ MW/m}^2$ ) around  $T_{\text{sat}} + 20 \text{ K}$ .
- Transition boiling: fall of heat flux concomitant to a rapid increase of clad temperature.
- Film boiling: clad temperature higher than  $T_{\text{sat}} + 500 \text{ K}$ , low heat flux ( $1$  to  $2 \text{ MW/m}^2$ ).
- Rewetting phase starting around  $T_{\text{sat}} + 450 \text{ K}$  and leading to a second peak of heat flux.

Figure A.3. Boiling curve of the NSRR test NH



#### A.3.1.1. Modelling description

On the basis on the physical interpretation of the different regimes described above, a corresponding model has been implemented in the SCANAIR code [4]. A particular feature of the model is that the boiling curve

is not preset: the heat flux in the conduction phase and the value of the CHF result from a time-dependent process. Therefore, the computed boiling curves are power history-dependant. The heat transfer regimes and their modelling are described hereafter.

a. Heat conduction phase.

Pre-Boiling Crisis heat transfer is simulated by the transient heat conduction in a perfectly stagnant liquid water up to the critical temperature ( $T_{crit} = T_{sat} + \Delta T_{onb}$ ). In the current model for NSRR experiments with a clad heating rate comprised between 7000 K/s to 10 000 K/s,  $\Delta T_{onb}$  has been set to the experimentally observed value of 20 K. Above the saturation temperature and up to the critical temperature, the physical properties of the saturated liquid apply. In that regime, the conduction heat flux at the clad periphery is equal to the heat flux in the fluid at the clad surface.

b. Vaporisation phase and boiling crisis.

A basic semi-empirical model relies on the assumption that, for NSRR heating rates, considerable vaporisation of the fluid occurs at a temperature equals to the critical temperature (i.e.  $T_{sat} + 20$  K here) and leads to a clad temperature plateau until a certain thickness of fluid is vaporised. Simultaneously, imposing a fixed clad surface temperature induces a misbalance between the conductive heat flux in the clad and in the fluid. Once the vaporised thickness exceeds a threshold (experimentally fitted on NSRR Surface Effect Tests to  $3 \cdot 10^{-5}$  m), the Boiling Crisis is triggered and the transition boiling heat transfer regime is activated. In this model, the CHF is not determined by a correlation: it corresponds to the clad heat flux at the time of Boiling Crisis.

c. Transition boiling and film boiling.

The transition and film boiling regimes are simulated with a Heat Transfer Coefficient (HTC) approach. The HTC for the transition boiling is represented by an exponential function of the clad temperature that first decreases and then, for temperatures higher than  $T_{sat} + 450$  K, asymptotically tends to the film boiling HTC estimated with the Sakurai's correlation [5] with an adjustment coefficient (value: 5) fitted on the NSRR experiments.

d. Rewetting.

The rewetting temperature corresponds to the temperature of minimum heat flux ( $T_{sat} + 450$  K).

e. Post-rewetting.

The Churchill and Chu correlation [6] simulating the natural convection is used when the clad surface temperature drops below the saturation temperature.

#### A.3.1.2. Validation of the modelling on NSRR experiments

The NSRR Surface Effect Tests were simulated with the SCANAIR code with the present model. A sensitivity study on the main parameters of the modelling was simultaneously carried out. The computed CHF's are close to the experimental ones, as can be seen in Figure A.4. The uncertainty on the computed CHF is about +/- 15%. The increase of the CHF versus the maximum linear heat rate is well reproduced.

The Figure A.5 illustrates the computed clad temperature evolution in the Surface Effect Test 1H. The duration of the dry out phase is well reproduced by the model.

Figure A.4. Comparison calculated-experimental CHF's

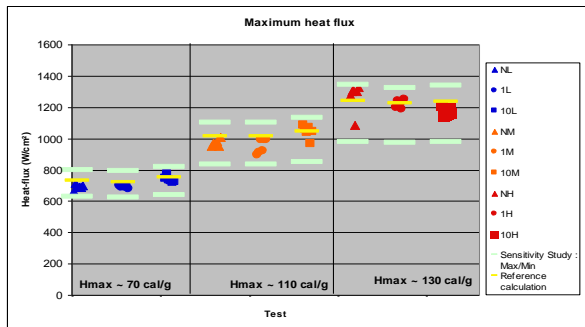
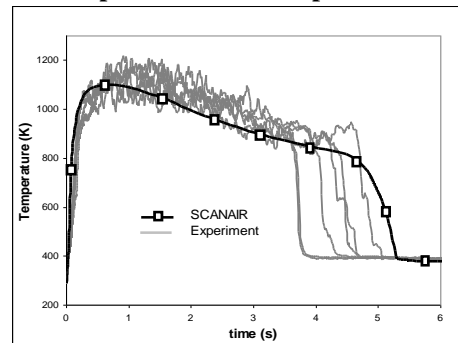


Figure A.5. Test 1H - comparison of calculated and experimental clad temperature



### A.3.2. Clad elasto-viscoplastic behaviour

The non-reversible mechanical deformation is assumed to be the superposition of an instantaneous plastic deformation and a viscoplastic (or creeping) deformation. The partition of the mechanical deformation is written as:

$$\varepsilon_{mec} = \varepsilon_{el} + \varepsilon_{pl} + \varepsilon_{vp}$$

This decomposition allows the modelling of fast deformation during the clad loading and, in the same time, slower deformations during the creeping phase. When the transient is not sufficiently energetic to heat up the clad to transition temperature, the creeping effects can be neglected and a perfect plastic model is able to model accurately the clad behaviour. In case of water cooling, if the Departure of Nucleate Boiling (DNB) is reached, high temperatures are reached and clad creeping must be modelled by using a viscoplastic law. The code is therefore able to compute clad ballooning with the limitation of the small deformations.

The plastic contribution  $\varepsilon_{pl}$  to the mechanical deformation is modelled with a perfect plastic law given by Prandtl Reuss' law. The viscoplastic contribution  $\varepsilon_{vp}$ , aimed at modelling the high temperature secondary creeping ("dislocation creeping"). It is activated over a limit temperature of 600°C. The viscoplastic formalism is based on the Norton formalism in which parameters are identified with burst tests.

The tensorial form of the Norton viscoplastic law can be written:

$$\dot{\varepsilon}_{vp} = \frac{3}{2} \dot{\varepsilon}_{vp} \frac{s}{\sigma} \quad \text{with} \quad \dot{\varepsilon}_{vp} = \frac{2}{\sqrt{3}} A(T, f_\alpha) e^{\left(-\frac{Q(T, f_\alpha)}{T}\right)} \left(\frac{2}{\sqrt{3}} \bar{\sigma}\right)^{m(T, f_\alpha)}$$

where  $s$  is the deviatoric part of the stress tensor,  $T$  the temperature,  $f_\alpha$  the  $\alpha$ -phase fraction and  $Q$  the activation energy.

Because Zircaloy creeping velocities become significant after the transition to the  $\beta$ -phase, the kinetic of phase transformation is described by the Holt's law:

$$\frac{\partial f_\alpha}{\partial t} = F(f_\alpha, T)$$

## A.4. Analysis of the results

In this section, the SCANAIR specific developments will be tested through the BGR/RIA test results [1].

### A.4.1. RT3 experiment

The test RT-3 was performed on a 47 GWd/tU irradiated fuel rod, initially pressurized at 2.1 MPa with pure Helium. The fuel enthalpy reached 138 cal/g during the pulse-irradiation, and the test resulted in no failure.

Calculated clad temperature evolution is illustrated in Figure A.6. Clad inner and outer temperature reached respectively 850°C and 800°C, with a considerable temperature gradient of about 500°C in the cladding in the early PCMI phase and a DNB occurrence at about 0.04 s.

As the fuel-clad gap reopens, the clad creep under pressure loading can start (at about 0.3 s) leading to an additional strain of about 1% (see Figure A.7). Calculations are in good agreement between average and maximum experimental hoop strain.

Figure A.6. BGR test RT3- computed clad temperatures

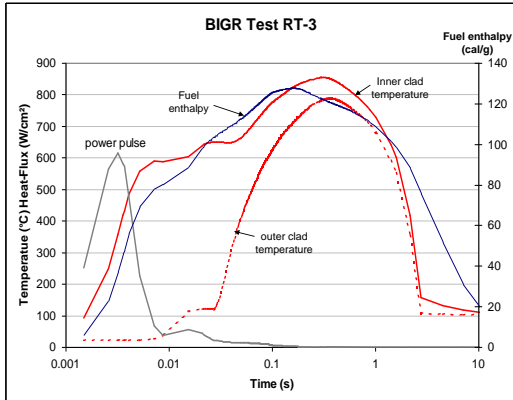
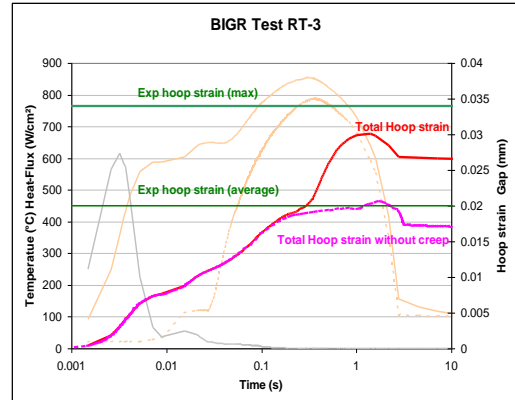


Figure A.7. BGR test RT3- computed clad hoop strain



**A.4.2. Residual deformation of BGR tests**

All the BGR/RIA tests have been calculated with SCANAIR V6. As illustrated in Figure A.8, fission gas induced swelling became significant above a fuel enthalpy about 120 cal/g. When fission gas swelling is added to thermal expansion in the code, the average clad strain is well explained by the PCMI induced by the pellet swelling. It is not sufficient to explain and reproduce the maximum clad strain which is about 2-4% higher than the average strain. An additional strain, related to clad creeping, has to be taken into account. Figure A.9 shows the comparison of the measurements (averaged and maximum measured strain) with SCANAIR calculations (with or without creeping). It can be observed a significant overestimation of the calculated maximum clad strain for the non failed rods with an initial 2MPa helium pressure, due to the fact that SCANAIR creep deformation is strongly dependent of the filling pressure. Nonetheless, a good agreement is obtained for low initial pressure test (as seen for RT12).

Figure A.8. Comparison of SCANAIR calculations with BGR average residual strain

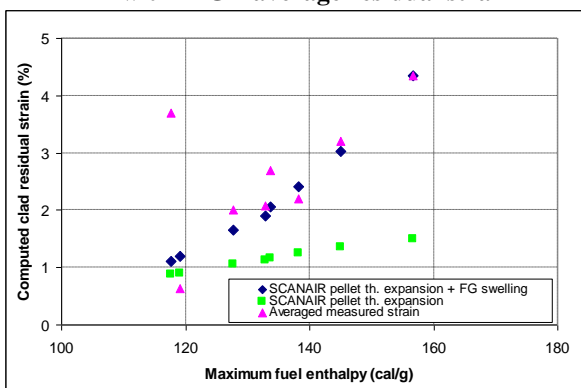
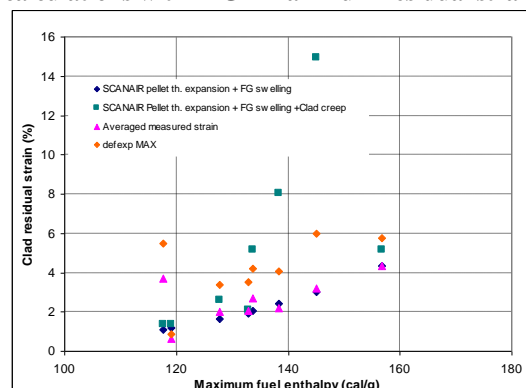
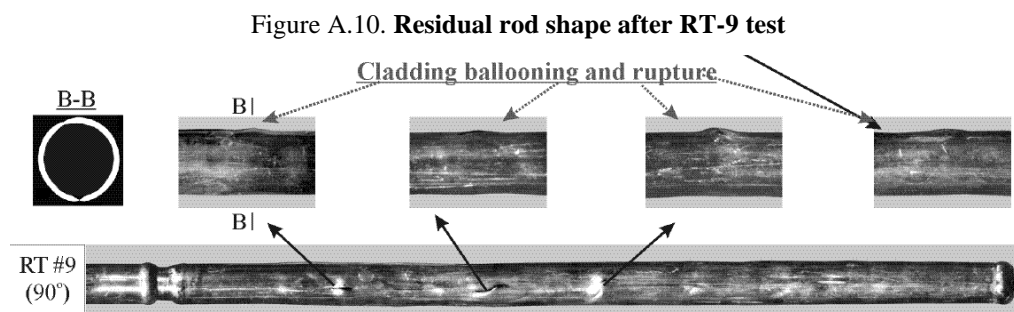


Figure A.9. Comparison of SCANAIR calculations with BGR maximum residual strain



By the same time, the failed rods (RT8-11) cannot be explained by the pellet swelling only (thermal+fission gas swelling) because the maximum measured deformation of failed tests ranged between 8 and 18%.

The SCANAIR modelling, which deals with an instantaneous pressure equilibrium between all the free volumes (including the plenum) is not appropriate to the BGR experiments where it has been observed the presence of multiple local balloons (axial and azimuthal) that are not interconnected for gas transfer (Figure A.10). In fact, a local balloon model (axial and azimuthal) with a local deformation criterion, which could be related to total elongation or striction, has to be used to predict the rod failure in BGR tests.



#### A.4.3. Comparison with NSRR test TK-1

A local but azimuthally homogeneous balloon, with an axial extension 2 to 3 times larger than in BGR tests, has been observed in the NSRR TK-1 test [7]. One possible explanation of this difference could be the fact that axial and azimuthal transfer of gas is easier for NSRR pulses because of a 2 times larger power pulse. Thus, an azimuthally pressure equilibrium may take place in TK-1 while the BGR clad deformation is characterised by local (axial and azimuthal) instability, especially for tests at high enthalpy with a clad temperature about 900°C.

#### A.4.4. Towards an appropriate modelling of post-DNB clad deformation

It has been seen that the post-DNB clad deformation depends on pellet thermal expansion and fission gas swelling, on clad temperature and on gas transfer and available expansion volume. Thus, fission gas swelling models and thermo-hydraulic models validated on NSRR experiments can be used. The problem of gas transfer and available expansion volume is more complex because it may depend on the energy injection rate and on the filling pressure. In this framework, a joint JAEA-IRSN Fission Gas Dynamics (FGD) tests in the NSRR reactor is scheduled in order to investigate gas transfer during fast transients. Actually, experimental results from NSRR and BGR tests may not be directly transposed to PWR cases.

### A.5. Conclusions

The SCANAIR code, improved through a BGR/NSRR heat transfer model, validated by Japanese NSRR experiments, and a Norton viscoplastic clad mechanical behaviour, is able to simulate the rod thermal behaviour in BGR tests. Concerning the clad mechanics, it has been seen that a pellet swelling model is able to simulate the average rod deformation. Nonetheless, the current clad creep model associated with the free volume equilibrium assumption is not suited to predict the maximum clad deformation and the possible post DNB rod failure because they do not simulate local balloons. Furthermore, it has been shown that the clad deformation is strongly dependent on transient gas transfer. In consequence, further work is needed to access the post-DNB clad behaviour in PWR conditions.

## Part B. Analysis of a boron dilution accident with SCANAIR V6

### B.1. Introduction

A new version of the RIA fuel modelling code SCANAIR due to French IRSN has recently been delivered to the VTT Technical Research Centre of Finland. Previously an old version of the code, SCANAIR V4, has

been in use and under development as well as the predecessor version V2 before that. The development work at VTT related to the SCANAIR code has mainly been focused on the improvement of the mechanical modelling of fuel during RIA and also on the thermal hydraulics modelling of capsule RIA tests.

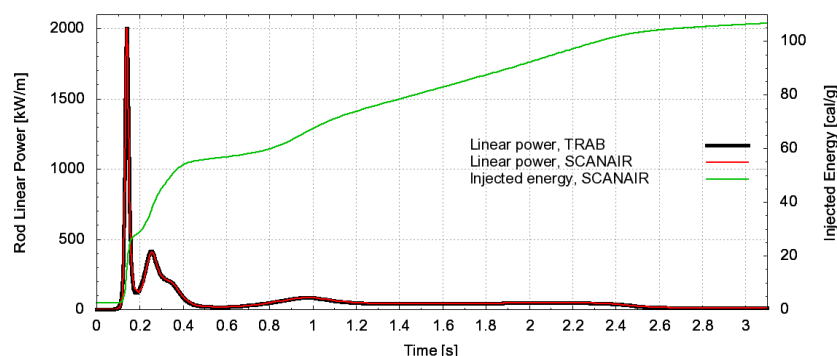
This part of the paper describes the introduction of SCANAIR V6 at VTT by a calculation of a hypothetical RIA scenario in which a slug of diluted coolant water flows into a borated power reactor core. The calculation is based on previous simulations of the transient concerning VVER type Loviisa nuclear power plant core modelled with VTT's neutronics and thermal hydraulics codes. From amongst the initialising events of RIA, boron dilution accident has been chosen for the analysis because more dramatic consequences are expected than with a control rod ejection accident. The assumed amount of injected diluted water is not based on safety analyses or any code calculation but has been chosen so that the fuel and cladding temperatures would rise to bring the rod near the failure limit. This type of scenario is not a design basis accident and in reality it has been concluded that it does not pose a serious threat to the safe operation of a reactor. Though, it is well suited to test the performance and the capabilities of the new code version of SCANAIR.

VTT has several calculation tools to compare SCANAIR calculation results of thermal hydraulics for instance. The thermal hydraulics of SCANAIR V6 has been validated for PWR conditions as well as for capsule experiments characterised by stagnant water under normal conditions.

## B.2. Case description of the boron dilution RIA

Various boron dilution accident scenarios related to the Loviisa NPP have been extensively studied at VTT during the last decade [8]. The accident case presented in this paper has also been calculated previously with the SCANAIR V2. This accident scenario begins with 1% initial power at the start-up of the reactor. Coolant pump of an isolated loop is started incorrectly against the closed main gate valve in the cold leg while the other five coolant pumps are already in operation. The main gate valve is then opened and 3 m<sup>3</sup> of diluted water from the hot leg eventually enters one of the 60° sectors of the core. The full width at half maximum of the resulting RIA power pulse is 20.1 ms and the injected energy according to the SCANAIR calculation during the first power peak is 28.5 cal/g and after the secondary peak 56.0 cal/g as one can see from Figure B.1. The linear power calculated from the rod total power reaches a maximum value of 2 002 kW/m. The position of the fresh fuel rod to be analysed has been chosen from the loading pattern based on the highest expected exertion to the fuel bundle.

Figure B.1. Power history of the transient. Total injected energy



## B.3. Calculation tools and the preparation of the SCANAIR input data deck

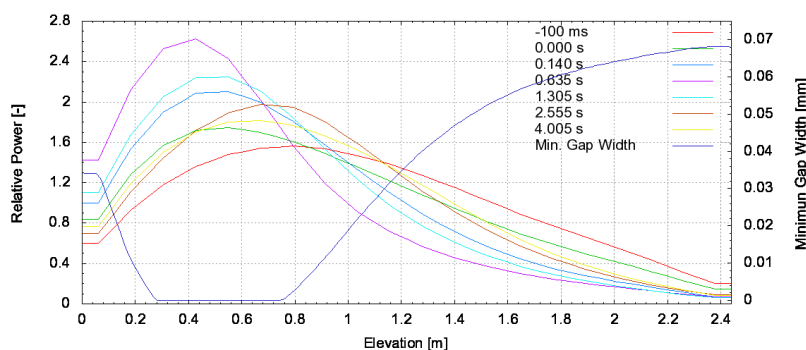
The course of the accident has been previously calculated with the full core neutronics code HEXTRAN and the thermal hydraulics code SMABRE (five equation model + drift flux correlation) that has been coupled with HEXTRAN. HEXTRAN is a 3-D reactor dynamics code developed at VTT to model the hexagonal VVER plant core. HEXTRAN has a dynamic coupling with SMABRE which has also been developed at VTT. A hot rod calculation has been conducted based on the HEXTRAN/SMABRE results

with 1-D neutronics code TRAB due to VTT. The coolant channel flow area used with SCANAIR is the effective flow area applied to the TRAB calculation that takes the various hot channel factors into account.

Thermal hydraulics boundary conditions needed for the SCANAIR input data deck have been extracted from TRAB and HEXTRAN output files. These are inlet coolant mass flow and temperature and coolant pressure. Transient power history has been extracted from TRAB results as well as the axial power profiles (Figure B.2). The time span of the available power and boundary condition history is from 0 to 50 seconds and this data is used without any filtering. Transient itself starts soon after 28.8 s which has been selected as a zero point of the accident when plotting the graphs. This is the time when the diluted boron water enters the reactor core whereas the zero point of the transient modelling with HEXTRAN/SMABRE is actually the time when the main gate valve is opened.

A new axial power profile is set for all time values available, thus 778 different axial power profiles are placed to the input data deck. Axial profile is peaked to the lower part of the rod and does not change too much during the transient so fewer axial profiles would also qualify (Figure B.2). The radial power profile is set in the TRAB input to be uniform and therefore flat radial profile is used also in the SCANAIR input with all axial zones. This is presumably a good approximation for fresh fuel although the correct shape should take account the shelf-shielding effect that depress the thermal neutron flux at the centre of the rod causing the radial profile to peak slightly on the fuel surface.

Figure B.2. Axial power profiles extracted from TRAB output. Minimum gap width at axial locations during the transient, SCANAIR



Initialisation of burn-up dependent data in the input data deck has previously been conducted with ENIGMA steady-state fuel performance code. The current version of ENIGMA in use is 5.9b with VTT applied improvements. A distinct module has been programmed previously in order to transfer irradiation data from ENIGMA to SCANAIR and this module should also be used with the new version of SCANAIR. However, the calculation presented in this paper solely considers unirradiated fuel so no ENIGMA calculation is needed. Nominal values for fuel manufacturing parameters for VVER fuel are used.

The thermal hydraulics model is the 1-D SCANAIR default one with one phase modelling. Boiling phenomena are modelled by heat exchange correlations and boiling curves which means that bulk boiling region is not accessible with this choice [9]. There is also an option for 2-D and two phase calculation mode but the development efforts seem to be aimed at the heat exchange correlation approach. Heat exchange correlations have been validated on specific experiments in the PATRICIA test facility for PWR conditions.

The fuel rod is divided into 20 axial nodes with HEXTRAN calculation and into 41 axial points with TRAB. Fuel rod is split to 40 axial nodes for the SCANAIR calculation and each of these nodes is refined by dividing uniformly to 4 parts, totalling the number of axial meshing to 160. Radially the rod is divided to 20 radial nodes which are again refined by splitting. The most inner node is split to 2 and the few outer nodes are split to graduated amount of meshes. This is important with high burn-up fuel where the radial power profile is peaked to the outer zones of the pellets but now with the fresh fuel rod the refinement should not have that much significance. Finally the cladding is divided into 15 radial meshes.

As injected energies are high, elasto-viscoplastic laws are used for UO<sub>2</sub> fuel and Zr-1%Nb cladding. Norton viscoplastic law for M5-like cladding is applied and because the fuel rod is fresh no oxide layer is supposed. Recommended default water properties for PWR are being utilised.

A fixed time step size is applied until the beginning of the transient and then switched to an automatic time management.

#### **B.4. Analysis of the results**

The main findings of the boron dilution accident are presented graphically in Figures B.1 – B.12.

Previously with SCANAIR V2 there were convergence difficulties with the cladding temperature calculation when the limit for DNB was reached. This forced the calculation to be conducted with an altered coolant flow preventing the DNB limit to be reached. Therefore the temperatures of the cladding were more or less wrong. With the new version of SCANAIR, the maximum fuel temperature is 2 382 °C and that for cladding 1 082 °C (Figure B.4). Fuel maximum temperature is 163 °C lower than once calculated with SCANAIR V2, and the maximum cladding temperature is about 460 °C higher than earlier. The new results are in good agreement with TRAB calculation, only slightly lower due to higher clad-to-coolant heat flux calculated by SCANAIR (Figure B.5).

The amount of parameter data that can be extracted from TRAB output files is in this case limited. Then again with SCANAIR, for example no evolved oxide layer thickness can be found from the output files. The Zr-1%Nb cladding has nevertheless good corrosion resistance and the oxidation rate should be low. According to TRAB, axially maximum oxide layer is 0.95% of the cladding total thickness.

Radially averaged fuel maximum enthalpy reaches a value of 142 cal/g (594 J/g) which slightly exceeds the 140 cal/g (586 J/g) limit for fuel failure set by the Finnish Radiation and Nuclear Safety Authority, STUK (Figure B.3). However, the value is lower than the limit for assurance of fuel coolability, 230 cal/g (963 J/g). The value is also lower than the one previously calculated with SCANAIR V2. According to the SCANAIR calculation, fuel and clad do not melt and the central hole stays open during the whole transient.

PCMI occurs only at the lower zones of the rod as can be seen from Figure B.2 where the minimum gas gap widths are presented. The hottest part of the fuel is around the 36<sup>th</sup> axial node and therefore the clad to coolant heat flux in that node is plotted in Figure B.4. From the figure one can see the different boiling regimes. DNB occurs at time 0.41 s and the transition boiling lasts until 1.08 s. After that the film boiling follows until clad quenching at 15.29 s. Maximum clad to coolant heat flux is presented in Figure B.5. TRAB results show quite similar behaviour compared to SCANAIR even though no peak in the heat flux at quenching is present with TRAB.

From Figure B.7 one can see that the maximum hoop strain is 0.56%. This is quite close to the one calculated with SCANAIR V2. Unfortunately no more data concerning stresses or strains is available for comparison. The absence of fission gases in the fresh fuel means that no additional strains are present because of FGR.

The evolution of coolant boundary conditions can be seen from Figures B.8, B.10 and B.11. The maximum coolant temperature rise over the channel is calculated to be about 70 °C. SCANAIR does not perform any coolant pressure calculation. In the real world, there is a small pressure difference over the channel. The calculated outlet coolant mass flow depicted in Figure B.9 is not the same as with TRAB but the time scale of the deviation is quite small. The reason for this behaviour is not clear and needs to be further analysed.

In Figure B.12 the development of rod radial dimensions at the axial node 36 over the transient is presented. One can also see the rod internal pressure history from the figure. The results are in alignment with those presented in Figures B.2 and B.7 and seem sensible. During the PCMI the cladding is pushed by the expanded fuel pellet after which the heated cladding is pressed by the elevated coolant pressure.

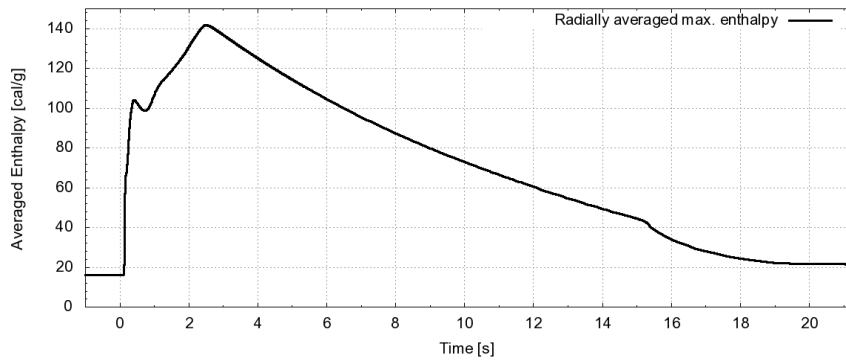


Figure B.3. Radially averaged, axially maximized fuel enthalpy, SCANAIR. Enthalpy slightly exceeds the limit for fuel failure, 140 cal/g, set by the Finnish Radiation and Nuclear Safety Authority, STUK.

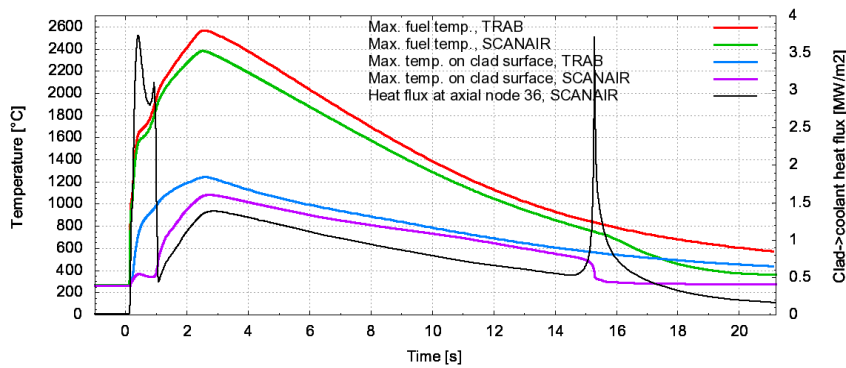


Figure B.4. Fuel maximum temperature and maximum cladding surface temperature according to SCANAIR and TRAB. Clad to coolant heat flux at the hottest axial node, 36 (36/160).

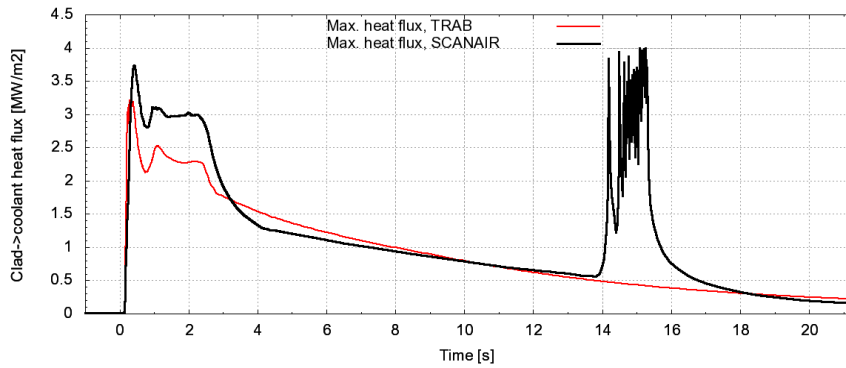


Figure B.5. Maximum heat flux from clad to coolant according to SCANAIR and TRAB.

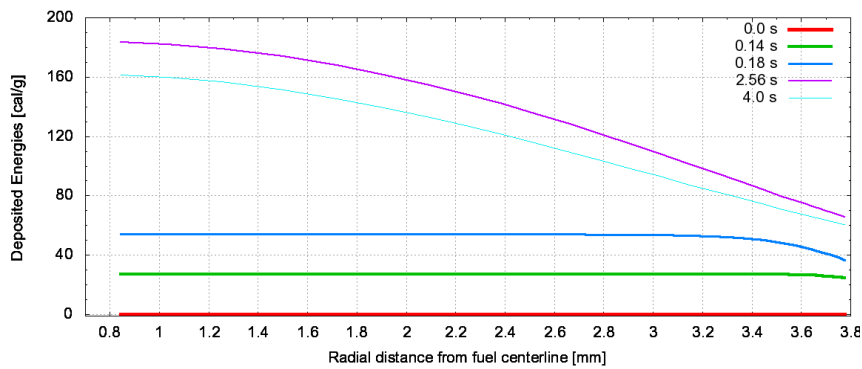


Figure B.6. Maximum deposited energy in fuel.

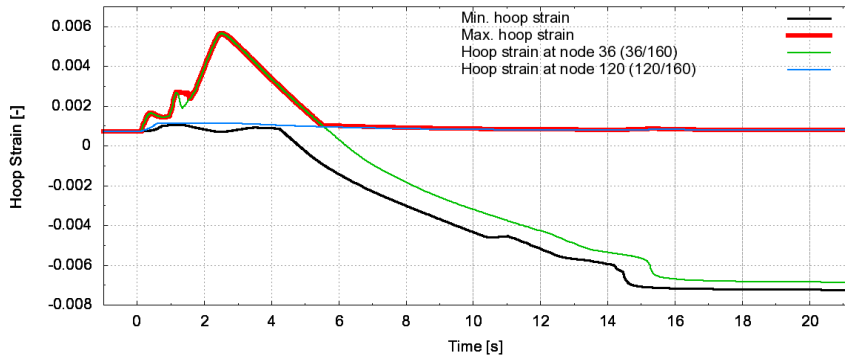


Figure B.7. Cladding hoop strains at clad surface.

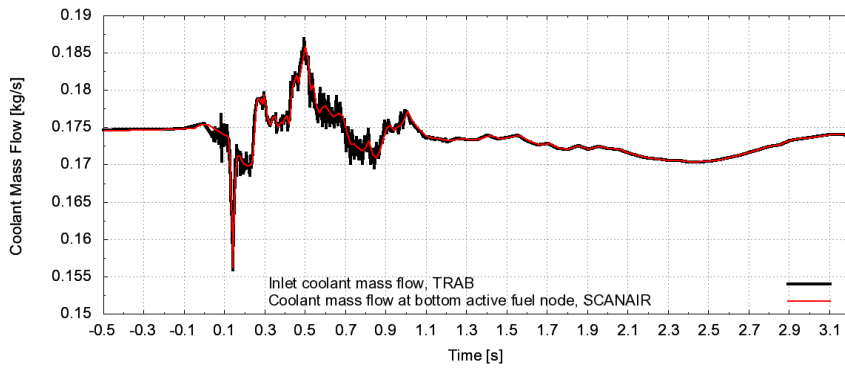


Figure B.8. Inlet coolant mass flow.

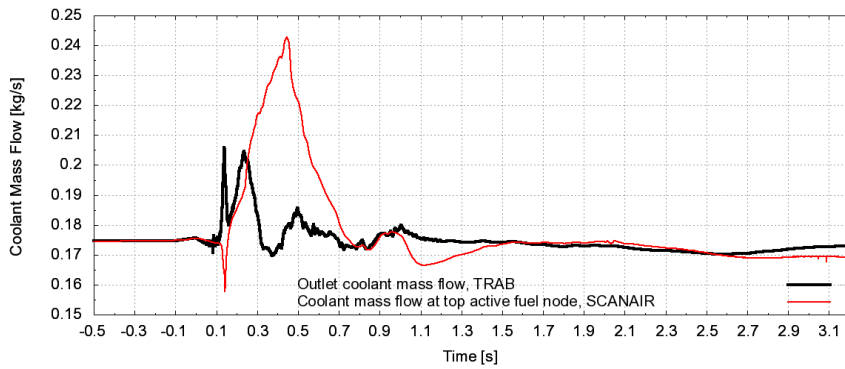


Figure B.9. Outlet coolant mass flow.

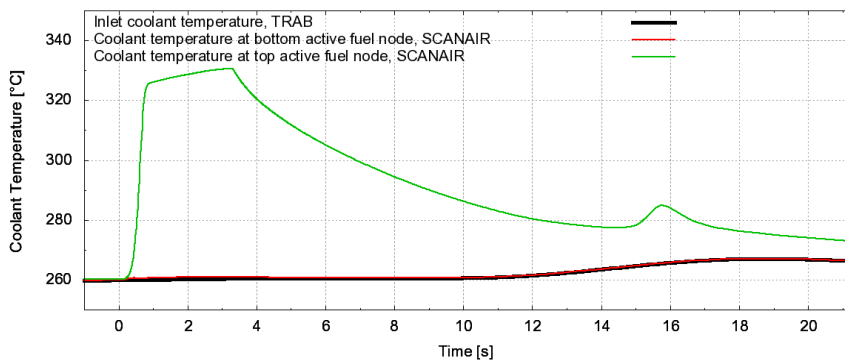


Figure B.10. Coolant temperature.

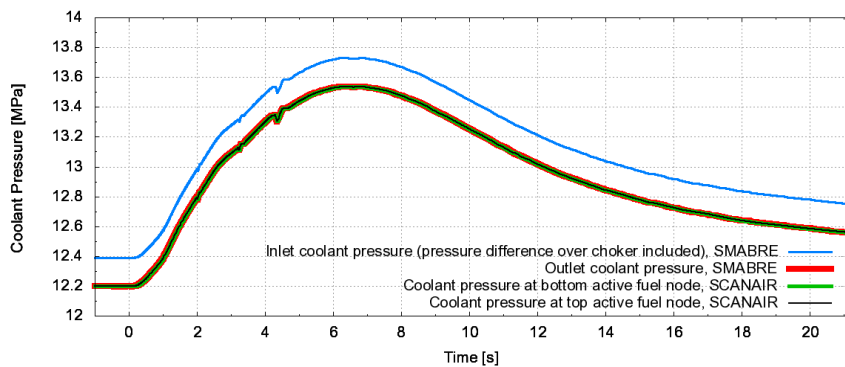


Figure B.11. Coolant pressure. SCANAIR does not perform pressure calculation as it reads it the code manual and as one can see from the figure.

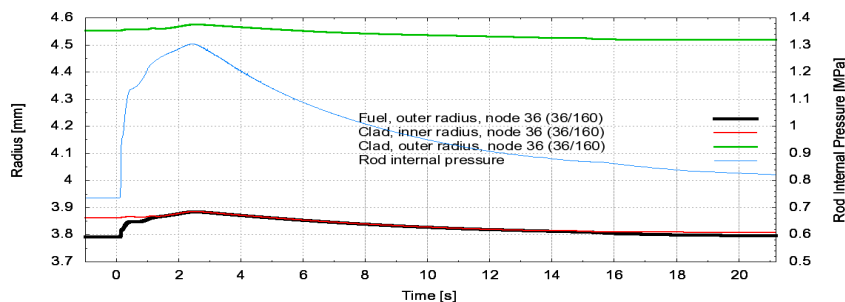


Figure B.12. Fuel outer radius and clad inner and outer radius in axial node 36. Rod internal pressure.

## B.5. Conclusions

As a starting point for RIA analyses with a new version of the SCANAIR code at VTT, a boron dilution accident previously calculated with SCANAIR V2 was recalculated. A limited amount of result parameters were compared with the results of VTT's neutronics code TRAB. Divergence problems encountered previously when reaching the DNB limit were not present anymore. Fuel and cladding temperatures produced by SCANAIR were in good agreement with those calculated with TRAB. More comparison of the SCANAIR results, for example with those of VTT's thermal hydraulics code GENFLO, is suggested.

The SCANAIR V6 transient fuel performance code has now been introduced at VTT.

## Summation

The SCANAIR V6 code due to IRSN of France has been developed to model the mechanics, thermal hydraulics and FGR behaviour of a single fuel rod during reactivity initiated accidents. For VVER fuel, the code has been validated against Russian BGR narrow pulse experiments. The thermal hydraulic conditions with these capsule tests are characterised by stagnant water under ambient conditions. SCANAIR V6 has also been validated on a specific PATRICIA separate effects programme to extend the capabilities of the code to model PWR conditions. As an application, a boron dilution accident in VVER-440 type reactor has been successfully calculated with SCANAIR V6.

## Acknowledgement

SCANAIR V6 has been delivered to VTT under the IRSN-VTT bilateral co-operation agreement in the field of nuclear safety and radiation protection.

## References

- [1] L. Yegorova et al., “Experimental Study of Narrow Pulse Effects on the Behavior of High Burn-up Fuel Rods with Zr-1%Nb Cladding and UO<sub>2</sub> Fuel (VVER Type) under Reactivity-Initiated Accident Conditions: Program Approach and Analysis of Results”, NUREG/IA-0213 Vol. 1 & 2, (2005).
- [2] E. Federici et al., “The SCANAIR Code Version 3.2: Main features and Status of Qualification”, Proc of IAEA TCM on Fuel Behavior Under Transient and LOCA Conditions, Halden, Norway, (10-14 September 2001).
- [3] V. Bessiron, T. Sugiyama, T. Fuketa, “Clad to coolant heat transfer in NSRR experiments”, J. Nucl. Sci. Tech. 44[5].
- [4] T. Sugiyama, T. Fuketa, “Effect of cladding pre-oxidation on rod coolability during reactivity accident conditions”, J. Nucl. Sci. Tech. 41[11], 1093-1090 (2004).
- [5] A. Sakurai, M. Shiotsu, K. Hata, “Correlations for subcooled pool film boiling heat transfer from large surfaces with different configurations”, Nucl. Eng. Des. 120[2-3], 271-280 (1990).
- [6] J.H. Lienhard, A heat transfer textbook (MIT course), 3<sup>rd</sup> edition, Phlogiston Press, 452- 454, (2001).
- [7] T. Fuketa, 22<sup>nd</sup> NSRR meeting (1998).
- [8] P. Siltanen, M. Antila, R. Kyrki-Rajamäki, T. Vanttola: “Analysis of Core Response to the Injection of Diluted Slugs for the Loviisa VVER-440 Reactors”, OECD/NEA/CSNI/ Specialist Meeting on Boron Dilution Reactivity Transients, State College, Pennsylvania, U.S.A., (18-20 October 1995).
- [9] A. Moal, F. Lamare, J.C. Latché, E. Fédérici, V. Bessiron: “SCANAIR reference documentation version V\_6\_6”, (27 October 2008).

## Application of the SCANAIR Code for VVER Conditions – Boron Dilution Accident

RIA Workshop – Paris, France  
9-11 September 2009

A. ARFFMAN,  
VTT Technical Research Centre of Finland  
B. CAZALIS,  
Institut de Radioprotection et de Sûreté Nucléaire, France




IRSN FRANCE VTT TECHNICAL RESEARCH CENTRE OF FINLAND

### Outline of the Presentation

- Validation of SCANAIR V6 Code, due to IRSN, for VVER fuel
  - ▶ Validation calculations conducted at IRSN
  - ▶ Russian BGR narrow pulse tests
  - ▶ Implemented new features to the Code
  - ▶ Assessment of the results
- Application at VTT: a boron dilution accident
  - ▶ Introduction of the new Code version SCANAIR V6 at VTT
  - ▶ This accident type was chosen to have more dramatic consequences in power reactor application
  - ▶ Calculation is based on previous analyses of the accident with VTT's neutronics and thermal hydraulics codes




IRSN FRANCE VTT TECHNICAL RESEARCH CENTRE OF FINLAND

### Russian BGR tests

- Study of VVER high burnup fuel behaviour during RIA with Russian fast-pulse graphite research reactor BGR
- Twelve fuel rodlets fabricated from VVER-440 and VVER-1000 mother rods irradiated up to average burnup of 60 MWd/kg<sub>0</sub> and 47-49 MWd/kg<sub>0</sub>, respectively
- Rodlets were pressurized with Helium to the internal pressure of 2.0 or 2.1 MPa except two which were unpressurized (0.1 MPa)
- Pulse full width at half maximum: 2.5-3.1 ms
- Capsule tests
  - ▶ Thermal hydraulics characterised by stagnant water under normal conditions
  - ▶ Need to implement proper clad-to-coolant heat transfer model
- Also modelling of the viscoplastic behaviour of clad mechanics had to be implemented




IRSN FRANCE VTT TECHNICAL RESEARCH CENTRE OF FINLAND

### Thermal hydraulics of SCANAIR V6

- Thermal hydraulics of SCANAIR is based on 1-D and 1-phase modelling with mass and energy conservation equations → bulk boiling region is not accessible
- NSRR/BIGR heat transfer model
  - Validated on Japanese NSRR Surface Effect Tests
  - Different heat transfer regimes are modelled (conduction, vaporization, boiling crisis, transition boiling, film boiling, rewetting, post-rewetting)
  - Parameter values are adjusted according to NSRR experiments
  - Heat exchange coefficient approach is used
- For PWR conditions, a specific heat transfer model has been validated on PATRICIA Separate Effect Tests

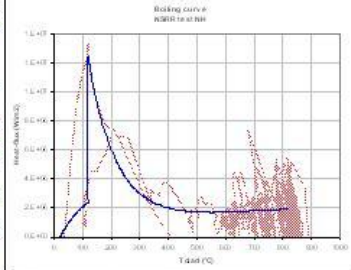


Figure 1: Example of a boiling curve from NSRR test

T
 VTT

IRSN FRANCE VTT TECHNICAL RESEARCH CENTRE OF FINLAND

### Mechanics of SCANAIR V6

- Clad elasto-viscoplastic model has been implemented to SCANAIR V6 to take account high cladding temperatures resulting from DNB
- Activated over a limit temperature of 600°C
- Norton viscoplastic law is used to model the viscoplastic contribution of clad mechanical deformation

$$\epsilon_{mec} = \epsilon_{el} + \epsilon_{pl} + \epsilon_{vp}$$

- Creeping and clad ballooning can be modelled with the limitation of small deformations

T
 VTT

IRSN FRANCE VTT TECHNICAL RESEARCH CENTRE OF FINLAND

### Findings of the BIGR analyses (1/2)

- Average clad strain can be explained by thermal expansion and fission gas swelling (significant above fuel enthalpy of about 120 cal/g) but strain related to clad creep has to be taken into account for maximum clad strain
- SCANAIR creep deformation is strongly dependent on the filling pressure → a significant overestimation of the calculated maximum clad strain for non-failed rods with an initial 2 MPa internal pressure, a good agreement obtained for low initial pressure (0.1 MPa) tests
- Multiple local balloons, both axial and azimuthal, are observed with failed fuel rods, and the modelling of those would require a local balloon model with a local deformation criterion not yet present in SCANAIR

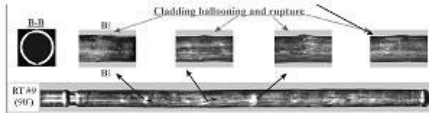


Figure 2: Rodlet shape after the RIA pulse

T
 VTT

IRSN FRANCE VTT TECHNICAL RESEARCH CENTRE OF FINLAND

### Findings of the BGR analyses (2/2)

- SCANAIR modelling relies on the not necessarily correct assumption of instantaneous pressure equilibrium between all free volumes
- Local balloon is present also with NSRR tests but it is azimuthally homogeneous
- An explanation could be the two times larger power pulse with NSRR tests easing the gas transfer

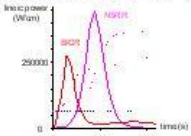


Figure 3: BGR and NSRR power pulse

- Fission gas swelling model and thermal hydraulic models validated on NSRR experiments can now be used but the issues related to the gas transfer and available expansion volume need more clarification
- Problems may depend on the energy injection rate and on the filling pressure

✖ T VTT

IRSN FRANCE VTT TECHNICAL RESEARCH CENTRE OF FINLAND

### Application of SCANAIR V6: VVER-440 boron dilution accident

#### SCANAIR Code history at VTT

- Different SCANAIR Code versions have been in use and under development at VTT already a number of years
- The development of the previous version, V4beta, concentrated on the implementation of heat transfer correlations for capsule RIA tests and on the improved mechanical model developed at VTT
- Other Code versions were the different subversions of SCANAIR V2
- The BGR RIA tests have also been calculated at VTT with VTT modified SCANAIR V4beta
- New Code version was recently in 2009 delivered to VTT according to the IRSN-VTT bilateral co-operation agreement

✖ T VTT

IRSN FRANCE VTT TECHNICAL RESEARCH CENTRE OF FINLAND

### Boron dilution accident

- Purely hypothetical onset of RIA, not a design basis accident
- Some amount of diluted coolant water somehow enters the borated reactor core → large amount of possible scenarios
- Control rod ejection accident in a VVER is expected not to pose a serious threat, more severe effect is supposed with boron dilution accident when the extent of dilution is sufficient
- The installed automation and operating procedures at VVER type Loviisa NPP (Finland) minimizes the risk of the accident
- Various boron dilution accident scenarios related to the Loviisa NPP have been extensively studied at VTT during the last decade

✖ T VTT

Specification of the chosen scenario

- Accident begins with 1 % initial power at start-up of the reactor
- 3 m<sup>3</sup> of diluted water from the hot leg enters one of the 60° sectors of the core
- The assumed amount of injected diluted water is not based on safety analyses or any code calculation but has been chosen so that the fuel and cladding temperatures would rise to bring the rod near the failure limit
- The position of the fresh fuel rod to be analysed has been chosen from the loading pattern based on the highest expected exertion to the fuel bundle
- Full width at half maximum of the resulting RIA power pulse is 20.1 ms
- Injected energy according to the SCANAIR calculation during the first power peak is 28.5 cal/g and after the secondary peak 56.0 cal/g

Figure 4. Power history of the transient.  
Total injected energy.

Applied calculation tools at VTT

- The course of the accident has been previously calculated with the full core neutronics code HEXTRAN and the thermal hydraulics code SMABRE (both due to VTT)
- HEXTRAN is a 3-D reactor dynamics code developed to model the hexagonal VVER plant core and it has a dynamic coupling with SMABRE
- A hot rod calculation has been conducted based on the HEXTRAN/SMABRE results with 1-D neutronics code TRAB due to VTT
- For the SCANAIR calculation, power history, thermal hydraulic boundary conditions and time-dependent axial power profiles have been extracted from TRAB and HEXTRAN output files

Figure 5. Some of the axial power profiles extracted from TRAB output. Minimum gap width at axial locations during the transient, SCANAIR.

Preparation of the input data deck

- In the past, initialization of burn-up dependent data in the SCANAIR input data deck has been conducted at VTT with ENIGMA steady-state fuel performance code. The current version of ENIGMA in use is 5.9b with VTT applied improvements
- Now with fresh fuel, no ENIGMA calculation is needed
- Recommended default water properties for PWR are being utilized
- As injected energies are high, elasto-viscoplastic laws are used for UO<sub>2</sub> fuel and Zr-1%Nb cladding
- Nominal values for fuel manufacturing parameters for VVER fuel are used

IRSN FRANCE VTT TECHNICAL RESEARCH CENTRE OF FINLAND

### Calculation results (1/4)

- The same calculation has also been conducted previously with the SCANAIR V2
- Then there were convergence difficulties with the cladding temperature calculation when the limit for DNB was reached  
→ coolant flow had to be altered in order to prevent DNB ever happening
- Now no problems with the calculation were encountered
- During the accident, radially averaged fuel maximum enthalpy reaches a value of 142 cal/g (594 J/g) which slightly exceeds the 140 cal/g (586 J/g) limit for fuel failure set by the Finnish Radiation and Nuclear Safety Authority, STUK (Figure 6).

**Figure 6:** Radially averaged, axially maximized fuel enthalpy, SCANAIR.

IRSN FRANCE VTT TECHNICAL RESEARCH CENTRE OF FINLAND

### Calculation results (2/4)

- Maximum fuel temperature is 2 382 °C and that for cladding 1 082 °C
- These are in alignment with TRAB results, only slightly lower due to higher clad-to-coolant heat flux calculated by SCANAIR
- From the heat flux profile one can see the different boiling regimes in the hottest axial zone

**Figure 7:** Fuel maximum temperature and maximum cladding surface temperature according to SCANAIR and TRAB. Clad-to-coolant heat flux at the hottest axial zone, 36 (36/160).

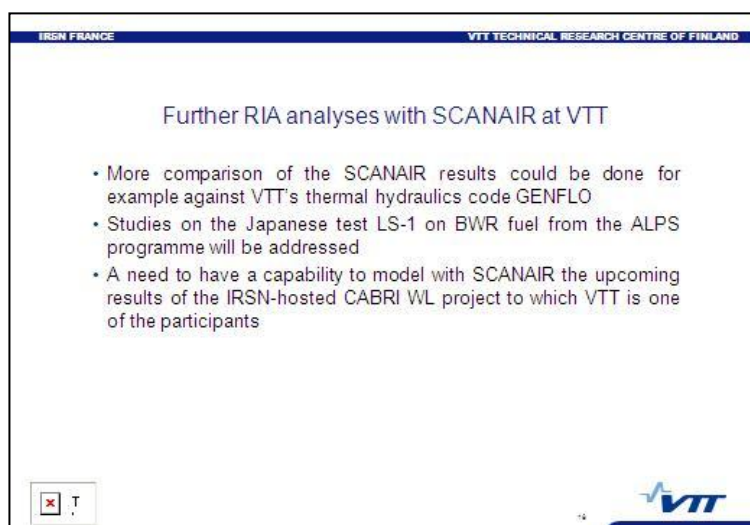
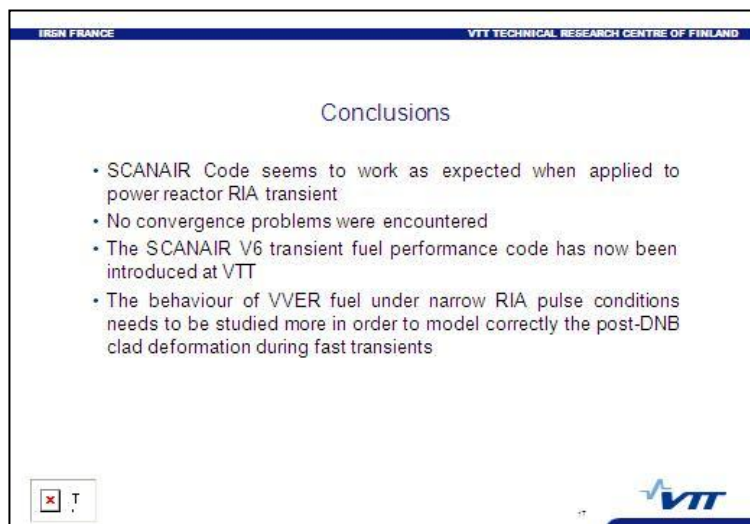
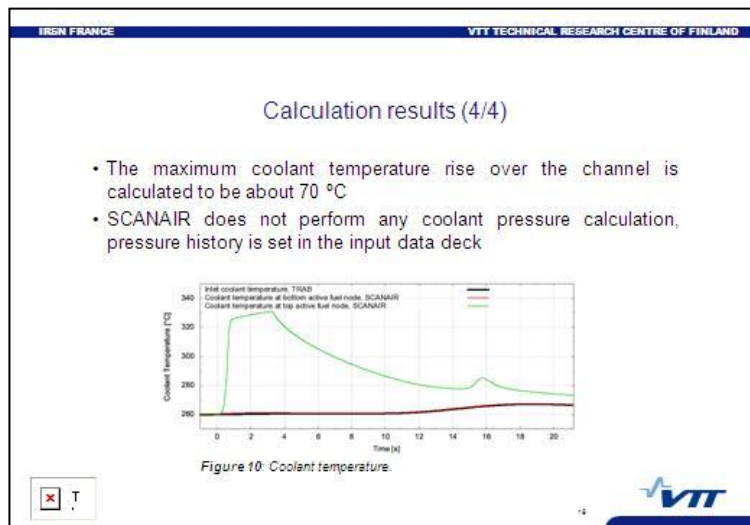
IRSN FRANCE VTT TECHNICAL RESEARCH CENTRE OF FINLAND

### Calculation results (3/4)

- SCANAIR maximum clad-to-coolant heat flux shows quite similar behaviour compared to TRAB, Figure 8
- Also the peak at rewetting is present with SCANAIR
- PCMI occurs only at the lower zones of the rod (Figure 5)
- During the PCMI the cladding is pushed by the expanded fuel pellet (max. hoop strain 0.56 %) after which the heated cladding is pressed by the elevated coolant pressure, Figure 9

**Figure 8:** Maximum heat flux from clad to coolant according to SCANAIR and TRAB.

**Figure 9:** Cladding hoop strains at clad surface.





## ANALYSIS OF MIXED-OXIDE FUEL BEHAVIOR DURING RIA TESTS USING FALCON MOD01

**Robert Montgomery**  
ANATECH Corp., USA

**Ken Yueh**  
EPRI, USA

**Odelli Ozer**  
EPRI, USA

**John Alvis**  
ANATECH Corp., USA

### 1. Introduction

The final version of acceptance criteria are being developed in the United States (US) for use in the safety analysis of the hot-zero power (HZIP) and hot-full power (HFP) Reactivity Initiated Accidents (RIA) in Pressurized Water Reactors (PWRs) and Boiling Water Reactors (BWRs). Recently, the staff at the US Nuclear Regulatory Commission (NRC) issued Interim RIA acceptance criteria within Revision 3 of the Standard Review Plan (NUREG-0800) for use in new reactor certification and licensing [1]. These criteria attempt to account for exposure induced changes in fuel rod behavior at higher burn-up. The interim RIA acceptance criteria have been developed using an empirical approach with limited consideration for the differences between RIA-simulation tests and LWR RIA events or  $UO_2$  and Mixed Plutonium-Uranium (MOX) fuel.

The Electric Power Research Institute (EPRI), under the auspices of the Fuel Reliability Program Working Group 2 – Fuel Regulatory Issues, has undertaken an effort to evaluate the impact of irradiation on MOX fuel rod behavior during an RIA event. RIA-simulation tests have shown that irradiated MOX fuel pellets at similar burn-up can experience a larger expansion response compared to  $UO_2$  pellets due to the dispersed distribution of high burn-up structure of plutonium agglomerates throughout the pellet [2]. This enhanced pellet expansion increases the clad loading at a given fuel enthalpy level in comparison to  $UO_2$  fuel.

This paper summarises the development and verification of a MOX fuel pellet transient gaseous swelling model for use in the FALCON fuel performance code and the evaluation results of MOX fuel rods being tested at the Japan Atomic Energy Agency (JAEA) Nuclear Safety Research Reactor (NSRR). The FALCON code, developed under the sponsorship of EPRI, uses a fully two-dimensional finite element analysis methodology to model the thermal and mechanical behavior of the fuel and cladding under a variety of irradiation conditions [3]. The fuel performance code, integrated with the MOX pellet model, was then applied to the analyses of eight (8) fuel rods tested at the NSRR facility. The test program is composed of seven tests conducted at cold conditions and one test performed in the high temperature test capsule.

### 2. Model development

A transient gaseous swelling model for MOX fuel pellets was developed for FALCON using the RIA-simulation experiments CABRI REP Na-6, Na-7, Na-9 and Na-12 [2]. Post-test examinations and on-line measurements of REP Na-6 and Na-9 indicate that these rods experienced cladding strain levels significantly higher than that expected based on MOX fuel pellet thermal expansion alone. Furthermore, REP Na-7 failed suddenly indicating a rapid transition from PCMI loading to uncontrolled pressure loading on the cladding.

During the rapid energy deposition of an RIA event, loading on the clad develops in two stages [4]. The first stage is PCMI loading enhanced by gaseous swelling caused by the controlled expansion of the fission gas residing within the fuel matrix either on the grain boundaries or within the grains, and is additive to the pellet thermal expansion. The second stage occurs when the gas pressure begins to overcome the confinement provided by the fuel matrix. This loss of confinement is due to one or more of the following effects: material softening under high temperature, grain boundary separation by the expansion of intergranular bubbles, or loss of cladding contact during cool down. This two-stage loading can potentially lead to two types of failure regimes: 1) during Stage 1, the cladding may fail by displacement-controlled PCMI loading, depending on the level of cladding embrittlement or 2) during Stage 2, the cladding may fail by force-controlled loading caused by the mechanical instability of the pellet induced by the fission gas in the fuel matrix.

The development of a transient gaseous swelling model for MOX fuel focused on two important aspects, 1) calculation of the gas pressure evolution within idealised fission gas bubbles contained in the high burn-up structure of the fuel pellet matrix and 2) the local stress in the fuel matrix adjacent to the fission gas bubbles.

### 2.1. Fission gas bubble pressure evolution model

The gas concentration and volume of gas bubbles in high burn-up structure material are not adequately known to allow for the development of a mechanistic model that describes the expansion process during rapid heating. The proposed model is semi-empirical and is based on the Ideal Gas Law formulation. Ignoring the surface tension effects of small bubbles, the gas pressure within a bubble can be approximated by the following expression:

$$P_b = n_b R T_g / V_b \quad (2.1)$$

where:

$P_b$  is the gas pressure within the bubble  
 $n_b$  is the number of moles of gas within the bubble  
 $T_g$  is the temperature of the gas within the bubble  
 $V_b$  is the volume of the bubble  
 $R$  is the gas constant

By making the reasonable assumption that the change in the bubble volume is proportional to the local change in the volumetric expansion of the fuel, the bubble volume can be approximated by the following equation:

$$V_b = V_{ob} (1 + \Delta V_b / V_{ob}) = V_{ob} (1 + D_v \varepsilon_v) \quad (2.2)$$

where:

$V_{ob}$  is the initial bubble volume at the start of the transient  
 $\Delta V_b$  is the change in bubble volume during the transient  
 $\varepsilon_v$  is the local volumetric strain in the fuel matrix during the transient  
 $D_v$  is an empirical constant of proportionality

Substituting Eq. 2.2 into Eq. 2.1 yields,

$$P_b = C_g T_g / (1 + D_v \varepsilon_v) \quad (2.3)$$

where:

$$C_g = n_b R / V_{ob} \quad (2.4)$$

As can be seen in Eq. 2.4,  $C_g$  depends on the gas content, through  $n_b$ , and the initial bubble volume  $V_{ob}$ , both of which depend on burn-up, thus making  $C_g$  burn-up dependent.  $D_v$  is not so clearly defined, as it

depends on the bubble shape and distribution in the fuel matrix, the local burn-up, the fuel compliance, and perhaps a number of other factors. Both  $C_g$  and  $D_v$  can be empirically quantified from MOX RIA experiments as shown in the following section.

The gas pressure described by Eq. 2.3 is calculated in the fuel as a local body force. The result is an additional loading component related to local fuel temperature and volume expansion. The product ( $C_g T_g$ ) provides the increase in gas pressure due to rising temperatures, whereas, the denominator provides the decrease in gas pressure due to volume expansion of the bubbles.

## 2.2. Gas-bubble spatial distribution and effective porosity

The presence of MOX agglomerates uniformly distributed in the  $UO_2$  fuel matrix results in local burn-up accumulation in the agglomerates. This, in turn, leads to localised regions of high fission gas concentrations that precipitate a cluster of small bubbles in the vicinity of the agglomerates [5, 6]. For modeling purposes, the gas bubbles associated with the MOX agglomerates are assumed to have a uniform volumetric distribution characterised by an effective porosity  $\rho_b$ , which evolves as a function of burn-up. An expression for the effective porosity is derived using an idealised form of bubble shape and distribution. Each bubble has a radius of  $r_b$  and is separated by a  $UO_2$  matrix ligament of thickness  $2t_b$ . The stress ( $\sigma_b$ ) within the spherical ligament separating the gas bubbles can be approximated by:

$$\sigma_b = \frac{P_b r_b}{2t_b} \quad (2.5)$$

The bubble radius to ligament thickness ratio can be determined from the porosity of the fission gas bubbles. Using an idealised cubic volume of material, each of the eight spherical bubbles contributes  $\frac{1}{4}$  volume to the total bubble volume in the cube ( $V_b$ ) yielding:

$$V_b = \frac{8}{3} \pi r_b^3 \quad (2.6)$$

The total volume of the cube is given by:

$$V_c = (2t_b + 2r_b)^3 \quad (2.7)$$

The porosity of gas bubbles in the cubic volume of material ( $\rho_b$ ) is obtained from the ratio of the gas bubble volume to the total volume, i.e.:

$$\rho_b = \frac{\frac{8}{3} \pi r_b^3}{(2t_b + 2r_b)^3} = \frac{\pi r_b^3 / 3}{(t_b + r_b)^3} \quad (2.8)$$

Rearranging Equation 2.8 yields:

$$\frac{r_b}{t_b} = \frac{1}{\left(\frac{\pi}{3\rho_b}\right)^{1/3} - 1} \quad (2.9)$$

The stress in the ligament can now be written as a function of the bubble pressure and the local bubble porosity by substituting Equation 2.9 into Equation 2.5:

$$\sigma_b = \frac{P_b}{2} \left[ \left( \frac{\pi}{3\rho_b} \right)^{1/3} - 1 \right]^{-1} \quad (2.10)$$

The expression above provides a condition of equilibrium between the ligament stress and the gas pressure as a function of the fission gas bubble density. The behavior of the fuel pellet remains stable as long as this state

of equilibrium remains in effect. However, as the bubble pressure continues to rise, the confining stress  $\sigma_b$  may no longer be capable of confining the rising pressure and a state of local instability can develop.

### 3. Benchmarking of model parameters

As a first step in the benchmarking process, the gaseous swelling model equations were implemented in FALCON. The computations are performed at the element integration points, where local field variables that are needed for calculating model parameters are defined or calculated. These include burn-up, temperature, effective porosity, yield stress, bubble pressure, stresses and strains. To allow FALCON computations to proceed, the model parameters,  $C_g$ ,  $D_v$ , and  $\rho_b$  were initially assigned approximate numerical values. These were then modified through an iterative analysis process.

The four MOX REP-Na tests (REP Na-6, Na-7, Na-9, and Na-12) were analyzed, making use of the test results that provide information about the cladding strain response and failure conditions during the test. This data includes flow channel sodium displacement data for REP Na-6, REP Na-7, and REP Na-9, post-test permanent cladding strains measured for REP Na-6 and REP Na-9, and data for REP Na-12. The sodium displacement in the flow channel during the early part of the power pulse is caused by the cladding radial and axial expansion. The displaced sodium data for the REP-Na tests provides the evidence for the evolution of cladding deformations during the early energy deposition phase of the event. To compare the strain histories from FALCON to the sodium displacement data, a numerical scheme was developed calculating the evolution of the fuel rod volume change from calculated cladding displacement history. Once coolant heating from the fuel rod begins, the dilation of the sodium coolant will dominate the sodium volume displacement data. This effect is not considered in the FALCON calculations at this time.

The coefficients  $C_g$ ,  $D_v$  and  $\rho_b$  are burn-up dependent, and were benchmarked simultaneously through iterative FALCON analyses of the REP Na tests. The coefficients  $C_g$  and  $D_v$  govern the gas pressure generation through equation 2.3, where  $C_g$  prescribes the gas content and  $D_v$  provides the ability of the fuel matrix to accommodate the bubble expansion, which is a form of a "damping" mechanism for the rise in bubble pressure due to loss of confinement and increase in bubble volume.

The analysis procedure employed to benchmark the model parameters used the following steps:

1. All three burn-up-dependent coefficients, namely,  $C_g$ ,  $D_v$  and  $\rho_b$ , are varied until the calculated displaced sodium volume is matched with the measured displaced sodium volume for REP Na-6, REP Na-7 and REP Na-9, which was determined from the flow channel time-history data.
2. These three coefficients are fine tuned against the post-test permanent cladding strains measured for REP Na-6, REP Na-9, and the failure condition of REP Na-7 and no-failure condition of REP Na-12.
3. All four REP Na cases were analyzed in series, alternating between the above three steps, and the procedure was continued until the best match for each of the four coefficients is obtained.

The FALCON results for the CABRI MOX experiments using the final set of model coefficients are shown in Figure 1 and summarised in Table 1. Figure 1 contains a comparison of the FALCON calculated displaced sodium volume and the measured displaced sodium volume for REP Na-6 and REP Na-7 as a function of injected enthalpy. Table 1 summarises some of the key parameters calculated by FALCON and compares them to post-test measurements. The calculated displaced sodium volume agrees well with the measured data for both REP Na-6 and REP Na-7. The rapid increase in displaced sodium volume at an injected energy of  $\sim 105$  cal/gm for the measure data in REP Na-7 was caused by the expulsion of sodium out of the flow channel when fission gas and fuel material was dispersed upon fuel rod failure. This behavior is not included in the FALCON calculation and leads to the divergence in results at the higher injected enthalpy.

Comparison of the calculated residual hoop strain shown in Table 1 to the measured values for REP Na-6 and REP Na-9 finds that the FALCON results agree well with REP Na-9 and slightly over-predicts the

strain for REP Na-6. Comparisons of the FALCON calculated cladding radial deformation and post-test measurements for test Rep Na-9 are presented in Figure 2. The calculated cladding hoop strain (elastic + plastic) at the time of failure for REP Na-7 is ~2% which is consistent with the cladding strains obtained from post-test examinations of REP Na-7.

The comparison of the calculated cladding deformations to the experimentally determined cladding deformations for the MOX REP Na tests demonstrates that FALCON combined with the gaseous swelling enhanced-PCMI model can accurately represent the thermo-mechanical behavior of MOX fuel under RIA conditions.

Figure 1. Displaced sodium volumes as a function of injected energy for REP Na-6 and REP Na-7 RIA tests

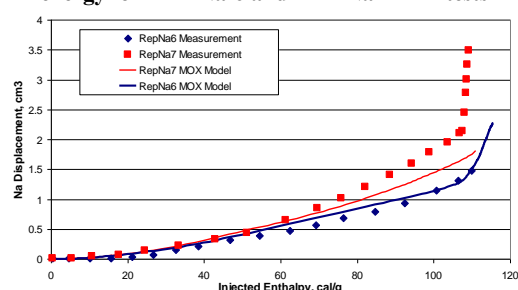


Figure 2. Comparison of FALCON calculated deformations to experimental measurements for REP Na-9

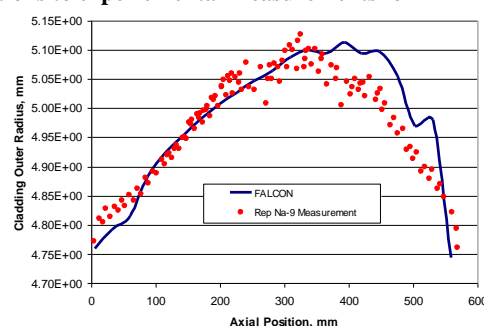


Table 1. Summary of MOX test cases used in quantifying model parameters

Case	Burnup	Enthalpy	Measured Residual Hoop Strain	Calculated Hoop Strain
	GWd/MTU			
RepNa-6	47	126	2.6	3.5
RepNa-7	55	175	1.0 - 2.6	2
RepNa-9	28	197	7.5	7.1
Repna-12	64	100	2.5	2.6

#### 4. Verification using NSRR MOX experiments

A total of eight (8) MOX fuel test specimens were subjected to pulse irradiation experiments in the NSRR as part of the Japan Atomic Energy Agency (JAEA) RIA test program. The NSRR is a modified TRIGA reactor able to achieve a maximum reactivity insertion of \$4.6 with a corresponding pulse width of approximately 4.4 milliseconds. NSRR has the capacity to conduct tests using either a room temperature (RT) capsule or a newly designed hot temperature (HT) capsule [7].

The RT capsule is a sealed pressure vessel containing an instrumented test fuel rod with stagnant water. A length of test fuel is installed into the capsule is approximately 300 mm in total length with fueled region of 100 to 120 mm. The HT capsule can be used at coolant temperatures up to 286°C at the corresponding saturation pressure. The test fuel segment in the HT capsule is only 130 mm total length with a fuel stack height of approximately 50 mm.

The test fuel rods summarised in this paper were extracted from commercial fuel rods irradiated between 45 and 59 GWd/tU. Table 2 provides information on the base irradiation characteristics and the test conditions for these test rods. Four additional MOX test segments base irradiated in the Japanese Materials Test Reactor (JMTR) were analyzed as part of the verification of FALCON. These test rods had a burn-up of ~20 GWd/tU and experienced peak fuel enthalpy levels of ~140 cal/gm.

The test rod of DW-1 was sampled from a fuel rod irradiated in Dodewaard NPP of the Netherlands. It is a 8×8 BWR fuel rod containing MOX pellets fabricated using the MIMAS (Micronized Master Blend) process with Zircaloy-2 cladding with a zirconium liner. The average burn-up of the test rod was 45 Wd/MTU with an oxide layer thickness of 10 µm average and 40 µm maximum.

The BZ series of tests are test segments sampled from fuel rods irradiated in the Beznau NPP of Switzerland. The test BZ-1 was fabricated from a 14×14 PWR fuel rod containing MOX pellets produced with the SBR (Short Binderless Route). The cladding was Zircaloy-4. The average burn-up was 48 GWd/MTU. The cladding oxide layer was 30 μm with an average hydrogen content of 340 ppm. The test segments BZ-2 and BZ-3 were sampled from a different fuel rod than BZ-1. This fuel rod was also a 14×14 PWR with Zircaloy-4 cladding but the fuel pellets were with the MIMAS process. The fuel burn-up was 59 GWd/MTU and the cladding oxide thickness was 20 μm and the hydrogen content was 160 ppm.

Table 2. Test conditions

Test ID	DW-1	BZ-1	BZ-2	BZ-3
Rod Type	8x8	14x14	14x14	14x14
Cladding	Zr-2 with Zr-liner	Zr-4	Zr-4	Zr-4
MOX Pellet Production	MIMAS	SBR	MIMAS	MIMAS
Initial Pu Enrichment, %	6.4	5.5	5.6	5.6
Burnup, GWd/MTU	45	48	59	59
Average Cladding Oxide Thickness, μm	10	30	20	20
Average Hydrogen Content, ppm	50	340	160	160
Coolant Temperature, °C	20	20	20	281
Coolant Pressure, Mpa	0.1	0.1	0.1	6.6
Inserted Reactivity, \$	4.6	4.6	4.6	4.53
Initial Fuel Enthalpy*, cal/g	0	0	0	16
Peak Fuel Enthalpy, cal/g	121	164	154	143

\* Based on 20°C enthalpy

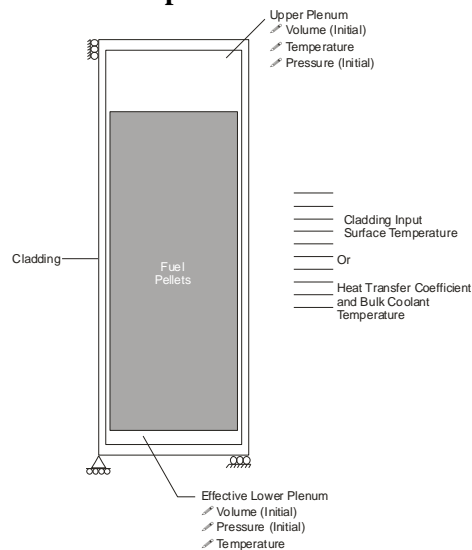
### 5. Results and discussion

An asymmetric finite element model of the test segments was developed for comparison to actual test data. A schematic representation of the FALCON model is presented in Figure 3.

Table 3. Segment geometry used in FALCON

Test ID	DW-1	BZ-1	BZ-2	BZ-3
Clad OD, mm	12.3	11.2	11.2	11.2
Clad Thickness, mm	0.813	0.737	0.737	0.737
Liner Thickness, mm	0.08	n/a	n/a	n/a
Gap Thickness, mm	0.112	0.102	0.102	0.102
Pellet OD, mm	10.4	9.5	9.5	9.5
Fuel Stack Height, mm	83	117	110	51

Figure 3. Schematic representation of the FALCON model



Models of DW-1, BZ-1, BZ-2 and BZ-3 were executed using both the modified version of FALCON incorporating the MOX model and the standard version of FALCON. Comparisons of the FALCON results to available measured data are presented in Table 4. Results of the FALCON simulations of test DW-1 and BZ tests are presented in Figures 4 through 9. The FALCON results using the MOX model are very good when compared to the measured data.

Table 4. Comparisons of the FALCON results to available measured data

Test	Burnup GWd/MTU	Injected/Failure Enthalpy cal/g	Measured Residual Hoop Strain	Calculated Hoop Strain	Maximum Calculated SED MJ/M <sup>3</sup>	CSED MJ/M <sup>3</sup>	Cladding Temperature at Max SED or SED=CSED °C		Calculated Failure Enthalpy cal/g
							MOX Model	FALCON	
DW-1	45	121	0.41% average 0.55% max	0.7% MOX Model 0.6% FALCON	18 MOX Model 17 FALCON	20	48 MOX Model 39 FALCON	-	
BZ-1	48	76	Failed	1.5% MOX Model 1.3% FALCON	24 MOX Model 24 FALCON	12	25 MOX Model 25 FALCON	103 MOX Model 113 FALCON	
BZ-2	59	130	Failed	1.3% MOX Model 1.1% FALCON	22 MOX Model 21 FALCON	14	35 MOX Model 29 FALCON	118 MOX Model 119 FALCON	
BZ-3	59	126	-	5.0% MOX Model 1.0% FALCON	21 MOX Model 15 FALCON	23	497 MOX Model 340 FALCON	-	

5.2. DW-1 comparison

In the test DW-1, the test segment reached a peak fuel enthalpy of 121 cal/g without cladding failure. Limited departure from nucleate boiling was reported to occur during the later portion of the test. The measured cladding residual hoop strain was 0.55% at maximum with an average of 0.41% [8]. Results of the cladding surface temperature calculations are presented in Figure 4 along with the cladding thermocouple data. The high cladding temperatures associated with the short time DNB are not predicted by the FALCON calculations. Comparisons of the FALCON calculated cladding radial deformation and post-test measurements for test DW-1 are presented in Figure 5. Good agreement is observed between the calculated and measure results. The evolution of the Strain Energy Density (SED) as a function of the cladding mid-wall temperature for the MOX model compared to the un-modified version of FALCON is presented in Figure 6. This figure shows that the peak SED is achieved at a time when the cladding temperatures are below 50°C. The cladding deformations and SED show only small variations between MOX and UO<sub>2</sub> fuel pellets for the DW-1 test performed at room temperature conditions.

Figure 4. Cladding surface temperature as a function of time for test DW-1

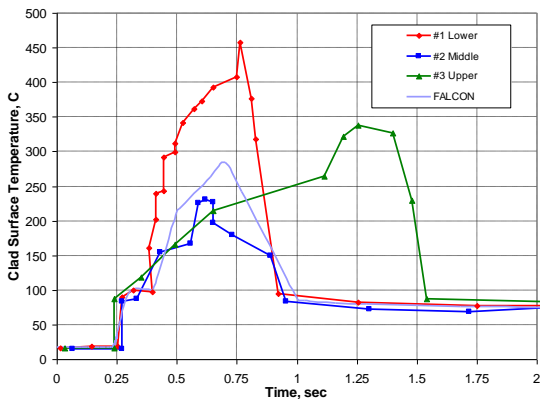


Figure 5. Cladding deformation for test DW-1

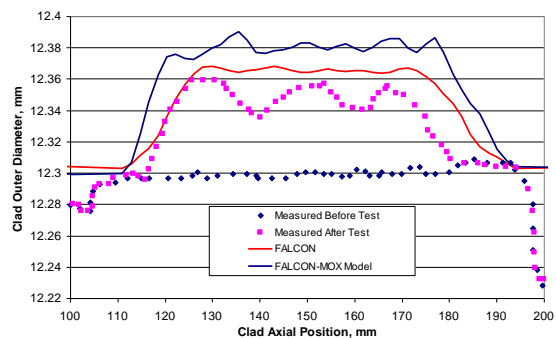
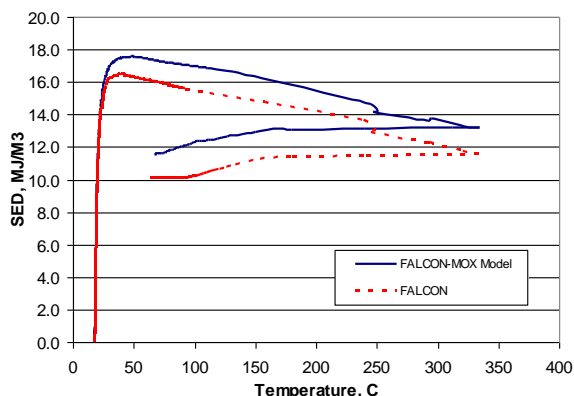


Figure 6. SED as a function of the cladding mid-wall temperature for test DW-1



### 5.3. BZ test series comparisons

Tests BZ-1 and BZ-2 were performed with the coolant at room temperature and ambient pressure conditions. Both tests resulted in cladding failure due to PCMI at fuel enthalpies of 74 cal/g for BZ1 and 117 cal/g for BZ-2 [8]. Test BZ-3, the sister segment to BZ-2, was performed within the high temperature/pressure capsule with a coolant temperature of 281°C and 6.6 MPa of pressure. Cladding failure was not observed in the BZ-3 test up to a peak fuel enthalpy level of 143 cal/gm. Results of the cladding hoop strain calculations are presented in Table 4 for BZ-3.

The evolution of the SED as a function of the cladding mid-wall temperature from FALCON with and without the MOX gaseous swelling model is presented in Figures 7-9 for tests BZ-1, BZ-2 and BZ-3, respectively. These figures show that there is little variation between MOX and UO<sub>2</sub> for the tests conducted at room temperature and ambient pressure (tests BZ-1 and BZ-2). However, there appears to be a significant impact of MOX gaseous swelling enhancement on the PCMI loading at the higher temperatures seen in test BZ-3 conducted in the high temperature capsule. The sharp increase in SED observed in Figure 9 is associated with the high cladding temperatures that occurred as a result of DNB during the test and does not result from low temperature PCMI during the early part of the energy deposition.

Figure 7. SED as a function of the cladding mid-wall temperature for test BZ-1

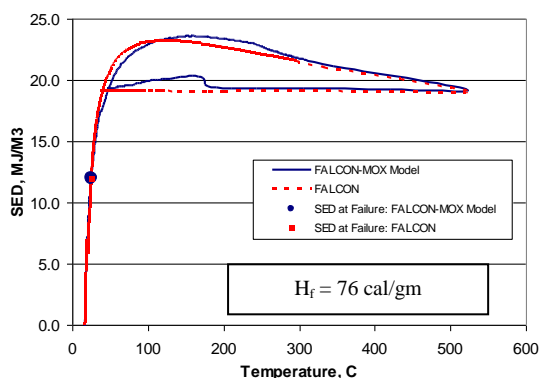


Figure 8. SED as a function of the cladding mid-wall temperature for test BZ-2

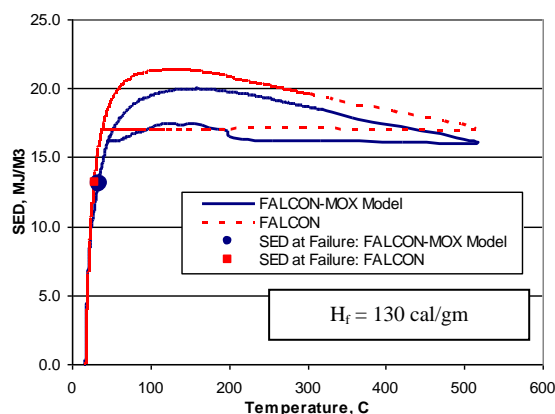
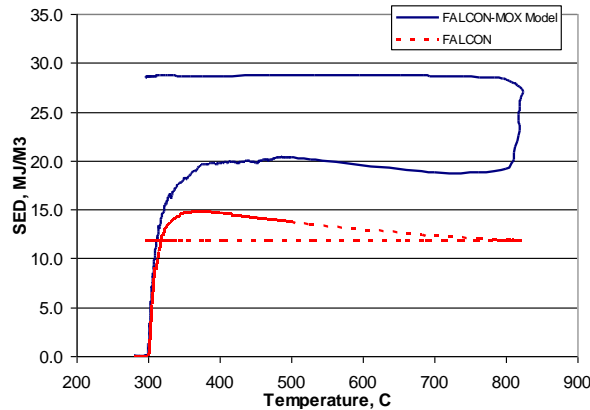


Figure 9. SED as a function of the cladding mid-wall temperature for test BZ-3



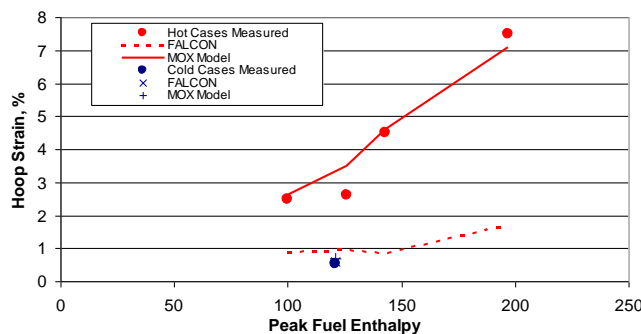
**6. Discussion**

The comparison of the calculated results to available experimental measurements for the MOX tests demonstrates that FALCON combined with the gaseous swelling enhanced-PCMI model can accurately represent the thermo-mechanical behavior of MOX fuel rods under RIA conditions.

MOX fuel behavior during RIA transients differs from that for UO<sub>2</sub> fuel in certain respects because of the added effect of fission gas loading. In UO<sub>2</sub> fuel, the loading on the cladding during the power pulse is governed solely by classical PCMI, which evolves in direct proportion to the nearly adiabatic fuel thermal expansion. This process can be referred to as prompt-PCMI. Subsequent reversal in the pellet thermal expansion caused by heat loss due to conduction generally marks the end of prompt-PCMI. In MOX fuel, cladding loading evolves as a two-phase process: a fuel thermal-expansion-dominated phase where gaseous swelling enhances the PCMI loading but does not govern it and a gaseous swelling-dominated phase. The gaseous swelling model developed in Section 2 treats these two phases simultaneously as a continuous process, and the aggregate effect of both phases is what is delivered to the cladding in the form of enhanced PCMI. Gaseous-swelling-dominated loading can be considered delayed-PCMI.

The delayed-PCMI appears to coincide with higher cladding temperatures as observed in Figure 10, which displays the measured cladding strains compared to the FALCON analysis with and without the MOX model for the non-failed tests from the CABRI and NSRR test programs. The data shows that gaseous dominated loading is significant for those cases conducted at high temperature such as the REP Na test series and test BZ-3. As evidenced in Figure 9, the SED accumulation during prompt-PCMI occurs when heat conduction has not caused significant heating of the cladding. However, higher cladding temperatures cause a lower material modulus and yield stress, thus providing less mechanical restraint on the fuel pellet. As a result, the SED accumulation during delayed-PCMI occurs during most of the heat conduction phase when the cladding reaches the maximum temperature. This type of behavior is absent in UO<sub>2</sub> fuel, where the SED beyond the prompt-PCMI phase will show a slightly decreasing trend due to the elastic unloading of the cladding.

Figure 10. Comparison of FALCON calculated cladding hoop strain and measured values as a function of peak fuel enthalpy during power pulse



Prompt-PCMI appears to dominate at the cold cladding conditions represented in test DW-1. For the tests conducted at room temperature and ambient pressure conditions, mechanical loading reaches a maximum, and so does the cladding strain and SED, during the power pulse at a point in the transient when heat conduction has not had sufficient time to heat the cladding much above the pre-transient temperature.

## 7. Conclusions

The use of a transient gaseous swelling model for MOX fuel pellets developed for FALCON demonstrates that pellet thermal expansion combined with gaseous swelling enhanced-PCMI can accurately represent the thermo-mechanical behavior of MOX pellets during rapid energy deposition. The comparison of the calculated results to the available experimental measurements for the MOX tests finds that gaseous swelling enhanced-PCMI is an important contributor to the mechanical behavior of MOX fuel rods under RIA conditions. In addition, the results suggest that for the room temperature tests, the loading on the cladding is governed primarily by classical PCMI, which evolves in direct proportion to the nearly adiabatic fuel thermal expansion and there is little difference between UO<sub>2</sub> and MOX fuel response. However, RIA tests run either in CABRI or the high temperature/pressure capsule at NSRR have higher cladding temperatures and as a result, the gaseous swelling of the MOX fuel pellets becomes a more dominant clad loading mechanism during the later portion of the transient. These results indicate that the pellet expansion process of MOX fuel pellets can be influenced by the ability of the cladding to provide mechanical restraint.

The model development and evaluation process has found that the MOX fuel pellet expansion process leading to cladding deformation can be several times higher than that arising from UO<sub>2</sub> pellets at equivalent peak fuel enthalpy levels. The interim failure criteria established in revision 3 of NUREG-0800 is based on the lower bound of adjusted RIA-simulation tests that includes MOX fuel. However, the more severe loading response in irradiated MOX fuel pellets, caused by the widely distributed high burn-up structure throughout the pellet, should be accounted for prior to finalisation of the acceptance criteria.

## References

1. U.S. Nuclear Regulatory Commission, Standard Review Plan for the Review of Safety Analysis Reports for Nuclear Power Plants, NUREG-0800, Appendix B, Rev. 3. (2007).
2. J. PAPIN, et al., "Summary and Interpretation of the CABRI REP-Na Program", *Nuclear Technology*, Vol. 157, March (2007).
3. Fuel Analysis and Licensing Code: FALCON MOD01: Volume 2: Users's Manual, EPRI, Palo Alto, CA: 2004. 1011308.
4. D. SUNDERLAND, et. al., "Evaluation of Recent RIA-Simulation Experiments with the FALCON Fuel Performance Code." Proceedings of the 2004 International Meeting on LWR Fuel Performance, Orlando, Florida (2004).
5. T. KAMEYAMA, et. al., "Analyses of Burn-up at Plutonium Spots in Uranium-Plutonium Mixed Oxide Fuels in Light Water Reactors by Neutron Transport and Burn-up Calculations", *Journal of Nuclear Science and Technology*, Vol. 34 (1997).
6. F. LEMOINE, "Estimation of the Grain Boundary Gas Inventory in MIMAS/AUC MOX Fuel and Consistency with REP-Na Test Results", *Journal of Nuclear Science and Technology*, Vol. 43 (2006).
7. T. SUGIYAMA, et. al., "Failure of High Burn-up Fuels Under Reactivity-Initiated Accident Conditions", *Annals Nucl. Energy*, 36, 380 (2009).
8. M. UMEDA, "MOX Fuel Behavior during RIA", *2007 Fuel Safety Research Meeting (FSRM 2007)*, Tokai, Japan, (May 2007).

## Analysis of Mixed-Oxide Fuel Behavior During RIA Tests Using FALCON MOD01

John Alvis  
Robert Montgomery  
**ANATECH**  
Linking Theory and Practice

Ken Yueh  
Odelli Ozer  
**EPRI** | ELECTRIC POWER  
RESEARCH INSTITUTE

Presented at the  
OECD/NEA Workshop  
Nuclear Fuel Behavior during Reactivity Initiated Accidents  
Paris, France  
September 9 – 11, 2009

**ANATECH**  
Linking Theory and Practice

**EPRI**

### Overview

- Background/Motivation
- MOX Pellet Expansion Model Development
- Model Benchmarking Using CABRI Experiments
- Analysis of Recent NSRR MOX Tests
- Observations

OECD/NEA RIA Workshop, September 9-11, 2009 -3-

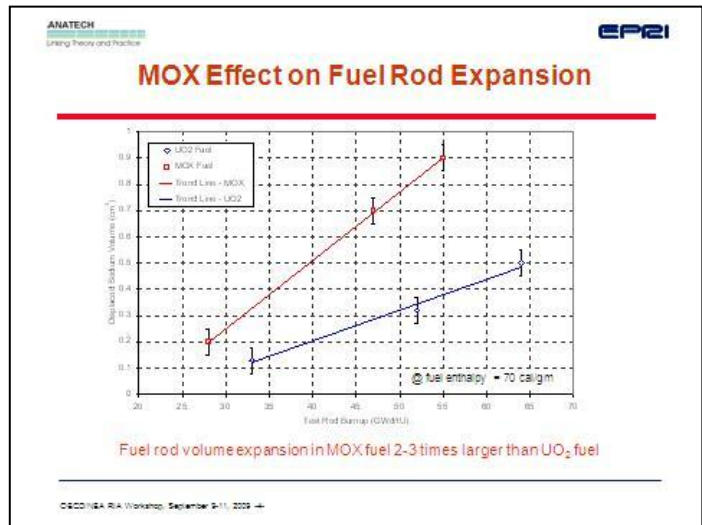
**ANATECH**  
Linking Theory and Practice

**EPRI**

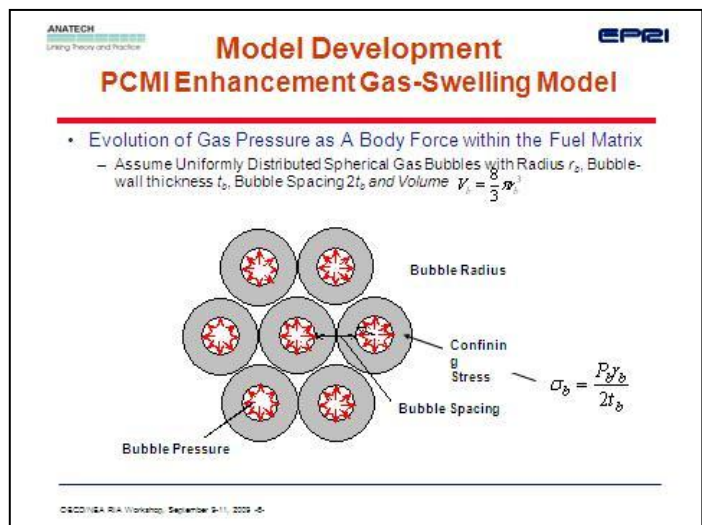
### Background/Motivation

- Interim RIA acceptance criteria have been developed using an empirical approach
  - Limited consideration for the differences between RIA-simulation tests and LWR RIA events or  $UO_2$  and Mixed Plutonium-Uranium (MOX) fuel
- RIA-simulation tests have shown that irradiated MOX fuel pellets at similar burnup can experience a larger expansion response compared to  $UO_2$ 
  - Post-test examinations and on-line measurements of REP Na-6 and Na-9 find cladding strain levels significantly higher than that expected based on MOX fuel pellet thermal expansion alone
  - Enhanced pellet expansion increases the clad loading at a given fuel enthalpy level in comparison to  $UO_2$  fuel

OECD/NEA RIA Workshop, September 9-11, 2009 -3-



- ANATECH  
Using Theory and Practice
- EPRI
- ### MOX Pellet Expansion Model Development
- A transient gaseous swelling model for MOX fuel pellets was developed for FALCON
  - The development of a transient gaseous swelling model for MOX fuel focused on two important aspects
    - Calculation of the gas pressure evolution within idealized fission gas bubbles contained in the high burnup structure of the fuel pellet matrix
    - The local stress in the fuel matrix adjacent to the fission gas bubbles
  - RIA-simulation experiments CABRI REP Na-6, Na-7, Na-9 and Na-12 were used in the semi-empirical approach
- CSCE/ISA RIA Workshop, September 9-11, 2009 -5-



ANATECH  
Lining Theory and Practice

EPRI

### MOX Gas Swelling Model Formulation

---


$$P_b = n_b R T_g / V_b \quad V_b = V_{ob} (1 + D_v \varepsilon_v)$$

$$P_b = C_g T_g / (1 + D_v \varepsilon_v) \quad C_g = n_b R / V_{ob}$$

$P_b$ : Bubble Gas Pressure  
 $T_g$ : Gas Temperature  
 $V_b$  &  $V_{ob}$ : Bubble Current and Initial Volume  
 $n_b$ : Number of Gas Moles in Bubble  
 $R$ : Gas Constant  
 $\varepsilon_v$ : Bubble Volumetric Expansion  
 $C_g$ : Gas Pressure Evolution Coefficient  
 $D_v$ : Bubble Volume Evolution Coefficient

$C_g$ : Depends on burnup because  $n_b$  and  $V_{ob}$  depend on burnup  
 $D_v$ : Depends on bubble shape and bubble distribution

**Note:  $C_g$  is a pressurization coefficient,  $D_v$  is a damping coefficient**

CSCD/ISA RIA Workshop, September 8-11, 2009 -7-

ANATECH  
Lining Theory and Practice

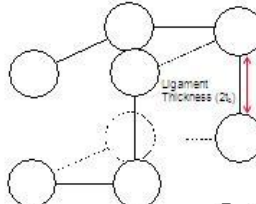
EPRI

### Pellet Instability Model

---

Consider Cube of Fuel Material with Volume  $8(t_b + r_b)^3$  & Porosity  $\rho_b$

Schematic Representation of Porosity in the Fuel Matrix  
(Bubble Spacing is Exaggerated for Clarity)



$$\rho_b = \frac{\frac{8}{3}\pi r_b^3}{(2t_b + 2r_b)^3} \quad \sigma_b = \frac{P}{2} \left[ \left( \frac{\pi}{3\rho_b} \right)^{1/3} - 1 \right]$$

**Condition of Instability:** When the confining stress  $\sigma_b$  reaches the fuel yield strength  $\sigma_y$ , local gas confinement is no longer possible, and the bubble begins to swell rapidly.

**Onset of Instability**  $\rightarrow$   $P_{crit} = 2 \sigma_y \left[ \left( \frac{\pi}{3\rho_b} \right)^{1/3} - 1 \right]$

$P_b = C_g T_g / (1 + D_v \varepsilon_v)$  when  $P_b > P_{crit}$

CSCD/ISA RIA Workshop, September 8-11, 2009 -8-

ANATECH  
Lining Theory and Practice

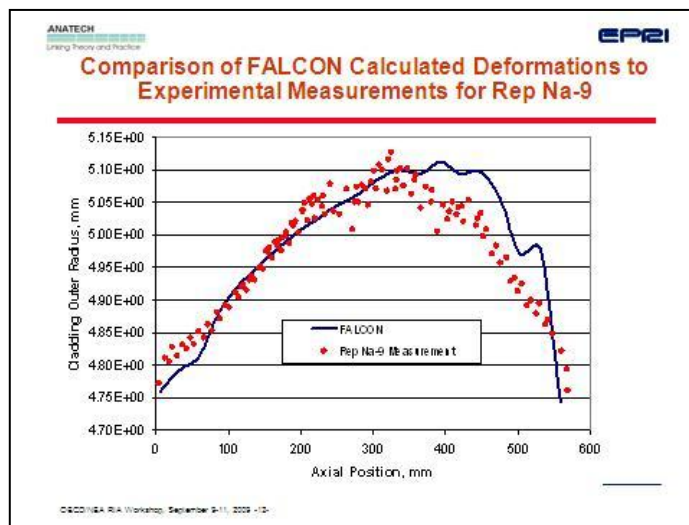
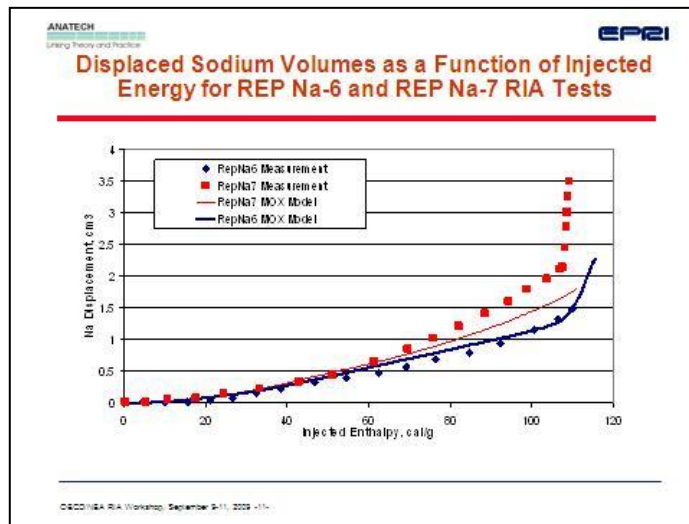
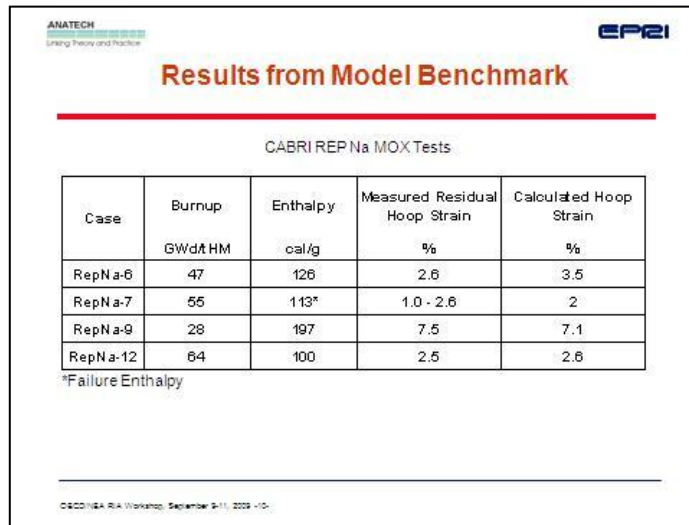
EPRI

### Model Benchmarking Using CABRI Experiments

---

- All three burnup-dependent coefficients were varied until the calculated displaced sodium volume matched the measured displaced sodium volume for REP Na-6, REP Na-7 and REP Na-9
- The coefficients were fine tuned against the post-test permanent cladding strains measured for REP Na-6, REP Na-9, and the failure condition of RepNa-7 and no-failure condition of REP Na-12.
- All four REP Na cases were analyzed in series, alternating between the above steps, and the procedure was continued until the best match for all coefficients was obtained.

CSCD/ISA RIA Workshop, September 8-11, 2009 -9-



ANATECH  
Using Theory and Practice

EPRI

### Model Verification using NSRR MOX RIA Experiments

- Eight (8) MOX fuel specimens have been tested in the NSRR as part of the JAEA RIA test program
  - Four low burnup (~20 GWd/THM) test segments from rods irradiated in the ATR facility
  - Four high burnup segments extracted from commercial fuel rods
- The four high burnup test fuel rods have been analyzed with FALCON and the integrated MOX model
  - Verify the MOX pellet expansion model using post-test examination data
  - Evaluate differences between room temperature and hot zero power conditions

CSCE/NSRR RIA Workshop, September 9-11, 2009 -13-

ANATECH  
Using Theory and Practice

EPRI

### Comparisons of the FALCON Results to Available Measured Data

Test ID	DW-1	EC-1	EC-2	EC-3
Rod Type	8x8	14x14	14x14	14x14
Cladding	Zr-2.5wt% Zr-Ni	Zr-4	Zr-4	Zr-4
MOX Pellet Production	MIMAS	SBR	MIMAS	MIMAS
Initial Pellet Enrichment, %	6.4	5.5	5.6	5.6
Burnup, GWd/THM	45	48	59	59
Average Hydrogen Content, ppm	50	340	160	160
Coolant Temperature, °C	20	20	20	281
Coolant Pressure, MPa	0.1	0.1	0.1	6.6
Peak Fuel Enrichment, g/g	121	164	154	143

Test	Burnup, GWd/THM	Max Pellet Enrichment, g/g	Measured Residual Hoop Strain	Calculated Hoop Strain	SED, MPa	CESD, MPa	Calculated Failure Strain, g/g
DW-1	45	121	0.47% average (0.28% max)	0.7% MOX Model 0.85% FALCON	18 MPa (Model) 17 FALCON	20	-
EC-1	48	76	Failed	1.9% MOX Model 1.9% FALCON	24 MPa (Model) 24 FALCON	12	103 MPa (Model) 113 FALCON
EC-2	59	130	Failed	1.3% MOX Model 1.7% FALCON	22 MPa (Model) 23 FALCON	14	118 MPa (Model) 119 FALCON
EC-3	59	142	-	3.0% MOX Model 1.0% FALCON	21 MPa (Model) 19 FALCON	23	-

CSCE/NSRR RIA Workshop, September 9-11, 2009 -14-

ANATECH  
Using Theory and Practice

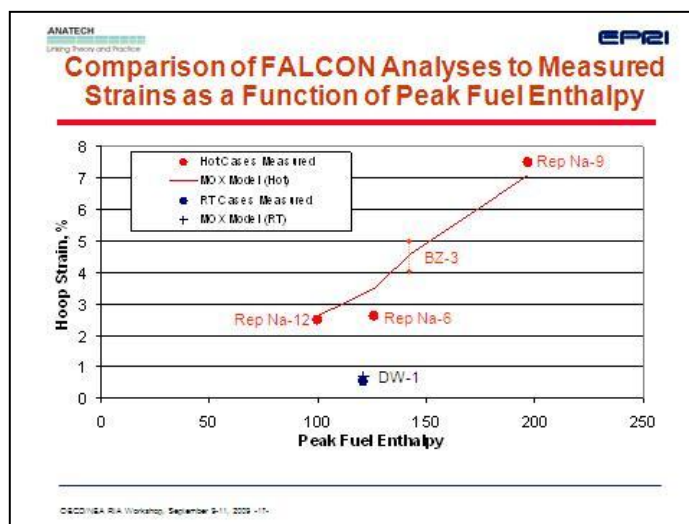
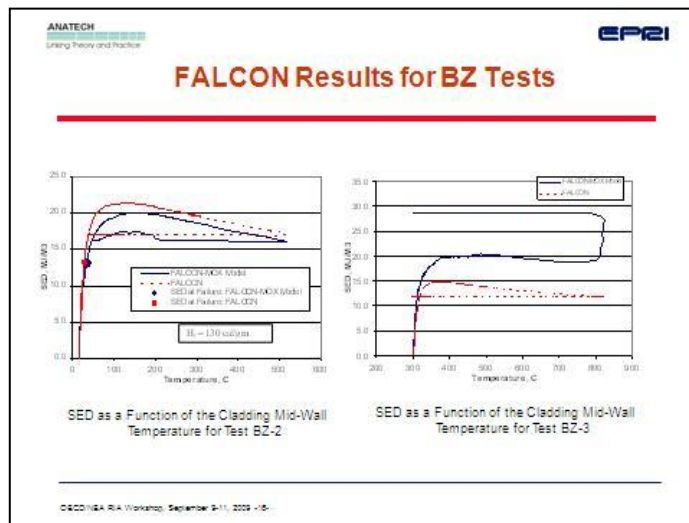
EPRI

### FALCON Results for Test DW-1

**Cladding Deformation for Test DW-1**

**SED as a Function of the Cladding Mid-Wall Temperature for Test DW-1**

CSCE/NSRR RIA Workshop, September 9-11, 2009 -15-



- ANATECH  
Lining Theory and Practice
- EPRI
- ### Key Observations
- The transient gaseous swelling model for MOX fuel pellets developed for FALCON accurately represent the thermo-mechanical behavior of MOX pellets during an RIA
  - For the room temperature tests:
    - Clad loading is governed by classical PCMI
    - Little difference between UO<sub>2</sub> and MOX fuel response
  - For high temperature tests:
    - Gaseous swelling becomes a dominate clad loading mechanism
    - MOX pellet expansion process can be influenced by the mechanical restraint of the cladding
  - Development of fuel rod failure criteria for application to hypothetical control rod ejection accidents must consider the differences between UO<sub>2</sub> and MOX fuel response
- © OECD/NEA RIA Workshop, September 9-11, 2009 -15-

**SESSION THREE**

**Code Assessment**

**Parametric Study of Fuel Rod Behaviour during the RIA using the Modified Falcon Code**

Grigori Khvostov and Martin Zimmermann (PSI, Switzerland); Guido Ledergerber (KKL, Switzerland)

**Major Sensitivities of Modelling a High Burn-up Fuel Rod with FRAPCON-3/FRAPTRAN Codes**

Maria Teresa del Barrio, Isabel Vallejo and Luis Enrique Herranz (CIEMAT, Spain)

**Capabilities of TRANSURANUS Code in Simulating Power Ramp Tests from the IFPE Database**

Martina Adorni, Davide Rozzia, Alessandro Del Nevo and Francesco D'Auria (GRNSPG, Italy)



## PARAMETRIC STUDY OF FUEL ROD BEHAVIOUR DURING THE RIA USING THE MODIFIED FALCON CODE

**Grigori Khvostov, Martin A. Zimmermann**

Laboratory for Reactor Physics and Systems Behaviour, Paul Scherrer Institut, Switzerland

**Guido Ledergerber**

Kernkraftwerk Leibstadt AG, CH 5325 Leibstadt, Switzerland

### Abstract

Presented in the paper are the results of a parametrical study with the use of optimised modules of the FALCON code (FALCON-PSI) that addresses the effects of the selected characteristics of fast thermal transients (e.g., impulse width), fuel rod design (e.g., active fuel attack length) and boundary conditions (e.g., the coolant conditions) on fuel behaviour during a RIA. Specifically, the analysis of the governing processes for the fuel rod behaviour during the RIA events simulated in the experimental facility of the Nuclear Safety Research Reactor (NSRR, Japan) are in the focus of the present study. The results obtained can be useful for a better transfer of the NSRR test results in relation to the corresponding behaviour in LWRs and furthermore might also support the planning of future additional experiments.

### 1. Introduction

A Reactivity Initiated Accident (RIA) is an extremely infrequent event, which is categorised as accident ( $10^{-4} \dots 10^{-6}/\text{yr}$ ) for the Light Water Reactors (LWRs). Consequently, the vast majority of information necessary for safety analysis of the corresponding Design Basis Accidents (DBAs) has been obtained from special experimental programmes [1] simulating conditions typical of RIA (ALPS, CABRI, etc.). A good complement to the knowledge gained from the experimental studies can be derived from theoretical models (fuel behaviour codes) that are validated using the experimental data. Conversely, the fuel behaviour codes can be used to better target the experimental research by exploring the parameter space of interest. In addition, the code analysis is also invaluable for the interpretation of the test results by gauging the relative importance of the different processes on PCMI during RIA for a range of conditions.

The Paul Scherrer Institut (PSI) with support from the Swiss Nuclear Utilities (*swissnuclear*) has been taking active part in one of the most comprehensive of the corresponding experimental programmes, ALPS (i.e., Advanced LWR fuel Performance and Safety research programme), which has been performed by the JAEA (Japan). The Swiss contribution consists of the provision of high-burn-up fuel samples, after pre-irradiation in the Leibstadt NPP, a 3600 MW BWR, respective Post Irradiation Examination (PIE) [2], as well as sophisticated modelling [3] of the fuel behaviour during base irradiation and under RIA conditions. The modelling results discussed in this paper represent a step in the latter direction. Specifically, after considerable amount of experimental information had been accumulated in relation to the limiting fuel enthalpy at room temperature and atmospheric pressure, a new series of tests has recently been launched [4] using typical operational conditions of LWRs (e.g., coolant temperature of 559 K and pressure of 70 bar for BWR). Furthermore, some modifications in the design of the test-fuel rod have become necessary for the new type of experiments.

It therefore appears as worthwhile to apply an integral fuel behaviour code independent from JAEA to discriminate the effects of the coolant conditions from the possible effects of the design change. Besides, open questions are still surfacing with regard to representativity of the ALPS tests (and some others), e.g., the use of relatively small values for the impulse Full Widths at Half Maximum (FWHM) compared to values expected from RIA transients in LWRs [5].

The present paper aims at a fresh interpretation of early and more recent NSRR RIA tests and the effects identified might be considered in the planning of future experiments.

## 2. Main RIA-related features of FALCON (PSI) analysis

The FALCON fuel analysis and licensing code [6] has been used to perform the present study. FALCON is a FEM-based code providing comprehensive 2-D analysis of the thermo-mechanical and thermo-physical behaviour of the fuel rods under base irradiation, during power ramps (slow power transients) and fast transients, including the RIA and LOCA. The code has been proven to be applicable to the analysis of the above-mentioned types of fuel behaviour [7], RIA included, through the strict validation and verification procedures, which were carried out by the primary code developer (Anatech Corp. -USA) and proprietor (EPRI -USA). PSI is EPRI's licensee and a dedicated user of the FALCON code. Furthermore, the code has been recently enhanced at PSI by means of coupling with the fission Gas Release and gaseous SWelling Advanced (GRSW-A) model [8].

The GRSW-A model analyzes simultaneously the processes of Fission Gas Release (FGR), gaseous swelling and microstructural evolution in the uranium dioxide fuel subjected to elevated temperature and/or irradiation to a high burn-up. The most important processes addressed in the model are: (1) The group of intragranular processes including the kinetics of point defects in the lattice and gas mono-atom diffusion, as well as nucleation, migration, coalescence, irradiation-induced resolution and point-defect-diffusion-controlled growth of gaseous pores and bubbles; (2) The behaviour of High Burn Structure (HBS), which is analyzed using the phenomenological model for the intragranular polygonisation coupled with the mechanistic model for the gaseous pores formation and growth, considering fission gas release into the fuel rod free volume as one of the possible outcomes of the overall fission gas behaviour; (3) The process of high-temperature recrystallisation. Specifically, the analysis addresses the phenomenon of equiaxed-grain growth with emphasis on the corresponding effects on the grain-boundary fission gas and gaseous porosity; (4) The behaviour of as-fabricated intragranular pores that is closely related to the macroscopic processes of irradiation-induced densification and high-temperature sintering.

After having been coupled with GRSW-A, the modified FALCON code has been subject to verification and validation [9]. Particular attention is paid to the code validation for RIA-type events [3].

### *Thermo-mechanical behaviour*

The material behavior description of the FALCON code covers the extensive range of effects, from elastic response to the elastic-plastic-creep strain-rate dependent (viscoplastic) response in high temperature and high power regimes. The latter seems to be essentially important for the adequate modeling of the fuel rod subject to the RIA. Admittedly, the use of large strain theory is crucial for adequate modeling of the cladding response to the LOCA. Besides, this capability of the analysis can eventually become relevant to the RIA as well, e.g., at high FGR resulting in a high excessive internal gas pressure in the rod free volume in combination with the increase in cladding temperature due to the DNB.

With regard to the cladding strain-stress conditions during the RIA, an important feature of the corresponding analysis can arise from the short-term occurrences of the extremely high temperature gradient in the cladding, which is shown by the examples in Fig.1. This must result in the considerable additional thermo-mechanical stresses in the outer part of the cladding compared to any other normal and off-normal conditions of the fuel rods.

### *Thermo-physical behaviour*

The thermo-physical part of the FALCON code includes the solution of the unsteady-state thermal conductivity problem in the pellet in consideration of the evolution of the radial non-uniformity of the volumetric power due to the excessive build-up of the fissile Pu on the pellet periphery during the base irradiation. These capabilities of the analysis allow capturing the behaviour of the fuel temperature profile in the early quasi-adiabatic phase of the fast thermal transients, as shown in Fig. 2. Specifically, the calculated local temperature shows up the distinct upswing towards the pellet periphery, which qualitatively follows after the profile of the volumetric heat generation unless the temperature distribution is forced to the standard shape by the processes of thermal conductivity and heat transfer.

Figure 1. Calculated cladding temperature during a RIA test for the two types of coolant conditions  
 RTLP: RT-capsule of the NSRR. HTHP: HTHP-capsule of the NSRR.  
 Note: Calculation assumes no DNB during the RIA simulated.

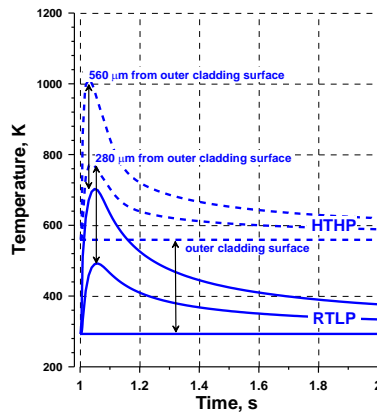
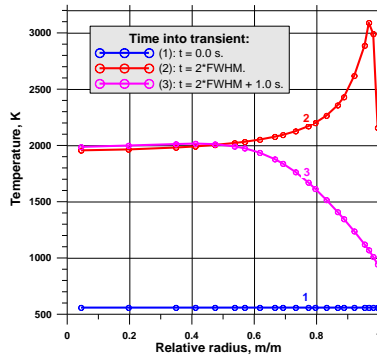
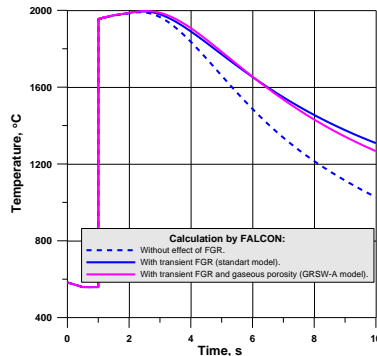


Figure 2. Calculated evolution of temperature profile across the pellet over a RIA simulated  
 Pellet-averaged burn-up: 70 MWd/kgU



As for the micro-structural state and FGR of the pellets, it can hardly have an essential influence on the early quasi-adiabatic phase of the transient and, thereby, has very minor impact on the peak temperature of the fuel during the RIA. However, a visible effect of the FGR on the temperature decay after the energy insertion is predicted by FALCON (both with and without the GRSW-A model) due to the reduction in the pellet-cladding heat conductance co-efficient, which is shown in Fig.3.

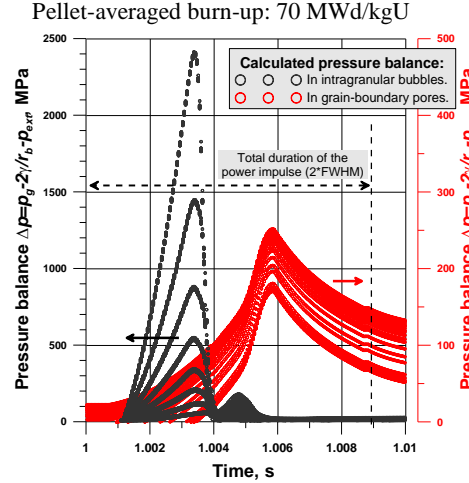
Figure 3. Calculated centre-line fuel temperature during RIA simulated (calculation using FALCON-PSI against standard FALCON models with and without effect of FGR)  
 Pellet-averaged burn-up: 70 MWd/kgU



**Fuel-pellet swelling and FGR**

From the viewpoint of modelling the fuel structure evolution and fission gas behaviour, the characteristic feature of the fast enough RIA events is the predicted drastic increase of the gas pressure in the bubbles, which accompanies the increase in temperature after the prompt energy insertion into the fuel (Fig.4).

Figure 4. Calculated evolution of excessive pressure in the bubble and pores caused by prompt energy insertion during RIA simulated (calculation with FALCON-PSI)



The restraining, or even totally ‘prohibiting’, effect of the intragranular bubble over-pressure on the bubble coalescence was already discussed in [3]. Below proposed is a simple approach to the quantification of the corresponding effect on the rate of bubble coalescence, by the example of the coalescence process caused by the bubble random motion.

Let’s consider a simple hydrostatic stress in the isotropic fuel material surrounding a spherical bubble, which is induced by the bubble over-pressure  $\Delta P$ :

$$\Delta P = P_g - 2\gamma/R - P_{ext}$$

where  $\Delta P$  is the pressure balance on the surface of the pore,  $P_g$  the gas pressure in the bubble,  $\gamma$  the specific bubble surface energy,  $2\gamma/R$  the capillarity pressure,  $P_{ext}$  the external pressure exerted on the bubble.

From the condition of the mechanical equilibrium, for the hydrostatic stress in the material element at the distance  $r$  from the centre of the bubble one can write:

$$\sigma = \Delta P \frac{R^2}{r^2}.$$

where  $\sigma$  is the hydrostatic pressure ( $\sigma = \sigma_{xx} = \sigma_{yy} = \sigma_{zz}$ ),  $r$  the distance from the bubble centre to the material element in question.

The equation for the elastic stress energy density,  $u$ , of the hydrostatic stress field reads:

$$u = \frac{\sigma^2}{2K}$$

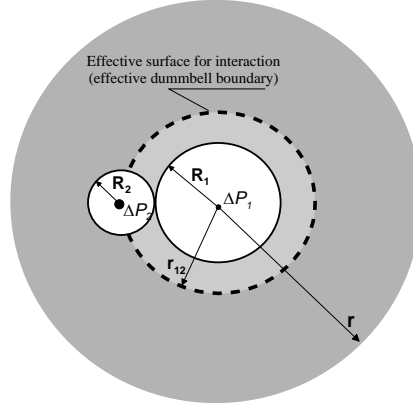
where  $K$  is the bulk modulus of the fuel material.

Assuming the additive superposition of the elastic stress fields induced by the two small closely-distanced bubbles, as shown in Fig.5, the elastic interaction energy density,  $u_{12}$ , can be approximately expressed as follows:

$$u_{12} = \frac{\sigma_1^2}{2K} + \frac{\sigma_2^2}{2K} - \frac{(\sigma_1 + \sigma_2)^2}{2K} \approx \frac{R_1^2 R_2^2}{K} \frac{\Delta P_1 \Delta P_2}{r^4}$$

where  $r$  is the effective distance from the fuel material element considered to the notional small dumbbell formed by the two bubbles in question.

Figure 5. Model schematics for the analysis of the effect of bubble over-pressure on coalescence rate



Consequently, the total interaction energy,  $E_{12}$ , can be estimated from the expression as follows:

$$E_{12} = \int_{r_{12}}^{\infty} u_{12} dV = 4\pi \frac{R_1^2 R_2^2}{K} \frac{\Delta P_1 \Delta P_2}{r_{12}}$$

where  $r_{12}$  is the distance between the interacting bubbles.

The equation for a mechanical force exerted by the elastic stress field of the bubble '1' on the bubble '2',  $F_{12}$ , is as follows (meaning that the force is positive in case of the repulsion, and vice versa):

$$F_{12} = -\frac{dE_{12}}{dr_{12}} = 4\pi \frac{R_1^2 R_2^2}{K} \frac{\Delta P_1 \Delta P_2}{r_{12}^2}$$

According to the general treatment of the bubble mobility [10], the biased motion velocity,  $V_2$ , of the bubble '2' towards/outwards the bubble '1' due to the force  $F_{12}$  can now be expressed as follows:

$$V_2 = M_2 F_{12}$$

where  $M_2$  is the bubble mobility.

The bubble mobility can be related to the bubble diffusion coefficient by the equation of Nernst-Einstein:

$$M_2 = \frac{D_2}{kT}$$

where  $M_2$  is the bubble mobility,  $D_2$  the bubble diffusion coefficient,  $k$  Boltzmann constant,  $T$  the local fuel temperature.

The classic equation of Chandrasekhar [11] for the rate of bubble coalescence due to random motion reads:

$$K_{12} = 4\pi(R_1 + R_2)(D_1 + D_2)C_1 C_2,$$

where  $K_{12}$  is the volumetric rate of bubble coalescence for the classes '1' and '2',  $C_1$  and  $C_2$  the concentrations of intragranular bubbles for the classes in question,  $R_1$  and  $R_2$  the effective radii of the interacting species,  $D_1$  and  $D_2$  the diffusion coefficients of the bubbles.

Let's re-write the above equation in a slightly modified form:

$$K_{12} = j_2 S_{12} C_1,$$

where  $j_2$  is the notional flux density of the species '2' (considered as points) through the effective interaction-surfaces (which is the surface of the hypothetic immobile sphere of radius  $R_{12} = R_1 + R_2$ , shown by broken curve in Fig.5),  $S_{12}$  the area of the effective interaction-sphere in question.

For the mentioned bubble flux density, one can write:

$$j_2 = V_{2R} C_2,$$

$$V_{2R} = \frac{D_1 + D_2}{R_1 + R_2}$$

where  $V_{2R}$  is the effective velocity of the drift of the bubble ‘2’ towards the bubble ‘1’ at the interaction-surface, which is caused by bubbles’ random motion only.

Consequently, the corrected form of the equation for the bubble coalescence rate could be obtained by the replacing of  $V_{2R}$  with the effective drift velocity,  $V_{2eff}=V_{2R}-V_2$ , reduced due to the assumed bubble interaction. Finally, the proposed equation for the bubble coalescence rate reads:

$$K_{12}^* = K_{12}(1 - k_{el}),$$

$$k_{el} = 4\pi \frac{R_1^2 R_2^2}{K} \frac{\Delta P_1 \Delta P_2}{(R_1 + R_2)kT}$$

where  $K_{12}$  is the unaffected value for the coalescence rate,  $k_{el}$  the dimensionless factor accounting for the effect of the assumed elastic interaction.

It is worthy of noting that the above-presented modified equation for the bubble coalescence rate is deemed to be applicable in case the expression in brackets on the right-hand-side falls into the range from zero to unity. The negative values obtained for  $K_{12}^*$  must be interpreted as the fully ‘prohibited’ coalescence between the corresponding species. Note that the non-modified classic equation for the coalescence rate remains in force in case one of, or both the interacting bubbles are in the state of equilibrium, or the over-pressure is not applicable, i.e., for the gas mono-atoms and atom-clusters treated by the model as ‘solid’ spheres.

Finally, after the appropriate modification in the treatment of the intragranular bubble interaction, the application in the modified FALCON code to the analysis of an intensive thermal transients has been resulting in the prediction of the evolution of the bubble size-distribution [see an example in Fig.6(a)] that is equivalent to the significantly lower intragranular fuel swelling, which is expected to occur before a considerable amount of intragranular gas has arrived at the grain boundary, than the swelling predicted without a modification of the kind in question.

Figure 6. Calculated evolution of the parameters of fuel micro-structure in the pellet centre over an intensive thermal transient (calculated with FALCON-PSI)

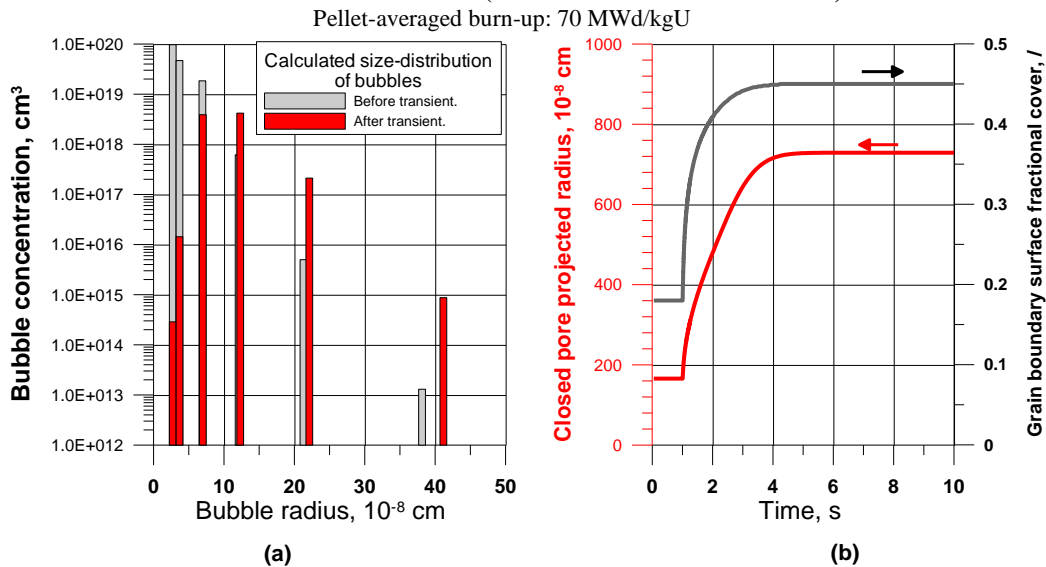
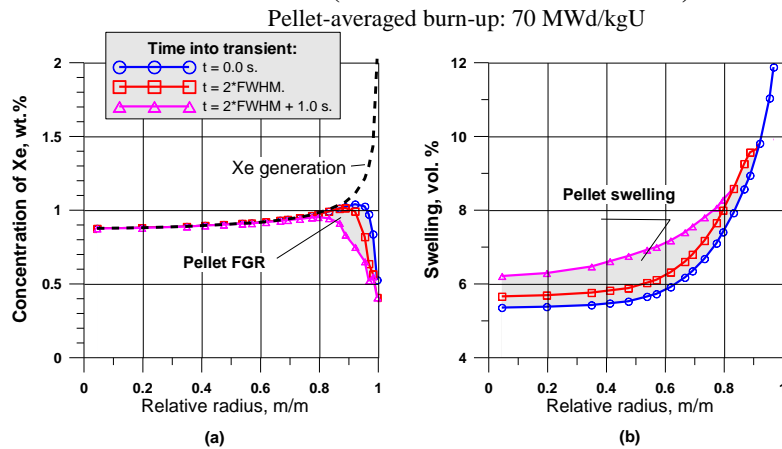


Figure 7. Calculated evolution of macroscopic characteristics of the pellet over an intensive thermal transient (calculated with FALCON-PSI)



The predicted evolution of the fuel microstructure related to the grain boundaries (closed pore size and grain-boundary fractional cover) is shown in Fig.6 (b). The swift over-pressurising due to the temperature elevation and the intragranular gas loss must lead to as fast intergranular FGR as in the cases of so-called burst-release. Moreover, the FGR enhancement in the failed rods due to the grain boundary separation by the gaseous-pore-growth has been shown feasible [3] by the corresponding parametric study, which accounted for the fuel oxidation after the contact with the coolant.

Finally, moving on to the results of the FALCON (PSI) analysis as applied to macroscopic fuel behaviour related to the predicted evolution in the fuel microstructure, one should note the more complicated character of the relationship between integral FGR and swelling of the pellets during the RIA, than in the power ramps or the base irradiation.

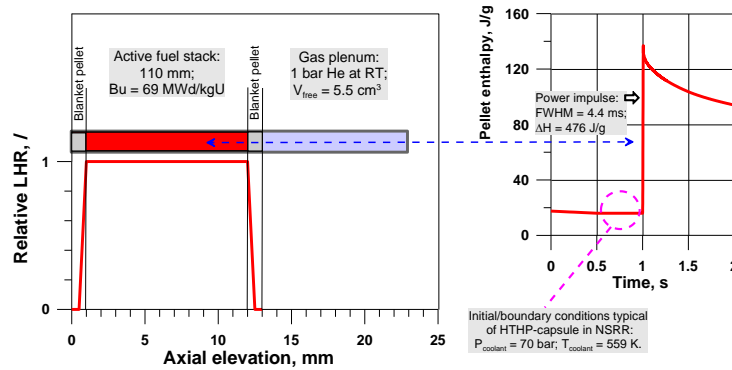
As shown in Fig.7 (a), the predicted impact of the pellet bulk and periphery on these two characteristics of the pellet behaviour can essentially differ from each other. Specifically, according to the calculation, the outer region of the pellet (with the exception for the very rim that is expected to retain quite a limited amount of fission gases after the base irradiation) has significantly higher propensity to FGR than the centre. This result of modelling is related to the combined effect of the HBS, which is formed during the base irradiation, and the above-mentioned upswing of the local temperature at the pellet periphery during the early phase of the RIA. Evidently, the intragranular polygonization and a large amount of the fission gases accumulated in the HBS-porosity allow for the significant FGR from the pellet zone in question, in spite of a very short duration of the high-temperature phase in this zone, compared to the centre. On the other hand, the relatively high temperature is expected to be sustained for a longer time in the central part of the pellet (see Figs.2, 3), while a lot of gas here is predicted to be retained in the grain interior of the fuel of the normal structure. Generally, this gas may not have enough time to be released, but quite enough to form the gaseous bubbles and pores and, thereby, to contribute to the transient pellet swelling [see Fig.7 (b)].

### 3. Results

#### *Base case for parametric study*

The parameters of the NSRR test LS-1 [12] have been used for the specification of the base case for the present parametric study, including test fuel rod geometry, fuel pre-irradiation conditions and the parameters of the power pulse, which is outlined in Fig.8. The LS-1 was carried out in the RT-capsule using the high-burn-up fuel sample pre-irradiated in the BWR KKL [2]. The analysis of the LS-1 test was performed - as a part of the FALCON (PSI) validation - and the results were published in [3]. However, the majority of the calculations of the present study have been performed assuming coolant conditions of the HTHP-capsule, which was recently used for the NSRR test LS2.

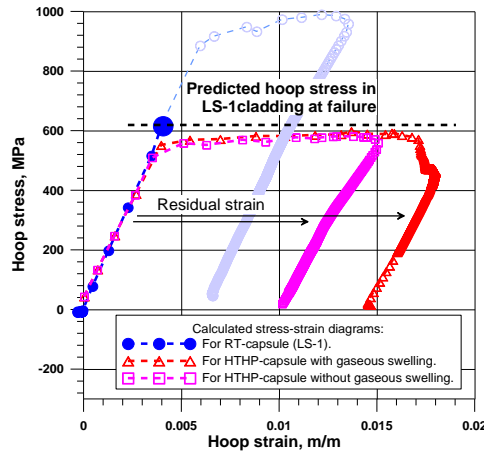
Figure 8. Fuel rod geometric presentation and test parameters accepted as the base case in present study



**Effects of coolant conditions on cladding strain-stress behaviour during RIA**

The assumed transition from the conditions of the RT-capsule to those of the HTHP has been shown to have a significant influence on the predicted strain-stress diagram, as presented in Fig.9 for the cladding outer element during the high-power and high-temperature phases of the test. Specifically, the switching from the elastic regime to the plastic regime in the high-temperature cladding is predicted to occur at a lower level of stress when compared to the values for the RT-capsule at the moment of fuel rod failure in the LS-1 test. Note that the latter value has been defined as the stress calculated by the code for the measured time of the cladding failure [12] in the LS-1 test.

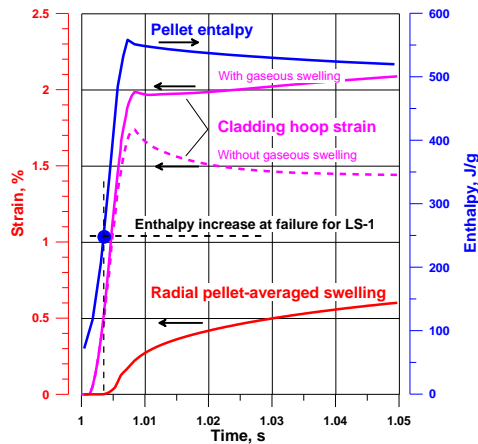
Figure 9. Calculated strain-stress diagrams for the cladding outer element during RIA test (calculated with standard FALCON and FALCON-PSI)



**Impact of gaseous pellet swelling on fuel rod mechanical behaviour during RIA**

As can also be seen from the results shown in Fig.9, gaseous swelling can cause a considerable increase in the residual cladding strain, for the HTHP conditions, where significant plastic deformations are predicted to occur. The important impact of the gaseous pellet swelling on the cladding strain is also shown in Fig.10 for the high-temperature cladding conditions. Besides, no impact of the gaseous swelling is expected to contribute to the cladding failure in the LS-1 test (conducted with the low-temperature cladding), according to our calculations.

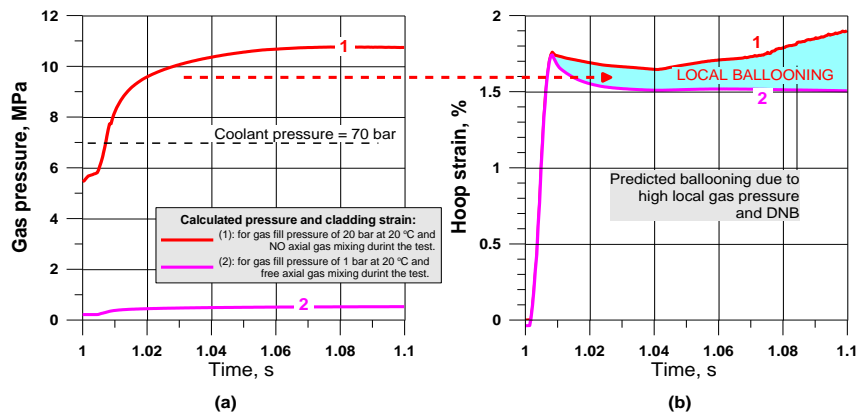
Figure 10. The calculated dynamics of strain in cladding inner element against pellet swelling and enthalpy during RIA test (calculated with FALCON-PSI)



### Effect of internal gas pressure

A crucial characteristic feature of the RIA tests conducted within the ALPS programme is the use of a low fill-gas pressure (e.g., atmospheric pressure at RT). Normally, in this case, the calculated inner gas pressure in the test fuel rod is well below the coolant pressure in the HTHP-capsule throughout the test, which is shown in Fig.11 (a). Under these conditions, a ballooning-type deformation of the cladding is not expected based on an extensive calculational study using several strong assumptions: Occurrence of DNB (resulting in the increase in cladding temperature above 750 °C, which is the limit temperature for the transition to high-temperature creep), FGR enhancement due to an assumed fuel hyper-stoichiometry (considering values for the O/U-ratio as high as 2.015 in the non-defected high-burn-up rod), and finally constrained axial mixing of the gas released during the transient. However, when the higher fill-gas pressure (namely: 20 bar at 20 °C, which is typical for a BWR fuel rod at a peak-pellet burn-up of ~70 MWd/kgU) is assumed in the calculation in addition to the above assumptions, a drastic increase of the cladding strain is predicted via high-temperature creep (i.e., the local ballooning of the cladding); this is shown in Fig.11 (b).

Figure 11. The calculated dynamics of internal gas pressure against cladding strain during RIA test for the different assumptions on fill-gas pressure (calculated with FALCON-PSI)

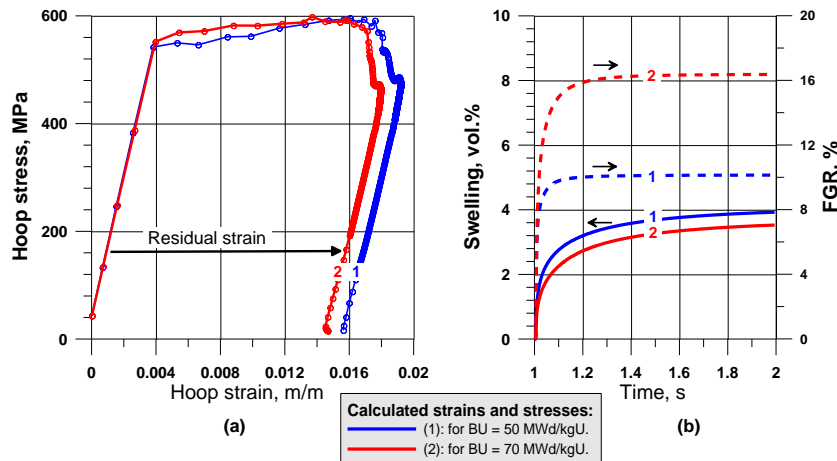


### Effect of high fuel burn-up

It is no doubt that the hypothetical transition from a pellet burn-up of 50 MWd/kgU to 70 MWd/kgU must result in the significant increase in the transient FGR [see Fig.12 (b)]. This prediction is related to the fact that the increase in the pellet burn-up is credited with a significant transformation of the fuel structure at the pellet periphery, which is expected to cause a higher propensity to both steady-state and transient FGR

(see the corresponding discussion in the previous Chapter). Inversely, in line with the discussion of the previous Chapter, the extension of the HBS-zone must result in a reduction of the non-restructured pellet zone, which has been shown to contribute in a most efficient manner to the overall pellet swelling. As a result, the calculated transient pellet swelling and cladding strain have been shown to stay at a meta-stable level (or even slightly decrease) for the burn-up increase in question, which is shown in Figs.12 (a) and (b).

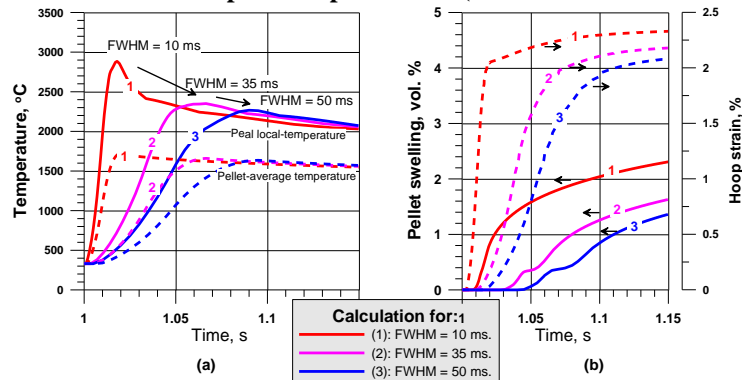
Figure 12. **The calculated mechanical response of cladding against pellet swelling and FGR during RIA test for two levels of fuel burn-up (calculated with FALCON-PSI)**



**Effect of impulse width**

The numerical research has been performed with FALCON (PSI) into the effects of the impulse width (using the values of FWHM in the range from 5 ms to 50 ms, under all the other conditions being kept the same), which is illustrated in Fig.13. As seen from the results of the calculation for the fuel temperature, the most significant effect is expected for the peak-local temperature, which is usually reached at the pellet outer surface just after the energy insertion. Evidently, this prediction is related to the fact that for the slower impulses the early high-power phase of the transient can no longer be treated as quasi-adiabatic when compared to the shorter impulses, because more time is available for (1) heat conduction and (2) thermal conductivity to act and thereby flatten out the outer peak of the fuel temperature. On the other, the effect of the impulse width that is related to the heat conduction through the pellet-cladding gap refers to the energy dissipation from quite a limited outer layer of the pellet, while the predicted volume-average temperature remains nearly unaffected [see Fig.13(a)].

Figure 13. **The calculated dynamics of fuel temperature against pellet swelling and cladding strain for the different values of the power impulse width (calculated with FALCON-PSI)**



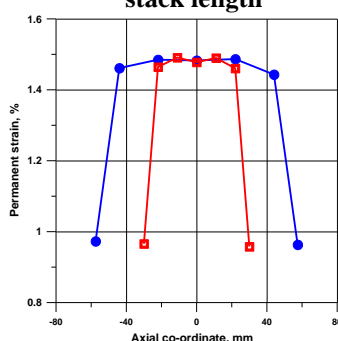
Consequently, the overall effect of the power pulse width on the residual cladding hoop strain is expected to be essentially dependent on the corresponding effect on the gaseous pellet swelling and its relative contribution

when compared to the pure thermal expansion. For example, the calculation presented in Fig.11 was performed with the assumption of the fuel being effectively hyper-stoichiometric ( $O/U=2.015$ ) during the high-power and high-temperature phases of the transient, which suggests an enhancement of the transient FGR and gaseous swelling. A certain increase in the cladding hoop strain has thus been predicted by this analysis, due to the hypothetical increase of the FWHM in question, which is shown in Fig 13 for the impulse FWHM in the range from 10 ms to 50 ms.

### *Effect of active fuel length*

One of the modifications to be undertaken in the NSRR RIA-test facility to provide the testing at high cladding temperature is the reduction on the active fuel length in the fuel rods tested [13]. Consequently, there has been a concern about possible effects of this modification on the fuel behaviour under the RIA simulated, particularly on the critical enthalpy for failure. One of the conceivable reasons for these effects could be an increase in the ratio of the heat-exchanging surface to the active fuel volume, while another is a possible impact of the axial thermal conductivity. Calculations to investigate the impact of the active fuel stack length have been performed using the conditions of the base case (see Fig.1), but considering the active fuel stack length of 11 cm (just like for the testing in the RT-capsule) against the one of 6 cm (which is more typical for the HTHP-capsule). As shown in Fig. 14, our calculation did not confirm the concern: The predicted cladding peak strains are nearly the same for the both cases considered, keeping in mind that the permanent cladding strain due to a thermal transient is deemed to be a relevant indicator for estimating the relative probability of the fuel failure, given all the other conditions are kept the same.

Figure 14. **Predicted residual cladding strain in response to a RIA test for two values accepted for active fuel stack length**



## 4. Summary and conclusions

Presented in the paper are the results of a parametrical study with the use of the special version of the FALCON code (FALCON-PSI) that addresses the effects of the selected characteristics on fuel behaviour during the RIA-simulating transients in the Nuclear Safety Research Reactor (NSRR), namely for:

- The effects of coolant conditions on cladding strain-stress behaviour during RIA.
- The impact of gaseous pellet swelling on fuel rod mechanical behaviour.
- The effects of internal gas pressure.
- An additional insight into effects of high fuel burn-up.
- The effect of impulse width.
- The effect of active fuel length in the test-fuel-rod.

Moreover, the analysis of the governing processes for the fuel rod thermo-physical and thermo-mechanical behaviour during the RIA events simulated in the experimental facility of the NSRR is in the focus of the present study, as well.

Although the present paper doesn't deal with any new experimental data, it aims at a fresh interpretation of early and more recent NSRR RIA tests and the effects identified might be considered in the planning of future experiments.

## Acknowledgment

This work was partly funded by the Swiss Federal Nuclear Safety Inspectorate (ENSI) in the framework of the STARS project. Some specific studies have been supported by *swissnuclear* through its expert group on fuel safety.

The authors also would like to thank T. Fuketa and T. Sugiyama from JAEA for their review of the paper.

## References

- [1] “Review of High Burn-up RIA and LOCA Database and Criteria”, NEA/CSNI/R(2006)5.
- [2] G. Ledergerber, et al., “Characterisation of High Burn-up Fuel for Safety Related Fuel Testing”, JNST, 43, 1006-1014 (2006).
- [3] G. Khvostov, M.A. Zimmermann, T. Sugiyama, T. Fuketa, “On the use of the FALCON code for modeling the behaviour of high burn-up BWR fuel during the LS-1 pulse-irradiation test“, Proc. Int. Conf. on the Physics of Reactors, PHYSOR'08, (14-19 September 2008), Interlaken, Switzerland, (CD-ROM, FP213).
- [4] T. Sugiyama, M. Umeda, H. Sasayima, M. Suzuki and T. Fuketa, “Effect of Initial Coolant Temperature on Mechanical Fuel Failure under Reactivity-Initiated Accident Conditions”, TOP FUEL 2009, Paris, France, September, (2009).
- [5] Hakim Ferroukhi and Martin A. Zimmermann: “Study of the PWR REA pulse width for realistic UO<sub>2</sub> and MOX core designs using 3D kinetics methods”, Annals of Nuclear Energy (2009), doi:10.1016/j.anucene.2009.04.007.
- [6] *Fuel Analysis and Licensing Code: FALCON MOD01: Volume 1: Theoretical and Numerical Bases*, EPRI, Palo Alto, CA: (2004). 1011307.
- [7] *Fuel Analysis and Licensing Code: FALCON MOD01: Volume 3: Verification and Validation*, EPRI, Palo Alto, CA: (2004). 1011309.
- [8] G. Khvostov, “A Dynamic Model for Fission Gas Release and Gaseous Swelling Integrated into the FALCON Fuel Analysis and Licensing Code”, Paris, France, September, (2009).
- [9] Luis E. Herranz, I. Vallejo, G. Khvostov, J. Sercombe, G. Zhou. “Insights into Fuel Rod Performance Codes during Ramps: RESULTS of a CODE BENCHMARK based on the SCIP PROJECT”, TOP FUEL '09, Paris, France, September, (2009).
- [10] D.R. Olander, Fundamental aspects of the nuclear fuel reactor elements, US Energy Research and Development Administration, (1976).
- [11] S. Chandrasekhar, Rev. Mod. Phys. 15: 1 (1973).
- [12] T. Sugiyama, M. Umeda, T. Fuketa, H. Sasajima, Y. Udagawa and F. Nagase, “Failure of high burn-up fuels under reactivity-initiated accident conditions”, Proc. Int. Conf. on the Physics of Reactors, PHYSOR'08, (14-19 September 2008), Interlaken, Switzerland, (CD-ROM, FP118).
- [13] T. Sugiyama, “PCMI Failure of High Burn-up Fuel under High Temperature RIA Conditions”, Presentation at Fuel Safety Research Meeting 2009, Tokai, Japan, (2009).

PSI  
 Laboratory for Reactor Physics and Systems Behaviour  
 Nuclear Energy and Safety Department

## Parametric Study of Fuel Rod Behaviour during the RIA Using the Modified FALCON Code

G. Khvostov<sup>1)</sup>, M.A. Zimmermann<sup>2)</sup>, G. Ledergerber<sup>2)</sup>

<sup>1)</sup> Paul Scherrer Institut, Switzerland  
<sup>2)</sup> Kernkraftwerk Leibstadt AG, Switzerland

Top Fuel 2009 Meeting, Paris, France - September 9-10, 2009 PSI/LRS/KG41/Paper 2009 (1)

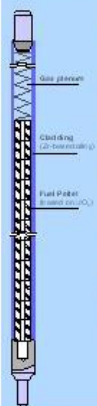
PSI  
 Laboratory for Reactor Physics and Systems Behaviour  
 Nuclear Energy and Safety Department

## Contents

- Main RIA-related features of FALCON (PSI) analysis.
  - ✓ Thermo-mechanical behaviour.
  - ✓ Thermo-physical behaviour.
  - ✓ Fuel-pellet swelling and FGR.
- Results of the parametric study.
  - ✓ Base case for the study.
  - ✓ Effects of coolant conditions on cladding strain-stress behaviour during RIA.
  - ✓ Impact of gaseous pellet swelling on fuel rod mechanical behaviour during RIA.
  - ✓ Effect of internal gas pressure.
  - ✓ Effect of high fuel burn-up.
  - ✓ Effect of impulse width.
  - ✓ Effect of active fuel length.
- Summary and conclusions

Top Fuel 2009 Meeting, Paris, France - September 9-10, 2009 PSI/LRS/KG41/Paper 2009 (2)

PSI  
 Laboratory for Reactor Physics and Systems Behaviour  
 Nuclear Energy and Safety Department

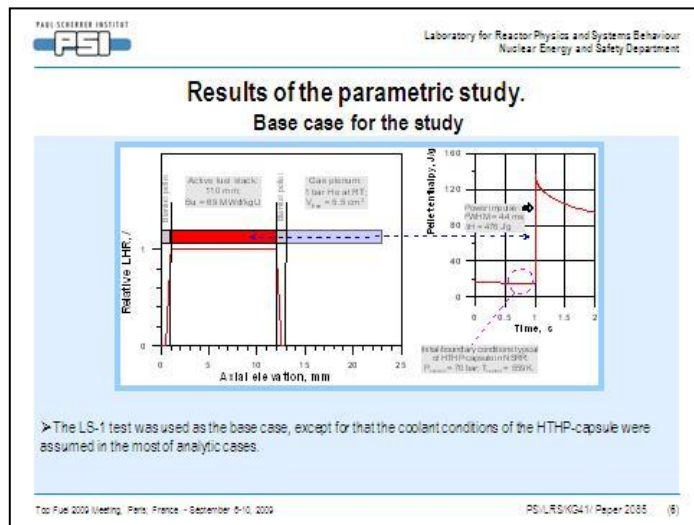
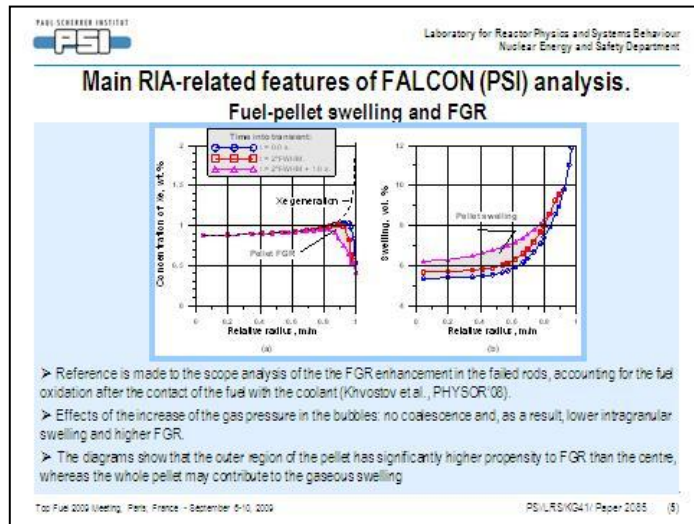
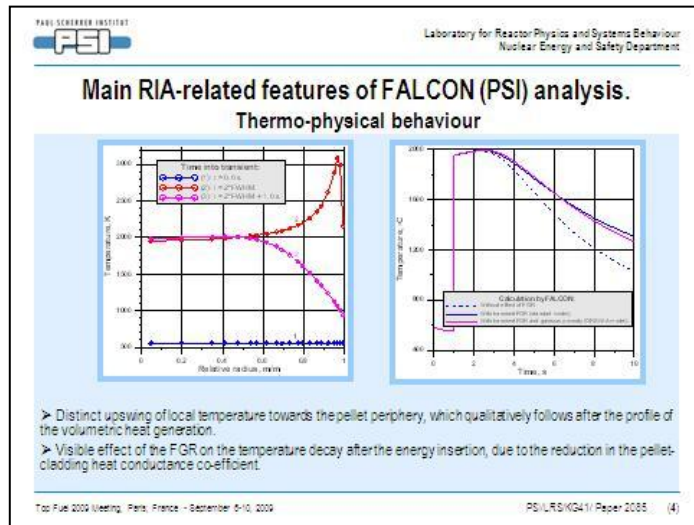


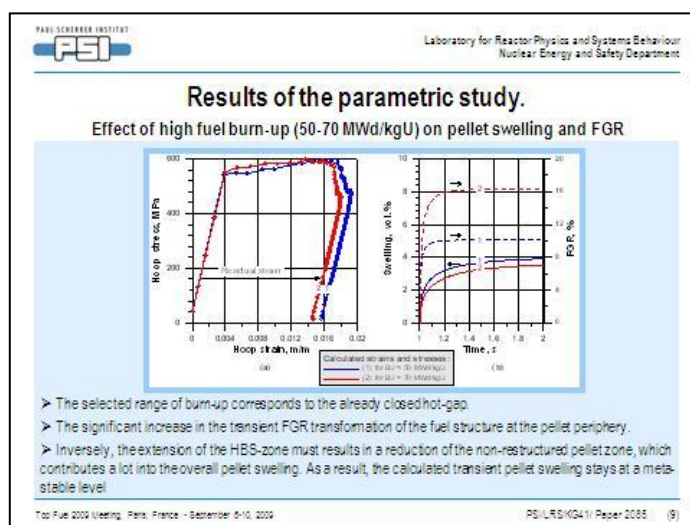
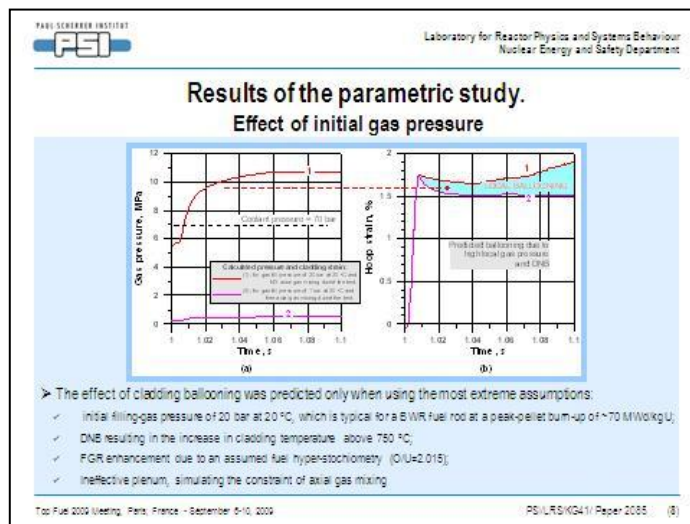
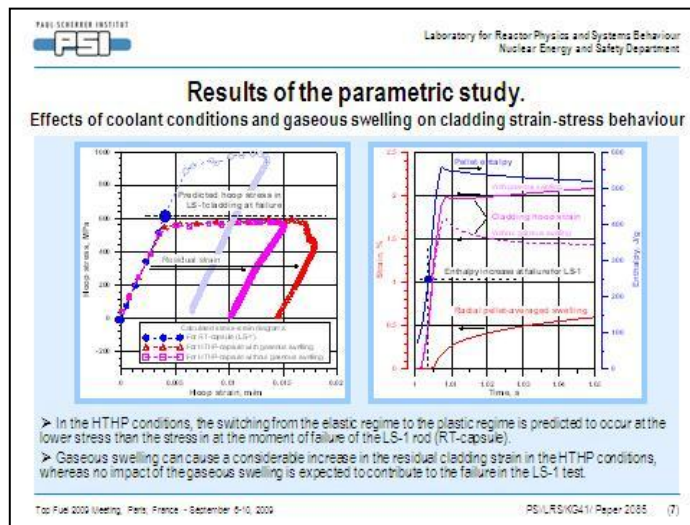
❑ The FALCON fuel analysis and licensing code has been used to perform the present study.

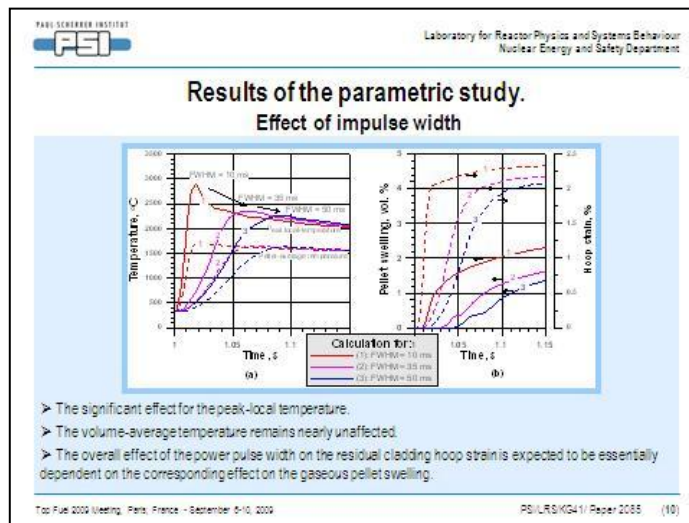
- ❑ The code is under development by Anatech Corp. (USA), while under property of the Electric Power Research Institute (EPRI-USA).
- ❑ The solution processor of FALCON is based on the FEM, that allows for 2-D analysis with representation of the fuel-rod-elements geometry using both r-z and r-θ systems of co-ordinates.
- ❑ The code makes it possible to analyze under both steady states and fast transients conditions.
- ❑ Provides possibility of replacing the default model with the user-developed ones

❑ The code has recently been coupled with a model (sub-code) that provides detailed calculation of fuel swelling, micro-structural evolution and FGR.

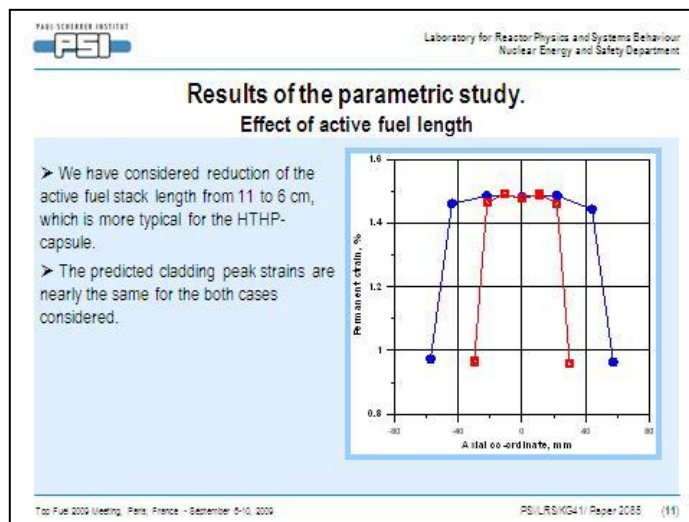
Top Fuel 2009 Meeting, Paris, France - September 9-10, 2009 PSI/LRS/KG41/Paper 2009 (3)







- > The significant effect for the peak-local temperature.
- > The volume-average temperature remains nearly unaffected.
- > The overall effect of the power pulse width on the residual cladding hoop strain is expected to be essentially dependent on the corresponding effect on the gaseous pellet swelling.



PSI Laboratory for Reactor Physics and Systems Behaviour  
Nuclear Energy and Safety Department

### Summary and conclusions

- (1) The analysis of the governing processes for the fuel rod thermo-physical and thermo-mechanical behaviour during the RIA was in the focus of the present study.
- (2) The effects of the selected characteristics of the test-fuel-rods and boundary conditions on fuel behaviour during the simulated RIA were investigated.
- (3) The present work aims at a fresh interpretation of early and more recent NSRR RIA tests and the effects identified might be considered in the planning of future experiments

Top Fuel 2009 Meeting, Paris, France – September 6-10, 2009 PSI/LRS/KG4-1/ Paper 2085 (12)

## MAJOR SENSITIVITIES OF MODELLING A HIGH BURN-UP FUEL ROD WITH FRAPCON-3/FRAPTRAN CODES

**M.T. del Barrio, I. Vallejo, L.E. Herranz**  
CIEMAT-Unit of Nuclear Safety Research, Spain

### 1. Introduction

The main objective of a safety tool related to fuel rod analysis is to estimate as close as possible the fuel performance both under steady-state and transient conditions. During the last years, a significant effort to extend codes domain up to burn-ups higher than those currently reached has been done. In addition, a considerable interest has been also arisen on accidental conditions of high burn-up fuel rods, especially under reactivity initiated (RIA) and loss of coolant accidents (LOCA), due to the possible inadequacy of the failure criteria so far accepted. Regarding RIA, actual safety criteria were developed several decades ago for fresh or low burn-up fuel rods, fairly away from that currently achieved. Moreover, fuel rod geometries and cladding materials have been modified since the criteria were developed. So, both codes and new safety criteria assessment require integral and separate effects tests in order to understand and model the changes or emergence of new operative mechanisms in current fuel rods at high burn-up.

Up to date several experimental programmes have been carried out in order to investigate the fuel rod behaviour during a RIA event. Some of them, as those executed at Impulse Graphite Reactor (IGR), Nuclear Safety Research Reactor (NSRR)<sup>1</sup> facilities or Argonne National Laboratory (ANL)<sup>2</sup> were performed under fuel rod conditions far away from that currently achieved. In order to analyze the behaviour of present fuel rod designs at medium and high burn-up, a comprehensive RIA program<sup>3</sup> was launched in 1992 by the former French Nuclear Safety and Protection Institute. In a first phase of the investigation program, the nine REP-Na tests performed mainly demonstrated the detrimental effect of the high corrosion levels in Zr-4 mechanical properties, and the potential influence of the fission gases as an additional loading mechanism on the cladding failure<sup>4</sup>. Afterwards, the CABRI International Program (CIP), launched in 2000 under the auspices of the OECD and a broad international cooperation<sup>5</sup>, has tried to address the remaining opened questions. The program also included separate effect tests in cladding materials and modelling, in order to improve the understanding of phenomena involved in the transient. The transient tests carried out so far in the CABRI facility have been performed under liquid sodium cooling conditions. Because of the better coolant properties of sodium with regard to water, just the PCMI stage, before the rapid overheat of the cladding for thermal conduction can be analyzed through these tests.

---

<sup>1</sup> OECD, "Nuclear Fuel Safety Criteria Technical Review". Result of OECD/CSNI/PWG2 Task Force (2001).

<sup>2</sup> D.E. BASSETTE, "Initial and boundary conditions to LOCA analysis – an examination of requirements of Appendix K". 10<sup>th</sup> International Conference on Nuclear Energy, Baltimore MD, April (2000).

<sup>3</sup> F. SCMITZ and J. PAPIN, "High Burn-up Effect on Fuel Behaviour under Accident Conditions: the test CABRI REP-Na", *Journal of Nuclear Materials*, vol. 270, pp. 55-64 (1999).

<sup>4</sup> J. PAPIN, B. CAZALIS, J. M. FRIZONNET, J. DESQUINES, F. LEMOINE, V. GEORGENTHUM, F. LAMARE, and M. PETIT, "Summary and Interpretation of the CABRI REP-Na Program", *Nuclear Technology*, vol. 157, pp. 215-229 (2007).

<sup>5</sup> J. PAPIN, M. PETIT, C. GRANDJEAN, and V. GEORGENTHUM, "IRSN R&D Studies on High Burn-up Fuel Behaviour under RIA and LOCA Conditions" *Transactions of the Top\_Fuel 2006 International Meeting on LWR Fuel Performance*, Salamanca, Spain (2006).

The main purpose of this study is to assess the uncertainties associated to a RIA transient analysis. To do so the analytical tool used is the FRAPTRAN code <sup>6</sup>, sponsored by the U.S. NRC and developed by the PNNL is applied for licensing analyses of single fuel rod performance under transient power conditions up to fuel average burn-up of 65 GWd/tU. The fuel rod characterisation at EOL of base irradiation necessary for the transient code initialization was provided by the FRAPCON-3 steady-state code.

Two RIA tests (CIP0-1 and CIP0-2), carried in fall of 2002 at the CABRI facility, with high burn-up and advanced claddings, have been selected to assess the code capability to deal with such events. A global relative uncertainty range can be obtained by the use of the raw FRAPCON-3 end-of-life characterisation in the transient code. In order to determine the relative uncertainty range, just due to the transient simulation, that attributable to the steady state estimation can be minimised by fitting the end of life FRAPCON-3 estimations as much as possible to available data. The uncertainty quantification (i.e. the absolute uncertainty range in the RIA estimation) can be obtained through comparison with the two measured variables, permanent clad hoop strain along the rod length and time-dependent clad axial elongation. The results obtained should provide an idea of the accurateness that can be attained through the simulation of the PCMI stage of a RIA with high burn-up and advanced cladding.

This work has been done under the CSN-CIEMAT collaboration agreement on Thermo Mechanical Behaviour of High Burn-up Fuel.

## 2. CIP0 tests

Two high burn-up test rodlets (CIP0-1 and CIP0-2) were submitted to a RIA within the CIP0 series in the framework of the CABRI International Program. None of the test rod failed during the power pulse transient.

### 2.1. The experiment CIP0-1

CIP0-1 rodlet was submitted to a RIA transient at the CABRI reactor under sodium cooling conditions on November 29th 2002<sup>7</sup>. The rodlet was refabricated from a father rod irradiated during five cycles in a PWR up to an average rod burn-up of 68 GWd/tU (with maximum burn-up of 75.4 GWd/tU) measured by gamma-scanning at the Studsvik laboratories<sup>8</sup>. The cladding material was ZIRLO with a mean oxide layer of 77  $\mu\text{m}$  in the rodlet section. During the CIP0-1 test the rodlet was submitted to isothermal hot shut-down representative conditions: 280 °C sodium coolant temperature and channel sodium velocity of 4 m/s. The transient had 32.4 ms width at half maximum with a specific energy deposited at PPN of 99 cal/g after 1.2 s<sup>9</sup>.

#### 2.1.1. Father rod characterisation

Table 1 summarises the general design specifications of the CIP0 1 father rod prior to the base irradiation and Table 2 presents the deviation of the FRAPCON-3 estimations at the EOL of the base irradiation. The EOL FRAPCON-3 (version 3.3) estimations provide the characterisation of the rodlet necessary for the FRAPTRAN initialisation. The best estimation of the base irradiation is required because the transient code predictions will be affected in some extent for the fuel rodlet characterisation prior the power pulse.

<sup>6</sup> M. E. CUNNINGHAM, C. E. BEYER, P. G. MEDVEDEV and G. A. BERNA "FRAPTRAN: A Computer Code for the Transient Analysis of Oxide Fuel Rods" NUREG/CR-6739, Vol. 1, PNNL-13576 (2001).

<sup>7</sup> J.C. MÉLIS, M., FAURY, C. MARQUIÉ and J. PAPIN "CABRI CIP0-1 Preliminary Results". NUREG/CP-0185, Proceedings of the 2003 Nuclear Safety Research Conference (2003).

<sup>8</sup> P. EKBERG, "Non-Destructive Examination of Two Fuel Rods Irradiated Five Cycles in Vandellós-2, intended for STUDEFAB Refabrication". Studsvik Nuclear AB. Studsvik/N(H) 01/046 (2001).

<sup>9</sup> A. ROMANO, H. WALLIN, M.A. ZIMMERMANN, and R.CHAWLA, "Modelling the CABRI High-Burn-up RIA Test CIP0-1 Using an Extended Version of the FALCON Code". Nuclear Engineering and Design, vol. 236, pp. 284–294 (2006).

Table 1. Design specifications of CIP0-1 father rod

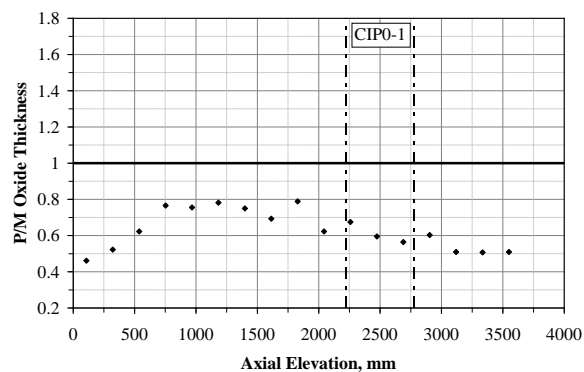
Characteristic	Value
Fuel material	UO <sub>2</sub>
Cladding Material	ZIRLO
Free volume, m <sup>3</sup>	19.69E-6
Active length, m	3.6576
Filling gas	He
Filling pressure, MPa	2.35

Table 2. CIP0-1 FRAPCON-3 estimations at the EOL of base irradiation

Item	Error, %
Rod average burn-up	-2.39
Maximum burn-up,	-1.79
Cladding elongation	13.41
Plenum pressure (at 1bar and 273K)	-37.57
Final free volume (at 1bar and 273K)	29.61
Total gas volume (at 1bar and 273K)	-18.92
FGR	-45
Oxide thickness range (min – max)	(-56) – (-53)

The father rod estimations obtained by FRAPCON-3 can be considered as acceptable; the highest deviations are shown in Fission Gas Release (FGR) and oxide thickness predictions. Fig. 1 compares the oxide thickness predicted by FRAPCON-3 together with the measured data in relative terms. It must be pointed that the current FRAPCON-3 version estimates the ZIRLO oxide thickness decreasing the Zr-4 corrosion rate by a numerical factor<sup>10</sup>. Other cladding properties different of oxide thickness or hydrogen pick-up are not modified by the steady-state code and those of standard Zr-4 are used. In spite of the FRAPCON-3 modification for ZIRLO corrosion rate, the code underestimates the oxide thickness in almost a 50%. Regarding the zone reconditioned for CIP0-1, the range error is about 33% 43%.

Figure 1. Predicted to measured CIP0-1 oxide thickness at EOL of base irradiation



The amount of gases released estimated by FRAPCON-3 is about a 45% lower than that measured. In principle, this discrepancy is not significant in the further transient analysis since the gases of the father rod were removed and the rodlet was re-pressurised with helium prior the transient. However, alternative parametric studies have shown that CIP0-1 FGR underestimation cannot be imputable to oxide thickness estimation inaccuracy and such deviation can be attributable to uncertainties in fuel temperature

<sup>10</sup> D.D. LANNING, C. E. BEYER and K. J. GEELHOOD, "FRAPCON-3 Updates, Including Mixed-Oxide Fuel Properties". NUREG/CR-6534, Vol. 4. PNNL-11513, (2005).

estimations<sup>11</sup>. Some parametric calculations have showed that a 7% increase of the fuel centreline temperature (fuel temperature uncertainty<sup>10</sup> in FRAPCON-3 is about 10 to 15%) results in a much better agreement with data (the error decreased from 57% to 19%).

### 2.1.2. Test rodlet

After the base irradiation, the test rodlet was refabricated in Studsvik from the span 5 of the father rod. The active length<sup>9</sup> of the refabricated rodlet was of 0.541 m with a mean oxide thickness of 77  $\mu\text{m}$ . The maximum burn-up of the rodlet section at the end of the base irradiation was about 75 GWd/tU. The refabricated rodlet was pressurised with 3 bar of helium at 20°C.

## 2.2. The experiment CIP0-2

The CIP0-2 rodlet was tested at the CABRI experimental reactor on 8th November 2002 under sodium cooling conditions. The rodlet was reconditioned from the span 5 of a father rod irradiated during six cycles in a French PWR Nuclear Power Plant<sup>5</sup>. The advanced cladding material was M5 and showed a mean oxide layer of about 20  $\mu\text{m}$  at the end of the base irradiation. The RIA transient<sup>5</sup> had a power pulse half width of 28 ms with a deposited energy of 90 cal/g at PPN after 1.2 s.

### 2.2.1. Father rod characterisation

Table 3 presents the main design specifications of the CIP0-2 father rod prior to the base irradiation and Table 4 summarises the most important deviations found after the base irradiation simulation performed by FRAPCON-3.

Table 3. Main design specifications of CIP0-2 father rod

Characteristic	Value
Fuel material	UO <sub>2</sub>
Cladding Material	M5
Free volume, m <sup>3</sup>	18.2E-6
Filling gas	He
Filling pressure, MPa	1.5

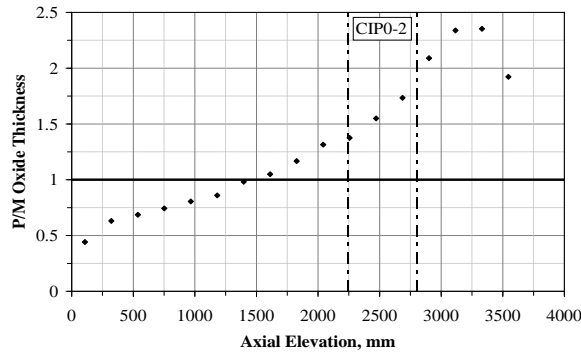
Table 4. CIP0-2 FRAPCON-3 estimations at the EOL of base irradiation

Item	Error, %
Rod average burn-up	0.57
Maximum burn-up,	6.45
Cladding elongation	41.18
FGR	0.69
Oxide thickness range (min – max)	(-50) – (115)

As can be shown in the above table, FRAPCON-3 FGR estimation agrees quite well with measurements. Fig. 2 compares in relative terms the FRAPCON-3 oxide thickness estimation against the one measured. The figure shows that neither the qualitative nor the quantitative oxide profile is fitted. The highest difference with measurements is shown at the upper zone of the fuel rod at the higher clad temperature estimations. It must be pointed out that the current FRAPCON-3 version<sup>10</sup> estimates the M5 oxide thickness just by decreasing in a numerical factor the corrosion rate of the standard Zr-4 and greater than that used for ZIRLO. So, such a deviation could be likely due to M5 oxidation kinetic differs from that of standard Zr-4.

<sup>11</sup> M.T. DEL BARRIO and L.E. HERRANZ, "FRAPTRAN Predictability of High Burn-up Advanced Fuel Performance: Analysis of the CABRI CIP0-1 and CIP0-2 Experiments" Proceeding of the 2007 International meeting on LWR fuel performance. San Francisco, California, 30 Sept. – 3 Oct., (2007).

Figure 2. Predicted to measured CIP0-2 oxide thickness at EOL of base irradiation



2.2.2. Test rodlet

The CIP0-2 rodlet was reconditioned from the span 5 of the father rod<sup>5</sup>. The active length of the refabricated rodlet was of 0.558 m. The refabricated rodlet was pressurised with 3 bar of helium at 25°C.

3. Transient simulation

The simulations of the CABRI-CIP0 RIA tests were performed by using the FRAPTRAN (version 1.3) transient code.

3.1. Code considerations

Some remarks respect to mechanical properties in FRAPTRAN code should be considered:

- No ZIRLO and M5 mechanical properties are available in FRAPTRAN code. Standard Zr-4 mechanical properties are used instead.
- Non-slip fuel-clad contact is assumed either.
- FRAPTRAN does not model FGR during the power pulse.

3.2. Simulation approaches

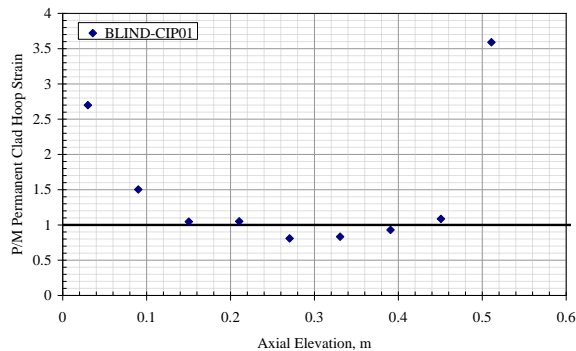
3.2.1. Blind case

It has been considered as Blind Case, the FRAPTRAN simulation obtained just taken into account the raw FRAPCON-3 estimations at the end of the base irradiation. The transient code comparison with the available experimental data will provide a global relative uncertainty range of a RIA simulation, which will include both base irradiation and transient uncertainties.

3.2.1.1. Permanent clad hoop strain

Fig. 3 presents in relative terms the permanent clad hoop strain blind estimations along the CIP0-1 rod length.

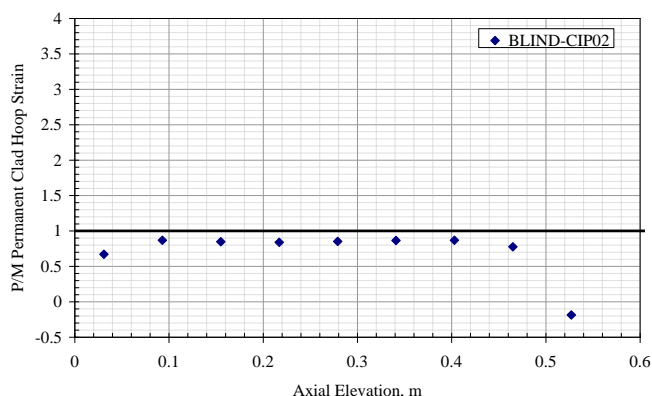
Fig. 3. CIP0-1 predicted to measured permanent clad hoop strain for blind case



The maximum estimation difference is found at the extremes of the rodlet, where the absolute hoop strain is lower. It must be highlighted that the represented points are an average of the measurements at that rod elevation and, all the estimated points fall into the data dispersion band. Avoiding the rodlet extremes, in the centre zone of the rod, the most significant because is where the strain is higher; the global uncertainty on permanent clad hoop strain can be enclosed to the  $\pm 20\%$ .

A similar evaluation is shown in the Fig. 4 for the CIP0-2 test. As in the previous test, the maximum divergence is found at the rodlet extremes where strain is experimentally expected to be lower. In spite of the different clad material, the global uncertainty can be also enclosed in a 20% of underestimation in the zone that presents the harder mechanical impact.

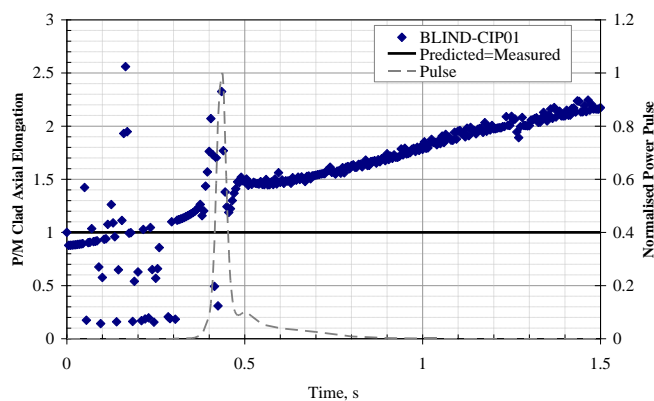
Figure 4. CIP0-2 predicted to measured permanent clad hoop strain for blind case



3.2.1.2. Clad axial elongation

Fig. 5 presents the CIP0-1 ratio of predicted and measured clad elongation as a function of the transient time.

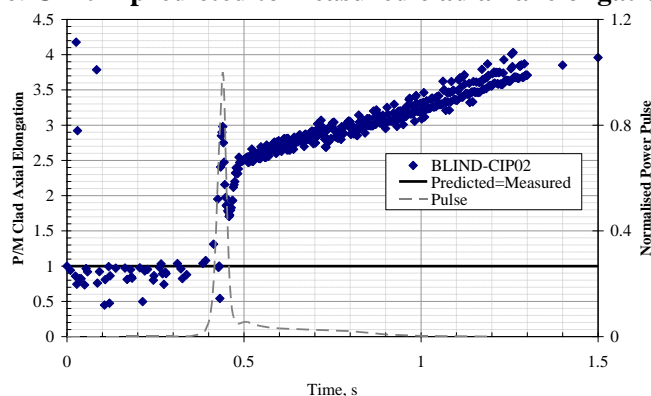
Figure 5. CIP0-1 predicted to measured clad axial elongation ratio



As a result, FRAPTRAN trends to overestimate the ZIRLO clad elongation. Just after the power pulse, the code overshoot data in nearly a factor 1.5 (divergence peak between 0.35-0.45 s is not real and is due to a meaningless peak in the measurements result of the transformation of the raw signal). Such a multiplicative factor even increases with time since the code clad relaxation estimation is lower than that experimentally observed. It has been assessed that these results are not attributable to uncertainties in oxide thickness or coolant heat transfer.

CIP0-2 clad axial elongation is evaluated in Fig. 6. Code overestimation after the power pulse is also observed for M5 cladding material, where the overestimation is even more significant. Just after the pulse the clad axial elongation is overestimated in about a factor 2.5, and divergence slope is even higher than that found in CIP0-1 test.

Figure 6. CIP0-2 predicted to measured clad axial elongation ratio



### 3.2.2. Open case

With the aim of determining the relative uncertainty range, just due to the transient simulation, that attributable to the steady state estimation has been minimised by fitting the end of life FRAPCON-3 estimations as much as possible to available data in the rodlet zone.

In order to do so, CIP0-1 FRAPCON-3 simulation has been improved by decreasing the saturation condition of the FRAPCON-3 FGR model in a 47%. In addition, the corrosion rate was reduced around 26% respect to that of Zr-4 clad material in CIP0-1 base irradiation in order to fit the oxide thickness in the rodlet zone at the end of the base irradiation. The Table 5 presents the deviation obtained through the fittings above mentioned at end of base irradiation when is compared to measured values.

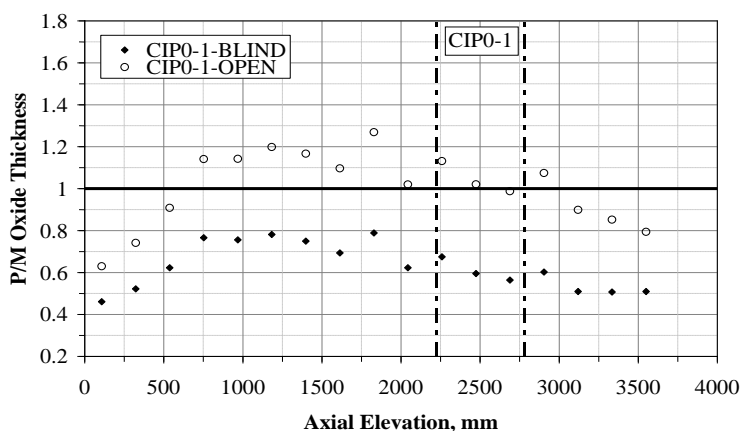
Uncertainties from the irradiation estimates concerning gap size could affect the mechanical response of the cladding. Unfortunately, no gap size data is available after base irradiation to be directly applied in the Open Case. Difference in gap size between Blind and Open Case (about 2 microns in CIP0-1 and 0.6 microns in CIP0-2 at hot conditions) is merely a consequence of the different irradiation history resulting from the FRAPCON-3 modifications made to fit the end of base irradiation. A larger gap size than that estimated by FRAPCON-3 at the end of the base irradiation would result in a later fuel-clad contact, so, the load on the clad would be imposed during a shorter time and then, the axial cladding elongation could be lower. Parametric studies have been made to assess the influence of gap size at end of base irradiation on FRAPTRAN/transient estimations<sup>11</sup>. As result, excessively low gap sizes were necessary to fit the mechanical response of the transient code. Then, despite the major effect of gap size on RIA transient, such huge uncertainties are not expected from steady-state calculation.

Table 5. Estimations at the EOL of the base irradiation of the CIP0-1 father rod through FRAPCON-3 fitting

Item	Error, %
Rod average burn-up	-2.39
Maximum burn-up,	-1.79
Cladding elongation	13.41
Plenum pressure (at 1bar and 273K)	-24.82
Final free volume (at 1bar and 273K)	30.75
Total gas volume (at 1bar and 273K)	-1.45
FGR	0.27
Oxide thickness range (min – max)	-1.2 – -13 (at rodlet zone)

Figure 7 presents in relative terms the improvement in the oxide thickness estimation through the FRAPCON-3 fitting narrowly focused in the rodlet zone.

Figure 7. Predicted to measured oxidation thickness ratio comparison in open and blind cases at the end of the CIP0-1 base irradiation



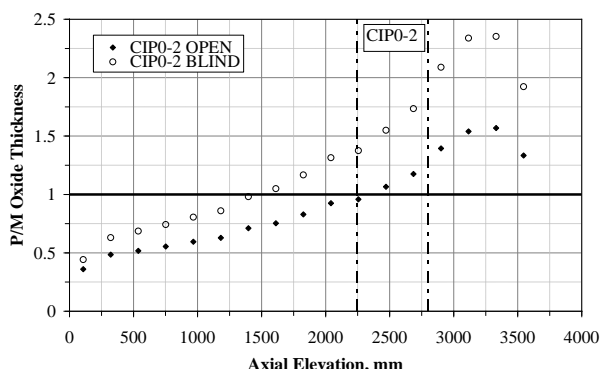
Regarding CIP0-2, the fitting of the base irradiation has been performed through the modification of the corrosion rate in a factor 0.30 with regard to that of Zr-4 standard. Besides, the irradiation growth model for Zr-4 has been modified in a factor 0.7.

Table 6. Estimations at the EOL of the base irradiation of the CIP0-2 father rod through FRAPCON-3 fitting

Item	Error, %
Rod average burn-up	0.57
Maximum burn-up,	6.45
Cladding elongation	-1.47
FGR	-3.63
Oxide thickness range (min – max)	-4 – 17 (at rodlet zone)

Fig. 8 compares the oxide thickness estimation in relative terms between the blind and the open case with the FRAPCON-3 fittings. As can be observed, the oxide thickness development with axial rod length is not properly settled with just a multiplicative factor. So, the oxide thickness has been focused to be fitted mostly in the zone of the rodlet.

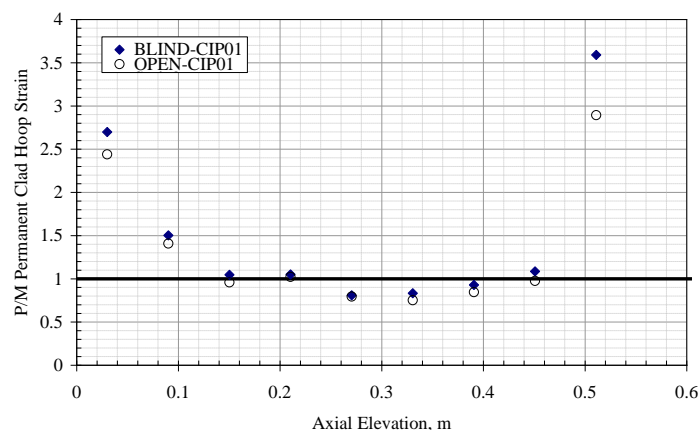
Figure 8. Predicted to measured oxidation thickness ratio comparison in open and blind cases at the end of the CIP0-2 base irradiation



### 3.2.2.1. Permanent clad hoop strain

Fig. 9 compares the previous estimations of CIP0-1 permanent clad hoop strain with the FRAPTRAN predictions obtained through the fitting of the FRAPCON-3 estimations at the end of base irradiation.

Fig. 9. CIP0-1 predicted to measured permanent clad hoop strain in open and blind cases comparison



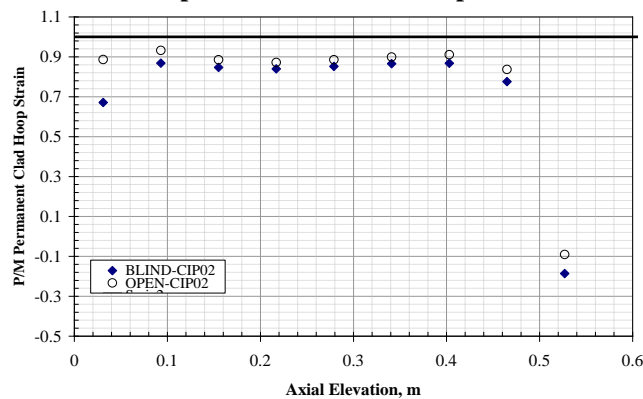
In the open case, the CIP0-1 FRAPTRAN permanent cladding hoop strains are slightly lower than the blind case. As can be observed, the decrease in relative terms is much significant at the rodlet extremes. However, just slightly difference is observed between blind and open case at the zone of the higher mechanical strain. So, it can be deduced that the uncertainty in this variable is not directly attributable to deviation in oxide thickness estimations at the end of the base irradiation. Such behaviour bring into highlight that in-clad hydrogen content effect on the cladding mechanical response could not properly implemented in the transient code. Although a failure model based on uniform plastic hoop elongation estimated by means of the exceeding hydrogen content in the cladding is incorporated in the FRAPTRAN code<sup>12</sup>, however, such variable seems not to directly affect the mechanical on permanent clad hoop strain. FRAPTRAN mechanical response is mainly affected by clad temperature, fast neutron fluence and cladding cold work. So, the detrimental in the cladding mechanical properties can not be directly attributable to clad corrosion or hydrogen content by the use of FRAPTRAN code.

Regarding CIP0-2 in the open case, a slightly increase in the FRAPTRAN estimations of permanent clad hoop strain is observed for blind and open cases in Fig .10. In this case is also corroborated that the influence of oxide thickness at the end of base irradiation does not affect straightforwardly the FRAPTRAN estimations. It could be expected that a decrease in oxide thickness will result in a lower permanent hoop strain as a consequence of a minor detriment of the initial clad mechanical properties; however, an increase in the FRAPTRAN variable is observed. In the CIP0-1 the behaviour is similar, since the oxide thickness is increased in the open case and a decrease in the FRAPTRAN permanent clad hoop strain is predicted. So, a decrease in CIP0-2 the oxide thickness prediction during base irradiation will result in lower fuel temperatures, and thus, lower FGR, as can be appreciated when the FRAPCON-3 results for the blind and the open case of the CIP0-2 at the end of the base irradiation are compared. Therefore, it seems that simulation results are more sensitive to the amount of fission gas release during steady state irradiation than to cladding oxidation rate. In other words, FRAPTRAN estimations seem to be mostly affected by thermal behaviour during the base irradiation than loss of the mechanical properties at high burn-up.

In any case, it seems to be confirmed that steady-state deviations do not affect appreciably the transient results. The uncertainty observed in permanent clad hoop strain is mainly due to the transient simulation and it is in the  $\pm 20\%$  range in the zone of higher mechanical impact.

<sup>12</sup> K.J. GEELHOOD, C. E. BEYER and M. CUNNINGHAM, "Modifications to FRAPTRAN to Predict Fuel Rod Failures Due to PCMI during RIA-Type Accidents". LWR Fuel Performance Meeting, Orlando, Florida, USA (2004).

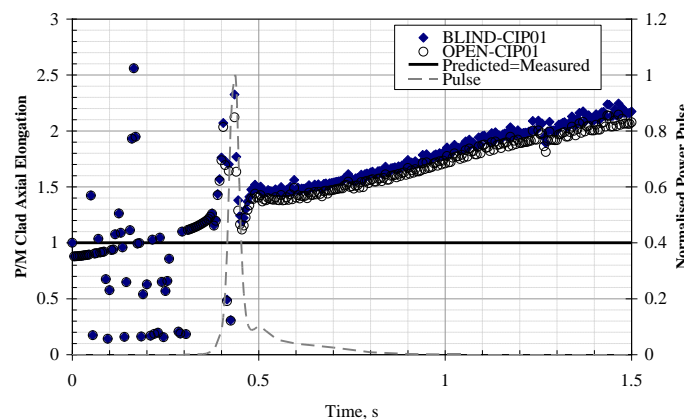
Figure 10. CIP0-2 predicted to measured permanent clad hoop strain in open and blind cases comparison



3.2.2.2. Clad axial elongation

Fig. 11 compares the previous estimations of clad axial elongation of the CIP0-1 with the FRAPTRAN predictions obtained through the fitting of the FRAPCON-3 estimations at the end of base irradiation.

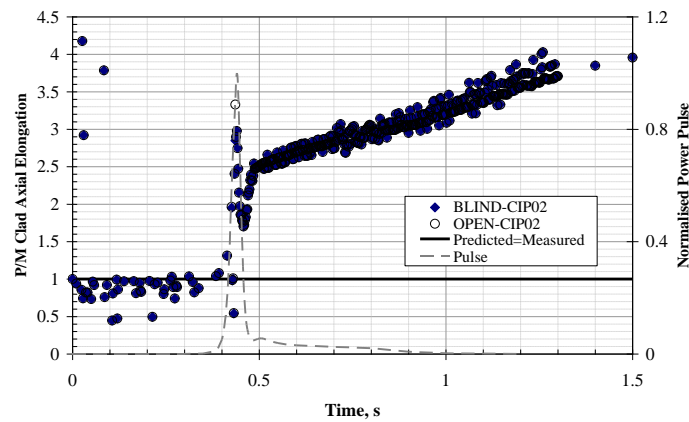
Figure 11. CIP0-1 predicted to measured permanent clad axial elongation in open and blind cases comparison



FRAPTRAN clad axial elongation predictions for open case are slightly lower than that of the blind case. Once again, FRAPTRAN overestimation of clad axial elongation can not be attributable to FRAPCON-3 end of base irradiation deviation. The slight difference starts to be significant during and after the power pulse. However, just slightly difference is observed between blind and open case at the zone of the higher mechanical strain in clad hoop strain. This result agrees with the previous observed on FRAPTRAN estimations of permanent clad hoop strain. The higher is the oxide thickness at the end of the base irradiation, the lower elongation or strain of the cladding. Another time, there is a more significant influence in FRAPTRAN predictions of the thermal development during base irradiation than effects in the transient estimation of the clad oxidation or hydrogen content on the clad mechanical properties.

Similar conclusion can be adopted for CIP0-2 clad axial elongation. In this test, differences between open and blind estimations on axial clad elongation are minima. So, the decrease in oxide thickness does not affect the FRAPTRAN estimations on clad axial elongation. It must be pointed out that the oxide thickness of the M5 cladding at the end of the base irradiation is much lower than that of the ZIRLO one. So, a decrease of a 50% on the oxide thickness corresponds to a much lower amount of oxide thickness in the M5 cladding. The estimations results also reveal that, as expected during the PCMI RIA phase, the influence of the steady-state irradiation on the transient estimation is more sensitive in the hoop than in axial direction.

Figure 12. CIP0-2 predicted to measured permanent clad axial elongation in open and blind cases comparison



### Conclusions and final remarks

This paper has tried to identify the major uncertainties influencing modelling of a RIA event on a high burn-up fuel rod when FRAPCON-3 and FRAPTRAN are used to simulate base irradiation and power transient, respectively. A global relative uncertainty range has been obtained by the input in FRAPTRAN of the raw FRAPCON-3 estimations at the end of the base irradiation. On the other hand, the relative uncertainty range, just due to the transient simulation, can be achieved when the deviation of the steady state estimation is minimized by fitting the end of life FRAPCON-3 estimations as much as possible to available data. The absolute uncertainty range in the RIA estimation can be then obtained through comparison with the two measured variables, permanent clad hoop strain along the rod length and time-dependent clad axial elongation.

Some of the main outcomes of this work can be summarised as follows:

- According to the results presented above, simulation of RIAs in high burn-up fuel (i.e., closed gaps) is hardly affected by potential uncertainties coming from the fuel rod characterisation provided by steady state codes.
- Detriment of the mechanical properties at high burn-up seems not to be properly assessed by the code. Cladding oxidation level primarily affects the fuel rod thermal behaviour whereas its impact in the codes' mechanical response is almost negligible.
- Nevertheless, even though a 20% deviation in cladding hoop strain may seem to be acceptable, one should keep in mind that a better estimate of axial elongations could lead to changes in the rest of strain components.

OECD/NEA Workshop on Nuclear Fuel Behavior during RIAs

**MAJOR SENSITIVITIES OF MODELLING A HIGH BURNUP FUEL ROD WITH FRAPCON-3/FRAPTRAN CODES**

M.T. del Barrio, I. Vallejo, L.E. Herranz  
 Unit of Nuclear Safety Research  
 Nuclear Fission Division - Department of Energy  
 CIEMAT, Avda. Complutense, 22  
 28040 Madrid (Spain)

1. INTRODUCTION & OBJECTIVE  
 2. CIP0 TESTS. FATHER ROD CHARACTERISATION  
 3. TRANSIENT SIMULATION  
 4. CONCLUSIONS AND FINAL REMARKS

Unit of Nuclear Safety Research Paris (France), 09.09.09

OECD/NEA Workshop on Nuclear Fuel Behavior during RIAs

**1. INTRODUCTION & OBJECTIVE**

Experimental programmes investigate fuel behaviour in RIAs:

- > IGR
- > NSRR
- > ANL...

} Conditions far away from currently achieved

- RIA programme (1992) → REP-Na (9 tests)
- CABRI (CIP) (2000) under sodium cooling conditions

Purpose of this study: Assess uncertainties ( $\Delta$ ) associated to RIA transient (CIP01&CIP02) at  $\uparrow$ Bu and advanced cladding

↓  
How?

Unit of Nuclear Safety Research Paris (France), 09.09.09

OECD/NEA Workshop on Nuclear Fuel Behavior during RIAs

**1. INTRODUCTION & OBJECTIVE**

EOL FRAPCON-3 characterization to obtain  $\Delta$  range just due to transient:

1. Raw FRAPCON-3: **BLIND CASE** (Far measured data??)
2. Fit FRAPCON-3 to avail. measured data: **OPEN CASE**
3. Quantification for  $\Delta$  in RIA with 2 measur.
  - Clad  $\epsilon_{s,p}$  post transient
  - Clad  $\epsilon_z(t)$  during transient

Unit of Nuclear Safety Research Paris (France), 09.09.09

OECD/NEA Workshop on Nuclear Fuel Behavior during RIAs

## 2. CIPO TESTS. FATHER ROD CHARACTERISATION

> CIPO1: <Bu>=68 GWd/tU, Bu<sub>max</sub>=75.4 GWd/tU  
Design father rod  
FRAPCON-3 at EOL of BI

CHARACTERISTIC	VALUE
Fuel material	UO <sub>2</sub>
Cladding Material	ZIRLO
Free volume, m <sup>3</sup>	19.69E-6
Active length, m	3.6576
Filling gas	He
Filling pressure, MPa	2.35

ITEM	ERROR, %
Rod average burnup	-2.39
Maximum burnup	-1.79
Cladding elongation	13.41
Plenum pressure (STP)	-37.57
Final free volume (STP)	29.61
Total gas volume (STP)	-18.92
FGR (%)	-45
Ox. Thick. range (min-max)	(-56) - (-53)

STP= 1 bar, 273 K  
RIA: 29/11/2002, ΔE=99 cal/g

**BLIND CASE**

Unit of Nuclear Safety Research Paris (France), 09.09.09

OECD/NEA Workshop on Nuclear Fuel Behavior during RIAs

## 2. CIPO TESTS. FATHER ROD CHARACTERISATION

> CIPO1: <Bu>=68 GWd/tU, Bu<sub>max</sub>=75.4 GWd/tU  
FRAPCON-3 at EOL of BI

ITEM	ERROR, %
Rod average burnup	-2.39
Maximum burnup	-1.79
Cladding elongation	13.41
Plenum pressure (STP)	-24.82
Final free volume (STP)	30.75
Total gas volume (STP)	-1.45
FGR (%)	0.27
Ox. Thick. range (min-max)	*(-1.2) - (-13)

\* At rodlet zone

- FGR model: Ns ↓47%
- Corrosion rate: ↓≈26% from Zr-4

**OPEN CASE**

Unit of Nuclear Safety Research Paris (France), 09.09.09

OECD/NEA Workshop on Nuclear Fuel Behavior during RIAs

## 2. CIPO TESTS. FATHER ROD CHARACTERISATION

> CIPO2: Father rod irradiated Six cycles  
Design father rod  
FRAPCON-3 at EOL of BI

CHARACTERISTIC	VALUE
Fuel material	UO <sub>2</sub>
Cladding Material	M5
Free volume, m <sup>3</sup>	18.2E-6
Active length, m	3.6576
Filling gas	He
Filling pressure, MPa	1.5

ITEM	ERROR, %
Rod average burnup	0.57
Maximum burnup	6.45
Cladding elongation	41.18
FGR (%)	0.69
Ox. Thick. range (min-max)	(-50) - (115)

RIA: 08/11/2002, ΔE=90 cal/g

**BLIND CASE**

Unit of Nuclear Safety Research Paris (France), 09.09.09

OECD/NEA Workshop on Nuclear Fuel Behavior during RIAs

## 2. CIPO TESTS. FATHER ROD CHARACTERISATION

> CIPO2: Father rod irradiated Six cycles  
FRAPCON-3 at EOL of BI

ITEM	ERROR, %
Rod average burnup	0.57
Maximum burnup	6.45
Cladding elongation	-1.47
FGR (%)	-3.63
Ox. Thick. range (min-max)	*(-4) - (17)

\* At rodlet zone

**OPEN CASE**

- Irrad. Growth model:  $\epsilon_z \downarrow 30\%$
- Corrosion rate:  $\downarrow \approx 70\%$  from Zr-4

Unit of Nuclear Safety Research Paris (France), 09.09.09

OECD/NEA Workshop on Nuclear Fuel Behavior during RIAs

## 3. TRANSIENT SIMULATION

Mechanical properties (FRAPTRAN, v1.3):

- > No ZIRLO&M5 available in FRAPTRAN
- > Standard Zr-4 used
- > Non-slip-fuel-clad contact assumed
- > FRAPTRAN: No model FGR during pulse

Simulation approaches: Quantification for  $\Delta$

**BLIND CASE**

Raw FRAPCON-3

COMPARISONS  
with exp. data

**OPEN CASE**

Fit FRAPCON-3 minimize  
deviations predictions-data

Unit of Nuclear Safety Research Paris (France), 09.09.09

OECD/NEA Workshop on Nuclear Fuel Behavior during RIAs

## 3. TRANSIENT SIMULATION

> CIPO1  
Clad  $\epsilon_{\theta,p}$  post transient  
In centre global  $\Delta \pm 20\%$

Clad  $\epsilon_z(t)$  during transient

- ❖ OPEN slightly lower than BLIND
- ❖  $\Delta$  Not attributable to deviation in Ox after BI or clad hydrogen in transient

Unit of Nuclear Safety Research Paris (France), 09.09.09

OECD/NEA Workshop on Nuclear Fuel Behavior during RIAs

### 3. TRANSIENT SIMULATION

> **CIPO2**  
 Clad  $\epsilon_{\theta,p}$  post transient  
 In centre global  $\Delta \pm 20\%$

P/M Permanent Clad Hoop Strain

Axial Elevation, m

◆ BLIND-CIPO2  
● OPEN-CIPO2

Clad  $\epsilon_z(t)$  during transient

P/M Clad Axial Elongation

Time, s

◆ BLIND-CIPO2  
● OPEN-CIPO2  
— Predicted-Measured  
- - Pulse

Normalised Power Pulse

↑ dev. in Oxide (BI) ⇒ ↑ dev. in  $\epsilon_z$

❖ OPEN slightly higher than BLIND  
 ❖ Minima differences BLIND ⇔ OPEN for  $\epsilon_z(t)$

Unit of Nuclear Safety Research Paris (France), 09.09.09

OECD/NEA Workshop on Nuclear Fuel Behavior during RIAs

### 4. CONCLUSIONS AND FINAL REMARKS

- ✓ FRAPCON-3 - FRAPTRAN simulations of RIAs with  $\uparrow Bu$  hardly affected by  $\Delta$  coming from characterisation during BI
- ✓ Detriment of mechanical properties at  $\uparrow Bu$  not properly assessed by the code
- ✓ 20% deviation in  $\epsilon_{\theta,p}$  acceptable but a better estimate of  $\epsilon_z$  could change the other strain components

Unit of Nuclear Safety Research Paris (France), 09.09.09

OECD/NEA Workshop on Nuclear Fuel Behavior during RIAs

### ACKNOWLEDGMENTS:

Authors thank the Spanish Regulatory Body (CSN) for the financial support of this work carried out under the collaboration agreement TERMOCAQ

Unit of Nuclear Safety Research Paris (France), 09.09.09



## CAPABILITIES OF TRANSURANUS CODE IN SIMULATING POWER RAMP TESTS FROM THE IFPE DATABASE

**Martina Adorni, Davide Rozzia, Alessandro Del Nevo, Francesco D'Auria**  
University of Pisa, Italy

### 1. Introduction

TRANSURANUS is a computer program for the thermal and mechanical analysis of fuel rods in nuclear reactors.<sup>1,2,3</sup> The TRANSURANUS code consists of a clearly defined mechanical–mathematical framework into which physical models can easily be incorporated. The mechanical–mathematical concept consists of a superposition of a one-dimensional radial and axial description (the so called quasi two-dimensional or 1½-D model). The code was specifically designed for the analysis of a single cylindrical rod.

In the current paper, the application of the TRANSURANUS code to the Studsvik BWR Inter-Ramp<sup>4</sup> and PWR Super-Ramp<sup>5</sup> Projects are presented. The activity has been performed in the framework of an agreement between JRC-ITU and the University of Pisa and also of the IAEA FUMEX III project.

The objective of the activity is the assessment of the fission gas release model of TRANSURANUS code version “v1m1j08”, against the above mentioned databases. It constitutes an independent verification of a new model that was implemented at ITU for dealing with release during rapid power changes<sup>6</sup>.

The dataset of the BWR Inter-Ramp and PWR Super-Ramp Projects are part of the International Fuel Performance Experiments (IFPE) database<sup>7, 8</sup>. The first addresses the behavior of twenty standard-type unpressurised BWR fuel rods, including preceding base irradiation, during the over-power ramping. Two different values of base irradiations burn-up were adopted for the experimental database: about 10 and 20 MWd/kgU. The latter addresses the behavior of twenty-eight light water reactor fuel rods when subject to power ramps (twenty-six are modeled for the current activity), after base irradiation to high burn-up (28 to 45 MWd/kgU).

Pre-, during-, and post- irradiation, non destructive and destructive examinations were executed, in order to determine and understand the behavior of the fuel rods, but also to provide suitable data, useful for code validation.

---

<sup>1</sup> Lassmann K., A. Schubert, P. Van Uffelen, Cs. Gyory, J. van de Laar, “Transuranus Handbook version “v1m1j06”, EC, JRC, ITU, July 2006.

<sup>2</sup> Lassmann K., “TRANSURANUS: a fuel rod analysis code ready for use”, J. of Nuclear Material 188 (1992) 295-302.

<sup>3</sup> Van Uffelen P., “Modelling of Nuclear Fuel Behaviour”, Publications Office, JRC Publications, Report EUR 22321 EN, European Commission, 2006.

<sup>4</sup> Mogard H., et al., “The Studsvik Inter-Ramp Project”, Final Report of the Inter-Ramp Project, STIR-53, Studsvik AB Atomenergi, Studsvik, Sweden, 1979.

<sup>5</sup> Djurle S., et al., “The Super-Ramp Project”, Final report of the Super-Ramp project, STIR-32, Studsvik AB Atomenergi, Studsvik, Sweden, 1984.

<sup>6</sup> P. Van Uffelen, A. Schubert, J. van de Laar, C. Györi, "Development of a transient fission gas release model for TRANSURANUS", Water Reactor Fuel Performance Meeting, 19-23 October 2008, Seoul, Korea.

<sup>7</sup> OECD/NEA, “The Public Domain Database on Nuclear Fuel Performance Experiments for the Purpose of Code Development and Validation, International Fuel Performance Experiments (IFPE)”, Website: [www.nea.fr/html/science/fuel/ifpelst.html](http://www.nea.fr/html/science/fuel/ifpelst.html), 2008.

<sup>8</sup> Chantoin P., E. Sartori, J.A. Turnbull, “The Public Domain Database on Nuclear Fuel Performance Experiments (IFPE) for the Purpose of Code Development and Validation”, ANS, Topical Meeting on Light Water Reactor Fuel Performance, Portland, Oregon, 2-6 March 1997.

The experimental data were used for assessing the TRANSURANUS capabilities in predicting the fission gas release. Focus is given on the prediction of the different FGR model options available in the code. The objective of the activity has been fulfilled developing forty-six input decks suitable for the assessment of TRANSURANUS code version “v1m1j08”<sup>9,10</sup>. The assessment is focused on fission gas release models available in TRANSURANUS code version “v1m1j08”, with particular emphasis to the new “TFGR model” which is implemented for taking into account the events of rapid power variations. The current paper reports the main outcome of the assessment of the calculations. Conclusive remarks of the activity are provided in the last section.

### **2.1. Description of the BWR inter-ramp experiment**

Between 1 July, 1975 to 1 July, 1979, 20 standard-type unpressurised BWR fuel rods were irradiated and power ramped in the R2 research reactor of Studsvik (Sweden). Individual fuel rod power histories were recorded in great detail, non-destructive and selectively detailed destructive examinations were also made in order to determine the fuel rod changes<sup>4</sup>

The objectives of the BWR-Inter-Ramp Project<sup>4</sup> were to establish the fail-safe operating limits of 20 standard-type, unpressurised BWR fuel rods on over-power ramping at the burn-up levels of 10 and 20 MWd/kgU. This program also provided suitable data for model development and benchmarking. The over-power ramping is to be performed at a fast ramp rate of about 4 kW/m-min with the preceding base irradiation performed to represent the conditions in a typical commercial BWR power reactor. The study also investigated:

- The influence of three main design parameters on fuel rod performance under power ramping:
  - Cladding heat treatment (re-crystallized anneal vs cold work plus stress relief anneal).
  - Pellet/cladding diametral gap size.
  - Fuel density.
- The failure mechanism and associated phenomena.

The long term pre-ramp irradiation of the rods was performed in the Boiling Capsule (BOCA), introduced in 1973, of the Studsvik R2 research reactor. The BOCA Inter Ramp Project (BIRP) consisted of a pressurised container containing 4 fuel rods.

The power ramp irradiation was performed in the pressurised water loops of the R2 research reactor, containing one rod. The power ramp tests were performed as follow<sup>4</sup>:

- 24 hours conditioning irradiation at the same linear heat rating of the previous cycle, in order to minimise the influence of zero-power period of several weeks.
- Power ramp at a constant rate of 4 kW/m-min (~65 W/m-s).
- Ramp terminal level irradiation at ramp terminal power level held for 24 hours or until failure.

Eleven out of twenty tested rods failed and two non failed rods have been found to contain incipient cracks.

### **2.2. Description of the PWR super-ramp experiment**

The Studsvik Super-Ramp Project investigated the failure propensity of typical light water reactor test fuel rods when subjected to power ramps, after base irradiation to high burn-up. The Project power ramped 28 individual PWR test fuel rods in a PWR subprogram, analyzed in the current paper, and 16 test fuel rods in a BWR subprogram.

<sup>9</sup> Adorni M., A. Del Nevo, F. D’Auria, “Verification of TRANSURANUS Code Version v1m1j07 and v1m1j08 against BWR-Inter-Ramp Experiments”, University of Pisa, DIMNP NT 631(08) Rev. 1, December 2008.

<sup>10</sup> Adorni M., A. Del Nevo, P. Van Uffelen, F. Oriolo, F. D’Auria, “Assessment of TRANSURANUS fuel performance code against Studsvik Inter-Ramp BWR database”, ICONE-17 International Conference, Brussels, Belgium, 12-16 June 2009.

The principal objective of the Super-Ramp Project was to make a substantial and valid contribution to the understanding of the pellet cladding interaction (PCI) performance under power ramp conditions for commercial type LWR reactor test fuel irradiated to high burn-up. In particular, the main objectives of the PWR sub-program are here listed:

- Establish through experiments the PCI failure threshold of standard design PWR test fuel rods on fast power ramping at high burn-up.
- Investigate whether or not a change in failure propensity or failure mode is obtained as compared to the failure behavior at lower burn-up levels.
- Establish the possible increase in PCI failure power levels for candidate PCI remedy design fuel rods at selected burn-up levels.

Kraftwert Union AG/Combustion Engineering (KWU/CE) provided 19 fuel rods, which has been irradiated in the power reactor at Obrigheim (Germany). Westinghouse (W) provided 9 fuel rods following the base irradiation in the BR-3 reactor at Mol (Belgium).

The main features of the rods are here outlined:

Kraftwert Union AG type rods, UO<sub>2</sub> pellet column length of about 310 mm:

- PK1: 5 standard “A” rods, average axial peak position burn-up between 33 and 36 MWd/kgU.
- PK2: 5 standard “A” rods, average axial peak position burn-up between 41 and 45 MWd/kgU.
- PK4: 4 standard “A” rods plus Gd<sub>2</sub>O<sub>3</sub> (4%), average axial peak position burn-up between 33 and 34 MWd/kgU.
- PK6: 5 remedy “G” rods, large grain, average axial peak position burn-up between 34 and 37 MWd/kgU.

Westinghouse type rods UO<sub>2</sub> pellet column length of about 1136 mm:

- PW3: 5 standard rods rods, average axial peak position burn-up between 28 and 31 MWd/kgU.
- PW5: 4 remedy rods, annular pellets, average axial peak position burn-up between 32 and 33 MWd/kgU.

The power ramping of the experimental fuel rods were performed in the R2 reactor in the pressurised loop No 1 with forced circulation cooling simulating PWR coolant temperature and pressure conditions.

The power ramp tests were performed as follow<sup>5</sup>:

- Conditioning phase, with a rather slow increase of linear heat rating from an initial value to 25 kW/m (conditioning level) and 24 hours holding time at this value.
- Power ramp at a constant rate of 10 kW/m-min (~165 W/m-s) to a pre-selected ramp terminal level.
- Holding phase at ramp terminal level held for about 12 hours or until failure.

Nine out of twenty-eight tested rods failed.

### 3. Fission gas release options

The recommended URGAS algorithm with the (thermal) diffusion coefficient of H<sub>j</sub>. Matzke<sup>11</sup> and a constant athermal diffusion coefficient has been chosen for all the calculations. This option is used together with an intragranular fission gas release model.

The reference calculations are performed selecting the input parameter for the grain boundary fission gas behavior that activates the “TFGR model”, identified as option (C), Table 1. The model has been newly

<sup>11</sup> H. Matzke, "Gas release mechanisms in UO<sub>2</sub>-a critical overview", Radiation Effects, 1980, Vol. 53, pp. 219-242.

implemented in TRANSURANUS code to consider the additional release that can be observed in the event of rapid power variations. This model consists of two contributions: microcracking in case of power increase or reduction, and gas transport from the grain to the grain boundaries. The entire fission gas inventory stored at the grain boundaries is instantaneously released if transient conditions are met. This model should be invoked in case of power ramps. No values of the saturation limit for grain boundary gas input parameter is needed.

The “TRANSURANUS standard” option for code version “v1m1j07”, and available also in code version “v1m1j08”, is identified in the current report as option (A). This option refers to a model in which the grain boundary saturation concentration is a constant which can be set by an input variable.

The model referred to as option (B) in this report is a grain boundary fission gas behavior model similar to the previous one, in which the grain boundary saturation concentration depends on the temperature. Also in this case the grain boundary saturation concentration should be set as an input.

In the last case, option (D), the fission gas behavior at grain boundaries is not treated (i.e. the grain boundary saturation concentration is equal to zero) that should be considered as an “upper release limit”.

Table 1. FGR at grain boundary options

<b>Id</b>	<b>Model</b>	<b>Note</b>
<b>(A)</b>	TU standard	Standard option for code version “v1m1j07”. The grain boundary saturation concentration is a constant.
<b>(B)</b>	Simple grain boundary fission gas behavior model.	The grain boundary saturation concentration depends on the temperature.
<b>(C)</b>	TFGR model	Model option to be invoked during power ramps.
<b>(D)</b>	FGR at grain boundary is not treated.	“Upper release limit”.

#### 4. Boundary conditions

The boundary conditions implemented for the analysis are listed below:

- Linear heat rate at four axial positions.
- Cladding temperature histories at 4 axial positions.
- Fast flux.
- Pressure.

Outline of the maximum ramp rate, linear heat rate at ramp terminal level (RTL) and hold time at RTL are summarised in Table 2 (a) and (b) for the BWR Inter-Ramp and PWR Super-Ramp respectively.

Linear heat rate and temperatures are those at the given time which have been constant over the interval time step, i.e. the data are in histogram format. The rate of increase/decrease between different constant linear heat rate spans has been selected as 6 kW/m-h (Figure 1 (a) and (b) for the BWR Inter-Ramp and PWR Super-Ramp respectively). Inclination between two values of constant linear heat rate is calculated on the basis only of the peak linear heat rate position. In case of a time step that is too small to apply the above mentioned method, the measured slope of the database is maintained.

The power ramp has been “constructed” according to original ASCII files<sup>12,13</sup> together with data available from tables<sup>4, 5</sup>, i.e. considering the original files using the selected “6 kW/m-h” except for the ramp in which the rate has been taken directly from the tables.

<sup>12</sup> OECD/NEA, “Fast Power Ramps Failures of Unpressurised Fuel Rods”, NEA-1555 IFPE/INTER-RAMP, Website: [www.nea.fr/abs/html/nea-1555.html](http://www.nea.fr/abs/html/nea-1555.html), 1997.

Hold time at ramp terminal level is modeled according to the LHR histories from ASCII files<sup>12, 13</sup>, see Figure (a) and (b) for the BWR Inter-Ramp and PWR Super-Ramp respectively.

The coolant is not considered in the calculations since cladding temperature histories were provided from ASCII files<sup>12, 13</sup>.

Table 2 (a). BWR-inter-ramp experiments, maximum ramp rate and linear heat rate

BIRP No	Rod No	Rod label	F/NF	Max ramp rate [kW/mh]	LHR at RTL [kW/m]	Hold time at RTL [min]
1	1	LR1		288*	43.80	1440
	2	LR2		252	45.7	1440 <sup>12</sup> (84 <sup>4</sup> )
	3	LR3		234	50.1	103
	4	LR4		234	65.4	5
3	5	LR5		306	42.7	1440
	6	LS1		324	48.2	1440 <sup>12</sup> (35 <sup>4</sup> )
	7	LS2		234	43.8	1440
	8	TR1		252	42.2	1440
5	9	LS3		234	41.8	1440
	10	LS4		252**	50.7	92
	11	TS1		252	47.3	319
	12	DR1		270	43.2	1440
2	13	HR2		270	38.0	1440
	14	HR3		234	43.2	316
	15	HR4		252	46.1	1440
	16	HR5		252	47.9	1440
4	17	HS1		234	47.8	26
	18	HS2		234	41.0	59 <sup>12</sup> (1440 <sup>4</sup> )
	19	HS3		252	44.9	59
	20	BR1		234	51.0	1440

\* Pause of 2 minutes at 32 kW/m. \*\* From 29.6 kW/m with a rate of 0.28 kW/m-s to 40.8 kW/m

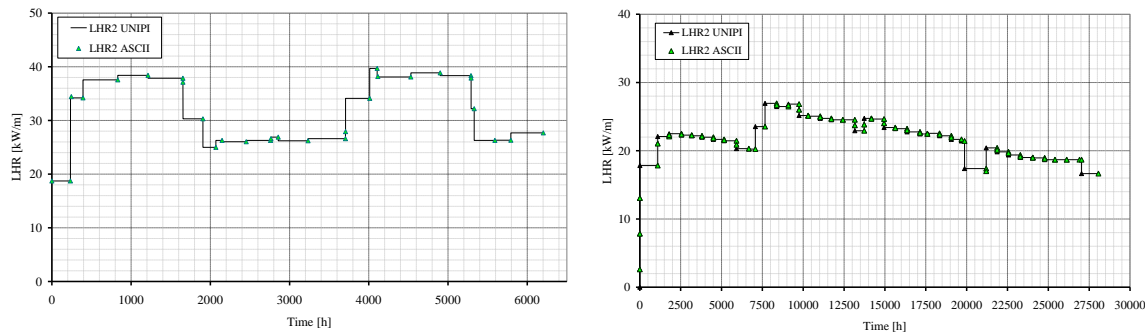
Table 3 (b). PWR-super-ramp experiments, maximum ramp rate and linear heat rate

BIRP No	Rod No	F/NF	Max ramp rate [kW/m-h]	LHR at RTL [kW/m]	Hold time at RTL [min]
PK1	1	NF	540	41.5	720
	2	NF	480	44.0	720
	3	NF	510	47.5	720
	4	NF	570	47.5	720
	S	NF	360	42.0	720
PK2	1	NF	510	41.0	720
	2	NF	570	46.0	720
	3	NF	510	49.0	720
	4	NF	510	44.0	1 <sup>s</sup>
	S	NF	510	44.0	720
PK4	1	NF	480	39.0	720
	2	NF	510	44.5	720
	3	NF	660	50.5	720
	S	NF	510	43.0	720
PK6	1	F	540	45.0	55
	2	NF	540	40.0	720
	3	NF	540	43.0	720
	4	F	600	44.0	60
	S	NF	600	41.0	720
PW3	1	F	600	40.0	22
	2	NF	600	35.3	720
	3	NF	600	37.2	720
	4	F	570	37.7	12
	S	F	600	40.5	17
PW5	1	F	540	42.7	118
	2	F	540	40.3	26
	3	F	540	38.2	38
	4	F	510	38.0	72

<sup>s</sup> Intentionally interrupted

<sup>13</sup> OECD/NEA, "SUPER-RAMP, PCI Failure Threshold for PWR and BWR Fuels", NEA-1557 IFPE/SUPER-RAMP, Website: [www.nea.fr/abs/html/nea-1557.html](http://www.nea.fr/abs/html/nea-1557.html), 2000.

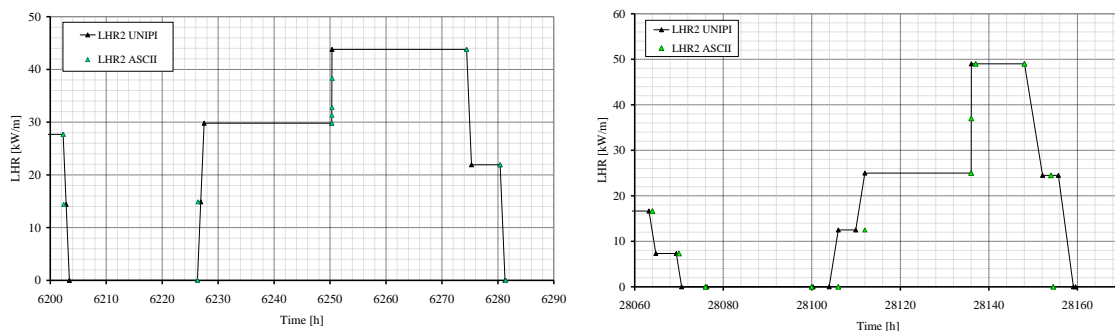
Figure 1. Base irradiation: implemented TU LHR history



(a) BWR Inter-Ramp Rod LR1 slice 2

(b) PWR Super-Ramp Rod PK23 slice 2

Figure 2. Power ramp: implemented TU LHR history



(a) BWR Inter-Ramp Rod LR1 slice 2

(b) PWR Super-Ramp Rod PK23 slice 2

## 5. Assessment of the TU code

In the following sections, results from analysis with the TRANSURANUS code version “v1m1j08” are presented. Then the FGR results of the two code versions are compared for base irradiation and power ramps.

## 6. Reference case results

With reference to Table 1, the option (C) (“TFGR model” for fission gas release at grain boundary) has been assumed as reference case for the current paper. However, the results of the post test calculations are reported together (and compared) with the analysis performed using the other three options available in TRANSURANUS code of fission gas release at grain boundary, option A, B and D of the same table.

In the following the results of FGR are discussed separately for the BWR Inter-Ramp and PWR Super-Ramp Projects.

Two figures are reported in order to summarise the outcomes of both experiments:

- Figure 3 reports the comparison between experimental measures and calculated results for both cases. This figure highlights the accuracy of the code results, evidencing the -50%+100% error.
- Figure 4 shows fission gas released (FGR) calculated with TRANSURANUS code options (C) and measured for both the databases, as a function of the ramp terminal level.

### 6.1. BWR inter-ramp: fission gas released

The experimental data of the FGR are measured during the PIE for 11 rods. Among them, nine were found non-failed and two (labeled HS1 and BR1 belonging to BIRP4) failed during the PIE. The evaluation of the FGR has been executed using two different methods based on the percentage of Kr and Xe, respectively.

The comparison between experimental measures and calculated results is summarised in Figure 3 (a) for PIE using Kr%. This figure highlights the accuracy of the code results, evidencing the -50%+100% error. Rod labels are reported with different colors, that represents different BIRP numbers.

Figure 4 (a) shows FGR calculated with TRANSURANUS code options (A) and (C) and measured with Kr%, as a function of the ramp terminal level. Higher values of FGR correspond to higher values of linear heat rate.

Calculations performed using option A and option B show very similar predictions in all the simulations, values above about 5.5% using these two options seem to be better predicted than lower ones. The “TFGR model” (option C, reference case) overestimates systematically the fission gas release for all cases except for rod No 12 DR1.

Evolution of linear heat rate for the hottest axial fuel slice and calculated fission gas release time trend for different TRANSURANUS model options is reported for the case of rod 16 in Figure 5 (a), focusing on power ramp. For the sake of clarity, in the same figure the linear heat rate history is reported as well. In the figure the calculated data for the end of the base irradiation and the power ramp from FRAPCON-3 are also reported, taken from<sup>14</sup>. The complete set of FGR time trends is reported in Ref. <sup>9</sup>. FGR time trend figures show that, considering the reference case (option C), a noticeable increment of fission gas release during the ramp and hold time at ramp terminal level is observed in all the cases. Moreover, the comparison with the experimental data shows a systematic overestimation of FGR (all cases except rod No 12 DR1).

The different behavior of rod DR1 may stem from a low density of the fuel compared to the other rods, leading to a large open porosity fraction. It should be mentioned that the open porosity is not directly taken into account in the fission gas release model of TRANSURANUS code.

Finally, in all the cases, as expected, the upper release limit overestimates the release of fission gas.

In summary:

- The two options A and B, which differ for the grain boundary saturation concentration modeling, constant in the first case and a function of the temperature the latter, exhibit negligible differences in the FGR predictions.
- Comparisons (on two rods) between TRANSURANUS and FRAPCON-3 codes reveal analogous results during base irradiation, as well as during power ramp. Considering the different FGR models applied in the TRANSURANUS simulations, the better results were obtained with the options A and B (only one result is reported in the current paper).
- The “TFGR model” (option C, reference case) overestimates systematically, the fission gas release due to the complete and immediate release of the FGR at the grain boundary at the power ramps occurrence.
- The upper release limit model (option D), overestimates systematically the final fission gas released - the grain boundary saturation concentration is set to 0.

## **6.2. PWR super-ramp: FGR**

Fission gas analysis was performed on all non-failed rods except PK1/S. The fission gas release values are based on the fraction released of the total fission gas present into the fuel rods. The two non-failed Westinghouse rods are not modeled for the current analysis.

---

<sup>14</sup> Lanning D. D., C. E. Beyer, G. A. Berna, “FRAPCON-3: Integral Assessment”, NUREG/CR-6534 Volume 3 PNNL-11513, December 1997.

The comparison between experimental measures and calculated results is summarised in Figure 3 (b). This figure highlights the accuracy of the code results, evidencing the -50%+100% error.

Figure 4 (b) shows FGR calculated with TRANSURANUS code options (A) and (C) and measured, as a function of the ramp terminal level.

Calculations performed using option A and option B show very similar predictions in all the simulations. These options underestimate systematically the FGR in all cases but rods PK1/4 and PK2/S. The “TFGR model” (option C, reference case) improve the prediction providing higher values of FGR.

Evolution of linear heat rate for the hottest axial fuel slice and calculated fission gas release time trend for different TRANSURANUS model options is reported for the case of rod PK2/3 in Figure 5 (b), focusing on power ramp. For the sake of clarity, in the same figure the linear heat rate history is reported as well.

Finally, the upper release limit case, option D, exhibits a very similar behavior of the option C, reference case.

In summary:

- The two options A and B, which differ for the grain boundary saturation concentration modeling, constant in the first case and a function of the temperature the latter, exhibit negligible differences in the FGR predictions. The results with both options underestimate systematically the FGR (all cases but two).
- The TFGR fission gas release model (option C, reference case):
  - overestimates the FGR in 4 out of 16 cases;
  - good agreement for 2 out of 16 rods;
  - underestimates the FGR all the remaining 10 out of 16 rods.
- The upper release limit model (option D) exhibits a very similar behavior compared to the reference case.

Figure 3. Summary of PIE and calculated values (options A, B, C and D) at the end of the experiments: fission gas released

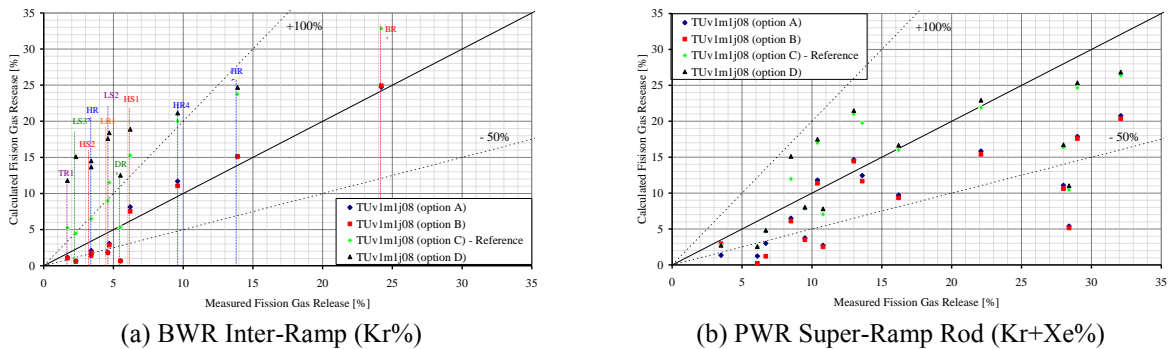


Figure 4. Calculated reference case: ramp terminal level vs fission gas released measured Kr% and calculated

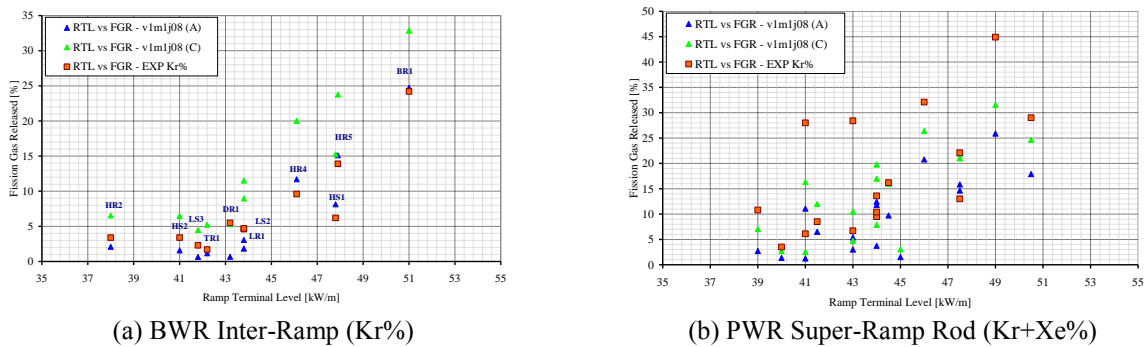
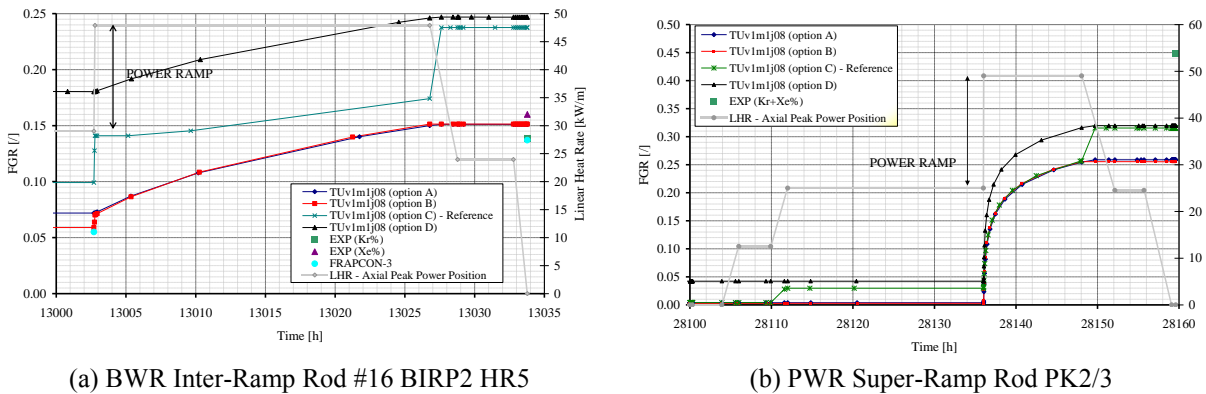


Figure 5. Calculated time trends of fission gas released (options A, B, C and D), experimental data, linear heat rate: zoom on ramp



(a) BWR Inter-Ramp Rod #16 BIRP2 HR5

(b) PWR Super-Ramp Rod PK2/3

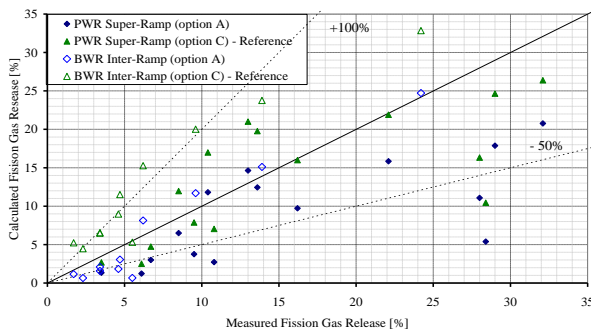


Figure 6. Summary of measured and calculated fission gas released: BWR inter-ramp and PWR super-ramp project

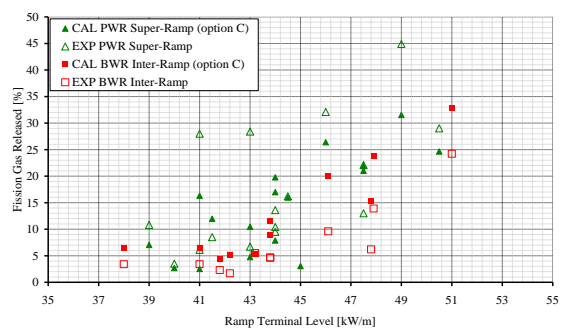


Figure 7. Summary of measured and calculated fission gas released vs ramp terminal level: BWR inter-ramp and PWR super-ramp project

## 7. Conclusions

The experimental data of twenty fuel rods irradiated in the BWR Inter-Ramp and twenty-six out of twenty-eight rods irradiated in the PWR Super-Ramp Projects have been compared with the simulations performed by TRANSURANUS code version “v1m1j08”. The activity is carried out in order to assess the performance of the new fission gas release model, “TFGR model”, implemented in the last version of the code, in predicting the fission gas release during power ramps. The reference calculations have been executed using this “TFGR model” (IGRBDM 3) of fission gas release at grain boundary.

The analyses performed allow stating the following conclusions:

- BWR Inter-Ramp (option A) exhibits the best prediction at high FGR values (above about 5.5%).
- BWR Inter-Ramp (option A):
  - Underestimates FGR for low values of ramp terminal level.
  - Overestimates higher FGR at higher values of ramp terminal level.
- BWR Inter-Ramp FGR calculated by (option C) overestimates systematically the FGR.
- PWR Super-Ramp (option A) underestimates systematically the experimental data in all cases but two (rods PK1/4 and PK2/S).
- PWR Super-Ramp (option C) underestimates the FGR for 10 out of 16 rods.

The activity presented in this paper represents an extension of the independent assessment of the FGR models carried out on the TRANSURANUS code. On the one hand the current simulations of the BWR rods in the Inter-Ramp project, indicate that the new “TFGR model” generally overestimates the FGR measured at end-of-life, whereas a different trend is evidenced by the PWR Super-Ramp Project simulations: underestimation

of FGR. On the basis of these results it seems therefore necessary to refine the model for ramp release. More precisely, one might consider only a partial venting of the grain boundary inventory during rapid power variations, rather than a total release as currently implemented. Nevertheless, this will require more experimental data to be analyzed.

## **8. Acknowledgments**

The authors wish to express their thanks to Enrico Sartori, for his effort in creating, maintaining and making available the OECD/NEA/NSC International Fuel Performance Experiments database. Gratitude is also expressed for Studsvik that made available to the scientific community, through the OECD IFPE database, the BWR Inter-Ramp and PWR Super-Ramp experimental data analyzed in the current paper in the framework of the IAEA FUMEX-III project.

The authors gratefully acknowledge the support and the kind availability of the fuel modeling team at ITU.



## UNIVERSITÀ DI PISA

DIPARTIMENTO DI INGEGNERIA MECCANICA,  
NUCLEARE E DELLA PRODUZIONE  
VIA DI OTTAVIANO 2, 56100 PISA

**OECD/NEA Workshop on Nuclear Fuel Behaviour  
during Reactivity Initiated Accidents**

*Paris, France 9-11 September 2009*

### Capabilities of TRANSURANUS Code in Simulating Power Ramp Tests from the IFPE Database

Gruppo Ricerca Nucleare S. Piero a Grado

Martina Adomi  
Davide Rozzia  
Alessandro Del Nevo  
Francesco D'Auria



## CONTENT

□	INTRODUCTION
□	OBJECTIVE OF THE ACTIVITIES
□	OUTLINE OF TRANSURANUS CODE AND CAPABILITIES
□	DESCRIPTION OF THE EXPERIMENTS
>	OBJECTIVE OF THE ACTIVITY
>	OBJECTIVES OF THE PROJECT
>	DESCRIPTION OF THE EXPERIMENTS
>	IRRADIATION PROGRAMS
□	MODELLING
□	RELEVANT RESULTS FOR VALIDATION
>	FISSION GAS RELEASE
□	SUMMARY
□	CONCLUSIONS

Nuclear Fuel Behaviour during RIAs, Paris, France, 9-11 September 2009
2/23



## INTRODUCTION

□	The fuel matrix and the cladding constitute the first barrier against radioactive fission product release.
□	The defense in depth concept requires the comprehensive understanding of fuel rod behavior and accurate prediction of the lifetime in normal operation and in accident condition as well.
□	Investigations of fuel behavior are carried out in close connection with experimental research operation feedback and computational analyses. → <b>IFPE Database: BWR Inter-Ramp, PWR Super-Ramp</b>
□	The experimental data are used for assessing the TRANSURANUS capabilities in predicting the fission gas release (FGR).

Nuclear Fuel Behaviour during RIAs, Paris, France, 9-11 September 2009
3/23



## OBJECTIVE OF THE ACTIVITY

Gruppo Ricerca Nucleare S. Piero a Grado

**Verification of TRANSURANUS code version v1m1j08 against BWR-Inter-Ramp and PWR-Super-Ramp databases.**

- ❑ Development and setup of **twenty** input decks modeling the fuel rods irradiated in the BWR-Inter-Ramp project and **twenty-six** in the PWR-Super-Ramp project as well as the boundary conditions available from the IFPE database (base irradiation and power-ramp).
  - The burnup values range between 10 and 45 MWd/kgU.
  - Pre-, during-, and post-irradiation, non destructive and destructive examinations are executed to:
    - determine and understand the behavior of the fuel rods
    - provide suitable data useful for code validation.
- ❑ Sensitivity calculations have been performed in order to address the impact of selected parameters and/or code options on the results.
- ❑ The analysis is focused on **fission gas release behavior under ramp test conditions** since a new FGR model, to be invoked in the event of rapid power variations, has been implemented in the TRANSURANUS code.

Nuclear Fuel Behaviour during RIAs, Paris, France, 9-11 September 2009
4/23



## OBJECTIVES OF THE PROJECT

Gruppo Ricerca Nucleare S. Piero a Grado

<p>❑ <b>BWR-Inter-Ramp:</b></p> <ul style="list-style-type: none"> <li>➢ Establishment of <b>fail-safe operating limits</b> of 20 standard-type, unpressurized BWR fuel rods on over-power ramping at the burn-up levels of <b>10 and 20 MWd/kgU</b>.</li> <li>➢ Investigation of influence of <b>three main design parameters</b> on fuel rod performance under power ramping:                             <ul style="list-style-type: none"> <li>• clad heat treatment;</li> <li>• pellet/clad diametral gap size;</li> <li>• fuel density.</li> </ul> </li> <li>➢ Investigation of <b>failure mechanism</b> and associated phenomena.</li> </ul>	<p>❑ <b>PWR-Super-Ramp:</b></p> <ul style="list-style-type: none"> <li>➢ Establishment of <b>fail-safe operating limits</b> of 28 standard-type, pressurized PWR fuel rods on over-power ramping at the burn-up levels exceeding <b>30 MWd/kgU</b>.</li> <li>➢ Establish the possible increase in <b>pellet clad interaction</b> failure power levels for candidate pellet clad interaction remedy design fuel rod at selected burnup levels.</li> <li>➢ Investigate whether or not a change in <b>failure propensity or failure mode</b> is obtained as compared to the failure behavior at lower burnup levels.</li> </ul>
---	--

Nuclear Fuel Behaviour during RIAs, Paris, France, 9-11 September 2009
5/23

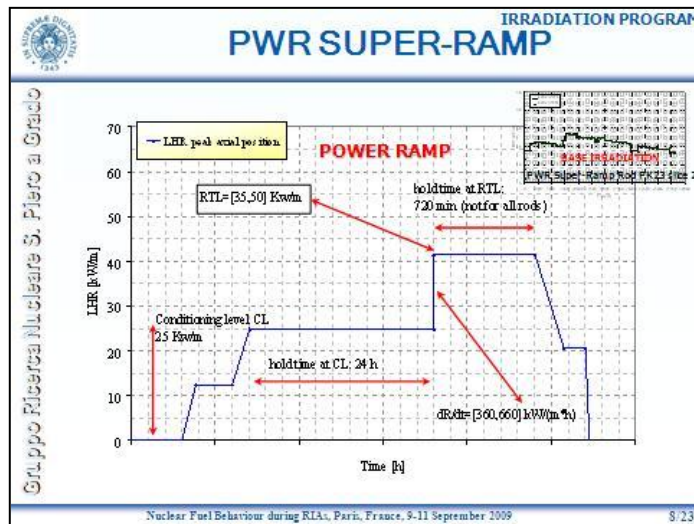
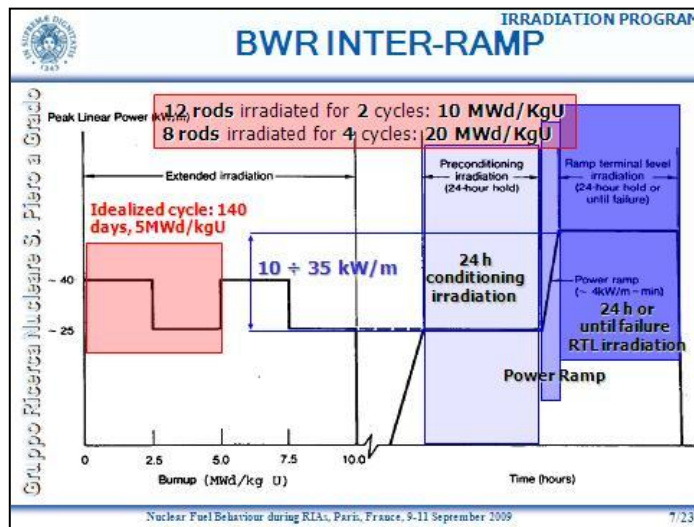


## DESCRIPTION OF THE EXPERIMENTS

Gruppo Ricerca Nucleare S. Piero a Grado

<p><b>BWR-Inter-Ramp</b></p> <p><b>BASE IRRADIATION</b></p> <p>❑ <b>Studsvisk R2 Research Reactor:</b></p> <ul style="list-style-type: none"> <li>➢ Material Testing Reactor (Sweden).</li> <li>➢ <b>50 MWth</b></li> <li>➢ Cooled and moderated by light water at <b>3.3 bar</b></li> <li>➢ Active length of the core was <b>60 cm</b>,</li> <li>➢ <i>Base irradiation in the Boiling Capsule Inter-Ramp Project (BIRP) pressurized container</i></li> </ul> <p><b>POWER RAMP</b></p> <p>❑ <b>Studsvisk R2 Research Reactor:</b></p> <ul style="list-style-type: none"> <li>➢ Power ramp in the high pressure loop</li> </ul>	<p><b>PWR-Super-Ramp</b></p> <p><b>BASE IRRADIATION</b></p> <p>❑ <b>Obrigheim Power Reactor:</b></p> <p>(group KWU)</p> <ul style="list-style-type: none"> <li>➢ Commercial type (Germany)</li> <li>➢ <b>1045 MWth</b></li> <li>➢ Cooled and moderated by light water at <b>14.5 MPa</b></li> <li>➢ Active length of the core was <b>2650 mm</b></li> </ul> <p>❑ <b>BR-3 Power Reactor:</b></p> <p>(group WJ)</p> <ul style="list-style-type: none"> <li>➢ Semi-commercial type (Mol, Belgium)</li> <li>➢ <b>40.9 MWth</b></li> <li>➢ Cooled and moderated by light water at <b>14 MPa</b></li> <li>➢ Active length of the core was <b>1600 mm</b></li> </ul> <p><b>POWER RAMP</b></p> <p>❑ <b>Studsvisk R2 Research Reactor:</b></p> <p>(group KWU and WJ):</p> <ul style="list-style-type: none"> <li>➢ Power ramp in the high pressure loop</li> </ul>
--	---

Nuclear Fuel Behaviour during RIAs, Paris, France, 9-11 September 2009
6/23



### FISSION GAS RELEASE OUTLINE OF TU CODE

TRANSURANUS code is used for the analysis

Fission gas release prediction is influenced by the modeling of the intergranular phenomena

#### Intergranular phenomena

- When the gas reaches grain boundaries, it precipitates on grain faces to form lenticular bubbles of the size of the order of  $\mu\text{m}$  which are immobile.
- Part of the gas inside these bubbles is transported back to the grain by fission spikes (**irradiation induced resolution**). When a **saturation concentration** is reached on the grain face, fission gas accumulates on the grain edge.
- If gas on the grain edges has also saturated, interlinkage occurs and the gas may be **released** to free volume.
- If grain growth occurs, single gas atoms as well as fission gas included in intragranular bubbles is **swept out**.

Nuclear Fuel Behaviour during RIAs, Paris, France, 9-11 September 2009 9/23

FISSION GAS RELEASE

## OUTLINE OF TU CODE

Gruppo Ricerca Nucleare S. Piero a Grado

**In the TRANSURANUS code four models are available**

- ❑ NO gas on the grain boundary.
- ❑ The grain boundary saturation concentration is a constant.
  - The release occurs when at grain boundary the fission gas reaches the saturation concentration, which is a constant. The value of the grain boundary saturation concentration is provided by an input variable (*Gas\_gb*).
- ❑ The grain boundary saturation concentration depends on the temperature.
  - The release occurs when at grain boundary the fission gas reaches the saturation concentration, which depends on temperature. The value *a'* of the grain boundary saturation concentration is provided by an input variable (*Gas\_gb*).

$$\sim \frac{a'}{T}$$

Nuclear Fuel Behaviour during RIAs, Paris, France, 9-11 September 2009 10/23

FISSION GAS RELEASE

## OUTLINE OF TU CODE

Gruppo Ricerca Nucleare S. Piero a Grado

**In the TRANSURANUS code four models are available (cont'd)**

- ❑ Complete and instantaneous release from the grain boundaries, when the conditions of a transient are fulfilled (to be invoked in the event of rapid power variations).
  - This model, has been implemented in order to take into account the additional release observed in the event of rapid power variation. It consists of two contributions:
    - **Microcracking** It takes into account the considerable fission gas burst in case of rapid power increase, which may be explained by the fact that changes in stresses cause microcracking, which in turn causes the entire fission gas inventory stored at the grain boundaries to be instantaneously released. This process is not thermally activated even if it requires to reach a specific temperature level.
    - Additional part due to the **gas transport from the grain to the grain boundaries** resulting from our power increase. This is because the diffusion coefficient increases only when power increases. This has no physical explanation and it is also not consistent with time constant of burst release.
  - In TU code the following thresholds are implemented:
 

$$T_{max} > 1500 (1 - b_{u_{max}} / 80)$$

$$\Delta q' > 3.5 \text{ kW/m}$$
  - No minimum power level is required, since it is redundant: with temperature (i.e. linear heat rate is approximately linearly dependent on the fuel central temperature).

Nuclear Fuel Behaviour during RIAs, Paris, France, 9-11 September 2009 11/23

FISSION GAS RELEASE

## MODELLING

Gruppo Ricerca Nucleare S. Piero a Grado

- ❑ Starting from the first input deck developed and set up for the simulation of the fuel rod 1 (identified with BIRP1, corresponding to the base irradiation and labeled LR1), further 19 different models, representing all the fuel rods irradiated in the "BWR-Inter-Ramp Project", have been prepared.
- ❑ Starting from the first input deck developed and set up for the simulation of the fuel rod 01-PK1/1, further 25 different models, representing all the fuel rods irradiated in the "PWR-Super-Ramp Project", have been prepared.
- ❑ Only the **active part of the fuel** is taken into account.
  - The active part has been divided into **4 slices, 3 or 6 slices**, according to the experimental data available.
  - Each axial part is represented, as far as possible, identical to the data available in the **Package NEA-1555/01 of the IFPE/INTER-RAMP or Package NEA-1557/01 of the IFPE/SUPER-RAMP** experiment belonging both to the **IFPE database**. Hypothesis were made for the linear heat rate BIC preparation.
  - Compensating natural uranium pellet are not taken into consideration in the model, as well as the relative gap volume.

Nuclear Fuel Behaviour during RIAs, Paris, France, 9-11 September 2009 12/23



## MODELLING

Gruppo Ricerca Nucleare S. Piero a Grado

- The boundary conditions used are:
  - > linear heat rate for each of the four axial positions;
  - > fast flux;
  - > cladding temperature histories for each of the four axial positions;
  - > pressure.
- The **TEMPERATURES** and **POWERS** from ASCII files available from IFPE database are those at the given time which have been constant over the interval time step, i.e. the data are in histogram format.
- Steady-state (implicit) analysis has been used for the calculations.
- The **coolant is not considered** in the calculations.
- The TU code options, models and correlations, selected are documented in detail, this should allow an easy review of the input deck.
- Recommended models are chosen when available.**

Nuclear Fuel Behaviour during RIAs, Paris, France, 9-11 September 2009
13/23



## MODELLING

FISSION GAS RELEASE

Gruppo Ricerca Nucleare S. Piero a Grado

**Fission gas release options**

- The recommended TU URGAS algorithm with the diffusion coefficients of H<sub>j</sub>. Matzke (thermal) and a constant athermal diffusion coefficient has been chosen for all the calculations (activated with the option **FGRMOD=6** and **idifSol=0** in the TU input deck). This option is used together an intragranular fission gas release model (IGRBDM).
- The reference calculation (C) has been performed using the new intergranular FGR model for power ramps (modified Koo model) selected by option **IGRBDM=3**.

No	IGRBDM	Gas_gb	Note
(A)	1	1E-4	"v1mlj07" TU standard
(B)	2	0.1773	-
(C)	3	-	"TFGR model"
(D)	0	-	"Upper release limit"

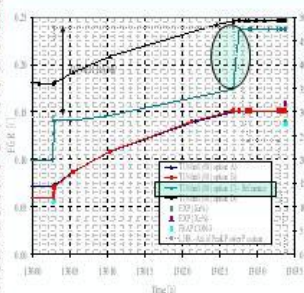
Nuclear Fuel Behaviour during RIAs, Paris, France, 9-11 September 2009
14/23



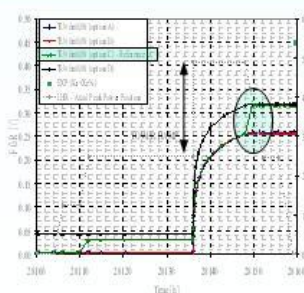
## RESULTS

FISSION GAS RELEASE

Gruppo Ricerca Nucleare S. Piero a Grado

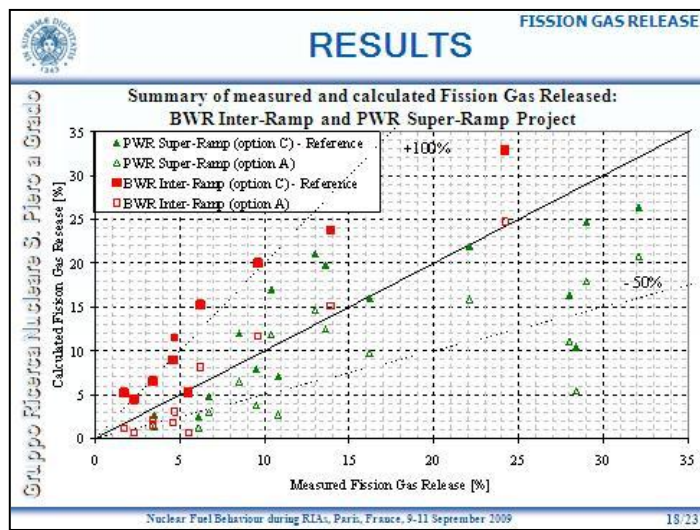
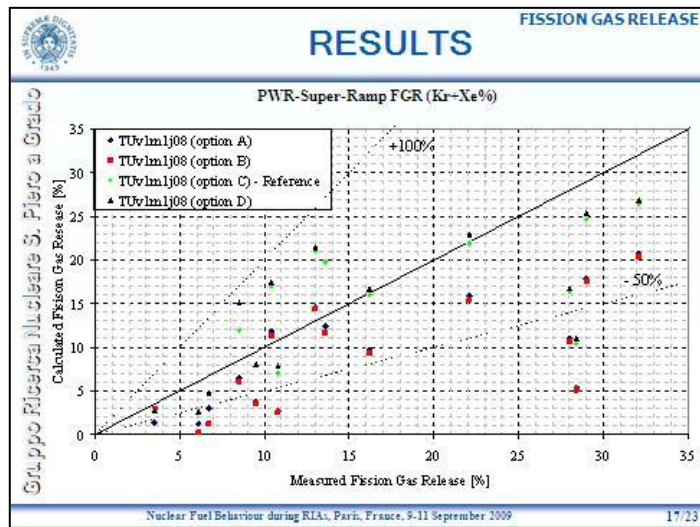
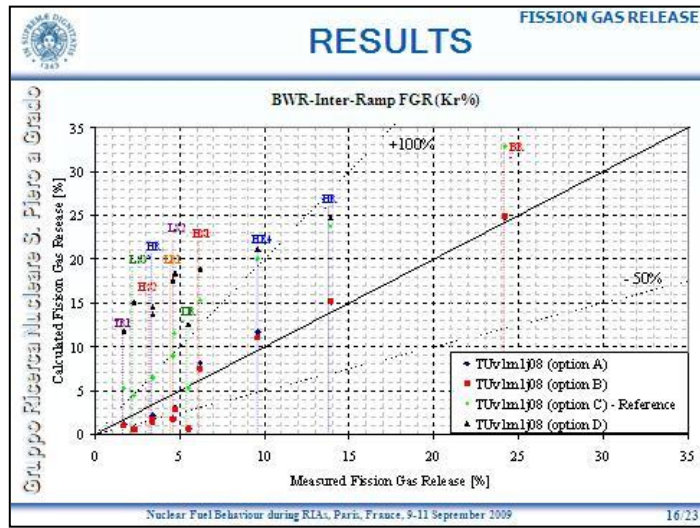


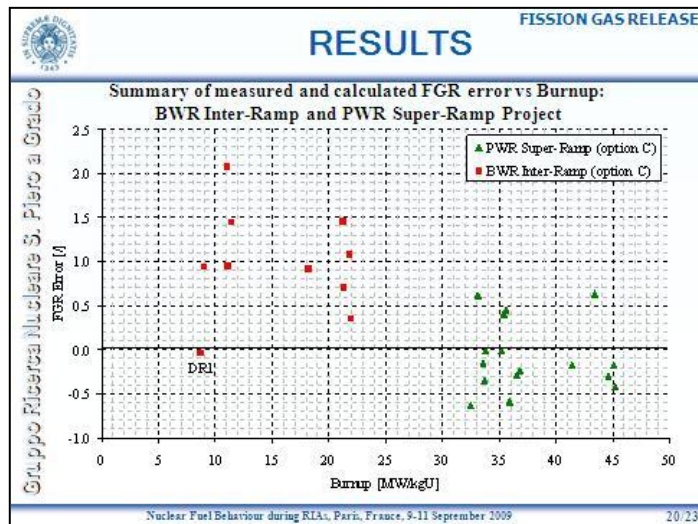
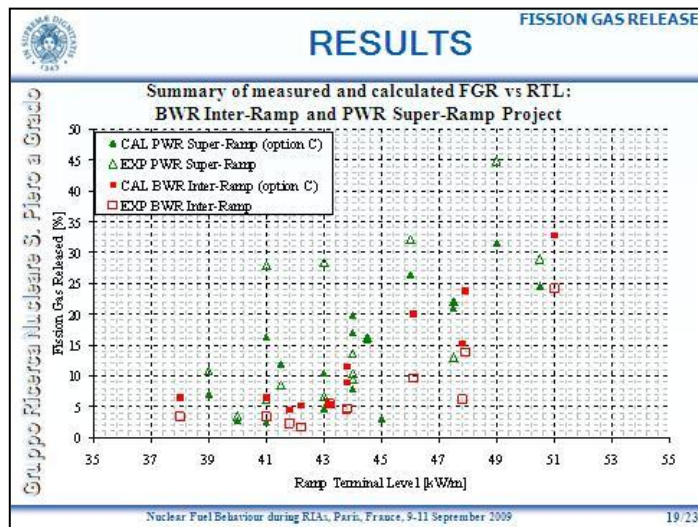
**BWR Inter-Ramp Rod #16 HR5**



**PWR Super-Ramp Rod PK2/3**

Nuclear Fuel Behaviour during RIAs, Paris, France, 9-11 September 2009
15/23





SUMMARY

Gruppo Ricerca Nucleare S. Piero a Grado

- The experimental data of **twenty** fuel rods irradiated in the BWR Inter-Ramp and **twenty-six** out of twenty-eight rods irradiated in the PWR Super-Ramp Projects have been compared with the simulations performed by TRANSURANUS code version "v1m1j08".
- The activity is carried out in order to assess the performance of the new fission gas release model, "**TFGR model**", implemented in the last version of the TRANSURANUS code, in predicting the fission gas release during power ramps.
- The reference calculations have been executed using this "**TFGR model**" of fission gas release at grain boundary.

Nuclear Fuel Behaviour during RIAs, Paris, France, 9-11 September 2009 21/23



## CONCLUSIONS (1/2)

The analyses performed allow stating the following conclusions.

**BWR Inter-Ramp:**

- ❑ The "TU standard" (option A) exhibits the best prediction at high FGR values (above about 5.5%). This option:
  - underestimates FGR for low values of ramp terminal level;
  - overestimates higher FGR at higher values of ramp terminal level.
- ❑ The "TFGR model" (option C, reference case) overestimates systematically the fission gas release, due to the complete and immediate release of the fission gas at the grain boundary at the power ramp occurrence.

**PWR Super-Ramp:**

- ❑ The "TU standard" (option A) underestimates systematically the experimental data in all cases but two (rods PK1/4 and PK2/5).
- ❑ The "TFGR model" (option C, reference case):
  - overestimation of the FGR for 4 out of 16 rods;
  - good agreement for 2 out of 16 rods;
  - underestimation of the FGR all the remaining 10 out of 16 rods.

Nuclear Fuel Behaviour during RIAs, Paris, France, 9-11 September 2009
22/23



## CONCLUSIONS (2/2)

- ❑ The activity represents an extension of the independent assessment of the FGR models carried out on the TRANSURANUS code.
- ❑ The current simulations of the BWR rods of the Inter-Ramp project indicate that the new "TFGR model" generally overestimates the FGR measured at end-of-life, due to the complete and immediate release of the FGR at the grain boundary.
- ❑ However, the results of the PWR Super-Ramp database show a general under-prediction for *higher burn-up* values for both models (A and C). Such a trend might be associated with the high burn-up structure (HBS) that should contribute with an additional release in the case of rapid power variations (quantitative contribution of the HBS under accidental conditions is still under discussion).

→ On the basis of these results it seems therefore necessary to refine the model for ramp release.

→ This will require an extension of the validation activity related to the power ramp tests (different burnup ranges) and to transient conditions (e.g. LOCA and RIA).

Nuclear Fuel Behaviour during RIAs, Paris, France, 9-11 September 2009
23/23

**SESSION FOUR**

**RIA Core Analysis**

**Analysis of PWR Control Rod Ejection Accident with the Coupled Code System Sketch-Ins/Trace by Incorporating Pin Power Reconstruction Model**

Tetsuo Nakajima and Tomohiro Sakai (JNES, Japan)

**A Survey of Available Margin in a PWR RIA with Statistical Methods and 3D Kinetics**

Javier Riverola and Tomas Nunez (ENUSA, Spain)



## **ANALYSIS OF PWR CONTROL ROD EJECTION ACCIDENT WITH THE COUPLED CODE SYSTEM SKETCH-INS/TRACE BY INCORPORATING PIN POWER RECONSTRUCTION MODEL**

**Tetsuo Nakajima**

Japan Nuclear Energy Safety Organisation (JNES), Japan

**Tomohiro Sakai**

Japan Nuclear Energy Safety Organisation (JNES), Japan

### **1. Introduction**

In Japanese nuclear safety review, the fuel failure threshold for the reactivity-initiated accident (RIA) was revised in 1998 based on the experimental data obtained with high burn-up fuels. The revised failure threshold related to PCMI is defined by the fuel enthalpy rise as a stepwise decreasing function with increasing fuel burn-up. In the safety analysis of RIA, it is required to calculate the pin powers of the reactor core with a high degree of accuracy in order to make the correct evaluation regarding the core design and safety margins.

The pin power distributions throughout the reactor core are commonly produced by synthesizing two-dimensional pin-by-pin calculations of assembly and three-dimensional nodal calculations of core. This conventional approach is insufficient to accurately predict the pin power distributions of the reactor core because the flux distributions within each assembly are not considered (i.e., the node averaged fluxes are used).

The pin power reconstruction model was incorporated in the 3-D nodal kinetics code SKETCH-INS[1] in order to produce accurate calculation of three-dimensional pin power distributions throughout the reactor core. The flux distributions within each assembly are correctly treated in this model.

In order to verify the employed pin power reconstruction model, the PWR MOX/UF<sub>4</sub> core transient benchmark problem[2] provided by the OECD/NEA and US NRC was analyzed with the coupled code system SKETCH-INS/TRACE by incorporating the model and the influence of pin power reconstruction model was studied. The description of the model and results of calculations are presented in this paper.

### **2. Coupled code system SKETCH-INS/TRACE**

The SKETCH-INS is a three-dimensional nodal code for solving neutron diffusion equations of steady-state and kinetics problems. The semi-analytic nodal method based on the nonlinear iteration procedure is used for spatial discretisation of diffusion equations. The time integration of neutron kinetics is performed by the fully implicit scheme with an analytical treatment of the delayed neutron precursors. The steady-state eigenvalue problems are solved by inverse iterations with Wielandt method, and the Chebyshev acceleration procedure is used for the neutron kinetics problems.

The TRACE code is a best-estimate system transient analysis code, which has a multidimensional thermal-hydraulic analysis capability [3]. The code solves the general transient two-phase coolant conditions in one and three dimensions using a realistic six-equation, two-fluid, finite difference model.

The 3-D nodal kinetics code SKETCH-INS was coupled with the thermal-hydraulic code TRACE. The coupling and data transfer between the two codes is organised by using the message-passing library Parallel Virtual Machine (PVM).

### 3. Pin power reconstruction model

The pin power reconstruction model employed in SKETCH-INS is based on the model used in SIMULATE-3 code [4]. The detailed pin power distributions within an assembly are reconstructed by synthesizing the local heterogeneous form function of each assembly into the global homogenized intranodal flux distribution:

$$P(x, y)_{reactor} = P(x, y)_{homogeneous} \cdot P(x, y)_{form\ function} \cdot \quad (1)$$

The local heterogeneous form function of each assembly is calculated by a 2-D lattice physics code. The intranodal power distributions are calculated from the groupwise nodal (homogenised) fission cross sections and flux distributions:

$$P(x, y)_{homogeneous} = \sum_{f_1} f_1(x, y) \cdot \Phi_1(x, y) + \sum_{f_2} f_2(x, y) \cdot \Phi_2(x, y). \quad (2)$$

The intranodal fast flux distribution  $\Phi_1$  is approximated by the following set of polynomial functions:

$$\Phi_1(x, y) = \sum_{i,j=0}^4 a_{i,j} \cdot R_i(x) \cdot R_j(y), \quad (3)$$

where

$$\begin{aligned} R_0(u) &= 1, & R_1(u) &= u, & R_2(u) &= \frac{1}{2}(3u^2 - 1), & R_3(u) &= \frac{1}{2}(5u^3 - 3u), \\ R_4(u) &= \frac{1}{8}(35u^4 - 30u^2 + 3), & u &= x \text{ or } y. \end{aligned}$$

The intranodal thermal flux distribution  $\Phi_2$  is approximated by the following set of functions:

$$\Phi_2(x, y) = \Phi_1(x, y) \cdot c_{00} + \sum_{\substack{i,j=0 \\ i=j \neq 0}}^4 c_{i,j} \cdot F_i(x) \cdot F_j(y) \quad (4)$$

where

$$\begin{aligned} F_0(u) &= 1, & F_1(u) &= \sinh(\kappa u), & F_2(u) &= \cosh(\kappa u), \\ F_3(u) &= \sinh(2\kappa u), & F_4(u) &= \cosh(2\kappa u), & \kappa &= h \cdot \sqrt{\sum_{a2} / D_2}, & u &= x \text{ or } y, \end{aligned}$$

and h is the node width.

The complete intranodal flux distributions of Eqs. (3) and (4) require 25 expansion coefficients, respectively. By neglecting all of the cross terms of coefficients in Eqs. (3) and (4) with i or j > 2, the expansion coefficients are reduced to 13 per node. The 13 expansion coefficients are obtained by the following 13 constraints for intranodal flux distributions. The 13 constraints on the flux expansion are the node-averaged flux, four surface-averaged fluxes, four surface-averaged currents and four corner-point fluxes. The 8 constraints except four corner-point fluxes are directly provided by the 3-D nodal calculations of SKETCH-INS. The corner-point fluxes are determined by averaging the four estimates of the corner-point fluxes provided by the calculations of SKETCH-INS.

**4. Verification of pin power reconstruction model**

The ability of SKETCH-INS pin power reconstruction model was verified against the PWR MOX/ $UO_2$  core transient benchmark problem. SKETCH-INS pin power distributions were calculated for the benchmark problem and SKETCH-INS result was compared with the PARCS solution [5],[6] which was provided by the host organisation of the benchmark.

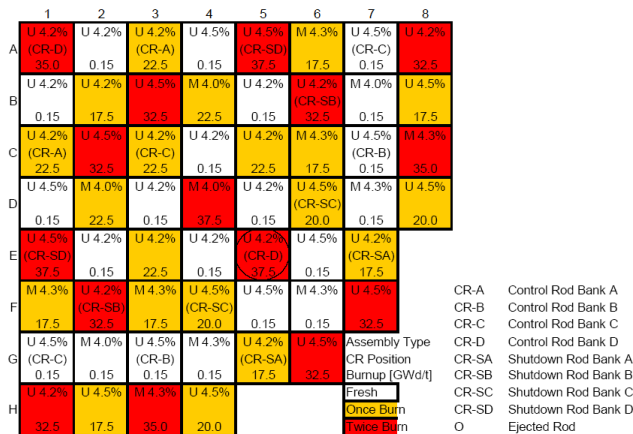
**4.1. Description of benchmark**

The PWR MOX/ $UO_2$  core transient benchmark problem is a PWR rod ejection problem to assess the ability of modern kinetics codes to predict the transient response of a core partially loaded with MOX fuel. In this benchmark problem, calculations were divided into four parts:

- Part I, 2-D fixed T-H conditions - calculate multiplication factor, rod worth, assembly and pin power.
- Part II, 3-D hot full power (HFP) conditions - calculate critical boron concentration, assembly and pin power.
- Part III, 3-D hot zero power (HZP) conditions - calculate critical boron concentration, assembly and pin power.
- Part IV, 3-D with Part III conditions - calculate transient response to control rod ejection accident.

The reactor core chosen for the simulation is based on four-loop Westinghouse PWR power plant similar to the reactor chosen for plutonium disposition in the US. The reactor core configuration is shown in Fig. 1.

**Figure 1. Core configuration (1/4 core)**



Fuel assembly type and number of assemblies loaded in the core are shown in Table 1. Main core and fuel design parameters are shown in Table 2.

**Table 1. Fuel assemblies loaded in the core**

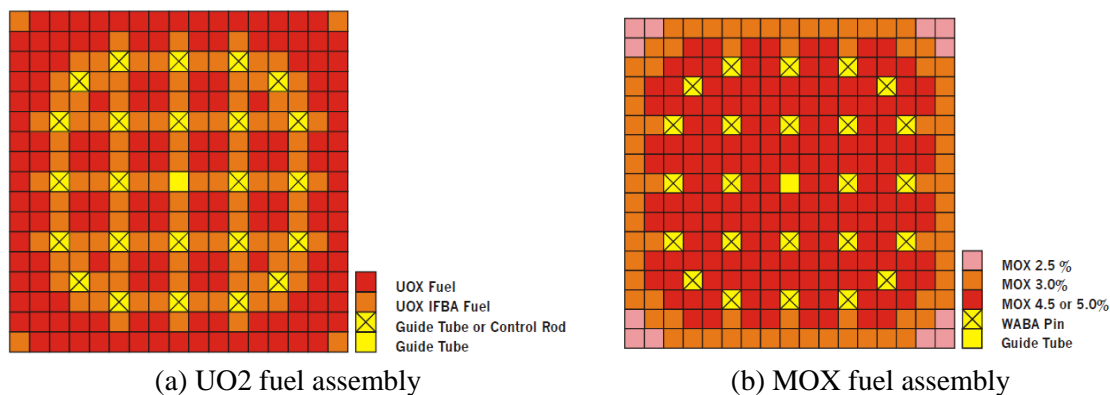
Fuel assembly type	Fresh fuel – 0 GWd/tHM	Once-burned fuel – 20.0 GWd/tHM	Twice-buened fuel – 35.0 GWd/tHM
$UO_2$ 4.2%	28	28	17
$UO_2$ 4.5%	24	24	20
MOX 4.0%	8	8	4
MOX 4.3%	12	12	8
Total number	72	72	49

**Table 2. Core and fuel design parameters**

Number of fuel assemblies	193
Power level (MWth)	3,565
Core inlet pressure (MPa)	15.5
Hot full power (HFP) core average moderator temperature (K)	580.0
Hot zero power (HZP) core average moderator temperature (K)	560.0
Fuel lattice, fuel rods per assembly	17×17, 264
Target discharge burn-up (GWd/tHM)	40.0-50.0
Maximum pin burn-up (GWd/tHM)	62.0

The configurations for the 17×17 UO<sub>2</sub> and MOX fuel assemblies are shown in Figure 2.

Figure 2. Fuel assembly configurations



A complete set of two-group macroscopic cross-sections and kinetic parameters defined for each assembly or cell type are provided together with discontinuity factors and pin power form functions. The cross-sections are given as functions of fuel temperature, moderator density and boron density.

#### 4.2. Results of benchmark for pin powers

##### 4.2.1. Comparison of pin power distributions at Part I conditions

SKETCH-INS pin power distributions were calculated for the benchmark problem of Part I and SKETCH-INS result was compared with the PARCS solution which was provided by the host organisation of the benchmark. Comparison of SKETCH-INS and PARCS pin power distributions at Part I (fixed T-H conditions) is shown in Figure 3. As shown in Figure 3, SKETCH-INS pin power distributions along diagonal line of core are consistent with the PARCS value. Root-mean-square (rms) differences in pin powers of six assemblies are less than 1.4% and the maximum difference is -6.8% in the peripheral assembly. SKETCH-INS predicts pin power distributions at Part I conditions with accuracy comparable to PARCS results.

##### 4.2.2. Comparison of pin power distributions at Part II conditions

Comparison of SKETCH-INS and PARCS pin power distributions at Part II (HFP conditions) is shown in Figure 4. As shown in Figure 4, SKETCH-INS pin power distributions along diagonal line of core are correctly predicted within a small difference of the PARCS value. Root-mean-square (rms) differences in pin powers of six assemblies are less than 1.6% and the maximum difference is 9.3% in the peripheral assembly. SKETCH-INS predicts pin power distributions at Part II (HFP conditions) with accuracy comparable to PARCS results.

##### 4.2.3. Comparison of pin power distributions at Part III conditions

Comparison of SKETCH-INS and PARCS pin power distributions at Part III (HZP conditions) is shown in Figure 5. As shown in Figure 5, SKETCH-INS pin power distributions along diagonal line of core are correctly predicted within a small difference of the PARCS value. Root-mean-square (rms) differences in pin powers of three assemblies are less than 1.8% and the maximum difference is 9.8%. SKETCH-INS predicts pin power distributions at Part III (HZP conditions) with accuracy comparable to PARCS results except three rodged assemblies of A1, C3 and E5.

Figure 3. Comparison of SKETCH-INS and PARCS pin power distributions at Part I conditions

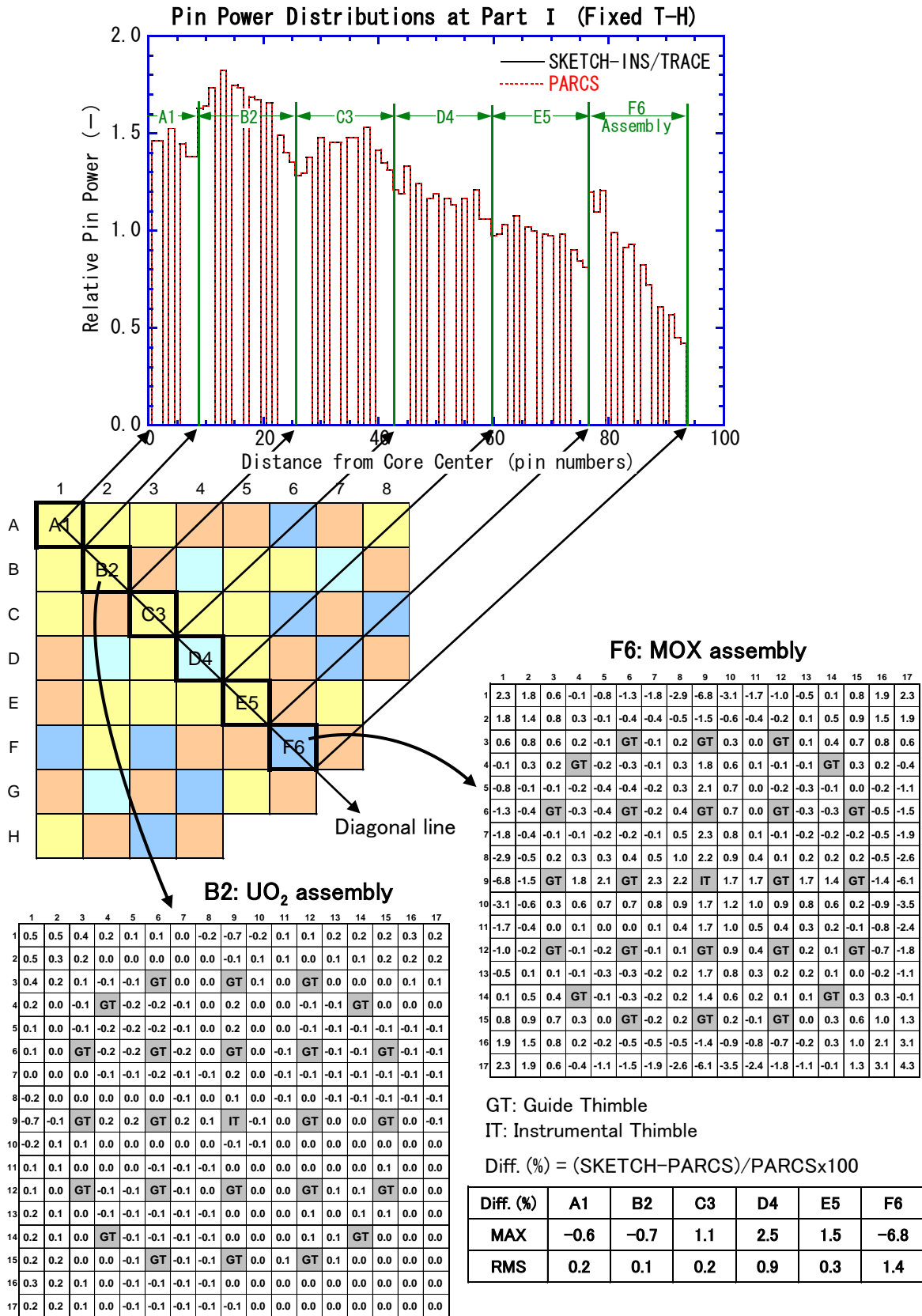


Figure 4. Comparison of SKETCH-INS and PARCS pin power distributions at Part II conditions

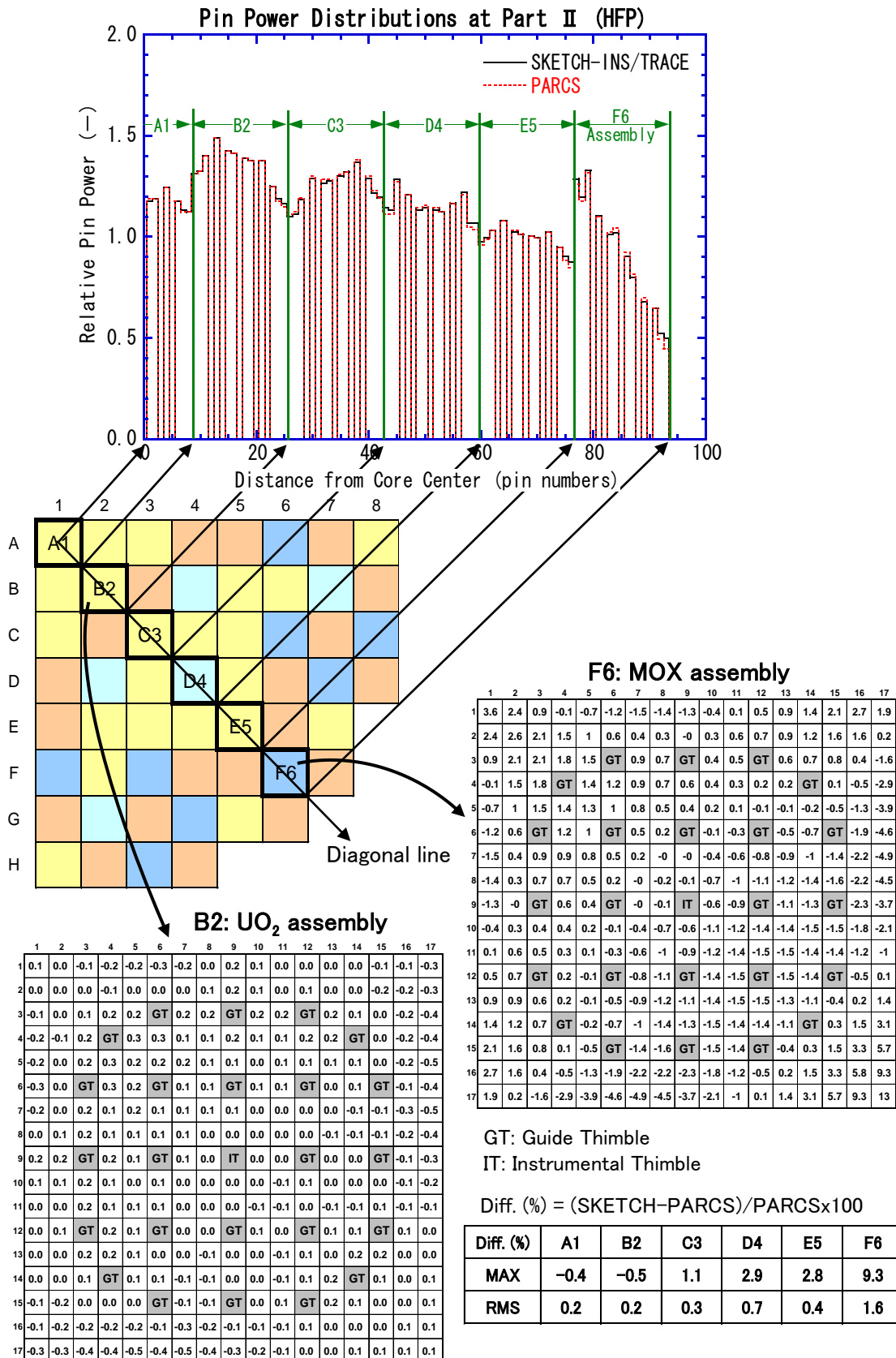
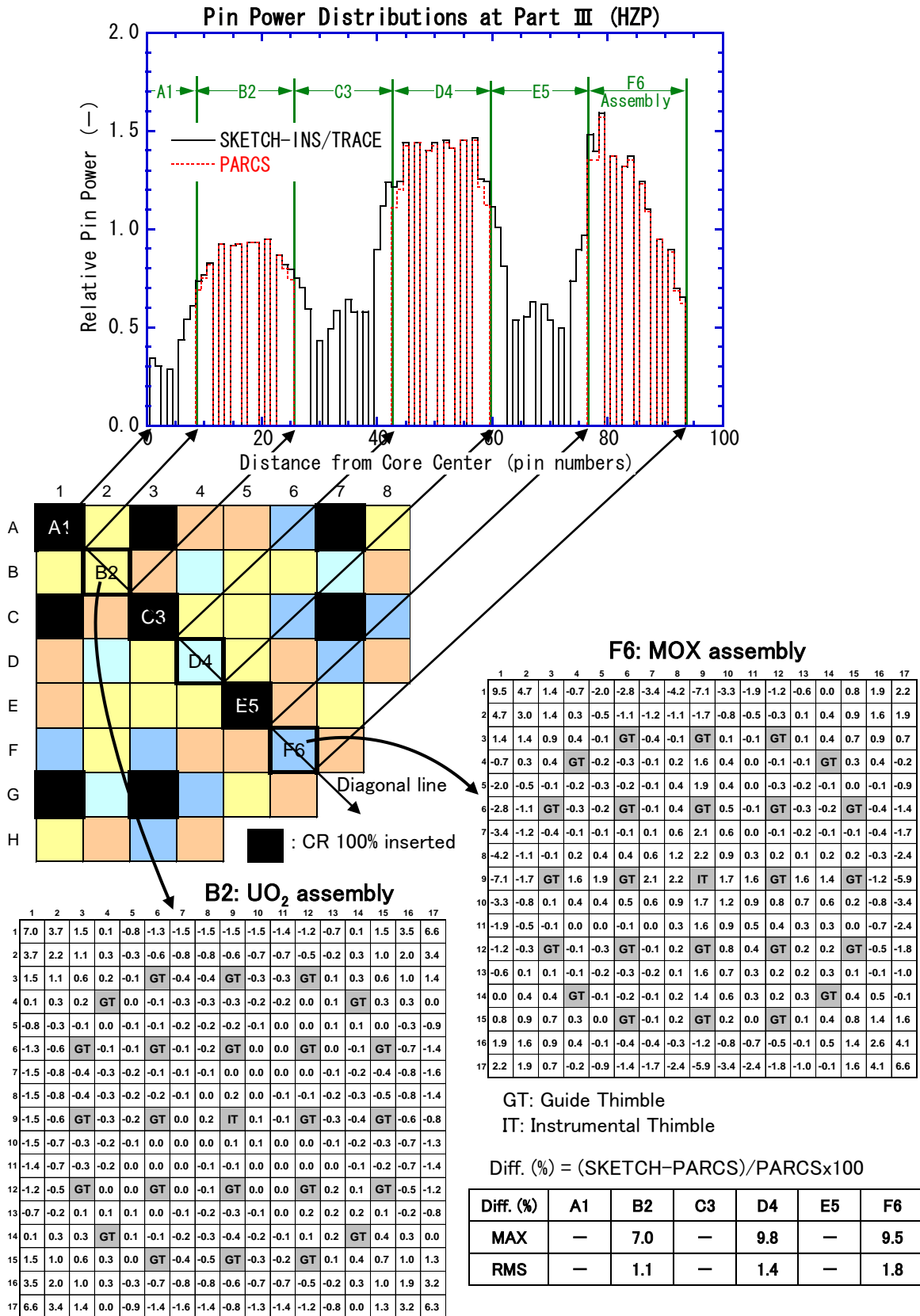


Figure 5. Comparison of SKETCH-INS and PARCS pin power distributions at Part III conditions



## 5. Analysis of Part IV control rod ejection benchmark problem by incorporating pin power reconstruction model

A PWR control rod ejection benchmark problem was analyzed with SKETCH-INS/TRACE by incorporating the pin power reconstruction model. As a part of the analysis, the influence of pin power reconstruction model was studied.

### 5.1 Core model and calculation conditions

The control rod ejection is performed from HZP, all control rod banks in, all shutdown rod banks out. The control rod pattern at HZP condition is shown in Figure 6. The ejected rod is located in the periphery of the core as shown in Figure 6. The control rod is assumed to be fully ejected in 0.1 seconds after which no reactor scram is considered.

The SKETCH-INS calculation was performed using full-core geometry for Part IV problem. A neutronics spatial mesh is defined with one node per fuel assembly in radial plane and 28 axial layers including reflectors in the SKETCH-INS model.

In the thermal-hydraulic calculation, the core region is modeled using 59 thermal-hydraulic channels. The axial spatial mesh has 24 layers. In the TRACE code, the CHAN component is used to simulate the reactor. The reactor boundary conditions are given using the FILL component on the bottom and the BREAK component on the top, which specify the mass flow rate and the reactor pressure respectively.

In the initial condition, a reactor is critical and a value of the boron concentration is calculated. The main calculation conditions used in the benchmark are shown in Table 3.

Figure 6. Control rod pattern at HZP conditions

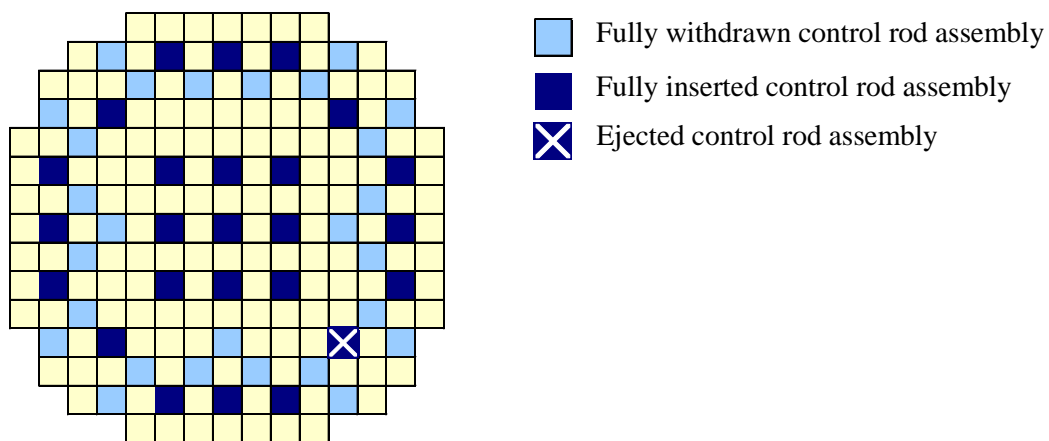


Table 3. Main calculation conditions for Part IV rod ejection benchmark problem

Initial power level ( $MW_{th}$ )	$3,565 \times 10^{-6}$
Coolant inlet pressure (MPa)	15.5
Coolant inlet temperature (K)	560
Control rod ejection time (s)	0.1
Delayed neutron fraction (%)	0.579
Prompt neutron lifetime ( $\mu s$ )	14.8

5.2 Results of calculations

5.2.1 Results of steady-state calculations

The core parameters in the initial condition at HZP were calculated and the steady-state results of SKETCH-INS/TRACE were compared with the PARCS solution. A comparison of SKETCH-INS/TRACE and PARCS solution is presented in Table 4. Figure 7 shows a comparison for the assembly power distribution at HZP with the PARCS solution. The core averaged axial power distribution is compared in Figure 8. The critical boron concentration of SKETCH-INS/TRACE is consistent with the PARCS solution. The maximum difference in the assembly power is only 0.7% and RMS of differences is 0.2%. The core averaged axial power distribution is in good agreement with the PARCS solution. The steady-state result of SKETCH-INS/TRACE is in good agreement with the PARCS solution.

Table 4. SKETCH-INS/TRACE results of Part IV control rod ejection benchmark problem and a comparison with PARCS solutions

Parameter		SKETCH-INS/TRACE	PARCS
Critical boron concentration (ppm)		1,340	1,341
Diff. in power assembly (%)	MAX	0.7	
	RMS	0.2	
Inserted reactivity (\$)		1.12	1.12
Time to the power peak (s)		0.34	0.34
Power at the peak (ratio to nominal)		1.48	1.42
Max. point pin peaking factor Fq (-)		9.92	9.87

Figure 7. Assembly power distribution at HZP

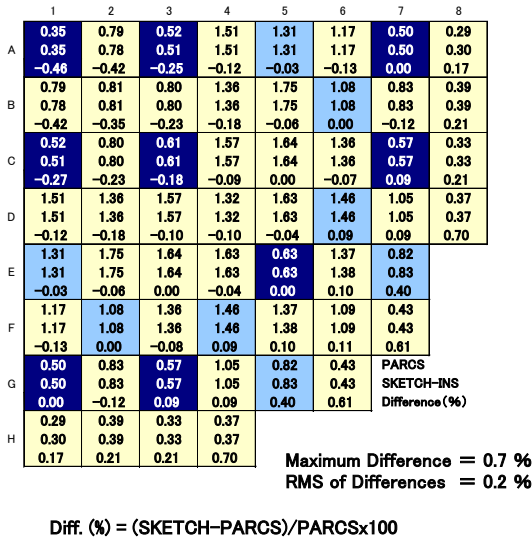
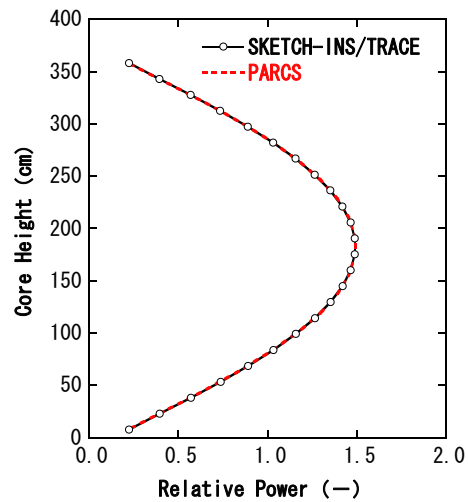


Figure 8. Core averaged axial power distribution at HZP



5.2.2 Results of transient calculations

The transient result and a comparison with the PARCS solution are also presented in Table 4. Figure 9 shows a comparison for the total reactor power with the PARCS solution, together with the average fuel temperature. Figure 10 shows a comparison for the reactivity components with the PARCS solution. Figure 11 shows a comparison for the point pin peaking factor Fq with the PARCS solution, together with the total reactor power on a logarithmic scale to nominal power. The inserted reactivity is consistent with the PARCS solution. However, the average fuel temperature during the transient is underestimated in SKETCH-INS/TRACE. The difference may be the result of different code models in the heat transfer

correlations. The fuel temperature difference causes the difference in the negative Doppler reactivity feedback, and hence SKETCH-INS/TRACE slightly overestimates the peak power. The maximum point pin peaking factor  $F_q$  is in good agreement with the PARCS solution.

A comparison results show that the coupled SKETCH-INS/TRACE code system can correctly predict the most important parameters in the rod ejection analysis; the time and value of the peak power.

Figure 9. Reactor power and fuel temperature time history

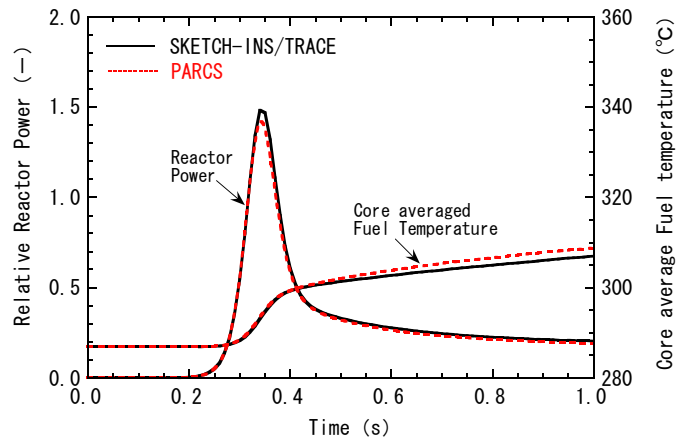


Figure 10. Reactivity components time history

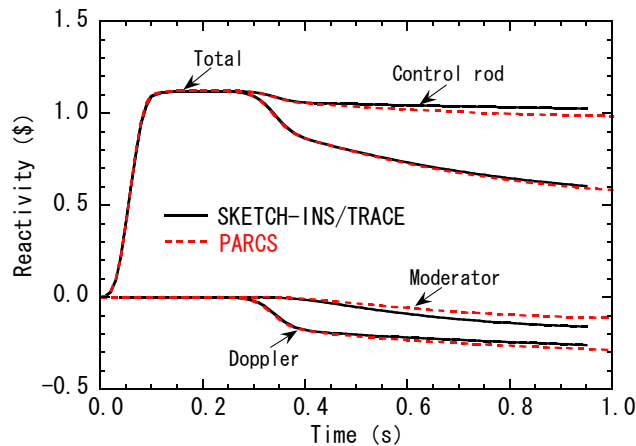
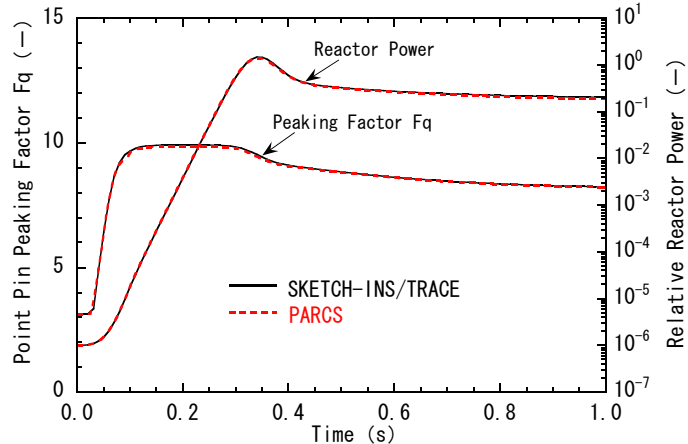


Figure 11. Point pi peaking factor  $F_q$  and reactor power time history



### 5.2.3 Pin power reconstruction effect on pin power and fuel enthalpy

A PWR control rod ejection problem was analyzed with SKETCH-INS/TRACE by incorporating the pin power reconstruction model. Figure 12 shows the change of pin power distributions during the transient in the diagonal line of the core, together with the pin power distributions within the assemblies around the ejected rod. As shown in Figure 12, pin powers within the assemblies around the ejected rod are considerably increased due to the ejection of control rod, especially in the fresh fuel assembly F6 which locates in the periphery of the core. In the highest assembly F6, pin powers are considerably biased toward the periphery of the core and the maximum pin power is occurred at the edge of assembly. This biased power distributions within the assemblies are correctly calculated by the pin power reconstruction model.

The pin power distributions during transient are commonly produced by synthesizing 2-D infinite lattice pin-by-pin calculations of assembly and 3-D nodal calculations of core. This approach is insufficient to accurately predict the pin power distributions of the core because the flux distributions within each assembly are not considered in this method (i.e., the node averaged fluxes are used). The SKETCH-INS pin power reconstruction model correctly produces pin power distribution by using the intranodal flux distribution, instead of node averaged fluxes.

Figure 13 shows the difference of pin power distribution between pin power reconstruction model and conventional node averaged flux model in the diagonal line of the core. A considerable difference was observed between two models within the peak assembly F6. The maximum local peaking factor in the peak assembly F6 is 1.47 with pin power reconstruction model and 1.16 with node averaged flux model. This 27% difference effects on the fuel enthalpy, significantly. Figure 14 shows a comparison for the fuel enthalpy trend between two models. As shown in Figure 14, the node averaged flux model considerably underestimates the fuel enthalpy increase compared that of pin power reconstruction model. The fuel enthalpy increase during the transient for pin power reconstruction model is 27% higher than the results with node averaged flux model. The pin power reconstruction model shows significant effect on the pin powers during transient and hence on the fuel enthalpy. In particular, the model is required to correctly predict the pin power distribution in the fuel assembly which has severely biased flux distribution within the assembly.

Figure 12. Change of pin power distributions during the transient

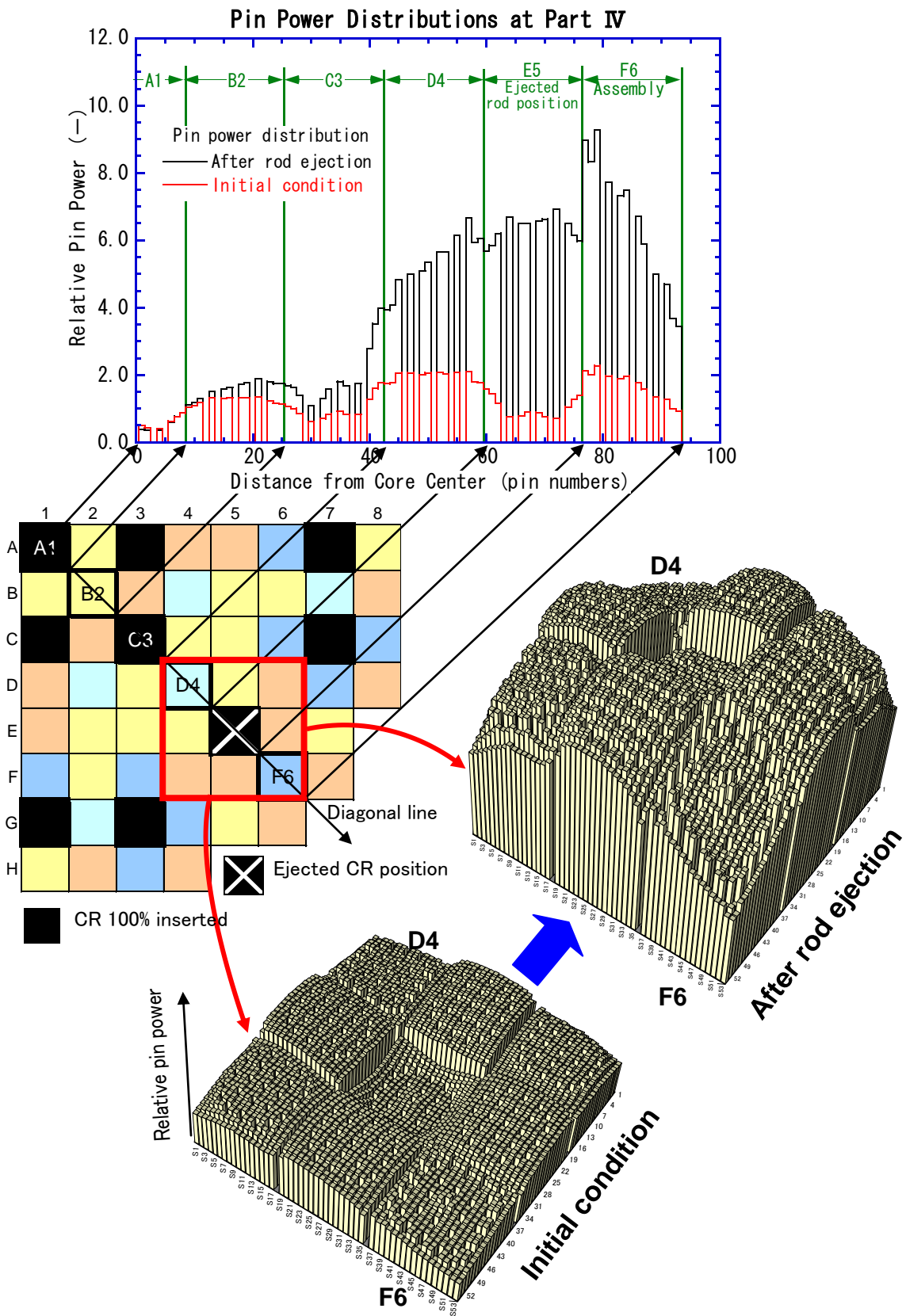


Figure 13. Comparison of pin power distributions between pin power reconstruction model and node averaged flux model

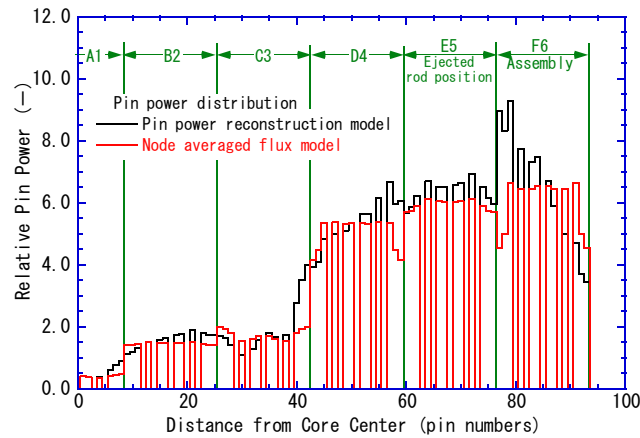
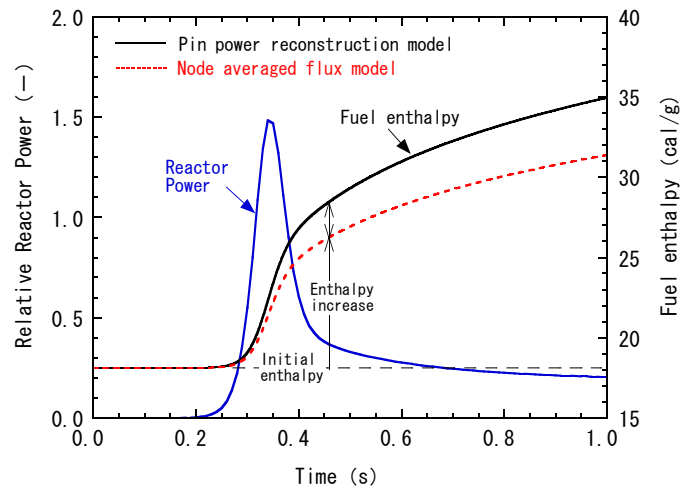


Figure 14. Comparison of fuel enthalpy time history between pin power reconstruction model and node averaged flux model



## 6. Summary

The pin power reconstruction model was incorporated in the 3-D nodal kinetics code SKETCH-INS in order to produce accurate calculation of three-dimensional pin power distributions throughout the reactor core. In order to verify the employed pin power reconstruction model, the PWR MOX/UO<sub>2</sub> core transient benchmark problem was analyzed with the coupled code system SKETCH-INS/TRACE by incorporating the model and the influence of pin power reconstruction model was studied.

SKETCH-INS pin power distributions for three benchmark problems were compared with the PARCS solutions which were provided by the host organisation of the benchmark. SKETCH-INS results were in good agreement with the PARCS results. The capability of employed pin power reconstruction model was confirmed through the analysis of benchmark problems.

A PWR control rod ejection benchmark problem was analyzed with the coupled code system SKETCH-INS/TRACE by incorporating the pin power reconstruction model. The influence of pin power reconstruction model was studied by comparing with the result of conventional node averaged flux model. The results indicated that the pin power reconstruction model has significant effect on the pin powers during transient and hence on the fuel enthalpy.

## References

- [1] “Modification of the Coupled Three Dimensional Neutronics and Thermal-Hydraulic code SKETCH-INS/TRACE”, JNES, JNES/SAE06-041, (2006) (in Japanese).
- [2] T. Kozłowski, T. J. Downar, “OECD/NEA and US NRC PWR MOX/UO<sub>2</sub> Core Transient Benchmark”, Final Specifications, Revision 2, NEA/NSC/DOC(2003)20, December (2003).
- [3] F. Odar, C. Murray et al., “TRACE V4.0 User’s Manual”, US NRC, (2004).
- [4] K. R. Rempe, K. S. Smith and A. F. Henry, “SIMULATE-3 Pin Power Reconstruction: Methodology and Benchmarking”, Nuclear Science and Engineering, 103, 334-342, (1989).
- [5] H. G. Joo, D. Barber, G. Jiang, and T. J. Downar, “PARCS, A Multi-Dimensional Two-Group Reactor Kinetics Code based on the Nonlinear Analytic Nodal Method”, PU/NE-98-26, September (1998).
- [6] T. Kozłowski, T. J. Downar, “Pressurised Water Reactor MOX/UO<sub>2</sub> Core Transient Benchmark”, Final Report, Revision 2, NEA/NSC/DOC(2006)20, December (2006).

**JNES** *OECD/NEA Workshop*  
*Nuclear Fuel Behaviour during Reactivity Initiated Accidents*

**Analysis of PWR Control Rod Ejection  
 Accident with the Coupled Code System  
 SKETCH-INS/TRACE by Incorporating  
 Pin Power Reconstruction Model**

*T.Nakajima/JNES*

September 9-11, 2009  
 Paris

**JNES** **Contents**

1. Introduction
2. Pin Power Reconstruction Model
3. SKETCH-INS/TRACE Code System
4. Verification of Pin Power Reconstruction Model
5. Analysis of PWR Control Rod Ejection Benchmark Problem with Pin Power Reconstruction Model
6. Summary

**JNES** **Introduction (1)** 1

- In safety analysis of RIA, it is required to calculate the pin powers of reactor core with a high degree of accuracy in order to make the correct evaluation regarding core design and safety margins.
- Pin power distributions in the reactor core are commonly produced by synthesizing 2-D pin-by-pin calculations of assembly and 3-D nodal calculations of reactor core.
- This conventional approach is insufficient to accurately predict the pin power distributions of reactor core because the flux distributions within each assembly are not considered (i.e., the node averaged fluxes are used).

**JNES** 2

## Introduction (2)

- In order to produce accurate 3-D pin power distributions throughout reactor core, pin power reconstruction model was incorporated in 3-D nodal kinetics code SKETCH-INS.
- In this pin power reconstruction model, flux distributions within assemblies are correctly treated.

**Node Averaged Flux Model**

**Pin Power Reconstruction Model**

**JNES** 3

## Pin Power Reconstruction Model (1)

- The detailed pin power distributions within an assembly are reconstructed by synthesizing the local heterogeneous form function of each assembly into the global homogenized intranodal flux distribution:

$$P(x, y)_{reactor} = P(x, y)_{homogeneous} \cdot P(x, y)_{form\ function}$$

- The local heterogeneous form function of each assembly is calculated by a 2-D lattice physics code.
- The intranodal power distributions are calculated from the nodal (homogenized) fission cross sections and flux distributions: :

$$P(x, y)_{homogeneous} = \sum_{f_1} \rho_1(x, y) \cdot \phi_1(x, y) + \sum_{f_2} \rho_2(x, y) \cdot \phi_2(x, y)$$

**JNES** 4

## Pin Power Reconstruction Model (2)

- The intranodal fast flux distribution is approximated by the following set of polynomial functions:

$$\phi_1(x, y) = \sum_{i,j=0}^4 a_{i,j} \cdot R_i(x) \cdot R_j(y)$$

where

$$R_0(u) = 1, \quad R_1(u) = u, \quad R_2(u) = \frac{1}{2}(3u^2 - 1), \quad R_3(u) = \frac{1}{2}(5u^3 - 3u),$$

$$R_4(u) = \frac{1}{8}(35u^4 - 30u^2 + 3), \quad u = x \text{ or } y.$$

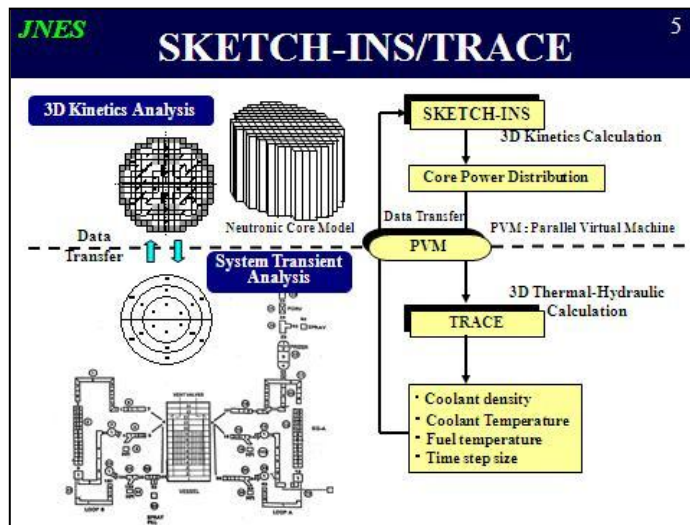
- The intranodal thermal flux distribution is approximated by the following set of functions:

$$\phi_2(x, y) = \phi_1(x, y) \cdot c_{00} + \sum_{i,j=0}^4 a_{i,j} \cdot F_i(x) \cdot F_j(y)$$

where

$$F_0(u) = 1, \quad F_1(u) = \sinh(\kappa u), \quad F_2(u) = \cosh(\kappa u),$$

$$F_3(u) = \sinh(2\kappa u), \quad F_4(u) = \cosh(2\kappa u), \quad \kappa = h \cdot \sqrt{\Sigma_{a2}/D_2}, \quad u = x \text{ or } y,$$



- JNES** 6
- ## SKETCH-INS Code
- **SKETCH-INS Characteristics**
    - Semi-analytic nodal method based on the nonlinear iteration procedure is used for spatial discretization of diffusion equations.
    - Time integration of neutron kinetics is performed by fully implicit scheme.
    - Two neutron energy groups
    - Six groups of delayed neutron precursors
    - Utilization of assembly discontinuity factors (ADFs)
    - Incorporation of pin power reconstruction model

**JNES** 7

## TRACE Code

- **USNRC TRACE code is a best-estimate system transient analysis code, which has a three-dimensional thermal-hydraulic analysis capability.**
- **The code solves the general transient two-phase coolant conditions in one, two, or three dimensions using a realistic six-equation, two-fluid, finite difference model.**

The diagram shows a detailed 3D model of a nuclear reactor core and its associated piping system, illustrating the complexity of the thermal-hydraulic analysis performed by the TRACE code.

**JNES** 8

## Verification of Pin Power Reconstruction Model

- The ability of SKETCH-INS pin power reconstruction model was verified against the PWR MOX/ $UO_2$  core transient benchmark problem provided by the OECD/NEA and US NRC.
- The PWR MOX/ $UO_2$  core transient benchmark problem is a PWR rod ejection problem to assess the ability of modern kinetics codes to predict the transient response of a core partially loaded with MOX fuel.
- SKETCH-INS pin power distributions were calculated for the benchmark problem and SKETCH-INS result was compared with the PARCS solution which was provided by the host organization of the benchmark.

**JNES** 9

## Description of Benchmark (1)

In the PWR MOX/ $UO_2$  core transient benchmark problem, calculations were divided into four parts:

1. **Part I: 2-D fixed T-H conditions** /calculate multiplication factor, rod worth, assembly and pin power/
2. **Part II: 3-D hot full power (HFP) conditions** /calculate critical boron concentration, assembly and pin power/
3. **Part III: 3-D hot zero power (HZP) conditions** /calculate critical boron concentration, assembly and pin power/
4. **Part IV: 3-D with Part III conditions** /calculate transient response to control rod ejection accident/

**JNES** 10

## Description of Benchmark (2)

The reactor core chosen for the simulation is based on four-loop Westinghouse PWR power plant.

**Core Configuration (1/4 Core)**

	1	2	3	4	5	6	7	8
A	U4.2% (CR-A)	U4.2% (CR-A)	U4.5% (CR-A)	M4.3% (CR-A)	M4.3% (CR-A)	U4.5% (CR-A)	U4.5% (CR-A)	U4.5% (CR-A)
B	U4.2% (CR-A)	U4.2% (CR-C)	M4.0% (CR-C)	U4.2% (CR-C)	U4.2% (CR-C)	M4.2% (CR-B)	U4.5% (CR-B)	U4.5% (CR-B)
C	U4.5% (CR-A)	M4.0% (CR-C)	U4.2% (CR-C)	U4.2% (CR-C)	U4.2% (CR-C)	M4.3% (CR-B)	M4.3% (CR-B)	U4.5% (CR-B)
D	U4.5% (CR-A)	M4.0% (CR-C)	U4.2% (CR-C)	U4.2% (CR-C)	U4.2% (CR-C)	M4.3% (CR-B)	M4.3% (CR-B)	U4.5% (CR-B)
E	U4.5% (CR-A)	M4.0% (CR-C)	U4.2% (CR-C)	U4.2% (CR-C)	U4.2% (CR-C)	M4.3% (CR-B)	M4.3% (CR-B)	U4.5% (CR-B)
F	U4.5% (CR-A)	M4.0% (CR-C)	U4.2% (CR-C)	U4.2% (CR-C)	U4.2% (CR-C)	M4.3% (CR-B)	M4.3% (CR-B)	U4.5% (CR-B)
G	U4.5% (CR-C)	M4.0% (CR-C)	U4.2% (CR-C)	U4.2% (CR-C)	U4.2% (CR-C)	M4.3% (CR-B)	M4.3% (CR-B)	U4.5% (CR-B)
H	U4.5% (CR-C)	M4.0% (CR-C)	U4.2% (CR-C)	U4.2% (CR-C)	U4.2% (CR-C)	M4.3% (CR-B)	M4.3% (CR-B)	U4.5% (CR-B)

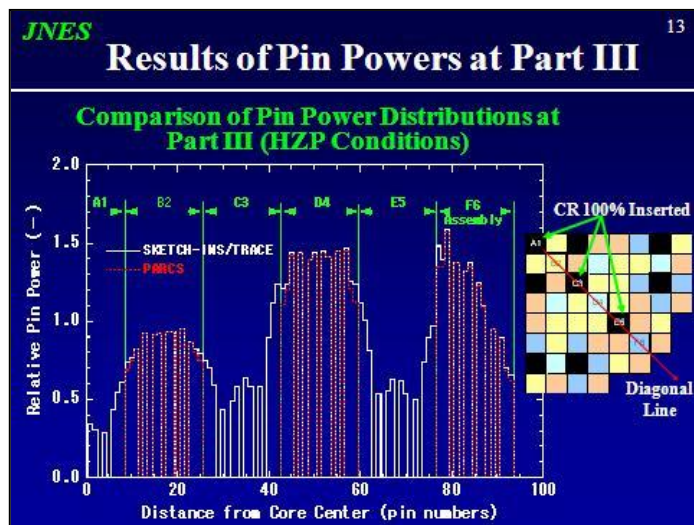
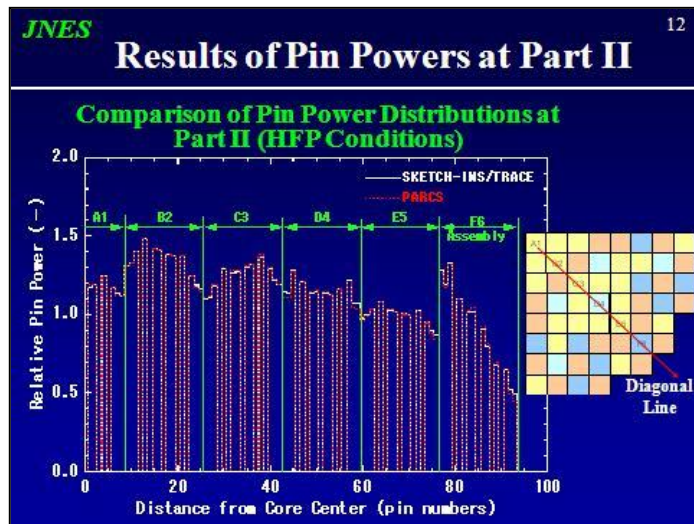
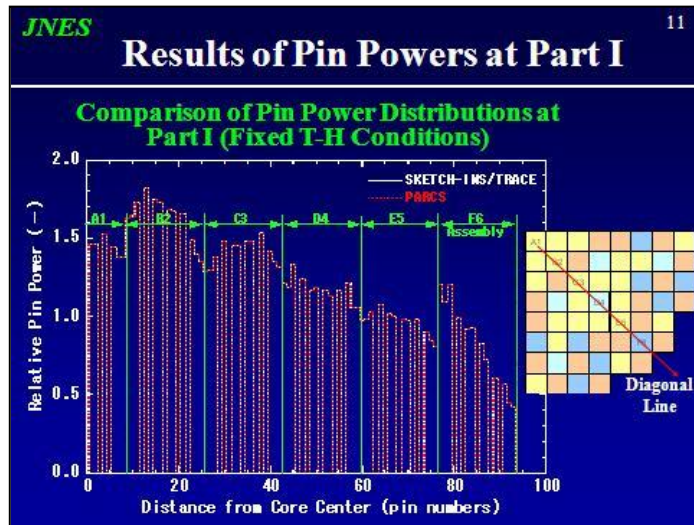
Geometry Type: CR Position  
 Legend: CR-A Control Rod Bank A, CR-B Control Rod Bank B, CR-C Control Rod Bank C, CR-D Control Rod Bank D, CR-SA Shutdown Rod Bank A, CR-SB Shutdown Rod Bank B, CR-SC Shutdown Rod Bank C, CR-SD Shutdown Rod Bank D, Ejected Rod

**$UO_2$  Fuel Assembly**

UO<sub>2</sub> Fuel  
 UO<sub>2</sub> Blank Fuel  
 Guide Tube or Control Rod  
 Ejected Rod

**MOX Fuel Assembly**

MOX 1.0%  
 MOX 2.0%  
 MOX 4.0 & 5.0%  
 MOX 8.0%  
 MOX 9.0%  
 MOX 10.0%  
 MOX 11.0%  
 MOX 12.0%  
 MOX 13.0%  
 MOX 14.0%  
 MOX 15.0%  
 MOX 16.0%  
 MOX 17.0%  
 MOX 18.0%  
 MOX 19.0%  
 MOX 20.0%  
 MOX 21.0%  
 MOX 22.0%  
 MOX 23.0%  
 MOX 24.0%  
 MOX 25.0%  
 MOX 26.0%  
 MOX 27.0%  
 MOX 28.0%  
 MOX 29.0%  
 MOX 30.0%  
 MOX 31.0%  
 MOX 32.0%  
 MOX 33.0%  
 MOX 34.0%  
 MOX 35.0%  
 MOX 36.0%  
 MOX 37.0%  
 MOX 38.0%  
 MOX 39.0%  
 MOX 40.0%  
 MOX 41.0%  
 MOX 42.0%  
 MOX 43.0%  
 MOX 44.0%  
 MOX 45.0%  
 MOX 46.0%  
 MOX 47.0%  
 MOX 48.0%  
 MOX 49.0%  
 MOX 50.0%  
 MOX 51.0%  
 MOX 52.0%  
 MOX 53.0%  
 MOX 54.0%  
 MOX 55.0%  
 MOX 56.0%  
 MOX 57.0%  
 MOX 58.0%  
 MOX 59.0%  
 MOX 60.0%  
 MOX 61.0%  
 MOX 62.0%  
 MOX 63.0%  
 MOX 64.0%  
 MOX 65.0%  
 MOX 66.0%  
 MOX 67.0%  
 MOX 68.0%  
 MOX 69.0%  
 MOX 70.0%  
 MOX 71.0%  
 MOX 72.0%  
 MOX 73.0%  
 MOX 74.0%  
 MOX 75.0%  
 MOX 76.0%  
 MOX 77.0%  
 MOX 78.0%  
 MOX 79.0%  
 MOX 80.0%  
 MOX 81.0%  
 MOX 82.0%  
 MOX 83.0%  
 MOX 84.0%  
 MOX 85.0%  
 MOX 86.0%  
 MOX 87.0%  
 MOX 88.0%  
 MOX 89.0%  
 MOX 90.0%  
 MOX 91.0%  
 MOX 92.0%  
 MOX 93.0%  
 MOX 94.0%  
 MOX 95.0%  
 MOX 96.0%  
 MOX 97.0%  
 MOX 98.0%  
 MOX 99.0%  
 MOX 100.0%  
 MOX 101.0%  
 MOX 102.0%  
 MOX 103.0%  
 MOX 104.0%  
 MOX 105.0%  
 MOX 106.0%  
 MOX 107.0%  
 MOX 108.0%  
 MOX 109.0%  
 MOX 110.0%  
 MOX 111.0%  
 MOX 112.0%  
 MOX 113.0%  
 MOX 114.0%  
 MOX 115.0%  
 MOX 116.0%  
 MOX 117.0%  
 MOX 118.0%  
 MOX 119.0%  
 MOX 120.0%  
 MOX 121.0%  
 MOX 122.0%  
 MOX 123.0%  
 MOX 124.0%  
 MOX 125.0%  
 MOX 126.0%  
 MOX 127.0%  
 MOX 128.0%  
 MOX 129.0%  
 MOX 130.0%  
 MOX 131.0%  
 MOX 132.0%  
 MOX 133.0%  
 MOX 134.0%  
 MOX 135.0%  
 MOX 136.0%  
 MOX 137.0%  
 MOX 138.0%  
 MOX 139.0%  
 MOX 140.0%  
 MOX 141.0%  
 MOX 142.0%  
 MOX 143.0%  
 MOX 144.0%  
 MOX 145.0%  
 MOX 146.0%  
 MOX 147.0%  
 MOX 148.0%  
 MOX 149.0%  
 MOX 150.0%  
 MOX 151.0%  
 MOX 152.0%  
 MOX 153.0%  
 MOX 154.0%  
 MOX 155.0%  
 MOX 156.0%  
 MOX 157.0%  
 MOX 158.0%  
 MOX 159.0%  
 MOX 160.0%  
 MOX 161.0%  
 MOX 162.0%  
 MOX 163.0%  
 MOX 164.0%  
 MOX 165.0%  
 MOX 166.0%  
 MOX 167.0%  
 MOX 168.0%  
 MOX 169.0%  
 MOX 170.0%  
 MOX 171.0%  
 MOX 172.0%  
 MOX 173.0%  
 MOX 174.0%  
 MOX 175.0%  
 MOX 176.0%  
 MOX 177.0%  
 MOX 178.0%  
 MOX 179.0%  
 MOX 180.0%  
 MOX 181.0%  
 MOX 182.0%  
 MOX 183.0%  
 MOX 184.0%  
 MOX 185.0%  
 MOX 186.0%  
 MOX 187.0%  
 MOX 188.0%  
 MOX 189.0%  
 MOX 190.0%  
 MOX 191.0%  
 MOX 192.0%  
 MOX 193.0%  
 MOX 194.0%  
 MOX 195.0%  
 MOX 196.0%  
 MOX 197.0%  
 MOX 198.0%  
 MOX 199.0%  
 MOX 200.0%  
 MOX 201.0%  
 MOX 202.0%  
 MOX 203.0%  
 MOX 204.0%  
 MOX 205.0%  
 MOX 206.0%  
 MOX 207.0%  
 MOX 208.0%  
 MOX 209.0%  
 MOX 210.0%  
 MOX 211.0%  
 MOX 212.0%  
 MOX 213.0%  
 MOX 214.0%  
 MOX 215.0%  
 MOX 216.0%  
 MOX 217.0%  
 MOX 218.0%  
 MOX 219.0%  
 MOX 220.0%  
 MOX 221.0%  
 MOX 222.0%  
 MOX 223.0%  
 MOX 224.0%  
 MOX 225.0%  
 MOX 226.0%  
 MOX 227.0%  
 MOX 228.0%  
 MOX 229.0%  
 MOX 230.0%  
 MOX 231.0%  
 MOX 232.0%  
 MOX 233.0%  
 MOX 234.0%  
 MOX 235.0%  
 MOX 236.0%  
 MOX 237.0%  
 MOX 238.0%  
 MOX 239.0%  
 MOX 240.0%  
 MOX 241.0%  
 MOX 242.0%  
 MOX 243.0%  
 MOX 244.0%  
 MOX 245.0%  
 MOX 246.0%  
 MOX 247.0%  
 MOX 248.0%  
 MOX 249.0%  
 MOX 250.0%  
 MOX 251.0%  
 MOX 252.0%  
 MOX 253.0%  
 MOX 254.0%  
 MOX 255.0%  
 MOX 256.0%  
 MOX 257.0%  
 MOX 258.0%  
 MOX 259.0%  
 MOX 260.0%  
 MOX 261.0%  
 MOX 262.0%  
 MOX 263.0%  
 MOX 264.0%  
 MOX 265.0%  
 MOX 266.0%  
 MOX 267.0%  
 MOX 268.0%  
 MOX 269.0%  
 MOX 270.0%  
 MOX 271.0%  
 MOX 272.0%  
 MOX 273.0%  
 MOX 274.0%  
 MOX 275.0%  
 MOX 276.0%  
 MOX 277.0%  
 MOX 278.0%  
 MOX 279.0%  
 MOX 280.0%  
 MOX 281.0%  
 MOX 282.0%  
 MOX 283.0%  
 MOX 284.0%  
 MOX 285.0%  
 MOX 286.0%  
 MOX 287.0%  
 MOX 288.0%  
 MOX 289.0%  
 MOX 290.0%  
 MOX 291.0%  
 MOX 292.0%  
 MOX 293.0%  
 MOX 294.0%  
 MOX 295.0%  
 MOX 296.0%  
 MOX 297.0%  
 MOX 298.0%  
 MOX 299.0%  
 MOX 300.0%  
 MOX 301.0%  
 MOX 302.0%  
 MOX 303.0%  
 MOX 304.0%  
 MOX 305.0%  
 MOX 306.0%  
 MOX 307.0%  
 MOX 308.0%  
 MOX 309.0%  
 MOX 310.0%  
 MOX 311.0%  
 MOX 312.0%  
 MOX 313.0%  
 MOX 314.0%  
 MOX 315.0%  
 MOX 316.0%  
 MOX 317.0%  
 MOX 318.0%  
 MOX 319.0%  
 MOX 320.0%  
 MOX 321.0%  
 MOX 322.0%  
 MOX 323.0%  
 MOX 324.0%  
 MOX 325.0%  
 MOX 326.0%  
 MOX 327.0%  
 MOX 328.0%  
 MOX 329.0%  
 MOX 330.0%  
 MOX 331.0%  
 MOX 332.0%  
 MOX 333.0%  
 MOX 334.0%  
 MOX 335.0%  
 MOX 336.0%  
 MOX 337.0%  
 MOX 338.0%  
 MOX 339.0%  
 MOX 340.0%  
 MOX 341.0%  
 MOX 342.0%  
 MOX 343.0%  
 MOX 344.0%  
 MOX 345.0%  
 MOX 346.0%  
 MOX 347.0%  
 MOX 348.0%  
 MOX 349.0%  
 MOX 350.0%  
 MOX 351.0%  
 MOX 352.0%  
 MOX 353.0%  
 MOX 354.0%  
 MOX 355.0%  
 MOX 356.0%  
 MOX 357.0%  
 MOX 358.0%  
 MOX 359.0%  
 MOX 360.0%  
 MOX 361.0%  
 MOX 362.0%  
 MOX 363.0%  
 MOX 364.0%  
 MOX 365.0%  
 MOX 366.0%  
 MOX 367.0%  
 MOX 368.0%  
 MOX 369.0%  
 MOX 370.0%  
 MOX 371.0%  
 MOX 372.0%  
 MOX 373.0%  
 MOX 374.0%  
 MOX 375.0%  
 MOX 376.0%  
 MOX 377.0%  
 MOX 378.0%  
 MOX 379.0%  
 MOX 380.0%  
 MOX 381.0%  
 MOX 382.0%  
 MOX 383.0%  
 MOX 384.0%  
 MOX 385.0%  
 MOX 386.0%  
 MOX 387.0%  
 MOX 388.0%  
 MOX 389.0%  
 MOX 390.0%  
 MOX 391.0%  
 MOX 392.0%  
 MOX 393.0%  
 MOX 394.0%  
 MOX 395.0%  
 MOX 396.0%  
 MOX 397.0%  
 MOX 398.0%  
 MOX 399.0%  
 MOX 400.0%  
 MOX 401.0%  
 MOX 402.0%  
 MOX 403.0%  
 MOX 404.0%  
 MOX 405.0%  
 MOX 406.0%  
 MOX 407.0%  
 MOX 408.0%  
 MOX 409.0%  
 MOX 410.0%  
 MOX 411.0%  
 MOX 412.0%  
 MOX 413.0%  
 MOX 414.0%  
 MOX 415.0%  
 MOX 416.0%  
 MOX 417.0%  
 MOX 418.0%  
 MOX 419.0%  
 MOX 420.0%  
 MOX 421.0%  
 MOX 422.0%  
 MOX 423.0%  
 MOX 424.0%  
 MOX 425.0%  
 MOX 426.0%  
 MOX 427.0%  
 MOX 428.0%  
 MOX 429.0%  
 MOX 430.0%  
 MOX 431.0%  
 MOX 432.0%  
 MOX 433.0%  
 MOX 434.0%  
 MOX 435.0%  
 MOX 436.0%  
 MOX 437.0%  
 MOX 438.0%  
 MOX 439.0%  
 MOX 440.0%  
 MOX 441.0%  
 MOX 442.0%  
 MOX 443.0%  
 MOX 444.0%  
 MOX 445.0%  
 MOX 446.0%  
 MOX 447.0%  
 MOX 448.0%  
 MOX 449.0%  
 MOX 450.0%  
 MOX 451.0%  
 MOX 452.0%  
 MOX 453.0%  
 MOX 454.0%  
 MOX 455.0%  
 MOX 456.0%  
 MOX 457.0%  
 MOX 458.0%  
 MOX 459.0%  
 MOX 460.0%  
 MOX 461.0%  
 MOX 462.0%  
 MOX 463.0%  
 MOX 464.0%  
 MOX 465.0%  
 MOX 466.0%  
 MOX 467.0%  
 MOX 468.0%  
 MOX 469.0%  
 MOX 470.0%  
 MOX 471.0%  
 MOX 472.0%  
 MOX 473.0%  
 MOX 474.0%  
 MOX 475.0%  
 MOX 476.0%  
 MOX 477.0%  
 MOX 478.0%  
 MOX 479.0%  
 MOX 480.0%  
 MOX 481.0%  
 MOX 482.0%  
 MOX 483.0%  
 MOX 484.0%  
 MOX 485.0%  
 MOX 486.0%  
 MOX 487.0%  
 MOX 488.0%  
 MOX 489.0%  
 MOX 490.0%  
 MOX 491.0%  
 MOX 492.0%  
 MOX 493.0%  
 MOX 494.0%  
 MOX 495.0%  
 MOX 496.0%  
 MOX 497.0%  
 MOX 498.0%  
 MOX 499.0%  
 MOX 500.0%  
 MOX 501.0%  
 MOX 502.0%  
 MOX 503.0%  
 MOX 504.0%  
 MOX 505.0%  
 MOX 506.0%  
 MOX 507.0%  
 MOX 508.0%  
 MOX 509.0%  
 MOX 510.0%  
 MOX 511.0%  
 MOX 512.0%  
 MOX 513.0%  
 MOX 514.0%  
 MOX 515.0%  
 MOX 516.0%  
 MOX 517.0%  
 MOX 518.0%  
 MOX 519.0%  
 MOX 520.0%  
 MOX 521.0%  
 MOX 522.0%  
 MOX 523.0%  
 MOX 524.0%  
 MOX 525.0%  
 MOX 526.0%  
 MOX 527.0%  
 MOX 528.0%  
 MOX 529.0%  
 MOX 530.0%  
 MOX 531.0%  
 MOX 532.0%  
 MOX 533.0%  
 MOX 534.0%  
 MOX 535.0%  
 MOX 536.0%  
 MOX 537.0%  
 MOX 538.0%  
 MOX 539.0%  
 MOX 540.0%  
 MOX 541.0%  
 MOX 542.0%  
 MOX 543.0%  
 MOX 544.0%  
 MOX 545.0%  
 MOX 546.0%  
 MOX 547.0%  
 MOX 548.0%  
 MOX 549.0%  
 MOX 550.0%  
 MOX 551.0%  
 MOX 552.0%  
 MOX 553.0%  
 MOX 554.0%  
 MOX 555.0%  
 MOX 556.0%  
 MOX 557.0%  
 MOX 558.0%  
 MOX 559.0%  
 MOX 560.0%  
 MOX 561.0%  
 MOX 562.0%  
 MOX 563.0%  
 MOX 564.0%  
 MOX 565.0%  
 MOX 566.0%  
 MOX 567.0%  
 MOX 568.0%  
 MOX 569.0%  
 MOX 570.0%  
 MOX 571.0%  
 MOX 572.0%  
 MOX 573.0%  
 MOX 574.0%  
 MOX 575.0%  
 MOX 576.0%  
 MOX 577.0%  
 MOX 578.0%  
 MOX 579.0%  
 MOX 580.0%  
 MOX 581.0%  
 MOX 582.0%  
 MOX 583.0%  
 MOX 584.0%  
 MOX 585.0%  
 MOX 586.0%  
 MOX 587.0%  
 MOX 588.0%  
 MOX 589.0%  
 MOX 590.0%  
 MOX 591.0%  
 MOX 592.0%  
 MOX 593.0%  
 MOX 594.0%  
 MOX 595.0%  
 MOX 596.0%  
 MOX 597.0%  
 MOX 598.0%  
 MOX 599.0%  
 MOX 600.0%  
 MOX 601.0%  
 MOX 602.0%  
 MOX 603.0%  
 MOX 604.0%  
 MOX 605.0%  
 MOX 606.0%  
 MOX 607.0%  
 MOX 608.0%  
 MOX 609.0%  
 MOX 610.0%  
 MOX 611.0%  
 MOX 612.0%  
 MOX 613.0%  
 MOX 614.0%  
 MOX 615.0%  
 MOX 616.0%  
 MOX 617.0%  
 MOX 618.0%  
 MOX 619.0%  
 MOX 620.0%  
 MOX 621.0%  
 MOX 622.0%  
 MOX 623.0%  
 MOX 624.0%  
 MOX 625.0%  
 MOX 626.0%  
 MOX 627.0%  
 MOX 628.0%  
 MOX 629.0%  
 MOX 630.0%  
 MOX 631.0%  
 MOX 632.0%  
 MOX 633.0%  
 MOX 634.0%  
 MOX 635.0%  
 MOX 636.0%  
 MOX 637.0%  
 MOX 638.0%  
 MOX 639.0%  
 MOX 640.0%  
 MOX 641.0%  
 MOX 642.0%  
 MOX 643.0%  
 MOX 644.0%  
 MOX 645.0%  
 MOX 646.0%  
 MOX 647.0%  
 MOX 648.0%  
 MOX 649.0%  
 MOX 650.0%  
 MOX 651.0%  
 MOX 652.0%  
 MOX 653.0%  
 MOX 654.0%  
 MOX 655.0%  
 MOX 656.0%  
 MOX 657.0%  
 MOX 658.0%  
 MOX 659.0%  
 MOX 660.0%  
 MOX 661.0%  
 MOX 662.0%  
 MOX 663.0%  
 MOX 664.0%  
 MOX 665.0%  
 MOX 666.0%  
 MOX 667.0%  
 MOX 668.0%  
 MOX 669.0%  
 MOX 670.0%  
 MOX 671.0%  
 MOX 672.0%  
 MOX 673.0%  
 MOX 674.0%  
 MOX 675.0%  
 MOX 676.0%  
 MOX 677.0%  
 MOX 678.0%  
 MOX 679.0%  
 MOX 680.0%  
 MOX 681.0%  
 MOX 682.0%  
 MOX 683.0%  
 MOX 684.0%  
 MOX 685.0%  
 MOX 686.0%  
 MOX 687.0%  
 MOX 688.0%  
 MOX 689.0%  
 MOX 690.0%  
 MOX 691.0%  
 MOX 692.0%  
 MOX 693.0%  
 MOX 694.0%  
 MOX 695.0%  
 MOX 696.0%  
 MOX 697.0%  
 MOX 698.0%  
 MOX 699.0%  
 MOX 700.0%  
 MOX 701.0%  
 MOX 702.0%  
 MOX 703.0%  
 MOX 704.0%  
 MOX 705.0%  
 MOX 706.0%  
 MOX 707.0%  
 MOX 708.0%  
 MOX 709.0%  
 MOX 710.0%  
 MOX 711.0%  
 MOX 712.0%  
 MOX 713.0%  
 MOX 714.0%  
 MOX 715.0%  
 MOX 716.0%  
 MOX 717.0%  
 MOX 718.0%  
 MOX 719.0%  
 MOX 720.0%  
 MOX 721.0%  
 MOX 722.0%  
 MOX 723.0%  
 MOX 724.0%  
 MOX 725.0%  
 MOX 726.0%  
 MOX 727.0%  
 MOX 728.0%  
 MOX 729.0%  
 MOX 730.0%  
 MOX 731.0%  
 MOX 732.0%  
 MOX 733.0%  
 MOX



**JNES Part IV Rod Ejection Benchmark** 14

- Part IV core transient benchmark is a PWR control rod ejection problem.
- The control rod ejection is performed from HZP conditions.
- The control rod is assumed to be fully ejected in 0.1 seconds after which no reactor scram is considered.

**Control Rod Pattern at HZP**

Parameters	value
Initial power level ( $MW_{th}$ )	$3.565 \times 10^{-4}$
Coolant inlet pressure (MPa)	15.5
Coolant inlet temperature (K)	560
Control rod ejection time (s)	0.1
Delayed neutron fraction (%)	0.579
Prompt neutron lifetime ( $\mu s$ )	14.8

■ Fuel Assembly  
■ Fully Withdrawn CR Assembly  
■ Fully Inserted CR Assembly  
✘ Ejected CR Assembly

**JNES Results of Part IV Benchmark** 15

**— Steady-State Calculations —**

**Assembly power distribution at HZP**

	1	2	3	4	5	6	7	8
A	0.85	0.78	0.52	1.51	1.21	1.17	0.58	0.28
B	0.45	0.74	0.51	1.51	1.21	1.17	0.58	0.28
C	-0.45	-0.42	-0.25	-0.12	-0.02	-0.12	0.09	0.17
D	0.78	0.81	0.88	1.86	1.75	1.82	0.82	0.28
E	0.78	0.81	0.88	1.86	1.75	1.82	0.82	0.28
F	-0.42	-0.35	-0.28	-0.15	-0.05	0.08	-0.12	0.21
G	0.52	0.28	0.51	1.57	1.64	1.26	0.57	0.22
H	0.51	0.28	0.61	1.57	1.64	1.26	0.57	0.22
I	-0.27	-0.28	-0.18	-0.08	0.08	-0.07	0.08	0.21
J	1.51	1.26	1.57	1.82	1.65	1.96	1.85	0.27
K	1.51	1.26	1.57	1.82	1.65	1.96	1.85	0.27
L	-0.12	-0.15	-0.18	-0.18	-0.08	0.08	0.08	0.24
M	1.21	1.25	1.64	1.65	0.61	1.27	0.22	
N	1.21	1.25	1.64	1.65	0.62	1.28	0.22	
O	-0.02	-0.05	0.08	-0.04	0.04	0.18	0.08	
P	1.17	1.05	1.26	1.96	1.27	1.88	0.45	
Q	1.17	1.05	1.26	1.96	1.28	1.89	0.45	
R	-0.12	0.08	-0.02	0.08	0.18	0.11	0.61	
S	0.58	0.22	0.57	1.85	0.22	0.45	0.45	
T	0.58	0.22	0.57	1.85	0.22	0.45	0.45	
U	0.48	-0.12	0.18	0.08	0.08	0.51	0.51	
V	0.28	0.28	0.22	0.17				
W	0.28	0.28	0.22	0.17				
X	0.17	0.21	0.21	0.24				

Maximum Difference = 0.7 %  
RMS of Differences = 0.2 %

Difference =  $\frac{\text{SKETCH-IMS/TRACE}}{\text{PARCS}} \times 100(\%)$

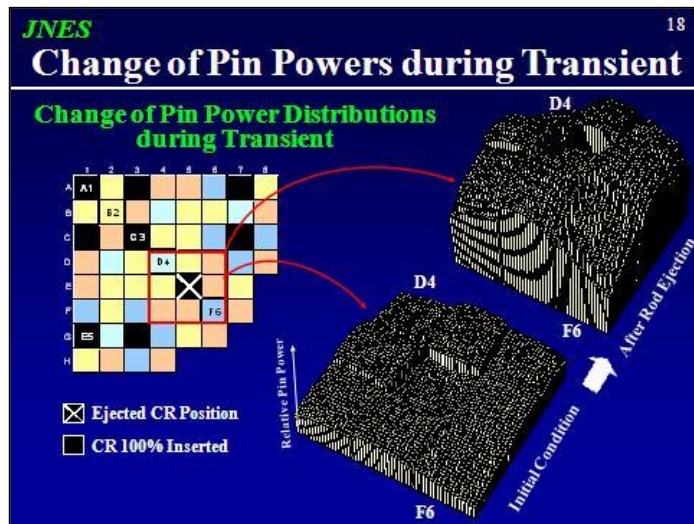
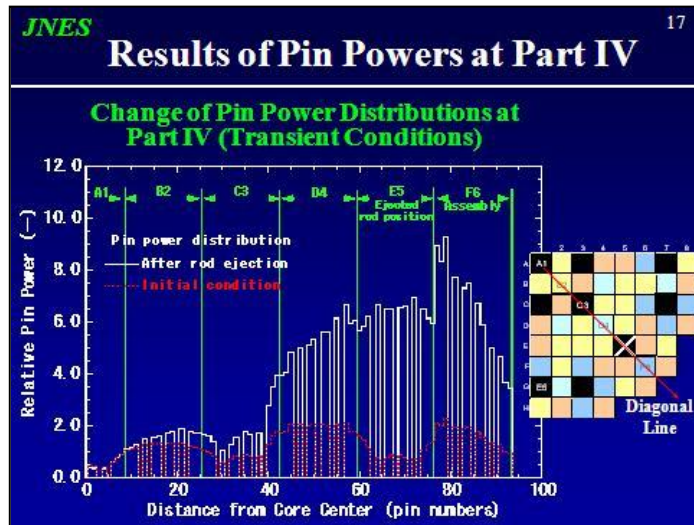
**Core averaged axial power distribution**

**JNES Results of Part IV Benchmark** 16

**— Transient Calculations —**

**Reactor power and fuel temperature**

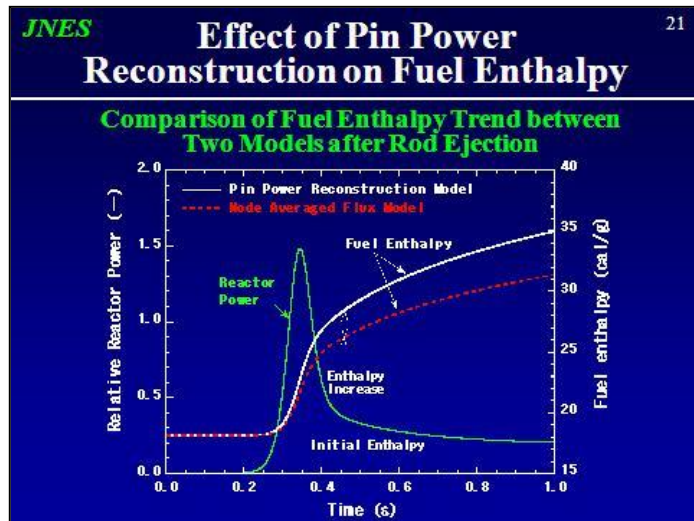
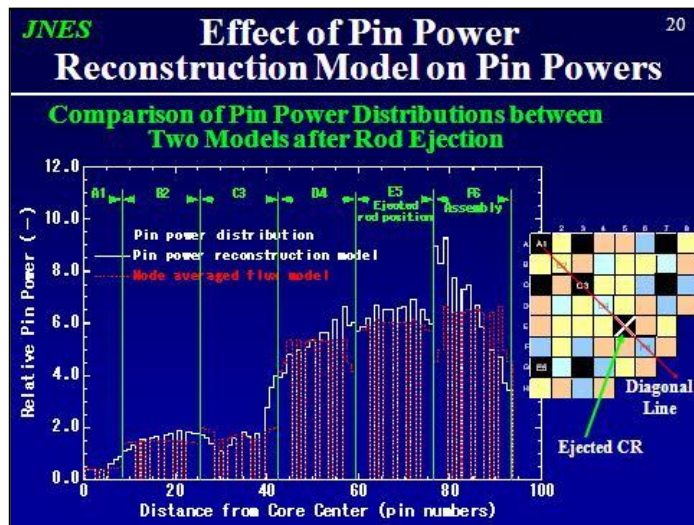
**Total reactivity and Reactivity Components**



**JNES** 19  
**Pin Power Reconstruction Effect on Pin Power and Fuel Enthalpy**

- Pin powers within the assemblies around ejected rod are considerably increased, especially in the fresh fuel assembly F6 which locates in the periphery of the core.
- In the highest assembly F6, pin power distributions are considerably biased toward the periphery of the core.
- This biased power distributions within the assemblies are correctly calculated with the pin power reconstruction model by using intranodal flux distribution, instead of node averaged fluxes.
- The pin power reconstruction effect on the pin power and fuel enthalpy was studied by comparing with the result of conventional node averaged flux model.

F6



- JNES** 22
- ## Summary
- Pin power reconstruction model was incorporated in the 3D nodal kinetics code SKETCH-INS in order to produce accurate 3D pin power distributions throughout the core.
  - A PWR control rod ejection benchmark problem was analyzed with the coupled code system SKETCH-INS/TRACE by incorporating the pin power reconstruction model.
  - SKETCH-INS pin power distributions for benchmark problems were in good agreement with the PARCS results.
  - The influence of pin power reconstruction model was studied by comparing with the result of conventional node averaged flux model.
  - The results indicated that the pin power reconstruction model has significant effect on the pin powers during transient and hence on the fuel enthalpy.

## A SURVEY OF AVAILABLE MARGIN IN A PWR RIA WITH STATISTICAL METHODS AND 3D KINETICS

**Javier Riverola Gurruchaga**  
ENUSA Industrias Avanzadas, S.A., Spain

**Tomás Nuñez Rodríguez**  
ENUSA Industrias Avanzadas, S.A., Spain

### Abstract

This paper investigates the recovery of margin in a PWR RIA simulation with 3D kinetics, due to statistical techniques. The chosen reference core is a typical 12 feet, 17x17 PWR, with very low leakage loading pattern strategy and gadolinium oxide as burnable poison. The PARCS calculated average nuclear power and nodal power are transferred to a hot spot model for a sequential calculation of fuel temperature and enthalpy responses allowing for independent hypothesis in both calculations. The hot spot analysis is done with a pellet type model with RELAP. The analysis is done at HZP and EOC, since this state is the most limiting one respect to the enthalpy rise criterion, compared to other burn-up condition or initial power cases. In this work, the enthalpy increase is estimated with several statistical methods of propagation of uncertainties: order statistics, parametric statistics, surface response and sensitivities. A discussion on the advantages and disadvantages of each method is also presented. This statistical analysis is also useful to confirm a previous classification of parameters and assumptions according to their importance for the simulation, and found to be consistent with the state of the art in the published literature. These parameters include ejected rod worth and ejection time, delayed neutron fraction and yields, nuclear power peaking factor, and Doppler.

### 1. Introduction

This paper is a survey of the margin that can be restored from the results of a reactivity insertion accident (RIA) simulation with 3D kinetics by the use of statistical methods. In previous investigations, ENUSA has utilised PARCS and RELAP codes in order to simulate this accident under the BE bounding approach, in which codes are realistic in nature, but code inputs are conservative with all uncertainties simultaneously applied in the most penalising sense [1]. This approach is purely deterministic.

In this research, the same realistic codes are used, but credit is given to the fact that some of the inputs can follow a pdf, whilst the conservative status for the rest of the inputs and the whole set of simulation basis is maintained. Thus, the output parameter (Y) as well as the margin to a Safety Limit (L) has an associated probability distribution. This approach is known as Best Estimate plus uncertainties (BEPU).

The reference core is a representative three loop, 12 feet PWR, representative of the Spanish PWR fleet of Westinghouse design. There are 157 fuel assemblies with a 17x17 array of 0.95 cm OD rods of a Zirconium alloy. The fuel management strategy is very low leakage loading pattern with Gadolinia as burnable poison and 18 month cycle length. The analysis in this paper is performed at hot zero power and end of cycle (HZP EOL), since it is the most limiting condition, as it is discussed below. The output result is the enthalpy deposition in the hot spot during the transient, which is likely to be related to the new criteria, and albeit not yet applicable to the current regulation, it is taken as the parameter of interest.

The following sections present the results obtained with different methods of propagation of uncertainties and they are compared to the conservative deterministic case. Besides, the ranking of importance of the input parameters is confirmed.

## 2. Description of the model

### 2.1. PARCS model

By using a detailed 3D advanced nodal code, the macroscopic cross sections corresponding to EOC were calculated at homogeneous HZP reference conditions and the first-order partial derivatives were obtained from a series of perturbation calculations, and based on the design reference model, a PARCS core model was built. The nodalization employed for this core model has been the following: each fuel assembly has been represented in 2x2 radial nodes and twenty-four axial nodes. Additionally, two other axial nodes were set up to represent the upper and lower axial reflectors. The radial reflectors have been modelled as additional non-fuel assemblies with the same 2x2 radial node geometry. To specify the node wise cross-sections assignment, the fuel has been lumped in five radial regions: “inner” fresh fuel, “outer” fresh fuel, once burned fuel, twice burned fuel, and finally, a special region with a unique assembly, the assembly where the ejected rod is positioned.

Previous calculations and sensitivity analysis performed in the past with this model [1], showed enough agreement to the more detailed 3D nodal reference core model, specially at the EOC limiting condition, not only from the axial and radial power distributions viewpoint but also from the core reactivity parameters (ejected rod worth, rod banks worth, Doppler and power defects, MTC, etc). Adjustments to kinetics and reactivity parameters need to be made through the cross section module of PARCS to adapt to the prescribed simulation state.

### 2.2. RELAP model

The calculation of fuel temperature and enthalpy deposition at the hot spot is performed by means of a pellet-type RELAP model. The transient core average nuclear power and heat flux peaking factor are determined in a previous calculation with PARCS and then transferred to the RELAP pellet model as boundary conditions.

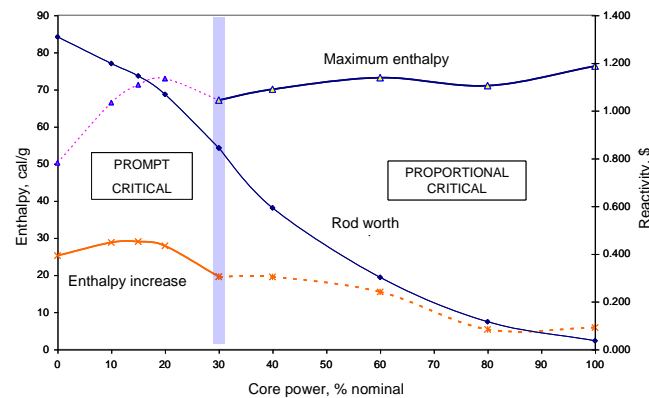
Radial heat conduction is considered but no axial conduction is assumed. Conservative low gap conductance values were determined to maximise the adiabatic behaviour of the hot rod during the transient. Suitable properties have been considered for the UO<sub>2</sub> and the burn-up effects have been considered as well. Heat transfer from clad to coolant is forced convection, local boiling or film boiling depending on the phase of the transient. No DNBR calculation was implemented at this stage.

## 3. Selected operating state: HZP – EOC

The most important parameters in a realistic RIA analysis are very dependent on the fuel exposure and core power. EOC and low power is the worst state possible due to several reasons. In one hand, both ejected rod worth ( $\Delta\rho$ ) and heat flux peaking factor ( $F_q$ ), are maxima, as well as the delayed neutron fraction ( $\beta$ ) is minimum. At EOC,  $\Delta\rho$  is maximum because of the lack of competition with other poisons, and per Technical Specifications requirements, the control rod insertion limits are higher (deeper) at HZP than at greater relative power levels. Thus, when the rod is ejected, the relative power is greatly distorted and shifted to the ejection location; the greater is  $\Delta\rho$ , the greater is  $F_q$ , so it is expect to have maximum  $F_q$  values at EOC-HZP. In the other hand, the fissile composition of the fuel varies with burn-up. Pu-239 has been builtup from neutron capture and beta decay processes. The contribution of this actinide to the total number of fissions in the reactor becomes important at EOC. As a result, the net delayed neutron fraction becomes smaller than at BOC.

The sensitivity of the energy deposition to the power has been studied with an EOC realistic model. It was found that the transition threshold from prompt to proportional criticality is between 30% to 40% of the nominal thermal power (see Figure 1). Below this point, the case of 15% of core power is the most limiting one from the enthalpy rise standpoint, although in a very small quantity. At power greater than 30%, there is no power pulse at all and, although the total enthalpy in the hot spot during the transient may be higher, the enthalpy rise is relatively not important anymore. Except at zero power, this calculation was performed assuming that all three pumps were in operations. With these results in mind, one can define a HZP case, with due penalties in the ejected rod worth and peaking factor, which bounds all prompt critical cases.

Figure 1. Realistic enthalpy and reactivity vs. power



#### 4. Uncertainties in the input and output parameters

Code predictions are uncertain due to several sources of uncertainty, such as code models as well as uncertainties of plant and fuel parameters. This lack of knowledge can be categorised in epistemic and stochastic uncertainties.

The first type is related to the question of what the exact value of an input parameter is. Depending on the case, some parameters can be measured or calculated imperfectly so that the actual value is known only to a certain degree of accuracy and one must describe the parameter within a probability distribution. Regarding RIA analysis, fuel parameters like ejected rod reactivity ( $\Delta\rho$ ), Doppler reactivity defect (DD), delayed neutron fraction ( $\beta$ ), moderator temperature reactivity coefficient (MTC), etc., material properties, plant measured parameters, among other, can be considered as epistemic parameters. Besides, some of the protection system characteristics, like the scram delay time and rod insertion interval, high neutron flux scram set point, can also be included in this category. In addition, some empirical correlations between physical parameters to close the constitutive equations are also affected by uncertainty. All these uncertainties propagate to the output.

In the other hand, predictive models are not perfect and they are simplifications of a complex reality. There may be a number of different accidental scenarios and actuations of the safeguards and the variability due to possible events and, consistently with the single failure criterion, component failures have to be conservatively assumed in a conservative deterministic. In the case of the RIA analysis of this paper, the maximum worth control rod is ejected at a fixed location from the maximum insertion limits allowed by the Technical Specifications. Also, some initial and boundary conditions, or status of the plant are assumed at the worst state, pressure feedback is not credited, the hot spot is assumed coincident with the greatest burn-up location, axial heat transfer in the rod is neglected, only two primary pumps are assumed in operation, etc. All these assumptions deal with stochastic uncertainty and provide intrinsic conservatism or bias to the evaluation model [2].

If a probabilistic approach is taken for some of the input variables, the resulting output is not deterministic anymore and it is described with a probability distribution. Therefore, the safety statement or criterion verification is not that  $Y \leq L$ , but  $P\{Y \leq L\} \geq Q$ , that is, the result of the calculation (Y) is lower than the safety limit (L) with a probability at least Q. Furthermore, since the sample is not infinite, then this statement can be made only within some confidence level [2, 3].

At this time, the current regulation does not account for the rod failure mechanism by PCMI yet. However, it is foreseen that the fuel enthalpy increase at the hot spot for prompt critical RIAs will be a parameter of interest. Therefore, this one will be the safety output in this exercise. Since no Safety Limit L for the

enthalpy increase has been specified by the regulatory authorities yet, only an estimation of the maximum  $\Delta h$  with a 95% coverage and 95% confidence level, can be made with no attempt to make any statement on the margin to the limit L.

## 5. Statistical estimation of $\Delta h$ on a 95/95 basis

### *Generation of the input/output sample*

In order to be conservative, it is assumed in this exercise that all the input probability distributions are uniform. The first step is to determine the sampling ranges for each one of the 29 selected input variables. The maximum value is assigned to the conservative high (or low) value that would have in a pure deterministic simulation. The other limit of the sampling range is obtained by subtracting two times the measurement uncertainty to the conservative limit. If the parameter does not come from a measurement nor it is surveilled in the plant, but it derives from calculations with a design code, only one uncertainty is subtracted. In this later case, no credit is given to values than are lower than those calculated with design codes.

Next, 59 sets of input parameters are randomly generated. It is necessary to confirm that the pdf of the inputs is the one assumed for each parameter; this stage is less critical in this research because all the input pdf were assumed uniform. Also, a check for independency among all the inputs is performed by means of a Pearson product moment [correlation](#) coefficient between each pair of variables. Finally, all 59 PARCS-RELAP cases are run to obtain the  $\Delta h$  value corresponding to each run case.

### *$\Delta h$ 95/95 with Order Statistics*

According to Wilks's formula [4], the worst result out of 59 cases is a conservative estimation of the 95% one sided tolerance of the population with at least 95% confidence level. Advantages of this method are: (i) the number of cases is independent of the number of inputs in the simulation and uncertainties are propagated together, (ii) it is an output distribution free method, (iii) the outcome is direct and no post processing is needed, (iv) a representative worst run can be identified, (v) it is suitable for complex computer simulations. Disadvantages are: (i) the estimation can be over conservative, and (ii) if more than one output is to be calculated with the same coverage, a larger number of runs are needed. Further details of this method are given in [5].

In this research, the maximum result out of 59 runs was 55.8 cal/g. Therefore:

$$\Delta h_{order\ stat}^{95/95} = 55.8 \text{ cal/g} .$$

### *$\Delta h$ 95/95 with parametric statistics*

The main advantages are: (i) if the number of runs is large enough, say more than 30 runs, the result is not very sensitive to the number of runs, so it is a robust method, (ii) there is no extra conservatism, (iii) the uncertainty in the output is quantifiable, (iv) provided that the pdf is correctly identified, the method is rich in the information that can be obtained from the output parameter. Disadvantages are: (i) no representative worst run can be identified, and (ii) it is necessary to identify the pdf associated to the output.

An Anderson Darling normality test was applied to the series of  $\Delta h$  results. In this case, significant evidence in favour of normality hypothesis was obtained (P-value = 0.46 > 0.05), see Figure 2. Besides, the skewness  $\gamma_1$  (asymmetry) and kurtosis excess  $\gamma_2$  (peakness) coefficients of the sample:

$$\gamma_1 = \frac{\sum (\Delta h_i - \Delta h_{avg})^3}{(N-2)s^3} = 0.35 \text{ and } \gamma_2 = \frac{\sum (\Delta h_i - \Delta h_{avg})^4}{(N-3)s^4} - 3 = 0.24 ,$$

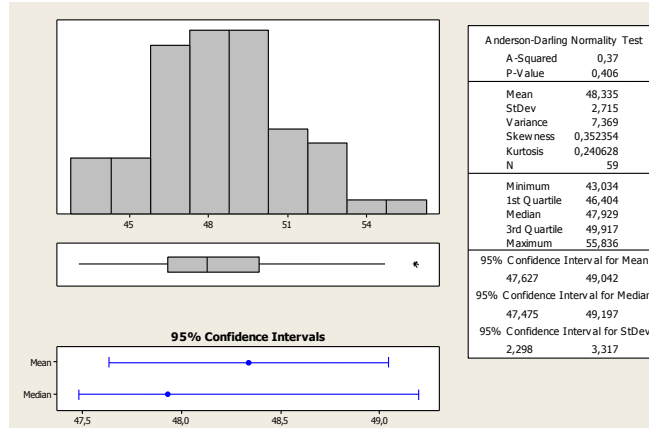
are closer to the characteristic values of a normal distribution (0.0, 0.0) than those of a uniform distribution (0.0, -1.2). Consequently, the assumption of a normal distribution is solid and parametric statistics can be

used for the further estimation of tolerances. This assumption is rather consistent with a visual inspection of the shape. Therefore:

$$\Delta b_{Param\ stat}^{95/95} = \Delta b_{avg} + K_P \cdot s_{\Delta h} = 48.335 + 2.03 \times 2.715 = 53.9 \text{ cal/g,}$$

where  $\Delta h_i$  is the sample mean,  $K_P$  is factor for one-sided tolerance limit for a normal distribution, and  $s$  is the sample standard deviation. Per the Owen tables, with a probability coverage  $P$  of 0.95 and a confidence level of 0.95, and a simple size of 59,  $K_P$  is 2.03.

Figure 2. Main statistics summary for  $\Delta h$  (cal/g)



$\Delta h$  95/95 with Montecarlo – Surface response method

Since a very large number of runs are necessary in a Monte Carlo analysis, and due to the complexity of the calculations with PARCS, a pure Monte Carlo analysis is not feasible. Instead, taking advantage of the existence of 59 runs already performed for the order statistics evaluations we can derive a surface response (SR), and then carry out the Monte Carlo analysis. Please note that the SR could also be developed from any other set of runs under a specification of a factorial design.

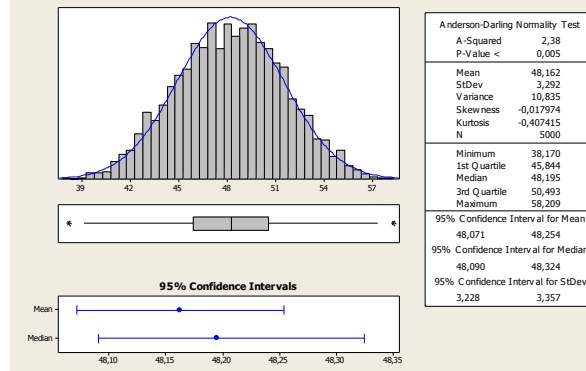
The SR was obtained by means of a stepwise regression process with forward selection based on the Pearson correlation coefficient, adding only those parameters statistically significant. The SR is described by the following linear expression:

$$\Delta b \approx 48.34 + 0.0286(DD - 1528) + 0.0854(\Delta\rho - 769) + 2.07(F_Q - 24) - 13243(\beta - 0.004542) - 200(\text{fracdc} - 0.031) + 0.282(MTC - (-28.7)) \pm 1.49,$$

where,  $\Delta h$  is the enthalpy increase at the hot spot (cal/g),  $DD$  is the Doppler defect from zero power (pcm),  $\Delta\rho$  is the ejected rod worth (pcm),  $F_Q$  is the heat flux peaking factor at the hot spot,  $\beta$  is the delayed neutron fraction,  $\text{fracdc}$  is the direct moderator heating fraction, and  $MTC$  is the moderator temperature coefficient (pcm/°C). The regression coefficient is  $r = 97.2\%$ , and the sample standard deviation of the errors is  $s = 0.61$  cal/g. A linear regression was preferred in this exercise to other more complex expressions because it provides individual sensitivities while the degree of correlation is very satisfactory.

Finally, 5000 random values were sampled from each parameter and the predicted  $\Delta h$  was calculated. An additional variable was considered for the regression error. The estimated enthalpy increase with the SR expression is presented in Figure 3.

Figure 3. Main statistics summary for SR - Δh (cal/g)



For the sake of conservatism, rather than inferring normality, the 95% upper bound is calculated with a distribution free test like Kolmogoroff-Smirnoff [6]. Thus, for a 95% coverage, the upper bound corresponds the  $\xi$  value such that  $F(\xi) + \lambda / \sqrt{n} = 0.95 + 1.35 / \sqrt{5000} = 0.969$ , which turns out to be  $\xi = 54.16$  cal/g. Therefore:

$$\Delta b_{SR}^{95/95} = 54.16 \text{ cal/g.}$$

The adimensional sensitivities for the important parameters can be calculated as follows:

$$S_{DD} = \left( \frac{\partial \Delta b}{\partial DD} \right) \cdot \frac{DD_{mean}}{\Delta b_{mean}} = 0.0286 \times \frac{-1528}{48.34} = -1,$$

$$S_{RO} = \left( \frac{\partial \Delta b}{\partial \Delta \rho} \right) \cdot \frac{\Delta \rho_{mean}}{\Delta b_{mean}} = 0.0854 \times \frac{-769}{48.34} = +2.44,$$

$$S_{FQ} = \left( \frac{\partial \Delta b}{\partial F_Q} \right) \cdot \frac{F_Q_{mean}}{\Delta b_{mean}} = 2.07 \times \frac{24}{48.34} = +1.1, \text{ and}$$

$$S_{\beta} = \left( \frac{\partial \Delta b}{\partial \beta} \right) \cdot \frac{\beta_{mean}}{\Delta b_{mean}} = -13243. \times \frac{0.004542}{48.34} = -1.24 .$$

These sensitivities are close to the theoretical sensitivities of Δh in a RIA event [7].

#### Δh 95/95 with SRSS

A very easy method of estimating the upper bound, which involves only a few sensitivity calculations, is the square root of sum of squares (SRSS). However, conservatism is not guarantee and one needs to assume linearity and independency of the all parameters, which cannot be demonstrated in all situations. The result is strictly valid only, if all distributions are of the same type. There is no representative case either.

In the RIA simulation, the SRSS upper bound estimation can be done by just seven computer runs: one corresponding to the mid point of all parameters (Δh<sub>0</sub>), and one sensitivity run for each individual parameter (ΔΔh<sub>i</sub>). All the other inputs have been considered stochastic.

$$\Delta b_{SRSS}^{95} \square \Delta b_0 + \frac{1.645}{\sqrt{3}} \sqrt{\sum (\Delta \Delta b_i)^2} = \dots = 53.7 \text{ cal/g.}$$

#### Conservative case

Another final run was done with all uncertainties applied in the worst sense together, resulting  $\Delta b_{all} = 61.0$  cal/g.

### Summary of results

The upper bound enthalpy increase at the hot spot obtained with each method is summarised in Table 1. Also, the most important parameters in the RIA simulation is presented in Table 2.

Table 1. **Upper bound enthalpy increase at hot spot**

Method	Enthalpy increase, cal/g	Margin to conservative
Conservative	61.0	-
Order statistics	55.8	8.5%
Parametric statistics	53.9	11.6%
Monte Carlo/surface response	54.2	11.2%
SRSS	53.7	12%

Table 2. **High and medium rank parameters**

High rank	<ul style="list-style-type: none"> <li>• Doppler defect, DD</li> <li>• Ejected rod worth, <math>\Delta\rho</math></li> <li>• Heat flux peaking factor, FQ</li> <li>• Delayed neutron fraction, <math>\beta</math></li> <li>• Number of pumps, flow at the hot spot (*)</li> </ul>
Medium rank	<ul style="list-style-type: none"> <li>• Direct moderator heating fraction</li> <li>• MTC</li> <li>• Scram delay time</li> <li>• Number of stucked rods</li> <li>• Post dryout heat transfer at the hot spot</li> <li>• Fuel and clad conductivity in the core model</li> <li>• Fuel and clad conductivity at the hot spot</li> <li>• Radial power distribution within the rod (*)</li> </ul>

Note (\*) – These parameters were considered deterministic in this simulation, but the importance was determined in a previous sensitivity calculation.

## 6. Conclusion

The recoverable margin in the RIA analysis with PARCS and RELAP, due to the utilisation of statistical techniques was calculated and found to greater than 8%, depending on the statistical method. This margin can be even higher if less conservative input pdf are considered.

Besides, the most important parameters of the simulation were identified and are consistent with those ones the state of the art in the published literature. These parameters include ejected rod worth and ejection time, delayed neutron fraction and yields and nuclear power peaking factor, and Doppler.

## References

- [1] J. Riverola, T. Nuñez. – “A Generic Assessment of the RIA Interim Criteria in a Typical 3 Loop 12 Feet PWR with 3D Methods”. Top Safe 2008, Dubrovnik, Croatia.
- [2] Task 3-Safety Margin Evaluation Methods, NEA/SEN/SIN/SMAP (2006)3 August (2006).
- [3] R. Mendizabal, F. Pelayo – “Regulatory Challenges Posed by the Best-estimate plus Uncertainty Methodologies”. Top Safe (2008), Dubrovnik, Croatia.
- [4] S.S. Wilks – “Determination of Sample Sizes for Setting Tolerance Limits,” Annals of Mathematical Statistics, vol. 12, (1941).
- [5] H. Glaeser – “GRS Method for Uncertainties and sensitivity Evaluations of Code Results and Applications”. Science and Technology of Nuclear Installations, Vol. (2008).
- [6] A. Kolmogoroff – “Confidence Limits for an Unknown Distribution Function”, Annals of Mathematical Statistics.
- [7] D.J. Diamond, C.Y. Yang, and A. Aronson – “Sensitivity Studies for the PWR Rod Ejection,” BNL-NUREG-67013.

# A survey of Available Margin in a PWR RIA with Statistical Methods and 3D Kinetics

Javier Riverola, Tomás Núñez  
OECD/NEA RIA Workshop  
Paris, September 2009



## Introduction

- Since PCMI consideration, RIA margin greatly reduced
- Need to avoid potential restrictions in loading pattern and fuel usage!
- Margin recovery:
  - Advanced cladding materials
  - Remove excessive conservatism in input and assumptions
  - Use of 3D methods with deterministic or probabilistic treatment
- Objective of this exercise:
  - Estimate recoverable **margin with statistical methods**
  - **Compare** different statistical methods
- Scope? PWR Wh 3 loops - 12feet - 17x17 at EOC-HZP

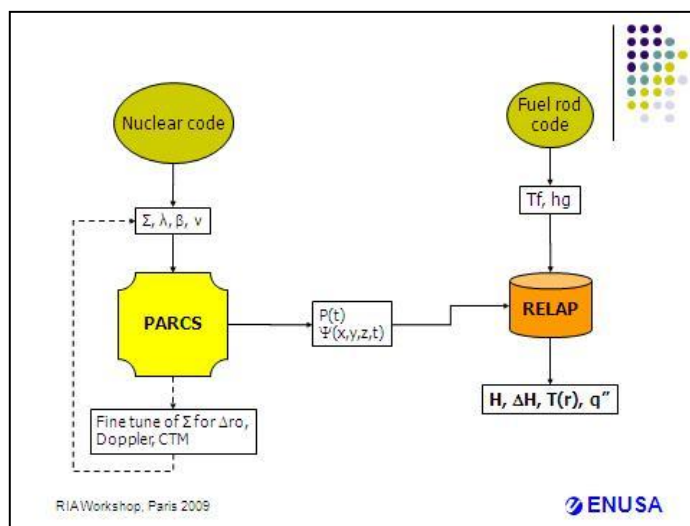
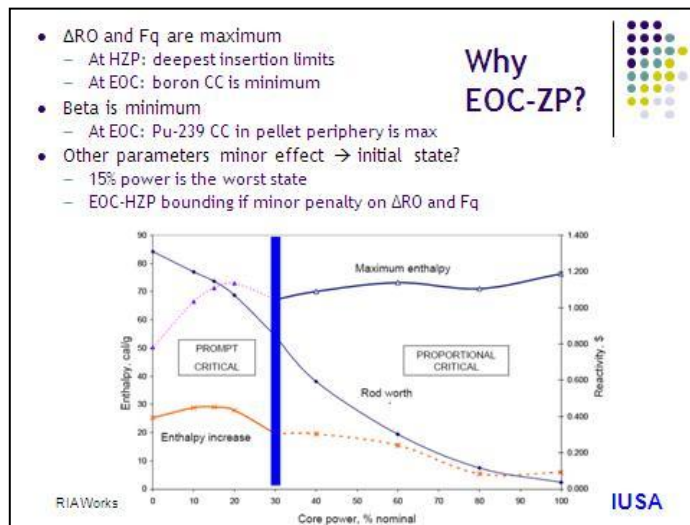
RIAWorkshop, Paris 2009



PCMI, high burnup, new regulations, ...  
We need margin!

RIAWorkshop, Paris 2009





## PARCS

- **Code**
  - 3D simulator
  - External XS from advanced nodal code
- **Model**
  - Modifications: more regions, doppler model, properties...
  - 1/2 core - each assembly 2x2 radial - 24 axial + 2 axial reflectors
  - Fine tune to match a reference solution for radial, axial distributions at given conditions
- **Simulation:**
  - Rod expulsion H-14 from RIL in 0.10 s

ENUSA

$$\frac{1}{V} \frac{d\Phi}{dt} = (1-\beta)(\nu\Sigma_f\Phi + \nu\Sigma_{f2}\Phi_2) + \sum_{k=1}^6 \lambda_k C_k - D_1 \cdot \nabla^2 \Phi - \Sigma_a \Phi - \Sigma_{a2} \Phi_2$$

$$\frac{1}{V} \frac{d\Phi_2}{dt} = \frac{\text{dispersionnelle groupé} \nu\Sigma_{f2}\Phi_2}{\Sigma_{a2}\Phi_2} - \frac{D_2 \cdot \nabla^2 \Phi_2}{\text{diffusion}} - \frac{\Sigma_{a2}\Phi_2}{\text{absorption}}$$

$$\frac{\partial C_k}{\partial t} = \beta_k (\nu\Sigma_{f1}\Phi_1 + \nu\Sigma_{f2}\Phi_2) - \lambda_k C_k, \quad k = 1, \dots, 6$$



$$\Sigma = \Sigma_{ref} + \left( \frac{\partial \Sigma}{\partial bororo} \right) \Delta bororo + \left( \frac{\partial \Sigma}{\partial T_m} \right) \Delta T_m + \left( \frac{\partial \Sigma}{\partial d} \right) \Delta d + \left( \frac{\partial \Sigma}{\partial \sqrt{T}} \right) \Delta \sqrt{T}$$

$$\left( \frac{\partial \Sigma_{ref}}{\partial \sqrt{T}} \right)_{ref} \propto \text{Doppler}, \quad \left( \frac{\partial \Sigma_{ref}}{\partial T_m} \right)_{ref} \propto \text{C7M}, \quad \left( \frac{\Delta \Sigma_{ref}}{\Delta Z} \right)_{ref} \propto \Delta d$$

RIAWorkshop, Paris 2009 ENUSA

## RELAP

- Pellet type - radial conduction
- Heat transfer: from single phase forced convection to post dryout, specified by tables
- Input is power, Fq vs. time vs. time
- Output is h, Tf, Tc, oxidation vs. Time
- Some conservatisms:
  - Hot spot coincident with max burnup
  - No credit to pressure increase
  - No axial HT
  - HT gap and clad very conservative

RIAWorkshop, Paris 2009 ENUSA

## Choice of random input variables

- **Stochastic** : models are not perfect, simplification of reality
  - What happens?
  - Deterministic BIAS
  - Examples: rod location, plant initial state, accidental scenario, safeguards actuation and component failures per single failure criterion, model simplifications, ...
- **Epistemic** : imperfect measurement or calculation
  - What is the exact value?
  - Propagate to the output
  - Deterministic OR probabilistic treatment of uncertainties
  - Examples:  $\Delta RO$ , Doppler,  $\beta$ , MTC, Fq, fuel props., empirical correlations, scram characteristics (29 input variables in this exercise, uniform pdf)

RIAWorkshop, Paris 2009 ENUSA



### 4 - SRSS

- Square root of sum of squares
- Only a few cases needed
- Conservatism not guaranteed
- Need to assume linearity, independency, same pdfs (or corrective factors)
- UB  $\Delta h_{95/95} = 53.7 \text{ cal/g}$

$$\Delta h = \Delta h_0 + \frac{1.645}{\sqrt{3}} \sqrt{\sum (\Delta \Delta h_i)^2}$$

RIAWorkshop, Paris 2009 

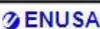
### Comparison of methods

Method	$\Delta$ Enthalpy, cal/g	Margin to deterministic	Comment
Deterministic	61.0	Ref	-
Order (OS)	55.8	8.5%	Easy for few outputs, overconservative
Parametric (PS)	53.9	11.6%	Robust and rich, need more insight
MC-SR	54.2	11.2%	Similar to PS, still an approximation
SRSS	53.7	12%	Good for quick estimation, but conservative?

RIAWorkshop, Paris 2009 

### Variance analysis → Important parameters

High rank	<ul style="list-style-type: none"> <li>• Doppler defect</li> <li>• Ejected rod worth</li> <li>• Fq</li> <li>• Beta</li> <li>• Number of pumps (hot spot)</li> </ul>
Medium rank	<ul style="list-style-type: none"> <li>• Direct moderator heating</li> <li>• MTC</li> <li>• Scram delay time</li> <li>• Number of stuck rods</li> <li>• Post dryout heat transfer at hspot</li> <li>• Fuel and clad properties</li> <li>• Pellet radial distribution</li> </ul>

RIAWorkshop, Paris 2009 

## Conclusions



- Significant margin available thru 3D and statistic analysis (depends on the assumptions of epistemic vars)
  - 3D (kinetics and power redistribution) :: about 40% (previous research)
  - Statistic approach :: 8.5 % or more
- All statistical methods provide a similar margin benefit
- OS is more suitable for very few outputs, otherwise, PS is adequate
- Ranking if important parameters consistent with published works
- Future work? Fq and  $\Delta\sigma$  reductions vs. burnup increase



## **SESSION FIVE**

### **Revision and Application of Safety Criteria**

#### **Expectation to RIA Criteria to be Applicable for Fuel under High Duty**

Hajime Fujii (MNF, Japan); Noyomu Murakami and Satoshi Imura (MHI, Japan)

#### **Swiss Regulatory RIA Criteria and the Verification Procedures by the Operators**

Andreas Gorzel (ENSI, Switzerland)

#### **Example of Application of the IRSN Approach to Assess Safety Criteria for Reactivity Initiated Accidents**

Christine Sartoris, Aude Taisne, Marc Petit, Francois Barré and Olivier Marchand (IRSN, France)

#### **Burnup Dependent RIA Criterion for VVER Fuel (P004)**

Zoltan Hózer (KFKI, Hungary)

#### **An Analytical Criterion to Prevent PCMI Fuel Rod Cladding Failure during RIA Transients**

Christian Bernaudat, S. Cambier, J. Guion and Serge Benjamin (EDF, France)

#### **Development of Acceptance Criteria for Safety Analysis of Control Rod Ejection and Control Rod Drop Accidents Using a Mechanistic Approach**

Robert Montgomery and John Alvis (ANATECH Corp., USA); Ken Yueh and Odelli Ozer (EPRI, USA)



## EXPECTATION TO RIA CRITERIA TO BE APPLICABLE FOR FUEL UNDER HIGH DUTY

**Hajime Fujii**

Mitsubishi Nuclear Fuel Co., Ltd., Japan

**Nozomu Murakami, Satoshi Imura**

Mitsubishi Heavy Industries, Ltd., Japan

### Abstract

Fuel cladding integrity during RIA event mainly depends on cladding ductility, and which is affected by hydrogen concentration and moreover hydride morphology and its distribution. Hydrogen is supposed to be the most important key parameter to cladding failure mechanism during RIA event. For the purpose, fuel industry has been developing various kinds of new cladding materials to resist corrosion/hydriding. To access the adaptability of such new materials to RIA criteria, further study, such as the pulse test focusing on hydrogen content/distribution, manufacturing process and so on, is necessary and such effect should be considered into RIA criteria certainly. M-MDA<sup>TM</sup> is proposed as one of the advanced cladding candidate for NSRR and CABRI test program. Typical performances of M-MDA<sup>TM</sup> cladding are presented.

### 1. Introduction

RIA criteria is one of the most concerned fuel safety related issues on high burn-up utilisation of LWR fuel. Japanese NSRR and French CABRI have been providing a number of pulse test data and current RIA PCMI failure threshold in Japan, which index is enthalpy rise as a function of local burn-up, is mainly established by those results. Fuel cladding integrity during RIA event mainly depends on cladding ductility, and which is affected by hydrogen concentration and moreover hydride morphology and its distribution. Hydrogen is supposed to be the most important key parameter to cladding failure mechanism during RIA event. For the purpose, fuel industry has been developing various kinds of new cladding materials to resist corrosion/hydriding. To access the adaptability of the material to RIA criteria, further study, such as the pulse test focusing on hydrogen content/distribution, manufacturing process and so on, is necessary and such effect should be considered into RIA criteria certainly.

As one of the new cladding material, M-MDA<sup>TM</sup>, which will be applied to future high duty usage in PWR has been confirmed its excellent corrosion resistance in the LTA program up to 73 GWd/t. The high burn-up M-MDA<sup>TM</sup> fuels are proposed to be subjected to RIA simulated pulse experiments both in NSRR and in CABRI. Therefore, the M-MDA<sup>TM</sup> provides the comprehensive and internationally accessible database for future high demanding fuel.

With regards to M-MDA<sup>TM</sup>, two types of manufacturing processes, Stress-Relieved(SR) and Recrystallised(RX) were irradiated as LTA in a commercial PWR. Pulse experiment not only with SRA but also with RXA materials of the same alloy irradiated under the same operation cycle is principal to assess and understand the effect of hydrogen morphology due to texture difference. In this paper, typical performances and extensive study plan of M-MDA<sup>TM</sup> cladding are presented in relation to expectation to upcoming study on RIA criteria from the point of PWR fuel vendor's view.

### 2. M-MDA<sup>TM</sup>

#### 2.1. M-MDA<sup>TM</sup> performance

Table 1 shows the chemical composition of M-MDA<sup>TM</sup> in comparison with the conventional cladding materials. M-MDA<sup>TM</sup> inherits an excellent performance from MDA which is applied in high burn-up fuel (step2 fuel) in Japan, while its corrosion resistance and hydrogen pick-up fraction are improved by optimisation of alloying elements.

Table 1. Chemical composition of M-MDA, MDA and Zircaloy 4

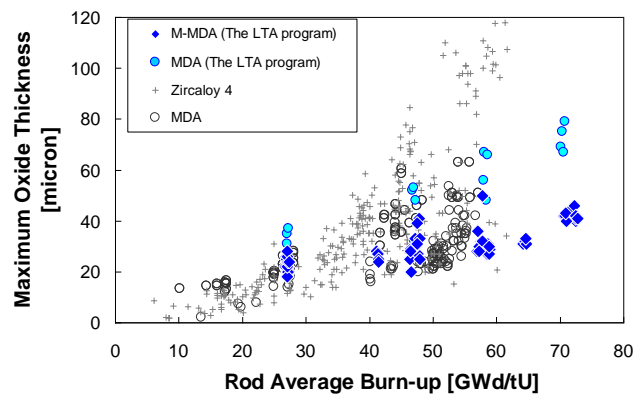
	Nb	Sn	Fe	Cr	Zr
M-MDA	0.45-0.55	0.4-0.6	0.27-0.33	0.36-0.44	balance
MDA	0.45-0.55	0.7-0.9	0.18-0.24	0.07-0.13	balance
Zircaloy 4	-	1.2-1.7	0.18-0.24	0.07-0.13	balance

In order to demonstrate the in-core performance of M-MDA<sup>TM</sup> cladding, irradiation test of LTA with M-MDA<sup>TM</sup> cladding inside was carried out in the Spanish commercial PWR plant Vandellós II<sup>1,2</sup>.

Several numbers of fuel rods consisting of M-MDA<sup>TM</sup> cladding tubes (M-MDA<sup>TM</sup> fuel rods) were loaded in the peripheral positions of four 17×17 PWR fuel assemblies. In the LTAs, as a reference material, MDA fuel rods were also loaded in the same LTAs and irradiation test at the same cycles.

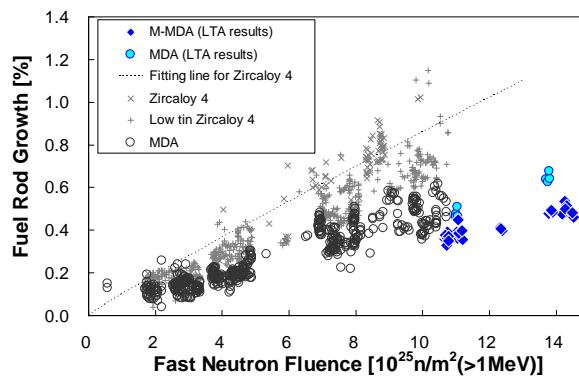
As shown in Fig.1, oxide thickness of M-MDA<sup>TM</sup> after high burn-up over 70GWd/tU is well improved and its corrosion rate is approximately 70% of that of MDA. This result convinces us that M-MDA<sup>TM</sup> is an appropriate cladding material for advanced fuel in the future from the viewpoint of corrosion resistance.

Figure 1. In-core corrosion performance of M-MDA<sup>TM</sup> and MDA fuel rods



As shown in Fig.2, fuel rod growth of M-MDA<sup>TM</sup> after high neutron fluence is enough suppressed and smaller than MDA. Therefore, M-MDA<sup>TM</sup> is an appropriate cladding material for advanced fuel in the future from the viewpoint of dimensional stability.

Figure 2. In-core fuel rod growth of M-MDA<sup>TM</sup> and MDA fuel rods



Since the chemical composition of M-MDA<sup>TM</sup> is not so different from the conventional cladding materials, the physical and thermo-physical properties of M-MDA<sup>TM</sup> related to fuel rod design and safety evaluation are comparable to the conventional cladding materials.

Since the modification of MDA to M-MDA<sup>TM</sup> in the chemical composition from the viewpoint of mechanical properties are quite small, and there is little difference in manufacturing process such as cold work, annealing temperature, surface finish, the texture and the mechanical properties of M-MDA<sup>TM</sup> are comparable to the conventional cladding materials. Accordingly, it is expected that the PCI (Pellet Clad Interaction) resistance of M-MDA<sup>TM</sup> is also comparable to MDA.

Since the physical properties, the thermo-physical properties, and the mechanical properties of M-MDA<sup>TM</sup> is comparable to the conventional cladding materials, LOCA related properties such as burst temperature, high temperature oxidation rate, and integrity after quenched of M-MDA<sup>TM</sup> is comparable to the conventional cladding materials.

In the LTA program, M-MDA<sup>TM</sup> rods with recrystallised heat treatment (M-MDA-RX) have been also irradiated in the same LTAs. Axial tensile tests on as-received and hydrogenated specimens were performed at elevated temperature, as shown in Figure 3. The total elongation of as-received M-MDA<sup>TM</sup>-SR was approximately 20% and it remained when hydrogenated up to around 800ppm. On the other hand, the total elongation of as-received M-MDA<sup>TM</sup>-RX was approximately 40%, while it degraded with increasing hydrogen concentration. But it still kept approximately 30% when hydrogenated up to around 800ppm. Such difference in influence of hydrogen upon ductility between SR and RX materials is ascribable to difference in hydride morphology as shown in Fig.4. Fig.4 shows the precipitated hydrides on M-MDA<sup>TM</sup>-SR and M-MDA<sup>TM</sup>-RX specimens observed by means of hydriding test in which metallographic observation was performed on the specimens which had been hydrogenated approximately 100ppm at 400°C and then cooled down to room temperature. Some of the hydrides precipitated on M-MDA<sup>TM</sup>-RX were oriented in the radial direction, while almost all of the precipitated hydrides on M-MDA<sup>TM</sup>-SR were oriented in the circumferential direction.

Figure 3. Total elongation of as-received and hydrogenated specimens of M-MDA<sup>TM</sup>

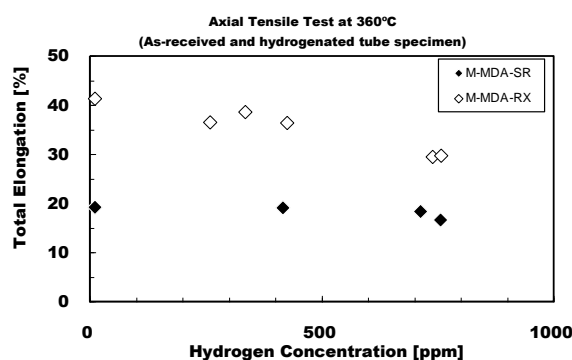
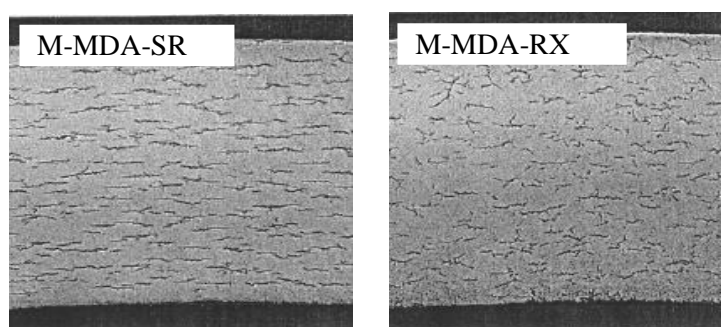


Figure 4. Hydrides precipitated on M-MDA<sup>TM</sup>



## 2.2. Study programs

As mentioned above, it is convinced that M-MDA<sup>TM</sup> cladding has well improved corrosion resistance and no degradation in the other properties related to fuel rod design and safety evaluation in comparison with the conventional cladding materials such as MDA. As the final step of demonstration to utilise it in the commercial reactor, it is scheduled to obtain further data by means of post irradiation examinations in hot cells, in which several non-destructive tests and destructive tests such as tensile tests and hydrogen analysis will be performed. Moreover, M-MDA<sup>TM</sup> fuels are proposed to be studied in international project, such as Halden, SCIP and safety related studies such as ALPS and CABRI program. Pulse experiment not only with SRA but also with RXA materials of the same alloy irradiated under the same operation cycle is principal to assess and understand the effect of hydrogen morphology due to texture difference.

## 3. Expectation for RIA criteria

In Japan, current RIA PCMI failure threshold consists of an index of enthalpy rise as a function of local burn-up, which was established based on wide range of RIA simulated pulse experiment data. USNRC proposes new PCMI criteria of PWR fuel as a function of cladding oxidation<sup>3</sup>. It is understood that hydrogen is important to be regulated since it affects cladding ductility during RIA event and hydrogen pick-up is almost proportional to the cladding waterside corrosion. There has been still a strong demand for more efficient operation of LWR such as higher burn-up, up-rating, and optimisation of operation cycle, therefore, our fuel industry has a role to supply reliable fuel under such a high duty condition. In this context, reasonable RIA PCMI criteria considering appropriate benefit for less corrosion and hydriding cladding material is expected to be established. We think that the effect of hydrogen on cladding ductility is also influenced by hydrogen morphology as well as hydrogen concentration. For the purpose, SRA and RXA material of the same M-MDA<sup>TM</sup> alloy irradiated under the same operation cycle can contribute for assessing and understanding the effect of hydrogen morphology due to texture difference. In the ALPS program will include those materials for RIA simulated pulse experiments in NSRR and the materials are also proposed for CABRI waterloop programs in the near future. We believe that such outcome of the experiments will provide the comprehensive and internationally accessible database for establishing reasonable criteria.

## 4. Conclusion

Fuel cladding integrity during RIA event mainly depends on cladding ductility, and which is affected by hydrogen concentration and moreover hydride morphology and its distribution. Hydrogen is supposed to be the most important key parameter to cladding failure mechanism during RIA event. A reasonable RIA PCMI criteria considering appropriate benefit for less corrosion and hydriding cladding material is expected to be established. We think that the effect of hydrogen on cladding ductility is also influenced by hydrogen morphology as well as hydrogen concentration. For the purpose, SRA and RXA material of an advanced material, M-MDA<sup>TM</sup> alloy can contribute for assessing and understanding the effect of hydrogen morphology due to texture difference. In the ALPS program will include those materials for RIA simulated pulse experiments in NSRR and the materials are also proposed for CABRI waterloop programs in the near future. We believe that such outcome of the experiments will provide the comprehensive and internationally accessible database for establishing reasonable criteria.

## References

- [1] S. Watanabe, et al., "Performance of M-MDA<sup>TM</sup> cladding in the commercial reactor up to 73GWd/tU", Proc. 2008 WRFPM, Seoul, Korea, 2008.
- [2] S. Watanabe, et al., "DEVELOPMENT OF MODIFIED MDA (M-MDA), PWR FUEL CLADDING TUBE FOR HIGH DUTY OPERATION IN FUTURE", Proc. 2007 LWR fuel performance meeting, San Francisco, USA, 2007.
- [3] USNRC, NUREG-0800 Rev.3, Mar 2007.

OCED/NEA Workshop Nuclear Fuel Behaviour during Reactivity Initiated Accidents 

## Expectation to RIA criteria to be applicable for fuel under high duty

Hajime FUJII<sup>1</sup>, Nozomu MURAKAMI<sup>2</sup>, Satoshi IMURA<sup>2</sup>

1 Mitsubishi Nuclear Fuel Co., Ltd.  
2 Mitsubishi Heavy Industries, Ltd.

 **MITSUBISHI NUCLEAR FUEL CO., LTD.**

OCED/NEA Workshop Nuclear Fuel Behaviour during Reactivity Initiated Accidents 

## Contents

1. Introduction
2. RIA PCMI criteria
3. M-MDA
4. Conclusion

1

OCED/NEA Workshop Nuclear Fuel Behaviour during Reactivity Initiated Accidents 

## Introduction

- **Advanced PWR fuel for future**
  - **Plant operation**
    1. Longer fuel cycle (13 → 24 EFPM)
    2. Plant power uprate
    3. Burnup extension (Reducing fuel cycle cost and spent fuel)
  - **Key features for advanced PWR fuel**
    1. Enhanced corrosion resistant advanced cladding
    2. Even more improved fuel reliability
    3. Keeping enough safety margin

2

OECD/NEA Workshop Nuclear Fuel Behaviour during Reactivity Initiated Accidents

**MNF**  
MATERIAL NUCLEAR FUEL

## Introduction (cont'd)

- **RIA Criteria**
  1. One of the most concerned fuel safety related issues on high burnup utilization
  2. Hydrogen : the most important key parameter to cladding failure mechanism during RIA event, not only concentration but also hydride morphology and distribution

↓

- **Needs for advanced cladding with less H**
  1. M-MDA™ cladding is one of the advanced cladding
  2. M-MDA™ is proposed for RIA simulated pulse experiments in ALPS-2 and CIP

3

OECD/NEA Workshop Nuclear Fuel Behaviour during Reactivity Initiated Accidents

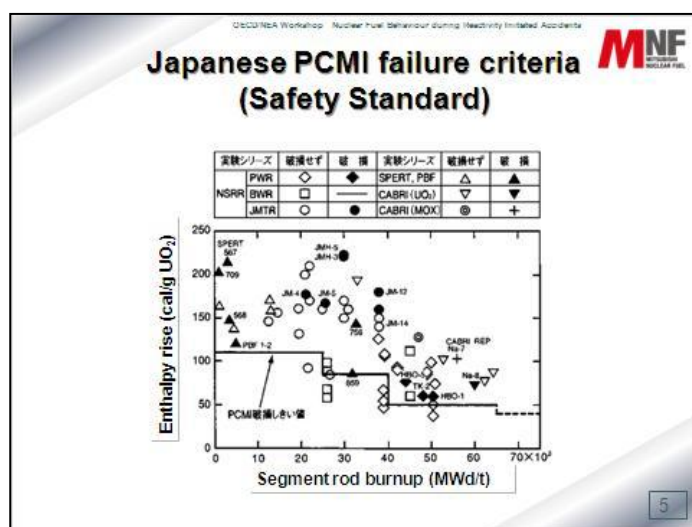
**MNF**  
MATERIAL NUCLEAR FUEL

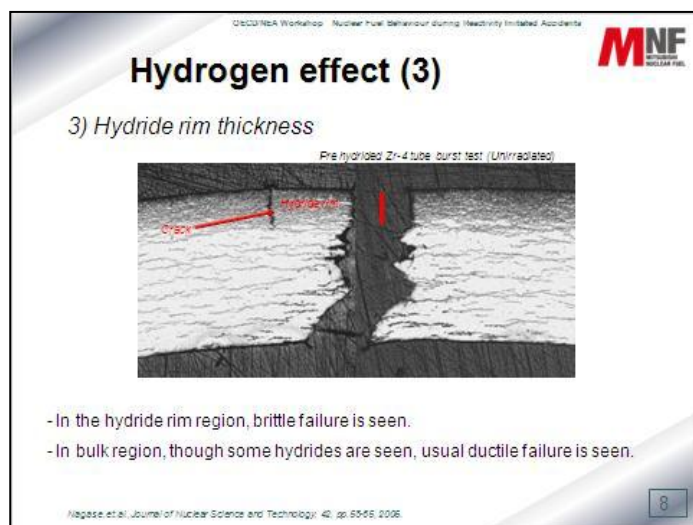
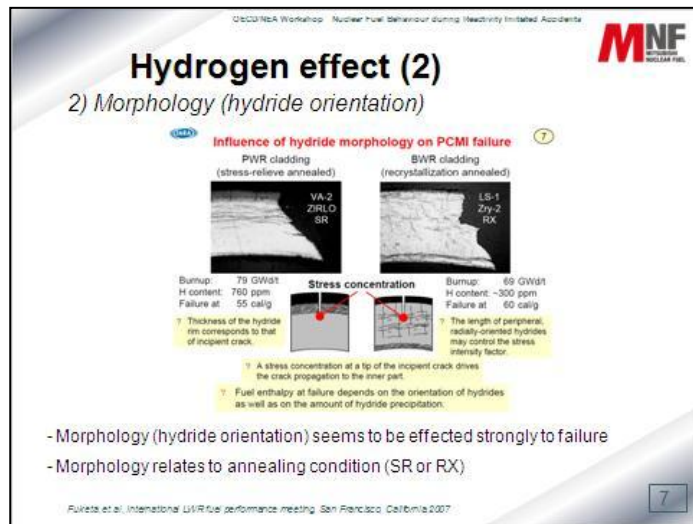
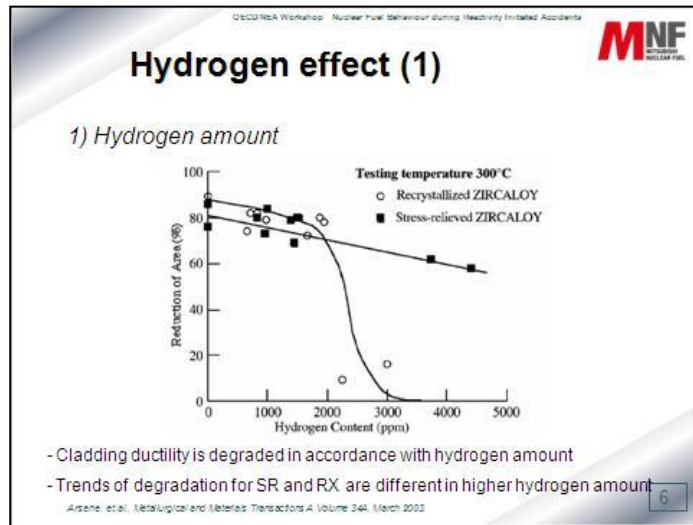
## Current RIA Criteria in Japan

- Defined in Japanese regulatory standard
- All are used "Enthalpy" as index
  - a) Preventing fuel disperse  
230 cal/g –  $\alpha$  (melting point effect)
  - b) Preventing oxidations/bursting  
170 cal/g –  $\beta$  (depends on differential pressure)
  - c) Preventing PCMI failure  
Enthalpy rise vs burnup (see next Figure)

*Practically, RIA-PCMI failure criteria is the most concern issue for high burnup utilization*

4





OECD/NEA Workshop Nuclear Fuel Behaviour during Reactivity Initiated Accidents



## Hydrogen effect (brief summary)

- Hydrogen is a key factor and should be considered to criteria properly.
- Hydrogen pickup amount is usually used as index how degrade. But it is not adequate to express.
- Other factors, like hydride orientation, hydride rim thickness, are also important to be considered.
- However, there is no common opinion which index is better to evaluate hydrogen effect to ductility.

9

Nagase et al., Journal of Nuclear Science and Technology, 45, pp.65-66, 2008

OECD/NEA Workshop Nuclear Fuel Behaviour during Reactivity Initiated Accidents

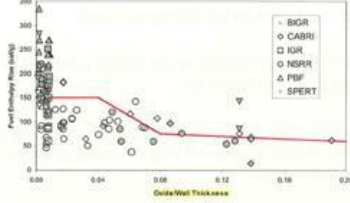


## NRC new RIA-PCMI criteria

- o As mentioned, PCMI failure is affected by hydrogen.
- o In PWR, hydrogen pickup amount is almost proportional to oxide thickness. Oxide thickness is representative for hydrogen amount.
- o This index (oxide thickness) approach is one of reasonable treatment since oxide thickness is measurable on-site.
- o Even though, hydride orientation/rim thickness are not considered explicitly, however, each data results include such properties.



### PWR Failure Criteria



10

OECD/NEA Workshop Nuclear Fuel Behaviour during Reactivity Initiated Accidents



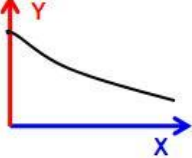
## Concerns for RIA-PCMI criteria

**X-axis (currently, burnup / oxide index)**

- o Current PCMI criteria is defined as a function of local burnup.
- o PCMI failure is strongly affected by hydrogen amount & morphology.
- o Index of burnup is not represent for cladding performance.
- o **Now it is acceptable to use parameter like oxide thickness instead of burnup. In future proper index should be studied from point of hydrogen effect.**

**Y-axis (currently, enthalpy index)**

- o Enthalpy index is a thermal energy property. It is not directly related to cladding failure index (like, stress, strain).
- o However, fast transient phenomena like RIA, **it is reasonable to use such enthalpy index.**
- o From the point of energy index, SED might be another applicable index. However, if SED is chosen, interaction between pellet behaviour and cladding behaviour should be more studied.



11

OC/CSNI/NEA Workshop Nuclear Fuel Behaviour during Reactivity Initiated Accidents 

### Future study item

- For PCMI-failure criteria, proper index which can express cladding performance degradation should be applied to criteria.
- Enthalpy (rise) index is still useful for fast transient.
- For future study, it is favorable to combine cladding mechanical failure mechanism and applied load from pellet during RIA.
- ALPS2 and CIP (with PROMETRA) are interesting program.
- SCIP program outcome is also valuable for hydrogen effect for mechanical failure during RIA.

12

OC/CSNI/NEA Workshop Nuclear Fuel Behaviour during Reactivity Initiated Accidents 

### Advanced cladding M-MDA™

- M-MDA™ (Modified MDA)
  - ◆ Corrosion resistance is highly improved, but the basic properties are maintained, with :
    - Optimization of Sn, Fe, Cr content
    - Inheritance of Nb content

Alloys	Sn	Nb	Fe	Cr
Zircaloy 4	1.2-1.7	-	0.2	0.1
MDA	0.8	0.5	0.2	0.1
<b>M-MDA™</b>	<b>0.5</b>	<b>0.5</b>	<b>0.3</b>	<b>0.4</b>

- Mechanical, LOCA, and basic properties of M-MDA™ are comparable to MDA which has a lot of in-reactor experience.

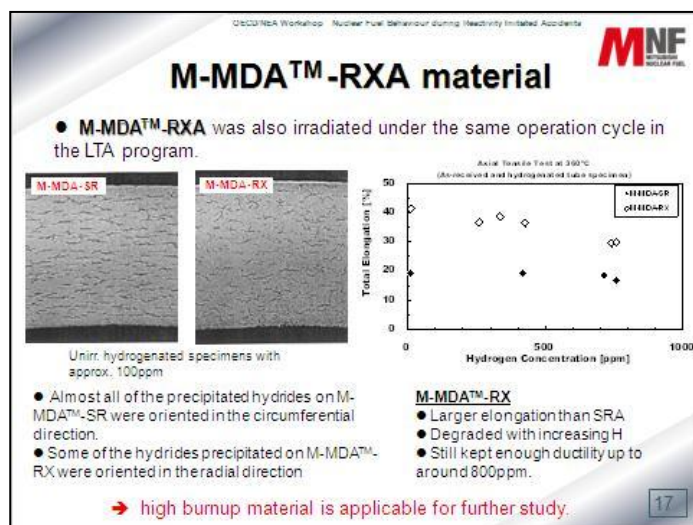
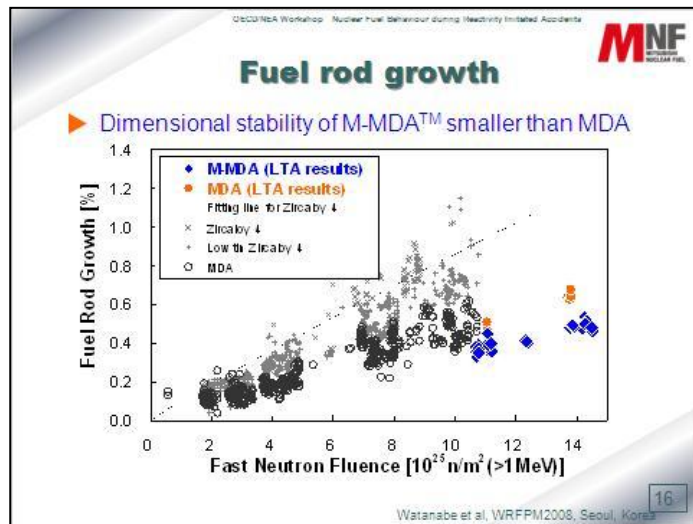
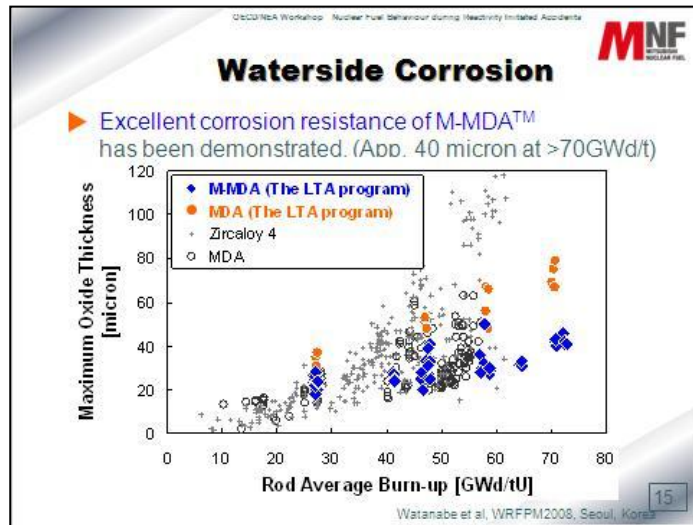
13

OC/CSNI/NEA Workshop Nuclear Fuel Behaviour during Reactivity Initiated Accidents 

### LTA irradiation in commercial reactor

- ▶ 4 LTAs with M-MDA™ and MDA fuel rods have been irradiated in Vandellòs II.
- ▶ Operative conditions are as follows ;
  - Nominal cycle length : 18 months
  - Core avg. LHR : ~18.93kW/m
- ▶ 4 cycles irradiation has been completed.
  - M-MDA fuel rods has achieved app. 73GWd/t with very low corrosion and no failure.

14



OECD/NEA Workshop Nuclear Fuel Behaviour during Reactivity Initiated Accidents

**MNF**  
MULTI-NATIONAL FUEL

## M-MDA™ future

Activities for M-MDA™ use is steadily in-progress.

- ▶ Irradiation effect (hydrogen pickup, ductility,...) will be studied in the Hot Cell PIE Program.
- ▶ In-pile creep data and corrosion data under severe (high duty) condition have been obtained in Halden Joint program (on-going).
- ▶ International collaboration : Highly burnt M-MDA™ materials were proposed to following projects
  - Lift-off : Halden joint program (Halden)
  - PCI : SCIP-2 (Studsvik)

18

OECD/NEA Workshop Nuclear Fuel Behaviour during Reactivity Initiated Accidents

**MNF**  
MULTI-NATIONAL FUEL

## M-MDA™ for Safety study

- Hydrogen is a key parameter for RIA-PCMI criteria.
- **M-MDA™** SRA and RXA material can contribute for assessing and understanding the effect of hydrogen morphology due to texture difference.
- RIA simulated test programs
  - **M-MDA™** is proposed to ALPS2 and CIP
  - Comprehensive and internationally accessible database for establishing reasonable criteria.

19

OECD/NEA Workshop Nuclear Fuel Behaviour during Reactivity Initiated Accidents

**MNF**  
MULTI-NATIONAL FUEL

## Conclusion

- ◆ RIA PCMI criteria considering appropriate benefit for less corrosion and hydriding cladding material is expected to be established.
- ◆ **M-MDA™** material can contribute for assessing and understanding the effect of hydrogen morphology due to texture difference (SRA and RXA).
- ◆ **ALPS2** program will include those materials for RIA simulated pulse experiments in NSRR and also proposed for **CABRI** water loop programs in the near future.
- ◆ Such outcome of the experiments are expected to provide the comprehensive and internationally accessible database for establishing reasonable criteria.

20



## SWISS REGULATORY RIA CRITERIA AND THE VERIFICATION PROCEDURES BY THE OPERATORS

A. Gorzel

Swiss Federal Nuclear Safety Inspectorate ENSI

### 1. Introduction

A major safety issue in the design of a new reactor core loading is the behaviour of the fuel during a postulated reactivity initiated accident (RIA). The considered cases in light water reactors are the control rod ejection in a pressurised water reactor (PWR) and the control rod drop in a boiling water reactor (BWR). During the RIA an energy pulse is created in the fuel that leads to a large power peak and a rapid expansion of the fuel. After the gap between the fuel and the cladding is closed there will be a radial deformation of the cladding which might lead to a failure of the cladding and even to dispersion of the fuel into the coolant.

To guarantee the integrity of the fuel or the coolability of the core, specific safety criteria have been established that gave upper limits for the enthalpy deposition in the fuel that based on results of experiments in test reactors. But newer results – mainly in the test reactors NSRR, CABRI and IGR – revealed that the cladding integrity threshold shows a strong dependency of the burn-up. This can be explained by a loss of ductility due to the formation of an oxide layer on the cladding surface which can lead to spalling of the oxide. Another reason for the embrittlement of the cladding material is the pick-up of hydrogen.

The national regulatory authorities tried to take the burn-up dependency of the deformation behaviour of the cladding into account. Fuel failure threshold curves were introduced or proposed e. g. by the Japanese NSC<sup>1</sup>, the KAERI<sup>2</sup> or the SKI<sup>3</sup>. The USNRC proposed an interim RIA-criteria in a Research Information Letter<sup>4</sup> (RIL) based on enthalpy limits that are dependent on the oxide thickness (PWR) resp. the hydrogen content of the cladding (BWR). Overviews of the international activities are given e. g. in a NEA report<sup>5</sup> or in<sup>6</sup>.

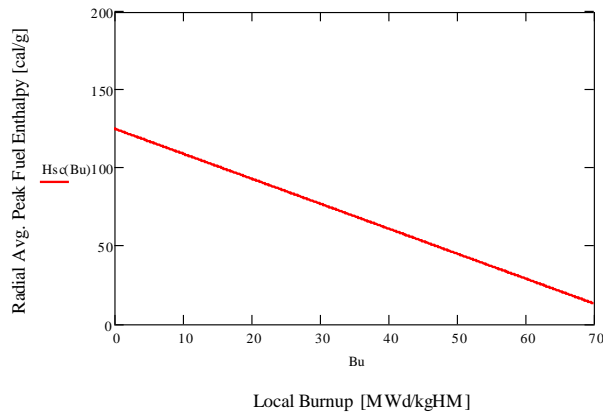
### 2. Regulatory proceeding in Switzerland

In 1994 the Swiss regulator HSK – predecessor of ENSI – defined the preliminary burn-up dependent safety criteria for RIA. To be sure that the protection goals are met even for high burn-ups, the HSK developed the so-called Swiss Curve (fig. 1), for which the compliance should guarantee the absence of cladding failure. During the following ten years, numerous RIA experiments were conducted, mainly in France (CABRI<sup>7</sup>) and Japan (NSRR<sup>8</sup>). Together with the improvement of the theoretical models, this led to the conclusion that the Swiss Curve represents a high degree of conservatism.

For this reason new safety criteria were established by the HSK in 2004 on the basis of criteria developed by the Electric Power Research Institute (EPRI) for UO<sub>2</sub> fuel<sup>9</sup> and by ANATECH for mixed oxide (MOX) fuel<sup>10</sup> in the framework of the “EPRI Robust Fuel Program”. The tendency by the operators to increase the local burn-ups had also to be considered in regulation. The new RIA criteria specify two different safety limits, the cladding integrity limit and the coolability limit. In the case of exceeding the integrity limit, the number of failed fuel rods would have to be determined as basis for radiological analyses for the verification of the regulatory demands. The coolability limit constitutes a “hard limit” which has to be met in any case, to preclude the dispersion of hot or even molten fuel into the coolant and therefore could challenge the coolability of the core.

For  $UO_2$  and MOX fuel specific burn-up dependent enthalpy curves for the coolability and the integrity limit were established for hot zero power (hzp) for PWR and BWR. For the BWR there is at the moment no specific MOX enthalpy limit for cold zero power (czp). For czp and  $UO_2$  fuel the compliance with the hzp integrity limit has to be shown for a local burn-up smaller than 40 MWd/kgU. If for a higher burn-up an enthalpy of 60 cal/g is exceeded, the operator has to provide additional evidence to meet the safety criteria. Since in a PWR there is a different start-up procedure, no verification has to be done for the PWR for the czp case. Fig. 2 and fig. 3 show the RIA criteria for  $UO_2$  and MOX fuel respectively.

Figure 1. **Provisional RIA fuel integrity limit (Swiss curve) from 1994**



The boundary conditions for the validity of the limits are:

- The cladding material is Zry-4 (PWR) resp. Zry-2 (BWR) or of a higher ductility than those materials.
- The oxide thickness is smaller than 100  $\mu\text{m}$ .
- The pulse width has to exceed 20 ms.
- No spallation of oxides is taken into account.

For power operation the strong negative reactivity feedback from the void leads to only a small increase of the fuel enthalpy. In this case the integrity limit is given by the thermal hydraulic criteria “Departure from Nucleate Boiling Ratio (DNBR)” (PWR) respectively the “Critical Power Ratio (CPR)” (BWR), but for MOX fuel at high burn-up the fuel enthalpy also has to be considered.

Figure 2. **RIA coolability (Hc) and fuel integrity limits for hzp (Hf) and czp (Hczp) conditions for  $UO_2$  fuel**

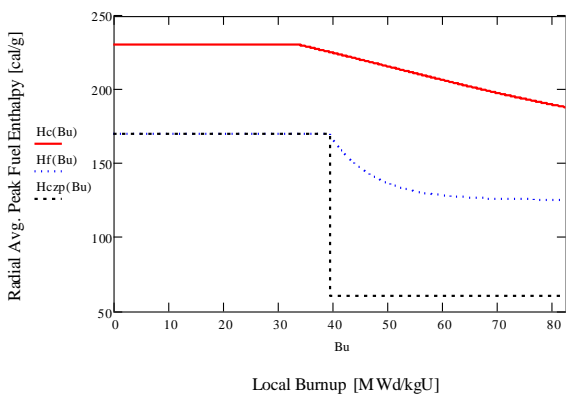
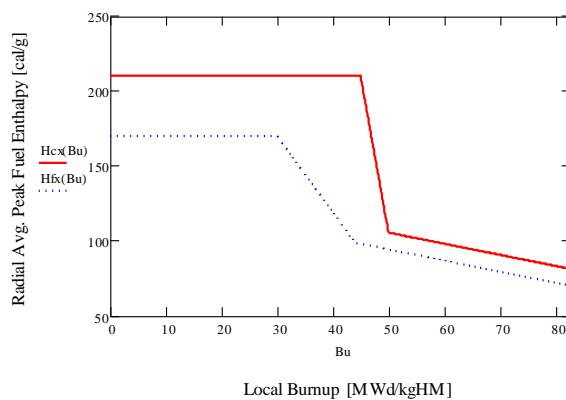


Figure 3. **RIA coolability (Hcx) and fuel integrity (Hfx) limits for MOX fuel**



### 3. Derivation of the RIA limits

#### 3.1. *UO<sub>2</sub> fuel*

The derivation of the RIA limits is described in detail in the according EPRI report<sup>9</sup>. The mechanical loading of the cladding during a RIA is described by the Strain Energy Density (SED) which represents the accumulation of the total mechanical energy during a RIA event. The cladding fails, if the SED exceeds a critical value CSED. The CSED of the cladding is mainly a function of temperature, fast neutron fluence, oxide thickness, hydrogen content and orientation of hydrides. It can be established on the basis of material tests with Zircalloy.

To establish the cladding integrity limit, the CSED as a function of the thickness of the oxide layer was derived by ductility tests with irradiated cladding material. The oxide layer thickness is expressed conservatively as a function of burn-up. The combination of these two steps results in the expression of the CSED as a function of burn-up. Analyses with the transient fuel rod code FALCON provides the SED as a function of burn-up and the radial averaged peak fuel enthalpy. By this way an enthalpy limit  $H_{lim}$  can be created as a function of local fuel rod burn-up which satisfies the condition  $SED(\text{burn-up}, H_{lim}) = CSED(\text{burn-up})$ .

The burn-up dependent coolability limit is derived by the condition that there is no local melting of the fuel. FALCON calculations revealed the conditions under which the melting is surely avoided. The analyses have taken into account the transient behaviour of the heat flux from the pellet to the cladding (incl. impacts of the gap) and the influences of the burn-up on the melting temperature, on the radial power distribution in the pellet and on the heat conductivity.

#### 3.2. *MOX fuel*

In principal the derivation of the RIA limits for MOX fuel was based on the same method as for UO<sub>2</sub> fuel, but another MOX specific phenomenon had to be taken into account. There have been four RIA tests with MOX fuel in the CABRI reactor which have shown that the mechanical loading of the cladding is not only produced by the thermal expansion of the pellet. The reason is the inhomogeneous structure of MOX fuel consisting of PuO<sub>2</sub> grains (agglomerates) in a UO<sub>2</sub> matrix. The PuO<sub>2</sub> grains have a very high local burn-up and thus are very porous and have a much higher content of fission gas in pores and at grain boundaries than the UO<sub>2</sub> matrix material. This creates a higher increase of the fission gas pressure and produces an enhanced pellet cladding mechanical interaction (PMCI) and thus a different RIA behaviour.

ANATECH has developed a semi-empirical model<sup>10</sup> that describes the impact of the enhanced transient release of fission gas on the mechanical loading of the cladding. This model was implemented in FALCON. The model describes the continuous transition between two different phases of the cladding load. In the beginning of the transient the thermal expansion of the pellet is the dominating effect. A minor contribution stems from the controlled expansion of fission gas pores in the Pu agglomerates. In the second phase the cladding load results mainly by an uncontrolled release of fission gas when the UO<sub>2</sub> matrix could not resist the pressure of the gas pores. The model was fitted to the CABRI MOX tests. One of the tests produced a cladding failure which was used to calculate a critical temperature beyond which pellet instabilities cannot be excluded.

The burn-up dependent coolability limit is derived by the condition that local melting of fuel in combination with the appearance of pellet instabilities can be excluded. The melting temperature of MOX fuel is dependent of the burn-up and the PuO<sub>2</sub> concentration and enrichment. The local PuO<sub>2</sub> enrichment of the agglomerates can be more than a factor of two higher than the average enrichment which was confirmed by post irradiation tests. This leads locally to higher burn-ups. For the derivation of the coolability limit it was conservatively supposed that the burn-up of the PuO<sub>2</sub> agglomerates is three times higher than the average value of the UO<sub>2</sub> matrix.

The pellet instability appears if the  $\text{UO}_2$  matrix cannot withstand the pressure of the fission gas pores. This happens above a critical fuel temperature when there is plastic deformation of the  $\text{UO}_2$  matrix<sup>10</sup>. This critical pressure is proportional to the temperature-dependent yield stress of  $\text{UO}_2$  and inversely proportional to the porosity of the  $\text{UO}_2$  matrix. Taken these aspects into account the semi-empirical model leads to a rapid decrease of the RIA coolability limit above a local burn-up of 45 MWd/kgHM (fig. 3).

The cladding integrity limit for MOX fuel is established in the same way as for  $\text{UO}_2$  fuel with the exception that there is a cladding failure if  $\text{SED} \geq \text{CSED}$  only in the prompt phase of the RIA. In the delayed phase characterised by the heat conduction into the cladding, the fuel rod fails if the condition of pellet instability is fulfilled additionally. Whereas at low- and middle-range burn-ups the first mechanism is dominant, there is a transition to the domination of the second mechanism beginning at 30 MWd/kgHM. In the region between 30 and 45 MWd/kgHM the cladding failure limit decreases rapidly because the ductility (and therefore the CSED) decreases along with an increased loading by the PCMI. Above 45 MWd/kgHM the CSED is constant and thus there is a weaker decrease of the limit (fig. 3). In the case of MOX the loading on the cladding increases linearly with increased burn-up. That is the reason that compared to  $\text{UO}_2$  fuel there is a steady decrease of the cladding limit over the entire burn-up range.

#### 4. Verification procedures by the operators

In Switzerland there are four operators with five operating nuclear power plants, three PWRs and two BWRs. In each plant the refuelling takes place once a year. For each new core design the cycle dependent verification to meet the RIA criteria has to be demonstrated by the operators. Generally the reactor cores of the plants are designed to fulfil the cladding integrity limit, so there is no need for radiological analyses which would be necessary if only the compliance of the coolability limit is demonstrated. As examples for possible ways of meeting the RIA criteria, the verification procedures of one BWR and one PWR operator are shown in the following.

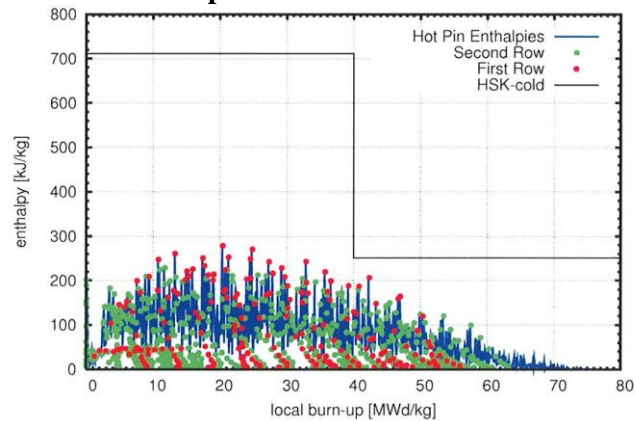
##### 4.1. BWR verification procedure

The control rod drop accident (CRDA) assumes a disconnection of an inserted control rod from the rod drive. In the licensing application for a new type of fuel assembly the operator has to verify that the RIA safety criteria for the CRDA can be met. The verification is based on 3D core analyses of an equilibrium cycle of the new fuel type.

The incremental reactivity produced by a dropped rod highly depends on the control rod pattern and the start and end position of the control rod. Therefore it is important to determine the control rod reactivity worth and the position of the control rod with the highest worth. For realistic calculations it is important to consider the restrictions for the movement of control rods – which aim in general at reducing the incremental rod worth as much as possible – and the resulting rod patterns. Based on this the limiting CRDA position is determined for begin of cycle (BOC), end of cycle (EOC) and several intermediate burn-up states.

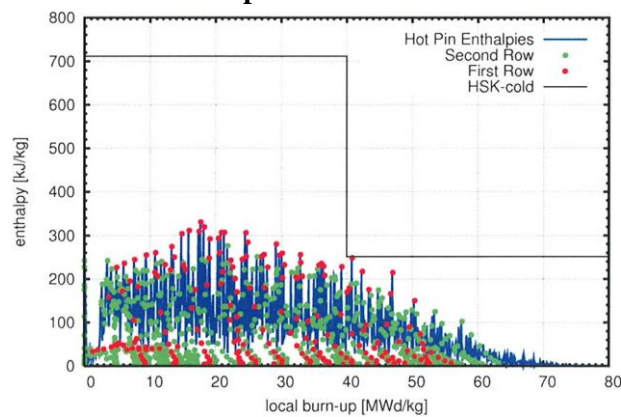
For the limiting control rods identified, dynamic 3D analyses with RAMONA are performed for czp and hzp conditions. The fuel enthalpy is determined as a function of the local burn-up. An example is shown in fig. 4. The pulse widths are also calculated. For state-of-the-art BWR fuel assemblies and core loadings they normally lie in the range between 60 and 100 ms.

Figure 4. Maximum fuel enthalpies with best-estimate incremental reactivity at czp



In the next step the control rod worth is successively increased until the RIA criterion is just met (fig. 5). The resulting rod worth is used in the licensing procedure for new core loadings as a limit value which must not be violated.

Figure 5. Maximum fuel enthalpies with increased control rod worth at czp



The same procedures are done for hzp conditions. In general the czp case is revealed to be the limiting one. For power operation it is demonstrated that the Minimum CPR limit is not violated. This is done – depending on the fuel supplier – either by a generic verification during the licensing procedure of a new fuel assembly type or on a yearly basis in the framework of the licensing of new core loadings.

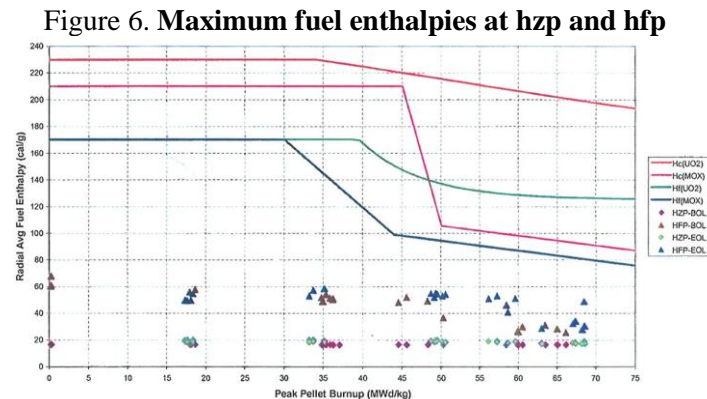
#### 4.2. PWR verification procedure

The RIA scenario for PWRs is the ejection of a control rod. One Swiss PWR operator has decided to demonstrate the fulfilment of the RIA criteria by cycle-specific calculations. The investigation is done for hzp and hfp conditions at BOC and EOC. The control rods are conservatively positioned at the rod insertion limit.

The 3D analyses are done by SIMULATE-3K which uses the restart files created by steady-state CASMO/SIMULATE core simulations. To include a certain degree of conservatism the following assumptions are made:

- No SCRAM for hfp.
- Conservative insertion velocity for SCRAM at hzp.
- Conservative ejection velocity for the highest worth rod.
- Increase of the worth of the ejected rod by 10%.

As can be seen in fig. 6, the RIA safety criteria are clearly met. The calculation revealed that there is no prompt criticality which is the reason for the low enthalpy increase. They also have shown that the power increase for hfp is smaller than 3%. Therefore there is no need for DNB analyses since this small power increase is covered by the DNB margin which for PWRs normally is the trip of the main coolant pumps.



## 5. Summary and conclusions

The numerous RIA experiments, mainly at CABRI and NSRR, together with progresses in the theoretical modelling and code development lead in 2004 to new RIA safety criteria in Swiss regulation. By this way the ten year old Swiss curve that from today's standpoint represents an over-conservative approach could be replaced.

The operators have found different ways to proof the compliance with the RIA criteria for each new core loading. All of them have in common the use of state-of-the art transient 3D reactor core codes. They are used to directly calculate the released enthalpies in the fuel or to correlate the enthalpy to reactivity increases. The procedures of compliance used by the operators have been accepted by the Swiss regulator and are meanwhile well proven.

Nevertheless and despite the firm conviction that the RIA safety criteria are a credible regulatory tool ENSI is still observing and evaluating the ongoing experimental and theoretical international research activities regarding potential consequences on the RIA criteria. The Swiss regulator ENSI also supports actively the RIA research in particular and the fuel behaviour research in general by participation in numerous international research projects like the CABRI waterloop project, the Halden research reactor programme and the projected second Studsvik cladding integrity programme (SCIP II).

## References

- 1 The Nuclear Safety Commission of Japan, Treatment of High Burn-up Fuels for Safety Evaluation in Reactivity-Initiated Events of Commercial LWRs, 1998.
- 2 C. Nam et al., A statistical Approach to Predict the Failure Enthalpy and Reliability of Irradiated PWR Fuel Rods during Reactivity-Initiated Accidents, Nuclear Technology, Vol. 136, November 2001.
- 3 J. In de Betou et al., Assessment of Burn-up dependent Fuel Rod Failure Threshold under Reactivity-Initiated Accidents in Light water Reactors, Ibidem, September 2004.
- 4 RIL N. 0401, An Assessment of Postulated Reactivity-Initiated Accident for Operating Reactors in the U.S., March 2004.
- 5 Nuclear Energy Agency, Review of High Burn-up RIA and LOCA Database and Criteria, NEA/CSNI/R(2006)5.
- 6 Ralph O. Meyer, An Assessment of Fuel Damage in Postulated Reactivity-Initiated Accidents, Nuclear Technology, Vol. 155, September 2006.
- 7 J. Papin et al., Summary and Interpretation of the CABRI REP-Na program, Nuclear Technology, Vol. 157, March 2007.
- 8 T. Nakamura et al., High Burn-up BWR Fuel Behaviour under Simulated Reactivity Initiated Accident Conditions, Nuclear Technology, Vol. 138, 2002.
- 9 EPRI Report 1002865, Topical report on Reactivity Initiated Accident: Basis for RIA Fuel and Core Coolability Criteria, June 2002.
- 10 ANATECH Report No. ANA-03-0638, Development of RIA Limits for Mixed UO<sub>2</sub> and MOX Cores in Swiss Reactors, January 2004.



Schweizerische Eidgenossenschaft  
Confédération suisse  
Confederazione Svizzera  
Confederaziun svizra

Swiss Federal Nuclear Safety Inspectorate ENSI

## Swiss Regulatory RIA Criteria and the Verification Procedures by the Operators

Andreas Gorzel

Swiss Federal Nuclear Safety Inspectorate ENSI

OECD/NEA RIA-Workshop, 09-09 – 09-11-2009, Paris



### Introduction

**RIA:**

- Control Rod Ejection (PWR)
- Control Rod Drop (BWR)

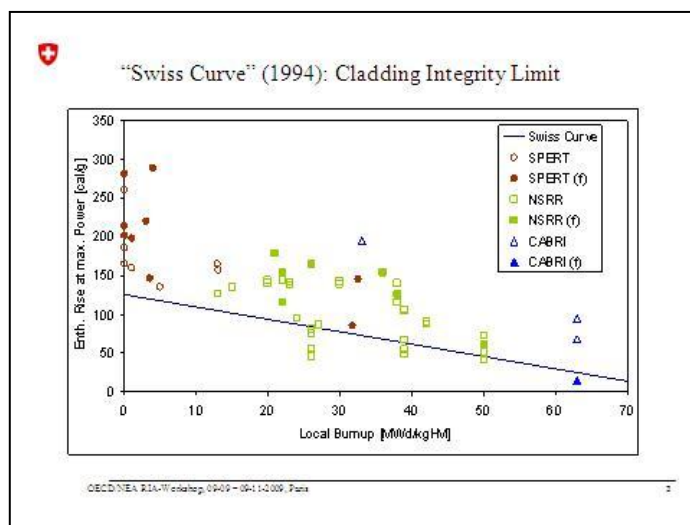
NSRR-, CABRI-, IGR-Results:

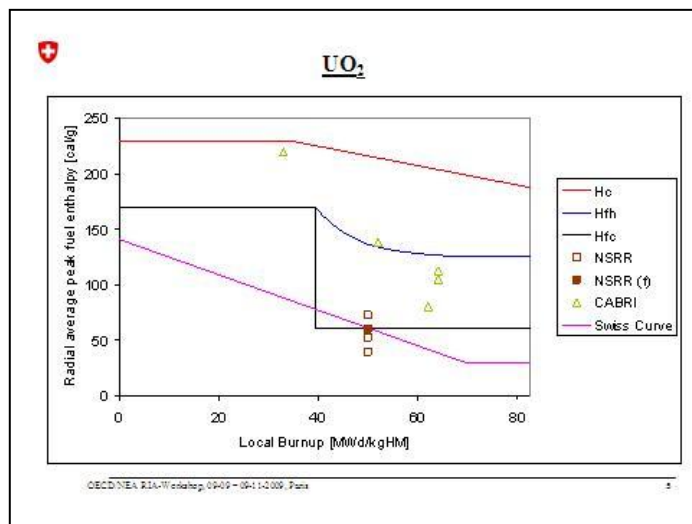
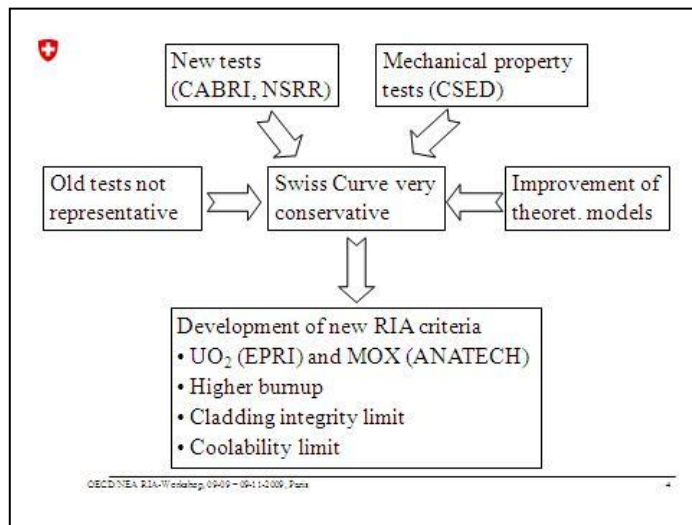
Cladding integrity dependent of

- Oxidation (Loss of ductility, spallation)
- H-Pickup (Embrittlement)

➡ Regulators: Preliminary burnup dependent criteria

OECD/NEA RIA-Workshop, 09-09 – 09-11-2009, Paris 2





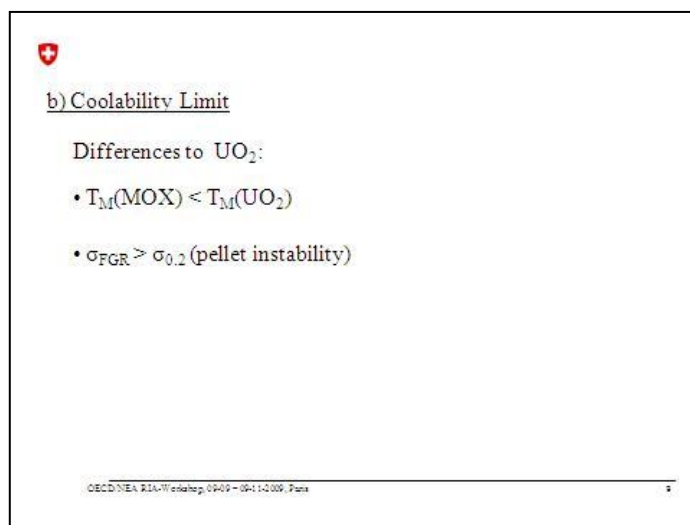
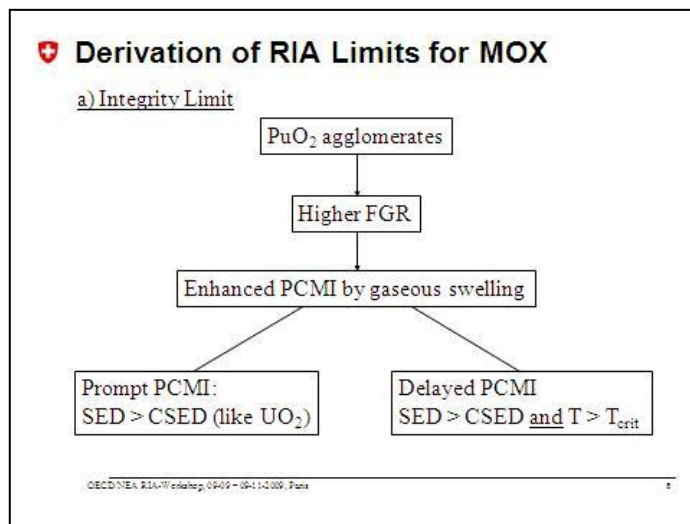
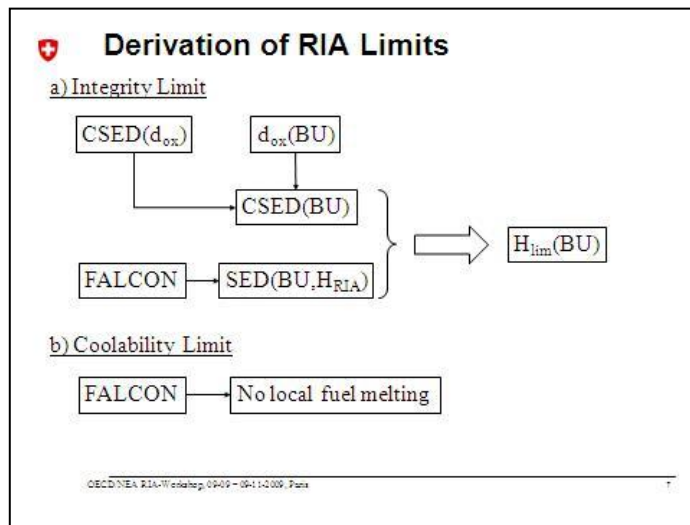
Boundary conditions:

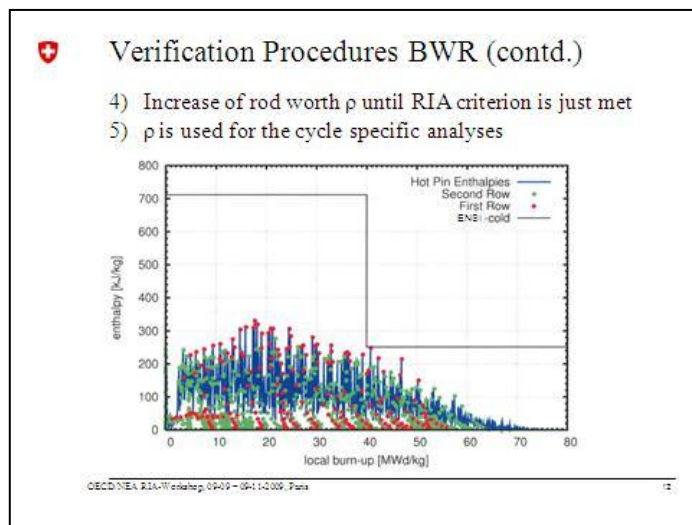
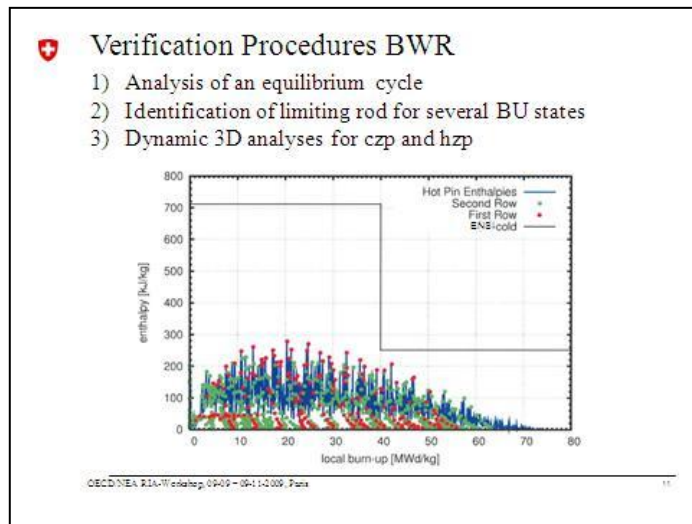
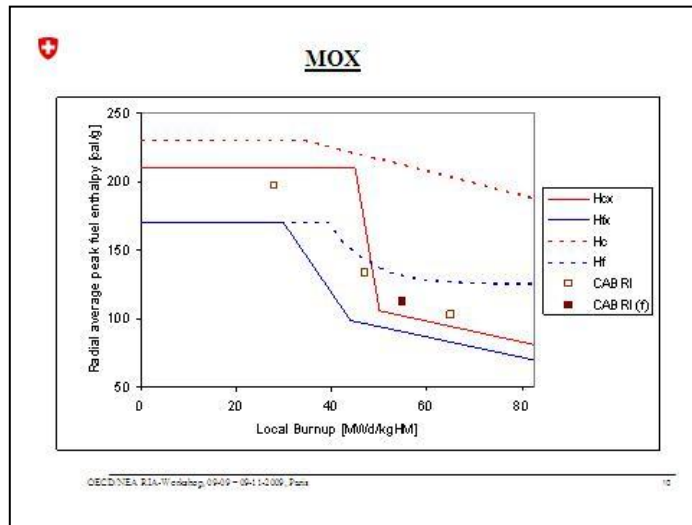
- Zry-4 (PWR) resp. Zry-2 (BWR) or of a higher ductility
- Oxide thickness < 100 μm
- Pulse width > 20 ms
- No spallation of oxides

Criteria for power operation:

Thermal limits concerning film boiling (DNB, PWR) respective dryout (MCPR, BWR) must not be violated

OECD/NEA RIA-Workshop, 0409-0411-2009, Paris 6



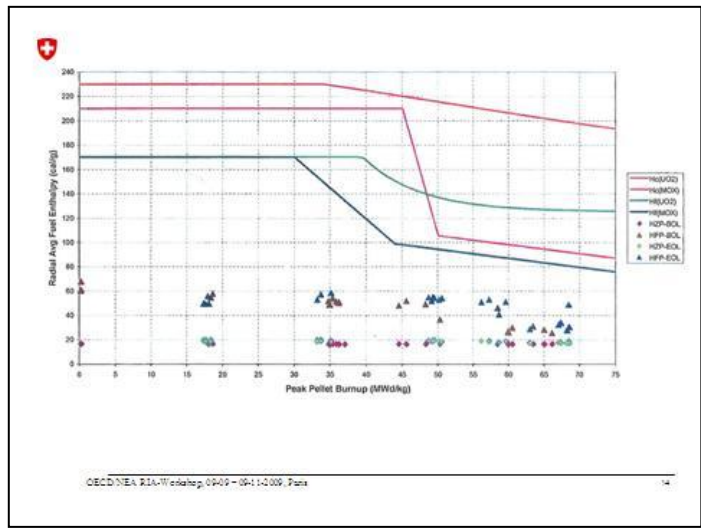


**Verification Procedures PWR**

Cycle specific 3D analysis under conservative assumptions:

- No SCRAM for hfp
- Conservative insertion velocity for SCRAM at hzp
- Conservative ejection velocity for the highest worth rod
- CR at rod insertion limit
- Increase of the worth of the ejected rod by 10 %

OECD/NEA RIA Workshop, 0409 – 04/1-2009, Paris 12



**Summary and Conclusions**

New RIA experiments }  
 Theoretical modelling } ⇒ New RIA criteria

Compliance is shown by SOA transient 3D codes

ENSI supports national and international research

- CABRI International Project
- Paul Scherrer Institute
- Studsvik Cladding Integrity Project II
- Halden Reactor Project

OECD/NEA RIA Workshop, 0409 – 04/1-2009, Paris 15



## **EXAMPLE OF APPLICATION OF THE IRSN APPROACH TO ASSESS SAFETY CRITERIA FOR REACTIVITY INITIATED ACCIDENTS**

**C. Sartoris**

Institut de Radioprotection et de Sûreté Nucléaire (IRSN), France

**A. Taisne, M. Petit, F. Barré, O. Marchand**

Institut de Radioprotection et de Sûreté Nucléaire (IRSN), France

### **Abstract**

Since the start of the 1990s, optimisation of PWR core management has led utilities to consider the use of fuel assemblies with higher burn-up and to introduce MOX fuel in these reactors. The clear evidence of specific aspects of highly irradiated fuel that could affect the transient rod behaviour during a RIA and the lack of data on irradiated MOX fuel, created the need to both verify and/or adjust the current safety criteria and to evaluate the corresponding margins.

In this context, IRSN has developed a large research program mainly based on experimental tests, including CABRI tests. The CABRI REP-Na program, conducted with Electricité de France (EDF) support, was devoted to increase the knowledge of highly irradiated fuel (UO<sub>2</sub> and MOX) behaviour experiencing fast power transients as RIA in a PWR. The goals were to identify and quantify the main physical phenomena that can lead to rod failure resulting from Pellet-Clad Mechanical Interaction (PCMI) and fuel ejection without significant clad heat up (limitation due to the use of sodium as coolant).

Several CABRI REP tests on UO<sub>2</sub> and MOX rods with a Zircaloy-4 cladding were carried out between 1993 and 1998 in the sodium loop of the CABRI reactor (Cadarache center). The tests results have revealed rod failures for enthalpy values less than the SPERT one (140 cal/g for irradiated fuels). The CABRI tests showed clearly that it was necessary to redefine criteria for high burn-up fuel.

IRSN is developing a consistent and original approach to assess safety criteria for Reactivity Initiated Accidents. This approach is based on:

- A thorough understanding of the physical mechanisms involved in each phase (PCMI and post-boiling phases) of the RIA, supported by the interpretation of the experimental database. This experimental data is constituted of global test outcomes, such as CABRI or NSRR experiments, and analytical program outcomes, such as PATRICIA tests, intending to understand some particular physical phenomena.
- The development of computing codes, modelling the physical phenomena. The physical phenomena observed during the tests mentioned above were modelled in the SCANAIR code. SCANAIR is a thermalmechanical code calculating fuel and clad temperatures and strains during RIA. The CLARIS module is used as a post-calculation tool to evaluate the clad failure risk based on critical flaw depth. These computing codes were validated by global and analytical tests results.
- The development of a methodology. The first step of this methodology is the identification of all the parameters affecting the clad brittleness. Besides, an envelope curve resulting from burst tests giving the hydride rim depth versus oxidation thickness is defined. After that, the critical flaw depth for a given energy pulse is calculated then compared to the hydride rim depth. This methodology results in an energy or enthalpy limit versus burn-up.

This approach can be followed for each phase of the RIA. An example of application is presented to evaluate a PCMI limit for a Zircaloy-4 cladding UO<sub>2</sub> rod at Hot Zero Power.

This approach will be applied to MOX fuel, other cladding materials and other initial power levels. This methodology will also be applied for the post-boiling phase, for which another failure mode is expected.

## 1. Introduction

Since the start of the 1990s, optimisation of PWR core management has led utilities to consider the use of fuel assemblies with higher burn-up and to introduce MOX fuel in these reactors. Current safety criteria for reactivity initiated accident (RIA) have been formulated on the basis of the available experimental database (from SPERT, PBF and early NSRR experiments) that was restricted to fresh or slightly irradiated UO<sub>2</sub> fuels (up to 30 GWd/tU for UO<sub>2</sub> fuel). However, the clear evidence of specific aspects of highly irradiated fuel that could affect the transient rod behaviour during a RIA and the lack of data on irradiated MOX fuel, created the need to both verify and/or adjust the current safety criteria and to evaluate the corresponding margins. As a result, various organisations in most countries operating reactors<sup>1,2,3</sup> are assessing the RIA limits that apply to current and future fuels, in terms of component materials as well as burn-up.

In this context, the IRSN has developed a large research programme based mainly on experimental tests, including the CABRI tests<sup>4</sup>. The CABRI REP-Na programme was conducted with EDF support. The UO<sub>2</sub> part of the programme was also supported by the US Nuclear Regulatory Commission (NRC). The test results revealed rod failures for enthalpy values less than the SPERT failure threshold of 140 cal/g for irradiated fuels.

In the same time, the IRSN decided that it was necessary to develop its own methodology for deriving RIA safety limits, to be used as a tool for giving technical advice on revising the RIA criteria.

This paper presents the IRSN approach and its application to the case of a UO<sub>2</sub> rod clad with Zy-4, in the PCMI phase of a RIA initiated at hot zero power.

## 2. IRSN approach for RIA criteria

The IRSN approach is based on:

- A thorough understanding of the physical mechanisms involved in each phase of an RIA, supported by interpretation of the experimental database.
- Developing a methodology and computing codes.
- Identifying the relevant parameters using the above methodology.

This approach is derived in four steps.

### 2.1. Step 1: interpreting recent research programmes

In order to be able to derive pertinent RIA safety limits, it is fundamental to gain a good understanding of the phenomenology involved during the transients, in particular for high burn-up fuel. The IRSN achieves this goal by setting up a general programme of global and analytical tests and by developing the SCANAIR code<sup>5</sup> for interpretation.

<sup>1</sup> Del Barrio, M. T., Herranz, L. E., 2002. Failure Criterion of a Fuel Rod during Reactivity Initiated Accidents” – CIEMAT Report DFN/SN-03/OP-02.

<sup>2</sup> Jernkvist, L.O., Massih A.R., 2004. Assessment of Core Failure Limits for Light Water Reactor Fuel under Reactivity Initiated Accidents. SKI Report 2005:16.

<sup>3</sup> Landry, R., USNRC [Memorandum from Ralph Landry to Thomas Martin dated] January 19, 2007. Technical and Regulatory Basis for the Reactivity Initiated Accident Interim Acceptance Criteria and Guidance. ML070220400.

<sup>4</sup> Papin, J., Cazalis, B., Frizonnet, J. M., Desquines, J., Lemoine, F., Georgenthum, V., Lamare, F. and Petit, M., March 2007. Summary and Interpretation of the CABRI REP-Na Program. Nuclear Technology –157 N°3, 230-250.

<sup>5</sup> Moal, A., Lamare, F., Latché, J.C., Federici, E., Besson, V., 2008. SCANAIR Reference Documentation Version V\_6\_5.

### *Global and analytical tests*

The global tests consisted in the CABRI REP-Na programme and the global tests performed in the NSRR test reactor in Japan were also analysed.

The CABRI REP-Na programme goals were to identify and quantify the main physical phenomena that can lead to PCMI-induced rod failure and fuel ejection during the first phase of an RIA transient without significant clad heat-up (limitation due to the use of sodium as coolant). The test results revealed rod failures for enthalpy values less than the old SPERT failure threshold of 140 cal/g for irradiated fuels.

Extensive evaluation of the experimental results and theoretical interpretation of the tests has resulted in numerous outcomes, related to clad straining, rod failure mechanisms for UO<sub>2</sub> fuel, changes in fuel microstructure, fission gas behaviour, transient oxide spalling, gas and fuel ejection after rod failure, and specific aspects of MOX fuel behaviour.

In particular, post-test examinations showed that UO<sub>2</sub> rod failure with initially spalled Zy-4 cladding can occur within a large range of low enthalpy levels (from 30 to about 80 cal/g<sup>6</sup>).

The CABRI International Programme (CIP), conducted by IRSN with EDF support, in the framework of an OECD project, is expected to provide new information, particularly for the post-boiling phase of the RIA, due to the presence of the new water loop (with water as coolant at 280°C and 155 bar).

The numerous NSRR global tests were also analysed. Due to the ambient temperature of the water (room temperature tests), the physical phenomena were enhanced and brittle cladding failure, when it occurred, was easily detected. The High Temperature High Pressure tests to come will be very useful to confirm our results.

The purpose of the analytical tests was to improve understanding of specific physical phenomena. In particular:

- PATRICIA tests <sup>7</sup> were carried out to characterise heat transfers between the cladding and the coolant during fast transients. These experiments were conducted in the PATRICIA facility operated by the CEA in Grenoble. These experiments mainly highlighted that transient phenomenology differs significantly from steady state conditions. In particular, the critical heat flux is much higher in transient conditions.
- PROMETRA tests <sup>8</sup> on mechanical behaviour of the cladding are still being conducted. A very large database of test results was compiled and important conclusions were drawn. In particular, the PROMETRA programme demonstrated the extremely deleterious effect of hydrogen on cladding material resistance. Specifically, the IRSN concluded from these experiments that **oxide spallation during reactor operation must be avoided because it leads to a configuration in which the mechanical strength of the cladding is no longer predictable.**

### *Identifying failure modes*

Using and analysing the available database improved knowledge about the physical phenomena during the RIA transient and confirmed the need to change the criterion. During the first phase of the transient (PCMI phase), the thermal expansion of the fuel, exceeding that of the cladding, is governed by the power pulse.

<sup>6</sup> Papin, J., Cazalis, B., Frizonnet, J. M., Desquines, J., Lemoine, F., Georghentum, V., Lamare, F. and Petit, M., March 2007. Summary and Interpretation of the CABRI REP-Na Program. Nuclear Technology –157 N°3, 230-250.

<sup>7</sup> Bessiron, V., 2007. Modelling of Clad-to-Coolant Heat Transfer for RIA Applications. Journal of Nuclear Science and Technology 44, N°2, 211-221.

<sup>8</sup> Cazalis, B., Desquines, J., Poussard, C., Petit, M., Monerie, Y., Bernaudat, C., Yvon, P., Averty, X., 2007. The PROMETRA Program: Fuel Cladding Mechanical Behavior under High Strain Rate. Nuclear Technology 157, N° 3.

The cladding undergoes an extreme increase in stress without significant clad heat-up, since the pellet-to-clad heat transfer is slow. During this phase, the cladding failure mode is fracture-induced by hydride embrittlement. A second phase (“post-boiling” phase) may appear later, governed by the clad-to-coolant heat exchange. Due to the power increase in the fuel, heat exchange between the fuel rods and the water increases. The coolant reaches its saturation temperature. If the coolant temperature continues to rise, a vapour film may form that reduces clad-to-coolant heat exchange and strongly increases cladding temperature. For these temperature levels, fission gas is released and the internal fuel rod pressure increases, loading the cladding, whereas its mechanical strength decreases. The cladding may reach its plasticity limit. At the same time, cladding creep takes place. The cladding deforms and the stresses due to the release of fission gas are relieved. The cladding may fail over a given strain limit.

*Developing interpretation tools; extrapolation to reactor conditions*

Due to the high cost of performing integral tests and the availability of fuel rods for experimentation, few tests are available, and they are often not fully representative of an RIA transient in PWR conditions. It is impossible when performing global tests to consider all values of the range of parameters encountered in PWRs. For example, tests are performed for a given fuel rod, i.e. for specific fuel and cladding materials, geometry and enrichment and at a given burn-up and power history. It is obviously impossible to test all characteristics of the rods. In the same way, the integral tests cannot consider all the pulse shapes, coolant pressures, temperatures, flow rates, etc., that can be encountered in PWRs. A well-validated computational tool thus needs to be developed to extrapolate to a full range of PWR parameters and to perform sensitivity studies on a large range of conditions.

This computer code package is also essential for expressing the new limit with different parameters. For example, it may be interesting to convert a limit expressed as the maximum injected energy versus burn-up, into the corresponding maximum fuel enthalpy rise versus burn-up, or versus the corresponding zirconia thickness.

**The FRAPCON-3.3 code**<sup>9</sup> is developed by Pacific Northwest National Laboratory (PNNL) for the NRC. It calculates the parameters characterising the initial state of a typical fuel rod before the RIA, based on the power history the rod undergoes in the reactor.

FRAPCON was assessed<sup>10</sup> by comparing its predictions for fuel temperatures, fission gas release, rod internal void volume, fuel swelling, cladding creep/growth, and cladding corrosion/hydrating to data from integral irradiation experiments and post-irradiation examination programmes. The FRAPCON-3.3 code is adapted for burn-up as high as 65 GWd/tU for UO<sub>2</sub> and MOX fuels, and for Zy-4, ZIRLO and M5™ claddings. Higher burn-up calculations are extrapolations.

**SCANAIR**<sup>11</sup> is a thermo-mechanical code developed by IRSN simulating a fuel rod surrounded by coolant that undergoes an RIA. The SCANAIR code couples three modules:

- The first calculates fission gas migration and release into the rod gap.
- The second deals with mechanics (calculates the stresses and strains in the fuel and in the cladding).
- The third evaluates the fuel, cladding and coolant temperatures.

<sup>9</sup> Berna, G.A., Beyer, C.E., Davis, K.L., Lannung, D. D., 1997. FRAPCON-3: A Computer Code for the Calculation of Steady-State, Thermal-Mechanical Behavior of Oxide Fuel Rods for High Burn-up. NUREG/CR-6534, Vol. 2, PNNL-11513.

<sup>10</sup> Lannung, D. D., Beyer, C.E., Berna, G.A., 1997. FRAPCON-3: Integral Assessment. NUREG/CR-6534, Vol. 3, PNNL-11513.

<sup>11</sup> Moal, A., Lamare, F., Latché, J.C., Federici, E., Bessiron, V., 2008. SCANAIR Reference Documentation Version V\_6\_5.

The SCANAIR code is qualified based on the CABRI REP-Na tests<sup>12</sup> and the NSRR, BGR and CIP tests. These tests validate the thermal module, particularly by determining the thermal conductivity in the gap between the fuel and the cladding. They also validate the mechanical module, and the clad-to-coolant heat exchange calculations.

The clad mechanical properties are validated with the results of the PROMETRA programme<sup>13,14</sup> (conditions representative of the strain rate).

The clad-to-coolant heat transfer is modelled and qualified:

- In PWR conditions based on the PATRICIA tests.<sup>15</sup>
- In NSRR conditions (20°C, 1 bar) based on the NSRR tests.<sup>16</sup>

Today, the SCANAIR qualification level is very satisfactory for UO<sub>2</sub> and MOX fuels and for Zy-4 and M5™ claddings, and the code is used by the IRSN, EDF and other international users for reactor applications.

The brittle failure module **CLARIS** is a post-processing module of SCANAIR. It aims at determining whether an initial flaw, will propagate through the cladding for a given RIA thermo-mechanical load. To determine this, at each time-step of the SCANAIR calculation, CLARIS determines the critical Rice J-integral value<sup>17,18</sup>, which validates the brittle strength of the cladding material. It is evaluated based on cladding toughness:

$$J_C = \frac{K_{IC}^2 (1 - \nu^2)}{E}$$

with  $\nu$ ,  $E$  and  $K_{IC}$  being respectively the Poisson's ratio, the Young's modulus and the material toughness.

Cladding toughness,  $K_{IC}$ , depends on the cladding temperature and hydrogen content.

Simultaneously, the detrimental effects of the mechanical load are evaluated using the Rice J-integral. A J-integral database was previously calculated for different clad temperatures  $T$ , clad strains  $\epsilon$ , clad thicknesses  $e$  and crack depths  $a$ . It is illustrated by the figure 1, for given clad temperature and clad thickness. The crack depth is considered as a parameter.

<sup>12</sup> Papin, J., Cazalis, B., Frizonnet, J. M., Desquines, J., Lemoine, F., Georgenthum, V., Lamare, F. and Petit, M., March 2007. Summary and Interpretation of the CABRI REP-Na Program. Nuclear Technology –157 N°3, 230-250.

<sup>13</sup> Cazalis, B., Desquines, J., Poussard, C., Petit, M., Monerie, Y., Bernaudat, C., Yvon, P., Averty, X., 2007. The PROMETRA Program: Fuel Cladding Mechanical Behavior under High Strain Rate. Nuclear Technology 157, N° 3.

<sup>14</sup> Desquines, J., Cazalis, B., Bernaudat, C., Poussard, C., Averty, X., Yvon, P., 2005. Mechanical Properties of Zircaloy-4 PWR Fuel Cladding with Burn-up 54-64 MWj/kgU and Implications for RIA Behavior. Journal of ASTM International Vol. 2, N°6.

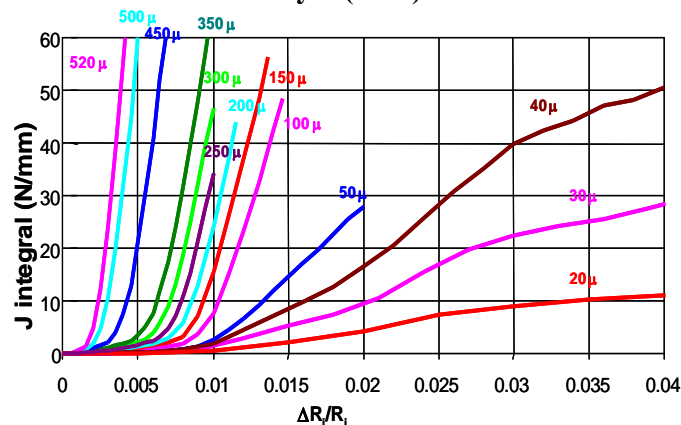
<sup>15</sup> Bessiron, V., 2007. Modelling of Clad-to-Coolant Heat Transfer for RIA Applications. Journal of Nuclear Science and Technology 44, N°2, 211-221.

<sup>16</sup> Bessiron, V., Sugiyama, T., Fuketa, T., 2007. Clad-to-Coolant Heat Transfer in NSRR Experiments. Journal of Nuclear Science and Technology 44, N°5, 723-732.

<sup>17</sup> Hutchinson, J.W., 1968. Singular Behaviour at the end of a tensile crack in a hardening material. Journal of the mechanics and physics of solids, pp13-31.

<sup>18</sup> Rice, J.R., Rosengren, G.F., 1968. Plane strain deformation near a crack tip in a power law hardening material. Journal of mechanics and physics of solids – pp1-12.

Figure 1. J-integral chart for irradiated Zy-4 (SRA) at 350°C influence of crack depth “a”



In practice, the flaw depth  $a$  is unknown, but based on comparison of the J-integral value and the critical J-integral value, CLARIS calculates the critical flaw depth ( $a_c$ ) as the crack depth such that  $J=J_C$ . In other terms, the critical flaw depth is the minimum size of a crack that would propagate at the considered energy level.

For the **CLARIS module**, Georgenthum<sup>19</sup> compares the critical flaw depth calculated by CLARIS and the hydride rim depth observed on the rods tested in CABRI and NSRR. This study validates the CLARIS calculations for the PCMI phase and Zy-4 claddings.

As concerns the fission gas behaviour, the CABRI REP-Na tests calculation with SCANAIR show<sup>20</sup> that the fission gas module, inherited from Fast Breeder Reactor models, has to be improved to modelise the grain boundary behaviour and the fission gas release adequately. For the post-boiling phase limit calculation, a simplified gas module will be elaborated. The results of the CABRI International Programme (CIP) will be useful for improvement and qualification. In addition, the IRSN is carrying out additional analytical studies on this subject.

## 2.2. Step 2: failure limit derivation: developing a methodology

Since the RIA transients involve two phases with very different physical phenomena, the investigation of this limit was naturally divided into two parts, each of them relating to one phase: the PCMI phase and the post-boiling phase. The methodology developed by the IRSN is the same for each of these phases:

- Step A: developing analytical tools

This step consists in:

- Understanding the physical phenomena involved, as explained in Section 2.1.
- Modelling them adequately.
- Validating the model using the experimental database.

- Step B: identifying the most sensitive parameters and selecting the reference case

In order to select assumptions for further calculations of the limit, parametric studies are necessary to identify the parameters that influence rod behaviour during an RIA, in particular parameters that characterise the rod initial state.

A conservative trend or value is determined for each parameter. The least influential parameters are set to their penalising value and the most influential parameters to their best-estimate value. This

<sup>19</sup> Georgenthum, V., Sugiyama, T. Udagawa, Y., Fuketa, T., Desquines, J., WRFPM 2008. Fracture Mechanics Approach for Failure Mode Analysis in CABRI and NSRR RIA tests.

<sup>20</sup> Papin, J., Cazalis, B., Frizonnet, J. M., Desquines, J., Lemoine, F., Georgenthum, V., Lamare, F. and Petit, M., March 2007. Summary and Interpretation of the CABRI REP-Na Program. Nuclear Technology –157 N°3, 230-250.

constitutes a reference case that is later used to develop the limit. It is followed by a sensitivity study on specific influential parameters.

- Step C: evaluating the failure limits and sensitivity studies for the RIA phase studied

Assumptions are derived from the previous step, and a methodology is applied. A computer code package is used to determine the failure limit for the RIA phase studied. Sensitivity studies are then performed with the most influential parameters.

### **2.3. Step 3: mechanical consequences of rod failure**

In the case of rod failure, the second barrier (primary circuit) may be damaged by the pressure loading resulting from hot fuel interaction with the coolant. This subject will be assessed in another later paper.

### **2.4. Step 4: core coolability**

In case of rod failure inducing fuel relocation or rod excessive strain, the core coolability may be questioned. The core coolability will not be addressed in this paper, but in a future one.

## **3. Application of the methodology to the PCMI phase: failure limit derivation**

### **3.1. Step A: developing analytical tools**

For the PCMI phase, the calculations are run with the following codes:

- The FRAPCON irradiation code<sup>21</sup>, which calculates the parameters characterising the initial state of a typical fuel rod before the RIA, based on the power history the rod undergoes in the reactor.
- The thermo-mechanical SCANAIR transient code<sup>22</sup> is used to evaluate strain and temperature of the fuel and cladding from the initial state and for given pulse characteristics, etc.
- The failure module CLARIS<sup>23</sup> performs the calculation of the corresponding critical flaw depth.

The calculation chain is summarised in diagram 1.

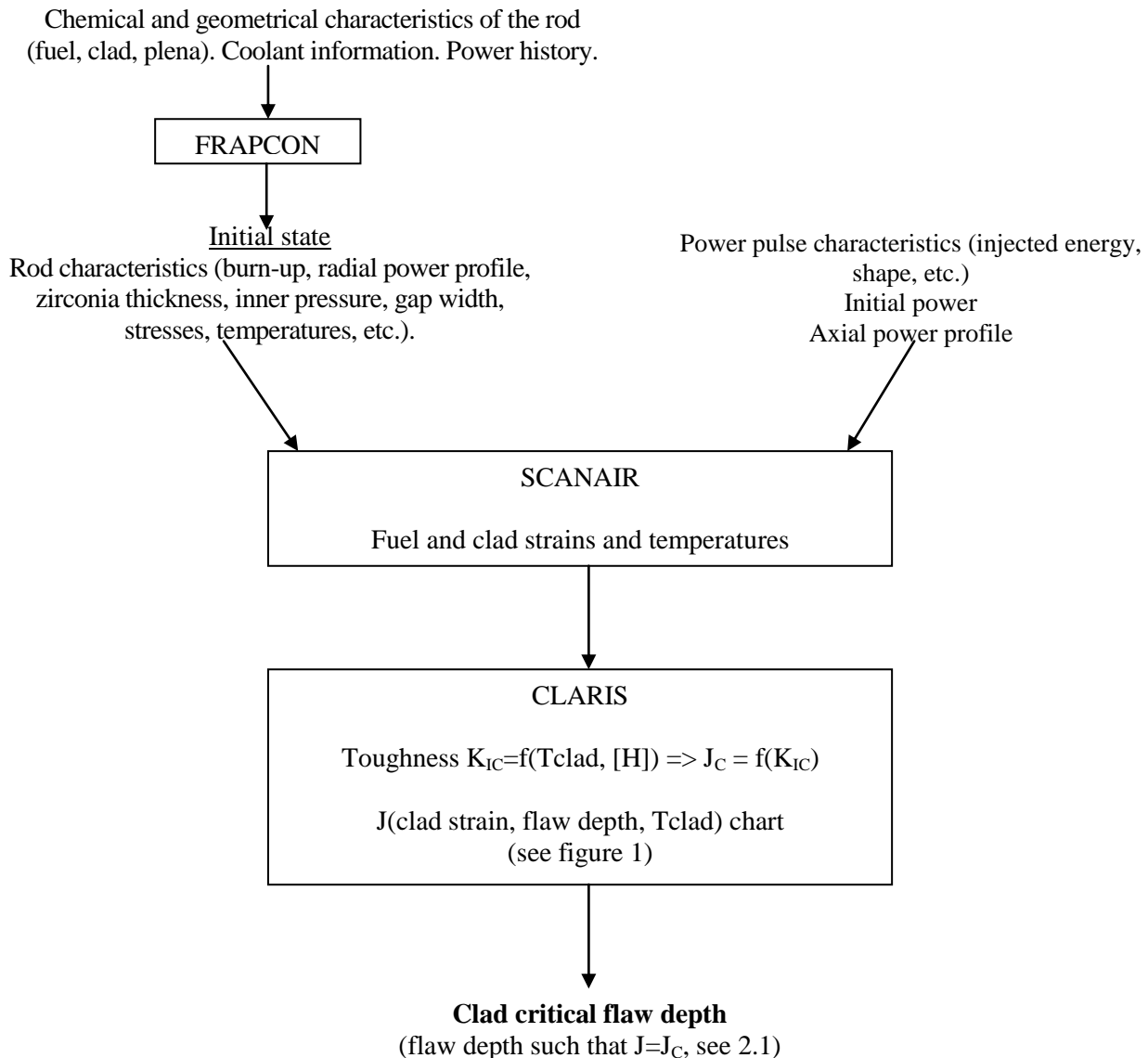
---

<sup>21</sup> Lannung, D. D., Beyer, C.E., Berna, G.A., 1997. FRAPCON-3: Integral Assessment. NUREG/CR-6534, Vol. 3, PNNL-11513.

<sup>22</sup> Moal, A., Lamare, F., Latché, J.C., Federici, E., Bessiron, V., 2008. SCANAIR Reference Documentation Version V\_6\_5.

<sup>23</sup> Georgenthum, V., Sugiyama, T. Udagawa, Y., Fuketa, T., Desquines, J., WRFPM 2008. Fracture Mechanics Approach for Failure Mode Analysis in CABRI and NSRR RIA tests.

Diagram 1. **Computer code package used for PCMI limit calculation**



### 3.2. Step B: identifying the most sensitive parameters and selecting the reference case

#### 3.2.1. Determining a penalising set of parameters influencing PCMI-induced clad failure

The first stage consists in listing all the parameters that potentially influence clad failure and sorting them in order of their influence. Assumptions must be made about their values based on their influence to establish the PCMI limit.

Among these parameters:

- Some can be referred to as “uncertain” parameters: their value is known, with some uncertainty. These parameters are the roughness of contact between fuel and cladding, the heat-exchange coefficient with water, the radial power profile in the fuel pellets, fuel thermal conductivity, cladding toughness, hydride concentration, and the initial gap.

- Some can be referred to as “fixed” parameters, i.e. they can have very different values according to the conditions. These parameters will be successively chosen at different values. They are the power at the initial state, the zirconia thickness, the injected energy and the full width at half maximum for the power pulse (assumed triangular).

These parameters are sorted by modelling the SCANAIR/CLARIS response  $ac^{24}$  as a linear combination of the 11 parameters plus their mutual interactions. Table 1 below shows the two values given to each of the parameters.

Table 1. Minimal and maximal values of the 11 parameters

1	2	3	4	5	6	7	8	9	10	11
Roughness	Clad-coolant heat exch. coef.	Radial power profile	UO <sub>2</sub> conductivity	Toughness KIC	Hydride concentration [H]	Initial gap	Initial power	Zirconia thickness	Inj. energy	fwhm
0.1 µm	-10%	Flatten	-5%	-5MPa√m	* 0.85	1 µm	0%Pn	70 µm	80 cal/g	10 ms
4 µm	+10%	Peaked	+5%	+5MPa√m	* 1.15	10 µm	40%Pn*	100 µm	110 cal/g	30 ms

\* 100% Pn corresponds to a lineic power of 172 W/cm.

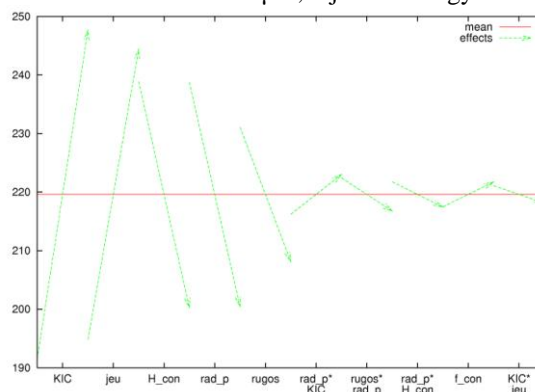
The SCANAIR computation of all these cases and the matrix calculation make it possible to determine the model coefficients and to sort the parameters by order of influence.

The second step of this study uses previous polynomial modelling to determine a set of uncertain parameters that minimises the critical flaw depth. The polynomial model is used and for each combination of “fixed” parameters, it is determined whether the uncertain parameters must be minimised or maximised.

Figure 2 illustrates the case where all “fixed” parameters are chosen at their low value (initial power = 0%, zirconia thickness = 70 µm, injected energy = 80 cal/g, fwhm = 10 ms). The uncertain parameters are shown on the abscissa, and the value of the critical flaw depth  $ac$  is shown on the ordinate.

The uncertain parameters are indicated in order of their influence. The arrows show the variation of the critical flaw depth  $ac$  when the considered parameter changes from its low value to its high value. For example, the first and most influential parameter is KIC (cladding toughness). When set at its low value, the critical flaw depth is about 193 µm; at its high value it becomes about 247 µm. In other words, when KIC rises, the value of  $ac$  increases. Therefore, to be penalising, the value of KIC must be minimised. In the same way, the initial gap must be minimised, the hydride concentration must be maximised, etc. The interaction between some parameters also appears to be influential; for example, the interaction between the radial power profile and the fracture toughness is more influential than fuel conductivity.

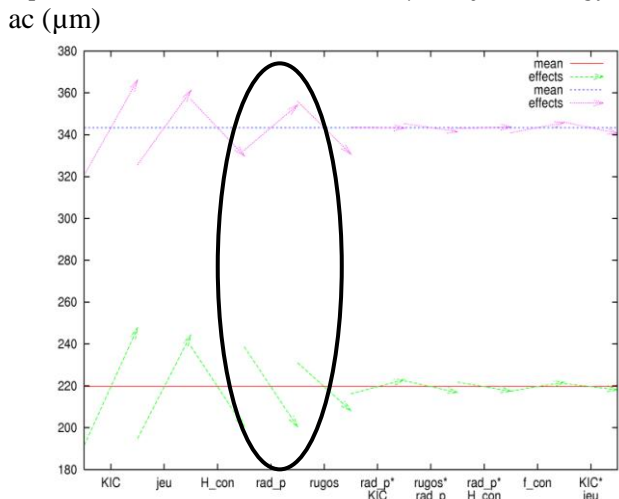
Figure 2. Trends of the most influential parameters in decreasing order for the case {initial power = 0%, zirconia thickness = 70 µm, injected energy = 80 cal/g, fwhm = 10 ms}



<sup>24</sup>  $ac$ : critical flaw depth: if the flaw in the clad is greater than this limit, the crack propagates and the clad is assumed to fail. The smaller the value of  $ac$ , the less resistant the clad is to brittle failure.

In Figure 2, all the “fixed” parameters are set to their low value. If the value of the full width at half maximum is set to its high value (30 ms instead of 10 ms), the diagram becomes that shown in Figure 3 below (upper row of arrows):

**Figure 3. Trends of the most influential parameters in decreasing order for the case**  
 {initial power = 0%, zirconia thickness = 70 μm, injected energy = 80 cal/g, fwhm = 10 ms}  
 and for the case {initial power = 0%, zirconia thickness = 70 μm, injected energy = 80 cal/g, fwhm = 30 ms}



First, it can be observed that decreasing the fwhm from 30 ms to 10 ms makes the mean critical flaw depth reduce by about 120 μm.

Besides, this figure shows that the radial power profile does not always have the same effect on the critical flaw depth. In half of the cases, the radial profile needs to be maximised to be penalising; in the other half, it needs to be minimised.

One possible penalising set is as follows:

**Table 3. Penalising set of uncertain parameters**

Fuel roughness	Max.	UO <sub>2</sub> conductivity	Min.
Heat-exc. coef.	Max.	KIC	Min.
Radial profile	?	[H]	Max.
		Initial gap	Min.

Regarding the radial profile, two values (minimum and maximum) were systematically studied and the most penalising case was then selected.

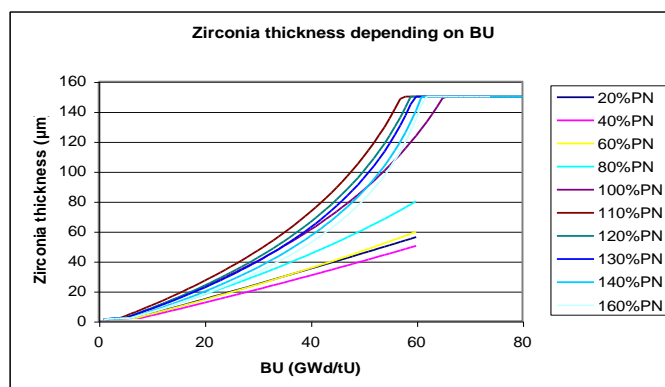
### 3.2.2. Determining the influence of power history on initial state parameters

Among the influential parameters identified above, some relate to the initial state of the rod. The influence of the rod’s power history is investigated as regards zirconia thickness, clad temperature, clad strains and clad stresses. The FRAPCON code was used to simulate different power histories. The main conclusions of this study are:

- The two axial profiles studied (flat and sinusoidal) lead to approximately the same local zirconia thickness provided that the local axial burn-up is the same.
- It is difficult to predict the power history influence on zirconia thickness, which is linked in a complex way to burn-up by the mean of the oxidation rate, the neutron flux and the clad temperature. Nevertheless, some calculations for constant power histories have shown (see figure 4) that zirconia

thickness varies considerably with power and that for a UO<sub>2</sub> rod, 110% of nominal power leads to maximal zirconia thickness.

Figure 4. **Zirconia thickness versus BU for a UO<sub>2</sub> rod clad with Zy-4**



Plastic strain and circumferential stress in the cladding are directly dependant on cladding creep during plant operation. In France, power plants often change their power to adjust to electricity demand. For the moment, FRAPCON does not deal with these conditions. So assumptions have to be made to address this pre-conditioning of the cladding:

- For hot zero power conditions, the initial clad hoop stress is assumed to be zero.
- For an initial power of 40% nominal power, the initial clad hoop stress will be assumed to be 150 MPa based on several calculations, performed with creep modelling whenever possible.

### 3.2.3. Power pulse

For simplification reasons, the power pulse is considered triangular. This triangle is a surrogate of the first part of the pulse that causes the fast mechanical loading of the cladding. Nevertheless, realistic PWR power pulses include a second part, a tail that continues injecting energy in the fuel. The effect of the pulse tail on clad behaviour needs further investigation.

## 3.3. Step C: evaluating the failure limits and sensitivity studies

### 3.3.1. Preliminary note about spalled rods

The CABRI-REP-Na tests, in particular REP-Na1, REP-Na8 and REP-Na10, showed that the failure enthalpy level of initially spalled zircaloy-4 clad rods is rather unpredictable<sup>25</sup>. Spalled rods were thus not considered in developing this limit. For the IRSN, provisions should be taken to ensure the absence of spalled rods in reactors, for example by limiting the maximum admissible zirconia thickness.

### 3.3.2. Assumptions for deriving the PCMI limit

Numerous assumptions have been made, as a result of the studies presented above (step B).

The main outcomes of these studies are reviewed below:

- The less influential parameters (heat exchange coefficient and UO<sub>2</sub> thermal conductivity) are taken at their nominal values, which were calculated by SCANAIR, and were respectively increased and decreased by the corresponding uncertainty values.

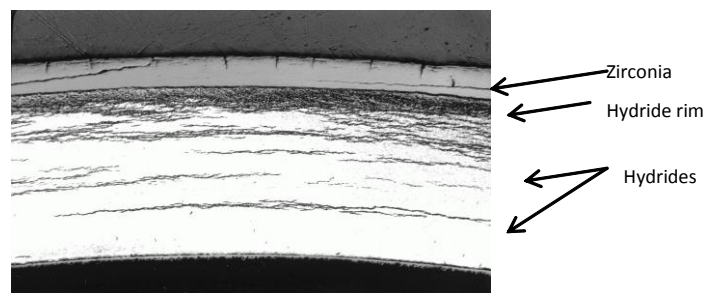
<sup>25</sup> Papin, J., Cazalis, B., Frizonnet, J. M., Desquines, J., Lemoine, F., Georgenthum, V., Lamare, F. and Petit, M., March 2007. Summary and Interpretation of the CABRI REP-Na Program. Nuclear Technology –157 N°3, 230-250.

- The more influential parameters of fuel roughness, clad toughness and hydride concentration were fixed at their best-estimate value. Sensitivity studies will be conducted at a later time.
- The radial power profile was systematically maximised and minimised and the most penalising case was kept.
- The RIA was assumed to occur at hot zero power; the initial gap is thus zero and the initial circumferential clad stress is zero.
- For the zirconia thickness, two options were selected: a maximum value (max eZrO<sub>2</sub> option) given by the 110% nominal power history for UO<sub>2</sub> (see paragraph 4.2.2 for explanation), and a medium value (mean eZrO<sub>2</sub> option) which is the mean of the extreme values for a given BU. This avoids systematic FRAPCON calculations. Only a few specific FRAPCON calculations were needed.
- The axial power profile was flat and the axial local BU was used for the BU.
- The pulse shape was triangular and its full width at half maximum was initially 30 ms. Because more flexible reactor core management would lead to lower values, leading to narrower power pulses, fwhm of 20 ms and 10 ms were also considered.

### 3.3.3. Determining the failure limit

The presence of hydrides in the cladding is the consequence of zirconium oxidation during plant operation, producing hydrogen atoms in solution in the zirconium matrix. When the hydrogen concentration exceeds its solubility, it precipitates, forming zirconium hydrides. When their concentration grows up, these hydrides accumulate at the periphery of the cladding, so that a rim thickness can be defined as exemplified in figure 5.

Figure 5. Metallographic examination of VA-1 (before NSRR test)



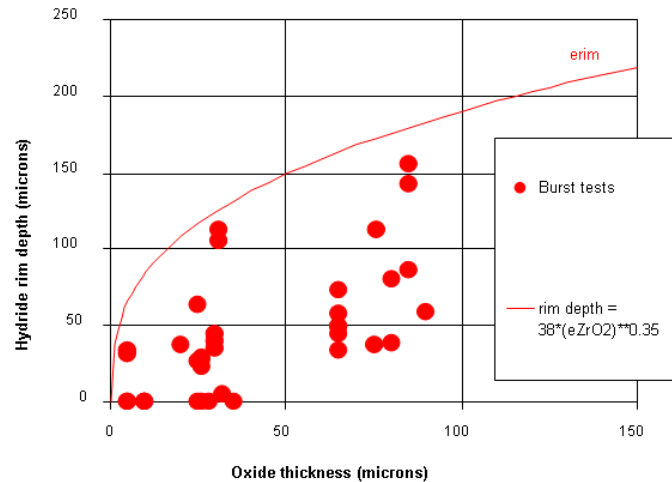
The methodology requires the knowledge of the hydride rim thickness which is assumed equal to a crack depth and compared to the critical flaw depth.

For the Zy-4 claddings, the hydride rim thickness (or depth) was expressed as  $erim = 38 \times e_{ZrO_2}^{0.35}$  ( $erim$  and  $e_{ZrO_2}$  in microns). This limit, plotted in Figure 6, is determined based on burst test results.

The burst tests were performed at 350°C with a controlled strain rate of  $3 \cdot 10^{-4}$ /s on irradiated, stress-relieved zircaloy-4 claddings. This experimental programme was performed at the CEA as part of the EDF monitoring programme. Several outer oxide layer thicknesses were tested varying between 10 and 90 microns. The burst pressure was shown to depend strongly on the oxide layer thickness. Burst tests performed on spalled samples were excluded from the analysis. The significant dependence of burst pressure on oxide layer thickness was explained by the existence of a hydride rim layer on the outer wall of the burst pressure samples. One of the major advantages of burst tests is that the weakest areas are expected to fail, in this case the deepest hydride rim layer. The hydride rim layer embrittles the cladding, and is thus similar to an incipient crack.

A classical elasto-plastic failure mechanics analysis allowed the conversion of the test failure pressure into the hydride rim depth that would induce this failure pressure. The hydride rim thickness was then plotted versus oxide thickness (see Figure 6).

Figure 6. Hydride rim thickness versus oxide thickness for Zy-4 claddings



Due to the spread of the results (e.g. for an oxide thickness of about 30 microns, the hydride rim can vary from 0 to about 120 microns), a penalising coefficient is taken into account (arbitrary +20%). A sensitivity study is done below to evaluate the influence of this coefficient.

It should be noted that these results are extrapolated beyond an oxide thickness of 90 microns.

The brittleness limit of the cladding is evaluated by comparing the critical flaw depth calculated by CLARIS (see above) and the clad hydride rim thickness. It has been observed that the incipient crack depths correspond to the hydride rim depth.<sup>26</sup> Thus, if the critical flaw depth exceeds the rim thickness, it can be considered that the cladding fails.

For a given burn-up, the injected energy level given to SCANAIR is adjusted iteratively so that the calculated critical flaw depth is as close as possible to the limit erim ( $\times 1.2$  if considered).

Developing a PCMI limit by comparing the critical flaw depth calculated by the module brittle failure module CLARIS and the hydride rim depth is the key point of the IRSN approach.

#### 3.3.4. Results

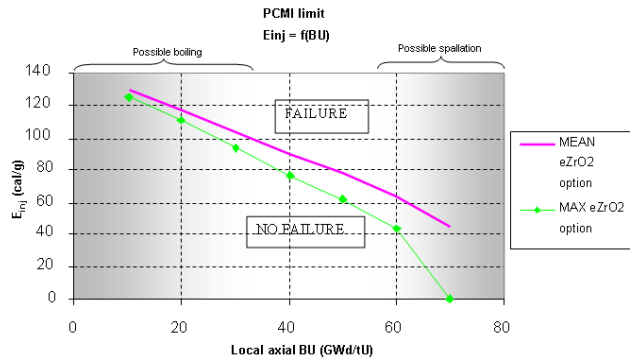
The results presented below are PCMI limits, with two validity boundaries:

- For low burn-ups, a possible boiling phase is expected: the low zirconia thickness allows water to boil, generating higher clad temperatures and clad strains. The expected failure mode is no more a PCMI one but a failure mode due to excessive strains. The failure limit will probably occur for energy levels higher than the PCMI calculated limit.
- For high burn-ups, clad spallation cannot be excluded and is extremely probable above 100  $\mu\text{m}$  of zirconia thickness.

For a  $\text{UO}_2$  rod clad with Zy-4, and for an initial state of hot zero power, the PCMI limit is plotted in Figures 7 to 11.

<sup>26</sup> Georghum, V., Sugiyama, T. Udagawa, Y., Fuketa, T., Desquines, J., WRFPM 2008. Fracture Mechanics Approach for Failure Mode Analysis in CABRI and NSRR RIA tests.

Figure 7. PCMI limit (UO<sub>2</sub> rod clad with Zy-4). Maximum injected energy versus local BU.



The maximum zirconia thickness option uses the maximum zirconia thickness calculated for a given burn-up. The mean zirconia thickness option uses the mean of the maximum thickness and the minimum thickness calculated for a given burn-up, as explained in Section 3.2.2 and as shown in Figure 4.

The figure 7 shows that the maximum permissible energy is lower for the maximum oxide thickness option than for the mean option, and the difference increases with burn-up, as oxide thickness is increasingly scattered at higher burn-ups. This can be avoided by expressing the limit as a function of oxide thickness, keeping in mind that a given oxide thickness can correspond to very different burn-ups.

The PCMI limit can be expressed using different parameters. Several examples are given below.

Figure 8. PCMI limit (UO<sub>2</sub> rod clad with Zy-4)

Maximum injected energy versus zirconia thickness.

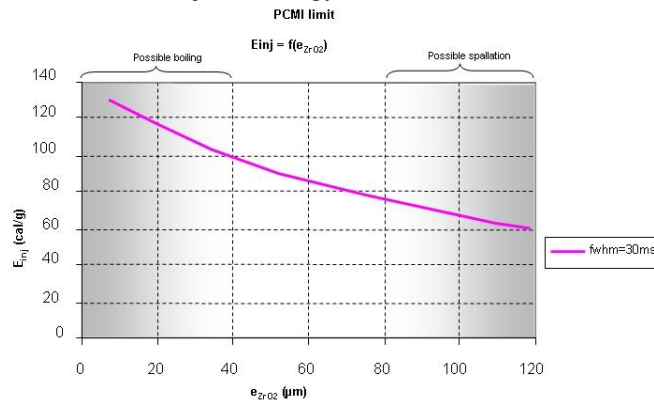


Figure 9. PCMI limit (UO<sub>2</sub> rod clad with Zy-4)

Maximum enthalpy and maximum enthalpy rise versus zirconia thickness.

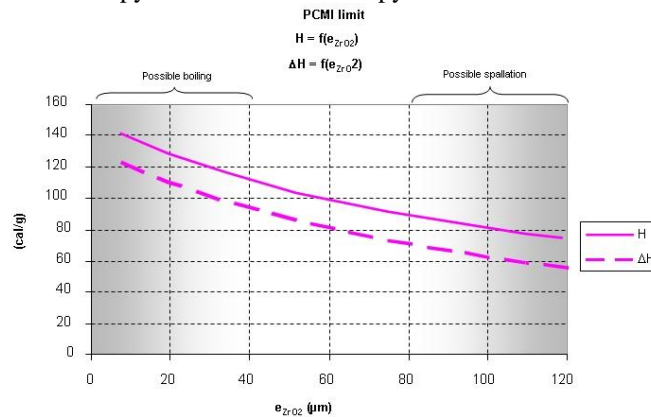


Figure 10. PCMI limit (UO<sub>2</sub> rod cladded with Zy-4)  
Maximum injected energy versus zirconia thickness/clad thickness ratio.

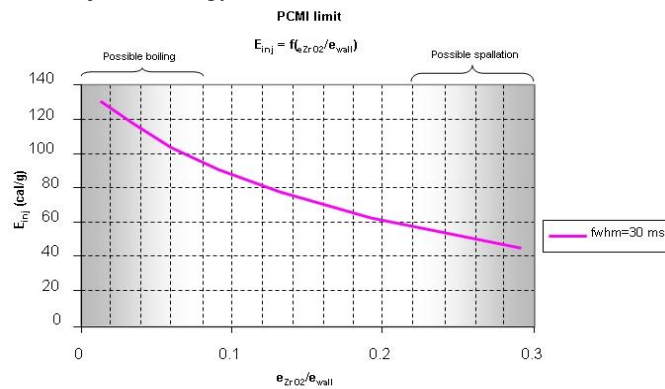
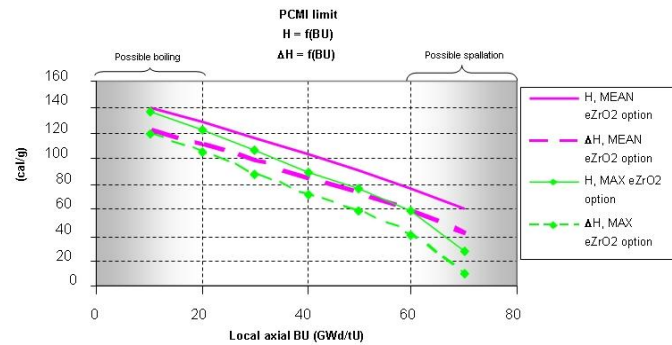


Figure 11. PCMI limit (UO<sub>2</sub> rod cladded with Zy-4)  
Maximum enthalpy and maximum enthalpy rise versus local BU.



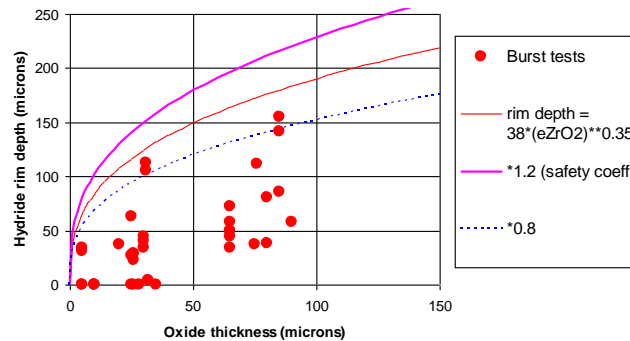
**Additional evaluations**

The PCMI limit was evaluated in two additional ways.

The first one involved the following conditions:

- Without the penalising coefficient (1.2) applied to the failure criterion (see Fig. 12).
- With a multiplying coefficient of 0.8 applied to the failure criterion (see Fig. 12), to evaluate the sensitivity of the results to this parameter.

Figure 12. Different hydride rim depths considered



The figure 13 shows that the limit is almost unchanged for burn-ups greater than 20 GWd/tU: the maximum injected energy levels (about 7 cal/g higher for 60 GWd/tU) are similar whereas the critical flaw depth can vary up to 20%. This confirms that injected energy has a major influence on clad failure.

For burn-ups lower than 20 GWd/tU, the figure shows that this PCMI limit is very sensitive to hydride rim thickness.

The second evaluation determined the PCMI limit for narrower pulses (full width at half maximum of 20 ms and 10 ms).

As expected and shown in figure 14, the limit is lower for a narrower pulse. The narrower is the pulse, the faster is the mechanical loading of the cladding. At the same time, the fuel does not have enough time to heat the cladding, which stays relatively “cold”. These two phenomena – cold cladding and higher loading – promote brittle failure. As a consequence, the limit is lower in maximum injected energy.

The maximum difference is observed for lower oxide thicknesses. This difference decreases with oxide thickness because the oxide layer isolates the cladding from the coolant and allows it to heat up.

Fig. 13. Comparison of the PCMI limit (UO<sub>2</sub> clad with Zy-4) with different multiplying coefficients

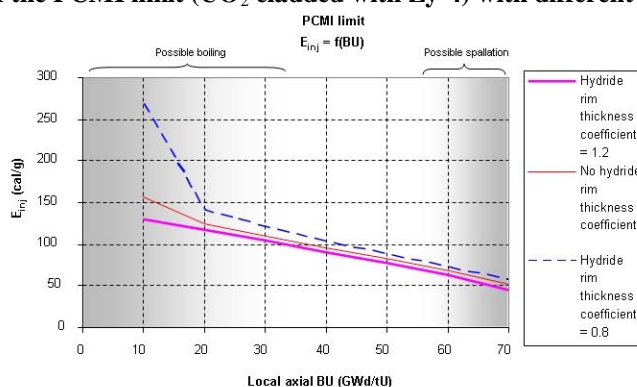
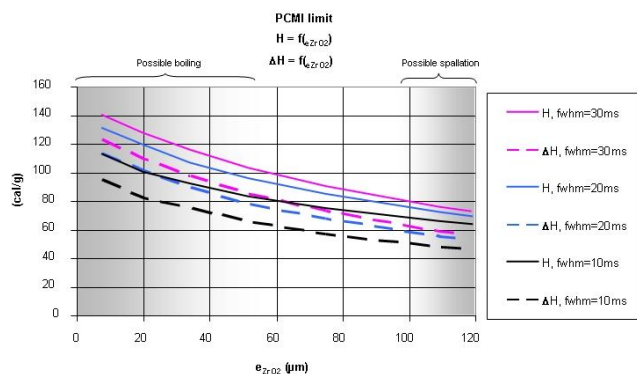


Fig. 14. PCMI limit (UO<sub>2</sub> rod clad with Zy-4)

Maximum enthalpy and maximum enthalpy rise versus zirconia thickness for 10 ms, 20 ms and 30 ms fwhm values

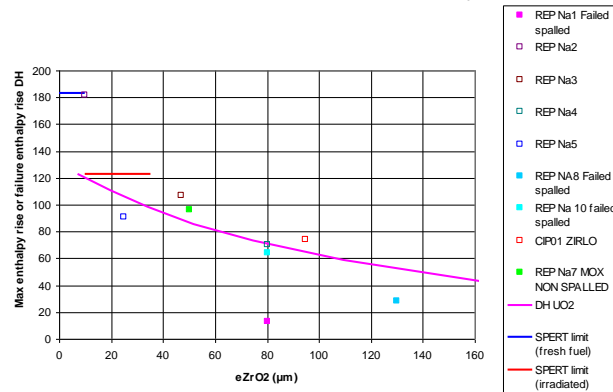


### 3.3.5. Sensitivity studies

As indicated in the assumption list, the results provided in this paper consider the more influential parameters (fuel roughness, clad toughness and hydride concentration) fixed at their best-estimate value. Sensitivity studies are planned to assess their influence on the PCMI limit when taken at more penalising values.

## 4. Comparison with RIA experimental results

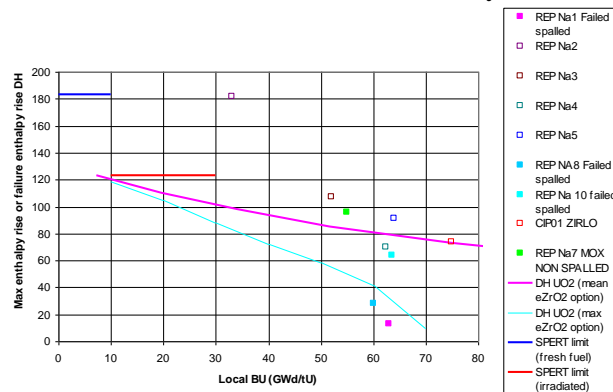
The next figure (figure 15) compares the PCMI limit obtained with the IRSN approach and the results of the REP-Na tests, for a UO<sub>2</sub> rod clad with zircaloy-4. The initial state is hot zero power. These global tests are so far the most representative of PWR thermo-hydraulic conditions.

Figure 15. Comparison of PCMI limit for UO<sub>2</sub> rods cladded with Zy-4 and CABRI REP-Na test results

The figure shows that some of the failed rods fall under the curve; but these rods (REP-Na1, REP-Na8 and REP-Na10) were spalled.

The only failed rod that was unspalled, the REP-Na7 MOX rod, is situated over the limit.

This limit can also be represented as a function of burn-up (see figure 16). For a representation with the burn-up as abscissa, it must be kept in mind that to a given burn-up, the corresponding zirconia thicknesses are scattered, as shown in figure 4. The figure 16 shows two limits: the thick (pink) curve, corresponding to the mean zirconia thickness option, and the thin (blue) curve, corresponding to the maximum zirconia thickness option (see paragraph 3.2.2 for explanation). In figure 16, the gap between REP-Na7 point and the limit is greater than in figure 15, because REP-Na7 zirconia thickness (50 µm) is lower than the mean zirconia thickness (about 92 µm) corresponding to a burn-up of 55 GWd/tU.

Figure 16. Comparison of the PCMI limit for UO<sub>2</sub> rods cladded with Zy-4 and CABRI REP-Na test results

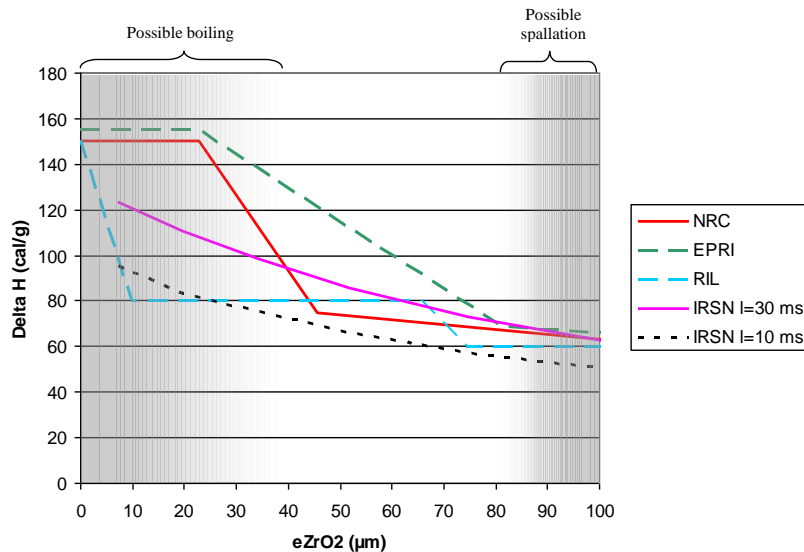
The future CABRI International Programme (CIP) is intended to provide new results to compare with, to enhance the relevance of this limit.

#### 4. Comparison with criteria developed in the US

The figure below (figure 17) positions the limit obtained with the IRSN approach for a UO<sub>2</sub> rod cladded with zircaloy-4 and compares it with different limits in the US:

- The "RIL" limit proposed in the Research Information Letter<sup>27</sup>.
- The limit developed by EPRI, indicated in the document<sup>17</sup> as an EPRI proposed lower bound PWR cladding failure limit based on presentation at RIA Public Workshop on November 9, 2006.
- The NRC limit<sup>28</sup>.

<sup>27</sup> Thadani A., USNRC [Memorandum from Ashok Thadani to James Dyer] March 31,2004. Research Information Letter N°. 0401. An Assessment of Postulated Reactivity-Initiated Accidents for Operating Reactors in the US ML 040920207.

Figure 17. Comparison of the PCMI limit for UO<sub>2</sub> rods clad with Zy-4 and US limits

The NRC PWR PCMI fuel cladding failure criteria is an empirical criteria, derived by standing the limit through numerous failed tests results (BIGR, CABRI, IGR, NSRR, PBF and SPERT tests). For some failed tests, a method is used<sup>29</sup> to translate the non-representative test conditions, such as the initial test temperature or pulse width, into an additional enthalpy rise, in order to evaluate the total enthalpy rise that would lead to the cladding failure in PWR conditions. As the NRC failure criteria takes account of the effect of a 10 ms wide pulse, the PCMI limit calculated by the IRSN for fwhm = 10 ms has been added (dashed points) for comparison.

The EPRI approach is based on the Critical Strain Energy Density, determined from mechanical property tests and depending on hydrogen content and temperature. As this parameter was initially a mean parameter, a statistical study was carried out to derive a lower bound CSED, encompassing 95% cases. Then, an analytical code was used to express this limit in terms of maximal enthalpy rise.

## 6. Conclusions and perspectives

The IRSN developed a consistent approach for establishing a safety limit, to be used as a tool to provide technical advice on revising RIA criteria. This approach is based on:

- Thoroughly understanding the physical mechanisms involved in each phase of the RIA, supported by the interpretation of the experimental database.
- Developing a methodology and computing codes.
- Identifying the relevant parameters using this methodology.

The methodology determines the failure limit related to each phase of the RIA. An example application was presented for a UO<sub>2</sub> rod clad with zircaloy-4 at hot zero power and follows each step of the methodology.

This example needs to be extended to MOX fuel, other cladding materials and other initial power levels. The methodology will also be applied to the post-boiling phase, where other failure modes are postulated.

The mechanical consequences of rod failure and core coolability will also be addressed.

<sup>28</sup> Landry, R., USNRC [Memorandum from Ralph Landry to Thomas Martin dated] January 19, 2007. Technical and Regulatory Basis for the Reactivity Initiated Accident Interim Acceptance Criteria and Guidance. ML070220400.

<sup>29</sup> Meyer, R. O., October 2005. An assessment of fuel damage in postulated reactivity-initiated accidents. Nuclear Technology, Vol.155.



## Example of Application of the IRSN Approach to Assess Safety Criteria for Reactivity Initiated Accidents

C. Sartoris

### IRSN Approach

In order to be able to assess the criterion that will be proposed by French utilities and to compare it with other international ones

4 steps :

- Interpretation of research programmes (CABRI, NSRR, analytical)
- development of a methodology for the clad failure limit derivation
- evaluation of the mechanical consequences of rod failure
- assessment of the core coolability

DECD-NEA RIA Workshop Paris 9-11 September 2009 2/18 IRSN

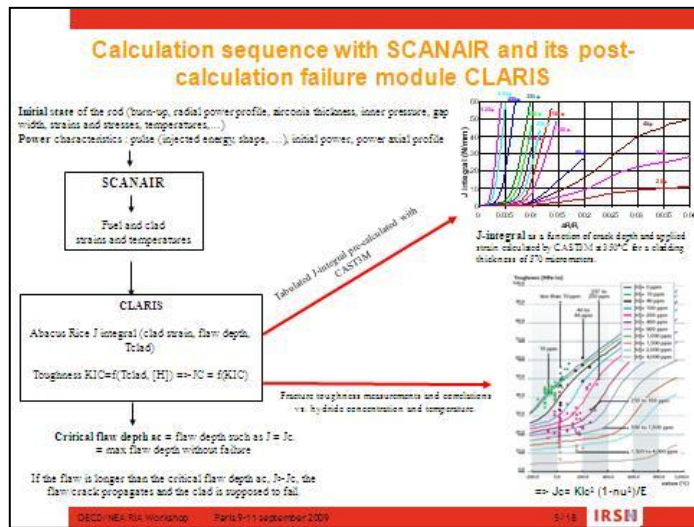
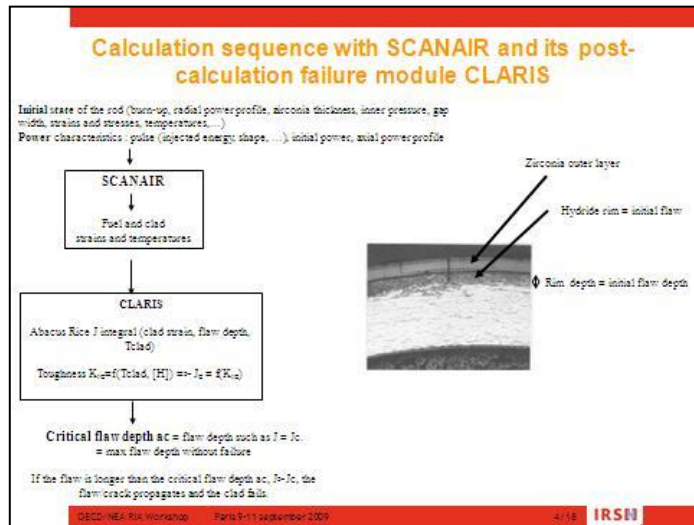
### Development of a methodology for a clad failure limit derivation

3 steps :

- development of calculation codes
- identification of the most influent parameters on the clad failure => selection of a reference calculation case ; effect of the base irradiation on the initial state of the rod
- evaluation of a failure limit and performance of associated sensitivity studies

└─> PCMI failure limit

DECD-NEA RIA Workshop Paris 9-11 September 2009 3/18 IRSN



### Identification of the most influent parameters on the PCMI clad failure and selection of a reference case

- Identification of the parameters  
 Examination of the SCANAIR input data deck, selection of the potentially influent parameters  
 PCMI phase => gas release and water boiling not taken into account

- red condition - and transient - parameters										
1)	2)	3)	4)	5)	6)	7)	8)	9)	10)	11)
Fuel roughness	h <sub>1</sub> (red-water)	Radial power profile	UO <sub>2</sub> Conductivity	Clad toughness K <sub>IC</sub>	Hydride Concentration	Initial gap	Initial power P <sub>0</sub>	Zirconia thickness zO <sub>2</sub>	Injected energy	γ <sub>hyd</sub> (m <sup>3</sup> )

\*option = Pulse Width at Half Maximum (energetic pulse)

- Modeling choice : linear + first order interaction between parameters

$$\text{SCANAIR response} = ac = \sum a_{i1} X_{i1} + \sum a_{ij} X_{i1} X_{j1}$$

- 2 values chosen for each parameter => a<sub>i</sub> and a<sub>ij</sub> coefficients values

ac : critical flaw depth.  
 If the flaw is longer than the critical flaw depth ac, it propagates and the clad fails.

DECD-NEA RIA Workshop Paris 9-11 September 2009 6/18 IRSN

### Identification of the most influent parameters on the PCMI clad failure and selection of a reference case

- Typical results
  - Order of influence:  
for  $P_0=0\%$ ,  $eZrO_2=70\ \mu\text{m}$ ,  $E_{inj}=80\ \text{cal/g}$ ,  $p_{whm}=10\ \text{ms}$   
KIC > initial gap > [H] > radial power profile, fuel roughness ...  
Interactions are also influent.
  - Penalizing set (ac minimal):  
For all combinations of ( $P_0$ ,  $eZrO_2$ ,  $E_{inj}$ ,  $p_{whm}$ ); penalizing trend:

Fuel roughness	h clad-water	Radial power profile	UO2 conductivity	Clad toughness KIC	[H]	Initial gap
+	+	Peaked/Flatten	-	-	+	-

DECD-NEA RIA Workshop Paris 9-11 September 2009 7/18 IRSN

### Effect of the base irradiation on the rod initial state

1 – Zirconia thickness  $eZrO_2$

- corrosion rate dp T, neutron flux
- BU dp power, time
- => the zirconia thickness prediction with BU is difficult

FRAPCON calculations  
Different constant power levels  
Flat axial power profile - uppermost axial slice

=> for the PCMI limit application, 2 zirconia options are retained: max  $eZrO_2$  and « mean »  $eZrO_2$

DECD-NEA RIA Workshop Paris 9-11 September 2009 8/18 IRSN

### Effect of the base irradiation on the rod initial state

2 – Clad hoop permanent strain and clad hoop stress

FRAPCON calculations with different power histories

=>  $\epsilon$  and  $\sigma$  tend to asymptotes with a rate that is very dependant on the considered creep law.  
In France reactors regularly change their power level to fit the demand => Creep law is important

Biblio : No adequate creep laws (adjusted on post-irradiation examinations)  
It is not possible to evaluate the initial stresses in the clad, depending on the power history, with a correct creep calculation

=> Assumptions:

=> for the PCMI limit application:

- $\sigma_0 = 0\ \text{MPa}$  for an initial power of 0
- $\sigma_0 = 150\ \text{MPa}$  for an intermediate initial power

DECD-NEA RIA Workshop Paris 9-11 September 2009 9/18 IRSN

### Summary of the assumptions for PCMI limit derivation

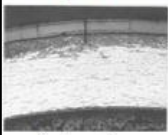
- 1 - Less influent parameters: fixed to their penalizing value
  - h clad-water: SCANAIR + uncertainty
  - UO2 conductivity: SCANAIR - uncertainty
- 2 - More influent parameters: fixed to their best-estimate value, then sensitivity studies to be performed
  - fuel roughness
  - toughness KIC = used by SCANAIR failure module
  - hydride concentration = evaluated by SCANAIR
- 3 - Radial power profile: calculated by FRAPCON for a reactor power of 100%PN and for the given BU, « flatten » and « peaked ».
- 4 - Zirconia thickness: maximum, mean
- 5 - Flat axial power profile and the considered BU is the axial local BU
- 6 - Initial gap zero and initial stress in the clad:
  - 0 MPa for an initial power of zero
  - 150 MPa for an intermediate initial power
- 7 - Triangular pulse shape, different fwhm values. Tail effect investigated later.

10/18 **IRSN**

### Evaluation of a PCMI failure limit (UO2/Zy-4, HZP)

**PRINCIPLE:**

The problem is:



Rod condition

+



RIA thermal-mechanical loading

Will it propagate?



Or not?

It propagates (and the clad is considered failed) if

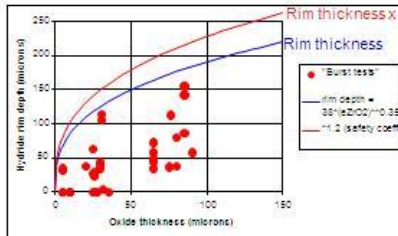
"real" flaw depth (hydride rim depth) > ac (critical flaw depth, SCANAIR calculation)

ac : critical flaw depth.  
If the flaw is longer than the critical flaw depth ac, it propagates and the clad fails.

11/18 **IRSN**

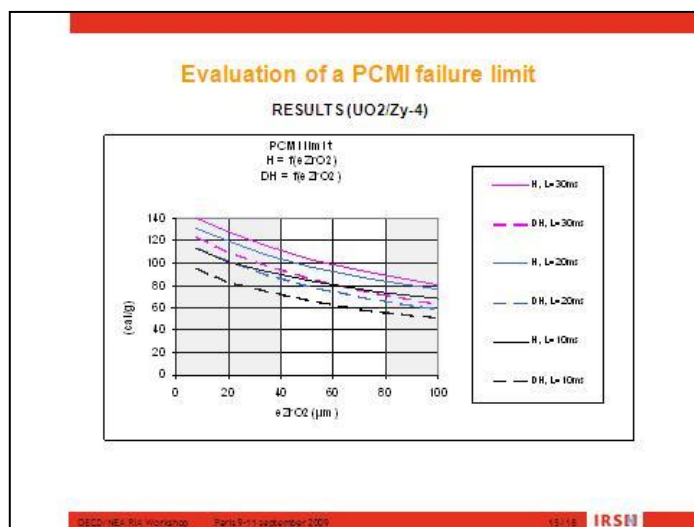
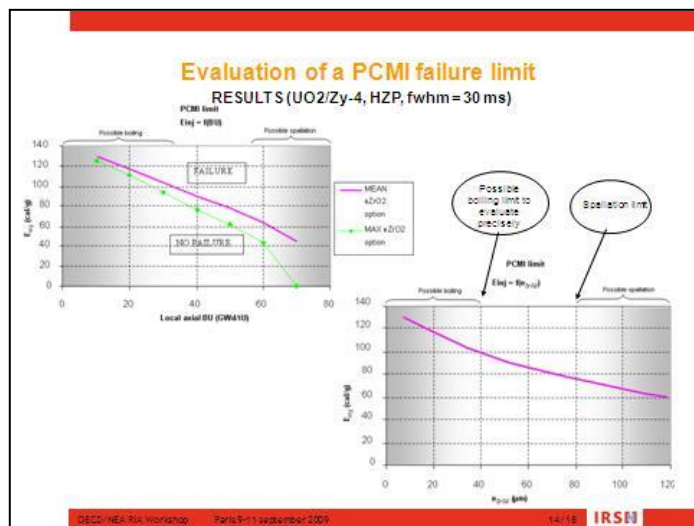
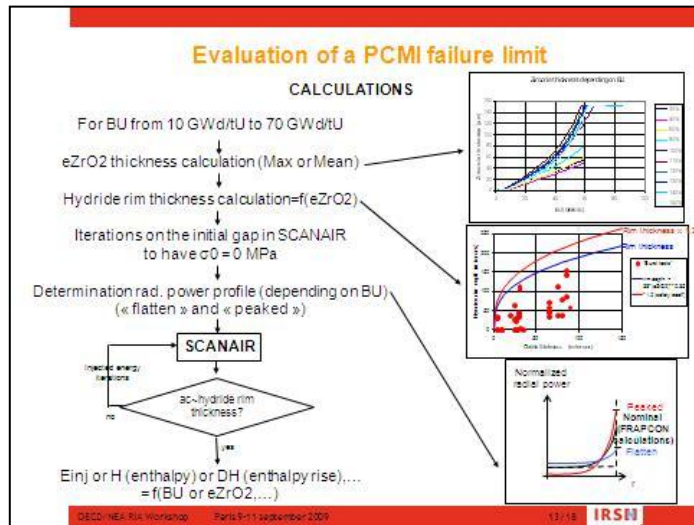
### Evaluation of a PCMI failure limit (UO2/Zy-4, HZP)

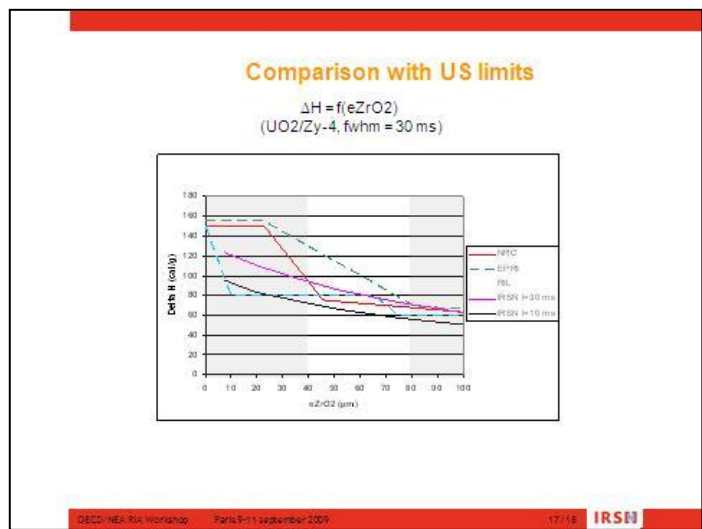
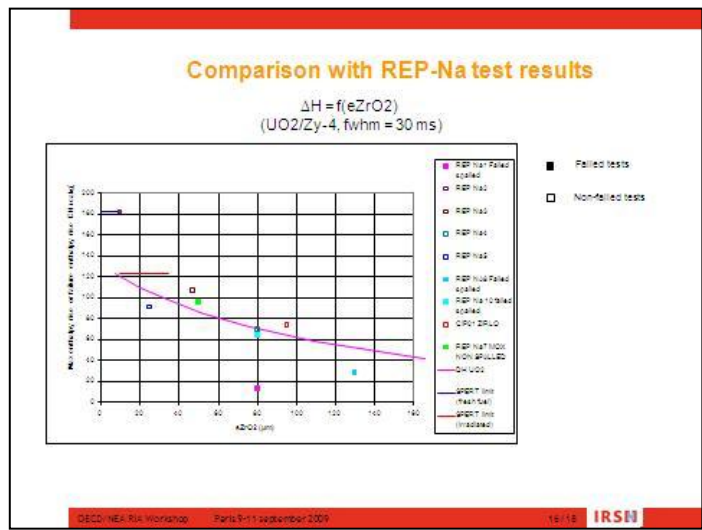
• "Real" rim depth  
EDF burst tests (oxidized Zy-4).  
CASTEM calculations => flaw depths corresponding to the tests burst stresses. These flaw depths have then been assimilated to hydride rim depths.



Scattered points => coeff. x 1.2

12/18 **IRSN**





### Conclusion

- The analytical approach of the IRSN, based on a good understanding of the physical phenomena involved and on the development of computational tools, has allowed to :
  - Elaborate some relevant assumptions
  - Elaborate an example of the PCMI limit for the case of a UO<sub>2</sub> rod clad with zircaloy-4 at hot zero power
- A similar work is under progress for MOX fuel and zirclo cladding
- Sensitivity studies are carried on to evaluate the impact of the most influent parameters.
- The post-boiling limit determination is under way
- The validity domains for PCMI limit and post-boiling limit must be worked out.
- Intermediate initial power levels will be considered

DECD-NEA-RIA Workshop Paris 9-11 September 2009 18/18 IRSN

## BURN-UP DEPENDENT RIA CRITERION FOR VVER FUEL

**Zoltán Hózer**

Hungarian Academy of Sciences KFKI Atomic Energy Research Institute, Hungary

### 1. Introduction

The RIA fuel safety criteria are under revision in the international community of fuel suppliers, authorities and research organisations. In the present paper the RIA fuel failure criterion will be reviewed for VVER fuel. Experimental data on the fuel failure behaviour under reactivity-initiated-accident (RIA) conditions produced in French and Japanese test reactors indicated low failure enthalpy for high burn-up fuel compared to fresh fuel<sup>1</sup>. However the high burn-up was not the only phenomenon influencing the fuel failure. The oxide scale on the external surface of the fuel rod, hydrogen content of the Zr cladding and the local hydriding seemed also be responsible for the failure at low enthalpy<sup>2</sup>. Furthermore differences have been found between Western design fuel and Russian type VVER fuel<sup>3,4,5</sup>. The burn-up dependence of fuel failure for VVER fuel was found much less, probably due to the low oxidation and hydrogen uptake during normal operational conditions compared to other PWRs.

### 2. RIA criteria in Hungary

Hungary operates four VVER-440 units. The currently applied fuel criteria are limited to VVER type fuel. Two RIA criteria are considered, both are expressed in term of fuel enthalpy:

- a. *Fuel fragmentation limit.* The objective of this criterion is to prevent fuel dispersal from the damaged fuel rod. Its value is 230 cal/g in Hungary. In other countries it varies between 200-280 cal/g.
- b. *Fuel failure limit.* The objective of this criterion is to prevent the loss of fuel integrity. Its value is 140 cal/g in Hungary. In other countries it may be higher and in some countries burn-up dependent criteria are discussed<sup>6</sup>.

The fragmentation limit is very high, such values as 230 cal/g can be hardly expected in reactor cases. For this reason only the second criterion will be reviewed here.

<sup>1</sup> R.O. Meyer, R.K McCardell, H.M. Chung, D.J. Diamond, H.H. Scott: A Regulatory Assessment of Test Data for Reactivity-Initiated Accidents, Nuclear Safety, vol 37, No.4, 1996, pp. 271-288.

<sup>2</sup> F. Nagase, K. Ishiyama, T. Furuta: Influence of Locally Concentrated Hydrides on Ductility of Zircaloy-4, NEA/CSNI/R(95)22, 1995, pp.433-443.

<sup>3</sup> V. Asmolov, L. Yegorova: The Russian RIA Research Program: Motivation, Definition, Execution and Results, Nuclear Safety, vol 37, No.4, 1996, pp. 343-371.

<sup>4</sup> L. Yegorova: Data Base on the Behaviour of High Burn-up Fuel Rods with Zr1%Nb Cladding and UO<sub>2</sub> Fuel (VVER Type) under Reactivity Accident Conditions, NUREG/IA-0156, NSI RRC KI 2179, 1998.

<sup>5</sup> L. Yegorova, K. Lioutov, N. Jouravkova, A. Salatov, O. Nechaeva, V. Smirnov, A. Goryachev, V. Ustinenko, I. Smirnov: Experimental study of Narrow Pulse Effects on the Behavior of High Burn-up Fuel Rods with Zr-1%Nb Cladding and UO<sub>2</sub> Fuel (VVER Type) under Reactivity-Initiated Accident Conditions. NUREG/IA-0213 Vol. 1,2,3. IPSN/DPAM 2005-275 NSI RRC KI 3230, 2006.

<sup>6</sup> J. Voglewede: Current status of RIA criteria in the United States, Fuel Safety Research Meeting 2009, Tokai-mura, Japan.

### 3. RIA tests with VVER fuel

Large number of RIA experiments has been performed in Russia on the IGR, GIDRA and BIGR reactors in order to study the behaviour of VVER fuel rods<sup>3,4,5,7,8,9</sup>. Capsule type experiments were carried out with fresh and irradiated fuel, furthermore some refabricated fuel samples were applied with fresh pellets and irradiated cladding. The effects of energy deposition, pulse width, pressurisation of fuel rods were tested. In most of the cases water fill was used, but some experiments were conducted in air as well.

According to the test results for highly pressurised fuel rods ballooning was the basic mechanism of cladding failure for both fresh and irradiated fuel. Peak fuel enthalpies, that correspond to the lower failure boundary was found the same ( $\approx 160$  cal/g) for both fresh and irradiated fuel. The conducted tests covered a wide range of pulse width, but showed no effect of this parameter on the failure threshold. The last series of experimental research programme on the BIGR reactor included some fuel samples with burn-up above 60 MWd/kgU<sup>5,9</sup>. The failure enthalpy was not measured during the VVER tests, these values were calculated with transient fuel behaviour codes. Part of the experiments was collected into well described databases and published in NUREG reports<sup>4,5</sup>.

In the present study the 26 VVER experiments were considered. The tests were performed in the IGR and BIGR reactors. The main parameters of the tests are summarised in Table 1.

Table 1. Russian RIA tests with VVER fuel

Test	Burn-up (MWd/kgU)	Oxide thickness ( $\mu\text{m}$ )	Pulse width (ms)	Peak enthalpy (cal/g)	Failure
IGR experiments					
H1T	51	5	800	151	No
H2T	50	8	760	213	Yes
H3T	50	10	820	212	Yes
H4T	50	5	760	110	No
H5T	50	8	840	176	Yes
H6T	50	5	800	87	No
H7T	47	5	630	187	Yes
H8T	48	5	850	61	No
H14T	0	5	900	61	No
H15T	0	5	900	195	Yes
H16T	0	5	850	121	No
H17T	0	5	950	91	No
H18T	0	5	850	85	No
H6C	0	5	800	219	Yes

<sup>7</sup> L. Yegorova, F. Schmitz, J. Papin: Mechanical Behaviour of Fuel Element During RIA Transients, Proc. of EUROSAFE, 18-19 November 1999, Paris.

<sup>8</sup> Yu Bibilashvili, N. Sokolov, O. Nechaeva, A. Salatov, F. Sokolov, V. Asmolov, L. Yegorova, E. Kaplar, Yu Trutnev, I. Smirnov, V. Ustinenko, V. Sazhnov, V. Smirnov, A. Goryachev: Experimental Study of VVER High Burn-up Fuel Rods at the BIGR Reactor under Narrow Pulse Conditions, Proc. of Int. Topical Meeting on LWR Fuel Performance on CD, 10-13 April 2000.

<sup>9</sup> O. Nechaeva, A. Medvedev, V. Novikov, et al.: "Researches of WWER fuel rods behavior under RIA accident conditions," in: Proceedings of the 5th International Conference on WWER Fuel Performance, Modelling, and Experimental Support, Albena, Bulgaria, September 29–October 3, 2003, 2204, pp. 309–318.

Table 1. Russian RIA tests with VVER fuel (Cont'd)

Test	Burn-up (MWd/kgU)	Oxide thickness (µm)	Pulse width (ms)	Peak enthalpy (cal/g)	Failure
BIGR experiments					
RT1	48	5	2.6	142	No
RT2	48	5	3.1	115	No
RT3	48	5	2.5	138	No
RT4	60	5	2.5	125	No
RT5	49	5	2.5	146	No
RT6	48	5	2.6	153	No
RT7	61	5	2.6	134	No
RT8	60	5	2.6	164	Yes
RT9	60	5	2.7	165	Yes
RT10	47	5	2.6	164	Yes
RT11	47	5	2.6	188	Yes
RT12	47	5	2.8	155	No

#### 4. Failure threshold derived from RIA experimental programmes

Several correlations and models have been proposed by different authors for the determination of RIA failure threshold<sup>10</sup>. The different approaches were based mainly on the evaluation of experimental data and/or numerical modelling.

C. Vitanza derived a correlation on the basis of CABRI experimental data<sup>11</sup>. His approach was intended to produce a simple correlation using the available experimental data and without the need for additional information on the tested fuel. The produced correlation can be used for the calculation of traditionally applied fuel enthalpy.

The proposed failure threshold is based on cladding deformation. CABRI REP Na data have been used and fuel failure has been considered as the strain level, which can not be tolerated by the cladding. 1% permanent strain was accepted for cladding with ductile mechanical characteristics. The failure threshold of embrittled cladding is the onset of permanent strain (0%). The criterion predicts well the CABRI data and Japanese NSRR tests. The correlation is based on three parameters: fuel burn-up, oxide layer thickness and pulse width. These parameters were available for the above described VVER tests (Table 1.) and so the correlation could be applied for the calculation of failure enthalpy of VVER fuel. The threshold is defined by the following equation<sup>11</sup>:

$$H_F = \left[ 200 \frac{25 + 10D}{Bu} + 0.3\Delta\tau \right] \left( 1 - \frac{0.85OX}{W} \right)^2 \quad (1)$$

where  $H_F$  - fuel enthalpy failure limit, cal/g       $\Delta\tau$  - pulse width, ms  
 Bu - burn-up, MWd/kgU      OX - oxide layer thickness, µm  
 D - hoop strain limit, %      W - as fabricated cladding thickness, µm

The range of applicability of equation (1) is limited by the following conditions:

- The calculated failure enthalpy is limited: if  $H_F > 200$ ,  $H_F = 200$

<sup>10</sup> Review of High Burn-up RIA and LOCA Database and Criteria, NEA/CSNI/R(2006)5, OECD, 2006.

<sup>11</sup> C. Vitanza: RIA Failure Threshold and LOCA Limit at High Burn-up, Journal of Nuclear Science and Technology, Vol. 43, No. 9, p. 1074–1079 (2006).

- Hoop strain is 1% for ductile and 0% for brittle cladding. Two transition functions are proposed, one with spalling oxide and one for cladding without spalling oxide layer. The failure strain drops from 1% to 0% as function of oxide layer thickness. For cladding with oxide scale less than 50 µm in both cases 1% is applied.
- Pulse width is also limited: if  $\Delta\tau > 75$  ms,  $\Delta\tau = 75$  ms.

### 5. Failure threshold for VVER fuel

The available VVER tests were analysed using the equation (1)<sup>12,13</sup>. In the experiments the exact failure enthalpy was not determined, only the peak value is known. So it was not possible to compare directly the calculated and measured failure limits. However, checking each test separately the calculated failure enthalpy could be compared to the peak fuel enthalpy. Correlation (1) was calculated using 1% hoop strain, 685 µm cladding thickness and 75 ms pulse width for the very long IGR tests. For fresh fuel 1 MWd/kgU burn-up was applied. The formula gave very high value for all fresh fuel IGR tests with long pulse width (630-950 ms), the failure enthalpy was limited by the maximum 200 cal/g value.

The analysis of results showed that the calculations were too sensitive to the pulse width value. For this reason a constant 75 ms pulse width was applied in all cases. There were several reasons to remove the pulse width from the proposed correlations. First of all the RIA tests (Russian and other as well) showed no significant dependence of the failure enthalpy on the pulse width. Furthermore the peak fuel enthalpy is calculated using the power history over the RIA time, so the peak fuel enthalpy value already includes the information on characteristic pulse width. Using constant pulse width the formula gave higher failure values than the measured peak enthalpy in tests with no fuel failure. In case of fuel failure the correlation indicated lower failure enthalpy than the measured value.

The burn-up dependence of VVER fuel failure enthalpy was calculated using the correlation with a constant oxide layers thickness of 10 µm, which is a conservative value for VVER fuel after long term operation and up to 65-70 MWg/kgU burn-up<sup>14</sup>. Using the characteristics of VVER fuel and applying 75 ms pulse width the (1) correlations can be written in a simplified form:

$$H_F = 21.9 + \frac{6827}{Bu + 1} \quad (2)$$

The experimental listed in Table 1. and the calculated curve using (2) equation are presented in Fig. 1. It can be well observed that most of the failed samples lie above the curve and most of the intact samples under the curve. It can be agreed that the correlation proved to be capable to describe the boundary between failed and intact fuels.

Beside the curve and experimental data the 140 cal/g limit is also shown in Fig. 1. The curve calculated by correlation (2) crosses this line at 57 MWd/kgU burn-up. It means that 140 cal/g limit should be applied for burn-up values less than 57 MWd/kgU and beyond that decreasing fuel enthalpy should be considered. The proposed burn-up dependent criterion is shown in Fig. 2.

<sup>12</sup> Z. Hózer, L. Maróti: Review of RIA Safety Criteria for VVER Fuel, NEA/CSNI/R(2003)8 vol.2. pp. 21-33.

<sup>13</sup> Z. Hózer: Review of RIA and LOCA criteria for VVER fuel, Proc. Int. Conf. WWER Fuel Performance, Modelling and Experimental Support, 2005, pp. 412-416.

<sup>14</sup> Markov D., Smirnov V., Polenok V., Volkova I.: Main results of post irradiation examinations of advanced WWER fuel, in: Proceedings of the 7<sup>th</sup> International Conference on WWER Fuel Performance, Modelling, and Experimental Support, Albena, Bulgaria, September 17–21, 2007, pp. 275–279.

Figure 1. Application of Vitanza correlation to VVER fuel with pulse width 75 ms and 10  $\mu\text{m}$  oxide scale thickness

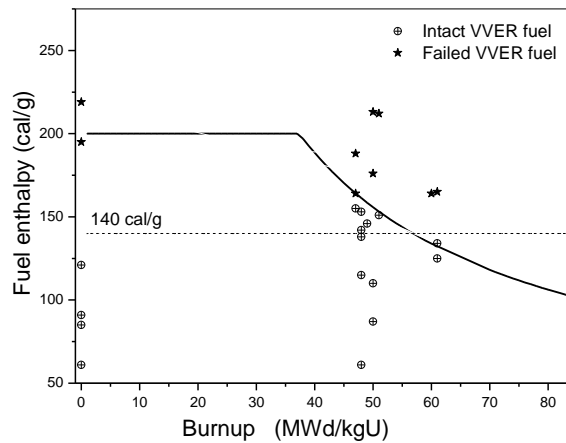
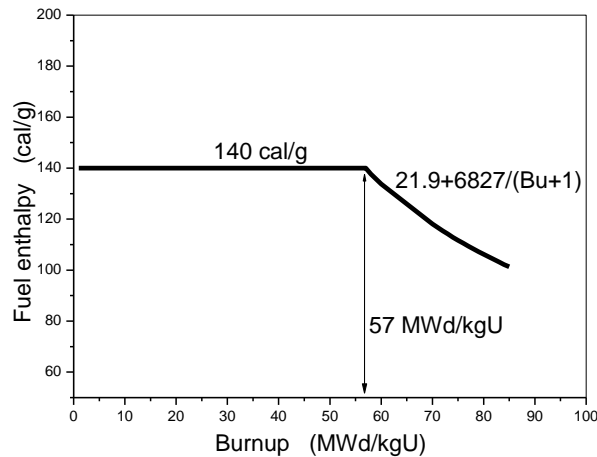


Figure 2. Proposed burn-up dependent RIA fuel failure criteria for VVER fuel



## 6. Conclusions

The Vitanza correlation for RIA failure enthalpy, have been applied for the evaluation of VVER tests. Experimental data from Russian IGR and BGR research reactors have been used. Considering the low corrosion of VVER fuel during normal operation and using the available data a simple burn-up dependent criterion has been produced to describe fuel failure during RIA events. The currently used 140 cal/g enthalpy criterion remains valid until 57 MWd/kgU burn-up and beyond this burn-up value the allowable fuel enthalpy is decreasing by a reciprocal function of burn-up. The validity of the criterion confirmed by experiments up to 61 MWd/kgU.

The proposed burn-up dependent fuel failure criterion is based on VVER experiments and pushes the advantage of high corrosion resistance of VVER fuel during normal operation. The correlation was derived from an equation which covers many PWR and BWR test results. So the correlation includes the main tendencies derived from those tests, too. The correlation is simple and can be easily extended if new experimental data becomes available. The validity of correlation is confirmed by experimental data above the current burn-up limit (55 MWd/kgU) applied for VVER-440 fuel in Hungary.

 Hungarian Academy of Sciences  
KFKI Atomic Energy Research Institute

---

## Burnup Dependent RIA Criterion for VVER Fuel

Zoltán Hózer

OECD/NEA Workshop  
Nuclear Fuel Behaviour during Reactivity Initiated Accidents  
Paris, France, September 9-11, 2009

 Hungarian Academy of Sciences  
KFKI Atomic Energy Research Institute

---

## Introduction

RIA experiments in France and Japan indicated low failure enthalpy for high burnup fuel compared to fresh fuel

Causes: high burnup + oxide scale + hydrogen content of Zr

Burnup dependence of fuel failure for VVER fuel was found much less (Russian tests), for low oxidation and hydrogen uptake during normal operation

2

 Hungarian Academy of Sciences  
KFKI Atomic Energy Research Institute

---

## RIA criteria in Hungary

1. **Fuel fragmentation limit.** The objective of this criterion is to prevent fuel dispersal from the damaged fuel rod. Its value is **230 cal/g** in Hungary. In other countries it varies between 200-280 cal/g.
2. **Fuel failure limit.** The objective of this criterion is to prevent the loss of fuel integrity. Its value is **140 cal/g** in Hungary. In other countries it may be higher and in some countries burnup dependent criteria are considered.

3



Hungarian Academy of Sciences  
KFKI Atomic Energy Research Institute

## RIA tests with VVER fuel

IGR, GIDRA and BGR reactors (Russia)

Capsule type experiments with fresh and irradiated fuel (max. 61 MWd/kgU), and refabricated samples with fresh pellets and irradiated cladding

basic mechanism of cladding failure:  
ballooning (for both fresh and irradiated fuel)



Hungarian Academy of Sciences  
KFKI Atomic Energy Research Institute

## Failure threshold

derived from RIA experimental programmes  
by C. Vitanza:

$$H_F = \left[ 200 \frac{25 + 10D}{Bu} + 0.3\Delta\tau \right] \left( 1 - \frac{0.85OX}{W} \right)^2$$

burnup
pulse width
oxide scale thickness

5



Hungarian Academy of Sciences  
KFKI Atomic Energy Research Institute

## Failure threshold for VVER fuel

D = 1% hoop strain limit

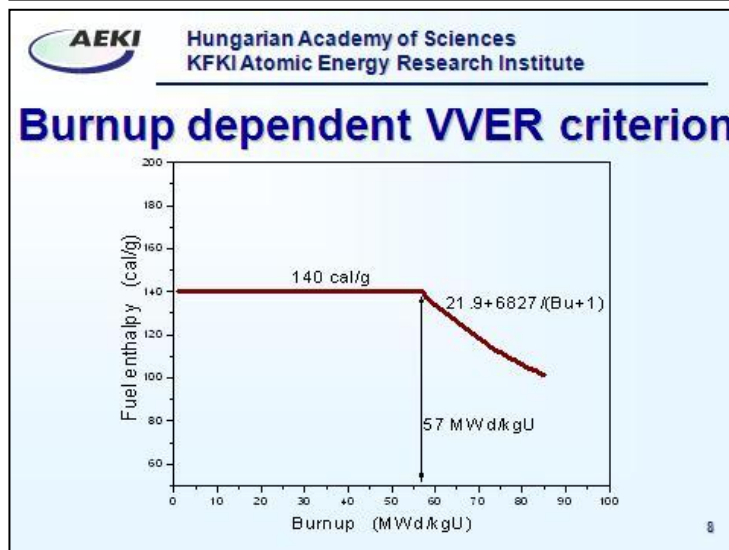
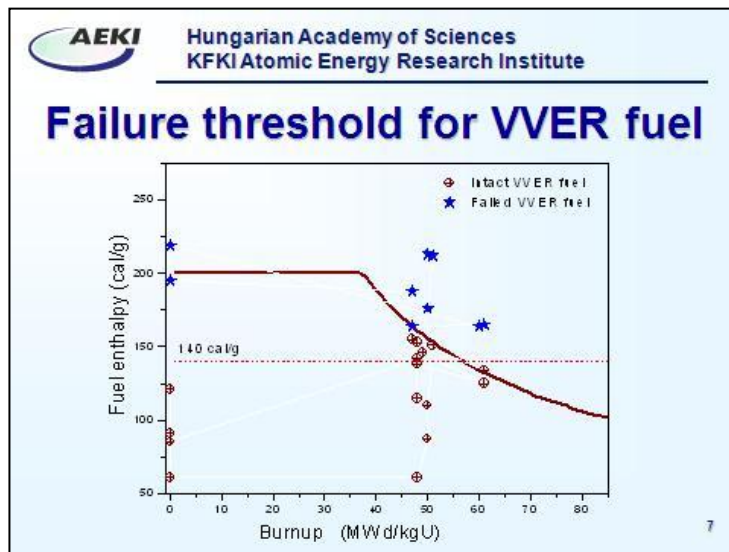
W = 685 μm cladding thickness

75 ms pulse width

10 μm oxide scale thickness

$$H_F = 21.9 + \frac{6827}{Bu + 1}$$

6



**AEKI** Hungarian Academy of Sciences  
KFKI Atomic Energy Research Institute

### Conclusions / 1

Burnup dependent criterion was derived from an equation which covers many PWR and BWR test results.

- The correlation is simple and can be easily extended if new experimental data becomes available.
- The correlation includes the main tendencies derived from PWR and BWR tests, too.

9



Hungarian Academy of Sciences  
KFKI Atomic Energy Research Institute

## Conclusions / 2

Considering the low corrosion of VVER fuel during normal operation and using the available data a simple burnup dependent criterion has been produced to describe fuel failure during RIA events.

The currently used 140 cal/g enthalpy criterion remains valid until 57 MWd/kgU burnup and beyond this burnup value the allowable fuel enthalpy is decreasing by a reciprocal function of burnup. The validity of the criterion confirmed by experiments up to 61 MWd/kgU.

10



## AN ANALYTICAL CRITERION TO PREVENT PCMI FUEL ROD CLADDING FAILURE DURING RIA TRANSIENTS

**C. Bernaudat\*, S. Cambier, J. Guion, S. Benjamin**

EDF/SEPTEN, Nuclear Fuel Division

12-14 Avenue Antoine Dutriévoz, F-69628 Villeurbanne Cedex

*\*Corresponding author*

### Abstract

This paper describes a new approach to define an analytical fuel rod cladding failure criterion during fast power transients such as reactivity initiated accidents (RIAs). Though cladding failure is not a safety issue in itself in such situations, a criterion aiming at precluding this risk is a useful decoupling limit allowing to meet the safety issues. Based on experimental results, a failure limit, expressed in critical strain energy density (CSED) as a function of the waterside corrosion level or rod average burn-up, has been determined. The CSED failure limit is then transposed for PWR conditions in terms of critical energy deposition (DHc) in the fuel. This is done by the means of CYRANO3 (steady-state) and SCANAIR (transient) calculations using relevant input data (rod design, power history, RIA transient shape, etc.). The DHc limit is a function of both rod average burn-up and initial linear power. It is applicable to UO<sub>2</sub>/Zr-4 rods submitted to rod ejection accidents (REAs), during which the cladding is subject to PCMI mechanical loading. It also precludes the risk of failure by oxidation and embrittlement at low burn-up. The robustness of the DHc failure criterion is ensured by the penalties and uncertainties taken into account at the different steps of its elaboration.

### 1. Introduction

#### 1.1. Regulatory background

In the French PWRs, the Rod Ejection Accident (REA) is considered as the reference event for all accidental situations in which a reactivity insertion is involved. According to the Nuclear Safety Authority guidelines, the following associated safety requirements for such situations are to be met:

- i) To assess the integrity of the 2<sup>nd</sup> containment barrier (i. e. the core vessel and its internal structures).
- ii) To maintain a fuel core coolable geometry.
- iii) To limit the dispersal of radioactive material in the environment.

The first and second requirements can be met by precluding phenomena such as fuel melting or dispersal of solid fuel particles in the coolant, in order to avoid coolant channel blockage or transmission of mechanical energy to the core vessel. The third one can be met if the number of potentially failed rods can be bounded.

Fuel rod cladding integrity is not a safety issue in itself, but a decoupling criterion based on the cladding integrity can be very useful since, when such a criterion is accurately defined and met, all the safety requirements are automatically met.

## ***1.2. REA phenomenology***

The first consequence of the reactivity insertion due to a rapid rod control cluster assembly (RCCA) removal from the core is a sharp power transient, which is radially localised within the core. In the fuel rods, the result is a very fast heating of the fuel column, first in the peripheral zones of the pellets, and then in the whole pellet cross-section. The pellets undergo thermal expansion, fracturation and (possibly in highly energetic transients) gaseous swelling, which result in pellet volume increase and important fission gas release.

During the first phase of the transient, the deformation of the fuel column induced by thermal expansion and (possibly) gaseous swelling results in pellet-cladding mechanical interaction (PCMI). This mechanical loading is strain-driven, and the associated cladding failure mechanism is ductility exhaustion of the cladding material, which is governed by the total elongation (TE) of the cladding material.

In the second phase of the transient, i. e. after DNB onset, clad ballooning can be triggered if the rod is over-pressurised. The cladding mechanical loading is then stress-driven (in fact, it is energy-driven, due to the limited quantity of available gas in the rod); the associated failure mechanism is plastic instability which is governed by the uniform elongation (UE) of the cladding material.

A third failure mechanism is possible if the cladding is submitted to a very high temperature: in this case, the oxidizing reaction between the cladding and the water becomes exothermic and can accelerate till cladding failure. The cladding temperature and time-at-temperature are the governing parameters for this mechanism.

## ***1.3. Historical background***

### *1.3.1. The RIA international full-scale test database before 1992*

Up to the mid 1980s, the RIA international full-scale test database was made-up of tests on fresh or low-burn-up fuel rods, performed in the USA (SPERT-CDC, PBF) and Japan (NSRR). On the basis of these tests, an empirical safety criterion was established: the fuel enthalpy per unit mass should not exceed 230 cal/g for fresh fuel and 200 cal/g for irradiated fuel. This criterion was applicable for burn-ups up to 33 GWd/tM.

In 1988, the French NPPs began to be operated according to improved core managements which led to higher fuel assembly discharge burn-ups, up to 47 GWd/tM: the GARANCE core management (four annual cycles) in 900 MW NPPs and the GEMMES core management (three 18-month cycles) in 1300 MW ones. But the RIA rod failure criteria had not been updated at that time.

More recently, in 1992, the Fuel Assembly (F/A) discharge burn-up was increased up to 52 GWd/tM. EDF wondered whether the old RIA criteria were still applicable for high-burn-up fuel and decided to launch, jointly with IRSN, an experimental programme centered on full-scale tests in the CABRI sodium loop. In November 1993, the result of the REP-Na1 test (rod failure at very low enthalpy ( $H_{max} = 30$  cal/g), with some fuel dispersal) showed that the old RIA criteria were no longer relevant. This was confirmed several months later with the HBO test series performed in NSRR (failure at  $H_{max} = 60$  cal/g for HBO-1).

### *1.3.2. The CABRI REP-Na programme and the empirical “safety domain”*

The CABRI REP-Na programme consisted in:

- i) 14 full-scale tests (including REP-Na1) in the CABRI sodium loop, performed between 1993 and 2002<sup>1</sup>.
- ii) The PROMETRA programme (still ongoing) dedicated to the characterisation of the cladding mechanical properties in high strain-rate conditions<sup>2</sup>.

- iii) The PATRICIA programme (achieved in 2001), dedicated to the study of thermal-hydraulics in PWR conditions (DNB onset, rewetting) for fast transients <sup>3</sup>.
- iv) The development of the SCANAIR code, dedicated to the simulation of the thermo-mechanical response of a fuel rod submitted to an RIA transient <sup>4</sup>.

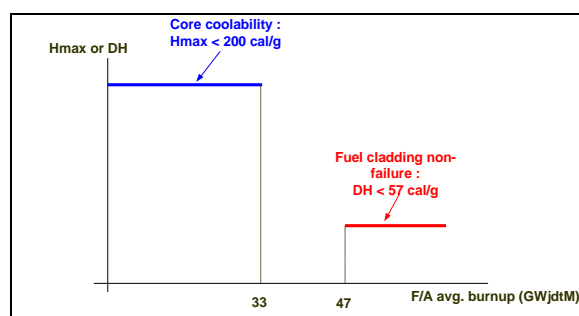
Based on the results of the full-scale tests, an empirical “safety domain”, which intends to preclude high-burn-up rod failure during an RIA, has been established. It is defined by five parameters and the corresponding bounding values <sup>5</sup>:

- i) Local burn-up  $\leq 64$  GWd/tM.
- ii) Waterside corrosion layer thickness  $\leq 120$   $\mu\text{m}$ .
- iii) Enthalpy deposition  $\leq 57$  cal/g.
- iv) Pulse width at mid-height  $\geq 30$  ms.
- v) Maximum cladding temperature  $\leq 700^\circ\text{C}$ .

This “safety domain” (Figure 1) has been successfully applied to most of the core managements which are in operation today, including the ones with MOX fuel and/or advanced cladding materials. But:

- When joined to the low-burn-up safety criterion, "the safety domain" is not constant, since it refers to different phenomena (core coolability at low burn-up and fuel rod failure at high burn-up) and is described by different parameters (max enthalpy at low burn-up, enthalpy deposition at high burn-up).
- The "safety domain" cannot be easily extended to new claddings, new fuels, new REP conditions without dedicated full-scale experiments.

Figure 1. Schematic view of the RIA empirical “safety domain”



### 1.3.3. Scope and outline of the paper

The paper is dedicated to the description of a new RIA rod failure criterion, based on mechanical tests on irradiated claddings and expressed in terms of a critical strain energy density (SED) vs. waterside oxidation level or average rod burn-up. The SED criterion is then transposed in terms of enthalpy deposition vs. rod burn-up and initial linear power for PWR conditions. The criterion is thus applicable to UO<sub>2</sub>/Zy-4 rods, whose cladding is submitted to PCMI loading and at every burn-up level, up to 69 GWd/tM. Clad failure by oxidizing/embrittlement is taken into account, but failure by ballooning and burst is not considered.

## 2. Failure by oxidation/embrittlement

Cladding failure by oxidation/embrittlement has been extensively studied in the past. In 1979, Van Houten <sup>6</sup>, on the basis of an extensive literature review, determined a failure limit expressed in equivalent temperature vs. time-at-temperature. According to this limit, the threshold for failure by accelerated oxidation (1482°C) corresponds to a temperature maintained during ca. 30 seconds.

Moreover, Shiozawa et al. <sup>7</sup> showed, on the basis of full-scale tests performed in NSRR on fresh fuel rods, that an energy deposition of 240-270 cal/g was necessary to reach this temperature threshold, with a boiling crisis during less than 10 seconds. For low burn-ups, a energy deposition limit at 240 cal/g

precludes the risk of clad failure by oxidation/embrittlement. This is also confirmed by the results of the full-scale PBF tests: such rod failures by fragmentation (consecutive to extensive cladding oxidation) were observed only in 4 tests, with max enthalpies reaching 285 cal/g.

### 3. Failure by PCMI: the CSED criterion

#### 3.1. Why choose the SED as a failure criterion?

The local strain energy density (SED) in the cladding is defined by:

$$SED = \int_{\varepsilon_0}^{\varepsilon_f} \sum_{i=r,\theta,z} \sigma_i \cdot d\varepsilon_i \quad (1)$$

where  $\sigma_i$  and  $\varepsilon_i$  are the components of the local stress and strain tensors (radial, hoop and axial directions), the integration being carried out between an initial strain  $\varepsilon_0$  (prior to the transient) and the maximal (or failure) strain  $\varepsilon_f$ . It has been chosen as the most relevant parameter to define a failure criterion for the following reasons:

- i) The three components of the stress and strain tensors are taken into account, along with the material constitutive law (relationship between stresses and strains, including anisotropy).
- ii) It is defined as a stress linked to a strain increment, which is a relevant criterion for a strain-driven mechanical loading (which is not the case for a criterion based on the sole stress).
- iii) It allows to take into account an initial stress state in the cladding, e. g. resulting from an RIA transient initiated at non-zero power (which cannot be taken into account with a criterion based on the sole strain).

#### 3.2. Assessment of the SED-to-failure for zircaloy-4 claddings

The definition of a critical SED (i. e. SED-to-failure) for zircaloy-4 claddings has been already described<sup>8</sup> and will be only briefly recalled here.

##### 3.2.2. Definition of the critical SED

###### 3.2.2.1. First step: definition of an experimental database

An experimental database has been build up with mechanical tests on both as-received and irradiated claddings, such as hoop tensile tests on machined rings and biaxial burst tests on plain tubes. Some tests have been discarded:

- Axial tensile tests on double-winged specimens, because the failure mode is not representative of the in-reactor situation.
- Tests at low temperatures (i. e. < 280°C), in which hydrogen embrittlement is exacerbated.
- Tests on specimens with a spalled zirconia layer, because the cladding is embrittled by the formation of hydride lenses.

Finally, a set of 90 mechanical tests has been considered; these tests encompass the following conditions : peak pellet burn-up from 0 to 68 GWd/tM, temperatures from 280 to 600°C, strain rate from  $2 \cdot 10^{-5}$  to  $5 \text{ s}^{-1}$ , zirconia layer thickness from 0 to 120  $\mu\text{m}$ .

###### 3.2.2.2. Second step: transposition to reactor case

During an RIA in reactor conditions, the mechanical loading of the cladding is assumed to be close to an equibiaxial one. But the mechanical tests mentioned above (hoop tensile tests and biaxial burst tests) are far from equibiaxial. Therefore some corrections have to be made on the failure strains. Based on the work of Fan & Koss<sup>9</sup>, corrective factors depending on the hydrogen content in the material have been determined and are to be applied on failure strains. These factors are formulated as follows:

- For hoop ring tensile tests:

$$f_H = 0.568 * \exp(-0.0011 * [H]) \quad (2)$$

- For biaxial burst tests:

$$f_H = 0.889 * \exp(-0.001 * [H]) \quad (3)$$

where [H] is the averaged hydrogen content, in ppm.

### 3.2.2.3. Third step: calculation of the critical SED

The critical SED is then calculated for all tests of the experimental database. By splitting the elastic and viscoplastic components of the strain, we obtain the following formula:

$$SED = SED_e + SED_p = \int_0^{\varepsilon_e} E \varepsilon d\varepsilon + \int_{\varepsilon_e}^{\varepsilon_f} K \cdot \varepsilon^n \left( \frac{\dot{\varepsilon}}{\varepsilon_0} \right)^m d\varepsilon \quad (4)$$

where  $\varepsilon_e$  is the elasticity limit of the cladding material,  $E$  is its Young's modulus,  $\varepsilon_f$  is the strain-to-failure (corrected as is explained above),  $\dot{\varepsilon}$  is the test strain rate, and  $K$ ,  $n$ ,  $m$  and  $\varepsilon_0$  are the coefficients of the material constitutive law.

### 3.2.2.4. Fourth step: homogenisation

Finally, since some tests have been carried out at strain rates much lower than typical RIA ones, a corrective factor has been added to take into account strain-rate effects. Based on the formulation of the material constitutive law, the viscoplastic component of the CSED is corrected as follows:

$$SED_p^{RIA} = V^m \cdot SED_p \quad (5)$$

where  $V = \frac{\dot{\varepsilon}}{\dot{\varepsilon}^{RIA}}$  and  $\dot{\varepsilon}^{RIA} = 5s^{-1}$

### 3.2.3. CSED curve

A CSED curve is then build up as the lower bound for all the CSED values calculated for the entire experimental database. The CSED curve is well represented by the following equation, as a function of the waterside zirconia layer thickness:

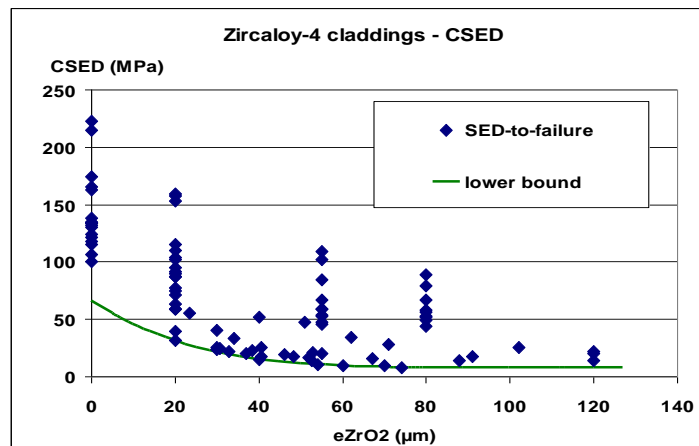
$$\begin{aligned} CSED &= 66.327 - 2.3536 * e + 3.3334 * e^2 \\ &- 1.6458 * e^3 \quad \text{if } e \leq 74.8 \mu\text{m} \\ CSED &= 8.0033 \quad \text{otherwise} \end{aligned} \quad (6)$$

where  $CSED$  is the SED-to-failure (in MPa) and  $e$  is the zirconia layer thickness (in  $\mu\text{m}$ ). This curve is illustrated on Figure 2 below, along with the points corresponding to the mechanical test database.

Cladding PCMI failure is clearly dominated by the thickness of the highly hydrided and embrittled zone which appears in the outer region of the cladding wall. The formulation of the CSED as a function of waterside zirconia layer thickness is a way to implicitly take into account the local inhomogeneity of the cladding material due to the build-up of this brittle layer, whose thickness corresponds to the length of incipient cracks in the cladding.

In this curve, the temperature doesn't appear as an explicit parameter. The curve bounds experimental results obtained at various temperatures; so it can be applied to real or postulated RIA transients, during which the cladding temperature varies with spatial position and time.

Figure 2. CSED as a function of cladding waterside corrosion level



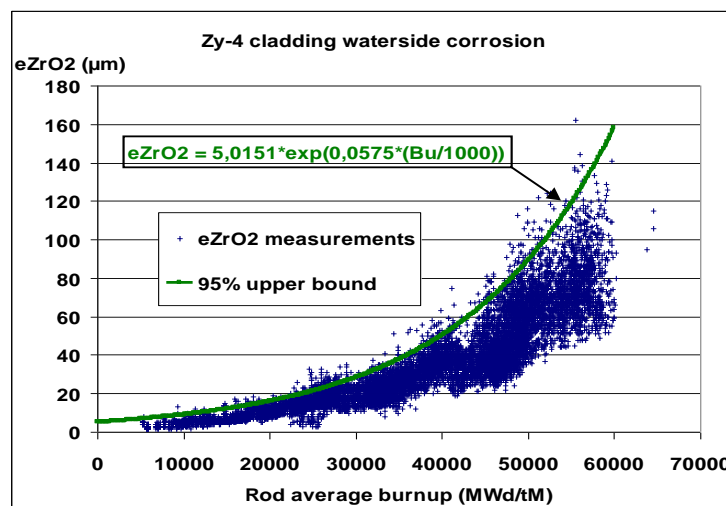
3.2.4. Transposition as a function of rod averaged burn-up

The CSED is then expressed as a function of the rod average burn-up, by the means of a bounding correlation between the burn-up (in GWd/tM) and the maximum zirconia layer thickness (in µm). Based on a large amount of measurement results (more than 14000 points), a 95% upper bound correlation can be determined according to the following equation (Figure 3):

$$e_{ZrO2} = 5.0151 * \exp(0.0575 * Bu) \quad (7)$$

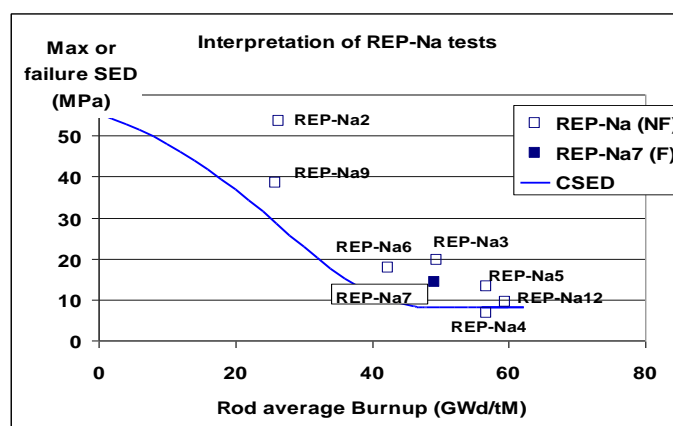
where Bu is the rod average burn-up in GWd/tM.

Figure 3. 95% bounding correlation between rod average burn-up and zirconia layer thickness



The final expression of the CSED curve is obtained by combining eqs. (6) and (7) above. Figure 4 shows the CSED curve as a function of rod average burn-up, compared with the maximum SED (or SED-to-failure) calculated from the interpretation of the CABRI REP-Na full-scale tests on Zy-4-clad rods with the SCANAIR code. As can be seen, the only test which led to rod failure with a sound cladding (REP-Na7) is represented by a point that is located well above the CSED curve.

Figure 4. CSED curve as a function of rod average burn-up, compared with the interpretation of REP-Na tests



### 3.3. Robustness of the CSED failure criterion

The robustness of the CSED criterion described above is assessed by the conservatisms that have been taken into account during the different steps of its elaboration:

- i) The corrective factors introduced to transpose the SED-to-failure to reactor case are penalised in order to take into account the experimental scatter in Fan & Koss's results.
- ii) The CSED curve has been chosen as a lower-bound for all the SED-to-failure values calculated for the experimental database.
- iii) The correlation between the rod average burn-up and the maximum zirconia layer thickness is an upper bound that covers 95% of the measurement points. Fig. 4 shows a posteriori that this choice leads to a reasonably conservative CSED curve; a 100% upper bound would have led to an overly conservative curve.

## 4. Transposition of the CSED criterion

### 4.1. Purpose

The purpose of this section is to present the transposition of the CSED PCMI criterion described above in more relevant quantities for safety studies, such as max fuel enthalpy or energy deposition per unit mass. This is done in order to allow performing REA studies by the means of simplified thermal calculations. This step is however limited to UO<sub>2</sub>/Zy-4 rods whose cladding is submitted to PCMI loading. So, MOX fuel and clad failure by ballooning are not considered here.

### 4.2. Specifications

The transposition of the CSED criterion must obey the following specifications:

- i) The criterion shall be applicable whatever the conditions of the power transient onset, such as rod burn-up and initial linear power.
- ii) It shall be applicable whatever the core management and the related fuel rod design considered.
- iii) Along with the conservatisms introduced in the build-up of the CSED curve (see § III.3. above), all uncertainties shall be taken into account; they concern rod design data (fabrication tolerances), rod irradiation (power history and modeling) and the cladding material constitutive law during the transient (since no uncertainty has been previously introduced in the build-up of the CSED curve).

### 4.3. Input data and calculations

The rod design data are taken from a recent F/A design from Areva-NP, which is to be operated in an improved core management in the French 1300MW NPPs. The rod cladding is assumed to be made of zircaloy-4. Table I below gathers the main rod design nominal data and the associated fabrication tolerances.

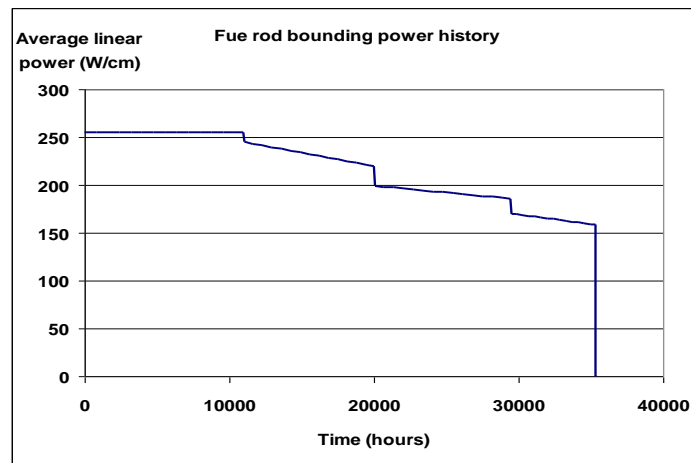
Table 1. Rod design data

Parameter	Nominal value	Tolerance
Pellet density (%TD)	95	± 1.5
Pellet diameter (mm)	8.192	± 0.012
Resintering rate (%DT)	0.5	± 0.5
Clad outer diam. (mm)	9.5	± 0.045
Clad wall thickness (mm)	0.57	± 0.044
Spring volume (cm <sup>3</sup> )	1.38	± 0.114
Plenum length (mm)	201.5	± 8.3
Filling pressure (bar, He + air)	20 + 1	± 0.7 (He)

The rod is assumed to be irradiated in a 1300 MW NPP, according to the postulated bounding power history (figure 5 below). The rod averaged end-of-life (EOL) burn-up is 69 GWd/tM.

The rod irradiation is simulated with the CYRANO3 thermal-mechanical code, developed by EdF. During this step, the uncertainties considered come from rod design data (see above) and some models implemented in the code, consistently with basic design studies: fuel thermal conductivity and solid swelling, fission gas release, cladding irradiation creep and waterside corrosion.

Figure 5. Rod bounding power history



The CYRANO3 calculations provide the pre-transient states of the rod for many burn-up values (i. e. from 10 GWd/tM up to EOL, by steps of 5 GWd/tM). For each burn-up and all the configurations considered (i. e. with all the uncertainties listed above), an RIA transient with a pulse width of 20 ms and different initial power levels (from 0 to 400 W/cm at peak power node) is assumed to be applied. The thermal-mechanical response of the rod is simulated with the SCANAIR code. For each case, the energy injected during the pulse is adjusted in such a way that the maximal local SED in the cladding is equal to the CSED corresponding to the given burn-up. The critical energy deposition  $DH_c$  corresponds to the maximum value of the enthalpy increase for this case.

Additional uncertainties and hypotheses are taken into account here :

- i) Since some zirconia spallation has been observed during the transient in some REP-Na tests, two extreme situations are considered: without any spallation and with complete removal of the zirconia layer.
- ii) An uncertainty is applied on the cladding material constitutive law (the uncertainty has been adjusted to bound all the experimental results).
- iii) During the pulse, the axial power profile is chosen as flat as possible; this case allows a maximum coolant heating ahead of the peak power node (PPN).

It should also be noticed that all SCANAIR calculations have been made considering a reduced initial pellet-clad gap, which depends on the local burn-up. This hypothesis allows to take into account a pellet-clad bonding at high burn-up, and is necessary to interpret correctly the REP-Na full-scale tests (in terms of rod diameter increase). Thanks to this hypothesis, all situations involving rod de-conditioning and reconditioning, such as a return to full power after an extended reduced-power operation (ERPO) period, are covered, in terms of stress level in the cladding prior to the transient, thus in terms of SED in the cladding during the transient.

#### 4.4. Calculational method for critical energy deposition

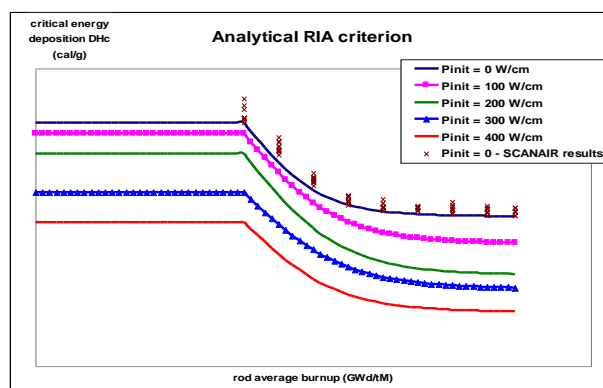
CYRANO3 and SCANAIR calculations have been performed by varying the 14 uncertain parameters (i. e. 8 rod design data (Table I), 5 models for base irradiation simulation (§ IV.3) and 1 for transient simulation). From these calculations, the penalising configurations (i. e. sets of parameters with or without uncertainty) have been determined. For each of these configurations, the critical energy deposition  $DH_c$  is calculated and the final value, for a given burn-up and initial linear power level, is the lowest of all the values of  $DH_c$  obtained. This approach, which has needed ca. 160,000 SCANAIR calculations, enables to obtain a curve that conservatively bounds all main parameters uncertainties. This is illustrated on Figure 6, which also shows the flyspeck corresponding to the calculation results obtained for zero initial power.

#### 4.5. Results

Since rod burn-ups under 30 GWd/tM correspond to very high values of the CSED (see fig. 4 above), only the  $DH_c$  values for burn-ups from 30 to 69 GWd/tM have been calculated. The critical energy deposition is a decreasing function of both rod average burn-up and initial linear power. For each power level, the  $DH_c$  evolution vs. burn-up is well represented by a hyperbolic tangent function.

In order to take into account a lower bound for the oxidation/embrittlement failure limit (see chap. II above), each curve is horizontally extended for burn-ups between 0 and 30 GWd/tM, with the  $DH_c$  value obtained at 30 GWd/tM. The complete formulations of the transposed failure criterion during an REA transient are illustrated on figure 6.

Figure 6. Analytical RIA criterion expressed in critical energy deposition per unit mass, as a function of rod average burn-up and initial linear power



It should be noticed that the highest initial power level considered (400 W/cm) does not necessarily correspond to full power operation, where RIA transients cannot be prompt-critical. In neutronic and thermal studies, many uncertainties and penalties are taken into account, and thus the local initial power can reach such high values, even for transients initiated at 30% or 40% of full core power.

#### **4.6. Application and robustness of the RIA analytical criterion**

The analytical RIA criterion described above is applicable to REA transients in the following conditions:

- i) Rods with UO<sub>2</sub> fuel and zircaloy-4 cladding.
- ii) Rod average burn-up: from 0 to 69 GWd/tM (corresponding to an EOL F/A average burn-up of 62 GWd/tM).
- iii) Initial linear power at PPN: from 0 to 400 W/cm.
- iv) Pulse width at mid-height: 20 ms or more.
- v) Cladding mechanically loaded by PCMI.

It can be conservatively applied to rods with improved cladding materials such as M5<sup>TM</sup> from Areva-NP or Optimised ZIRLO ® from Westinghouse.

The robustness of the criterion is ensured by:

- i) The conservatism introduced at each step of the build-up of the CSED curve (see § III.3. above).
- ii) The use of qualified calculation tools such as CYRANO3 for base irradiation and SCANAIR for RIA transient simulations.
- iii) The introduction of various uncertainties and penalties in the transposition of the CSED criterion : rod design data (fabrication tolerances), simulation of base irradiation (power history and CYRANO3 models), reduced initial pellet-clad gap, cladding material constitutive law, behavior of the waterside zirconia layer).
- iv) The choice of the lower bound for DHc among a lot of values obtained from different configurations.

### **5. Conclusions and perspectives**

In 1993, the result of the CABRI REP-Na1 test (the first RIA full-scale test on high burn-up fuel, which led to premature rod failure with some fuel dispersal) showed that the old RIA criteria were no longer relevant for high burn-up fuel. EDF and IRSN decided to launch a joined programme with the purpose of studying the high-burn-up fuel rod behavior during an RIA transient and establish new failure criteria for REA studies.

On this basis, a “safety domain” was empirically established to preclude rod failure during an RIA transient at high burn-up. But this situation was not fully satisfactory because this approach was not consistent with the previous criteria; furthermore the domain cannot be easily extended without new full scale experiments. So, a new approach was decided in order to define new criteria applicable to every fuel rod design and burn-up.

This approach is based on the assessment of a cladding failure criterion expressed in critical strain energy density. For this sake, an experimental database composed of mechanical tests on zircaloy-4 cladding has been analyzed. The SED-to-failure has been calculated and transposed to in-reactor conditions. Then, the CSED curve is defined as the lower bound for all tests and expressed as a function of rod average burn-up. This criterion has proven to be conservative on the basis of a comparison with the interpretation of the CABRI REP-Na full-scale tests.

The CSED curve is then transposed in terms of critical energy deposition (DHc) in the fuel. A fuel rod irradiation is simulated with EDF’s CYRANO3 code; uncertainties are addressed in both rod design data and models. Then, a RIA power transient is simulated with SCANAIR code at different burn-ups (from 30

to 69 GWd/tM) and different initial power levels (from 0 to 400 W/cm) and the critical energy deposition corresponding to the CSED in the cladding is determined. The different DHc curves are horizontally extended for low burn-ups (0-30 GWd/tM) in order to preclude the cladding failure risk by oxidation and embrittlement.

The RIA cladding failure criterion is thus applicable to UO<sub>2</sub> fuel with zircaloy-4 cladding, for burn-ups between 0 and 69 GWd/tM and initial linear power between 0 and 400 W/cm, with a clad mechanical loading by PCMI. It can be conservatively applied to fuel rods with advanced claddings such as Areva-NP's M5<sup>TM</sup> or Westinghouse's Opt ZIRLO®.

Further work is necessary in order to extend its validity and application domain:

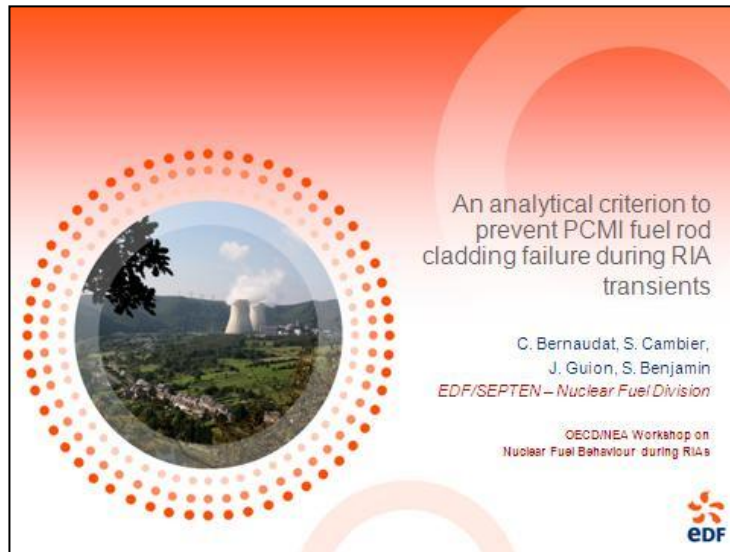
- i) Application to advanced cladding materials taking into account their improved behavior: this needs to calibrate constitutive laws for each material, based on mechanical tests such as PROMETRA tests on fresh and irradiated claddings.
- ii) Extension to cladding failure by ballooning and burst : this step needs a better knowledge of cladding large deformations at high temperatures, up to ca. 1200°C.
- iii) Extension to MOX fuel: compared to UO<sub>2</sub>, MOX fuel is characterised by larger fission gas release and swelling during an RIA transient, hence clad failure by ballooning could become predominant. An accurate estimation of this phenomenon needs to validate some hypotheses regarding the fission gas behaviour (fission gas release kinetics, axial gas flow within the rod).

### Acknowledgments

The authors are thankful to their colleagues from R&D Division of EDF for their contribution to the build-up of the cladding material constitutive law, and their colleagues from IRSN/DPAM/SEMCA for the fruitful discussions regarding the development of the SCANAIR code.

### References

- [1] J. Papin et al., *Synthesis of CABRI RIA tests interpretation*, Eurosafe 2003, (25-26 November 2003), Paris, France.
- [2] M. Balourdet et al, *The PROMETRA programme: assessment of mechanical properties of zircaloy-4 cladding during an RIA*, SMiRT 15, Seoul, South Korea.
- [3] V. Besson, *main outcomes from the PATRICIA program on clad-to-coolant heat transfer during RIAs*, NSRC (2002), (October 2002), Washington, USA.
- [4] E. Federici et al., *The SCANAIR code version 3.2: main features and status of qualification*, IAEA TCM on fuel behaviour under transient and LOCA condition, (10-14 September 2002), Halden, Norway.
- [5] B. Salles et al., *EDF-proposed safety domain for rod ejection accidents in PWRs*, ANS Topical Meeting on Reactor Fuel Performance, (April 2000), Park City, USA.
- [6] R. Van Houten, *Fuel rod failure as a consequence of departure from nucleate boiling or dryout*, NUREG-0562, (June 1979).
- [7] S. Shiozawa and M. Ishikawa, *A study of fuel behavior under reactivity initiated accidents – Review*, Jn. Nucl. Mat. 95 (1980), p. 1.
- [8] C. Bernaudat et al., *A new approach to study the rod ejection accident in PWRs*, WRFPM, (October 2005), Kyoto, Japan.
- [9] Y. Fan and D.A. Koss, *The influence of multiaxial state of stress on the hydrogen embrittlement of zirconium alloy sheet*, Metall. Trans. 16A (1985), p. 675.

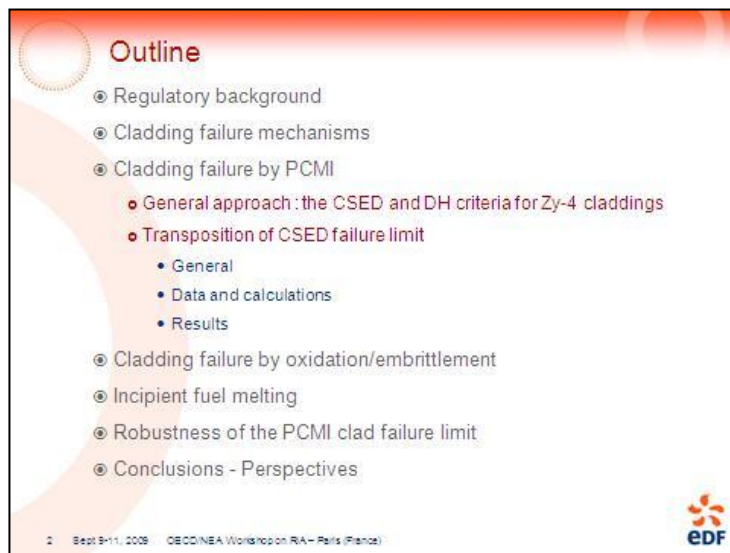


An analytical criterion to prevent PCMI fuel rod cladding failure during RIA transients

C. Bernaudat, S. Cambier,  
J. Guion, S. Benjamin  
*EDF/SEPTEN – Nuclear Fuel Division*

OECD/NEA Workshop on  
Nuclear Fuel Behaviour during RIAs

EDF



### Outline

- ⊙ Regulatory background
- ⊙ Cladding failure mechanisms
- ⊙ Cladding failure by PCMI
  - General approach : the CSED and DH criteria for Zy-4 claddings
  - Transposition of CSED failure limit
    - General
    - Data and calculations
    - Results
- ⊙ Cladding failure by oxidation/embrittlement
- ⊙ Incipient fuel melting
- ⊙ Robustness of the PCMI clad failure limit
- ⊙ Conclusions - Perspectives

2 Sept 9-11, 2009 OECD/NEA Workshop on RIA – Paris (France)

EDF



### Regulatory background

- ⊙ The rod ejection accident (REA) is the reference event for accidents involving reactivity insertion in the core
- ⊙ For accidental situation (4<sup>th</sup> category), the safety requirements are:
  - To maintain the integrity of the 2<sup>nd</sup> containment barrier,
  - To maintain a coolable geometry of the core, and
  - To limit the release of radioactive products
- ⊙ A comfortable way to meet the safety guidelines is to preclude fuel rod cladding failure
  - Fuel dispersal in the coolant is precluded
  - Cladding failure mechanisms are better known
  - Cladding failure criteria can be assessed on an experimental basis (full-scale or separate-effect tests)

3 Sept 9-11, 2009 OECD/NEA Workshop on RIA – Paris (France)

EDF

## Cladding failure mechanisms

- Oxidation/embrittlement:
  - Needs high temperature and sufficient time-at-temperature
- Pellet-Cladding Mechanical Interaction (PCMI):
  - Purely mechanical: no SCC or DHC possible
  - Strain-driven mechanism: failure by ductility exhaustion
  - Governing parameter = total elongation (TE)
- Ballooning/burst:
  - Stress-driven mechanism: failure by plastic instability (*in fact: energy-driven mechanism due to limited gas quantity and feedback of clad ballooning on rod inner pressure*)
  - Needs high temperature (DNB) and rod overpressurization
  - Governing parameter = uniform elongation (UE)
- Fuel incipient melting:
  - Needs high local energy deposition levels



4 Sept 9-11, 2009 OECD/NEA Workshop on RA - Paris (France)

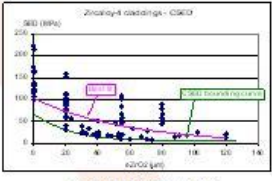
## PCMI loading : the approach

- The approach is based on the notion of CSED in the cladding ; but why choose such a criterion ?
  - CSED involves both strain and stress
  - All components of the tensors are considered
  - CSED is a relevant parameter to transpose the criterion to at-power transient
- The approach is similar to EPRI's one :
  - Determine a bounding CSED vs eZrO2 curve on the basis of a mechanical test database
  - Determine a bounding eZrO2 vs Bu correlation
  - Transpose the CSED curve as a function of rod Bu
  - Transpose CSED vs Bu in an energetic criterion :  $DH = f(Bu, Pini)$
  - Complete the criterion to include other cladding failure mechanisms

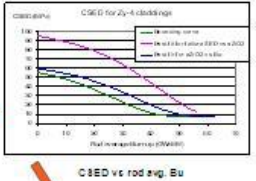


5 Sept 9-11, 2009 OECD/NEA Workshop on RA - Paris (France)

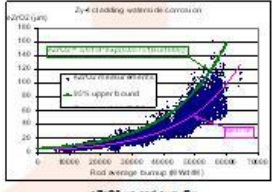
## PCMI loading : the CSED and DH criterion for Zy-4 claddings



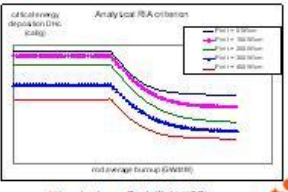
CSED (SED to failure) vs eZrO2



CSED vs rod avg. Bu



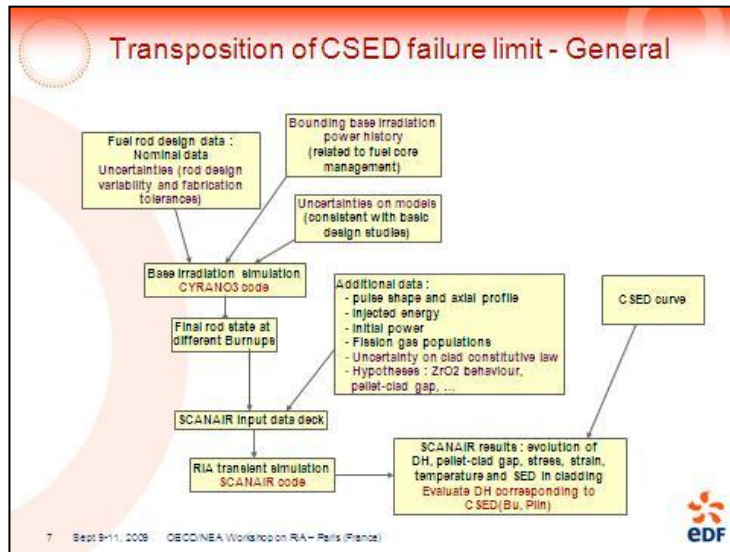
eZrO2 vs rod avg. Bu



DH vs (rod avg. Bu, Initial LHGR)



6 Sept 9-11, 2009 OECD/NEA Workshop on RA - Paris (France)



### Transposition of CSED failure limit : data and calculations (1/2)

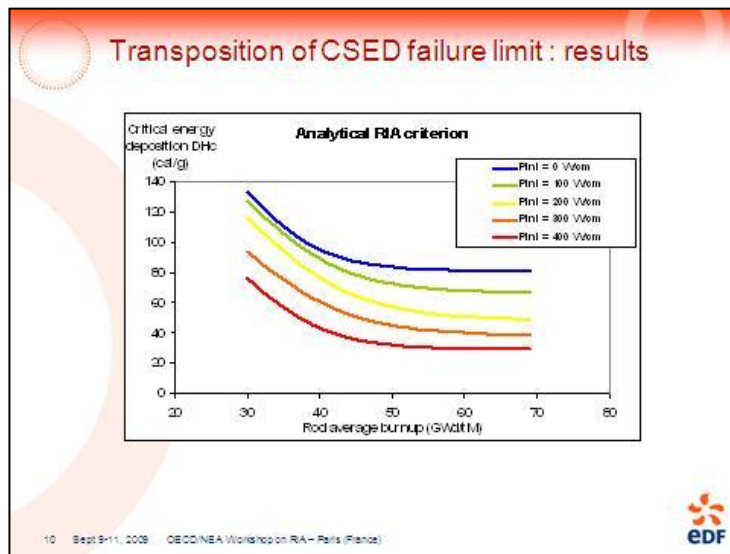
- Rod design data :
  - AFA3GLr-AA rod with UO<sub>2</sub> fuel and Zy-4 cladding
  - Uncertainties on 8 design parameters
- Rod irradiation :
  - Power history = bounding design PH for 18-month cycle core management (1300 MW NPPs)
  - Uncertainties on 5 irradiation models
- RIA transient :
  - Applied for Bu = 30 to 69 GWd/tM and Pini = 0 to 400 W/cm
  - Pulse shape typical of a HZP prompt-critical transient (L 1/2 = 20 ms)
  - Axial profile as flat as possible
  - ZrO<sub>2</sub> layer peels off or remains intact during the pulse
  - Uncertainty on cladding material constitutive law

8 Sept 9-11, 2008 OECD/NEA Workshop on RIA - Paris (France) EDF

### Transposition of CSED failure limit : data and calculations (2/2)

- Calculations have been performed for :
  - Many bounding configurations (obtained by combinations of the different uncertainties);
  - Rod avg. Bu = 30 to 69 GWd/tM by steps of 5 GWd/tM
  - Initial LHGR = 0 to 400 W/cm by steps of 100 W/cm
  - Injected energy = 40 to 200 cal/g (until CSED is reached)
  - ZrO<sub>2</sub> layer behaviour *during RIA transient*: completely removed or intact
- The whole transposition of the failure limit (CSED → DH(Bu, LHGR)) needs hundreds of CYRANO3 calculations and ca. 160,000 SCANAIR calculations
- For each initial LHGR, the critical energy deposition DH<sub>c</sub> is the lower bound for all configurations and is approximated by a simple formula :
 
$$DH_c(Bu) = A + B \cdot \tanh((Bu-30)/C)$$

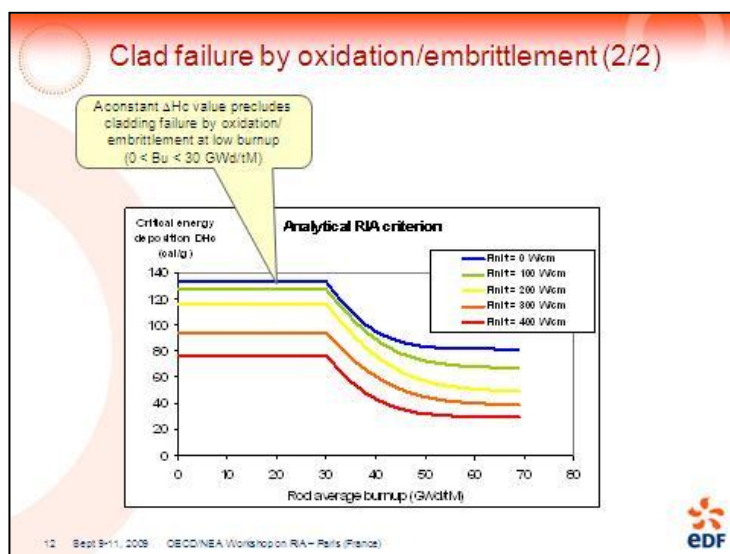
9 Sept 9-11, 2008 OECD/NEA Workshop on RIA - Paris (France) EDF

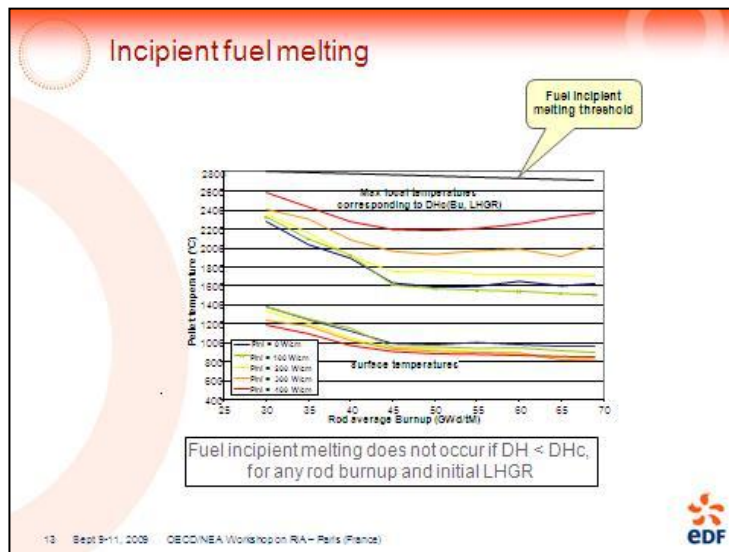


### Clad failure by oxidation/embrittlement (1/2)

- Van Houten et al., 1979 :
  - Cladding failure by oxidation/embrittlement needs a time-at-temperature of ca. 30 sec @ 1482°C (threshold for accelerated oxidation)
- Shiozawa et al., 1980 :
  - An energy deposition DH = 240 cal/g is necessary to reach such high cladding temperature
  - The DNB duration is less than 10 sec

11 Sept 9-11, 2008 OECD/NEA Workshop on RIA - Paris (France) EDF





- ### Robustness of the RIA clad failure limit
- CSED curve :
    - Based on experimental results transposed to in-reactor conditions (hoop strain-rate, stress biaxiality)
    - Bounding « eZrO<sub>2</sub> vs rod Bu » correlation
    - CSED curve = 100% LB for all experimental results
  - Calculation tools and models
    - CYRANO3 and SCANAIR are validated against experimental results
    - Same cladding material constitutive law for CSED curve assessment and rod overall behaviour modeling with SCANAIR
  - Uncertainties and penalties are taken into account:
    - Rod design data (design variability and fabrication tolerances)
    - Base irradiation (P/H and models, consistently with basic design studies)
    - Transient simulation:
      - Uncertainty on cladding material constitutive law
      - Pulse shape and axial profile
      - Bounding hypotheses for ZrO<sub>2</sub> layer behaviour during transient
      - Reduced pellet-clad gap to enhance PCMI loading
        - Based on fuel rod metallographies
        - Consistent with full-scale CABRI REP-Na test interpretation
        - Bounds all situations, including an RIA transient just after the end of an ERPO period
- 14 Sept 9-11, 2008 OECD/NEA Workshop on RA - Paris (France) EDF

- ### Conclusions
- A robust analytical fuel rod cladding failure limit has been established :
    - Based on a conservative CSED curve for Zr-4 claddings
    - Transposed in energy deposition (DH) as a function of rod average burnup (0 – 69 GWd/tM) and initial LHGR (0 – 400 W/cm)
    - With all relevant uncertainties and penalties taken into account
  - This failure limit precludes rod failure by oxidation/embrittlement, PCMI and incipient fuel melting
  - It is applicable to REA studies for:
    - UO<sub>2</sub> fuel of any design (and related core management)
    - Zircaloy-4 cladding (and conservatively improved cladding materials such as M5™ or Opt ZIRLO®)
    - Cladding mechanical loading by PCMI
    - RIA power transients with L1/2 ≥ 20 ms
- 15 Sept 9-11, 2008 OECD/NEA Workshop on RA - Paris (France) EDF



## Perspectives

- ⊙ Extend the application domain of the analytical RIA criterion :
  - MOX fuel
    - Specific features of MOX fuel : FG behaviour, He production and release
  - Advanced PWR 17x17 claddings : M5™, ZIRLO®, Opt ZIRLO®, ...
    - Cladding material constitutive law
    - CSED curve
  - Cladding failure by ballooning/burst
    - Cladding failure limit to be assessed by EDGARIA separate-effect tests
    - Needs some developments in the SCANAIR code (no instantaneous axial gas flow)
- ⊙ Experimental results to come will be analysed :
  - Full-scale tests (CABRI-WL, NSRR/HTHP)
  - Separate-effect tests (PROMETRA, EDGARIA, FGD)
- ⊙ Additional objective : benchmarking of the RIA codes :
  - Comparison between SCANAIR and EPRI's code FALCON

16 Sept 9-11, 2009 OECD/NEA Workshop on RIA - Paris (France)





**DEVELOPMENT OF ACCEPTANCE CRITERIA FOR SAFETY ANALYSIS OF CONTROL  
ROD EJECTION AND CONTROL ROD DROP ACCIDENTS USING A  
MECHANISTIC APPROACH**

**Robert Montgomery**  
ANATECH Corp., USA

**John Alvis**  
ANATECH Corp., USA

**Ken Yueh**  
EPRI, USA

**Odelli Ozer**  
EPRI, USA

Paper not available

## Development of Acceptance Criteria for Safety Analysis of Control Rod Ejection and Control Rod Drop Accidents Using a Mechanistic Approach

Robert Montgomery

John Alvis

**ANATECH**

Linking Theory and Practice

Ken Yueh

Odelli Ozer

**EPRI** | ELECTRIC POWER  
RESEARCH INSTITUTE

Presented at the  
OECD/NEA Workshop  
Nuclear Fuel Behavior during Reactivity Initiated Accidents  
Paris, France  
September 9 – 11, 2009

**ANATECH**  
Linking Theory and Practice

**EPRI**

### Presentation Overview

- Methods Used in Developing RIA Failure Thresholds
- Use of RIA Experiments in Fuel Rod Behavior Evaluations
- Mechanistic Approach to Develop Failure Threshold
- Treatment of Uncertainties Using Statistical Methods
- Conclusions

OECD/NEA RIA Workshop, September 9-11, 2009 -D-

**ANATECH**  
Linking Theory and Practice

**EPRI**

### Methods to Develop RIA Failure Threshold

- Possible Approaches
  - 1) Mechanistic method – e.g. EPRI Topical Report, June 2002, SKI
  - 2) Empirical method – e.g. RIL 0401, JNSC
- Both approaches use RIA-simulation experiments as initial basis for fuel rod failure threshold development
  - Goal is to identify fuel enthalpy (maximum or increase) necessary to cause cladding failure under LWR conditions
    - » Function of important state variables (burnup, oxide thickness, etc.)
  - Differences arise in how to use the RIA-simulation test data
    - » Mechanistic method – use data to develop and validate analysis methodology
    - » Empirical method – use data directly or adjusted with weighting factors (scaling)

OECD/NEA RIA Workshop, September 9-11, 2009 -D-

ANATECH  
Using Theory and Practice

EPRI

## Mechanistic Approach

---

- Develop analysis methodology for RIA
  - Use RIA-simulation test results (on-line and PTE) and analytical evaluations to gain understanding of fuel rod behavior
  - Identify active fuel rod deformation and failure mechanisms
    - » Develop cladding integrity model based on mechanical property tests representative of failure processes
  - Validate analysis methodology using RIA-simulation experiments
    - » Comparison to measured results (deformations, temperature, etc.)
    - » Ability to differentiate between failed and non-failed tests
- Failure threshold development for LWR conditions
  - Use validated analysis methodology as transfer function to develop failure threshold LWR hypothetical accident conditions
  - Account for important mechanisms affecting fuel rod behavior and the processes leading to cladding failure

---

© OECD/NEA RIA Workshop, September 9-11, 2009 -4-

ANATECH  
Using Theory and Practice

EPRI

## Empirical Approach

---

- Data evaluation
  - Correlate experimental results to single dependent variable
    - » Cladding outer surface oxide thickness or hydrogen content, without consideration for other burnup or temperature effects
  - May develop weighting (adjustment) factors to compensate for differences in test conditions (e.g. temperature, pulse width)
- Threshold development
  - Construct failure threshold using lower-bound empirical fit to experimental data
  - Use of weighting factors can produce results consistent with the mechanistic approach, if a realistic understanding of fuel behavior is used

---

© OECD/NEA RIA Workshop, September 9-11, 2009 -5-

ANATECH  
Using Theory and Practice

EPRI

## Empirical Evaluations of RIA Data

---

**Difficulties with Empirical Approach**

- Does not consider the fundamental mechanisms leading to cladding failure
- Generalizes individual rod behavior to all rods
- Approach can be biased by misinterpretation of a single rod (small data set of RIA-simulation tests)

---

© OECD/NEA RIA Workshop, September 9-11, 2009 -6-

ANATECH Leading Theory and Practice **EPRI**

## Best-Estimate Evaluations of RIA Experiments

- Use transient fuel rod behavior codes (e.g. FALCON, SCANAIR, FRAPTRAN, etc.) to understand fuel behavior
  - Evolution of pellet and cladding thermal and mechanical states
  - Demonstrate commonality and differences between various test conditions, rod types, etc.
  - Identify fuel rod conditions leading to cladding failure
- Use of separate effects tests in combination with analytical methods to:
  - Understand the key mechanisms operative in RIA-simulation experiments
  - Apply the results from RIA-simulation experiments to postulated accidents in LWR's

OECD/NEA RIA Workshop, September 9-11, 2009 -7-

ANATECH Leading Theory and Practice **EPRI**

## Key Observations from RIA Test Evaluations

- Pellet thermal expansion is the primary PCMI loading mechanism during the early phase of the power pulse
  - Applicable to  $UO_2$  fuel up to 75 GWd/tU
  - Consistency between CABRI and NSRR Experiments
- Cladding failure during PCMI loading is controlled by
  - Hydrogen content and hydride morphology
  - Temperature in the outer region of the cladding
- Cladding deformations beyond pellet thermal expansion
  - Decrease in strength due to cladding temperature  $>600^\circ\text{C}$
  - Secondary loading mechanisms: internal pressure or gaseous swelling

OECD/NEA RIA Workshop, September 9-11, 2009 -8-

ANATECH Leading Theory and Practice **EPRI**

## Considerations for PCMI Failure Threshold

- NSRR RIA tests at room temperature (CZP) over emphasizes role of corrosion/hydrogen on clad ductility
  - Recovery of cladding ductility at operating temperatures ( $280^\circ\text{C}$ ) increases fuel enthalpy at failure
- Evaluations show that irradiated MOX pellet expands more than  $UO_2$  at same enthalpy level
  - Using MOX data directly assumes no difference exists between  $UO_2$  and MOX fuel pellet response
  - Pellet expansion effects should be considered to adjust for  $UO_2$  limits
- Low failure enthalpy for BWR NSRR tests driven by  $20^\circ\text{C}$  temperature and narrow pulse width conditions
  - Wider pulse widths increase temperature
  - Higher temperature improves Zircaloy-2 and hydride ductility

OECD/NEA RIA Workshop, September 9-11, 2009 -9-

ANATECH EPRI  
Using Theory and Practice

### Development of RIA Fuel Rod Failure Threshold

---

- Construct Fuel Rod Failure Threshold Consistent with Neutronics Analysis Approach
  - Fuel rod enthalpy during a rod ejection accident is mostly a function of rod burnup and location in the reactor core
  - Failure threshold should be a function of burnup
  
- Analytical Approach to Develop LWR RIA Failure Threshold
  - Analytical approach required to account for differences between test conditions and postulated LWR RIA conditions
  - Develop failure model that considers the failure modes (PCMI, ballooning, etc.) and the important variables (H, T,  $\Phi$ , ...)
  - Construct irradiation performance data correlation, e.g. Corrosion vs. Burnup.
  - Thermal/mechanical analysis performed as a function of burnup to define clad loading during hypothetical control rod ejection accident

---

CSNI/NEA RIA Workshop, September 9-11, 2009 -10-

ANATECH EPRI  
Using Theory and Practice

### Mechanistic Approach to RIA Failure Threshold Development

#### How to link clad ductility to burnup ?

CSNI/NEA RIA Workshop, September 9-11, 2009 -11-

ANATECH EPRI  
Using Theory and Practice

### Results from Several Mechanistic Approaches

---

#### Results: Best-estimate rod failure thresholds

Comparison with similar studies of PWR HZP REA

\*Based on assumed oxide versus burnup correlation

CSNI/NEA RIA Workshop, September 9-11, 2009 -12-

ANATECH  
Lining Theory and Practice

EPRI

### Sources of Uncertainties in RIA Failure Threshold Development

---

- Mechanical properties used to develop cladding failure model (CSED, strain, etc.)
  - Experimental uncertainties, material variability, etc.
- Corrosion layer thickness accumulation and hydrogen content as function of burnup
  - Stochastic behavior of oxidation process and pickup fraction, coolant temperature and chemistry variations, etc.
- Accident analysis methodology used to define fuel rod thermal/mechanical response
  - Uncertainty in fuel and cladding behavior models impacts initial conditions and transient behavior

---

CSCE/NEA RIA Workshop, September 9-11, 2009 -13-

ANATECH  
Lining Theory and Practice

EPRI

### Treatment of Uncertainties in Failure Threshold Development

---

- Option 1 - Linear combination of uncertainties
 
$$CSED(Bu) = f(H = f(Ox = f(Bu) + \nu\sigma_{Ox})) + \nu\sigma_H$$
  - Simple approach that accounts separately for individual uncertainty ranges for key parameters
  - No method to quantify the uncertainty bounds
  - Could result in overly conservative failure model
- Option 2 - Statistical combination of uncertainties using Monte Carlo method
  - Requires probability density functions (PDFs) and cumulative density functions (CDFs) of oxide thickness, hydrogen content, and failure model
  - Better able to quantify uncertainty bounds, i.e. 95% lower bound

---

CSCE/NEA RIA Workshop, September 9-11, 2009 -14-

ANATECH  
Lining Theory and Practice

EPRI

### Statistical Approach to Develop Failure Threshold

---

- Use statistical approach to account for impact of uncertainties on cladding failure
  - Consider uncertainties in oxide thickness accumulation, hydrogen content, and mechanical properties (burst tests)
- Evaluate the uncertainties using standard statistical methods
  - Develop Gaussian or log-normal probability distribution functions (PDFs) for key variables (oxide thickness, hydrogen pickup, and mechanical properties)
- Use Monte Carlo technique to combine uncertainties
  - Results in scatter plot of failure model versus burnup
  - Develop lower 95% cladding failure model (e.g. CSED)
- Use lower 95% cladding failure model to construct failure threshold using analytical method
  - Enthalpy at failure versus burnup

---

CSCE/NEA RIA Workshop, September 9-11, 2009 -15-



ANATECH  
Using Theory and Practice

EPRI

## Observations from Statistical Evaluation

---

- Mean failure model is lower bound of high temperature tests using non-spalled rods
  - Confirms conservative nature of approach (use of burst tests, oxide accumulation, etc.)
  - 95% lower bound CSED model is below all failed high temperatures tests
  
- Statistical evaluation confirms adequacy of linear combination of uncertainties approach (Option 1)
  - Much easier to implement limits on oxide thickness or hydrogen content to reflect other fuel performance limits in linear combination of uncertainties approach

---

CSCE/NEA RIA Workshop, September 9-11, 2009 -19-

ANATECH  
Using Theory and Practice

EPRI

## Failure Thresholds Using Statistical Approach

---

**Function of Nodal Burnup**

This graph plots Fuel Energy Change (GJ/kg) on the y-axis (0 to 200) against Rod Average Burnup (GWd/tU) on the x-axis (0 to 80). It compares the 'Aggregative Approach' (solid line), 'Linear Approach (95% LB)' (dashed line), 'Linear Approach (95% LB)' (dotted line), '95% LB Tests' (red squares), and '95% LB Tests - Failed' (red circles). The linear approaches show a decreasing trend in energy change as burnup increases, while the test data points are scattered around these trends.

**Function of Oxide Thickness**

This graph plots Fuel Energy Change (GJ/kg) on the y-axis (0 to 180) against Best Estimate Oxide Thickness (microns) on the x-axis (0 to 120). It shows three curves for different oxide thickness limits: (20+25, 95% LB, 40 microns), (20+45, 95% LB, 80 microns), and (20+55, 95% LB, 112 microns). A 'Linear Approach - 95% LB' is also indicated. The curves show that higher oxide thickness limits result in higher fuel energy change for a given oxide thickness.

---

CSCE/NEA RIA Workshop, September 9-11, 2009 -20-

ANATECH  
Using Theory and Practice

EPRI

## Conclusions

---

- RIA-Simulation Experiments Provide Important Data on Transient Fuel Behavior
  - Use to understand phenomena and processes that control cladding failure
  - Provides a database for validation of analytical methods
  - Experiments can be used to support PCMI failure threshold development
  
- Mechanistic Methods Improve Traditional Empirical Approach to Threshold Development
  - Uses experience gained from RIA simulation tests
  - Accounts for differences between tests and hypothetical accident conditions
  - Allows use of statistical analysis to account for uncertainties in experimental data and analysis methods

---

CSCE/NEA RIA Workshop, September 9-11, 2009 -21-

**LIST OF PARTICIPANTS**



**LIST OF PARTICIPANTS****BELGIUM**

HOLLASKY, Nadine  
Bel V  
Rue de Walcourt, 148  
B-1070 Brussels

Tel: +32 2528 0244  
Fax: +32 2528 0102  
Eml: nadine.hollasky@belv.be

UMIDOVA, Zeynab  
Tractebel Engineering (GDF SUEZ)  
Avenue Ariane 7  
B-1200 Brussels

Tel: +32 4737 39464  
Fax: +32 7738 9000  
Eml: zeynab.umidova@gdfsuez.com

ZHANG, Jinzhao  
Safety Officer  
Modelisation & Calculations Nuclear Department  
Tractebel Engineering (GDF SUEZ)  
Avenue Ariane 7, Bte 1  
B-1200 Brussels

Tel: +32 2773 9843  
Fax: +32 2773 8900  
Eml: jinzhao.zhang@gdfsuez.com

**CANADA**

SUNDER, Sham  
Section Head, Fuel Behaviour Section  
AECL Chalk River Laboratories  
Mail Station 88  
Chalk River Ontario KOJ 1JO

Tel: +1 613 584 3311 - ext 44102  
Fax: +1 613 584 8220  
Eml: sunders@aecl.ca

**CZECH REPUBLIC**

HORKEL, Jan  
OZM Research s.r.o.  
Bliznovice 32  
CZ-53862 Hrochuv Tynec

Tel: +420 774 742 780  
Fax: +420 469 692 882  
Eml: horkel@ozm.cz

SHEJBAL, Jaromir  
UJP PRAHA a.s.  
Nad Kamínkou 1345  
CZ-15600 Praha Zbraslav

Tel: +420 227 180 302  
Fax: +420 227 180 390  
Eml: shejbal@ujp.cz

STECH, Svatobor  
Dukovany Nuclear Power Plant  
CEZ, Reactor Physics Dpt.  
Jaderna elektrarna Dukovany  
CZ-Dukovany, 67550

Tel: +420 561 103 690  
Fax: +420 561 104 980  
Eml: svatobor.stech@cez.cz

SVOBODOVA, Marie  
UJP PRAHA a.s.  
Nad Kamínkou 1345  
CZ-15610 Praha - Zbraslav

Tel: +420 227 180 326  
Fax:  
Eml: svobodova@ujp.cz

VALACH, Mojmir  
Nuclear Research Institute Rez, plc.  
Dept. of Reactor Technology  
Nuclear Safety and Power Division  
CZ-25068 - Rez-Husinec 130

Tel: +420 266 172 101 or 2464  
Fax: +420 266 172 100  
Eml: valach@nri.cz

ZIGMUND, Jan  
Jirankova 2281  
CZ-53002 Pardubice

Tel: +420 728 509 347  
Fax:  
Eml: dr.z@rapier.cz

## FINLAND

ARFFMAN, Asko  
VTT/ Technical Research Centre of Finland  
Tietotie 3, Espoo  
P.O. Box 1000,  
FI-02044 VTT

Tel: +358 207 224 312  
Fax:  
Eml: asko.arffman@vtt.fi

KELPPE, Seppo  
VTT Technical Research Centre of Finland  
P.O.B. 1000,  
Tietotie 3 Espoo,  
FI-02044 VTT

Tel: +358 405 899 932  
Fax: +358 207 225 000  
Eml: seppo.kelpe@vtt.fi

SAIRANEN, Risto  
STUK - Radiation and Nuclear Safety  
Authority of Finland  
P.O. Box 14  
FI-00881 Helsinki

Tel: +358 405 540 865  
Fax: +358 975 988 382  
Eml: risto.sairanen@stuk.fi

## FRANCE

BARRÉ, Francois  
IRSN/DPAM/SEMCA  
Bât. 702 - BP 3  
F-13115 Saint-Paul-lez-Durance Cedex

Tel: +33 4 42 19 94 15  
Fax: +33 4 42 19 91 66  
Eml: francois.barre@irsn.fr

BENJAMIN, Serge  
Service des Combustibles  
EDF/SEPTEN  
12-14, Avenue Dutriévoz  
F-69100 Villeurbanne Cedex

Tel: +33 4 7282 7233  
Fax: +33 4 7282 7711  
Eml: serge.benjamin@edf.fr

BERNAUDAT, Christian  
EDF/SEPTEN  
12/14 Avenue Dutriévoz  
F-69628 Villeurbanne Cedex

Tel: +33 4 7282 7138  
Fax: +33 4 7282 7713  
Eml: christian.bernaudat@edf.fr

BLANPAIN, Patrick International Expert AREVA NP SAS 10 Rue Juliette Recamier F-69456 Lyon Cedex 06	Tel: +33 4 7274 8927 Fax: +33 4 7274 8145 Eml: patrick.blanpain@areva.com
BOIREL, David IRSN/DSR/ST3C/BA2C BP 17 F-92262 Fontenay-aux-Roses Cedex	Tel: +33 1 5835 7294 Fax: +33 1 5835 9599 Eml: david.boirel@irsn.fr
BUSSER, Vincent IRSN/DPAM/SEMCA BP 702 – BP 3 F-13115 Saint-Paul-lez-Durance Cedex	Tel: +33 4 4219 9123 Fax: +33 4 4219 9166 Eml: vincent.busser@irsn.fr
CARASSOU, Sebastien CEA/Saclay Bât. 625P, p.119, Point Courrier 122 F-91191 Gif-sur-Yvette Cedex	Tel: +33 1 6908 2132 Fax: +33 1 6908 9324 Eml: sebastien.carassou@cea.fr
CAZALIS, Bernard IRSN/DPAM/SEMCA Bât 702 - BP 3 F-13115 Saint-Paul-Lez-Durance Cedex	Tel: +33 4 4219 9458 Fax: +33 4 4219 9166 Eml: bernard.cazalis@irsn.fr
CHAUMONT, Bernard IRSN/DSDRE BP 17 F-92262 Fontenay-aux-Roses Cedex	Tel: +33 1 5835 9374 Fax: +33 1 5835 8559 Eml: bernard.chaumont@irsn.fr
DESQUINES, Jean IRSN/DPAM/SEMCA Bat 702 - BP 3 F-13115 Saint-Paul-lez-Durance Cedex	Tel: +33 4 4219 9490 Fax: +33 4 4219 9166 Eml: jean.desquines@irsn.fr
FOUCHER-TAISNE, Aude IRSN/DSR/ST3C/BA2C BP 17 F-92262 Fontenay-Aux-Roses	Tel: +33 1 5835 9256 Fax: +33 1 5835 9599 Eml: aude.taisne@irsn.fr
GARAT, Veronique AREVA NP 10 Rue Juliette Récamier F-69456 Lyon Cedex 06	Tel: +33 4 7274 8203 Fax: +33 4 7274 8145 Eml: veronique.garat@areva.com
GEORGENTHUM, Vincent IRSN/DPAM/SEMCA Bât 702 – BP3 F-13115 Saint-Paul-lez-Durance Cedex	Tel: +33 4 4219 9536 Fax: +33 4 4219 9166 Eml: vincent.georgenthum@irsn.fr

GONNET, Michel  
AREVA NP  
1 Place de la Coupole  
F-92400 Courbevoie

Tel: +33 1 3496 3845  
Fax: +33 1 3496 3858  
Eml: michel.gonnet@areva.com

GRAFF, Stephanie  
IRSN/DSR/ST3C  
BP 17  
F-92262 Fontenay-aux-roses

Tel: +33 1 5835 9138  
Fax: +33 1 5835 9599  
Eml: stephanie.graff@irsn.fr

GRANDJEAN, Claude  
IRSN/DPAM/SEMCA  
Bât. 700 – BP3  
F-13115 Saint-Paul-lez-Durance Cedex

Tel: +33 4 4219 9546  
Fax: +33 4 4225 6468  
Eml: claude.grandjean@irsn.fr

GUION, Julien  
EDF/SEPTEN  
12 Avenue Dutrievoz  
F-69100 Villeurbanne

Tel: +33 4 7282 7147  
Fax: +33 4 7282 7711  
Eml: julien.guion@edf.fr

HACHE, Georges  
Senior scientific Advisor  
IRSN/DS/DIR  
BP 17  
F-92262 Fontenay-aux-Roses Cedex

Tel: +33 1 5835 9269  
Fax: +33 1 5835 8870  
Eml: georges.hache@irsn.fr

MARCH, Philippe  
IRSN/DPAM/SEREM  
BP 3  
F-13115 Saint-Paul-lez-Durance Cedex

Tel: +33 4 4219 9597  
Fax: +33 4 4219 9155  
Eml: philippe.march@irsn.fr

MARCHAND, Olivier  
IRSN/DPAM/SEMCA  
Bât 702 - BP 3  
F-13115 Saint-Paul-lez-Durance Cedex

Tel: +33 4 4219 9598  
Fax: +33 4 4219 9166  
Eml: olivier.marchand@irsn.fr

MARQUIE, Christophe  
IRSN/DPAM/SEREM/LR2E – Bât 729  
CEA Cadarache – BP 3  
F-13115 Saint-Paul-lez-Durance Cedex

Tel: +33 4 4219 9603  
Fax: +33 4 4219 9169  
Eml: christophe.marquie@irsn.fr

MICAELLI, Jean Claude  
Director  
IRSN/DPAM/DIR  
Bât 250 - BP3  
F-13115 Saint-Paul-lez-Durance Cedex

Tel: +33 4 4219 9613  
Fax: +33 4 4219 9157  
Eml: jean-claude.micaelli@irsn.fr

MOAL, Alain  
Institut de Radioprotection et de Sûreté Nucléaire  
IRSN/DPAM/SEMCA  
BP 702 – BP3  
F-13115 Saint-Paul-lez-Durance

Tel: +33 4 4219 9616  
Fax: +33 4 4219 9166  
Eml: alain.moal@irsn.fr

PETIT, Marc  
 Institut de Radioprotection et de Sûreté Nucléaire  
 IRSN/DPAM/SEMCA  
 Bât 702 - BP 3  
 F-13115 Saint-Paul-lez-Durance

Tel: +33 4 4219 9646  
 Fax: +33 4 4219 9166  
 Eml: marc.petit@irsn.fr

RIBEIRO, Fabienne  
 IRSN/DPAM/SEMCA  
 Bât 702 - BP3  
 F-13115, Saint-Paul-lez-Durance Cedex

Tel: +33 4 4219 9746  
 Fax: +33 4 4219 9166  
 Eml: fabienne.ribeiro@irsn.fr

SARTORIS, Christine  
 Institut de Radioprotection et de Sûreté Nucléaire  
 IRSN/DPAM/SEMCA  
 BP 702 – BP3  
 F-13115 Saint-Paul-lez-Durance

Tel: +33 4 4219 9651  
 Fax: +33 4 4219 9166  
 Eml: christine.sartoris@irsn.fr

SERCOMBE, Jérôme  
 CEA Cadarache  
 DEN/DEC/SESC – Batiment 151  
 F-13108 Saint-Paul-lez-Durance

Tel: +33 4 42 25 30 72  
 Fax: +33 4 42 25 29 49  
 Eml: jerome.sercombe@

TILLARD, Sylvie  
 IRSN/DPAM/SEREM  
 Bât 288  
 BP 3  
 F-13115 Saint-Paul-lez-Durance Cedex

Tel: +33 4 4219 9793  
 Fax: +33 4 4219 9155  
 Eml: sylvie.tillard@irsn.fr

WAECKEL, Nicolas  
 Electricité de France  
 12-14 Avenue Dutriévoz  
 F-69628 Villeurbanne Cedex

Tel: +33 4 7282 7426  
 Fax: +33 4 7282 7711  
 Eml: nicolas.waeckel@edf.fr

## GERMANY

HEINS, Lothar  
 AREVA NP GmbH  
 P.O. Box 1109  
 D-91050 Erlangen

Tel: +49 9131 900 95570  
 Fax: +49 9131 900 94078  
 Eml: lothar.heins@areva.com

HÜTTMANN, Andreas  
 Vattenfall Europe Nuclear Energy GmbH  
 Department E-HTK  
 Nuclear Technology – Reactor Core  
 D-Überseering 12

Tel: +49 40 6396 3946  
 Fax: +49 40 6396 2515  
 Eml: andreas.huettemann@vattenfall.de

KAEFER, Steffen  
 TUEV Energie- und Systemtechnik  
 Dudenstrasse 28  
 D-68167 Mannheim

Tel: +49 621 395 384  
 Fax: +49 621 395 644  
 Eml: steffen.kaefer@tuev-sued.de

MÄRTENS , Dietmar  
TÜV Nord EnSys Hannover  
Am TÜV 1  
D-30519 Hannover

Tel: +49 511 986 1894  
Fax: +49 511 986 1848  
Eml: DMAertens@tuev-nord.de

NEUMANN, Ralf-Dieter  
AREVA NP GmbH  
Paul-Gossen-Str. 100,  
P.O. Box 1109,  
D-91001 Erlangen

Tel: +49 9131 18 97110  
Fax: +49 9131 18 94345  
Eml: Ralf.Neumann@areva.com

OLMA, Bernd Joachim  
Institut für Sicherheits-  
technologie (ISTec) GbbH,  
D-85748 Garching

Tel: +49 89 3200 4516  
Fax: +49 89 3200 4300  
Eml: olm@istec.grs.de

SONNENBURG, Heinz Guenther  
Gesellschaft für Anlagen und  
Reaktorsicherheit (GRS)mbH  
D-85748 Garching

Tel: +49 89 3200 4578  
Fax: +49 89 3200 410578  
Eml: son@grs.de

## HUNGARY

HOZER, Zoltan  
Fuel Department  
Hungarian Academy of Sciences  
KFKI Atomic Energy Research Institute  
P.O. Box 49  
H-1525 Budapest

Tel: +36 1 275 4083  
Fax: +36 1 395 9293  
Eml: hozer@aeki.kfki.hu

## ITALY

ADORNI, Martina  
University of Pisa  
c/o prof. F. D'Auria  
Via Diotisalvi 2  
I-Pisa 56123

Tel: +39 050 22103 54  
Fax: +39 050 2210384  
Eml: m.adorni@ing.unipi.it

## JAPAN

FUJII, Hajime  
Mitsubishi Nuclear Fuel Co. Ltd.  
12-1, Yuraku-cho  
Chioda-ku  
Tokyo 100-0006

Tel: +81 3 5218 1821  
Fax: +81 3 5218 1839  
Eml: Hajime\_Fujii@mnf.co.jp

FUKETA, Toyoshi  
Senior Principal Researcher  
Nuclear Safety Research Center  
Japan Atomic Energy Agency  
2-4 Shirakata-Shirane, Tokai-mura,  
Naka-gun, Ibaraki-ken 319-1195

Tel: +81 29 282 5277  
Fax: +81 29 282 5429  
Eml: fuketa.toyoshi@jaea.go.jp

KAMIMURA, Katsuichiro  
Nuclear Energy System Safety Division  
Japan Nuclear Energy Safety Organisation  
TOKYU REIT Toranomom BLDG.7F,  
3-17-1 Toranomom, Minato-ku  
Tokyo, 105-0001

Tel: +81 3 4511 1751  
Fax: +81 3 4511 1897  
Eml: kamimura-katsuichiro@jnes.go.jp

NAGASE, Fumihisa  
Fuel Safety Research Group  
Reactor Safety Research Unit  
Nuclear Safety Research Center  
Japan Atomic Energy Agency  
Tokai, Naka-gun, Ibaraki-ken

Tel: +81 292 82 6386  
Fax: +81 292 82 5429  
Eml: nagase.fumihisa@jaea.go.jp

NAKAJIMA, Tetsuo  
Nuclear Energy System Safety Division  
Japan Nuclear Energy Safety Organization  
TOYKO REIT Toranomom Bldg. 3-17-1  
Toranomom  
Minato-ku, Tokyo, 105-0001

Tel: +81 3 4511 1792  
Fax: +81 3 4511 1898  
Eml: nakajima-tetsuo@jnes.go.jp

SUGIYAMA, Tomoyuki  
Fuel Safety Research Group  
Nuclear Safety Research Center  
Japan Atomic Energy Agency  
Tokai-mura, Naka-gun, Ibaraki-ken 319-1195

Tel: +81 29 282 5955  
Fax: +81 29 282 5429  
Eml: sugiyama.tomoyuki@jaea.go.jp

SUZUKI, Motoe  
Fuel Safety Research Group  
Nuclear Safety Research Center  
Japan Atomic Energy Agency  
2-4 Shirakata Shirane  
Tokai-mura, Naka-gun, Ibaraki-ken, 319-1195

Tel: +81 29 282 5295  
Fax: +81 29 282 5323  
Eml: suzuki.motoe@jaea.go.jp

## **KOREA (REPUBLIC OF)**

KIM, Oh-Hwan  
Korea Nuclear Fuel  
1047 Daedeokdaero, Yuseong-gu  
Daejeon, 305-353

Tel: +82 42 868 1877  
Fax: +82 42 868 1149  
Eml: ohkim@knfc.co.kr

KIM, Sun-ki  
Senior Researcher  
Korea Atomic Energy Research Institute  
1045 Daedeok Street, Yuseang  
Daejeon 305-373

Tel: +82 42 868 8661  
Fax: +82 42 863 0565  
Eml: kimsk@kaeri.re.kr

NAH, Wonjoon  
Korea Institute of Nuclear Safety  
19 Guseong-dong  
Yuseong-gu  
Daejeon 305-338

Tel: +82 428680205  
Fax: +82 428680045  
Eml: wjnah@kins.re.kr

SUNG, Song-Kee  
Korea Nuclear Fuel Company  
P.O. Box 14, Yuseong  
Daejeon 305-600

Tel: +82 42 868 1850  
Fax: +82 42 868 1868  
Eml: sksung@knfc.co.kr

WOO, Sweng-Woong  
Manager of Reactor & Safety Evaluation Department  
Korea Institute of Nuclear Safety  
19 Guseong-dong  
Yuseong-gu,  
Daejeon 305-338

Tel: +82 42 868 0215  
Fax: +82 42 868 0045  
Eml: k097wsw@kins.re.kr

#### **NETHERLANDS**

BAKKER, Klaas  
Nuclear Research & consultancy Group (NRG)  
P.O. Box 25  
NL-1755 ZG Petten

Tel: +31 224 56 43 86  
Fax: +31 224 56 86 08  
Eml: k.bakker@nrg.eu

#### **NORWAY**

VITANZA, Carlo  
Halden Reactor Project  
Os Alle 5  
N-1751 Halden

Tel: +47 69 21 23 55 (ext.51)  
Fax: +47 69 21 22 01  
Eml: carlo.vitanza@hrp.no

WIESENACK, Wolfgang  
OECD Halden Reactor Project  
Institut for Energiteknikk  
Os Alle 5  
N-1751 Halden

Tel: +47 69 21 2347  
Fax: +47 69 21 2201  
Eml: wowi@hrp.no

#### **SLOVAK REPUBLIC**

HATALA, Branislav  
VUJE Inc.  
Nuclear Safety Division  
Okruzna 5, Trnava 91864

Tel: +421 33 599 1172  
Fax: +421 33 599 1708  
Eml: hatala@vuje.sk

#### **SPAIN**

CONDE LOPEZ, Jose Manuel  
Head, Office of Research  
Consejo de Seguridad Nuclear  
C/ Justo Dorado 11  
E-28040 Madrid

Tel: +34 91 3460253  
Fax: +34 91 3460588  
Eml: jmcl@csn.es

PELAYO, Fernando  
 Head, Core Engineering Branch  
 Nuclear Technology Division  
 Consejo de Seguridad Nuclear  
 C/ Justo Dorado 11  
 E-28040 Madrid

Tel: +34 91 3460281  
 Fax: +34 91 3460496  
 Eml: fpl@csn.es

QUECEDO, Manuel  
 ENUSA  
 Santiago Rusinol 12  
 E- 28040 Madrid

Tel: +34 91 34 74 264  
 Fax: +34 91 533 69 53  
 Eml: mqg@enusa.es

REY, José M.  
 Core Engineering Branch  
 Consejo de Seguridad Nuclear  
 Justo Dorado, 11  
 E-28040 Madrid

Tel: +34 91 346 0215  
 Fax: +34 91 346 0588  
 Eml: jmrg@csn.es

RIVEROLA GURRUCHAGA, Javier  
 ENUSA  
 Santiago Rusinol 12  
 E-28040 Madrid

Tel: +34 91 347 4200  
 Fax: +34 91 347 4215  
 Eml: jrg@enusa.es

VALLEJO DIAZ, Isabel  
 Unidad de Seguridad Nuclear  
 Division de Fision Nuclear-Dpto. Energia  
 CIEMAT (Edf. 12)  
 Avda. Complutense, 22  
 E-28040 Madrid

Tel: +34 91 346 6257  
 Fax: +34 91 346 6233  
 Eml: isabel.vallejo@ciemat.es

## SWEDEN

GRIGORIEV, Viatcheslav  
 Studsvik Nuclear AB  
 SE-61182 Nyköping

Tel: +46 155 221 442  
 Fax: +46 155 263 150  
 Eml: slava.grigoriev@studsvik.se

IN DE BETOU, Jan  
 Swedish Radiation Safety Authority  
 Stralsakerhetsmyndigheten  
 Solna Strandväg 96  
 SE-17116 Stockholm

Tel: +46 8 799 42 91  
 Fax: +46 8 799 40 10  
 Eml: jan.indebetou@ssm.se

JERNKVIST, Lars Olof  
 Quantum Technologies AB  
 Uppsala Science Park  
 SE-75183 Uppsala

Tel: +46 18 509 690  
 Fax: +46 18 509 890  
 Eml: loje@quantumtech.se

RUDBACK, Elisabeth  
 Swedish Radiation Safety Authority  
 Solna Strandväg 96  
 SE- 17116 Stockholm

Tel: +46 8 799 4356  
 Fax: +46 8 799 4010  
 Eml: elisabeth.rudback@ssm.se

STEPNIEWSKI, Marek  
Vattenfall Nuclear Fuel AB  
Jamtlandsgatan 99  
SE-16287 Stockholm

Tel: +46 8 739 54 89  
Fax: +46 8 87 78 79  
Eml: marek.stepniewski@vattenfall.com

## SWITZERLAND

GORZEL, Andreas  
Swiss Federal Nuclear Safety Inspectorate  
Reactor and Fuel Engineering Section  
CH-5232 Villigen ENSI

Tel: +41 56 310 3815  
Fax: +41 56 310 3854  
Eml: andreas.gorzel@ensi.ch

KHVOSTOV, Grigori  
Fuel Behavior Group  
LRS/PSI  
CH5232 Villigen PSI

Tel: +41 56 310 4428  
Fax: +41 56 310 2199  
Eml: grigori.khvostov@psi.ch

ZIMMERMANN, Martin  
Head a.i.  
Laboratory for Reactor Physics and  
Systems Behaviour  
Paul Scherrer Institut  
CH-5232 Villigen PSI

Tel: +41 56 310 2733  
Fax: +41 56 310 2327  
Eml: martin.zimmermann@psi.ch

## UNITED STATES

ARIMESCU, Viorel-Ioan  
AREVA Fuel Expert  
AREVA NP Inc.  
2101 Horn Rapids Road  
Richland, WA 99354-5102

Tel: +1 509 375 8411  
Fax:  
Eml: ioan.arimescu@areva.com

BEYER, Carl E.  
Pacific Northwest National Laboratory  
902 Battelle Boulevard  
P.O. Box 999, MSIN K8-60  
Richland, WA 99352

Tel: +1 509 372 4605  
Fax: +1 509 372 6421  
Eml: carl.beyer@pnl.gov

CLIFFORD, Paul  
U.S. NRC  
11555 Rockville Pike  
Rockville, MD 20852

Tel: +1 301 415 4043  
Fax: +1 301 415 3577  
Eml: Paul.Clifford@nrc.gov

GEELHOOD, Ken  
Pacific Northwest National Laboratory  
902 Battelle Boulevard  
P.O. Box 999 MSIN K8-34  
Richland, WA 99352

Tel: +1 509 372 4556  
Fax: +1 509 372 6421  
Eml: Kenneth.Geelhood@pnl.gov

LANDRY, Ralph  
US NRC  
NRO/DSRA  
T10F4, 11555 Rockville Pike  
Rockville MD 20852

Tel: +1 301 415 1140  
Fax: +1 301 415 5153  
Eml: Ralph.Landry@nrc.gov

MONTGOMERY, Robert O.  
Anatech Corporation  
5435 Oberlin Drive  
San Diego, California 92121

Tel: +1 858 455 6350 x 133  
Fax: +1 858 455 1094  
Eml: rob@anatech.com

RASHID, Joseph  
Chairman  
Anatech Research Corp.  
5435 Oberlin Drive  
San Diego, California 92121

Tel: +1 858 455 6350  
Fax: +1 858 455 1094  
Eml: joe@anatech.com

VOGLEWEDE, John  
Office of Nuclear Regulatory Research  
US NRC, C-3A07M  
Washington DC, 20555

Tel: +1 301 251 7555  
Fax: +1 301 251 7423  
Eml: john.voglewede@nrc.gov

#### **INTERNATIONAL ORGANISATIONS**

TRICOT, Nicolas  
International Atomic Energy Agency  
Safety Assessment Section  
Division of Nuclear Installation Safety  
Wagramer Strasse 5, Room B0649  
A-1400 Vienna

Tel: +43 1 2600 25992  
Fax:  
Eml: N.Tricot@iaea.org

REHACEK, Radomir  
OECD/NEA Nuclear Safety Division  
Le Seine St-Germain  
12 bd des Iles  
F-92130 Issy-les-Moulineaux

Tel: +33 1 4524 1058  
Fax: +33 1 4524 1129  
Eml: radomir.rehacek@oecd.org